(2)

Ocean Engineering Studies

Compiled 1990

Volume I: Acrylic Submersibles

J. D. Stachiw

PUBLISHED BY
NAVAL OCEAN SYSTEMS CENTER
SAN DIEGO, CALIFORNIA

DISCLAIMER NOTICE

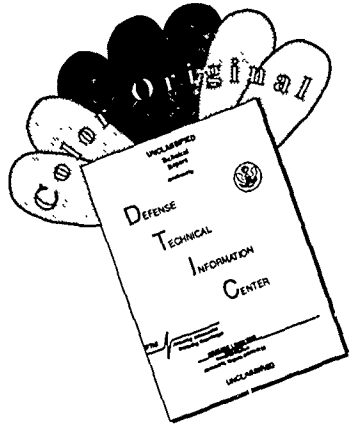

THIS DOCUMENT IS BEST QUALITY AVAILABLE. THE COPY FURNISHED TO DTIC CONTAINED A SIGNIFICANT NUMBER OF COLOR PAGES WHICH DO NOT REPRODUCE LEGIBLY ON BLACK AND WHITE MICROFICHE.

Foreword

Exploration of hydrospace requires manned and unmanned underwater vehicles capable of carrying observers and/or electro-optical devices to the very bottom of the sea. In either case, the vehicles must be provided with viewports through which the occupants can observe, and the cameras can record, the environment around them. Windows in these viewports must not only be clear but also strong enough to withstand the external hydrostatic pressure exerted by a column of water extending from the vehicle to the water's surface.

Pressure-resistant, acrylic-plastic windows were introduced into submersibles in 1947 by Professor Piccard. Since then, these windows have seen extensive service on undersea vehicles where they provided the occupants a clear, but limited view of hydrospace. However, even vehicles equipped with multiple viewports do not afford the occupants the desired panoramic view of the environment outside the vehicle. On the contrary, they accentuate the occupants' feelings of being enclosed in an opaque box with multiple peepholes that allow only tantalizing glimpses of the colorful environment.

This burdensome obstacle to unimpeded visual exploration of hydrospace could be eliminated by providing the crew of the submersible with a pressure-resistant, transparent cockpit. This cockpit would be mounted on top or in front of the opaque housing that encloses the functional subsystems of the submersible. To convert this concept into reality, many technical problems had to be solved. A transparent material with desirable structural properties had to be selected; a pressure-resistant enclosure, compatible with the structural characteristics of the material, had to be designed; and one, or several, economical fabrication techniques had to be developed.

The Navy achieved the goal of a crew compartment that was transparent with panoramic visibility, when, in 1970, the Naval Facilities Engineering Command launched the world's first two-man transparent submersible, *Nemo*, that had an operational depth of 600 feet. The pioneering transparent cockpit design gave rise to a whole class of oceanographic submersibles with transparent compartments and with a depth rating that has gradually been extended to 3000 feet by improving the structural performance of the transparent enclosure.

To preserve and disseminate the new engineering knowledge gained during the development of the transparent, pressure-resistant crew compartments for oceanographic submersibles, all the technical reports published on this subject have been collected. They are presented to the ocean engineering community in Volumes 1 and 2 of this monograph. This information should prove very helpful to any engineer contemplating the design of transparent, pressure-resistant, spherical hulls for submersibles.

J. D. Stachiw
Marine Materials Office
Ocean Engineering Division

TABLE OF CONTENTS: VOLUME I

R 676

Technical Report

DEVELOPMENT OF A SPHERICAL ACRYLIC PLASTIC PRESSURE HULL FOR HYDROSPACE APPLICATION

April 1970

Sponsored by

NAVAL FACILITIES ENGINEERING COMMAND

NAVAL CIVIL ENGINEERING LABORATORY

Port Hueneme, California

DEVELOPMENT OF A SPHERICAL ACRYLIC PLASTIC PRESSURE HULL FOR HYDROSPACE APPLICATION

Technical Report R-676

YF 38.535.005.01.006

by

J. D. Stachiw

ABSTRACT

A spherical, acrylic plastic capsule has been designed for protection of man against the external hydrostatic pressure present at continental shelf depths. Experimental and analytical studies have been conducted to evaluate the performance of both the spherical capsule design and the acrylic plastic construction material at continental shelf depths. Results from testing twenty-two 15-inch-outside diameter models and a large-scale prototype under short-term, cyclic, and long-term hydrostatic pressure indicate that the design and material chosen meet the requirements for safe operation at continental shelf depths. A prototype 66-inch-OD capsule of 2.5-inch wall thickness, and 4,000-pound positive buoyancy in seawater has been specifically developed for the NEMO (Naval Experimental Manned Observatory) system. The NEMO prototype capsule successfully withstood 105 simulated dives ranging from 250 to 2,400 feet prior to being tested to implosion at a simulated depth of 4,150 feet. The experimental data indicate that the full-scale NEMO capsule can be safely subjected to brief proof-test dives to 1,200 feet and routine operational manned dives of extended duration to 600 feet.

CONTENTS

INTRODUCTION

Statement of the Problem

Performance of useful tasks by man in hydrospace or on the ocean floor safely and efficiently requires good viewing and visibility. Ideally, underwater workers should retain stereoscopic, polychromatic vision in all directions. Furthermore, to optimize physical and mental efforts, it is desirable that the working environment be the gaseous mixture and pressure commonly referred to as "earth atmosphere." Since man immersed directly in water retains neither his terrestrial vision nor atmosphere, it is necessary to provide a protective capsule or habitat.

Pressure-resistant, transparent capsules can enclose man in a 1-atmosphere environment and at the same time not limit his vision in any manner. There are transparent structural materials such as plastics and glass for fabricating such pressure-resistant capsules. The major obstacles to their use are (1) the lack of data on the behavior of transparent materials under the biaxial and triaxial compressive stresses generally found in a pressure hull under cyclic or long-term external hydrostatic pressure, (2) the lack of proven designs for transparent capsules in which the penetrations in the form of hatches and feedthroughs have been incorporated, and (3) the lack of economical methods for fabricating transparent materials that result in reliable pressure-resistant capsules.

Because proven transparent capsule designs, methods of building them economically, and data on behavior of transparent material in such capsules under hydrostatic pressure have not been available, no transparent capsules have been built and used in hydrospace to date. If a pressure-resistant capsule incorporating hatches and feedthroughs could be designed to utilize transparent material for its pressure hull, and if such a capsule could be built from a transparent material that safely withstands the stresses generated by hydrostatic pressure, transparent capsules would replace in many cases the steel capsules with small portholes currently utilized in submersibles.

Objective of Study

The objective of this study was to explore analytically and experimentally the feasibility of constructing a 120-inch man-rated, pressure-resistant, transparent capsule for continental shelf operation with a minimum life of 2 years and 100 dives to its operational depth.

The capsule design was to be of general nature so that a scaled-down version could be incorporated into many available or foreseeable hardware systems designed for operation at continental shelf depths.

The data generated in this exploratory study were to serve two purposes: (1) they were to permit the cognizant certification authorities to assess the seaworthiness of the 66-inch-diameter* capsules built during this study for the NEMO system, and (2) they were to serve as a basis for design of other pressure-resistant, transparent capsules of the same material, but different configuration or dimensions.

Background Information

The idea that a pressure-resistant, transparent capsule is technically feasible and that its use will make exploration of hydrospace more comprehensive and effective is not new. It was suggested by Professor Piccard[1] in 1956 that such a capsule could replace steel pressure hulls. He proposed that a spherical capsule be assembled by bonding 12 spherical pentagons cast from acrylic plastic for use in bathyscapes instead of the steel capsules with viewports. In Professor Piccard's opinion, the wall of the capsule could be made thick enough to withstand safely a depth of 6,500 feet. Since he did not support the proposed concept of such a capsule with any experimental or analytical data, and very little was known about the behavior of acrylic plastic in complex biaxial and triaxial stress fields, the concept was considered on a par with science fiction. Because of the prevailing lack of interest in exploration of the oceans and the visionary nature of his proposal, the concept was not acted upon.

The next proposal for a spherical, transparent capsule was made by Perry[2] in 1961. He envisioned a transparent sphere assembled from two cast glass hemispheres joined by a mechanical lock located on the sphere's equator. According to him, such a capsule, when incorporated into a suitable submersible system, would permit the scientists to explore ocean depths in excess of 20,000 feet. The capsule would, according to him, withstand such depths

* For brevity, this and all further references to size will be understood to describe the outside diameter only.

because of the very high compressive strength of glass, which also becomes more impact resistant as it is stressed during submergence in the ocean. This concept was supported by analytical calculations and exploratory experiments with small-scale glass spheres. Although this concept extends the depth range considerably beyond Piccard's and imposes extremely high-stress loading on the capsule material (glass), it has been favorably received. Since 1963 exploratory research has been conducted by the Navy to develop Perry's concept into operational hardware.

Piccard's and Perry's concepts were specifically oriented to depths beyond the continental shelf, and only to submarines or bathyscaphs. Neither of these two concepts answered the growing need for the exploration and utilization of the continental shelf by means of divers supported by specialized mechanical systems operated by nondivers enclosed in 1-atmosphere, pressure-resistant capsules (Figure 1). To fill this gap, Navy scientists and engineers of the Naval Missile Center (NMC), Point Mugu, and the Naval Civil Engineering Laboratory (NCEL)[3] proposed research that would result in a transparent capsule for manned operations at continental shelf depth within the shortest possible time. Immediate practical application of the transparent capsule concept would consist of developing a 66-inch man-size capsule and mating it with life-support and winch-down subsystems resulting in a bottom tethered manned observatory with vertical water column mobility (Figure 2). Besides serving as the focal point for the acrylic plastic capsule project, NEMO (Naval Experimental Manned Observatory)* was to be utilized by NCEL engineers as an in-situ underwater control center to supervise and counsel Seabee diver teams performing ocean engineering construction experiments on the continental shelf floor, while NMC scientists were to use NEMO as an in-situ observatory for the scuba diver and porpoise performance studies.

Since the overriding requirement for NEMO was that it become operational within the shortest span of time, past concepts for transparent capsules were reviewed with this requirement in mind. Perry's concept for a glass capsule was rejected because at that time there were no molds in this country capable of reliably producing large glass hemispheres, and it appeared that funding in excess of available exploratory funds would be required to design and purchase such molds, develop the casting process, and test a sufficient number of such capsules to establish confidence limits for their performance. Instead, Piccard's concept employing spherical acrylic plastic pentagons was chosen.

* Earlier designated Naval Edreobenthic Manned Observatory.

The decision to select Piccard's concept had a sound engineering basis. First, considerably more is known about the engineering properties of acrylic plastic than those of massive glass. Much of this is data generated during the design of aircraft windows and canopies.[4,5] Second, acrylic plastic has already been successfully used in the construction of model-scale and full-scale pressure-resistant capsules with predictable collapse pressures.[6-10] Third, Commercial catalogs list acrylic plastic plate in sizes up to 4 x 6 feet and 4 inches thick which could be used for fabricating the spherical pentagon modules. Fourth, a wealth of experience and equipment exists for machining, thermoforming, and bonding acrylic plastic.

However, even with all this information, there was not sufficient hardware-oriented data to design with confidence a man-rated acrylic plastic capsule. There was, for example, insufficient information on the compressive strength of acrylic plastic in biaxial and triaxial stress fields generated by long-term or cyclic load application. The data from the testing of acrylic plastic windows for aircraft could serve here only as a general guide since the data applied primarily to tensile stresses, rather than compressive stresses. However, because the strength of acrylic plastic is somewhat less in tension than in compression, much of the tensile stress data could serve as the first-order conservative approximation for prediction of magnitudes in compressive stresses and strains.

The available research findings from testing acrylic plastic capsules under external hydrostatic pressure described in detail the response of different acrylic plastic capsule designs to short-term loading.[6-9] These findings do not cover long-term or cyclic loadings, which may cause the capsule to buckle through creep deformation or to fail by material fatigue, but they do indicate not only that Piccard's spherical pentagon concept is feasible,[10] but also that pressure capsules based on any sound engineering design can be built successfully from acrylic plastic.

The experience in fabrication of acrylic plastic components accumulated by the industry pertained primarily to acrylic plastic stock less than 1 inch in thickness. Most of the techniques developed for thin acrylic plastic stock, except possibly for thermoforming and bonding, were applicable also to the thick stock that would be utilized in the full-scale capsule. Thermoforming posed special problems because the transfer of heat through thick acrylic plastic sections is very slow, and thus special procedures are required for heating and cooling. Bonding of thick curved sections also posed special problems because contact-cementing large pressure hulls is not feasible and bonding of pressure hulls with a self-polymerizing cement had not been tried.

Thus, although some research data and experience in the application of acrylic plastic to the construction of pressure resistant structural components or whole structures existed, additional data and fabrication experience had to be generated before a man-size, acrylic plastic capsule could be designed and built for use at continental shelf depths.

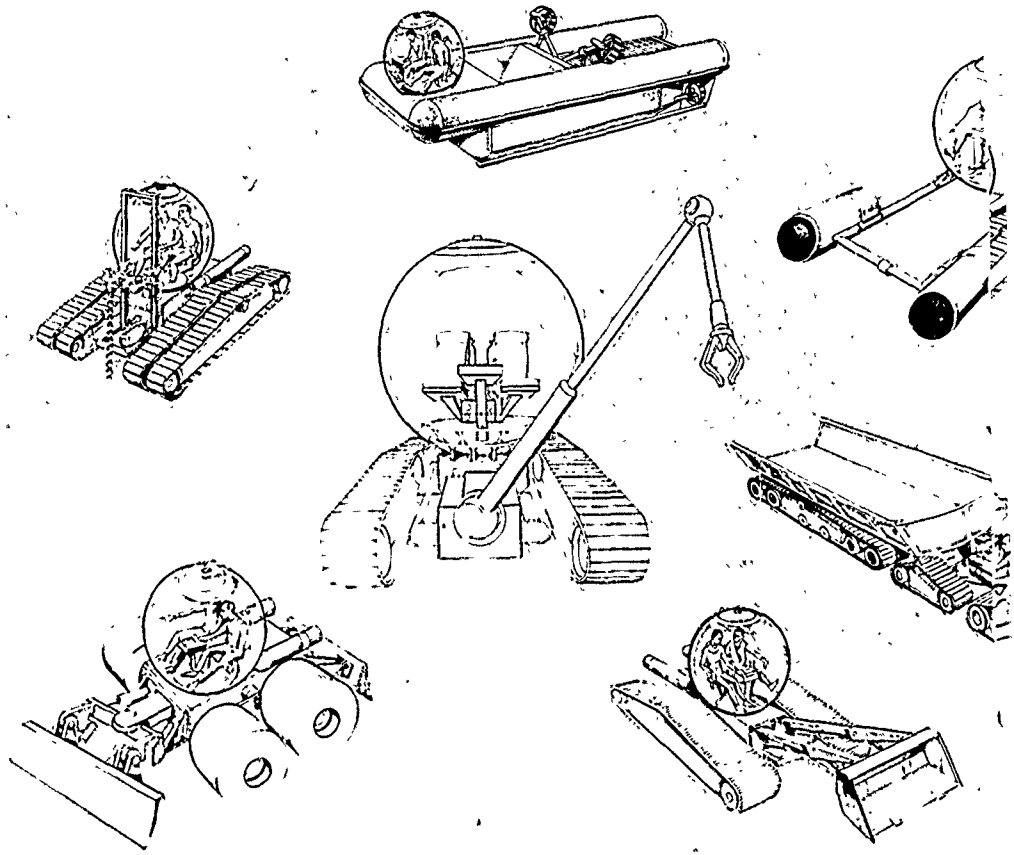

Figure 1 Typical applications for pressure-resistant acrylic plastic capsules in ocean engineering on the continental sh

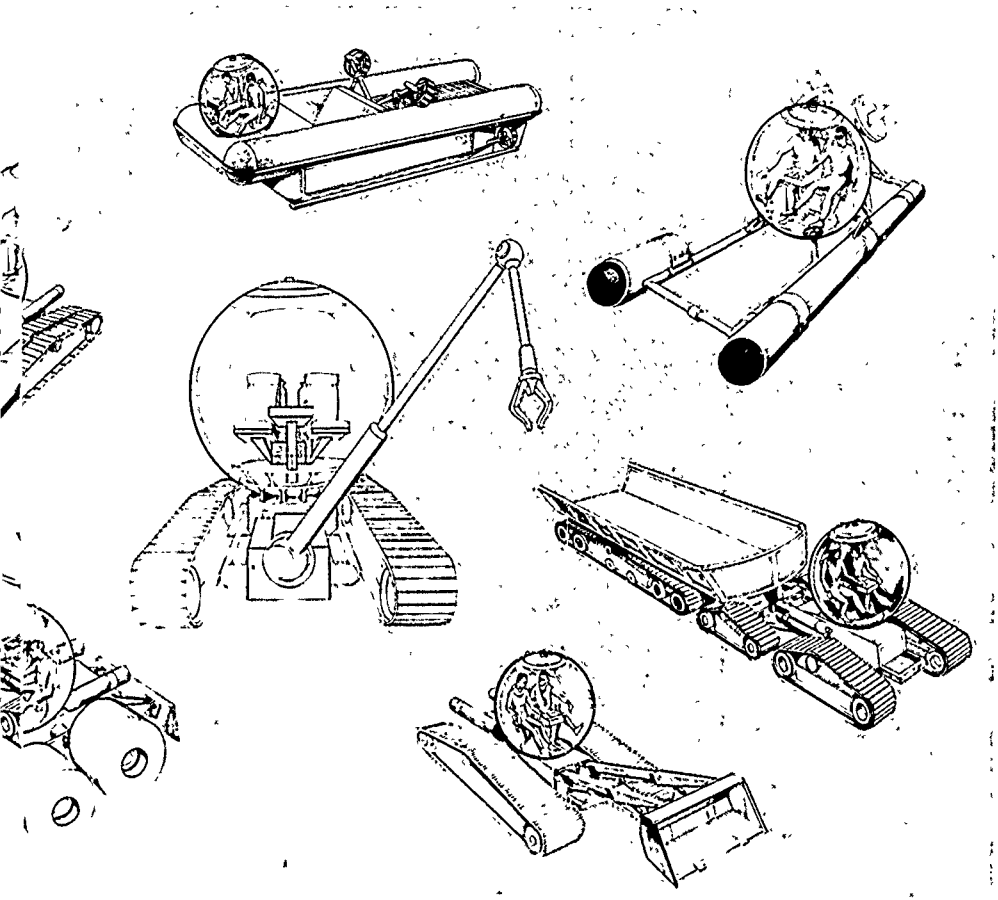

e 1 Typical applications for pressure-resistant acrylic plastic capsules in ocean engineering on the continental shelf.

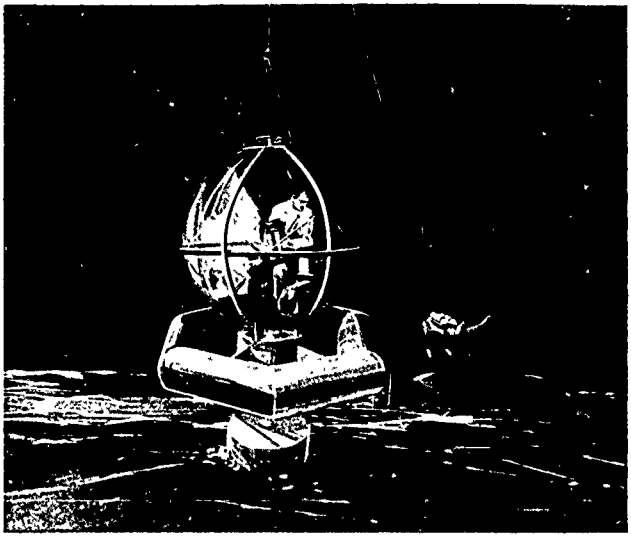

Figure 2. Engineering concept of the Naval Experimental Manned Observatory for continental shelf depths.

Scope of Investigation

The present study was limited to the investigation of a single 120-inch spherical capsule concept, grade G acrylic Plexiglas material, a single fabrication technique, and one operational depth. Only sufficient experimental investigations and analytical studies were to be performed to substantiate the adequacy of a single prototype 66-inch detailed capsule design for operation at continental shelf depth. The experimental data were limited to the recording of critical pressures, change of displacement, and strains of capsules under hydrostatic pressure. Analytical studies were limited to calculating critical pressure and strains under short-term loading, the only experimental condition for which analytical tools were in existence.

PROGRAM PLAN

The research and development program for the acrylic plastic capsule was conceived to progress through five consecutive phases that upon their successful completion would result in a proven 66-inch-prototype capsule for incorporation into the operational winch-down NEMO system.

Phase 1 – Develop an engineering design that will permit using a spherical acrylic plastic capsule as a safe, man-rated, pressure-resistant hull.

Phase 2 – Develop a reliable fabrication process for the construction of small-scale as well as large-scale, acrylic plastic capsules according to the design of Phase 1.

Phase 3 – Using scale models, evaluate experimentally (a) the design and fabrication process of the acrylic plastic capsule and (b) the performance of acrylic plastic as the main load carrying structural material.

Phase 4 – Validate the experimental data generated with small-scale models by fabricating and testing a large-scale prototype NEMO capsule.

Phase 5 – Develop a concept for the operational NEMO system that, besides the capsule subsystem, incorporates the life-support, winch, power supply, and control subsystems.

Since the successful completion of the study required facilities and personnel at NMC, Pacific Missile Range (PMR), and NCEL, a joint project was formulated between the three activities. The division of responsibility was according to area of specialization as follows:

Phase 1	Design	NMC and NCEL
Phase 2	Fabrication	PMR
Phase 3	Model Tests	NCEL
Phase 4	Prototype Tests	NCEL
Phase 5	System Concept	NMC

Since the study was exploratory with very modest funding, the coordination of the effort between the three activities was to be performed at the working level. All technical decisions were to be made on the basis of a consensus of engineering judgment expressed by the project personnel.

and casting process development was made. Other fabrication processes besides casting could be used to fabricate hemispheres which subsequently could be joined by bonding or by a mechanical lock. Casting is here again the only process available for producing hemispheres with the required thickness and out-of-roundness tolerances. Although the investment in hemispherical molds, casting equipment, and casting process development is less than for casting of monolithic spheres, it is still quite substantial.

It is only when the capsule can be assembled from many small structural modules that other fabrication processes can be effectively utilized to fabricate economically a monocoque sphere. Thus, instead of an expensive casting process, the much cheaper vacuum-assist mold forming can be applied to produce spherical sectors with uniform thickness and sphericity. The only limitation on this forming method is that the thickness to outside radius ratio (t/R_o) be less than 0.125 for spherical sectors up to a 75-degree spherical angle (as otherwise the temperatures required in forming become excessively high). (For larger sectors excessive variation in thickness also occurs due to unequal stretching of the acrylic plastic.) If the acrylic plastic sphere is broken down into 12 structural modules of pentagonal shape, the vacuum-assist, female mold forming technique becomes about the most economical fabrication process for spheres up to 6 feet in diameter and 4 inches in wall thickness (based on the 48 x 60-inch standard maximum size of acrylic plastic plates). Once the spherical sectors have been thermoformed, very little additional cost is required to machine them into pentagonal form. Spheres larger than 6 feet in diameter can be assembled from spherical pentagonal structural modules prepared by the vacuum-assist female mold form technique, but larger spheres would require use of premium-priced, oversize acrylic plastic plates. If procurement of oversize acrylic plastic plates is not feasible and 48 x 60-inch standard sheets are used, the structural modules would not be spherical pentagons of uniform size. The structural modules would either be spherical triangles of uniform size or they would vary both in configuration and in size. Thus, it can be seen that the spherical, pentagonal structural modules proposed by Piccard are, from the viewpoint of initial cost for fabrication equipment, fabrication process development, and fabrication process itself, the most economical approach to assembling a 66-inch monocoque sphere if thermoforming of flat acrylic plastic plates is substituted for casting of pentagons.

Since the objective of the NEMO concept was to provide a reliable operational capsule for continental shelf depth, and not to set depth records, no effort was made to design the capsule for the 6,000-foot depth originally postulated by Piccard for his acrylic plastic capsule concept. Aside from the four major design constraints, all design parameters were to be determined during the course of the study. Thus, the resulting design would closely match the operational requirements of the NEMO system.

Detail Design

Once the design parameters pertaining to material selection, shape configuration, operational depth, and assembly technique were selected, the detail design of the capsule could begin. The detail design was concerned with eight focal points:

(1) Means of ingress and egress for the capsule occupants

(2) Penetrations for electric and hydraulic conduits

(3) Attachment of the capsule to other structural systems

(4) Attachment of life-support equipment, chairs, and control console to the capsule interior

(5) Magnitude of permissible working stresses in the acrylic plastic and steel structural components

(6) Specification of construction materials

(7) Selection of hull thickness

(8) Structure and component dimensioning

Ingress and Egress. The access to the interior of the capsule could be achieved in several ways. The capsule could be separated into two hemispheres joined together by a mechanical lock that would permit opening of the top hemisphere for personnel access. Another approach to the same problem would consist of placing a hatch in the polar region of the sphere (Figure 3). The latter approach was chosen as it permitted egress from the capsule even when it was floating free on the ocean surface after emergency ascent without additional buoyancy systems. Although from a structural viewpoint an acrylic plastic hatch with a spherical bevel angle proposed by Piccard was the most desirable one (when closed it did not introduce any appreciable stress concentrations into the acrylic plastic hull), a metal hatch system with a spherical bevel angle was chosen for operational reasons (Figure 4).

The rationale behind this choice was that (1) an acrylic plastic hatch plug would soon lose its sealing ability because of surface scratches on the seal surface generated by equipment and personnel passing through the hatch opening, and (2) the metal would also act as efficient heat transfer surface to depress the temperature in the capsule's interior. Without such a cooling mechanism, pilots operating the capsule would soon become incapacitated by the heat generated in the capsule's interior. A metal hatch plug and matching ring insert would resist scratching more effectively and thus would prolong the operational life of the ingress–egress mechanism.

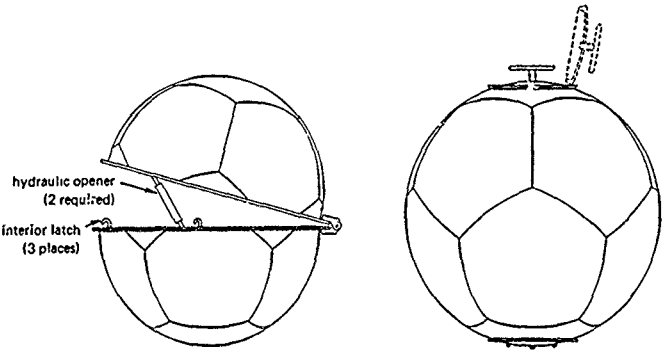

(a) Equatorial hatch.

(b) Polar hatch.

Figure 3. Basic approaches for providing access to the interior of a spherical acrylic plastic capsule.

Since a metal hatch system constitutes a serious mismatch of rigidity with the acrylic plastic hull, a concentrated effort was made to reduce the thickness of the metal hatch to a minimum, so that the mismatch and resulting stress raiser effect could be minimized. The engineering decision was to reduce the thickness of the metal hatch to the minimum value corresponding in strength to implosion pressure of the acrylic plastic hull.

One of the problems facing the designer in providing a metal hatch for the capsule was to find a means for firmly attaching the beveled metal hatch insert ring to the acrylic plastic hull so that the whole hatch assembly would not fall out when the capsule was tossed around on the ocean surface. An ingenious solution was found: secure the hatch insert ring to the acrylic plastic hull by means of a metal retainer flange located on the interior of the hull to which the hatch insert ring would be bolted. Direct contact between the metal retainer flange and the acrylic plastic hull was considered undesirable as it would lead to scoring of the acrylic plastic, and local stress concentrations when the curvature of the capsule decreased during hydrostatic loading. To forestall these conditions, a compliant rubber gasket would be interposed between the metal retaining flange and the acrylic plastic hull. In addition, the retaining flange would be provided with a convex spherical surface matching the concave interior curvature of the capsule. The flange cross-section was to decrease towards its outer edge to make the flange more compliant at the outer edge than at the inner edge at the bolt circle.

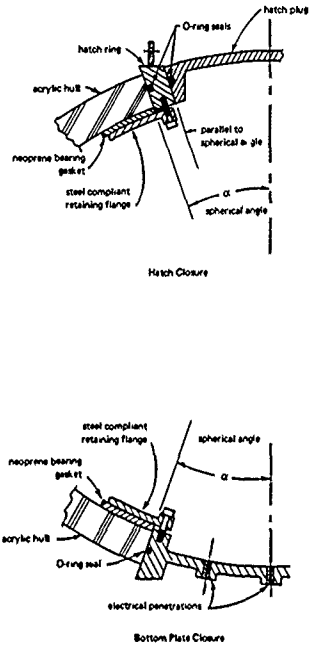

Figure 4. Hatch concept chosen for incorporation in the acrylic plastic capsule for the NEMO system.

Several sealing systems were considered for sealing the beveled hatch ring to the beveled bearing surfaces of the acrylic plastic capsule. Besides standard O-ring seals, rubber gaskets and epoxy adhesive were also considered. The O-ring seal was known to be reliable, but the groove in the metal would cause a contact stress raiser on the acrylic plastic bearing surface. A rubber gasket interposed between the metal and the acrylic plastic bearing surfaces would eliminate any stress concentrations, but would permit larger relative motion between the insert ring and the hull. Unless considerable force was constantly pressing the insert ring against the acrylic plastic, leakage would take place at the beginning of the dive until the capsule reached a substantial depth where hydrostatic pressure force would seal the hatch assembly against the acrylic plastic bearing surface.

Some thought was also given to using epoxy adhesive to bond the hatch insert ring in place permanently, thus eliminating both relative movement between the parts and the leakage. This approach, however, was discarded as it was known that the magnitudes of forces acting across the metal–acrylic plastic interface would be so large that the adhesive would shear, permitting the water to leak in. Although the advantages and disadvantages of the O-ring and the gasket sealing systems are about equal, the O-ring system was chosen for the acrylic plastic capsule because it utilized primarily off-the-shelf seals. If the stress raiser problem proved troublesome later, the rubber gasket system could be substituted.

Although the hatch system requires some arrangement for opening and locking the hatch by the occupants of the capsule, no thought was given to this problem during initial planning, because it was thought that any locking arrangement used in submersibles or by the chemical industry in autoclaves would be satisfactory for the NEMO capsule and would have very little if any bearing on the stress distribution in the hatch assembly or in the acrylic plastic hull.

Penetrations. Penetrations for electrical and hydraulic conduits represented a serious problem as they are sources of serious stress concentrations. Rather than have them distributed throughout the pressure hull, as is customary in steel pressure-resistant capsules, they were all placed in a single metal plate insert (Figure 4). This eliminated several design problems. First, a great number of penetrations in an acrylic plastic hull with the accompanying stress concentrations were replaced by a single penetration with a stress concentration approximately equal to that of the hatch. Second, placing all the penetrations associated with electrical and hydraulic feedthroughs in a metal plate eliminated all problems associated with drilling and tapping acrylic plastic. And third, placement of the individual penetrations in the metal plate made the incorporation of reinforcements around the many penetrations a relatively easy problem to solve. This was accomplished by placing the penetrations in a thicker section of the plate, where the effect of stress concentrations would not necessarily initiate failure of the whole plate. The location of the plate itself was optional, depending on other factors like (1) method of attaching the capsule to the submersible's exostructure and (2) method of attaching the life support, seats, and control console to the capsule.

The same method of sealing and attaching the penetrator plate to the acrylic plastic hull was to be utilized as for the hatch insert ring. Furthermore, by choosing the same diameter for the penetrator plate as for the hatch insert ring, no additional detail design would be needed for the seal and retaining flange.

External Attachment of Capsule. The attachment of the capsule to other structural systems posed a difficult problem to which several solutions were considered. The difficulty of attaching the capsule to another structural system lay in several design and operational constraints that had to be satisfied by the proposed attachment method. The design constraints that had to be satisfied were (1) no direct attachment to the acrylic plastic hull by means of steel bolts or screws, (2) no restraint was to be imposed on the decrease of capsule diameter during pressure loading, (3) the attachment was to be stiff enough to prevent excessive movement of the whole capsule with respect to the framework during raising or lowering of the NEMO structure in the ocean, (4) retention of as much panoramic visibility as possible for the capsule even

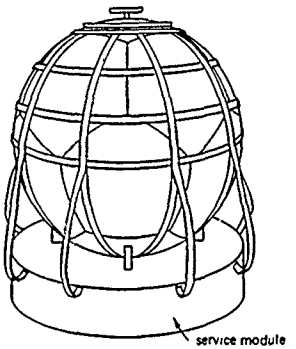

(a) Resting on deck.

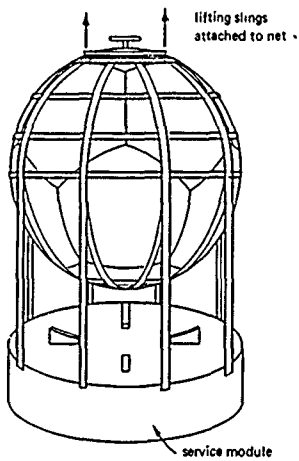

(b) Being lifted off the deck.

Figure 5. Net restraint concept for attaching the acrylic plastic capsule to the NEMO service module.

in the presence of structural members serving as the attachment, (5) the attachment was to work equally well regardless of whether the capsule was on deck, being lifted, floating on the ocean surface, or being winched down to operational depth, and (6) the attachment subsystem was not to generate excessive tensile stresses in the acrylic plastic capsule that could lead to a failure of a bonded adhesive joint whose minimum strength is approximately 40% less than of the parent material in tension.

Several design approaches were tried to arrive at a satisfactory attachment between the acrylic plastic sphere and the remainder of the NEMO structure. The most obvious solution to the problem, the placement of the capsule in a net (Figure 5), similar to the nets used for hanging gondolas under spherical balloons, had been immediately discarded as it did not satisfy three of the design constraints. Such a net would considerably restrict the panoramic visibility, it would permit excessive relative motion between the sphere and the remainder of the NEMO structure thus imposing severe stresses on hydraulic and mechanical control linkages between the control console inside the capsule and the operational components, and it would not provide any support for the capsule when it was being transported on land, or resting on deck of the ship.

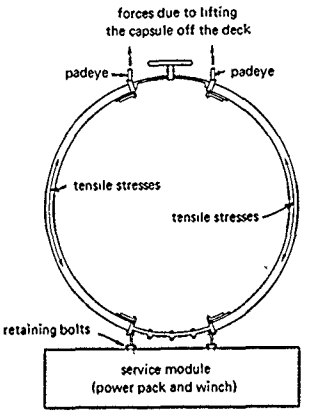

Figure 6. Bolt-on restraint concept for attaching the acrylic plastic capsule to the NEMO service module.

Another approach that was investigated and subsequently discarded was to attach the capsule to the service module by bolting on the metal penetrator plate where all of the feedthroughs were located (Figure 6). For this purpose, the penetrator plate would have to be located at the bottom of the capsule so that it could resist best the upward force generated by the buoyancy of the capsule when attached to the negatively buoyant service module. Such an attachment would possess some good points: (1) rigidity, (2) equal resistance to upward and downward forces, (3) ease of design and fabrication, and (4) unobstructed visibility. It has, however, two serious disadvantages: (1) it would generate considerable tensile stresses in the acrylic plastic joints when the NEMO system is lifted out of water by means of a line attached to the top hatch insert ring, and (2) it would generate flexure stresses in the acrylic plastic capsule when underwater currents impinge upon the capsule rigidly attached to the service module, thus creating a moment loading on the capsule. Of these two disadvantages, the first is the more serious.

Analysis of the shortcomings of the rigid attachment to the metal penetrator plate provided an approach to the problem that eliminated all the bad features of the previous design approach and retained all the good ones. In this design approach, the capsule was attached by bolting the metal penetrator plate to the service module, but the tensile stresses across the bonded acrylic plastic joints generated by hoisting operations were eliminated by the incorporation of pretensioned tie rods connecting the hatch insert ring to the penetrator plate located at the opposite pole of the capsule (Figure 7). With such an arrangement, the upward force applied to the hatch insert ring is transmitted to the service module through the tie rods rather than through the acrylic plastic hull. The incorporation of pretensioned tie rods introduces an additional compressive loading on the acrylic plastic hull when it is on deck, floating on the surface, or shallowly submerged. Because the tie rods are under tension, the acrylic plastic hull is placed under diametrical compression. If the

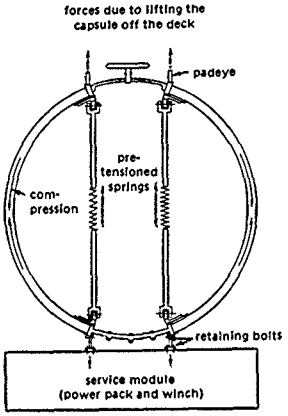

Figure 7. Tie-rod restraint concept for attaching the acrylic plastic capsule to the NEMO service module.

magnitude of pretension selected for the tie rods is larger than the forces applied to the hatch system during lifting, the joints in the acrylic plastic hull will never be subjected to tensile stresses due to lifting and will generally be under compression. In this manner, the danger of joint failure will be completely eliminated, as under compression the joints are self-wedging without any shear stresses at the joint surfaces. In the design of the pretensioned tie rods, the shrinkage of the capsule under hydrostatic loading at design depth had to be taken into account. If designed properly, the tie rods would be under the needed tension while the NEMO system is out of the water, while at design depth the tension would approach zero. In this manner the diametral compression of the capsule by tie rods will not be superimposed on the hydrostatic compression at design depth thus eliminating the danger of triggering the elastic collapse of the capsule by the localized tie-rod pretensioning forces. To achieve such a self-adjusting pretensioning system, a spiral spring with extension equal to diametral shrinkage of the capsule would have to be incorporated into each tie rod. The total force exerted by the springs in the tie rods while on deck would be equal to the buoyancy of the NEMO capsule while at the design depth it would decrease to almost zero.

The tie-rod system appeared to be an adequate solution to the attachment problem so long as the presence of several tie rods in the interior of the capsule was not considered objectionable. Since for some capsule sizes or possible non-NEMO system applications the presence of tie rods may be objectionable, additional approaches were considered that did not require the presence of tie rods. One of such proposed approaches utilized an external cage. To eliminate the tensile stresses associated with lifting of the NEMO system out of water or when it just floats on the ocean surface with the negatively buoyant power module pulling downward, an external rigid cage was added to the NEMO system (Figure 8). The point of contact between the NEMO capsule and the rigid cage was to be only at the polar metal plates

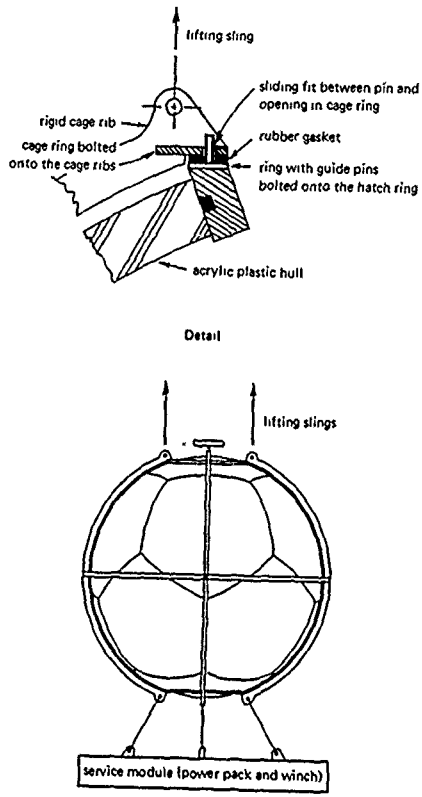

Figure 8. Rigid cage restraint concept for attaching the acrylic plastic capsule to the NEMO service module.

in the capsule. Since a rigid attachment to the cage at both top and bottom steel inserts was undesirable, as it would restrain the sphere radially during pressure application, a special joint was devised that permitted the sphere to change its radial dimension but at the same time resisted lateral forces applied to the sphere by waves on the ocean surface, or currents when submerged. The joint devised for this application consisted basically of pins attached to the polar metal plates that fitted into oversize holes in the cage framework. Thus, the sphere was permitted to change its diametrical dimension while at the same time the pin and hole joint restrained the whole capsule from lateral or vertical displacement that would cause it to strike the ribs of the cage. The sliding pin joint imposes only lateral and vertical but not diametral restraint. Because of this, no external tensile loading can act on the capsule, regardless whether the NEMO system is being lifted out of water or just floating on the ocean surface. The drawback of this capsule attachment to the NEMO service module was that the cage did reduce to some extent the panoramic visibility of which an acrylic plastic capsule is capable. Because of it, this attachment arrangement would not be as satisfactory from the optical viewpoint as the tie-rod attachment. There was, however, a compensating feature to the cage. If the cage members were spaced appropriately the cage could act as a protector against impacting the ship during launching operations. This protective feature of the cage was felt to compensate adequately for the loss of visibility caused by the cage.

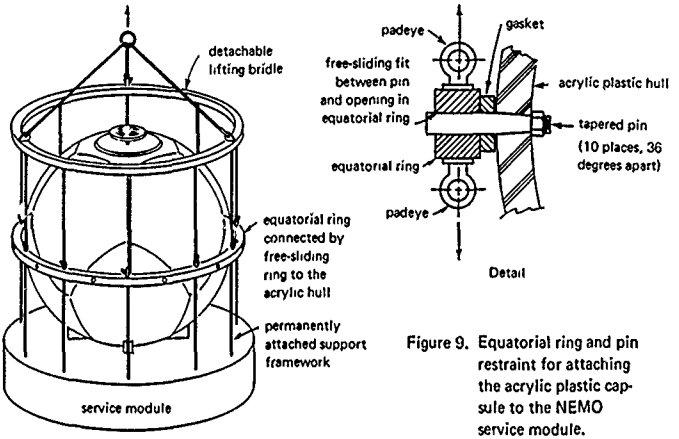

Figure 9. Equatorial ring and pin restraint for attaching the acrylic plastic capsule to the NEMO service module.

Another approach that was considered was an equatorial ring held in place by radial sphere penetrators (Figure 9). The sphere penetrators were to be tapered and made from plastic with elastic properties matching those of the acrylic plastic hull so that no stress raiser effect would be introduced by them. The fit between the pins and the matching holes in the equatorial ring was to permit sliding of the pins when they move radially inward with the shrinking capsule under hydrostatic loading. The capsule held by the equatorial ring basically would not be subjected to tensile loading as the major forces generated by lifting of the NEMO system out of water would be shunted around the acrylic plastic capsule via the lifting attachments to the equatorial ring. The only tensile loading acting on the acrylic plastic capsule would be caused here by the dead weight of the capsule suspended from the plastic penetrator pins when being lifted out of water. When floating on the ocean surface, there would be some tensile stresses in the hull, but they would be well distributed around the hull circumference by the radial sphere penetrators in the equatorial ring. In view of the rather low weight of the capsule and the large wall cross section, the tensile stresses generated by it would be low. Although the equatorial ring method of attaching the capsule to the NEMO service module is not particularly advantageous, it may become so if the NEMO capsules become part of some other system in which it is important to have the capsule attached to the submersible at its equator rather than at the poles as it is in the NEMO system.

Attachment of Equipment to the Interior of the Capsule. The interior of the capsule must contain certain subsystems that are needed to support the life of the crew and to allow them to control effectively the operation of externally located subsystems. These subsystems give the capsule vertical or horizontal mobility, and possibly the ability to perform work by the use of external manipulators. As a minimum, such subsystems located in the interior of the capsule would consist of life-support equipment, seats, control console, emergency power supply, communication gear, and cameras. All of this equipment must be securely attached to some rigid support that would prevent it from being tossed around during launch and retrieval operations on the ocean surface.

When pressure-resistant capsules are of steel, securing such equipment poses no design problem as the necessary brackets or framework can be directly attached to the steel capsule by means of bolts or welding. A different case presents itself for the acrylic plastic capsule. Since welding or bolting to the interior capsule wall is not permissible, other ways had to be considered for the securing of equipment. After considerable thought was given to this problem, four different approaches were arrived at for securing of equipment on the interior of the capsule:

1. The equipment was to be bolted to a floor that in turn was bonded to the wall of the capsule by means of a foamed-in-place plastic that completely filled the spherical sector space enclosed between the flat circular floor and the wall of the capsule below (Figure 10). The foamed-in-place plastic, for example styrofoam, would distribute evenly in the capsule the weight of the equipment and crew resting upon it. Because of the low modulus of elasticity of such material, it would permit the diameter of the acrylic plastic capsule to shrink considerably under hydrostatic loading without imposing a noticeable restraint. The disadvantage of this arrangement lay in the permanency of the foamed-in-place filler. Once the cavity below the floor was filled with foamed plastic, it would become very difficult to perform any maintenance or modification to the wiring and plumbing located below the floor.

2. The equipment and the floor were to be bolted to an internal cage that snugly fitted the interior dimensions of the acrylic plastic capsule (Figure 11). Elastomeric spacers were to be inserted between the ribs of the cage and the inner surface of the acrylic plastic capsule to permit the shrinkage of the capsule's internal diameter without transfer of load to the cage. The major shortcomings of this attachment method were the restriction of panoramic vision, difficulty of assembling such a cage in the cramped interior of the capsule from structural members small enough to pass through the hatch, and reduction of usable interior space.

3. The equipment and the floor were to be attached to the pretensioned tie rods (Figure 12). For such an arrangement, the tie-rod springs would be located near the top hatch so that the portion of the tie rods to which the floor and equipment were attached would not experience any displacement relative to the bottom metal plate to which hydraulic tubing and electrical leads were attached. The disadvantage of this arrangement lies primarily in the difficulty of packaging equipment with respect to the tie rods. Furthermore, problems would be encountered in the removal of equipment for maintenance and modification as in many cases the tie rods would have to pass through the equipment in order to exert proper vertical and lateral restraint.

4. The equipment was to be bolted to the floor, which in turn would be bolted to the bottom metal plate insert (Figure 13). Since the diameter of the floor is larger than that of the bottom metal plate, it cannot rest directly on the bottom plate but must be held some distance above the plate. To avoid having the floor rest on the compliant acrylic plastic hull while it is restrained by bolts to the rigid bottom metal plate, a spacer has been provided that keeps the floor a fixed distance above the bottom steel plates. A small clearance is provided between the edge of the floor and the inner wall of the capsule to allow for the shrinkage of the sphere without imposition of restraint on the sphere and compressive loading on the floor. Since all the equipment, occupants, and the floor rest on top of the bottom metal plate, approximately a 1,000-pound force acts upon it. Whether this downward-acting force generates tensile stresses across the bonded joints between individual pentagons depends on the method used for attaching the capsule to the NEMO exostructure and whether the capsule rests on deck, is being lifted, floats on ocean surface, or is submerged at its operational depth. When pretensioned tie rods are used on the interior of the capsule, and the bottom metal plate is rigidly attached to the ballast pod, no tensile stresses can be generated by the weight of the equipment in the interior of the capsule regardless of the stage of launch or retrieval operations. When the capsule is held in place by the external cage with sliding pin joints, tensile stresses are generated in the bonded joints when the capsule floats on the ocean surface. At that time, the bottom metal plate is not being supported by the external cage since the capsule has lifted off its bottom support in the cage and is pushing against its top seat in the cage. Furthermore, the hydrostatic pressure acting on the bottom pentagon from outside is not high enough to equal the downward force exerted from inside on the plate by the weight of equipment located in the capsule. Thus, the resultant force that is equal to the difference between (1) *the sum of the weights of bottom metal plate, polar pentagon, and internal equipment* and (2) *the upward-acting hydrostatic pressure on the bottom pentagon* generates tensile stresses

in the joints between the bottom polar pentagon and the adjacent pentagons. When the NEMO system is submerged more than 20 feet underwater, the upward acting hydrostatic pressure overcomes the downward acting weights of bottom plate and internal equipment relieving all the tensile stresses in the joints between individual spherical pentagons.

Working Stresses. The selection of a working stress level is always a very crucial engineering decision for internal or external pressure hulls whose catastrophic failure would kill the operating personnel. When the material selected has not been used previously for construction of pressure hulls, selection of a working stress level becomes highly subjective. The designer must draw heavily on experimental data peripheral to the problem at hand and on his engineering judgment.

Since acrylic plastic pressure hulls had not been designed or built previously for manned operation, no precedent existed on which to draw. There existed, however, two sources of experimental data that impinged on the design of acrylic plastic capsules. One was the body of experiments conducted over a period of years for determination of allowable stresses in acrylic plastic windows and canopies for aircraft.[4,5] The other source of data was the evaluation of acrylic plastic windows for undersea applications performed by NCEL and other laboratories.[12-15]

Although a wealth of experimental data has been generated by engineers during design and evaluation of aircraft windows and canopies, little of it is directly applicable to the design of an acrylic plastic pressure capsule. The windows and canopies in aircraft are (1) in tension and (2) cannot fail by elastic or plastic instability, while the acrylic plastic capsule is (1) in compression and (2) it generally fails by elastic or plastic instability. However, the aerospace research program provided the following information* relevant to the selection of working stress levels for the acrylic plastic capsule:

1. Under short-term tensile cyclic loading at a 6,000-psi stress and a 77^{o} temperature level, the life of acrylic plastic is about 10^{4} cycles.

2. Under long-term tension at a 6,000-psi stress and a 77^{o} temperature level, the acrylic plastic will rupture only after about 48 hours of sustained loading. At a 4,000-psi stress level, the material will not fail in less than 1,000 hours.

* Based on MIL-P-5425A and MIL-P-21105C materials.

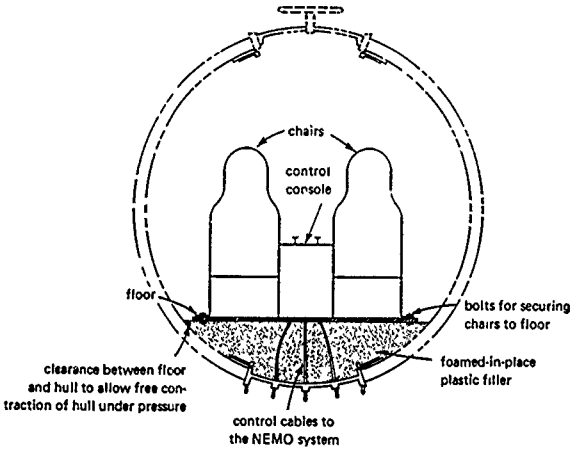

Figure 10. Foamed in-place restraint for securing of equipment inside the acrylic plastic capsule.

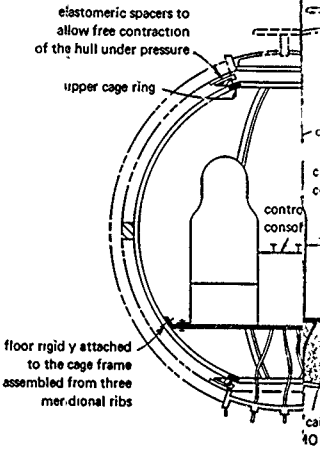

Figure 11. Internal cage restrai
inside the acrylic pl

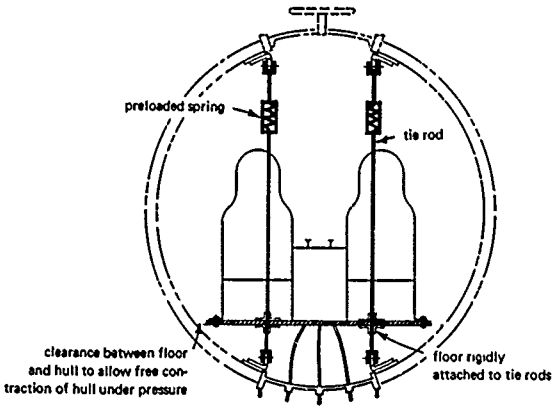

Figure 12. Tie-rod restraint for securing equipment inside the acrylic plastic capsule.

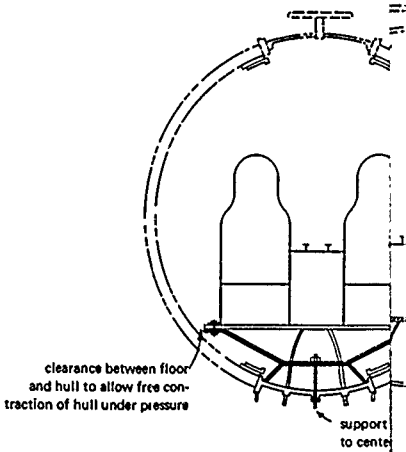

Figure 13. Polar plate restraint for secu
inside the acrylic caps

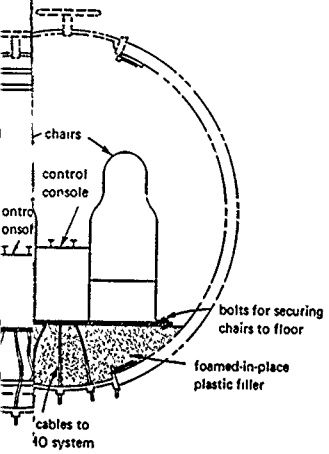

place restraint for securing of
inside the acrylic plastic capsule.

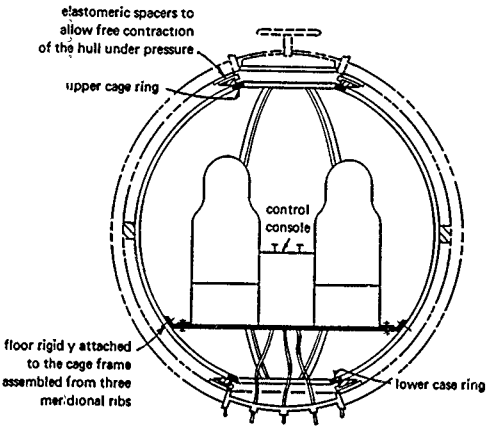

Figure 11. Internal cage restraint for securing equipment inside the acrylic plastic capsule.

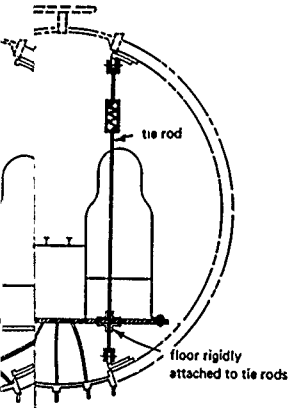

nt for securing equipment
lic plastic capsule.

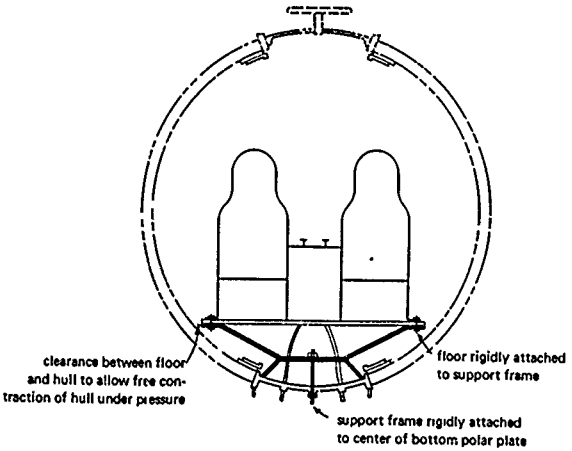

Figure 13. Polar plate restraint for securing equipment inside the acrylic plastic capsule.

3. The secant modulus of elasticity of acrylic plastic after 48 hours of sustained tensile loading in the 75 to 77°F range and at a 6,000-psi stress level is 90,000 psi; at a 4,000-psi stress level it is 200,000 psi; at a 3,000-psi stress level it is 300,000 psi; and at a 2,000-psi level it is 400,000 psi.

4. The strength and modulus of elasticity increase as the temperature of acrylic plastic is decreased from room temperature (75 to 77°F range). The increase is about 10% for the 30 to 35°F range.

5. There is no change in the impact strength of unnotched acrylic plastic bars with the decrease in temperature from the 75 to 77°F range to 30 to 35°F range.

6. The secant modulus of elasticity of acrylic plastic under sustained compressive loading in the 75 to 77°F range is 10 to 20% higher than for sustained tensile loading.

7. The compressive short-term strength of acrylic plastic is approximately 15,000 psi, while the tensile strength is 9,000 psi.

The data generated in the NCEL hydrospace window research program was less voluminous than in the aerospace research program but it had the advantage of being more directly applicable. In this research conical, flat disc, and spherical acrylic plastic windows were subjected primarily to compressive stresses, which either caused the windows to fail because of excessive stress magnitude or plastic instability. The results from the hydrospace window research program applicable to the capsule design were:

1. Time-dependent ultimate failure of acrylic plastic structural components by viscoelastic or viscoplastic instability caused by sustained compressive loading occurs in less than 24 hours only when the loading level is generally $\geq$70% of the short-term compressive strength. When the loading is $\leq$25%, the ultimate failure will definitely not occur in 10,000 hours.

2. Cyclic compressive loading may cause ultimate fatigue failure of acrylic plastic structural components in less than 100 cycles only when the loading is >50% of short-term compressive strength. When the loading is $\leq$25%, the ultimate failure will definitely not occur in 1,000 cycles.

From the rather general and only indirectly applicable information available at the time of design of the NEMO acrylic hull, two general conclusions could be made:

1. If the maximum operational depth of the hull was chosen to be at 20 to 35% of its implosion depth under short-term loading conditions the hull would probably be safe for long-term cyclic and sustained pressure service at the maximum operational depth so long as the fatigue life was not to exceed 1,000 dives of 8-hour, or 100 dives of 100-hour duration.

2. Since the low temperatures that commonly exist in the ocean at continental shelf depth make the test results obtained in the laboratory at room temperature (75 to 77°F) conservative for the design of hulls that will operate in the cooler ocean waters, there is no reason to conduct capsule evaluation tests under simulated ocean temperature, as lower temperatures are operationally much more difficult to maintain over long periods of time in pressure test facilities than room temperature.

Since the objective of the acrylic plastic pressure capsule program was to provide an operational system for continental shelf depth, the maximum operational depth had to be in the 600-to-1,000-foot range. The working stress in the hull had to be selected accordingly either for the 600- or the 1,000-foot operational depth. Because the exact relationship between the working stress level and the cyclic life of the acrylic plastic hull was not known, it was decided to select the greater depth of 1,000 feet as the maximum operational depth. A 1:3 relationship between the maximum working depth and the implosion depth under short-term loading was selected; implosion depth could be approximated with existing equations. In this manner, if the working stress corresponding to a 1,000-foot depth did not cause premature fatigue failure, the hull would be rated for a 1,000-foot operational service. If, on the other hand, the working stresses at a 1,000-foot operational depth caused premature cyclic failure (that is, in fewer than 1,000 dives to 1,000-foot depth) of the hull, then the working stress could be lowered by changing the operational depth of the hull from 1,000 feet to 600 feet. Since the 600-foot operational depth was also acceptable, such an arrangement was considered to be satisfactory and the working stress level was chosen to be 1/3 of the stress level associated with the calculated implosion pressure of the capsule under short-term loading. The working stress level was chosen on the basis of the relationship with the short-term hydrostatic loading of the capsule to implosion rather than on the basis of relationship with ultimate failure of an acrylic plastic test specimen under uniaxial compression because the fact that plastic instability must be considered in the evaluation of capsule failure. The compressive test of an acrylic plastic specimen does not take this into account.

In addition to selecting the working stress for the acrylic plastic, the appropriate working stress had to be selected for the metal hatch and bottom insert plate. The problem here was considerably simpler. Metals such as steel, titanium, or aluminum do not exhibit viscoelastic or viscoplastic behavior in the 32 to 120°F temperature range, and the response of metals to different compressive or tensile stress levels is well understood. Thus the selection of working stress here was more of a design than research problem. The metal hatch and polar plate could be designed to fail at higher

hydrostatic loading than the acrylic plastic hull, at equal loading, or at lesser loading. Designing it to fail at lower pressure than the hull would lower the overall safety of the capsule while designing it to fail at pressures above that of the acrylic plastic hull did not raise its overall safety, so a working stress level was chosen for metallic hull components that would cause them to fail at the same depth as the acrylic plastic capsule under short-term hydrostatic loading.

Specification of Materials. Although the decision had been made early in the research program to utilize acrylic plastic as the transparent hull material and metals for hatches and bottom penetration plate, a set of specifications had to be drawn up for their procurement.

Several grades of acrylic plastic are commercially available in the form of sheets and plates. The acrylic plastic is available in heat-resistant, unshrunk, utility grade (MIL-P-21105C); heat-resistant, preshrunk, optical grade (MIL-P-5425); modified cross-linked, preshrunk, optical grade (MIL-P-8184); and modified cross-linked, crack-propagation-resistant, prestretched optical grade (MIL-P-25690).

Since for the safe performance of the acrylic plastic capsule the most important material properties are compressive strength, shear strength, tensile strength, impact resistance and time-dependent viscoelastic or viscoplastic deformation, all of the existing acrylic plastic grades were carefully examined to determine which one of them best satisfied the material property requirements. A review of the material properties applicable to the NEMO capsule showed, however, that there was very little significant difference between the different grades of acrylic plastic materials with the possible exception of the stretched acrylic plastic that possesses significantly higher impact strength than all the other grades. A survey of acrylic plastic sheet producers revealed, however, that only MIL-P-21005C is available as a standard stock item in thicknesses to 4 inches; MIL-P-5425 could be obtained as a special order stock item at premium price from the suppliers, while the modified and prestretched acrylic plastic was simply not produced in the thicknesses above 1 inch. Further examination of standard commercial MIL-P-21105C plates of up to 4-inch thicknesses revealed that their optical properties are more than adequate for visual observation of hydrospace. Since MIL-P-21105C satisfied the operationally required optical criteria, was readily available in thicknesses to 4 inches, was the least expensive of all acrylic plastic material grades, and at the same time could satisfy the structural requirements of the capsule, it was chosen as the capsule material. The mechanical and physical properties of the heat-resistant, unshrunk, utility grade acrylic plastic (MIL-P-21105C) and the ASTM tests used in determining them are shown in Table 1.

Table 1. Physical and Mechanical Properties of Grade G Plexiglas Acrylic Plastic Used for Fabrication of NEMO Hulls

Physical Properties		
Property	Typical	Test Method
Hardness, Rockwell M	90	ASTM-D785-62
Hardness, Barcol	90	ASTM-D2583
Specific gravity	1.19 ± 0.01 (2 tests within 0.005)	ASTM-D792-64T
Refractive index; 1/8 inch	1.50 ± 0.01	ASTM-D542-50
Luminous transmittance; 1/8 inch	91%	ASTM-D1003-61
Haze, 1/8 inch	2.3	ASTM-D1003-61
Heat distortion temperature		
+3.6°F/minute at 264 psi	200°F	ASTM-D648-56
+3.6°F/minute at 66 psi	220°F	ASTM-D648-56
Thermal expansion/°F at 20°F	35×10^{-6}	Fed. Std 406 Method 2031
Water absorption; 1/8 inch		
24 hr at 73°F	0.3%	ASTM-D570-63T
To saturation	1.9%	ASTM-D570-63T

Mechanical Properties		
Property	Minimum Requirement	Test Method
Tensile strength, rupture (0.2 in./minute)	9,000 psi	ASTM-D638-64T
Tensile elongation, rupture	2% min to 7% max	ASTM-D638-64T
Modulus of elasticity, tension	400,000 psi	ASTM-D638-64T
Compressive strength, yield (0.2 in./minute)	15,000 psi	ASTM-D695-63T
Modulus of elasticity, compression	420,000 psi	ASTM-D695-63T
Flexural strength, rupture	14,000 psi	ASTM-D790-63
Shear strength, rupture	8,000 psi	ASTM-D732-46
Impact strength, 1 zod (per inch of notch)	0.4 ft-lb	ASTM-D256-56
Compressive deformation under load (4,000 psi at 122°F for 24 hr)	2.0% max	ASTM-D621-64

Only three groups of metallic materials were available at that time that, because of their corrosion resistance, could be considered for the selection of the hatch and bottom insert plate material. The three materials were titanium, stainless steel, and monel. Titanium was the most desirable one as its corrosion resistance was superior to the two other groups of materials. Its compressive strength and tensile strength were higher than for the other two groups of materials, and its specific gravity was the least, easing the opening of the lightweight hatch by the crew from the capsule's interior in an emergency. Unfortunately, the price of titanium forgings was about 500% higher than for the other materials, and this made its use inapplicable. Thus the choice was between monel and stainless steel, among which only type 316 satisfied the minimum requirement for corrosion resistance. Since the strength of type 316 stainless steel was about equal to that of the monel available, and since the desired shapes of type 316 stainless steel were more readily available from the suppliers, it was selected as the material for fabrication of the hatch and bottom insert plates. The mechanical and physical properties of the type 316 stainless steel are shown in Table 2.

Table 2. Properties of Type 316 Stainless Steel

Property	Typical
Mechanical	
Yield strength	30,000 psi
Tensile strength	75,000 psi
Elongation at failure	50%
Hardness	B 75
Chemical	
Carbon	0.08%
Chromium	17%
Nickel	12%
Molybdenum	3%

Selection of Capsule Dimensions. The acrylic plastic wall thickness was selected on the basis of (1) elastic theory for stress distribution and (2) elastic instability theory applied to a thick-walled perfect sphere without penetrations. These theories provide only approximations. Acrylic plastic is viscoelastic, rather than elastic and thus basically nonisotropic when stressed; the deformation of the material is not simply a function of stress but also of time and modulus of elasticity, which changes from point to point in the acrylic plastic hull according to the stress distribution.

However, under short-term loading the theory for thick-wall elastic stress distribution gives a good first-order approximation of what the wall thickness of the capsule should be in order to be within a specified compressive stress range. Although this theory does not predict the magnitude of stress raisers around the hatches, it was felt that if the average membrane stress level selected is low enough, the increase in stress generated by the presence of steel hatches will not surpass the ultimate tensile and compressive strength of the acrylic plastic and will not cause ultimate failure of the acrylic plastic material, although some viscoplastic deformation may take place.

The elastic stability calculations are also only approximations. The viscoelastic and viscoplastic time-dependent behavior of the acrylic plastic material negates the basic premises underlying the elastic stability calculations. But as in the calculation of stresses, it was felt that a first-order approximation is acceptable so long as the calculation of implosion pressure was limited to (1) the short-term loading case, in which the effect of time on viscoelastic behavior of material is minimized, and (2) the selected implosion pressure was higher than the operational pressure by some reasonably high safety factor.

Since *elastic instability* of external pressure hulls for shallow depths is generally the deciding factor in determining wall thickness,[16, 17, 18] it was used as the primary design consideration. The classical analytical expression for elastic instability developed by Zoelly in 1915 was originally derived[16] for perfect spheres.

$$p_{cr} = \frac{KE\left(\frac{t}{R_m}\right)^2}{\sqrt{1 - \mu^2}} \qquad (1)$$

where p_{cr} = critical pressure at which elastic instability occurs (psi)

E = Young's modulus (psi)

t = shell thickness (in.)

R_m = radius to midsurface of shell (in.)

μ = Poisson's ratio

K = buckling coefficient

Therefore, the buckling coefficient K = 1.15 derived by Zoelly applied only to small deflections. Because of the impossibility of obtaining perfectly spherical shells, the classical small deflection theory for elastic instability has been found to predict critical pressures that are actually 20 to 300% higher than experimental collapse pressures of spherical shells. Research[16, 17, 18] has shown that the deviation of experimental collapse pressure from the calculated critical pressure for perfect spheres is a function of deviations from nominal sphericity and nominal wall thickness. Therefore, attempts were made to modify the classical formula and to specify tighter dimensional tolerances for the spheres. The resulting semiempirical expression[16] of

$$p_{cr} = \frac{0.8E\left(\frac{t}{R_o}\right)^2}{\sqrt{1 - \mu^2}} \qquad (2)$$

where R_o is the external radius (in.), has been found to show good agreement with experimental data so long as the deviation in sphericity in shells is less than 0.03t and the minimum wall thickness value is used for the term t in Equation 2. To make this equation applicable to acrylic plastic material, one further modification is necessary. In place of Young's Modulus E, based on linear relationship between stress and strain, new terms must be substituted that reflect the nonlinear relationship between stress and strain in acrylic plastic material. The new term for E may be tangent modulus of elasticity, E_t, secant modulus of elasticity, E_s, or a hybrid expression of $\sqrt{E_s E_t}$ that takes both moduli into consideration. The new term for μ may be μ_v, a variable that also reflects the nonlinear relationship between stress and Poisson's ratio in acrylic plastic.

The secant modulus, tangent modulus, and variable Poisson's ratio are generally derived from typical uniaxial compression stress–strain curves of acrylic plastic test specimens. In order to arrive at the stress level in the sphere so that the proper E_s, E_t, and μ_v can be substituted into Equation 2, the following simplified equation was used

$$s = \frac{p(R_o)^2}{2R_m t} \qquad (3)$$

where s denotes average membrane stress, which for the purposes intended is of sufficient accuracy.

Thus, the resulting equation for prediction of instability-type failure in acrylic plastic shells can be stated as

$$P_{cr} = \frac{0.8\sqrt{E_s E_t}\left(\frac{t}{R_o}\right)^2}{\sqrt{1 - \mu_v{}^2}} \qquad (4)$$

When this formula is utilized, it is imperative that in order for the formula to predict critical pressure of an acrylic plastic sphere the material properties used in the formula must be obtained under stress rates that are identical to that used for implosion of the sphere. In practice, this means that, when the Equation 4 is used to predict the critical pressure of an acrylic plastic sphere under a short-term pressure loading condition (pressurization at some constant rate to implosion), the stressing rate of the material test specimens should be the same, or very close to the stressing rate of the sphere.

Thus as the first step in calculating the thickness of the spherical capsule, a stress–strain relationship had to be established for grade G Plexiglas under a stressing rate similar to the one to be used in short-term implosion tests of acrylic plastic capsules. Since the stress rate tentatively selected for capsule implosion tests was to be in the 800-to-1,000-psi/min range, similar stressing rates were used to determine the material properties of acrylic plastic (Figures 14a through 14d).

Utilizing the E_s, E_t, and μ_v determined by uniaxial tests and simultaneously solving Equations 3 and 4, the wall thickness required for implosion by the mechanism of general elastoplastic instability failure was calculated to be $t/R_o = 0.0685$ and the average membrane stress at critical pressure s_{avg} = 10,200 psi. At a critical pressure of 1,350 psi (equivalent to 3,000-foot depth) and an average stress level of 10,200 psi, the mechanical properties of acrylic plastic were determined to be E_s = 402,000 psi, E_t = 270,000 psi and μ_v = 0.375 (Figures 14a through 14d).

Once the t/R_o proportion of the sphere was established at 0.0685, detailed calculation of stresses could take place. Using the analytical expressions for distribution of stresses in a thick-walled sphere of elastic material

$$S_1 = S_2 = -p\left[\frac{R_o{}^3(R_i{}^3 + 2r^3)}{2r^3(R_o{}^3 - R_i{}^3)}\right] \qquad (5)$$

$$S_3 = -p\left[\frac{R_o{}^3(r^3 - R_i{}^3)}{r^3(R_o{}^3 - R_i{}^3)}\right] \qquad (6)$$

where S_1 = meridional membrane stress (psi)

S_2 = equatorial membrane stress (psi)

S_3 = radial wall stress (psi)

p = external hydrostatic pressure (psi)

R_o = external radius of sphere (in.)

R_i = internal radius of sphere (in.)

r = radius to point where stress is to be found (in.)

Solving Equations 5 and 6 for S_1 and S_3 when $p = 450$ psi (1,000-foot operational depth), the following stress values were determined for internal and external shell surfaces:

at R_o $\quad S_1 = S_2 = -3{,}330$ psi and $S_3 = -450$ psi

at R_I $\quad S_1 = S_2 = 3{,}550$ psi and $S_3 = 0$

From consideration of the calculated stresses, it appeared that the selection of the $t/R_o = 0.685$ wall thickness for the sphere on the basis of the elasto-plastic instability Equation 4 is probably satisfactory from the stress magnitude viewpoint also, as the general stress level in acrylic plastic at the operational depth of 1,000 feet appears to be less than 4,000 psi. If the stress magnitude level turned out subsequently to be too high because of the local stress raiser effect of metal plates in the polar penetrations, the reduction in operational depth from 1,000 to 600 feet (minimum continental shelf depth requirement) would probably lower the overall stress level sufficiently to bring the peak stress at the hatch penetration below ultimate failure stress level for acrylic plastic.

Selection of the hatch plate thickness presented a more complicated problem than the selection of acrylic plastic hull thickness. From the viewpoint of stresses in the hatch plate, it was desirable to make the plates as thick as possible, while from the viewpoint of stresses in the acrylic plastic bearing surface, it was mandatory to keep the thickness to the absolute minimum so that the mismatch in wall rigidity was minimized. Since neither the effect of hatch plate thickness on the stress concentration in acrylic plastic, nor the effect of acrylic plastic hull on the magnitude of stresses in the metallic hatch was known for sustained loading during a typical dive, either one of the viewpoints taken would result in an unknown quantity. Ultimately the viewpoint was taken that minimization of stress raiser effect in acrylic plastic was more important than minimizing the stress

level in the metallic plate. If the stresses in the hatch plate of chosen dimensions were found to be too high, an alloy with higher material properties could be substituted for the material originally chosen. This would result in no changes in hatch design, while increasing thickness of the acrylic plastic hull would require considerable redesign.

To calculate the minimum thickness of the metallic plates, the assumption was made that the metal plate is unaffected by the presence of the acrylic plastic hull bearing upon it. Therefore the stress in the plate could be approximated on the basis of membrane shell theory. Using a design stress of 13,500 psi (approximately 50% of minimum yield stress in type 316 stainless steel) and the thin shell membrane shell equation

$$p = \frac{2tS_1}{R_o} \tag{7}$$

a hatch thickness of $t/R_o = 0.0166$ was calculated for $p = 450$ psi. When the calculated hatch plate thickness was subsequently checked for its elastic stability with Equation 4, it was found to be elastically stable at operational depth. Its failure was predicted on the basis of Equation 4 to take place by plastic instability at pressures slightly in excess of 1,350 psi. Thus from the viewpoint of instability failure, the design would appear to be adequate as it would cause the hatch to fail at approximately the same depth as the rest of the acrylic plastic sphere. To forestall generation of excessive stress raisers around penetrations in the bottom metal plate, they were either reinforced by local thickening of the plate in the form of bosses or flanges, or they were subsequently filled by penetrators of approximately the same rigidity as the plate. Detailed stress analysis of the metal plates was not performed at that time as it was felt there was not sufficient information on the interaction between steel plate and acrylic plastic hull deforming viscoelastically or viscoplastically to make the analytical stress analysis more than a first order approximation.

Structural Component Dimensioning. This constituted the last step in the detail design of the acrylic plastic capsule. Before the detail design of the structural components could be initiated, a procedural question had to be resolved: Which acrylic plastic sphere size would be ultimately selected for the capsule program? Although some capsule dimensions have been calculated in nondimensional terms like t/R_o, and therefore apply to any size sphere, most dimensions of the capsule details must be based on dimensional human factors criteria (size of hatch, hatch locking mechanism, and others). Thus, once the decision was made to design a certain diameter capsule, a considerable waste of engineering and design time would occur if the diameter of the capsule was changed.

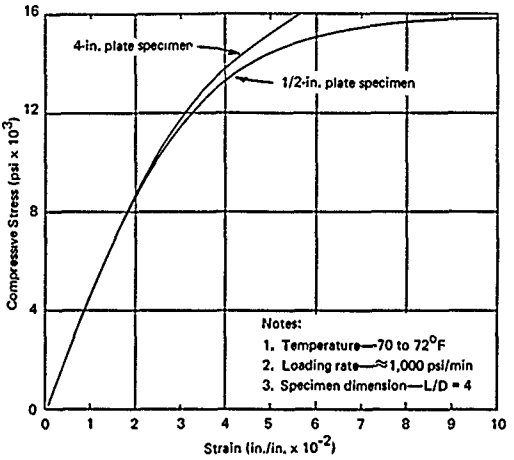

Figure 14a. Strain-versus-stress relationship for grade G Plexiglas acrylic plastic under uniaxial compression.

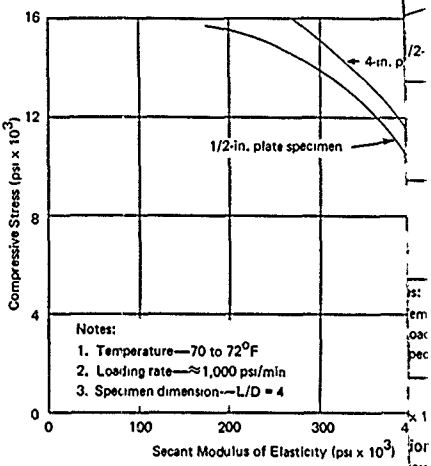

Figure 14b. Secant modulus of elasticity for grade acrylic plastic under uniaxial compres

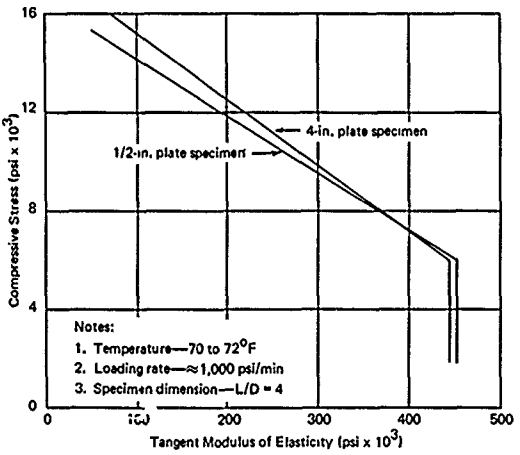

Figure 14c. Tangent modulus of elasticity versus stress for grade G Plexiglas acrylic plastic under uniaxial compression.

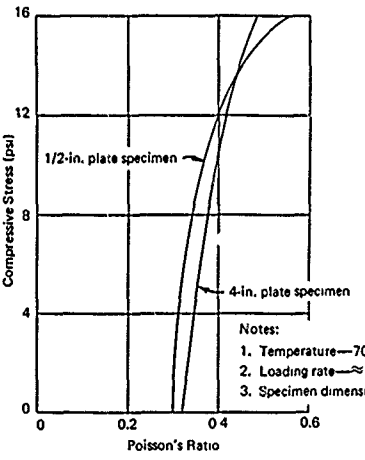

Figure 14d. Poisson's ratio versus stress for grade G Pl acrylic plastic under uniaxial compression

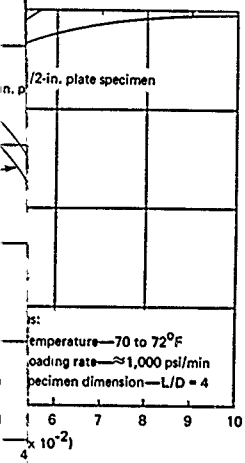

ionship for grade G Plexiglas
axial compression.

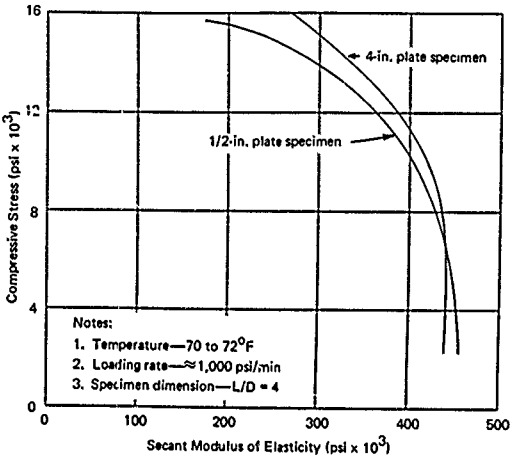

Figure 14b. Secant modulus of elasticity for grade G Plexiglas acrylic plastic under uniaxial compression.

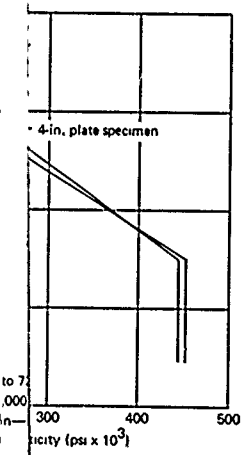

city versus stress for grade G
der uniaxial compression.

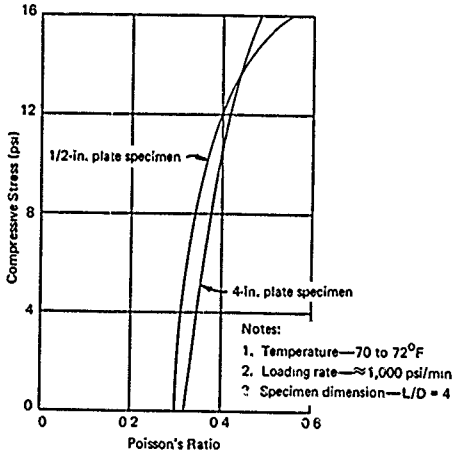

Figure 14d. Poisson's ratio versus stress for grade G Plexiglas acrylic plastic under uniaxial compression.

The diameter chosen at that time for the operationally most useful panoramic capsule concept was 120 inches. That diameter was arrived at on the basis of two considerations: (1) that this is the minimum size that will permit a two-man crew to remain comfortably on the ocean bottom submerged longer than a day, and (2) that this is the largest capsule for continental shelf depth that can be built around the required $t/R_o = 0.0685$ from 4.125 inch thick material, the thickest commercially available acrylic plastic plate. Since during the course of the acrylic plastic capsule program a smaller prototype operational capsule of 66-inch diameter was to be built, the operators would have to put up with scaled-down hatches, penetrations, attachments, etc., of less than ideal proportions from the human factors viewpoint. To permit as many subsequent changes in the capsule design as possible, only as many details were to be incorporated in the first capsule design as were needed to permit the construction of a 15-inch model for experimental validation of the capsule design. To save time in drafting and detail design, it was decided to bypass one step generally required between the formulation of the full-scale concept and the fabrication drawings for a scale model needed for experimental validation of the full-scale concept. The step bypassed was the detailed design drawing of the full-scale concept, which when scaled down and simplified would have become the fabrication drawing for the small-scale (15-inch) model. Thus, the fabrication drawings for the small-scale model of the capsule were prepared directly from the rough concept sketches. This shortcut made it possible to complete fabrication drawings of the small-scale capsule model in less than 2 months after the formulation of the concept. Because of the elimination of this step in arriving at small-scale model dimensions, the fabrication drawings for any subsequent capsules with diameters larger than 15 inches became only scaled-up versions of the 15-inch model capsule. There are some shortcomings associated with this approach. However, it was felt that the advantage of being able to check experimentally the quite radical concept before considerable time and money were expended on engineering the details of the concept offset the major shortcoming: freezing the design of the capsule during the first 2 or 3 months of the acrylic plastic capsule program before a thorough engineering study could be undertaken on the many feasible design trade-offs.

The resulting fabrication drawings (Figures 15 through 23) of the capsule model reflect quite faithfully the previously discussed conceptual approaches to (1) means of ingress and egress, (2) penetrations for electric and hydraulic circuits, (3) attachment of the capsule to other NEMO structural systems, (4) magnitude of working stresses, (5) specification of construction materials, and (6) hull thickness. No attempt was made to

include life-support equipment, railing, ladders, or any other structural components that have little influence on the stress distribution in the acrylic plastic capsule. It is well to point out, however, that the actual t/R_o ratio of the 15-inch models is somewhat smaller than that calculated previously in the section "Selection of Capsule Dimensions." There was only one reason for the t/R_o ratio of the 15-inch models to be in the 0.060 to 0.0685 range rather than at exactly 0.0685 as calculated: variation in thickness of commercial acrylic plastic plate from the nominal 0.5-inch plate thickness. Procurement of a nominal 0.625-inch-thick plate that subsequently could be ground to the specified 0.513-inch thickness would have produced models with the exact $t/R_o = 0.0685$ ratio, but only at the expense of 300% increase in the fabrication cost of each capsule model.

Although at a first glance the use of models with a somewhat thinner wall than calculated appeared to be quite unacceptable, there was a positive gain: the experimental data generated by destructive testing of models under short-term, long-term, or cyclic pressure loading would be conservative.

PHASE 2—FABRICATION PROCESS

The selection of the proper fabrication process posed considerable difficulties for two reasons: (1) it had to perform equally well in the fabrication of large-scale and model capsules, and (2) economical fabrication techniques for model capsules generally turn out to be uneconomical for large-scale capsules, and vice versa. For reasons already briefly discussed, the fabrication of the acrylic plastic capsule was chosen to conform closely to Professor Piccard's concept except for the introduction of material grades and shapes not commonly available in his day.

Acrylic Hull Fabrication

Material Selection. The material selected for the fabrication of both model capsules and any future full-scale capsules was grade G Plexiglas acrylic plate stock. This material is the commercial grade acrylic plastic widely available as an off-the-shelf plate and sheet stock item in many different sizes and thicknesses.

Although the acrylic plastic under the trade name of grade G Plexiglas was chosen for the NEMO program because of the proximity of a major supplier that carries this material in stock, other commercially available acrylic plastic plates with equivalent material properties sold under other trademarks (Swedlow 310, Acrylite, and others) probably could have been used with about the same success.

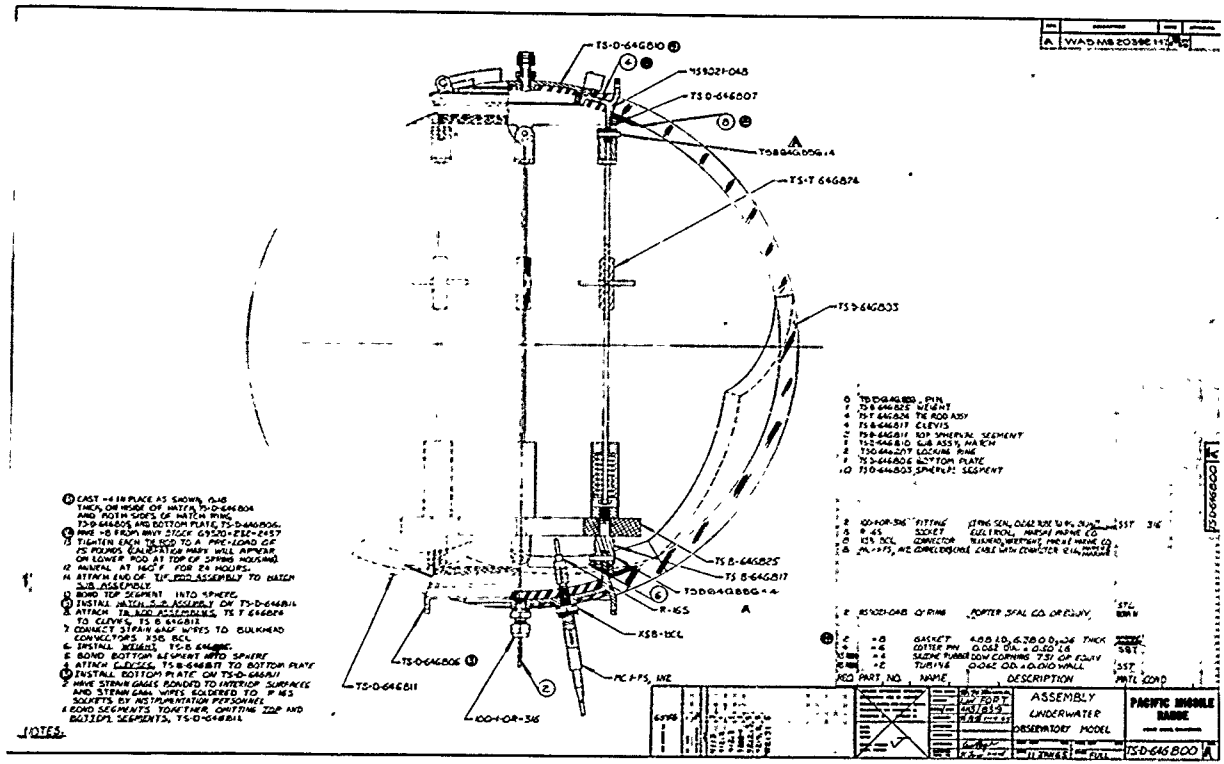

Figure 15. Design of model acrylic plastic capsule for the NEMO system: assembly.

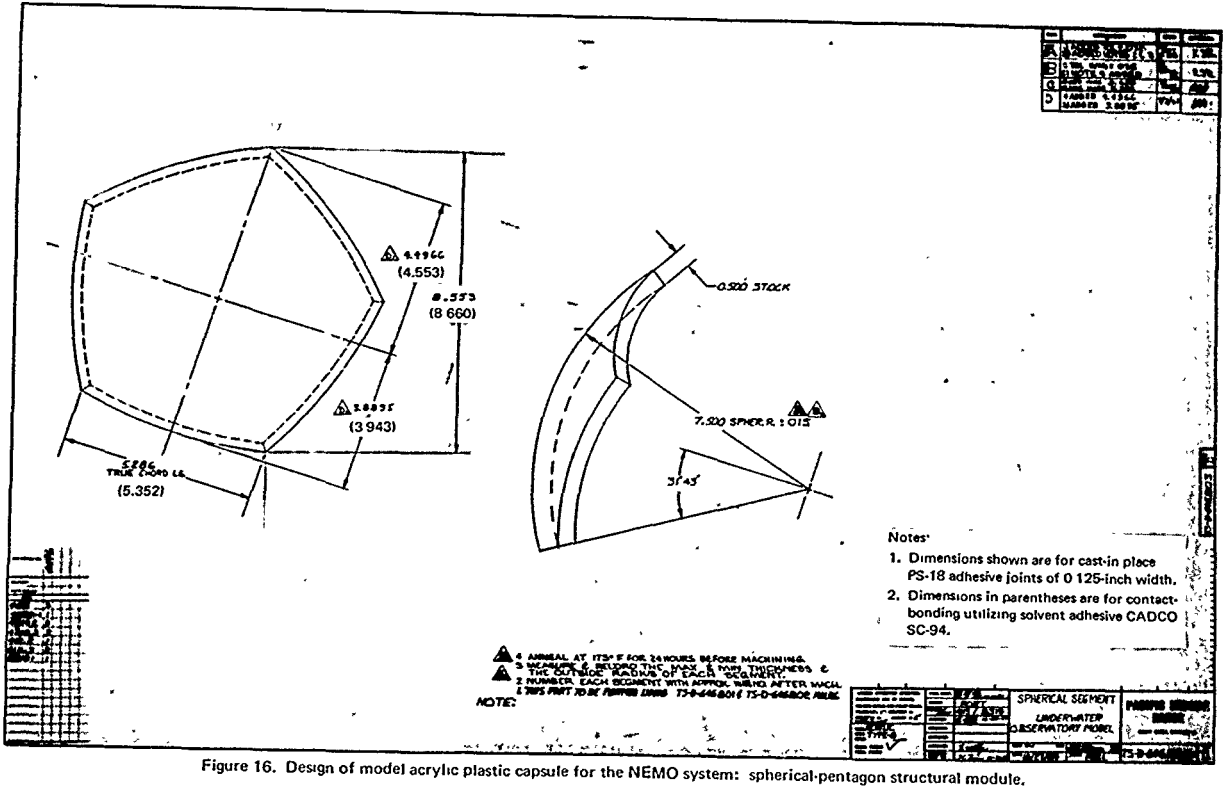

Figure 16. Design of model acrylic plastic capsule for the NEMO system: spherical-pentagon structural module.

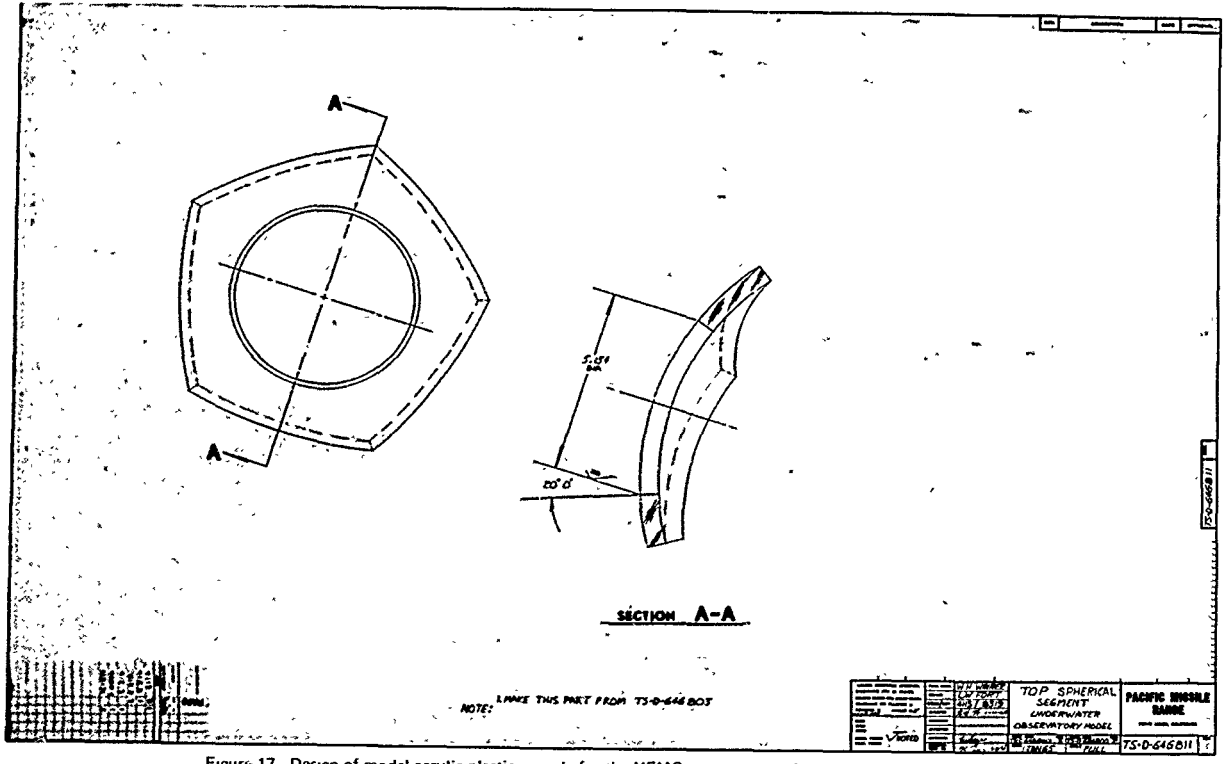

Figure 17. Design of model acrylic plastic capsule for the NEMO system: spherical pentagons with penetration.

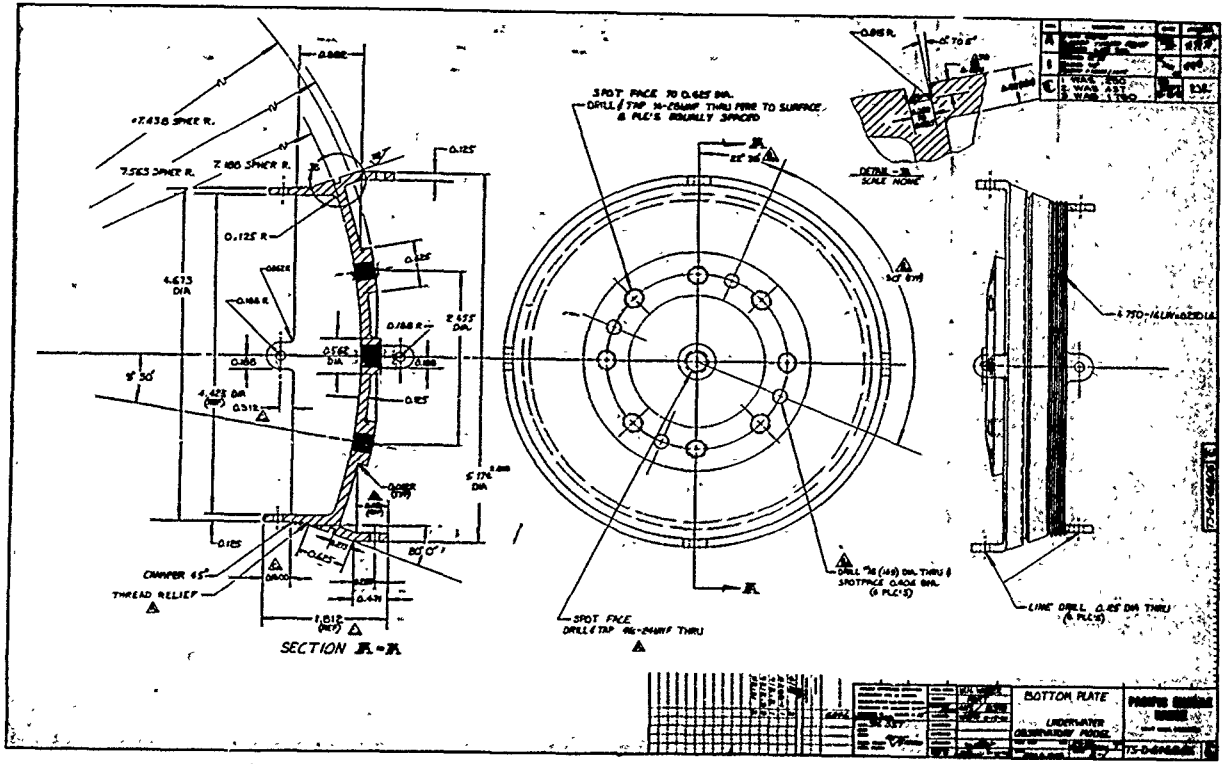

Figure 18. Design of model acrylic plastic capsule for the NEMO system: bottom penetration insert

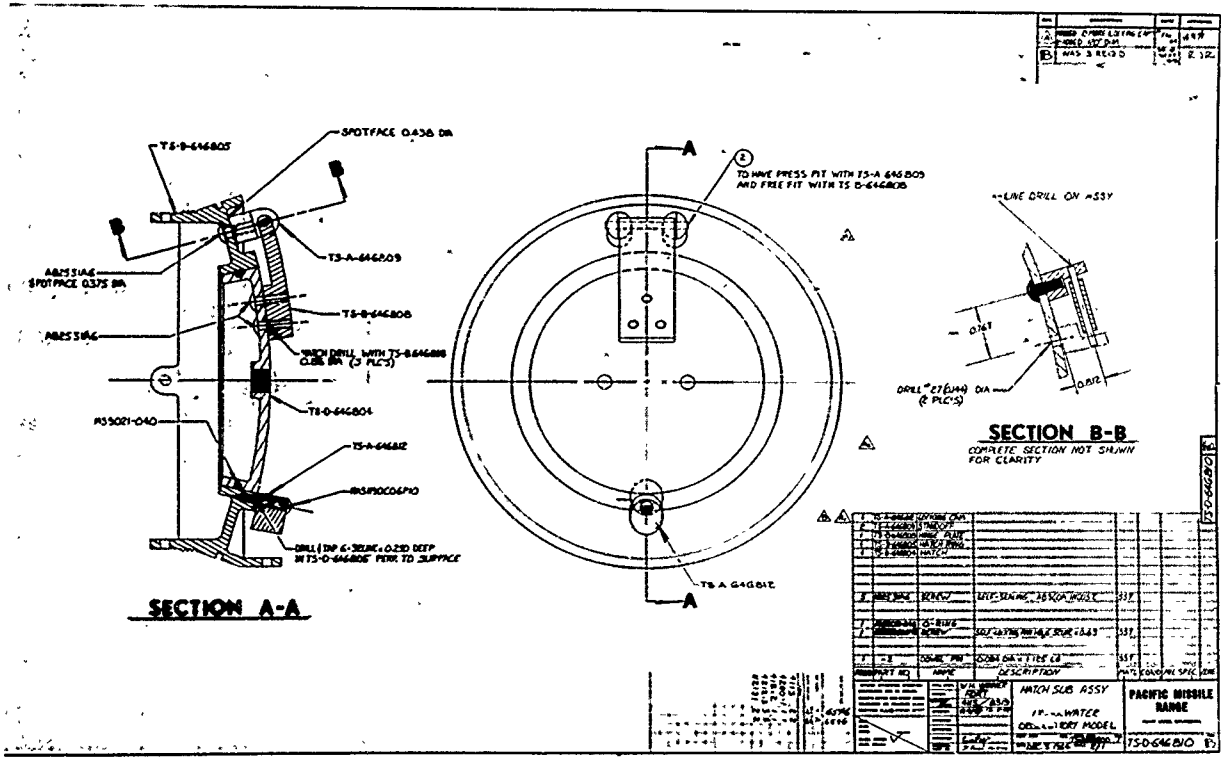

Figure 19. Design of model acrylic plastic capsule for the NEMO system: hatch subassembly.

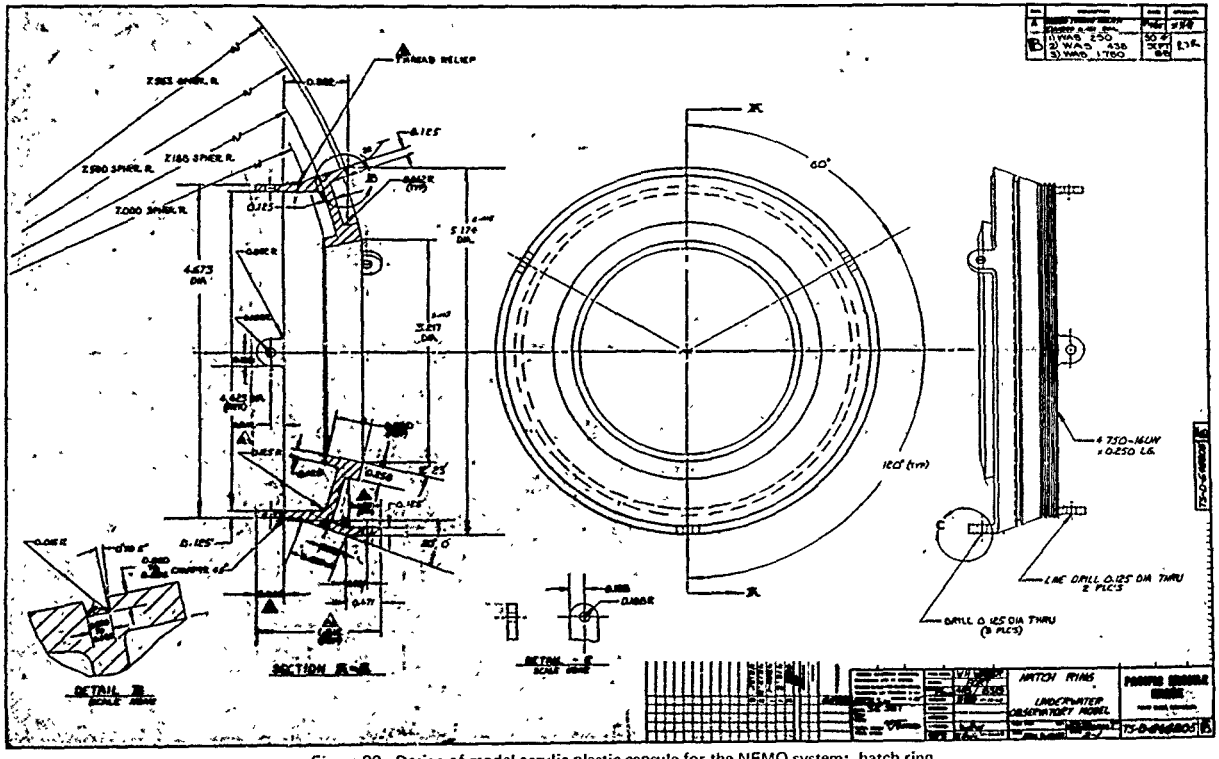

Figure 20. Design of model acrylic plastic capsule for the NEMO system: hatch ring.

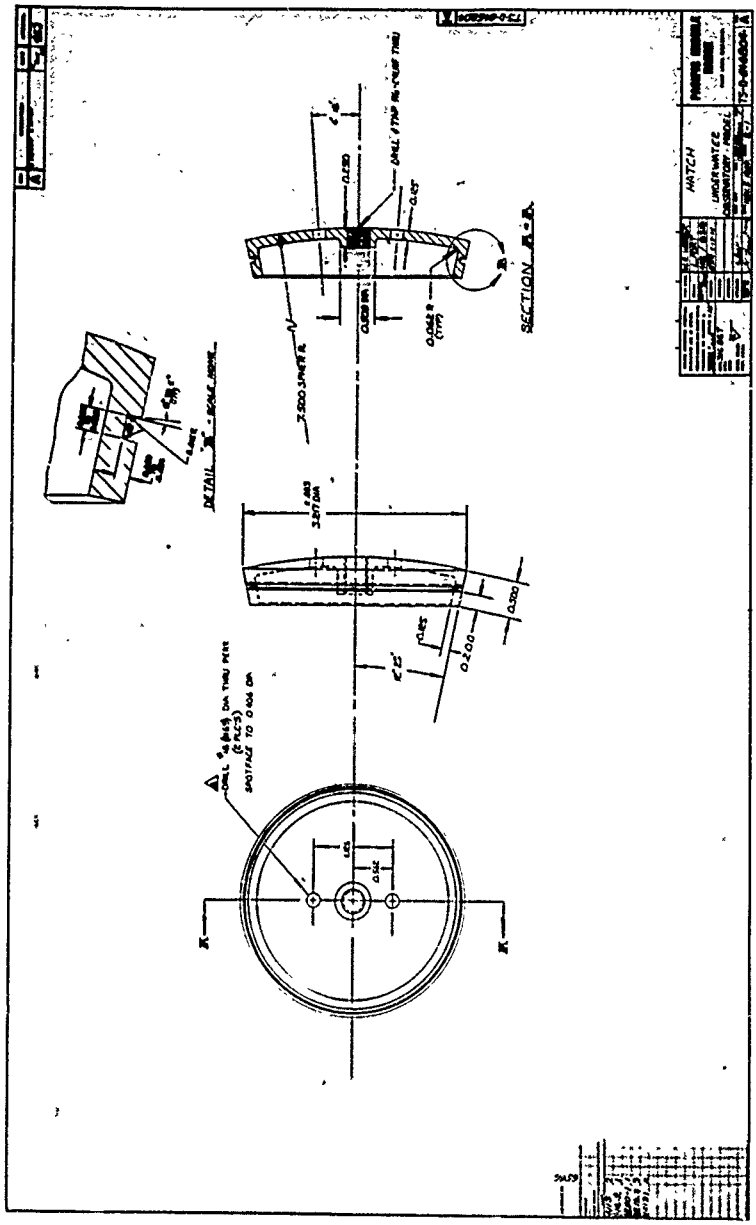

Figure 21. Design of model acrylic plastic capsule for the NEMO system: hatch plate.

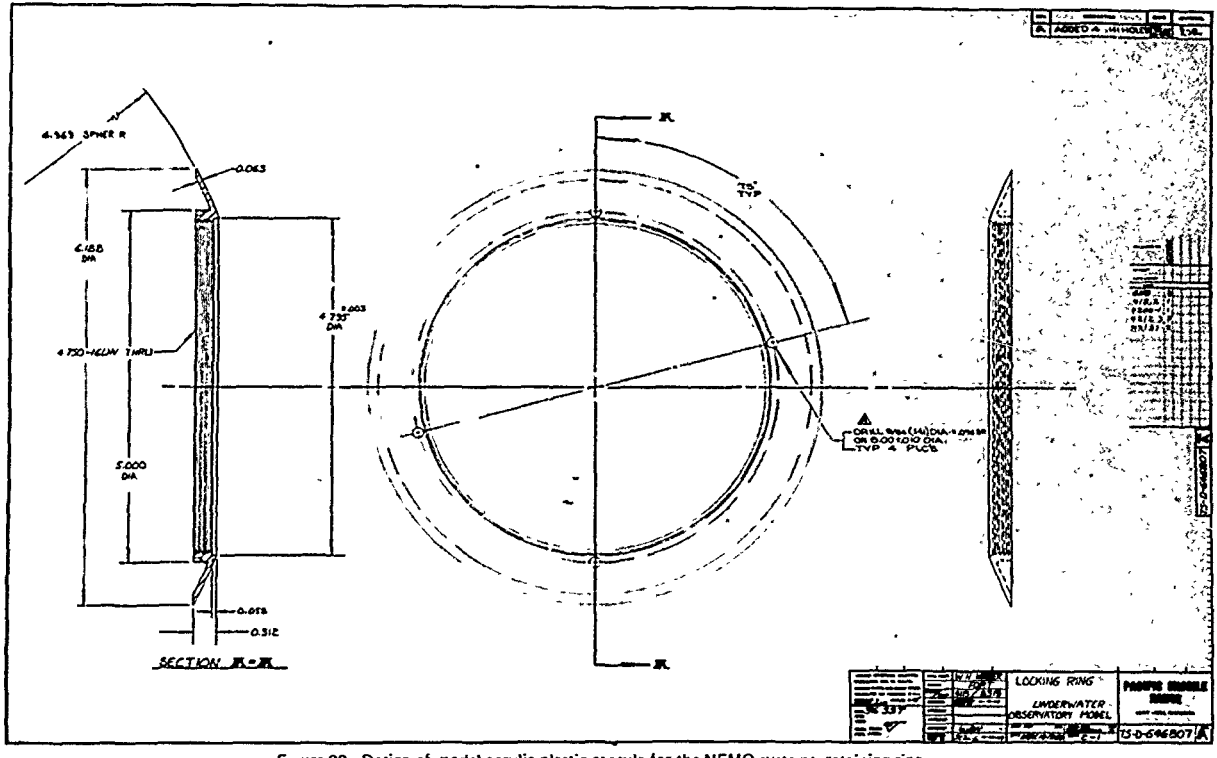

Figure 22. Design of model acrylic plastic capsule for the NEMO system: retaining ring

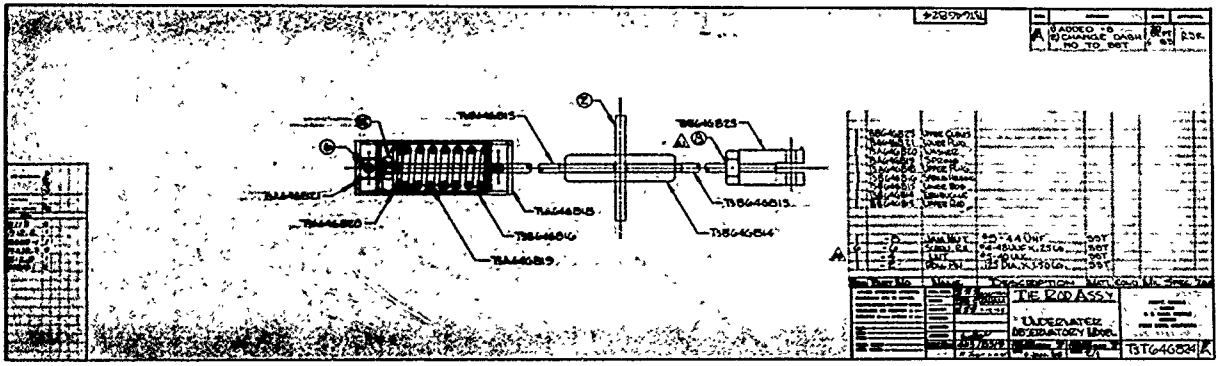

Figure 23. Design of model acrylic plastic capsule for the NEMO system: tie-rod subassembly.

No effort was made to utilize premium grade acrylic plastic materials, or acrylic plastic materials that have been chemically or physically modified (stretched acrylic for example). It was felt that in the exploratory phase of the program having as its objective the utilization of acrylic plastic as structural material for the hull of a submersible the most common available material should be utilized. Only after the exploratory phase of the acrylic plastic pressure hull program was successfully completed could other acrylic plastic materials be considered that, because of their special material properties, would improve either the fabrication process or the performance of acrylic plastic hulls.

The minimum properties of the commercial grade acrylic plastic plate stock used in the program are shown in Table 1. Since deviations from the material properties published by the material supplier could be expected, extensive tests were conducted on samples cut from plates that were subsequently used in the fabrication of model and large-scale capsules. No significant deviations were found between the material properties advertised by the manufacturer and the properties determined experimentally from test specimens, except for long-term compression creep (ASTM D621-51 at 4,000-psi load), which was found to be 2% in some of the 2.5-inch-thick plates instead of the advertised 0.5%. Plates with exceptionally high (larger than 2%) long-term compression creep were not utilized for the construction of the acrylic plastic capsules. No significant differences were found between the material properties of nominal 0.5-inch-thick acrylic plastic plates used in the fabrication of models and the 2.5-inch plate used in the fabrication of the 66-inch NEMO prototype. The data generated (Figures 14a through 14d) in the previously discussed testing of 0.5-inch and 2.5-inch acrylic plastic plates were used subsequently in the design of acrylic plastic hulls.

Forming. One of the major problems that had to be resolved successfully before spherical acrylic plastic capsules could be built from the pentagon-shaped structural modules of acrylic plastic plate was how to impart to the commercially available flat plates the desired curvature within tight dimensional tolerances. There were several different forming processes known that could be applied.

The flat acrylic plastic plates could be (1) free-blown to desired radius (2) blown into a spherical mold, (3) sagged into a spherically concave mold, (4) sagged over a spherically convex mold, (5) vacuum sucked into a concave mold, or (6) pressed into a concave mold by a convex male mold. Each of those forming processes possessed advantages and disadvantages that had to be carefully evaluated to arrive at the forming process best suited for the forming of structural hull modules.

A thorough evaluation indicated that free-blowing flat plates into spherical modules would result in the largest variation in spherical radius from one module to another, and pressing the flat plates between male and female molds of appropriate radii would result in the least variation. In addition, the free-blowing process produces the largest variation in thickness between different points on the module, while the pressing process produced not only a uniform thickness from point to point on a module, but also from one module to another. Thus, it was obvious that the forming process by pressing was the most applicable to fabrication of a spherical acrylic plastic capsule, in which undue deviations from sphericity and uniformity in thickness would exert a deleterious effect on its implosion pressure.

On the basis of this selection process, pressing dies were designed for the fabrication of 15-inch models and the 66-inch operational prototype (see Appendix A for detailed dimensions of the 66-inch capsule). However, only the dies for the model were built initially as it was felt that some experience in using them was required before the decision could be made to invest a considerable sum of money for fabrication of the dies for the prototype 66-inch acrylic plastic sphere. As soon as the press die assembly was built, it was placed in operation for molding structural modules for the 15-inch capsules.

Model structural modules were formed in a female die with a 7.5-inch concave radius and a male die with a 7-inch convex radius (Figure 24). The female die had holes in its bottom through which vacuum could be applied to the space between male and female dies. Both dies were placed in a vertical hydraulic press that applied sufficient force to bring the male die to its bottom position 0.5 inch above the female even if the acrylic plastic was several thousands of an inch thicker than 0.500. The alignment between the male and female dies was assured by rigid mounting in the press platens and by steel guide pins on the male die that fitted holes in the female die. Bottom stops were provided on the guide pins to assure that the male die would not move any closer to the female die than 0.5 inch even if the acrylic plastic blank was under 0.5 inch in thickness. Finish on the die surfaces contacting the acrylic plastic was 32 rms.

The first step in the forming process was bandsawing and subsequently turning in the lathe a 9.875-inch-diameter disc from nominal 0.5-inch grade G Plexiglas acrylic plastic stock. Subsequently, it was stripped of protective paper covering and was placed into an oven whose operational temperature was adjustable. After heating the acrylic plastic to the forming temperature (discussed below) at a rate of approximately 15^{o}F/minute, it was removed from the oven and placed into the open die assembly which was preheated by an electric heater in the press platens to 160^{o}F. Vacuum was immediately applied to the female die followed by closing of the die assembly with the

hydraulic press. After 3 minutes, the male die was raised while the application of vacuum continued. When the temperature of the formed acrylic plastic decreased to 160°F after about 12 minutes, the acrylic plastic was removed from the female mold and cooled on a workbench.

Although the supplier of acrylic plastic plate recommended heating the acrylic plastic to 340°F and the dies to 170°F prior to forming, some exploratory experiments were conducted to verify those settings. Experimentation indicated that although the magnitude of residual stresses in acrylic plastic after forming is inversely proportional to the temperature of the molds and of the acrylic plastic, the number and sizes of surface blisters and pits is directly proportional to the magnitude of those two temperatures. By varying the temperature of the acrylic plastic and of the dies, it was found that if the acrylic plastic was preheated to 310 to 320°F and subsequently placed into 160°F dies, the number and severity of surface blisters was not noticeable, while at the same time the residual stresses were not too excessive. Lowering the temperature of acrylic plastic to 260°F eliminated all surface bubbles and blisters, but introduced stresses of unacceptable magnitude.

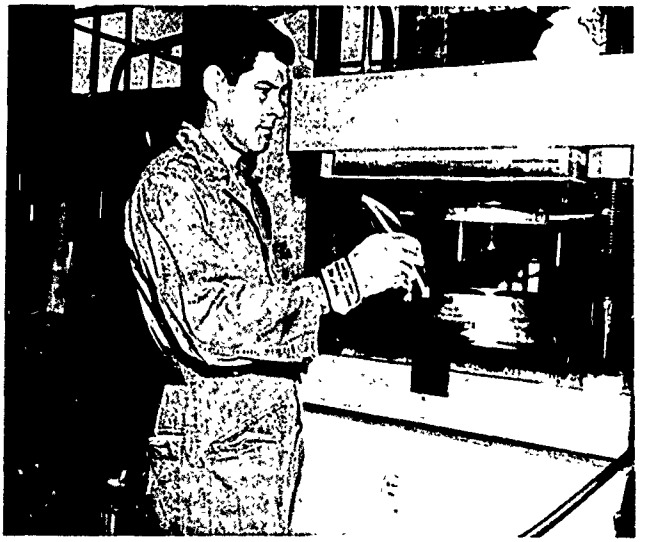

Figure 24. Hydraulic press with matched male and female die assembly for pressing spherical sectors for model capsules.

At the 310°F temperature of acrylic plastic and 160°F temperature of the dies, the residual maximum shear stress at the edge of the dished disc was measured photoelastically (see Appendix B for discussion of photoelastic effects in acrylic plastic) to be approximately 3,700 psi. The magnitude of residual stresses decreased somewhat towards the center of the formed disc. Thus, for example, the maximum shear stress 1.5 inches away from the edge of the disc was only 1,500 psi.

An attempt was made to eliminate the residual stresses by subsequent annealing of the formed spherical sector. The formed sectors were placed on a flat surface and inserted in a 170 to 180°F oven for 24 hours. After the sector had cooled to 95°F at a rate of approximately 7°F/hour, it was checked dimensionally and photoelastically. The dimensional check disclosed that the radius of curvature increased by approximately 0.020 inch while the magnitude of residual stresses decreased only very slightly. The basic change in residual stresses consisted of lowering the peak stresses by more evenly redistributing the residual stresses over the whole spherical sector surface. Because of the dimensional change generated in spherical sectors during annealing, it was decided in the future to anneal the spherical sectors only after they had been machined into pentagons and bonded into a sphere, as then they would be constrained by the spherical shape of the hull from changing their spherical radii excessively. An alternative approach was considered in which the spherical segments would be placed into a mold for annealing, so that the mold would give the sector even support and thus prevent changes in curvature due to sagging. Although this approach was considered feasible, it was not utilized as it was felt that the mold and the oven would be involved too long while individually annealing the 300 spherical sectors needed for fabrication of 25 acrylic plastic capsule models. However, individual annealing of spherical sectors was recommended for fabrication of the single 66-inch prototype capsule, as the individual annealing of only 12 sectors would not impose an undue time requirement on the available oven and mold.

The change in thickness of the acrylic plastic plate after thermoforming, but prior to annealing was measured. The thickness of the acrylic plastic disc, for example, changed from the previously uniform 0.494 inch to 0.485 inch in the center, to 0.480 inch along the edge (1/2 inch from the edge), and to about 0.470 to 0.475 midway between the center and the edge (Figure 25). These small changes in thickness were considered to be reasonable as the absolute change in thickness was actually less than 5%, and uniformity of thickness change within 3%.

Flat Blank

Material = grade G Plexiglas, unshrunk, nominal 0 5-in. plate
Flat blank diameter = 9-7/8 in.

Circumference of flat part = 31.0 in.
Actual thickness = uniform, 0 494 in.
Area of flat blank = 76 3 in.^{2}

Formed Spherical Sector

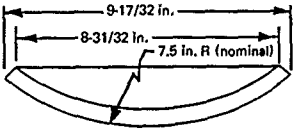

Cross Section at Centerline

Circumference of 8-31/32 in. chord = 28.17 in
Circumference of 9-17/32-in. chord = 29 95 in.
Length of the 7-in.-R arc = 9.7 in.
Length of the 7.5-in -R arc = 10.25 in.
Area of concave side = 71.5 in.^{2}
Area of convex side = 77.8 in.^{2}

Variation in Thickness of the Formed Part

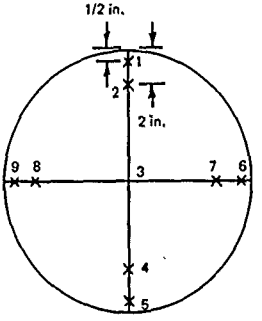

Location of Points on Flat Blank

Point No.	Thickness (in.)
1	0 481
2	0.478
3	0.485
4	0.477
5	0 480
6	0.480
7	0.473
8	0.473
9	0.477

Figure 25. Typical sphericity and thickness of spherical sectors after die pressing to 7.5-inch nominal radius of curvature.

In addition to thickness, the curvature of the spherical sector was also measured prior to annealing. In general, the curvature of the spherical sector was uniform and closely matched that of the female die. The external radius of the sector was within 0.000 to 0.005 inch of the mold curvature. The largest deviations occurred at the center and at the edge of the sector, while midway between the center and the edge there was the least deviation

in curvature. The measurement of the spherical radius on the thermoformed sector concluded the evaluation of the thermoforming process for fabrication of 15-inch model acrylic plastic hulls. Once the selected forming process was found to be feasible for forming the structural modules of the acrylic plastic capsule models, the feasibility of forming structural modules for the 66-inch prototype acrylic plastic capsule was explored.

The method of forming large-scale pentagon-shaped structural modules was similar, but not identical, to the method used for model structural modules. The reason for not following the forming technique developed for the scale models was the high cost of equipment (dies and presses) that this technique would require for forming structural modules for the prototype 66-inch acrylic plastic capsule. To decrease the costs of forming, it was decided to eliminate the male die, and thus also the requirement for a very expensive press. Although it was surmised that the elimination of the press-actuated male die would increase the deviations from desired sphericity and thickness, it was hoped that the increased deviation in sphericity from a nominal 33-inch-radius would not be of such magnitude as to make the pentagon-shaped spherical sectors unacceptable for pressure hull construction.

Thus a single female die, henceforth referred to as the mold, was designed and fabricated from aluminum. There was an important departure from the design philosophy used in designing the dies for the 15-inch model. In the previous case, the concave spherical radius of the female die was exactly equal to the nominal external radius of the hull. The female mold to be used in forming sectors for the 66-inch capsule had, however, a concave spherical radius 0.187 inch larger than the nominal external radius of 33 inches. This intentional discrepancy between the nominal sector and mold radii was based on the opinion of fabricating personnel that, because of the elimination of the hydraulic-press-actuated male die, the formed sector would not contact the whole surface of the mold, but just at the apex and at the edges. Thus, in their opinion, if a 33-inch-radius mold was used the curvature of the formed sector would be less than 33 inches in most places on the sector. On the other hand, if a 33.187-inch-radius mold was used, the curvature of the formed modules would be about 33 inches. In absence of convincing arguments to the contrary, it was decided to try this approach.

The thermoforming blank was prepared in the same fashion as were those for the 15-inch models. A circular 46.6 inch blank was first sawed on a bandsaw from a 48 x 60 x 2.5-inch plate of acrylic plastic (Figure 26) and then turned to a 46-inch disc with 200-rms edge finish in a vertical boring mill (Figure 27). One corner of the periphery was chamfered 1/8 of an inch for better support and sealing of the blank in the mold prior to forming.

During the bandsawing and milling operations, the masking paper was left on to protect the acrylic plastic against scratches. When the machining was completed, the masking paper was removed and the blank placed (chamfered edge downward) into the mold with the aid of a hoist equipped for this purpose with a vacuum-actuated suction disc. Four 0.125-inch-diameter holes were drilled 2 inches deep into the edge of the disc for placement of thermoelectric couples. After placement of thermoelectric couples, the mold and blank assembly were moved into a walk-in oven and the temperature control set at 165°F. After approximately 16 hours, the temperature control was set for 310°F. In approximately 8 hours, thermoelectric couples in the acrylic plastic indicated that a minimum temperature of 300°F was reached. At that time, a vacuum of 25 inches of mercury was applied to the mold. The blank sagged immediately and completely. After 15 minutes, the oven was turned off, but the vacuum was left on and the door closed to permit slow cooling of the acrylic plastic to 110°F. It took 16 hours for the temperature in the acrylic plastic to drop to 110°F. At that time, the doors to the oven were opened and the formed sector and the mold removed (Figure 28).

Since little was known about the formability of such thick acrylic plastic blanks in a vacuum mold, a careful postforming inspection was performed on the first molded acrylic plastic sector for the 66-inch capsule. The inspection consisted not only of accurately measuring the thickness of the formed sector, but also the sphericity of its concave surface. The sphericity of the concave mold was also measured, as without knowledge of deviations in its sphericity, few conclusions could be drawn on the causes of asphericity in the formed acrylic plastic sector.

The results of measuring the sphericity of the mold (Figure 29), as well as the sphericity and thickness of the formed acrylic plastic sector, are quite interesting (Figure 30). First, the sphericity of the mold was found to deviate at some points on the mold as much as 0.040 inch from the specified 33.000-inch radius of the formal sector, with the least deviation measured at a distance of 12.000 inches from the center of the mold as would be expected from a sphericity-measuring technique that used the surface of the mold at that location as reference datum. Second, the deviations from the nominal sphericity of the formed spherical sector followed closely the trend of the deviations of the surface mold. But since the sphericity of the sector was measured on its concave surface, and the thickness of the sector varied somewhat from point to point (Figure 30), a quantitative comparison between the sphericity of the convex surface on the sector and the sphericity of the concave surface on the mold could not be made accurately. Third, the radius of curvature on the concave surface of the sector appeared to be greater than the 30.500 inches specified.

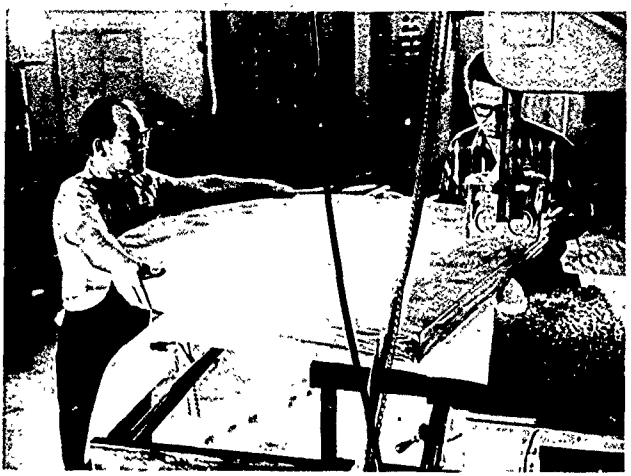

Figure 26. Sawing acrylic plastic plate stock into circular discs.

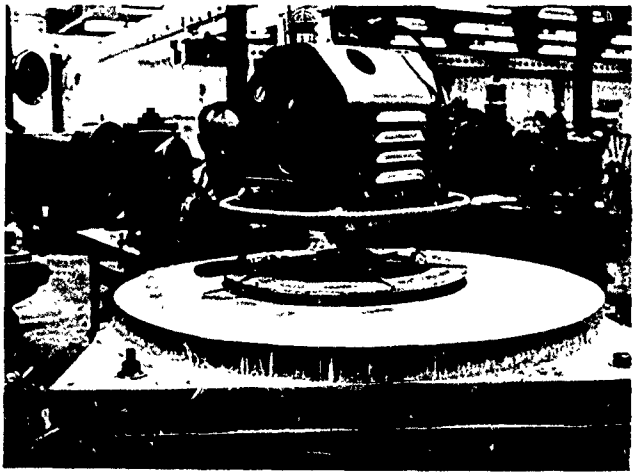

Figure 27. Turning edge of circular disc prior to placement in mold.

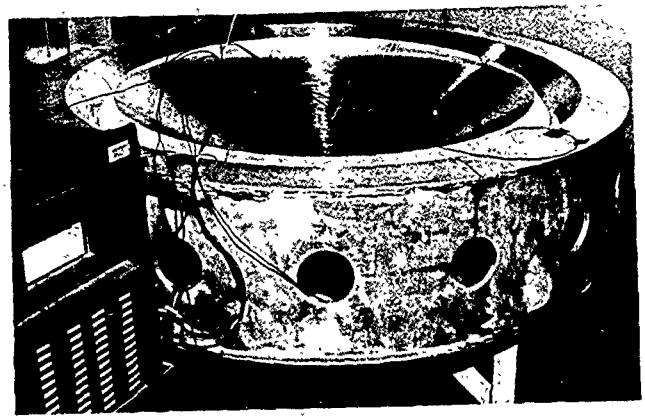

Figure 28. Circular disc after thermoforming at 300°F into spherical sector with a 33-inch radius of curvature; note thermocouples embedded in acrylic plastic for measurement of temperature.

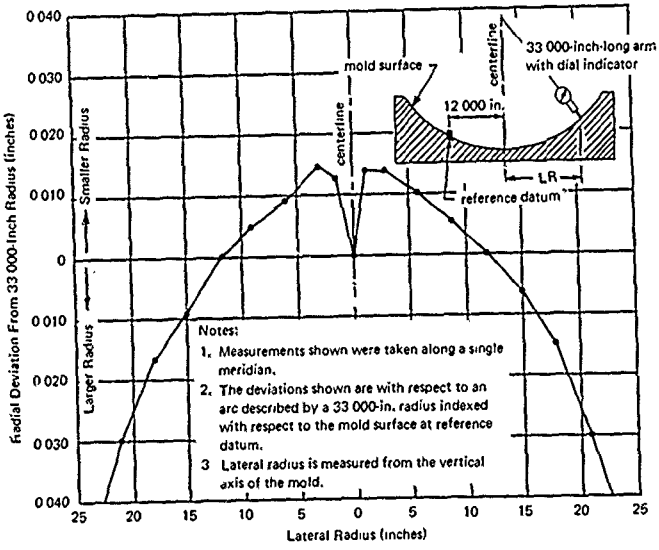

Figure 29. Actual sphericity of the mold for thermoforming sectors with 33-inch radius of curvature.

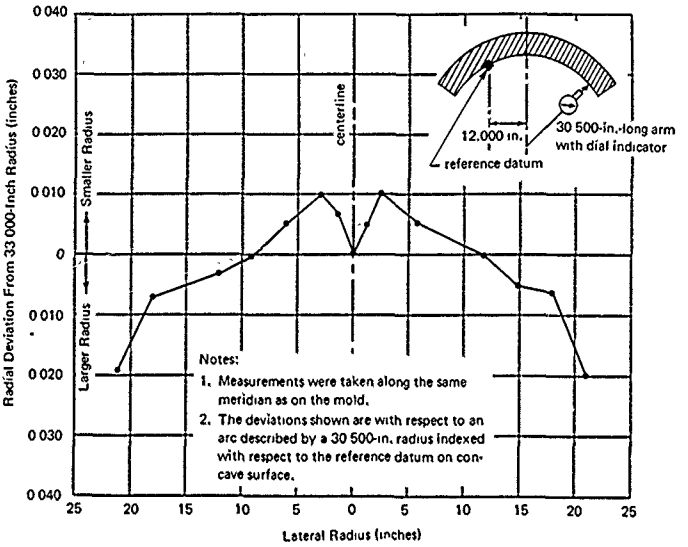

Figure 30a. Typical deviations from nominal 33-inch radius of curvature on thermoformed sector 18 for the 66-inch-diameter capsule.

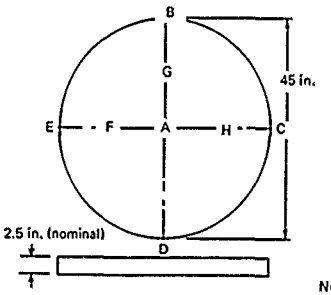

Location	Thickness Before Forming (in.)	Thickness After Forming (in.)
A	2.390	2.362
B	2.467	2.556
C	2.502	2 592
D	2.477	2.593
E	2.404	2.477
F	2.430	2.410
G	2.432	2.425
H	2.425	2.404
I	2.430	2.420

Note: The increase in thickness is caused by lateral shrinking of previously "unshrunk" grade G Plexiglas plate after it was subjected to 300°F forming temperature. The thinning out of the formed sector at the center is due to stretching of acrylic as the previously flat plate is forced to conform to the spherical surface of the mold.

Figure 30b. Effect of thermoforming on thickness of sector 18 for the 66-inch-diameter capsule.

In view of the fact that the deviations from sphericity of the formed sector were less than 1.0% of the specified radius, no real incentive existed to modify at that time the existing curvature of the mold by remachining it to an exact 33-inch radius. Besides, it was predicted (and subsequently verified by actual measurements) that the deviations from specified sphericity during the thermoforming process are minor compared to the deviations resulting from machining of the pentagons. However, the generated data on deviations in sphericity proved conclusively that specifying the nominal radius of curvature of the mold 33.187 instead of 33.000 inches produced thermoformed sectors with radii of curvature larger rather than smaller than the specified 33.000 inches. Thus, it is recommended that before additional 66-inch acrylic plastic spheres are fabricated, the curvature of the female mold be remachined accurately to the specified radius of curvature for the sphere.

Machining. The transformation of the spherical sectors into spherical pentagon modules was performed in two steps. The first step consisted of bandsawing the spherical sector into an oversized spherical pentagon (Figure 31). The second step, reducing the oversized spherical pentagon to the dimensions calculated for the spherical pentagon module, was performed on a vertical mill. For machining of model spherical pentagons, a manually operated mill was utilized (Figure 32), while for the machining of full-scale pentagons, a magnetic-tape-controlled mill was chosen (Figure 33). To facilitate the holding of the 33-inch-radius spherical sector in the bandsaw and in the vertical mill, a vacuum chuck (Figure 34) was designed and built by the shop personnel at the Pacific Missile Range. This chuck not only held the spherical sector in place but also served as a pneumatically operated indexing head for accurately locating the five straight beveled edges of the pentagon.

The machining of the large pentagons was performed with a 2-inch-diameter, helical-type milling cutter rotating at 3,800 rpm and fed at 10 in./min (Figure 33). A detergent and water cutting fluid was used to keep the cutter and the work piece cool so that serious stress concentrations would not be introduced into the spherical pentagon. The selected cutter, rotational speed, feed rate, and coolant resulted in a 63-rms finish for the beveled edges of the spherical pentagon.

Regardless of whether the pentagons were machined manually, as was the case with the model scale ones, or by preprogramed tape, as with the large pentagons, each pentagon had to be dimensionally checked before acceptance. The dimensional check consisted of measuring the linear distance between opposite tips of the pentagon with a specially built caliper having a 46-inch throat (Figure 35). Only if all the measurements between the opposite tips of the pentagon were within the specified dimensional range was the pentagon considered completed. To reduce the influence of temperature on the measurements, all readings were taken in the 65 to 75°F range. Although in the

beginning of the machining operation grave doubts existed whether pentagons could be machined to the dimensional tolerances specified (Appendix A) for the prototype 66-inch sphere, they soon were dispelled by these dimensional checks: the dimensional tolerances specified could be maintained. After the dimensions were checked, the large spherical pentagons were placed into contoured, padded plywood boxes (Figure 36); the model pentagons were stacked in shop baskets.

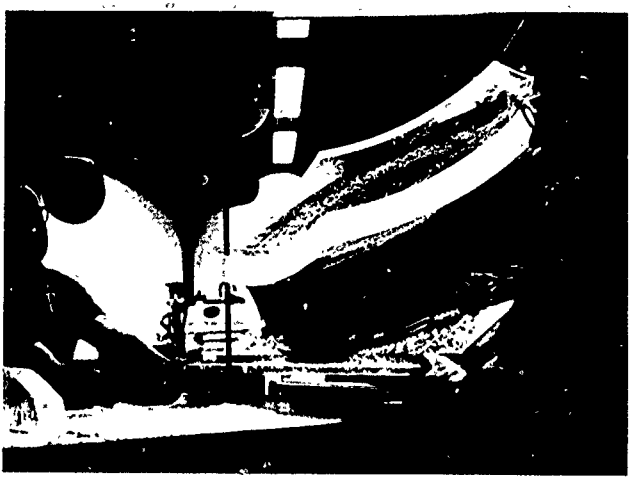

Figure 31. Sawing spherical sectors into rough spherical pentagon shape for the 66-inch-diameter capsule.

Annealing. No annealing of the model pentagons was performed after machining, as there were no contoured boxes or portable molds to support them during annealing. The annealing of the model pentagons was performed only after complete assembly and bonding of the model spheres, when the individual spherical pentagons could not readily change their curvature.

Large-scale spherical pentagons with a 33-inch spherical radius were annealed after completion of all the machining operations. This was performed to decrease the residual stresses introduced into the acrylic plastic by thermoforming, bandsawing, and milling. It was hoped that the decrease, if not complete elimination, of tensile stresses on the acrylic plastic surfaces would eliminate the tendency of acrylic plastic to craze on the machined surfaces.

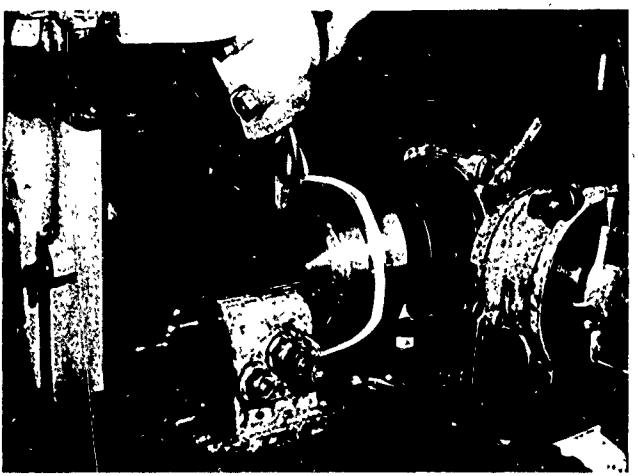

Figure 32. Milling the edges of spherical pentagon for the 15-inch-diameter capsule.

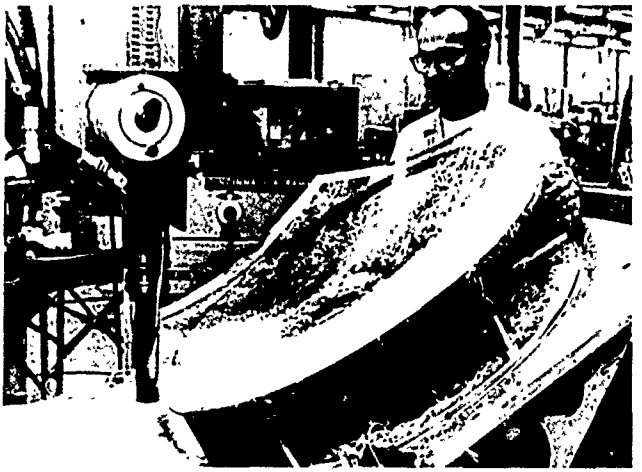

Figure 33. Milling the edges of spherical pentagon for the 66 inch diameter capsule.

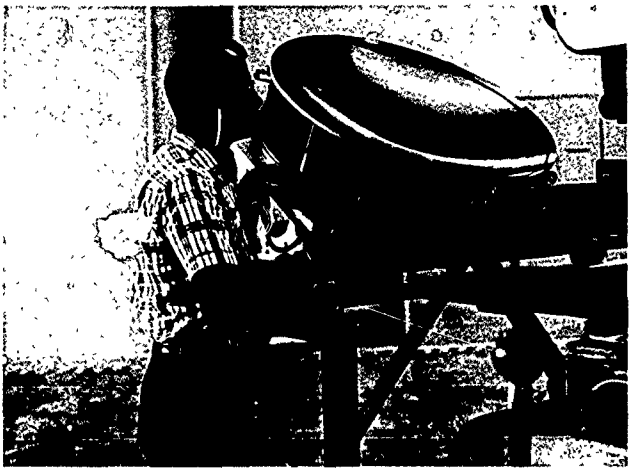

Figure 34. Indexing head with a vacuum operated chuck for the large spherical pentagons.

Figure 35. Dimensional check of large spherical pentagon prior to removing it from chuck.

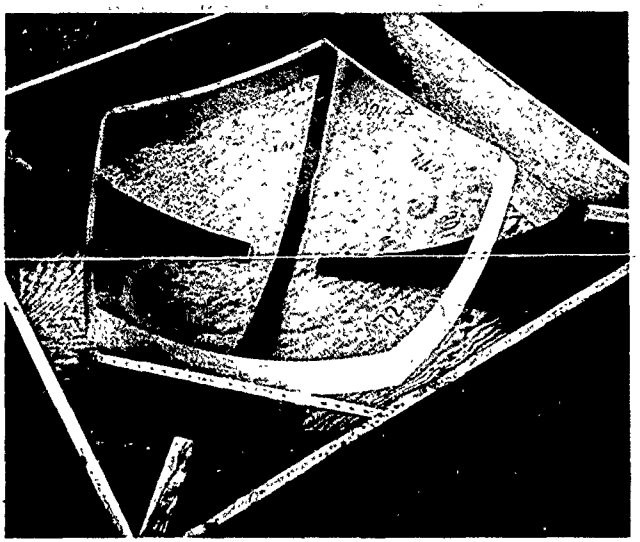

Figure 36. Storage of completed large pentagons between individual steps of the fabrication process.

Annealing of the large pentagons was performed in a walk-in oven. Each pentagon was placed there individually for 24 hours either in a wooden storage box, or in the mold, while the temperature was maintained at 160°F. After the annealing period, the temperature in the oven was slowly reduced to 100°F at which time the pentagon was removed from the oven.

Quality Control. Since it was predicted prior to the machining and annealing operations that some realignment of the curvature would take place on the full-scale pentagons when residual stresses were relieved, a dimensional check was made on all pentagons after all major steps in their fabrication were completed (Appendix A). Thus, a measurement of the sphericity and thickness was made on all spherical pentagons after annealing, but prior to assembly and bonding into a sphere. The effects of bandsawing, milling, and annealing on the sphericity of the pentagon can be seen by comparing the sphericity of the first thermoformed spherical sector (Figure 30a) to the sphericity of the annealed pentagon made from that sector (Figure 37).

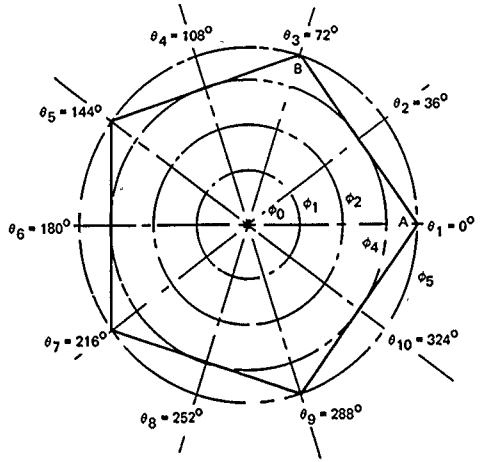

Typical Pentagon

φ angle

$\phi_0 = 0^\circ 0'$ $\phi_4 = 31^\circ 30'$

$\phi_1 = 10^\circ 30'$ $\phi_5 = 37^\circ 10'$

$\phi_2 = 21^\circ 0'$

Note:

1. Points A and B were marked to give orientation.
2. Angles ϕ_1 through ϕ_5 are angles through the center of the sphere.
3. Angles θ_1 through θ_{10} are measured from the center of the pentagon.
4. Pentagons are for the prototype 66 inch NEMO capsule.
5. ΔR denotes change in internal surface curvature from specified 30 500 inches; + indicates shorter radius, while – indicates longer radius.

Point	Pentagon 18	
	ΔR	Thickness
$\theta_1 - \phi_0$	+0 007	2 385
$\theta_1 - \phi_1$	-0 018	2.405
$\theta_1 - \phi_2$	-0 045	2.435
$\theta_1 - \phi_4$	-0 089	2.485
$\theta_1 - \phi_5$	-0.127	2 510
$\theta_2 - \phi_1$	0	2.405
$\theta_2 - \phi_2$	-0 015	2.435
$\theta_2 - \phi_4$	-0 065	2.465
$\theta_3 - \phi_1$	+0 015	2 400
$\theta_3 - \phi_2$	+0 013	2.405
$\theta_3 - \phi_4$	-0 038	2.435
$\theta_3 - \phi_5$	-0.083	2.470
$\theta_4 - \phi_1$	+0 023	2.390
$\theta_4 - \phi_2$	+0.017	2.400
$\theta_4 - \phi_4$	-0 024	2.420
$\theta_5 - \phi_1$	+0 018	2.395
$\theta_5 - \phi_2$	+0 017	2.405
$\theta_5 - \phi_4$	-0 039	2.450
$\theta_5 - \phi_5$	-0.100	2.475
$\theta_6 - \phi_1$	+0 004	2.395
$\theta_6 - \phi_2$	+0 020	2.400
$\theta_6 - \phi_4$	-0 073	2.460
$\theta_7 - \phi_1$	-0 010	2.400
$\theta_7 - \phi_2$	-0 014	2.430
$\theta_7 - \phi_4$	-0.134	2.570
$\theta_7 - \phi_5$	-0.187	2.550
$\theta_8 - \phi_1$	-0 023	2.415
$\theta_8 - \phi_2$	-0 070	2.485
$\theta_8 - \phi_4$	-0.168	2.555
$\theta_9 - \phi_1$	-0 028	2.428
$\theta_9 - \phi_2$	-0 074	2.485
$\theta_9 - \phi_4$	-0.140	2.545
$\theta_9 - \phi_5$	-0.180	2.560
$\theta_{10} - \phi_1$	-0 029	2.415
$\theta_{10} - \phi_2$	-0 065	2.410
$\theta_{10} - \phi_4$	-0.120	2.515

Figure 37. Typical deviations from nominal 33-inch radius of curvature on a completed spherical pentagon for a 66-inch diameter capsule.

Several conclusions can be made from that comparison. First, the deviations from specified sphericity are larger after machining operations than prior to them by a factor of 2 to 4. Second, even with the considerable increases in spherical deviations, they are less than 1% of specified radius.

Similar measurements (Appendix C) were taken on model pentagons (Figure 38). The only difference here was that the measurements did not reflect any deviations from sphericity due to annealing process, as the model pentagons were not annealed until they were assembled and bonded into spheres.

Bonding. Initially the assembly of both the models and the 66-inch spheres was planned to be by the solvent-cement technique. The arguments for this bonding technique were that (1) the tensile strength of solvent-bonded joints can be made to equal that of the parent material by proper curing schedule, (2) all the operational parameters of this bonding technique are well known, and (3) the joint, if properly made, is completely colorless and transparent.

Although the arguments cited in support of this technique are valid, the results from bonding the first model capsule were quite disappointing. Either the joints were full of air cavities (Figure 39) and surfaces unwetted by the solvent because of insufficient clearance between the individual pentagon for penetration of solvent, or the joints were completely wetted by the solvent, but because of too large a separation between pentagons, the solvent upon drying left a very weak joint.

The reasons for this unsatisfactory performance of solvent-cement technique were many. The major ones were (1) all the pentagons had to be bonded simultaneously so that mismatches between individual pentagons could be distributed over the whole sphere, (2) edges of pentagons were not presoaked in solvent prior to assembly because of physical impossibility of presoaking the five edges of all pentagons simultaneously prior to assembly, (3) joint clearances and clamping forces varied from point to point depending on the dimensional deviation from nominal pentagon dimensions, and (4) it was nearly impossible to apply a calibrated clamping restraint on the whole sphere during bonding.

In order to improve the quality of the joints, an attempt was made to control the clearances in the joints so that complete penetration of the joints by solvent would take place. After an exploratory investigation into this problem, it was found that a 0.005-inch clearance was required to create the capillary force that would draw the solvent into all the joint spaces. Unfortunately, the joint with a 0.005-inch clearance maintained by spacers had nearly zero strength as the evaporation of the solvent from the wide joint resulted in very inferior joint bond strength. The decrease of the joint clearance to 0.001 inch by placement of 0.001-inch-thick spacers resulted in higher joint bond strength, but did not permit the solvent to wet all the joint surfaces.

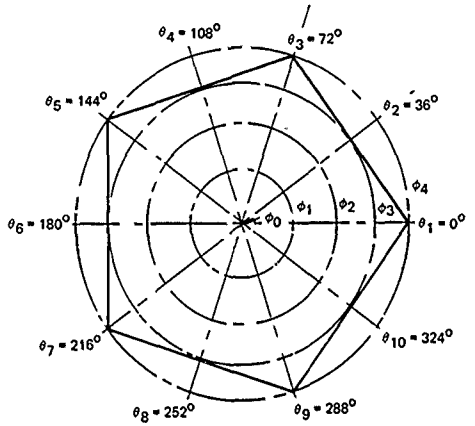

Pentagon Number 6

ϕ angle
$\phi_0 = 0^\circ 0'$
$\phi_1 = 10^\circ 30'$
$\phi_2 = 21^\circ 0'$
$\phi_3 = 31^\circ 30'$
$\phi_4 = 37^\circ 10'$

Note:

1. Mark on each pentagon the pentagon number at center and angle numbers at edge. These numbers should be maintained throughout fabrication of complete sphere.
2. Angles ϕ_1 through ϕ_4 are angles through center of sphere.
3. Angles θ_1 through θ_{10} are measured from the center of pentagon.
4. Δr denotes change in internal surface curvature from specified 7.000 inches; + indicates shorter radius, while − indicates longer radius.

Point	Δr	Thickness
$\theta_1 - \phi_0$	+0 003	0.485
$\theta_1 - \phi_1$	+0 0015	0 475
$\theta_1 - \phi_2$	0 000	0.475
$\theta_1 - \phi_3$	-0 006	0 475
$\theta_1 - \phi_4$	-0 018	0.485
$\theta_2 - \phi_1$	+0 0015	0.475
$\theta_2 - \phi_2$	0 000	0 475
$\theta_2 - \phi_3$	-0 011	0.475
$\theta_3 - \phi_1$	+0 0015	0.470
$\theta_3 - \phi_2$	0 000	0.472
$\theta_3 - \phi_3$	-0 004	0.475
$\theta_3 - \phi_4$	-0 018	0.485
$\theta_4 - \phi_1$	+0.002	0.472
$\theta_4 - \phi_2$	0.000	0 472
$\theta_4 - \phi_3$	-0 009	0.470
$\theta_5 - \phi_1$	+0.0015	0.475
$\theta_5 - \phi_2$	0 000	0.475
$\theta_5 - \phi_3$	-0.004	0.485
$\theta_5 - \phi_4$	-0.010	0.485
$\theta_5 - \phi_1$	+0 003	0.475
$\theta_6 - \phi_2$	0 000	0.485
$\theta_6 - \phi_3$	-0.009	0.485
$\theta_7 - \phi_1$	+0 001	0.472
$\theta_7 - \phi_2$	0.000	0.475
$\theta_7 - \phi_3$	-0 005	0.485
$\theta_7 - \phi_4$	-0 009	0 485
$\theta_8 - \phi_1$	+0 003	0.475
$\theta_8 - \phi_2$	0 000	0.482
$\theta_8 - \phi_3$	-0 007	0.485
$\theta_9 - \phi_1$	+0 0015	0.475
$\theta_9 - \phi_2$	0.000	0.480
$\theta_9 - \phi_3$	-0 004	0 487
$\theta_9 - \phi_4$	-0.009	0.492
$\theta_{10} - \phi_1$	+0 0025	0 475
$\theta_{10} - \phi_2$	0.000	0 475
$\theta_{10} - \phi_3$	-0 009	0 480

Figure 38. Typical deviations from nominal 7.5-inch radius of curvature on a completed spherical pentagon for 15-inch-diameter capsule model.

A procedure was finally developed for solvent bonding model capsules that produced high-strength bonds over 100% of the joint area (Figure 40). (1) assemble the model capsule with 0.005-inch spacers between pentagons, (2) place a clamping restraint on it in the form of rubber bands cut from auto inner tubes, (3) introduce solvent into the joint by means of a syringe (results in complete wetting of joint surfaces by capillary action), and (4) rapidly remove the spacers before the joint surfaces are bonded, thus permitting the clamping forces to bring the joint surfaces into intimate contact. This procedure was used to assemble and bond model NEMO capsules 1 through 11.

The annealing of the solvent-bonded model capsules consisted of placing them in an oven heated to 175°F and leaving them there for 24 hours at that temperature. The annealing process, however, did not eliminate completely the residual stresses in the joints introduced into the capsule by the bonding process (Figure 41). Since it was felt that the remaining residual stresses in the model capsule (approximately 1,300-psi shear stress in the joint area) would not significantly decrease the implosion pressure of the capsule, no further effort was made to eliminate the residual stresses after the single annealing operation described.

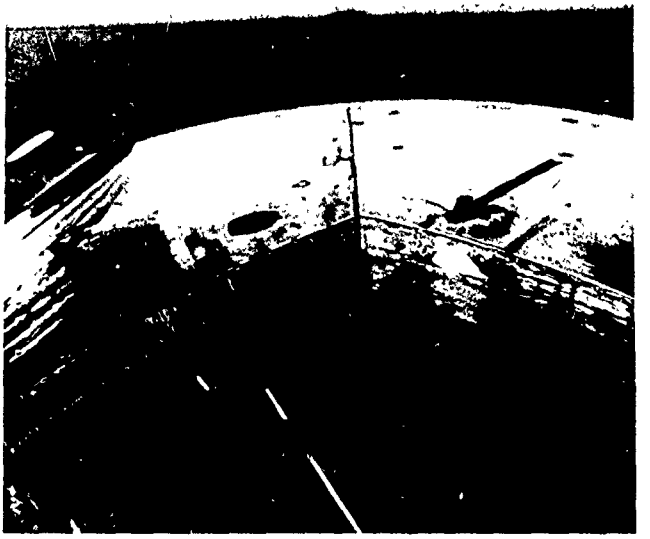

Figure 39. Typical air bubbles in an improperly solvent-bonded joint on the 15-inch-diameter capsule model.

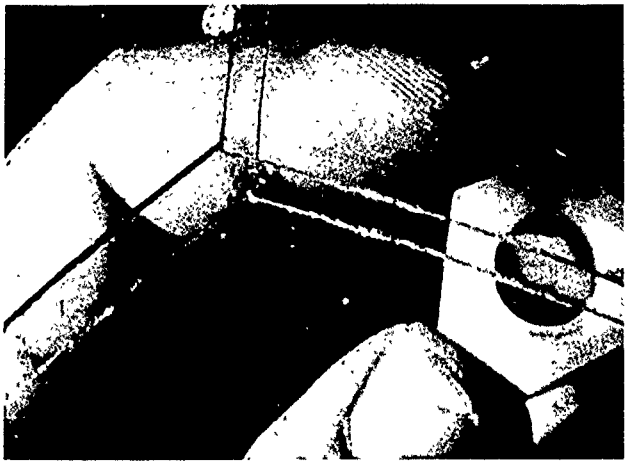

Figure 40. Typical sample of a properly solvent-bonded joint on a 15-inch-diameter capsule model.

Although the procedure developed for solvent bonding model capsules produced satisfactory joints, grave doubts existed whether this technique would produce satisfactory results for the large-scale capsule. It appeared that in order to solvent bond the large pentagons, the dimensional control of individual pentagons would have to be so strict as to make the fabrication cost unacceptable. Also, the cost of a clamping system for placing the solvent-bonded joints in a large sphere under uniform compression would, in all probability, be higher than the cost of fabrication up to the bonding stage. In view of these problems, it was decided to find a different joint bonding technique that, although being as costly as the solvent bonding technique for the models, would be distinctly less for the large-scale capsule.

The alternate bonding technique investigated was the cast-in-place adhesive. The prime characteristics of this bonding technique are: (1) the pieces to be bonded are maintained in a fixed relationship to each other by spacers that do not permit the pieces to contact each other, (2) the space between the acrylic plastic members is made fluid tight by placement of adhesive tapes over both sides of the space, (3) the adhesive is poured into the taped-over space by means of a funnel or squeeze bottle, and (4) filling the joint space is done in more than one pour, with the mechanical spacer being removed from the joint after the first increment of adhesive-filled joint has set, but before the succeeding increment of adhesive covers it (Figure 42).

Figure 41. Residual stresses in a solvent-bonded 15-inch-diameter capsule not removed by annealing operation; maximum shear stress approximately 1,300 psi.

The advantages of this bonding technique are: (1) the dimensional tolerances of spherical pentagons being bonded need not be tight because reasonable dimensional deviations are taken care of by the 0.100-to-0.150-inch-wide joint space, (2) there is no requirement for clamping forces on the members being bonded, (3) irregularly shaped surfaces can be joined, providing the joint space can be sealed on both sides with adhesive tape, (4) there is no requirement for fine finish on the acrylic plastic surfaces forming the two sides of the joint, and (5) the bonding of a large structure can proceed by small increments with each joint increment becoming set before the next pouring is performed.

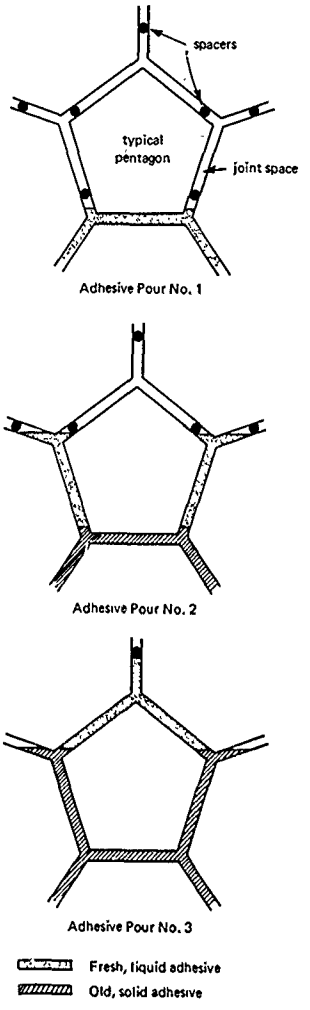

Figure 42. Procedure for casting of self-polymerizing joints in acrylic plastic capsules.

In view of the many advantages that such a bonding technique possesses for fabrication of large-scale acrylic plastic capsules, it was decided to evaluate this technique first on small-scale capsules and on joint-test specimens simulating the joint dimensions of the 66-inch capsule. Four cast-in-place adhesives were investigated: epoxy, polyester, PS-18 acrylic cement, and PS-30 acrylic cement. The epoxy and polyester adhesives were almost immediately discarded as the tensile strength of a joint between acrylic plastic members filled with these adhesives was less than 1,500 psi for epoxy and 1,000 psi for polyester. Although the compressive strength of these two adhesives was indistinguishable from that of the acrylic plastic parent material, the low tensile strength just made these adhesives noncompetitive with the PS-18 and PS-30 acrylic cements. When 2.5-inch-wide acrylic plastic blocks were bonded with acrylic cement in 0.125-inch-wide joints, it was found that the tensile strength for PS-18 was consistently higher than 5,000 psi, while for PS-30 it was higher than 4,000 psi (Table 3). Compressive strength of these joints was found to be of approximately the same magnitude as that of the parent acrylic plastic material, but their deformation under load was somewhat higher.

Table 3. Strength of Adhesive-Bonded Joints and Acrylic Plastic

(The test specimens were prepared by different technicians and at different times.)

Material[a]	Pretest Treatment			Type of Test	No. of Test Specimens	Ultimate Stress[b] (psi)		
	Age (days)	Temperature (°F)	Pressure			Maximum	Minimum	Average
PS-18 adhesive	1-5	65-75	1 atm (dry)	tensile[c]	10	8,280	5,150	6,700
				compressive[d]	4	17,800	16,980	17,120
	400	50-60	120-foot depth (seawater)	tensile	4	9,450	8,010	8,890
				compressive	4	16,950	16,400	16,700
PS-30 adhesive	1-5	65-75	1 atm (dry)	tensile	10	6,450	4,050	6,100
				compressive	4	17,300	15,750	16,610
	400	50-60	120-foot depth (seawater)	tensile	4	6,190	5,100	5,710
				compressive	4	16,800	15,300	16,300
grade G Plexiglas	700	65-75	1 atm (dry)	tensile	4	10,440	10,100	10,250
				compressive	4	18,740	17,650	18,150
	400	50-60	120-foot depth (seawater)	tensile	4	10,100	9,700	9,950
				compressive	8	17,900	16,920	17,380

[a] All of the bond test specimens were machined from 12 x 12 x 2.5-inch acrylic grade G Plexiglas blocks assembled by bonding 6 x 6 x 2.5-inch acrylic plastic plates with an 0.125-inch-wide adhesive joint.

[b] All test specimens tested at 65 to 75°F temperature and an 0.035-in./min load rate.

[c] Tensile specimens were 0.500 x 0.750 inch in cross section.

[d] Compressive specimens were 0.750 x 0.750 x 1.500 inches.

Since it was known that both PS-18 and PS-30 adhesive joints deteriorate in strength with age when exposed to atmospheric environment, it was questioned whether immersion in seawater accelerates this aging process further. To answer this question, a bonded acrylic plastic block was placed in the Pacific off Point Mugu at a depth of 120 feet. After 13 months of continuous submersion, the acrylic plastic block was retrieved, and material test specimens were machined from it. Because the block was rather small, and only a limited number of test specimens could be machined from it, only tensile and compressive test specimens were cut from it. These test specimens were tested at 70°F to establish the ultimate tensile and compressive strength of the PS-18 and PS-30 cast joint after 1 year's exposure to seawater.

When the test specimens were tested to destruction, it was found (Table 3) that the average tensile strength of the 0.125-inch-wide, adhesive-filled joints was 8,890 psi for PS-18 and 5,710 psi for PS-30 joints. Since no control block was bonded at the time when the ocean test specimen was fabricated and placed in the ocean, no accurate comparison can be made with test specimens exposed for 1 year to atmospheric environment. A general comparison, however, can be made with tensile and compressive strengths of PS-18 and PS-30 adhesive-bonded joints tested several days after bonding. The comparison between strengths of the fresh joints and those 1-year old but kept submerged in the ocean showed that no statistically significant decrease in tensile or compressive strength occurred for PS-18 or PS-30 adhesive-bonded joints. As a matter of fact, it appears that the strength of a PS-18 adhesive-bonded joint increased somewhat because of long-term immersion in the ocean (Table 3).

Tests were conducted also on grade G Plexiglas material after immersion in the ocean for 13 months to verify tests conducted by others[19, 20] indicating that there is no statistically significant degradation of material properties in acrylic plastic after long-term immersion in the ocean even at depths in excess of several thousand feet. Taking into consideration the experimental findings that neither the acrylic plastic nor the PS-18 adhesive joints deteriorated in strength during a 1-year immersion in seawater, it was decided to proceed with the construction of the full-scale acrylic plastic capsule utilizing PS-18 adhesive.

Although no particular problems were encountered during bonding of PS-18 joint test specimens, it remained to be seen how well this bonding technique would work in practice while bonding the spherical pentagons in a capsule. For this reason it was decided to discontinue bonding model capsules with the solvent-cement technique and to bond all the subsequent model capsules with PS-18 cement.

This was accomplished in the following manner: First, the spherical pentagons were made smaller (distance across tips decreased from 8.660 inches to 8.553 inches and true chord length from 5.352 inches to 5.286 inches) so that 0.125-inch-wide joints could be incorporated between the individual pentagons in the assembled hull. Second, an assembly jig was utilized that, although initially developed for providing precise alignment and clamping of all pentagons during solvent-bonding of joints (Figure 43), could be also used for accurate alignment and support of six pentagons during bonding operations employing cast-in-place adhesive. Third, after removal of all spacers between pentagons, the joint spaces were taped over on the interior and exterior surfaces of the hull with Rohm & Haas 670 cellophane fiber tape to contain the adhesive during casting. Fourth, the adhesive was mixed in the proportions recommended by the supplier, degassed under vacuum for approximately 15 minutes, and poured into the joint spaces by means of a gravity-fed funnel. The recommended procedure for mixing of PS-18 adhesive with a 60-minute pot life at room temperature was to dissolve one 2.4-gram capsule of catalyst (50-50 mix of granular benzoyl peroxide and camphor) in 113 grams of resin (methyl methacrylate monomer and methyl methacrylate polymer resin) followed by addition of 3 cc of promoter to the two already mixed components. Since the spacers were removed prior to taping over the interior surface of the joints between the six pentagons, the adhesive could be placed into all the joints of a hemisphere in one pour. Thus the adhesive was mixed in one batch and placed into the joint spaces in a single continuous pour. Fifth, upon setting of the adhesive which occurred in approximately an hour, the tapes were stripped from the joints and the six pentagons bonded into a hemisphere were removed from the jig. A similar procedure was repeated with the other six pentagons. Upon completion of the second hemisphere, both hemispheres were placed upon each other separated by spacers which, prior to placement of the tape on the exterior of the joint, were removed. The joint between the hemisphere was subsequently filled with adhesive. Sixth, the model was placed into an oven for annealing at 175°F for 24 hours. The residual stresses remaining in the capsule after annealing were of approximately the same magnitude and uniformity (Figure 44) as those resulting from solvent-bonding of model capsules (approximately 1,300-psi shear stress in the joints).

The successful casting of joints in the model capsules and subsequent testing that showed no significant difference in structural response to hydrostatic pressure from models bonded with solvent cement proved conclusively that casting of PS-18 adhesive into 0.125-inch-wide joints (Figure 45) was acceptable from both fabrication and operational viewpoints and thus should be applied to bonding of large-scale acrylic plastic capsules.

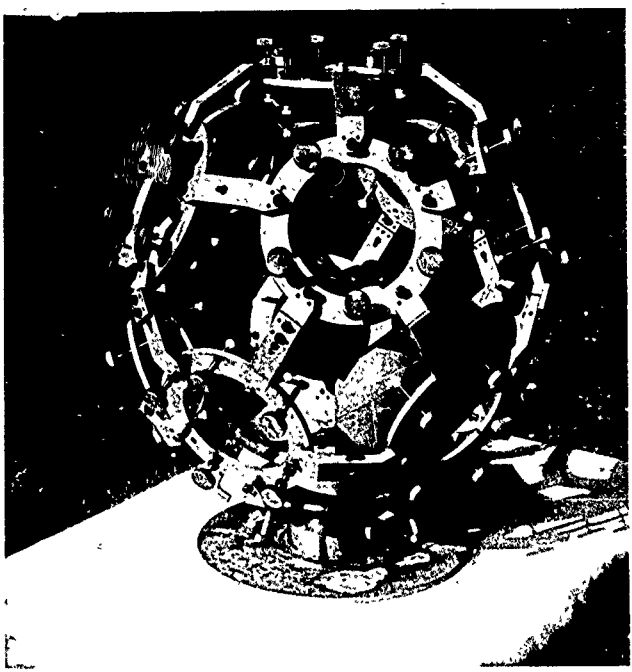

Figure 43. Jig for assembly of individual spherical pentagons into a 15-inch-diameter capsule.

Large-scale capsules were also fabricated from undersize spherical pentagons, that when assembled allowed an 0.125-inch joint space to exist between individual pentagons. Since the fabrication of an assembly jig for the large-scale capsule according to the same design that was used for the model scale capsule would have been expensive, a simpler jig was designed and built. The basic difference between the large-scale capsule jig and the model jig was that the large assembly jig permitted access for the shop personnel to the interior of the hemisphere to make the taping of joints on the interior easier.

The large-scale capsule was assembled and bonded like the models in three phases—the first two phases resulted in the assembly and bonding of pentagons into two hemispheres, while the third one culminated in the assembly of two hemispheres into a single sphere (Figures 46 through 50).

Figure 44. Residual stresses not removed by annealing in a 15-inch diameter capsule with cast-in-place joints.

This method of assembling and bonding the capsule possessed several disadvantages not present in the method of assembly used on solvent-bonded models, which permitted bonding of all 12 pentagons in one operation. These disadvantages were (1) difficulty in checking the sphericity of the assembled hemisphere prior to bonding, (2) distribution of dimensional mismatches between individual pentagons over the surface of a hemisphere only, and (3) inability to accomplish a perfect match between the irregular joint surfaces of the two mating hemispheres. But it was hoped that with proper attention to the sphericity and diameter of each individual hemisphere, a capsule could be assembled with small deviations from nominal diameter and sphericity.

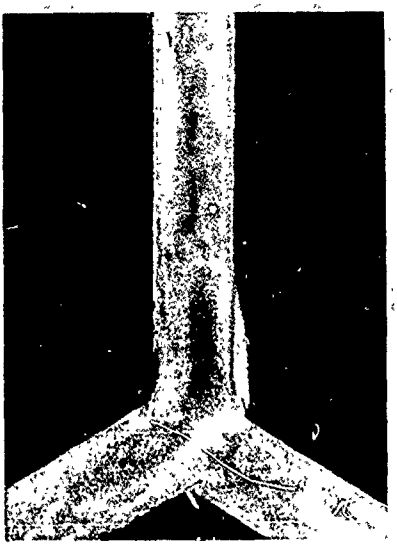

Figure 45.

Typical sample of a properly cast-in-place joint in a 15-inch-diameter capsule.

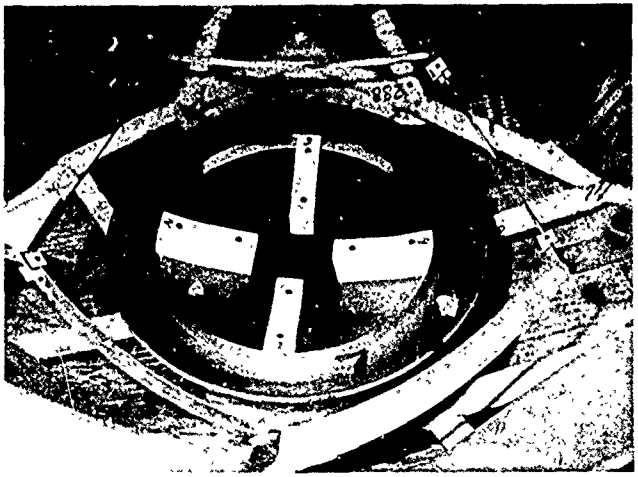

Figure 46. Jig with contoured spacers for centering the hemisphere for bonding.

Figure 47. Sealing of joint space between spherical pentagons prior to bonding.

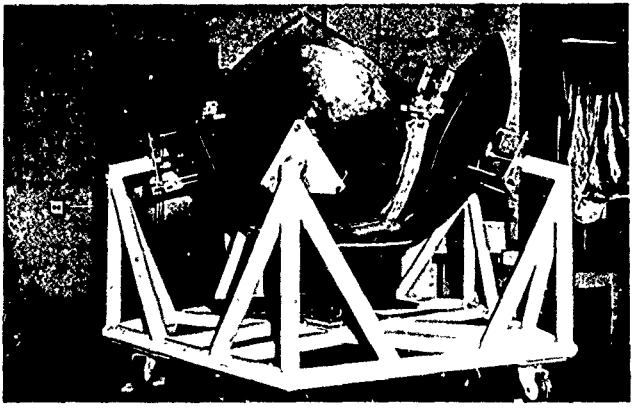

Figure 48. Acrylic plastic hemisphere assembled from six spherical pentagons prior to bonding operation.

Although the preparation for bonding was almost identical to the one used for scale models; considerably more difficulties were encountered in the bonding of the large-scale capsule. These difficulties can be placed into two categories: (1) mixing and pouring of large quantities of adhesive and (2) elimination of cavities and separation spaces in cast joints. The problem in the first category centered around mixing large quantities of adhesive components without inclusion of air bubbles and at the right temperature so that the mix would not set during pouring into the joints while at the same time retaining the ability to set in the joint within a short span of time. If the chemical reaction in the mix progressed too rapidly (because of the large mass of adhesive involved) during pouring, it not only generated an excess of bubbles but the adhesive would set in some portions of the joint prior to filling it completely. When this occurred, access holes had to be drilled through already-set adhesive to permit trepanning the voids in joint spaces so that they could be filled with adhesive by means of a syringe. On the other hand, when the mix reacted so slowly that several hours were required before it set, the components of the mix attacked the acrylic plastic surfaces of the joint causing them to craze. Since the exact temperature was not known to which the components of the mix had to be precooled to prevent premature setting during pouring while still permitting rapid setting in joint, the trial and error approach was utilized. The problem of arriving at a satisfactory mix temperature was further complicated by the variation in ambient temperature during the several day-long periods required for casting the joints. As a result, the placement of PS-18 into the joint spaces was a continuous trial and error operation. Some of the joint sections were filled with the adhesive without any trouble, while others had voids or separation spaces that had to be laboriously drilled out and refilled because of the too-rapid or too-slow setting of the adhesive. Since considerable shrinkage took place in the large volume of joint space, the tape covering the joint had to be placed over the joint in such a manner that the cast adhesive would develop an external bead over the joint. To form this bead, the tape was partially folded over the joint and, since the heat of the reaction in the cast adhesive may change the shape of the fold in the tape, it was stiffened locally in the fold area by aluminum foil. This aluminum foil provided a further advantage by giving the joint bead a smooth surface.

The troubles, however, did not terminate with the placement and setting of adhesive in the joint spaces, because small dispersed cavities (Figure 51) and separation spaces (Figure 52) were found in the joint after it had set. The separation spaces generally were found at the boundaries between individual pours. Only after a brief investigation into methods of eliminating them was it found that the removal of the surface skin from the preceding already set pour would in most cases eliminate the separation spaces between neighboring PS-18 pours in the joint. Separation spaces

that were already present in the joints because the surface of the preceding pour was not removed were eliminated in some cases by drilling or milling out (trepanning) the separation space and refilling it with fresh PS-18. No reliable method was found to prevent formation of small dispersed cavities in the set adhesive, although it can be hypothesized that a too-rapid setting rate (triggered by high ambient atmospheric temperature) was probably their cause. This hypothesis is substantiated by the fact that some of the pours resulted in completely cavity-free joints, while others had many cavities even though the chemical composition of the mix was identical in all cases. Most of the cavities were too small to merit a trepanning operation, particularly since it was felt that in joints subjected to operational tensile stresses less than 200 psi, the debilitating effect of cavities on the 4,000-to-5,000-psi ability of the joint to withstand 200-psi stresses was negligible. Only in very few cases where the cavities appeared to be interconnected was a trepanning operation performed and the cut refilled with fresh PS-18 adhesive. The trepanning and refilling of separation spaces in the joint, however, generally did not decrease the peak residual stress level at that location, and in most cases introduced many incipient fine cracks (Figures 53 and B-2b). For this reason, it was used only when the separation space penetrated the whole joint width creating a leak (three locations).

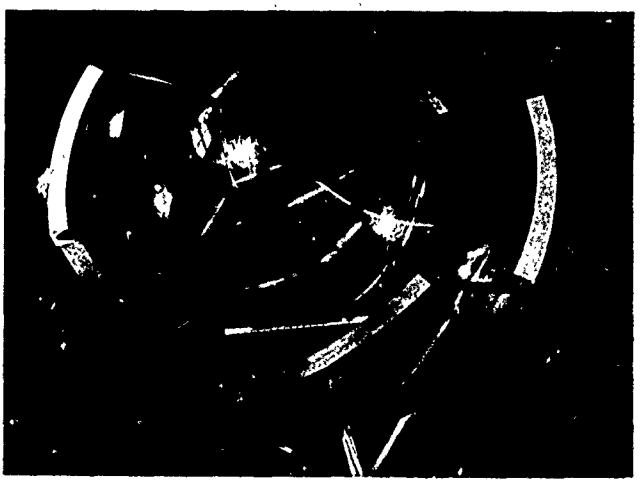

Figure 49. Bonded hemisphere after removal from assembly jig.

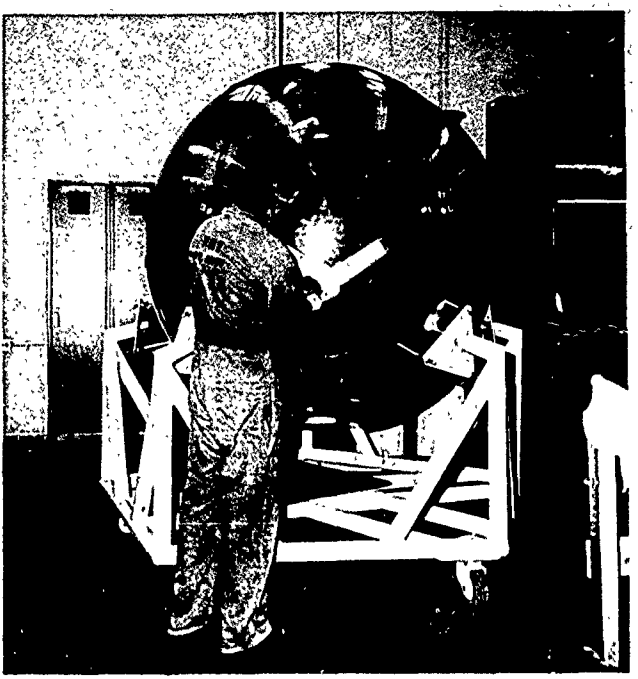

Figure 50. Preparing the two hemispheres for bonding together into a sphere.

Because of all the problems encountered during the bonding operations, the resulting joints in the 66-inch prototype capsule leave much to be desired and constitute a fruitful area for future improvement. However, one very valuable finding about joints could be expected from hydrostatic testing of the prototype large-scale capsule: *Successful, structural integrity of the hull and joints under both operational and proof pressures would serve as proof that the presence of discontinuities (dispersed cavities and separation spaces) in the joints is not a bar to safe operational performance of a spherical acrylic plastic capsule under external hydrostatic loading.* On the other hand, if the cavities and separation spaces served as fatigue crack initiators leading to early cyclic fatigue failure, future joints would have to be cast utilizing more refined casting techniques and under tighter quality control to prevent the occurrence of *any* cavities.

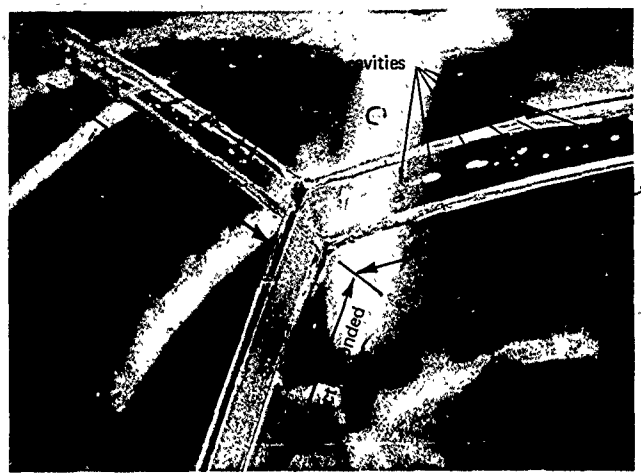

Figure 51. Typical cavities in an imperfectly bonded segment of a joint in 66-inch-diameter capsule.

After completion of bonding, the large-scale acrylic plastic hull was annealed for 124 hours at 160°F in a temperature-controlled oven. The annealing process did not remove all the residual stresses from the joints resulting from the bonding process. The residual stresses in the joints were found to be approximately of the same order of magnitude (but somewhat less) as the residual stresses in the model capsule (Figure 54). The basic difference between the residual stresses in the model capsule and the large-scale capsule was in distribution. In the model capsule, the stresses are fairly uniform in all of the joints, but in the large-scale capsule the magnitude of stresses varies markedly from one location to another in the joint. This, of course, is the result of bonding the joints in the large-scale capsule in small increments, each solidifying before the next one is cast. *Thus, it appears that casting of joints in small increments is less desirable than casting them in one or two increments, or preferably in a single operation.*

Polishing of the exterior and interior of the hull completed the fabrication of the large-scale acrylic plastic hull. Sphericity and diametral measurements revealed that zealous polishing of rough joints removed an excessive amount of acrylic plastic. The lesson that could be drawn from this is that *polishing should be performed with great care, and if the choice*

exists of removing an excessive amount of acrylic plastic versus having some roughness around joint mismatches, it is better to leave that roughness. Also, extreme care must be exercised not to exert so much pressure on the buffing wheel that local heating and galling of the acrylic plastic occurs. Since this care was not exercised at all times during buffing of the large-scale capsule, some surface areas on the acrylic plastic hull were locally scuffed.

Dimensional Inspection. At the completion of fabrication, each individual scale model was checked for its sphericity and diameter. This dimensional check together with previously conducted sphericity and thickness measurements of individual pentagons constituted the complete record for an individual NEMO model. Since the paperwork representing the complete dimensional record of each model NEMO is quite voluminous, only the dimensional record for one typical NEMO model has been included in this report (Appendix C). This dimensional record is briefly summarized here:

	NEMO Model 18	Nominal
Hull Thickness (in.)	0.515-0.465	0.500
Internal Radius (in.)	7.028-6.994	7.000
Outside Diameter (in.)	15.040-14.995	15.000

These deviations from the nominal can be considered representative for all the other scale models with one or two exceptions. One of the models, NEMO no. 1, had sphericity deviations considerably in excess of the representative values enumerated above. The internal sphericity and thickness of this model varied from 7.200 to 6.875 inches and from 0.495 to 0.450 inch, respectively. Although those sphericity deviations were considered unacceptable (1,000% larger than the permissible deviation of 0.03t) the NEMO Model no. 1 was used in the test program to determine the effect of excessive sphericity deviations on the collapse pressure of acrylic plastic hulls under long-term hydrostatic loading.

The measurement of thickness and sphericity on individual pentagons was performed utilizing micrometers and a dial gage mounted in a vertical mill. Upon assembly of pentagons into a sphere, the sphericity was measured with a female template and feeler gage while the diameter was measured with dial-indicator-equipped calipers.

Figure 52. Typical separation space in an improperly bonded segment of the joint in the 66-inch-diameter capsule.

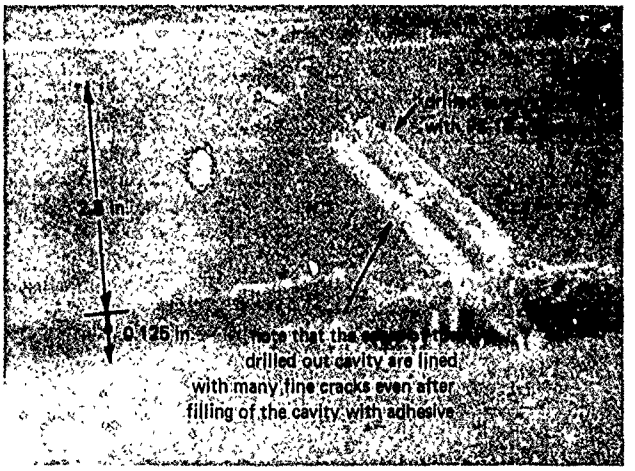

Figure 53. Results of a local trepanning operation in the joint of the 66 inch-diameter capsule.

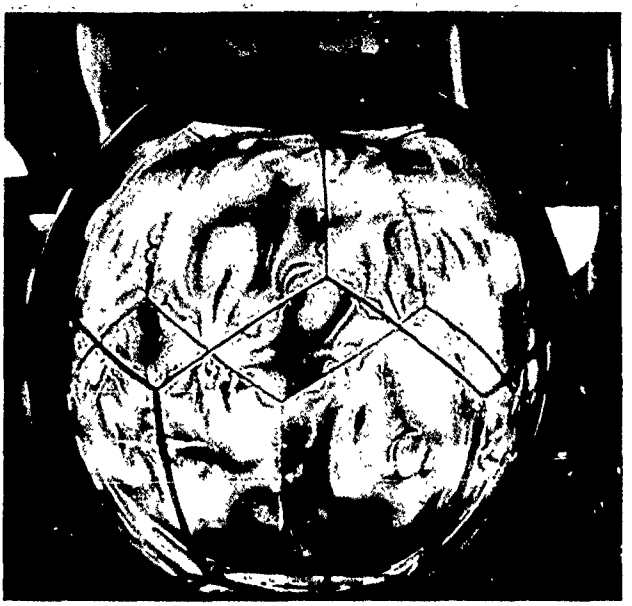

(a) Overview.

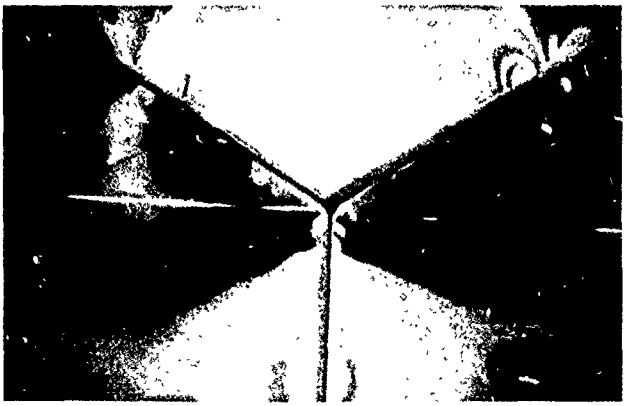

(b) Detail.

Figure 54. Residual stresses in the 66 inch diameter capsule not removed by the annealing operation.

Figure 55. Measuring the sphericity of the bonded 66-inch-diameter capsule with a template having a nominal radius of 33 inches.

The large-scale acrylic plastic capsule was dimensionally checked (Figures 55 and 56) in the same manner as the scale models by using a template, dial gage, feeler gages, and caliper mounted micrometers. All the dimensional control data taken on individual pentagons prior to assembly, and subsequently after bonding and annealing of the large-scale acrylic plastic hull has been included in this report (Appendix A) to serve as a standard of comparison for (1) future operational large-scale NEMO hulls and (2) show the effect scaling up models has on dimensional deviations. The dimensional control data of the large-scale NEMO hull can be summarized here by stating that the wall thickness and internal sphericity of individual pentagons prior

to assembly varied from 2.285 to 2.585 inches and 30.702 to 30.345 inches, respectively, while the external sphericity and the diameter of the assembled capsule varied from 33.134 to 33.000 inches and 66.158 to 65.920 inches, respectively. The difference between sphericity measurements taken on individual pentagons and on the finished hull are attributed in a large measure to (1) mismatch between individual pentagons during assembly, (2) excessive polishing and buffing of the joint surface areas, and (3) difference in measuring techniques (in one case dial indicator measurement of internal radius while in the other case template measurement of the external radius).

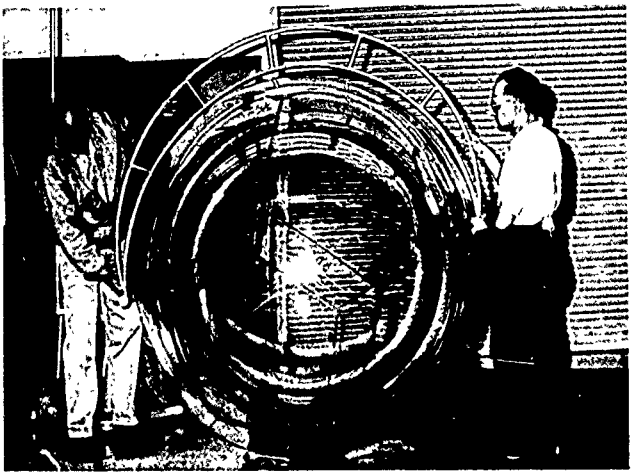

Figure 56. Measuring the diametral deviations of the bonded 66-inch capsule with a 66-inch-throat micrometer.

The magnitudes of sphericity, thickness, and diametral deviations from specified nominal values when related to the size of the large-scale capsule show that these deviations are approximately of the same magnitude as those measured on model capsules. While the relative sphericity deviation from the specified internal radius on scale models was within +0.09 and -0.4%, on the large-scale acrylic plastic hull it was within +0.50 and -0.66%. The relative diametral deviation from nominal diameter for scale models was within +0.26 and -0.03%, while the large-scale hull's diametral deviations were within +0.25 and -0.12%. Since the comparison of relative dimensional deviations has

shown that the large-scale hull presents approximately as perfect a sphere as the models, any data generated by testing of small-scale models should be considered as applicable to the prediction of large-scale capsule performance. Also, it can be hypothesized that scaling up acrylic plastic spherical capsule models results in large spheres with approximately the same relative dimensional deviations, providing the same fabrication method is used for model and large-scale capsules.

Before the discussion of relative dimensional tolerances is concluded, a point brought up in the discussion of the dimensional relationship between model and large-scale capsules should be reemphasized: Since in the fabrication of models it was found that the actual thickness of the hull consistently was *less* than specified, it was decided to order oversize material for the large-scale capsule so that even with the large tolerances on thickness of stock materials the hull thickness would not be below specified dimensions. Thus, 2.500-inch stock material was used in large-scale capsule, although 2.250-inch nominal thickness is actually required on the basis of geometrical scaling. Because of this, even though the hull thickness varied from 2.290 to 2.585 inches, it was always above the nominal thickness. This supports the author's assurance that *all the experimental data recorded on models is not only applicable, but even probably conservative since the models were actually 10 to 20% thinner than their nominal thickness arrived at by scaling down the actual large-scale capsule thickness.*

Polar Inserts

The steel structural components required for the assembly of top and bottom polar inserts for the model scale capsules were fabricated by turning 316 stainless steel bar stock in a lathe. Particular emphasis was placed on adherence to the tight angular and dimensional tolerances on the beveled bearing and sealing surfaces on the hatch ring, hatch and bottom plate. Since turning these components for the capsule was a typical metal machining operation, no research or development was necessary during their fabrication.

No problems were encountered in the fabrication of metallic inserts for the 66-inch capsule. The only basic difference between fabrication of the inserts for models and of the 66-inch capsule was the use of type 316L stainless steel and the welding of lifting lugs and bosses on the top hatch assembly instead of milling them out of a solid forging. To make the fabrication economical, the hatch ring, hatch plate, and bottom plate were ordered from suppliers as slightly oversized forgings for machining.

PHASES 3 AND 4—EVALUATION OF DESIGN AND FABRICATION

Capsule Test Specimens

The model capsule series consisted of 22 acrylic plastic hulls with nominal 15-inch outside diameter and 14-inch inside diameter. All were made of one-half-inch grade G Plexiglas plate stock that had been cut, thermoformed, and machined into spherical pentagons that subsequently were assembled and bonded with acrylic adhesives. The details of forming, machining, and bonding were discussed under "Fabrication Process." It is important to note here that models no. 1 through 11 were bonded with solvent-type adhesive while those numbered 11 through 22 were bonded with the self-polymerizing PS-18 cement.

Three distinctly different types of metallic polar plates were fabricated for the model NEMO series.

1. *Operational polar plates* represented faithfully scaled-down hatches and bottom plates proposed for the 120-inch capsule (Figures 19 and 57 through 62). All attempts were made here to reproduce all the working parts and details of the end plates that would be found in the 120-inch NEMO. The top hatch not only had a hatch that opened, but also the locking mechanism required for it. Since two different hatch designs (Figures 19 and 60) were proposed for the 120-inch capsule, two faithfully scaled-down hatch designs were also fabricated for the model capsules. The bottom plate in the operational end plates (Figure 18) incorporated all the penetrations planned for the large capsule. It was felt that if the operational polar steel inserts performed successfully on models without any difficulties (jamming of hatches, failure of electrical penetrators, pulling out of end plates under hoisting operations, or ripping out of retention flanges under hydrostatic loading), no unforeseen difficulties would be encountered during the operation of the proposed 120-inch NEMO system or any scaled-down version of it (for example, the 66-inch system).

Some of the models equipped with operational end plates had also internal tie rods connecting the top hatch with the bottom plate. The purpose of these pretensioned tie rods was to subject the acrylic plastic capsule to compressive preload while the capsule was out of water. Use of tie rods on some of the models was considered necessary to simulate the 120-inch NEMO that probably would utilize internal tie rods for reduction of tensile stresses in the sphere when it floats on sea surface. For the models, each of the four tie rods was preloaded 25 pounds. Together, they applied sufficient force on the polar plates to counteract the forces that would be exerted

upon the end plates by the internally or externally located equipment when the capsule was lowered on the sea surface. The spring assemblies (Figure 23) on the tie rods were of such design that when the capsule was submerged to its design depth of 1,000 feet and remained on station for 100 hours, the diametral decrease of the hull would match the original extension of the springs and thus the total tie-rod preload would decrease to zero. Upon depressurization of the capsule, the dilation of the hull would contract the springs again and the tie-rod system would again be under the specified preload of 100 pounds.

Some models were not equipped with internal tie rods in order to (1) simulate NEMO systems that would not utilize tie rods and (2) to compare experimentally the effect of preloaded tie rods on the critical pressure of the acrylic hulls.

All models equipped with operational polar plates were ballasted with properly distributed weights simulating the weight distribution on the 120-inch-diameter NEMO. A portion of the weights rested on the bottom plate simulating the weight of the crew, controls, and life support, while a sufficiently large weight was suspended from the bottom plate to give the whole model negative buoyancy (Figure 57).

2. *Simulated end plates* were structurally similar to the operational end plates but had none of the structural details or working parts found in the operational end plates (Figure 63). The simulated end plates were used on the majority of models (Figure 64) for economy. Since, however, they like the operational end plates were designed to fail in the 1,300-to-1,600-psi pressure range as were the acrylic plastic hulls, they were generally not employed in the model tests at low temperatures where the implosions were predicted to take place at pressures in the 2,000-psi range.

3. *Heavy-duty end plates* were simply metallic end plugs of the same thickness and curvature as the acrylic plastic hull closing off the polar openings in the acrylic plastic hull (Figure 65). The heavy-duty end plates were fabricated from 6AL-4Va titanium alloy to give them high strength while at the same time keeping their rigidity low so that the mismatch between the rigidities of the end plate and the hull did not generate undue stress concentrations in the acrylic plastic. The heavy-duty end plates were used only in those capsule models that were to be tested at low ambient temperatures that could increase the critical pressure of the acrylic plastic hulls above the design pressure of the operational or the simulated hatches of 316 stainless steel.

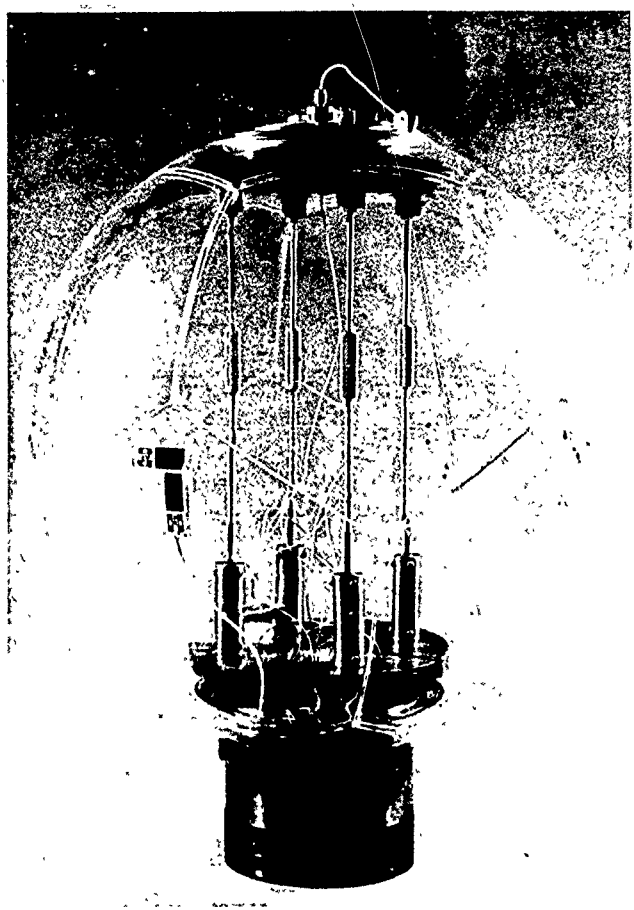

Figure 57. Operational 15 inch diameter model acrylic plastic capsule for the NEMO system: assembled.

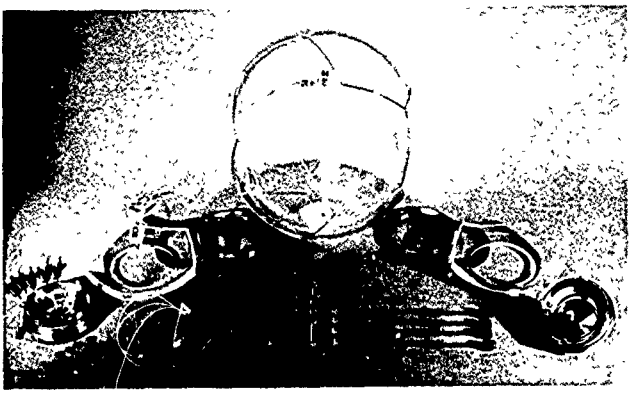

Figure 58. Operational 15-inch-diameter model acrylic plastic capsule for NEMO system: disassembled.

The large-scale test series consisted of a single 66-inch-OD and 61-inch-ID acrylic plastic hull equipped with operational end plates of type 316 stainless steel (Figure 66). The hull, as previously described under "Fabrication Process," was fabricated in much the same way as the model hulls. The bottom plate was a faithfully scaled-up copy of the operational bottom plate in the model NEMO with the exception of the internal retaining flange, which was bolted to the bottom plate instead of being threaded to it (Figure 67). The top hatch was also a scaled-up version of the operational hatch used in the NEMO models (Figure 68). The only difference between it and the working hatches in the models were the use of a bolted-on, instead of screwed-on, retaining flange (Figure 67) and the use of a planetary gear system, instead of a cam system, for the locking and unlocking mechanism. (For detailed dimensions, see Appendix A.) Pretensioned tie rods were not used as (1) there would not be sufficient room for them in a 66-inch capsule for manned operations and (2) absence of the rods subjected the hull to a more severe test condition in the pressure vessel than the capsule would see in actual service, where the external cage would resist the downward pull of external ballast.

Testing Program for Capsules

The capsule test specimens were tested for their structural integrity mostly by external hydrostatic loading. This type of loading was selected because it represents (1) the most severe loading condition to which the structure will be subjected in the ocean and (2) it is the loading condition

to which the structure will be subjected the largest percentage of time during its operational life. Since the test fixtures and test details associated with the hydrostatic testing of capsule specimens varied to some extent between the model and large-scale specimen tests, they will be described separately.

Testing of Models. Fifteen-inch capsule models were subjected to a large variety of hydrostatic tests in order to provide experimental data on as many facets of capsules' structural response to hydrostatic loading as possible. The hydrostatic pressure tests to which the model capsules were subjected can be divided into three general categories: (1) short-term tests, (2) long-term tests, and (3) cyclic tests. In addition to the hydrostatic tests, a single axial compression test was also performed.

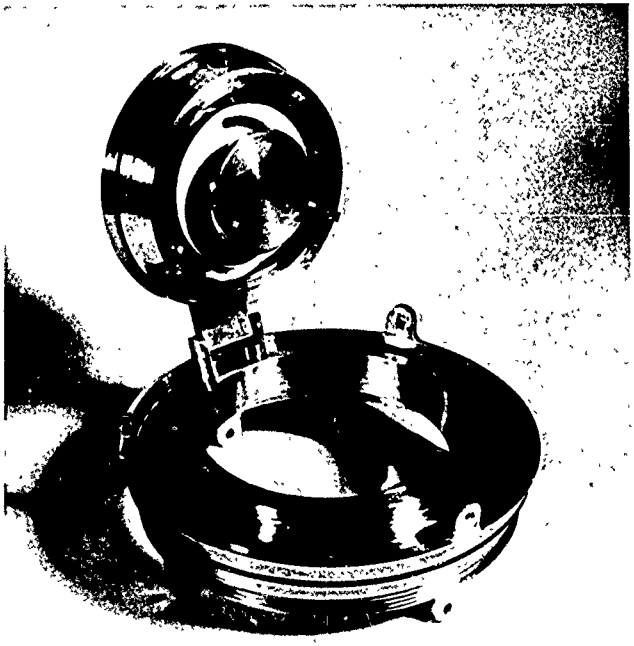

Figure 59. Hatch for the operational 15-inch-diameter model capsule: open.

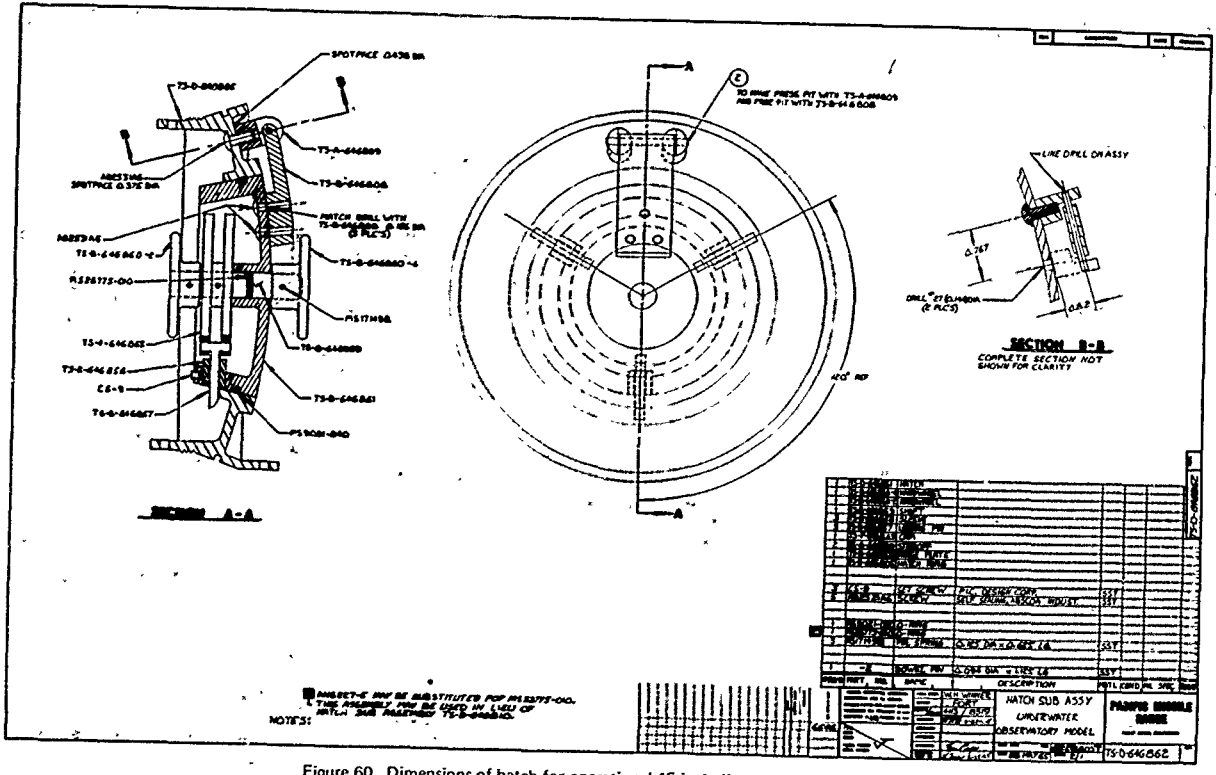

Figure 60. Dimensions of hatch for operational 15-inch-diameter model capsule.

Figure 61. Bottom polar penetration closure and retaining ring for the 15-inch-diameter model capsule: exterior view.

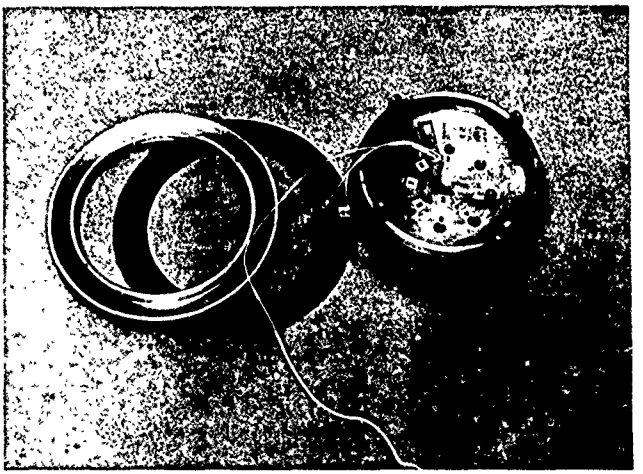

Figure 62. Bottom polar penetration closure and retaining ring for the 15-inch-diameter model capsule: interior view.

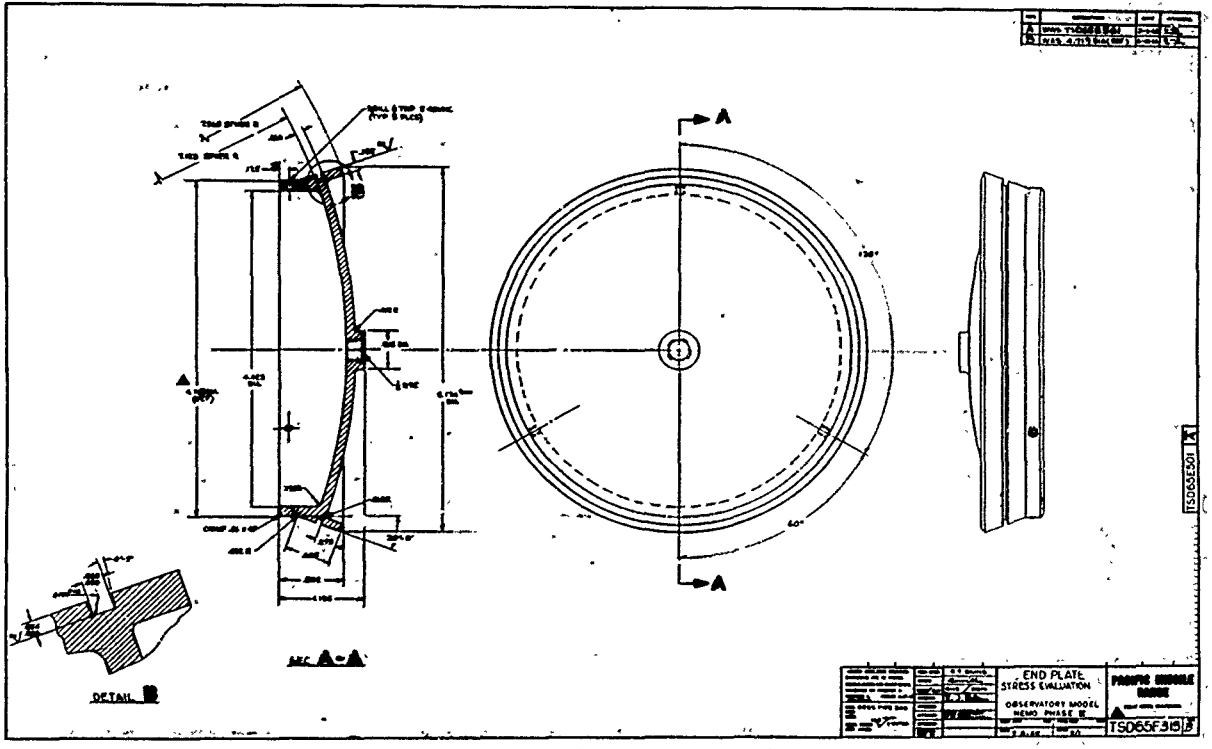

Figure 63. Detailed dimensions of simplified polar penetration closure.

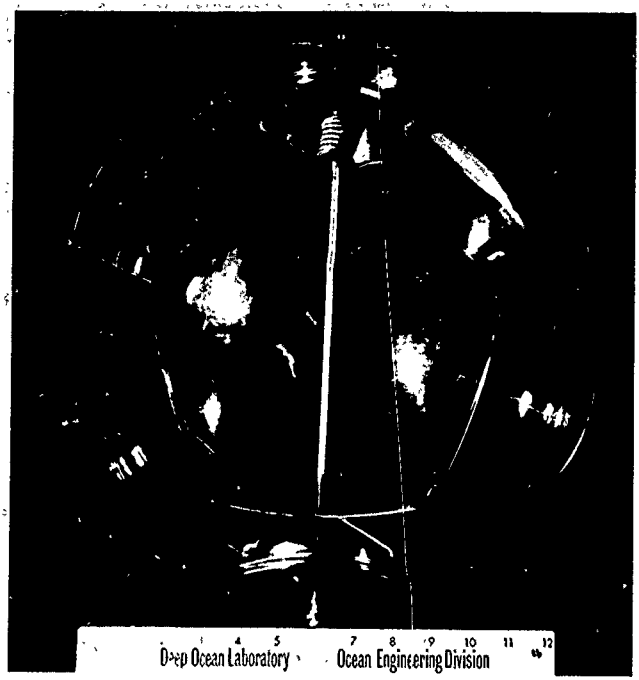

Figure 64. Model capsule of 15-inch diameter with simplified polar penetration closures: assembly. Note the single spring-loaded tie rod.

Short-term tests were performed on 11 capsules (Table 4). All of the models were equipped with tie rods except for capsules 0, 16 and 20. These tests were to provide immediate data on the maximum hydrostatic pressure the capsule can withstand under different temperatures in the 32 to 114°F range. Furthermore, the critical pressures at which implosion of the models occurred would serve as benchmarks to which critical pressures of models tested under long term (Table 5) and cyclic (Table 6) conditions could be compared to determine the effect of cycling, or long-term loading on their structural integrity. For all of these tests, water was used on the exterior and interior to insure proper temperature control. Since the water in the interior of the hull was vented to the atmosphere by tubing, its presence had no reinforcing effect on the hull.

Table 4. Short-Term Pressurization Tests on 15-Inch-OD x 14-Inch-ID Model Capsules

Specimen Number	Joints	Type of Penetration Closures	Temperature (°F)		Type of Failure	Pressurization Rate (psi/min)	Implosion Pressure (psi)
			Outside	Inside			
0	narrow	no penetrations in the hull	70	70	general implosion of acrylic plastic capsule	110	1,360
4	narrow	simple steel plates (Figure 63)	59	59		100	1,645
5	narrow	simple steel plates (Figure 63)	68	68		123	1,625
6	narrow	simple steel plates (Figure 63)	65	65		105	1,525
14	wide	simple steel plates (Figure 63)	45	45	general implosion of acrylic plastic capsule; yielding of end plates	102	1,800
18	wide	simple steel plates (Figure 63)	84	84	general implosion of acrylic plastic capsule	101	1,310
8	wide	simple thick titanium plates (Figure 65)	32	32		101	1,960
15	wide	simple titanium plates (Figure 63)	68	68		99	1,520
21	wide	simple thick titanium plates (Figure 65)	32	104		99	1,660
20	wide	simple steel plates and polycarbonate plugs (Appendix D)	100	100		102	1,175
16	wide	operational steel hatches with cam lock (Figures 59 and 60)	114	114		105	1,050

Notes: 1. Type 316 stainless steel used.
2. Acrylic plastic is grade G Plexiglas of nominal 1/2-inch thickness.
3. Narrow joints bonded with solvent cement
4. Wide joints bonded with PS-18 cement.

Table 5. Long-Term Pressurization Tests on 15-Inch-OD x 14-Inch-ID Model Capsules

Specimen Number	Joint	Type of Penetration Closures	Temperature (°F)		Type of Failure	Pressurization Rate (psi/min)	Sustained Pressure (psi)	Duration of Loading (minutes)
			Outside	Inside				
11	narrow	simple steel plates (Figure 63)	68	68	general implosion of acrylic plastic capsule	102	1,300	6
19	narrow	simple steel plates (Figure 63)	68	68		105	1,200	20
17	wide	simple steel plates (Figure 63)	68	68		107	1,100	150
1	narrow	operational steel hatches with dog lock (Figures 19, 20, and 21)	68	68		102	1,000	630
10	narrow	simple steel plates (Figure 63)	66	66		105	1,000	885
7	narrow	simple steel plates (Figure 63)	68	68		110	1,000	1,500
12	wide	simple steel plates (Figure 63)	70	70		100	925 max 895 avg 835 min	1,530
13	wide	simple steel plates (Figure 63)	64	64		106	910 max 899 avg 895 min	7,500
9	narrow	simple steel plates (Figure 63)	68	68		103	920 max 900 avg 880 min	4,330
3	narrow	simple steel plates (Figure 63)	73 max 60.0 avg 50.4 min	73 max 60.0 avg 50.4 min	local implosion in the center of a pentagon	107	810 max 755 avg 663 min	269,000[a]

continued

Table 5. Continued

Specimen Number	Joint	Type of Penetration Closures	Temperature (°F)		Type of Failure	Pressurization Rate (psi/min)	Sustained Pressure (psi)	Duration of Loading (minutes)
			Outside	Inside				
2	narrow	operational steel hatches with cam lock (Figures 59 and 60)	72 max 70.0 avg 68 min	72 max 70.0 avg 68 min	local implosion in the center of a pentagon	99	760 max 738 avg 720 min	22,300
7	narrow	simple steel plates (Figure 63)	83 max 67.4 avg 52 min	83 max 67.4 avg 52.0 min	no implosion	102	560 max 498 avg 440 min	1.08×10^6
9	narrow	simple steel plates (Figure 63)	82 max 68.5 avg 53 min	82 max 68.5 avg 53 min	no implosion	98	294 max 256 avg 200 min	1.13×10^6

Notes: 1. Type 316 stainless steel used.
2. Acrylic plastic is grade G Plexiglas of nominal 1/2-inch thickness.
3. Narrow joints bonded with solvent cement.
4. Wide joints bonded with PS-18 cement.
5. For tests where pressure and temperature fluctuated considerably, both maximum, average, and minimum values are given.

[a] Wall is approximately 10% thicker than in other models.

Table 6. Cyclic Pressurization Tests on 15-Inch-OD x 14-Inch-ID Model Capsules

Specimen Number	Joint	Type of Penetration Closures	Temperature (°F)		Type of Failure	Dwell at High Pressure (minutes)	Pressure (psi)	Dwell at 0 psi (minutes)	Number of Cycles
			Outside	Inside					
2	narrow	operational steel hatches with cam lock (Figures 59 and 60)	83 max 68 5 avg 50 min	same as outside	did not fail	7,200	550 max 487 avg 400 min	7,200	100
8	narrow	simple steel plates (Figure 63)	75 max 68 5 avg 59 min			1,440	520 max 490 avg 445 min	1,440	300
11	narrow	simple steel plates (Figure 63)	78 max 67 avg 56 min			720	520 max 491 avg 460 min	720	600
15	wide	simple steel plates (Figure 63)	80 max 68 avg 57 min			60	520 max 500 avg 490 min	60	4,000

Notes: 1. Type 316 stainless steel used.
2. Acrylic plastic is grade G Plexiglas of nominal 1/2-inch thickness.
3. Narrow joints bonded with solvent cement.
4. Wide joints bonded with PS-18 cement.
5. All capsules pressurized at 90 to 100-psi/min rate.
6. Since all of these tests were of long duration, considerable variation in pressure and temperature took place. For this reason not only the average, but also the minimum and maximum values are shown.

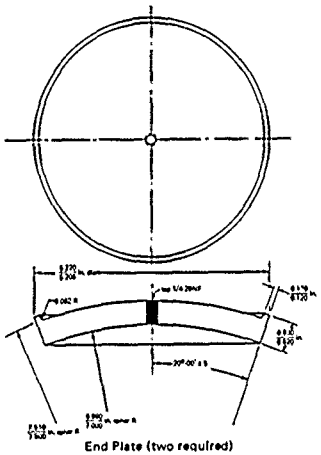

Figure 65. Heavy-duty polar penetration closures for low temperature implosion testing of 15-inch-diameter model capsules.

Hydrostatic loading of the capsules was performed in NCEL's 18-inch-diameter pressure vessel with a 20,000-psi pressure rating. Pressure was raised at a 90 to 110-psi/min rate based on the maximum planned descent rate for the large-scale operational NEMO system. The pressure was generated with pneumatically powered positive displacement pumps. Their operation generated some pulsations during the pressurization, but the small magnitude of these pulsations (approximately 10 psi) was considered insignificant for the purpose of these hydrostatic tests. In all of the short-term tests, the average pressurization rate of 100 psi/min was maintained until implosion of the model occurred. After implosion, the pressure vessel was opened and the fragments inspected for clues pointing to the source of failure (Figure 69).

Prior to performance of the short-term tests to implosion, some of the models were subjected to other types of hydrostatic tests. For example, Models 8 and 15 were subjected to cyclic loading prior to their implosion under short-term test conditions (see Table 6). Although subjecting the same model to other test conditions prior to short-term implosion testing is generally not desirable, the small number of models available for the evaluation of the capsule design made this test policy necessary.

Long-term tests were performed on 13 NEMO models (Table 5). These tests were to provide data on the structural response of acrylic plastic hulls to sustained hydrostatic loadings of different magnitudes. After the models imploded under the sustained loading, the duration of loading prior to implosion at a given pressure level would be compared to the short-term implosion pressure. The difference between these pressures would constitute a valid measurement of strength degradation as a function of load duration. Several pressure levels had to be chosen for the long-term test program to establish with sufficient accuracy the relationship between implosion pressure and duration of sustained loading.

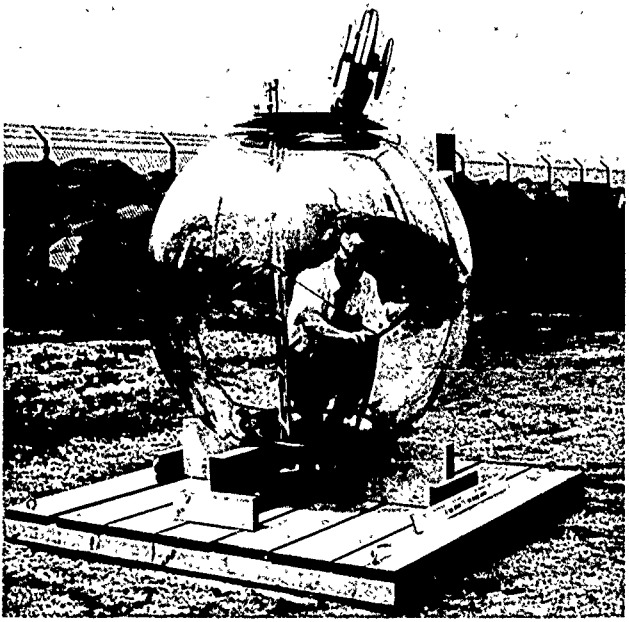

Figure 66. Large-scale capsule of 66-inch diameter for the NEMO system.

The pressure levels chosen for the long-term testing program were 1,300 psi, 1,200 psi, 1,100 psi, 1,000 psi, 900 psi, 750 psi, 500 psi, and 250 psi.* The large spread between the highest and lowest pressures selected for this testing program was based on the rationale that while the high-pressure loadings will cause the models to fail rapidly and thus permit generation of many data points within a short period of time, the low-pressure loadings will show that if the pressure is sufficiently low, implosion under long-term loading will not occur within any reasonable dive duration at operational depth. Using the data from both the high- and low-pressure tests, it will be possible to predict by interpolation the duration of loading preceding implosion for any sustained pressure level.

* Some tests were performed also at pressures of 4,500 psi, 4,000 psi, 3,500 psi, and 3,000 psi, but the model capsules used for those tests were 15-inch-OD x 13-inch-ID (Appendix E).

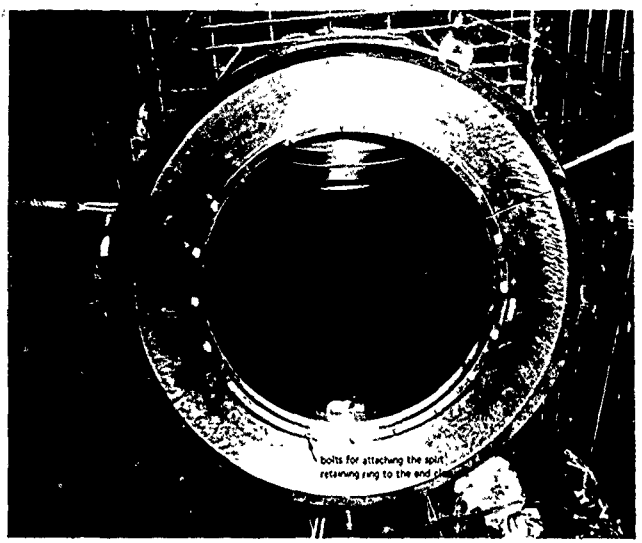

Figure 67. Split hatch retaining ring for top and bottom polar closures of the 66-inch-diameter capsule: view from the interior of the capsule.

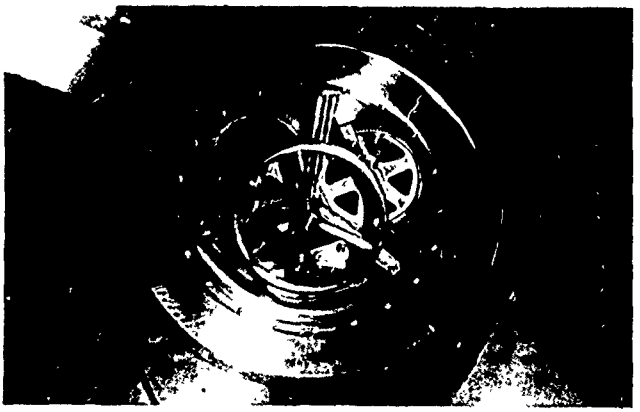

Figure 68. Hatch for the 66-inch diameter capsule: view from the interior of the capsule.

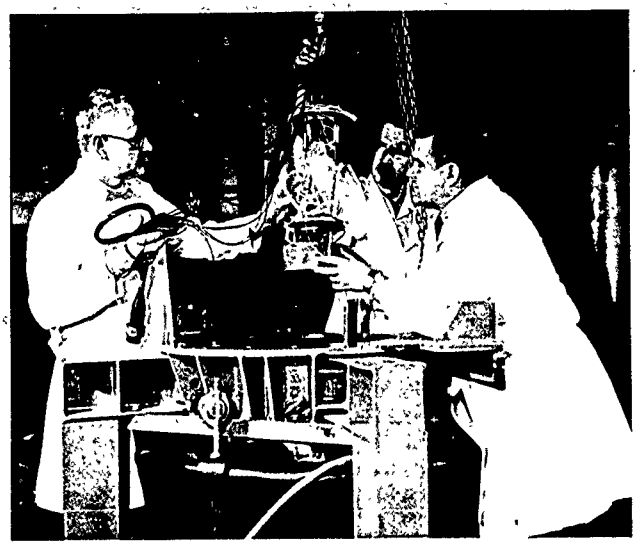

Figure 69. Removal of imploded 15-inch-diameter capsule from the 18-inch-diameter pressure vessel.

Models were tested under long-term loading conditions in hydrostatic pressure vessels specially built for this project. The pressure was raised at a 100-psi/min rate to the desired pressure level by pumping tap water into the vessel with pneumatically powered positive displacement pump. When the desired pressure level was reached, the line to the pump was closed. Since the pressure inside the vessel varied from day to day because of variations in room temperature and the progressive contraction of the hull under hydrostatic loading, daily pressure corrections were necessary. These pressure corrections were accomplished by opening the valve in the pipe connecting the vessel to the pump and increasing the pressure, or by opening the valve in the drainline and decreasing the pressure. The day-to-day pressure variations were generally less than 10 psi, although on some occasions they were as large as 70 psi when sudden temperature changes took place in the uninsulated building where the vessels were located.

The models undergoing the long-term tests were not filled with water prior to placement in the vessel, but were simply vented to the ambient atmosphere. Because of the large buoyancy that the models possess, lead ballast was attached to the bottom plates in the models. This test condition better simulated the loading conditions to which a large-scale capsule will be

subjected during its life as a part of the NEMO system. Some of the models (Table 5) were equipped with operational end plates while others had the simulated polar plates. Model 1 with operational polar plates was without tie rods. All models with simulated polar plates were pretensioned by means of the rods. The operational end plates were connected by means of four tie rods (Figure 57), and the simulated polar plates were connected by a single tie rod (Figure 64).

Two of the model capsules (2 and 11) were subjected to cyclic pressurization (Table 6) before being tested to destruction in the long-term tests. Because of their previous test history, a somewhat lower performance level during the long-term tests could be expected, and if it actually occurred, could be accounted for.

Cyclic tests were performed on four models (Table 6). The reason for choosing such a low number of models for cyclic tests was not a lack of appreciation for these tests but a lack of appropriate controls on the pumping system available for performance of cyclic pressurization tests. Different durations of cycles were selected for testing each model (Table 6). This decision was based on the rationale that since the effect of cycle duration on the cyclic life of an acrylic plastic pressure hull is unknown, cyclic tests with different durations must be utilized to cover the range of cycle profiles to which the NEMO system may be exposed during actual operation.

Pressurization and depressurization were both accomplished at a 100-psi/min rate by pneumatically powered positive displacement pumps. The temperature of the water during the performance of the cyclic tests was that of the ambient atmosphere, and therefore, as in the long-term tests, the temperature of the water varied from day to day within the 50 to 80°F range. The variations in ambient temperature were accompanied by variations in pressure as the water in the pressure vessel expanded or contracted with temperature. The variation in maximum pressure was particularly pronounced for the cyclic tests with long dwell time at the maximum pressure. The pressure, however, never exceeded 550 psi or went below 400 psi during dwell time at the nominal maximum pressure of 500 psi.

All the capsule models subjected to cyclic loading had no previous pressurization history except for Model 2, which had previously undergone two cyclic tests to 750- and 1,000-psi pressure levels with varying dwell times at maximum and minimum pressure. Since no damage in the model was observed prior to placing it in the regular cycling program, the effects of prior cycling history on the test results generated in the regular cycling program were considered insignificant. All of the models used for cycling tests were equipped with tie rods.

An *axial compression* test was performed on a single model capsule by pretensioning the internal tie rods connecting the polar metallic end plates. The objective of this test was to establish experimentally how serious the stresses would be in the acrylic plastic hull if the pretensioned tie rods were utilized in the capsule to place it under precompression prior to lifting it off the deck during launching operations. To simulate actual lifting operations, the tie rods inside the model were pretensioned to exert a total force of 100 pounds—equal in magnitude to the weight of the pod and anchor required for a 15-inch NEMO system. Since the weight of the pod and anchor increases with the cube of the diameter, while the wall section increases as the square of the diameter, the strains from testing the model would have to be scaled up for prediction of strains in larger capsules.

Testing the Large-Scale Capsule. Although the 66-inch large-scale capsule was also tested hydrostatically, there was a distinct difference between testing it and the model capsules described previously. While for the testing of models an attempt was made to provide a separate model for each kind of test, only one large-scale capsule specimen was available for the whole series of tests planned for the large-scale prototype. For this reason, the test results generated with the single large-scale capsule must be considered from the purely experimental viewpoint to a large measure as qualitative rather than quantitative. From the operational viewpoint, the fact that a single hull has been subjected to a diversity of tests is of course desirable, rather than objectionable because, during the operational life of a functional NEMO system, the capsule will also be subjected to a diversity of hydrostatic loading conditions.

All the hydrostatic tests on the large-scale capsule were performed in NCEL's 72-inch-diameter pressure vessel (Figure 70) which has a 5,500-psi pressure rating. Since the prime objective of the testing program for the single large-scale capsule was to generate a maximum of data in the shortest period of time without imploding the hull, only tests of short duration (24 hours or less) were performed, as they satisfied both requirements of the test program.

The pressurization rate for all the tests (Table 7) was selected to be 100 psi/min, identical to the pressurization rate applied to the capsule models. The maximum cycle pressure and temperature of the pressurizing medium varied from 100 to 1,070 psi and 32 to 70°F, respectively. For most of the tests, the interior of the hull was dry and open to atmospheric pressure; for a few of the cycling tests the interior was filled with water, which was vented to the atmosphere.

Figure 70. Placement of 66-inch diameter capsule in the 72-inch diameter pressure vessel at NCEL's Deep Ocean Laboratory. Note the cagelike test jig.

Table 7. Pressurization Tests on the Prototype 66-Inch-OD x 61-Inch-ID Acrylic Plastic Capsule

Type of Test	Number of Tests	Maximum Pressure (psi)	Duration of Sustained Loading	Temperature (°F)	Instrumentation	Damage
Long term	1	100	24 hr	68-70	strain gages	none
	1	200	24 hr	68-70	strain gages	none
	1	300	24 hr	68-70	strain gages	none
	1	400	24 hr	68-70	strain gages	none
	1	500	24 hr	68-70	strain gages	none
	1	600	24 hr	68-70	strain gages	none
	1	700	24 hr	68-70	strain gages	none
	1	800	24 hr	68-70	strain gages	none
	1	250	6 hr	68-70	water displacement	none
	1	500	6 hr	68-70	water displacement	none
	1	750	6 hr	68-70	water displacement	none
	1	500	4 hr	38	strain gages	none
	1	600	7 hr	36	strain gages	none
	1	700	5-1/2 hr	43	strain gages	none
	1	750	8 hr	42	strain gages	none
	1	850	8 hr	41	strain gages	none
Cyclic	5	500	6 hr each test	68-70	strain gages	none
	5	500	1 hr each test	68-70	strain gages	none
	7	500	15 min each test	68-70	strain gages	none
	13	500	2 min each test	68-70	strain gages	none
	20	500	4 hr each test	32-75	strain gages	none
	15	550	1 hr each test	32-40	none	none
	13	550	1/2 hr each test	32-40	none	none
	11	500	1 min each test	32-40	none	none
	1	1,070	10 min	34	none	none
Short term	1	1,850	none	70	none	imploded

Notes:
1. For all the tests the 66-inch capsule was secured to the protective cage by bolting the polar steel plate on the bottom of the capsule to the base of the cage.
2. The capsule was tested a total of 107 times.
3. The capsule was removed 25 times from the pressure vessel for inspection during the test program.
4. The capsule sustained a total of 375 hours under hydrostatic pressure prior to destructive implosion test.

For the performance of all the hydrostatic pressure tests, a special cagelike holding jig was designed and fabricated for NEMO. Its purpose was to protect the hull against impact when the capsule was placed into the vessel and to act both as an anchor and as a support for the either positively or negatively buoyant hull (depending on whether its interior was dry or filled with water). When the interior of the hull was dry, it exerted approximately 4,000 pounds of positive buoyancy force on the bottom plate anchored to the holding jig.

Although all the tests planned for the large-scale capsule were basically of cyclic nature, the objectives of these tests varied from one series of tests to another. In order to clarify these objectives, each series of tests will be discussed below in detail.

Time dependent strain under sustained pressure loading was to be determined by pressurizing the hull to the desired pressure level and holding it at that pressure until the time-dependent rate of strain increase stabilized itself for that pressure. Since the time-dependent strain rate varies from one sustained pressure level to another, the hull had to be held at different sustained pressures for a sufficient time to establish the strain rates. The test procedure established for this series of tests consisted of pressurizing the hull to 100-, 200-, 300-, 400-, 500-, 600-, 700-, and 800-psi pressure levels and holding it at each one of those levels for at least 24 hours. At the conclusion of every sustained pressure test, the pressure was decreased to 0 psi, so that the hull could relax between pressurization cycles. The relaxation periods varied from 45 to 188 hours. For this series of tests, the interior of the hull was dry and vented to the atmosphere. The ambient temperatures of the hull interior and exterior were maintained in the 68 to 72°F temperature range.

The effect of cycling on the magnitude of strains in the hull was to be investigated by pressurizing the hull to 500 psi, holding it at that pressure for a period of time, depressurizing it to 0 psi and holding it at that pressure for the same length of time as at maximum pressure. Since the relaxation period at 0 psi was not necessarily always sufficient to permit complete relaxation of the hull, some residual compressive strain would remain in the hull at the beginning of the new pressure cycle and would influence the strain during the succeeding pressurization cycle. By varying the length of dwell time at the 500-psi level in each cycle, the magnitude of residual strain in the hull was expected to vary from one series of cycles to another. By comparing the strain rates in the hull generated during long and short cycles, some indication of the effect of residual strains on the strain rates could be obtained. To vary the dwell time as much as possible, the dwell time at 500 psi was varied from 360 minutes to 2 minutes. For this series

of tests, the interior of the hull was kept dry and vented to the atmosphere. Ambient temperatures of the hull interior and exterior were maintained in the 68 to 72°F temperature range.

Displacement changes of the hull were investigated by a series of tests in which the pressure was varied from 250 to 750 psi. In each of the tests, the pressure was raised to the desired maximum pressure level, held there for 6 hours, and then followed by a depressurization and relaxation period of 18 hours. For those tests, the interior of the hull was filled with water vented to the atmosphere. During the pressurization of the hull, water was displaced from it because of the hull contraction, and the quantity of displaced water was used as a measure of hull contraction. The ambient temperatures both in the exterior and interior of the hull were in the 68 to 72°F range. Upon depressurization, the water displaced from the interior was siphoned back into the vessel interior, giving a measure of capsule relaxation during depressurization.

The effect of differential temperature on the strains in the hull was evaluated in a series of cyclic pressure tests from 0 to 500 psi with the dwell time at 500 psi being 4 hours and the relaxation time 20 hours. The temperature of the water surrounding the capsule was varied from 60 to 32°F, while the ambient temperature of the dry interior varied from 79 to 45°F. Because of the difference in internal and external ambient temperatures, a temperature gradient existed inside the wall of the acrylic plastic hull (Figure 71).

In addition to the tests to 500 psi, one brief test was run to 1,070 psi and another to 1,000 psi. Besides showing the capability of the hull to withstand a pressure 300% greater than the rated capability of the hull, these tests also supplied information on the strains in the hull at very high stress levels and the rate of relaxation after depressurization from such high excess pressures. The *scale effect* for crack-sensitive materials was determined by imploding the 66-inch capsule and comparing its short-term implosion pressure with the short-term implosion pressures previously determined by imploding 15-inch small-scale models. This test completed the testing program for the 66-inch prototype capsule.

Instrumentation

Long-term and cyclic tests on the 15-inch capsule models used only a minimum of instrumentation as it was not feasible to tie up electronic equipment for more than 1 year just for these tests. The instrumentation for almost all model capsules under long-term or cyclic pressure testing consisted only of temperature and pressure gages, from which data were read and recorded 3 times daily. The failure of the models was noted by a sudden drop in pressure. If failure did not occur prior to the termination of the test, the model was then carefully inspected upon removal from the vessel to ascertain the level of damage to the hull.

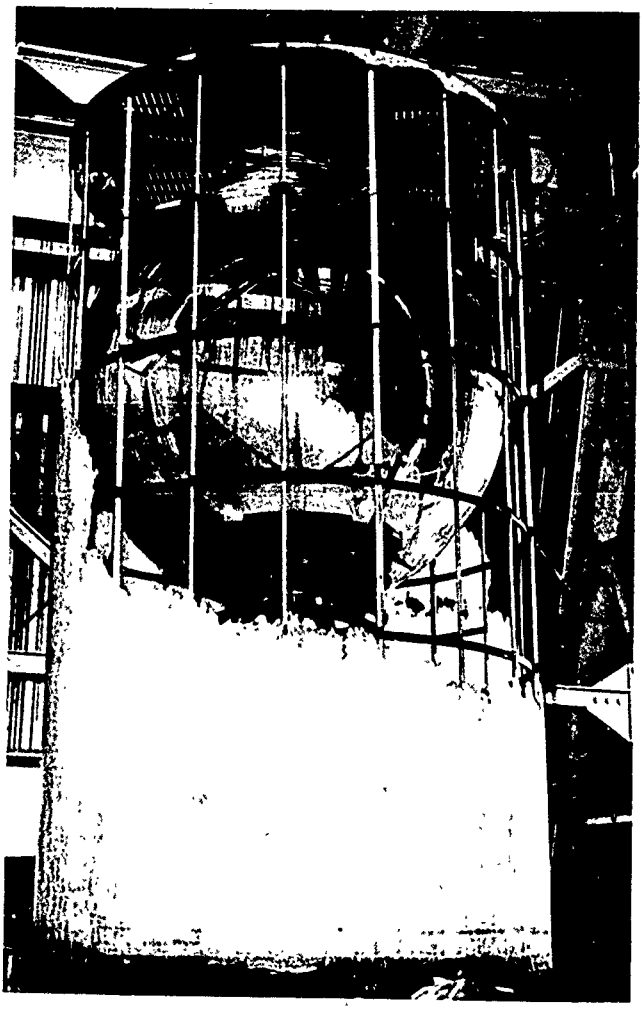

Figure 71. The 66-inch diameter capsule after the simulated arctic dive to the 2,400-foot depth. Note the accumulation of ice due to subfreezing water temperature.

A few of the models were equipped with a volume change measuring system to determine the magnitude of hull shrinkage under long-term loading (Figure 72). This instrumentation system consisted of distilled water filling the total interior volume of the model and tubing connecting the interior of the model to an accurate graduate located on the exterior of the pressure vessel. The shrinkage of the acrylic plastic hull under sustained pressure caused water to flow from its interior into the graduate. Readings of water level, temperature, and pressure were, at the initiation of the test, taken at 1-minute intervals for the first 15 minutes, every 5 minutes for the next 45 minutes, hourly for the next 7 hours, and 3 times daily thereafter until the model failed or was depressurized. When the model capsule was depressurized, the same data-recording process was repeated.

Only two models were strain-gaged (Figure 73), and then only four strain gages were used because of the limitation on the number of available electric penetrations in the test pressure vessel. However, it was hoped that by judicious placement of the strain gages a good representation of strain distribution in the hull could be obtained.

Short-term tests on model capsules utilized either strain-gage (Figure 74), volume-displacement, diameter-contraction, or photoelastic instrumentation. The strain-gage and the water-displacement instrumentation systems were identical to those used in the long-term tests. The diameter-contraction instrumentation consisted of a linear potentiometer inside the capsule placed between the polar steel end plates and an externally located read-out system calibrated to read in thousandths of an inch. The photo-elastic instrumentation consisted of a light source inside the acrylic plastic hull, circular polarizing sheets, a window in the pressure vessel end closure, and a camera mounted on the exterior of the pressure vessel end closure (Figure 75). During some of the tests, the camera was removed and visual observations of the photoelastic interference fringes were made instead.

Considerably more effort and expense were devoted to the instrumentation of the large-scale capsule because (1) only a single capsule specimen existed and (2) the testing of the large capsule was not as lengthy as that of models so that complex electronic equipment could be tied up for the tests. Some of the instrumentation systems were identical to those used on the models, while others, such as the strain-instrumentation system, were considerably more complex than a similar system on the model. The instrumentation for measurement of strains consisted of 81 channels for transmitting data generated by an equal number of electric resistance strain gages mounted on the exterior and interior hull surfaces. Eastman 910 contact adhesive was found to work best for bonding the gages to the hull and DOW Corning 105 silicone rubber with associated primer for subsequent waterproofing. The strains were recorded digitally on paper by a 90-channel BUDD DATRAN unit with a response capability of approximately 1 channel per second. Considerable trouble was encountered in the procurement of

waterproof instrumentation cables (Figures 76 and 77) that were not overly sensitive to hydrostatic pressure. Oversensitivity would unduly influence the strain readings recorded by the externally located balancing and recording unit. Even though care was taken in selection of cables, the recorded strain data may include some of the effect of hydrostatic pressure on the instrumentation cables. Tests conducted on the instrumentation cables have shown that although the effect of pressure on the cables was generally less than 10×10^{-6} in./in. (10 μin./in.) on the strain recording, a few of the cables were overly sensitive and increased the strain reading by as much as 100 μin./in.

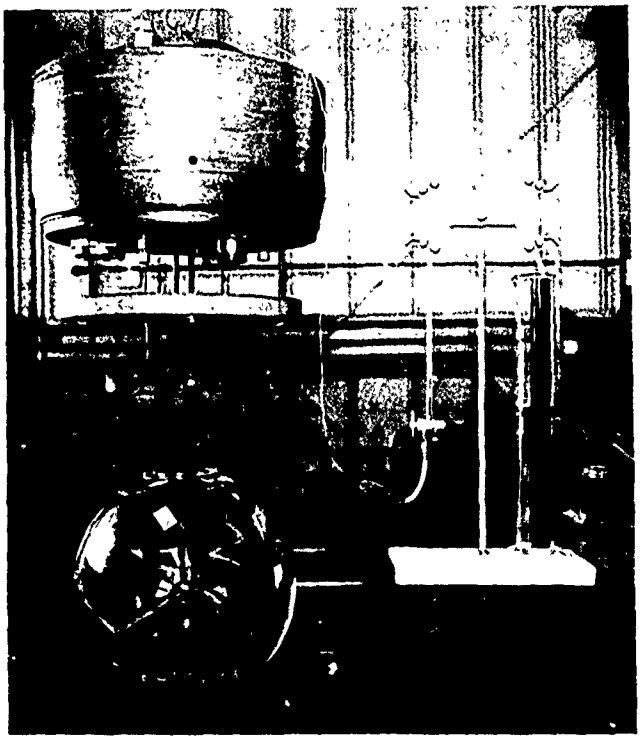

Figure 72. Typical test setup for measuring the change in volume of 15-inch diameter model.

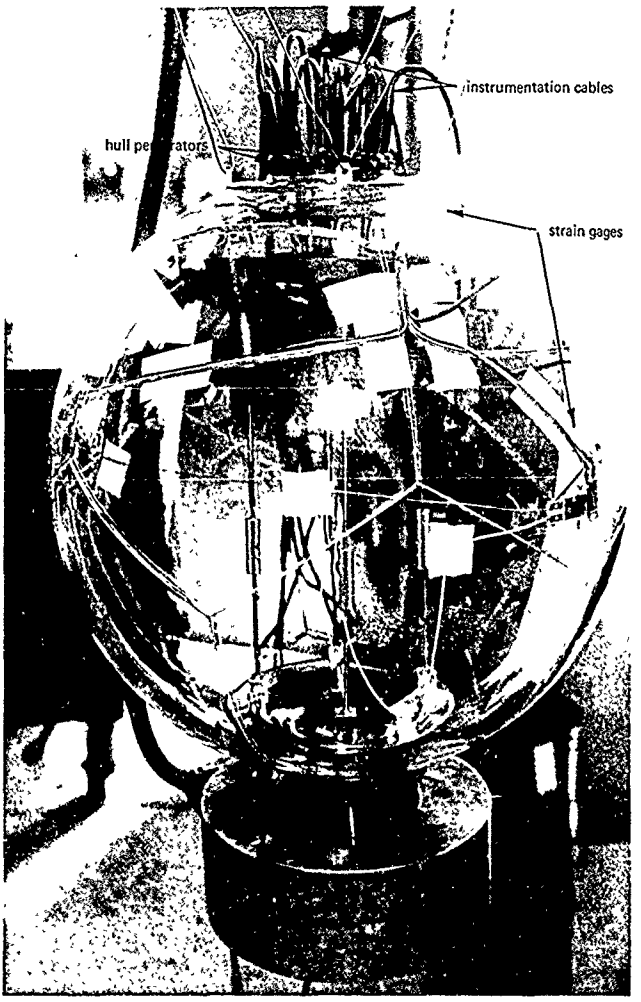

Figure 73. Typical strain gage instrumentation on a 15-inch-diameter capsule model overall view

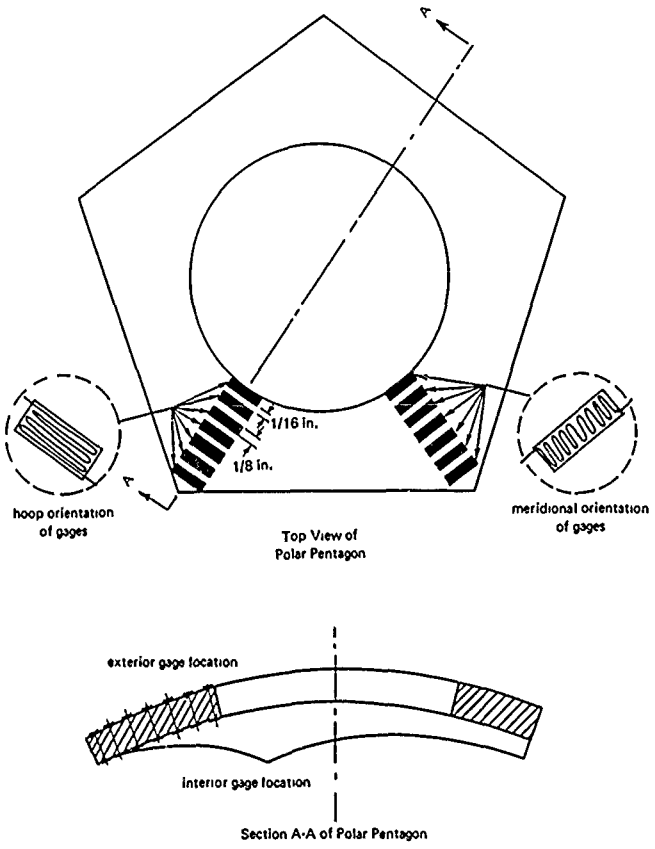

Figure 74. Location of strain gages on the 15-inch-diameter capsule near the polar openings.

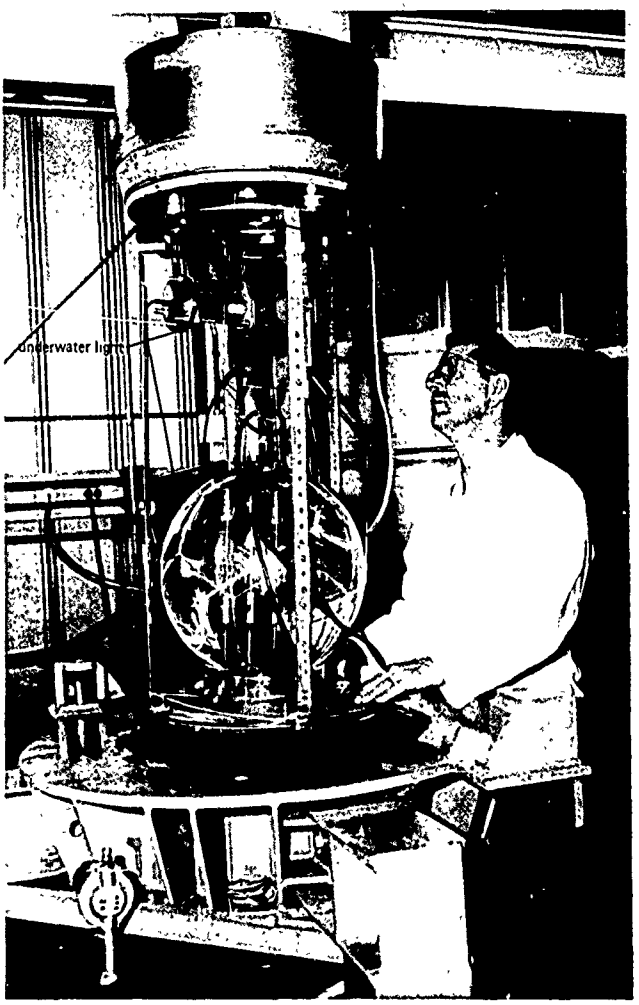

Figure 75. Test setup for measuring photoelastically the strain concentration around the steel polar insert in the 15-inch-diameter capsule under external hydrostatic pressure.

Figure 76. Cables and cable feedthroughs in the steel polar penetration closure for the strain gage instrumentation on the 66-inch-diameter capsule.

Figure 77. Termination of instrumentation cables at the head of the 72-inch pressure vessel.

TEST FINDINGS

Model Capsules

Short-term tests performed on 11 model capsules generated data on which several important findings are based:

1. The short-term implosion pressure of model capsules of same dimensions, construction, and dimensional tolerances tested at constant ambient temperature is repeatable from one sphere to another with only small deviations from the average (Table 4). For example, four NEMO capsules tested in the 59 to 68°F temperature range failed in the 1,520-to-1,645-psi pressure range, indicating less than a ±5% deviation from the group's average of 1,578 psi.

2. The presence of metal end plates in the acrylic plastic sphere does not significantly alter its short-term implosion pressure, as can be seen by comparing the 1,360-psi implosion pressure of a capsule at 70°F without metal inserts (Model 0) with the 1,578-psi average implosion pressure at 64°F of the NEMO capsules with metal end plates (Table 4).

3. Ambient temperature has a significant effect on the short-term implosion pressure (Figure 78): the short term implosion pressure was found to be an inverse linear function of the ambient temperature in the 32 to 114°F range used for testing of models.

4. A severe temperature differential across the thickness of the hull has no significant effect on the short-term implosion pressure. The implosion pressure of an acrylic plastic sphere under temperature differential test conditions appears to be related to the average temperature of the acrylic plastic hull. The acrylic plastic sphere with 104°F interior and 32°F exterior temperatures (average temperature of 68°F) failed at 1,660 psi which corresponds approximately to the implosion pressure of a sphere having interior and exterior temperatures in the 60 to 68°F range (Figure 78).

5. Ultimate failure in all short-term tests was catastrophic and accompanied by a loud noise. The speed of the implosion was rather slow, the duration of the implosion being on the order of 1 second. The failure mechanism was of a general, rather than a local nature. The fragments were small and the fracture surfaces ran across bond lines indicating that the bonded surfaces were not the planes of weakness along which the failure took place. No cracks were observed on the acrylic plastic bearing surface in contact with the metal end plate.

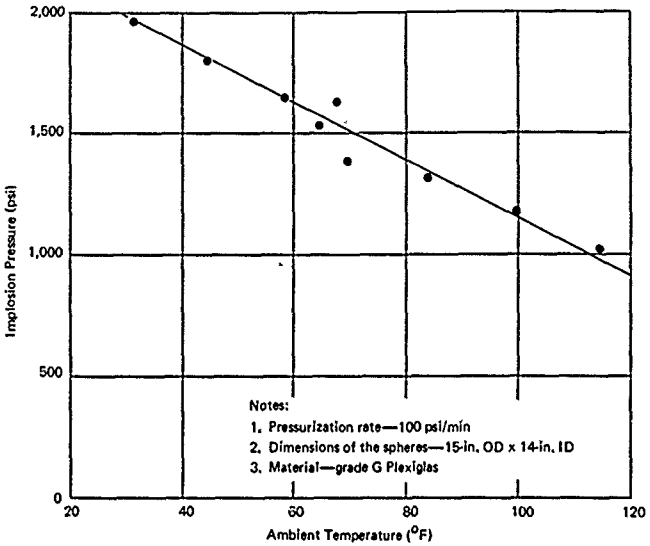

Figure 78. Implosion pressure of acrylic plastic capsule models as a function of ambient water temperature under short-term loading.

6. The magnitude of the volume decrease that the acrylic plastic spheres undergo with increase in short-term external hydrostatic pressure varies with ambient temperatures (Figure 79). The relationship between pressure and volume decrease is linear to pressures beyond 1,000 psi, except that (1) the volume decrease rate varies directly with temperature and (2) the linear-pressure-versus-volume-decrease relationship becomes nonlinear at lower pressure for high ambient temperature. Although the acrylic plastic spheres fail at different pressures, depending on the ambient temperature, the total decrease in volume at the moment of implosion is about the same for all of them: approximately 5% of the original sphere's displacement in water (equivalent to approximately 16,900 to 17,100 μin./in. average strain in the acrylic plastic).

7. Failure of the simple steel end plates of type 316 stainless steel used in some of the NEMO models takes place at approximately 1,800 psi (Figure 80). The failure takes place in the form of plastic buckling.

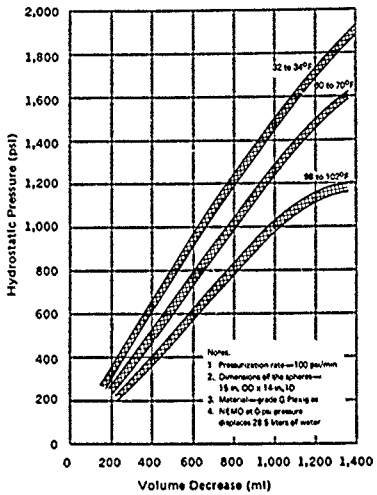

Figure 79. Change in displacement of acrylic plastic capsule models as a function of hydrostatic pressure under short-term loading.

8. All strains measured on the interior or exterior surfaces of the acrylic plastic hull were compressive. The meridional and hoop strains on the capsule models measured at their equator were of approximately the same magnitude. Their relationship to the hydrostatic pressure under short-term loading was linear to at least a 750-psi loading (Figure 81). The strains in the immediate vicinity of the steel end plates differed from those measured at the equator. This was indicated both by the magnitudes of strains measured there with electric resistance strain gages and by photoelastic techniques. From these readings, it appears that the maximum stress encountered around the steel end plate is at the very edge of penetration on the interior surface of the sphere. The meridional stress is in the elastic range of acrylic approximately 8 to 10 times higher than the stress measured at the equator at the same pressure (Figure 82). The circumferential stresses at the same location are, on the other hand, only 2 to 3 times higher than those found at the equator (Figure 83). In general, the distribution of stresses near polar penetrations indicates that bending moments are superimposed upon the membrane stresses in the vicinity of penetration through the acrylic plastic hull. Also, since at the 500-psi pressure the stress at the equator is in the 3,000-to-4,000-psi range, plastic redistribution of stresses probably takes place in the acrylic plastic at the edge of penetration.

Long-term tests performed on 13 model capsules over a period of 3 years (Table 5) at room temperature have shown that long-term sustained pressure loading is a very important test condition for acrylic plastic pressure hulls, as this test condition causes the acrylic plastic pressure hulls to fail in a mode that is not detectable by short-term tests. The major findings resulting from the long-term sustained hydrostatic tests of NEMO models are:

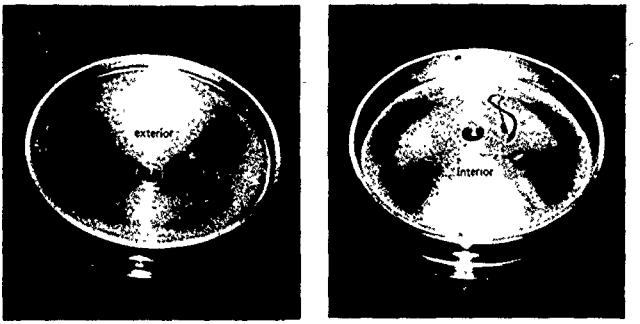

Figure 80. Simplified polar penetration closure for 15-inch-diameter capsule that failed by plastic instability and yielding at 1,800 psi of short-term hydrostatic loading.

1. Acrylic plastic capsules under external hydrostatic pressure exhibit time-dependent strains even at hydrostatic pressures as low as 250 psi (one-half the design pressure). The time-dependent strain rate at sustained long-term hydrostatic loading is a function of hydrostatic pressure: higher pressures generate higher strain rates. The time-dependent strain rate is also an inverse function of loading duration: the strain rate is largest immediately after load application and decreases in magnitude with duration of loading (Figures 84 through 86).

2. The magnitude of strain in a NEMO model after a given duration of sustained loading varies linearly with the magnitude of applied loading from 0 to 800 psi. This relationship becomes (Figure 85) markedly nonlinear at hydrostatic loadings above 800 psi for room temperature ambient test conditions. Although long-term tests were not conducted at other ambient temperatures besides room temperature, it can be postulated on the basis of research conducted by others with acrylic plastic tensile test specimens that both the magnitude of strain and the magnitude of hydrostatic pressure at which the linear relationship ceases will vary with the temperature. High temperatures will cause larger strains for the same pressure and duration of loading, while low temperatures will be accompanied by low strains under long-term loading.

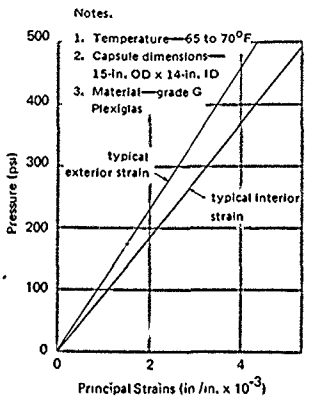

Figure 81. Strains on the equatorial region of the 15-inch-diameter capsule model as a function of short-term hydrostatic loading.

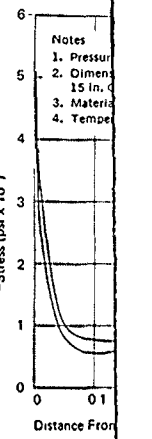

Figure 82. Mer
the
trat
of
of p
term

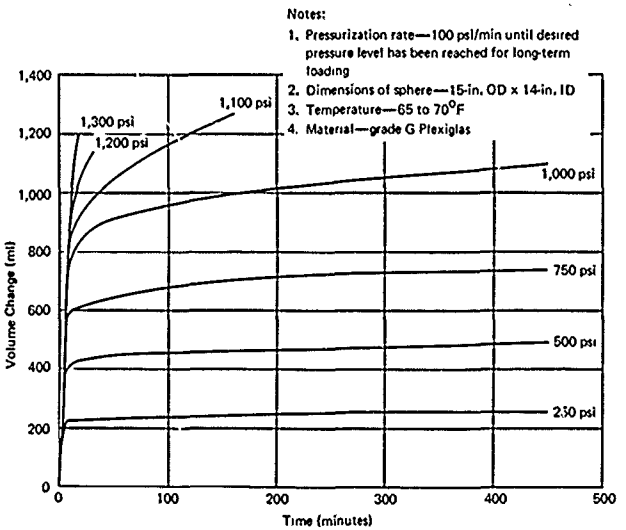

Figure 84 Change in displacement of 15-inch-diameter capsule as a function of hydrostatic pressure and duration of sustained loading; summary of all tests.

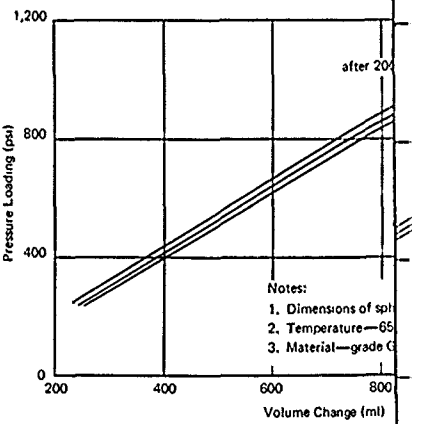

Figure 85. Comparison of displacement changes for under different hydrostatic pressure lo er 400 minutes of sustained pressurizatio ke

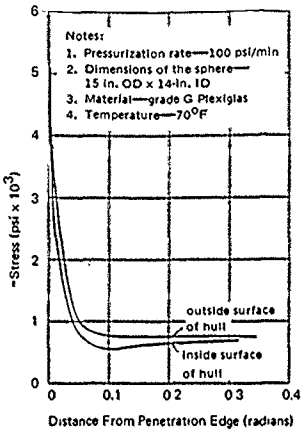

Figure 82. Meridional stresses around the simplified polar penetration closure as a function of distance from the edge of penetration under short-term hydrostatic loading.

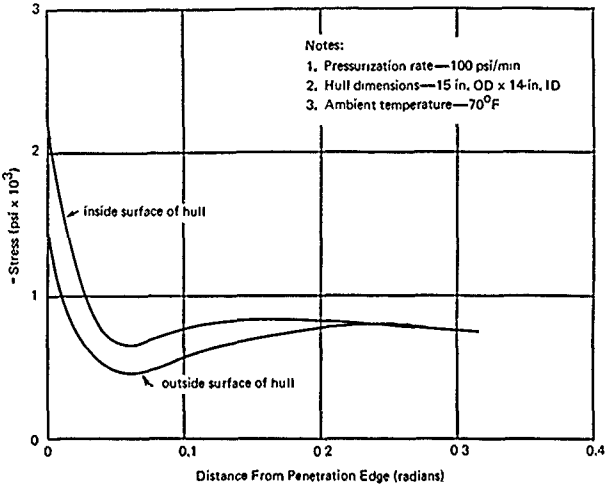

Figure 83. Hoop stresses around the simplified polar penetration closure as a function of distance from the edge of penetration under short-term hydrostatic loading.

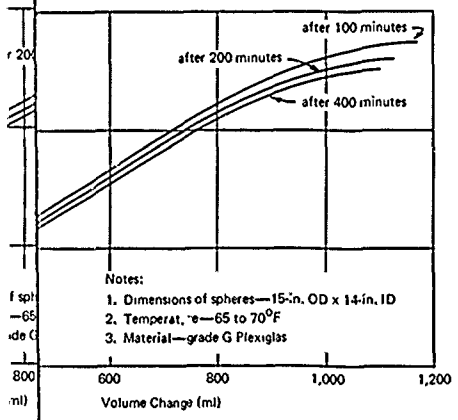

on of displacement changes in a 15 inch-diameter capsule
erent hydrostatic pressure loadings after 100, 200, and
es of sustained pressurization.

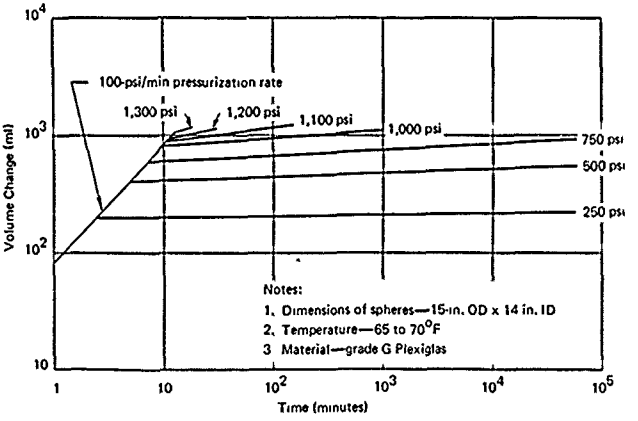

Figure 86. Linear plot of displacement change in a 15-inch-diameter capsule under sustained hydrostatic loading.

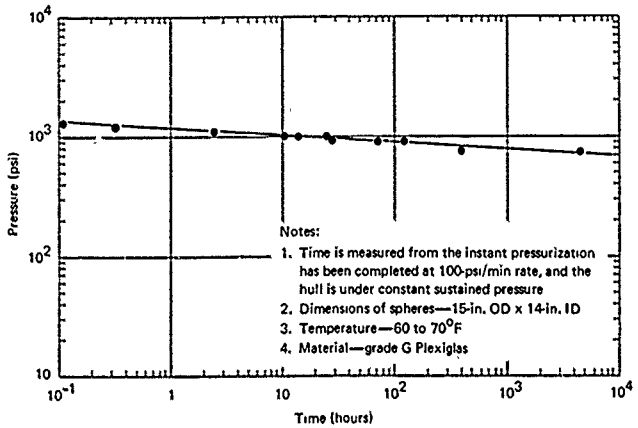

Figure 87. Implosion pressure as a function of sustained pressure duration at room temperature for 15-inch-diameter capsules.

3. Long-term sustained hydrostatic loading caused model capsules to fail at a lower pressure than short-term loading. The relationship between the magnitude of pressure and the duration of loading at which the models failed were represented by a linear graph when the test results were plotted on a log-log scale (Figure 87). When the critical pressure versus time relationship of Figure 87 was extrapolated, it was found that under a sustained pressure of 500 psi and in the 60 to 70°F ambient temperature range the time-dependent implosion of the model capsule would not take place before at least 10 years of exposure. At higher temperatures, since the time-dependent strain rate is higher, the implosion failure would occur sooner, while at lower temperatures, since the time-dependent strain rate is lower, the failure would occur later. For example, the model capsule under 750-psi long-term pressure loading at 70°F average ambient temperature failed after 366 hours, while another model (10% thicker) under the same magnitude of pressure loading, but at 60°F average temperature, failed after 4,500 hours.

4. The time-dependent failure of the model capsules was local in nature (Figure 88). It appeared to have been triggered by local deviations from sphericity and uniform wall thickness. Since local decrease in curvature or wall thickness causes a local increase in compressive membrane stresses, the time-dependent strains in this area would be higher also, thus further

aggravating the local imperfection. Ultimately the curvature decreases locally to such an extent that the flexure stress dominates the stress field. When the tensile component of the flexure stress overcomes the compressive membrane stress at the center of the flat spot on the interior surface of the capsule, failure of the acrylic plastic occurs (Figure 89). That the local failure occurs in flexure is substantiated by (1) the similarity of the failure surface on the interior of the hull (Figure 90) to the fracture on interior of flat disc acrylic plastic windows that fail in flexure (Figure 91) and (2) by the presence of the circular crack on the exterior surface of the hull at the location where the flexure hinge encircling the flat spot was located.

5. Crazing and cracks were found on the acrylic plastic bearing surfaces in contact with the steel end plates after conclusion of long-term sustained pressure loadings at 500-, 750-, and 900-psi pressure levels (Figures 92 through 95). No cracks or crazing were found in capsules subjected to long-term sustained loading at pressures less than 500 psi or higher than 900 psi. It is hypothesized that the formation of cracks on the acrylic plastic bearing surface in contact with the end plate depends on the magnitude of time-dependent strain (elastic and plastic components of strain) rather than stress in the bearing surface. The model capsule under 250-psi long-term sustained hydrostatic loading did not exhibit cracks because the magnitude of the time-dependent strain at that stress level is small even after 1 year of sustained loading. The models under pressure in excess of 900 psi also exhibited no cracks because although the *time-dependent strain rate* at these stress levels is very high, the *magnitude of time-dependent strain* is low at the moment of failure, as the failure of the model occurs within a relatively short time. Only in the 500-to-900-psi range of hydrostatic loading does the magnitude of time-dependent strain in the acrylic plastic bearing surface become sufficiently large to cause cracks in the acrylic plastic surface at the steel end plate, as the stress level is fairly high and the duration of sustained loading without implosion is long.

The cracks were not uniformly distributed across the thickness of the hull at the bearing surface but were primarily concentrated on the inner half of the wall. The deepest cracks were at the location on the bearing surface that corresponded to the bottom edge of the O-ring groove in the steel end plate. The cracks were circumferential with respect to the steel end plate and propagated themselves at right angles to the bearing surface. The depth of these cracks was greater in the model that was subjected to 750 psi for 4,500 hours (Figures 92 and 93) than in the model at 900 psi loaded for 72 hours. This could be explained by the fact that at the completion of the test the magnitude of time-dependent strain in the model loaded at 900 psi, although the stress level was higher on the latter.

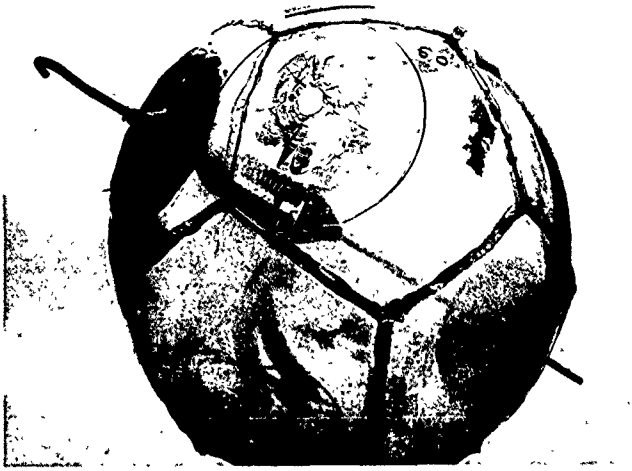

(a) Model 3.

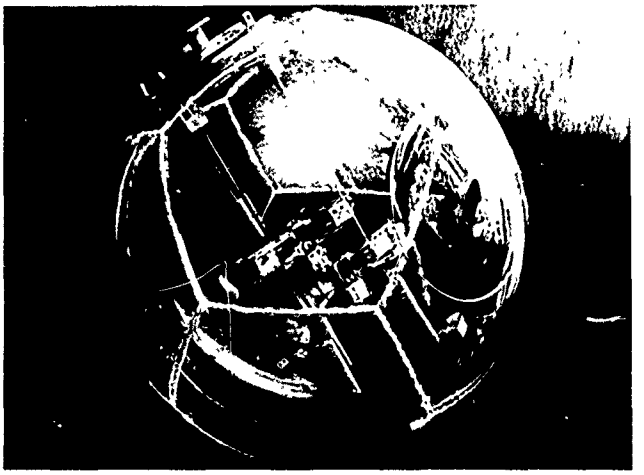

(b) Model 2.

Figure 88. Typical examples of localized, time-dependent, viscoelastic buckling of the 15-inch diameter capsules subjected to sustained 750-psi external hydrostatic pressure in 60-to-70°F temperature range until failure took place.

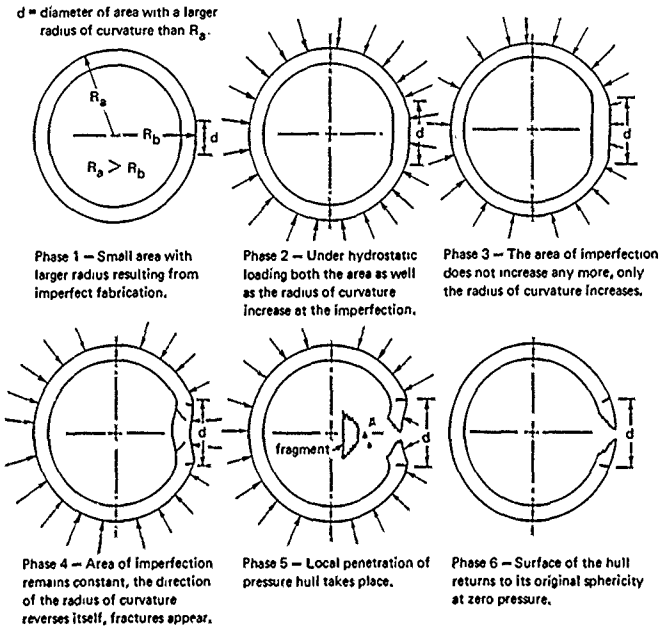

Figure 89. Mechanism of localized viscoelastic failure in an acrylic plastic hull under sustained external hydrostatic pressure.

6. The total decrease in volume of model capsules at the moment of their failure under long-term sustained hydrostatic pressure was approximately the same regardless of the sustained hydrostatic pressure level at which they were kept. The total decrease of volume just prior to implosion was somewhat less than in short-term pressure tests. The magnitude of volume decrease under long-term hydrostatic pressure was approximately 4% (Figure 86), as compared to 4.8% under short-term pressurization (Figure 79).

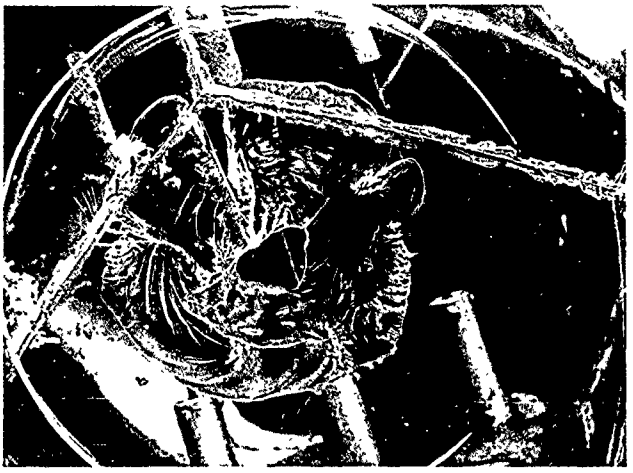

Figure 90. Fracture pattern in a localized viscoelastic capsule failure under sustained hydrostatic pressure.

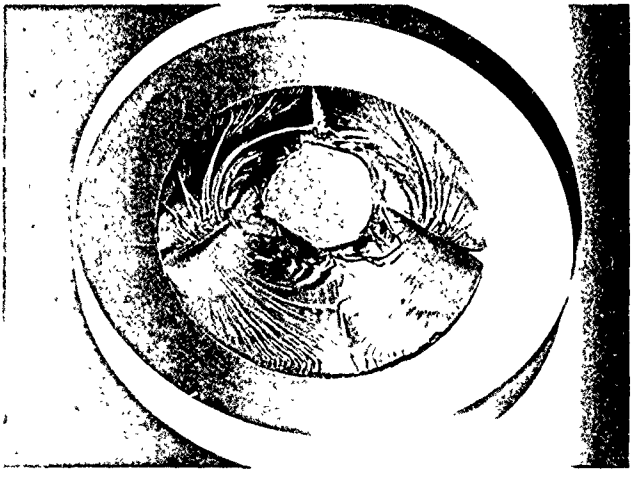

Figure 91 Fracture pattern in a flat disc acrylic plastic window that failed in flexure under short-term hydrostatic loading, high pressure face.

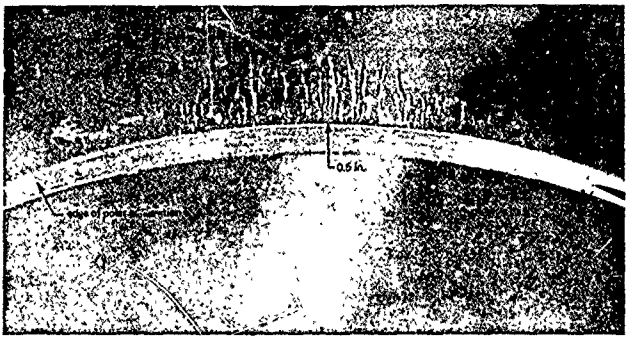

Figure 92. Cracks in beveled edge of acrylic plastic bearing surface for steel insert in a 15-inch-diameter capsule after 4,500 hours of sustained hydrostatic loading at 750 psi (looking at right angles to the external surface of the capsule).

Figure 93. Cracks in beveled edge of acrylic plastic bearing surface for steel insert in a 15-inch diameter capsule after 4,500 hours of sustained hydrostatic loading at 750 psi (looking at right angles to the beveled bearing surface).

Figure 94. Cracks in beveled edge of acrylic plastic bearing surface for steel insert in a 15-inch-diameter capsule after 72 hours of sustained hydrostatic loading at 900 psi (looking at right angles to the bearing surface).

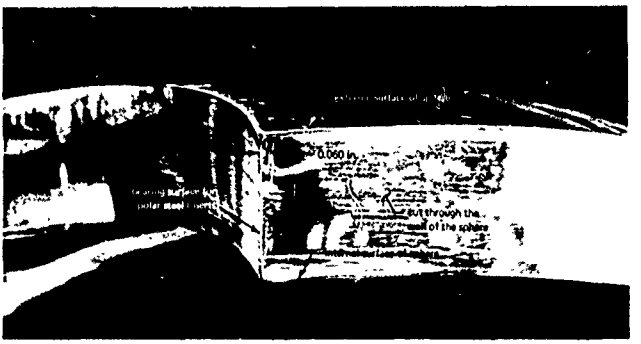

Figure 95. Cracks in the beveled edge of the acrylic plastic bearing surface for steel insert in a 15-inch diameter capsule after 72 hours of sustained hydrostatic loading at 900 psi (looking at right angles to a cut through the bearing surface).

This difference can be explained by the hypothesis that since local flat spots and thin sections of the hull cause the acrylic plastic hull to fail at lower pressure by straining locally at a higher viscoplastic rate than the rest of the hull, the rest of the hull does not have the opportunity to reach the compressive strain level at which implosion by general creep buckling mode occurs. Thus, the difference between the volume decrease under short-term and long-term sustained pressure can serve as an indicator of the severity of local deviations from sphericity and thickness in the acrylic plastic hull. The rather small difference between the volume decrease under short-term pressure loading (approximately 1,350 ml) and long-term pressure loading (approximately 1,150 ml) seems to indicate that the severity of local deviations in sphericity and thickness was rather low. This is, of course, substantiated by actual measurements of sphericity deviations which were on the order of 0.010 to 0.030 inch for the majority of the models.

Cyclic tests were performed on four capsule models to determine the effect of repeated pressurizations on the structural integrity of the acrylic plastic hulls. These tests produced results that are less conclusive than those from short-term and long-term sustained pressure tests, largely because there was only one test specimen for a given test condition and there were only four test conditions (Table 6). Because of these limitations, all the findings address themselves to the effects of three variables only: (1) number of cycles, (2) duration of pressure cycle, and (3) cumulative time under pressure. The effect of pressure magnitude is not discussed because only a single pressure level of 500 psi was used in the cyclic tests.

The cyclic test findings are:

1. None of the model capsules failed during pressure cycling from 0 to 500 psi (1,120 feet). The cyclic history at the termination of the tests was 4,000 cycles for the model with a 1-hour sustained loading during the pressure cycle, 600 cycles for the model with a 12-hour loading, 300 cycles for the model with a 24-hour loading, and 100 cycles for the model with a 120-hour loading.

2. No damage was visible in the model capsules except on the beveled acrylic plastic bearing surfaces in contact with the metal end plates. The damage was in the form of circumferential cracks in plane of the wall at right angles to the bearing surface, similar to those observed in some of the capsules under long-term loading. The cracks were concentrated below the inner half edge of the O-ring groove in the steel end plate.

3. By comparing the depth of cracks on the bearing surfaces of all the models cycled from 0 to 500 psi, it has been found that the deepest cracks were found in the model subjected to 100 cycles with a 120-hour dwell time at maximum and minimum pressures. Since the other three models completed

300, 600, and 4,000 cycles, respectively, the cause for the greater depth of cracks in the model with only 100 cycles could not be the number of stress cycles as otherwise the model with 4,000 cycles would have had the deepest cracks, while in reality it suffered only slightly from cracking (Figure 96).

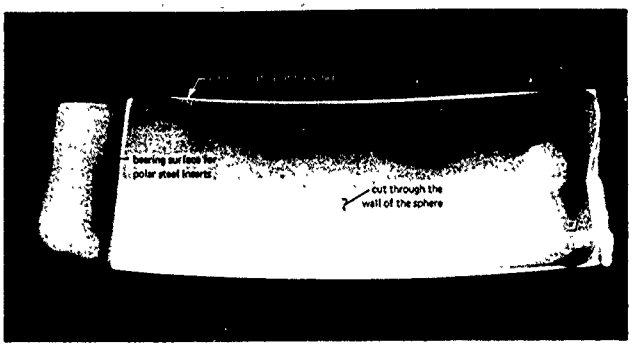

Figure 96. Beveled edge of the acrylic plastic bearing surface for the polar steel insert in a 15-inch-diameter capsule after 4,000 pressure cycles to 500 psi with 1-hour dwell times at 500 psi and 0 pressures.

Since the model with the 100 cycles was subjected to the longest duration cycles (120 hours at 500 psi) and had the longest cumulative time under pressure (12,000 hours at 500 psi) as compared to the others with 24-, 12-, and 1-hour cycles, respectively, it would appear that in all probability it was either the length of the individual cycle (magnitude of time-dependent strain) or the total cumulative time under pressure rather than the number of cycles that caused this model to have the deepest cracks. It would thus appear that the effect on the acrylic plastic bearing surfaces at penetrations in the capsule of a single long pressure cycle or total cumulative time under load is more severe than the effect of several short cycles of the same pressure level.

Further, it appears that from the two factors (length of individual cycle and cumulative duration of loading at 500 psi) the length of individual cycle is the more important one. This finding is based on the observation that the cracks were more prominent in Model 8 with 300 cycles and 24-hour individual cycle duration (total cumulative time under 500 psi is 7,200 hours) than in Model 11 with 600 cycles and 12-hour duration (total cumulative time of 7,200 hours). Since both models have equal cumulative time under load, while Model 8 has both the longer individual cycle and lesser number of cycles, it could not be either the number of cycles or cumulative time under load that caused it to have more severe cracks than Model 11.

4. The appearance of cracks in the acrylic plastic bearing surface at the penetrations is not a sign of impending implosion, as none of the models imploded during cycling, although the cracks became visible many cycles before the termination of the cycling program.

5. Pressure cycling capsules to a 500-psi pressure level does not appear to induce irreversible strains in the acrylic plastic, except probably locally on the steel polar closure–acrylic plastic interface. Both the decrease in hull volume, as measured by displacement of water, and the strains on the interior surface of the hull, as measured by electric resistance strain gages, have shown that even after a 120-hour pressure cycle the acrylic plastic hull returns to its original dimensions providing sufficient time is given for its relaxation at 0 pressure. This indicates that both the typical instantaneous and time-dependent strains generated in the acrylic plastic hull under a 500-psi loading in the 60 to 70°F temperature range are viscoelastic (Figures 97 and 98).

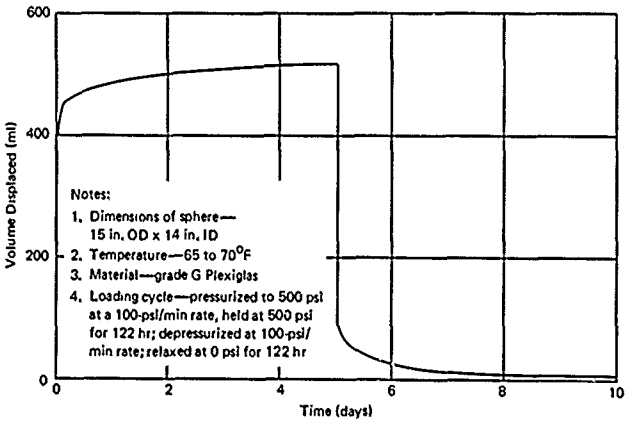

Figure 97. Change in displacement of a 15-inch-diameter capsule during a typical pressure cycle to 500 psi with subsequent relaxation period.

6. The acrylic plastic models were as viscoelastic at the conclusion of their cyclic testing programs as they were at their beginning. This is based on the observation that when the pressure in a given pressure vessel containing a capsule was raised to 520 psi and then the pressurization was terminated, the pressure dropped a certain amount in the isolated vessel during a 24-hour period due to a decrease in volume of the capsule. Since the decrease of

pressure in an isolated pressure vessel in a 24-hour period during the first pressure cycle was found to be equal to the pressure drop recorded in the same vessel during some later cycle, the decrease in volume of the capsule model was the same in both cases. For example, the pressure drop in 24 hours during the first pressure cycle on Model 8 was from 520 psi to 453 psi. Subsequently, the pressure drop was measured again during the 234th cycle and was also found to be from 520 to 453 psi.

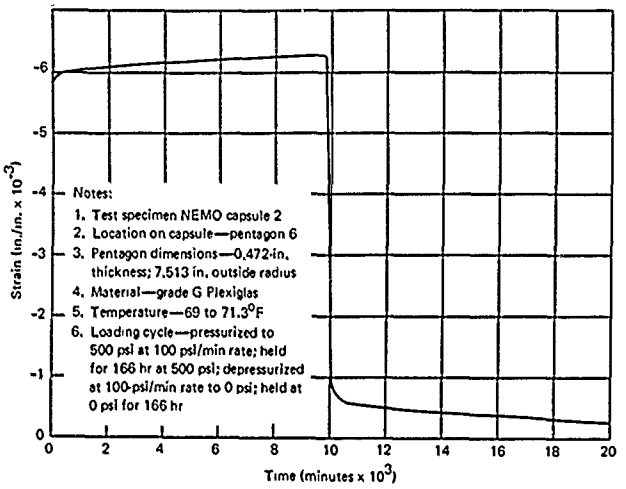

Figure 98. Typical viscoelastic strain on the interior of a 15-inch-diameter capsule in the equatorial region during a typical pressure cycle to 500 psi with subsequent relaxation period.

An *axial compression test* conducted on a single model capsule to simulate tie rod loadings produced only exploratory data. Since the electric resistance strain gages, located both on the exterior and interior of the hull, covered only a small area of the surface, a complete picture of the stress field in the acrylic plastic hull under axial compression was not obtained. The load was applied to the hull by internal tie rods attached to the circumference of the steel end plates. On the basis of this data (Figures 99 and 100), it has been found that:

1. The stresses generated by axial tie-rod pretension of 100 pounds are higher at the steel polar plate than at the equator. The meridional stresses at the penetration show compression on the exterior and tension on the interior.

The hoop stresses at the polar plate also show compression on the exterior surface of the hull and tension on the interior. The hoop stresses, both on the exterior and the interior, are smaller than meridional stresses.

2. The stresses at the equator of the acrylic plastic sphere were barely noticeable. The meridional stresses showed compression both on the outside and on the inside, while hoop stresses showed tension both on the outside and on the inside. The compressive meridional stress was higher on the inside than on the outside surface. The tensile hoop stresses were approximately equal for the outside and inside surfaces of the hull.

3. The tensile stresses caused by pretensioning of tie rods are so small as to constitute a negligible effect on the distribution of compressive stresses superimposed during hydrostatic pressure tests.

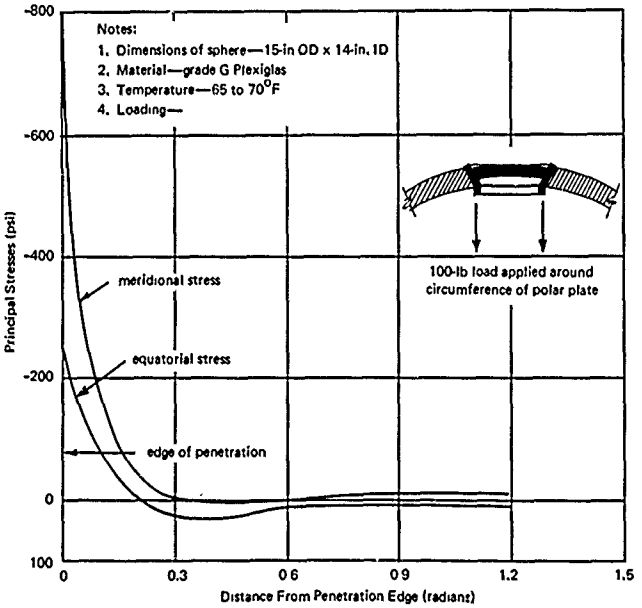

Figure 99. Stresses on the exterior of a 15-inch-diameter capsule under axial compression applied by internally located pretensioned tie rods.

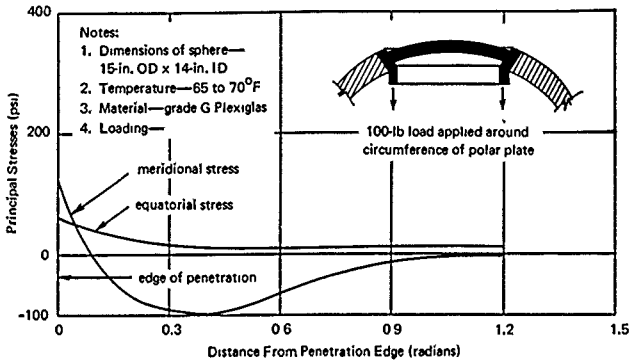

Figure 100. Stresses on the interior of a 15-inch-diameter capsule under axial compression applied by internally located pretensioned tie rods.

Large-Scale Capsule

Because only one 66-inch-OD x 61-inch-ID large-scale capsule prototype (NEMO capsule 0) was available for the determination* of the many facets of structural behavior exhibited by the acrylic plastic hull, it was much more exhaustively instrumented and produced considerably more data than the model capsules. This is particularly true of the strain data generated by 81 strain gages (Figure 101) during more than 100 pressure cycles of different periods and pressure magnitudes. Since the detailed evaluation of this voluminous strain data and its comparison with computer generated values[21] is a rather involved operation, the detailed discussion of experimental data were omitted from this report to be published as a separate report at a later date.[22] However, in order to make this report complete, the findings of the strain and stress analysis are presented here in the form of summaries (Figures 102 and 103); there are also discussions of tests that did not employ strain gage instrumentation systems.

Since all the tests performed on the large-scale capsule prototype were cyclic, even though of different period duration and maximum pressure level, the discussion of findings will be classified by type of response or physical characteristic rather than by test as was done in the discussion of findings for model capsules.

* The proof tests performed on the three production 66-inch NEMO capsules were very limited and therefore are not discussed in the main body of the report. (See Appendix F.)

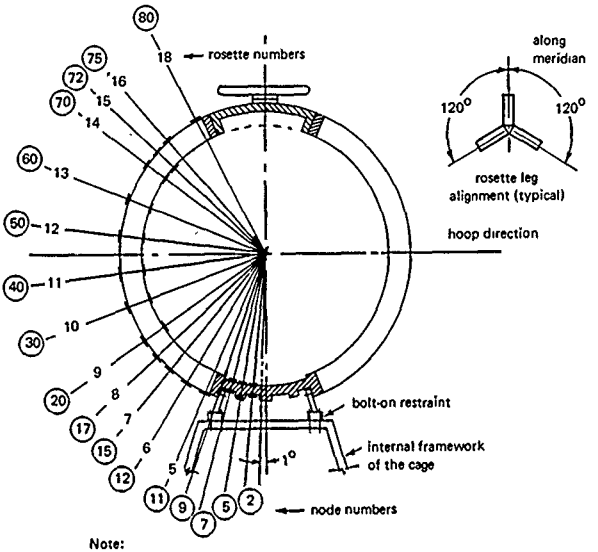

Figure 101. Location of strain gages on the 66-inch-diameter capsule for external pressure hydrostatic testing program.

Short-term strains and stresses in the large-scale capsule prototype were recorded at 27 locations (Figure 101) during all the pressurization in the 0-to-800-psi pressure range. Strains were also recorded at two locations during the differential temperature tests. The findings, based on strain gage recordings during the short-term pressurization from 0-to-500-psi pressure are:

1. The short-term strains in the acrylic plastic hull varied linearly with pressure (Figure 104). The maximum principal strains on the interior surface in the equatorial regions were approximately 20% higher than on the exterior surface of the hull. The magnitude of the principal strains on the interior surface of the equator at 500-psi short-term pressure and 68°F

temperature was in the region of 4,500 to 5,100 μin /in., while those on the exterior were in the 3,500 to 4,100-μin /in. range. The exact magnitude and distribution of strains in the acrylic plastic around the polar plates is not known because they were not instrumented in sufficient detail; there are indications that the ratios of strains at the polar plates to those at the equator were lower than those measured on the model. This was probably caused by the difference in polar plate fastening procedures used for the model and for the 66-inch capsule. While in the model the pretensioned tie rod seated the end plate with only a 100-pound axial force in the 66-inch capsule the polar plate was seated in the polar opening with approximately 100,000-pound force generated by 20 bolts reacting against the split retaining flanges. The very large seating force pretensioned the acrylic plastic around the polar plate to such an extent that only minor compressive strains could appear there during hydrostatic testing.

2. The strains in the steel bottom plate also varied linearly with pressure. The strains measured on the bottom steel plate varied from one location to another with the strains in one location approaching the yield point of type 316 stainless steel from which the end plates were made. The gage that measured the highest strain on the steel polar plate was rosette 3 located on the interior surface of the bottom plate in the immediate vicinity of the plate flange.

3. When the measured strains at 500-psi short-term pressurization and 68°F were converted into stresses, the magnitude of membrane stresses at the capsule's equator was found to be approximately 3,400 psi on the interior and 2,900 psi on the exterior. The highest measured stress in the steel end plate at rosette 3 was 27,000 psi (Figures 101 and 103).

Short-term volume decrease, measured with the same type of volume-displacement arrangement as in the model capsules, at 68°F was linear to 750 psi, the maximum pressure to which the sphere was pressurized in that test. The volume decrease was approximately 5.5 liters per each 100 psi of short-term pressure increase (Figure 105). When proper scaling factors were applied to the measured volume decrease of the prototype large-scale capsule, it was found to be the same as for the model capsules under short-term loading (Figure 106). Two separate scaling factors were employed. One factor accounts for the fact that the volume of a spherical hull varies as the cube of the radius. The other factor accounts for the fact that the actual wall thickness of the large-scale capsule was somewhat disproportionately thicker than that of the model capsule.

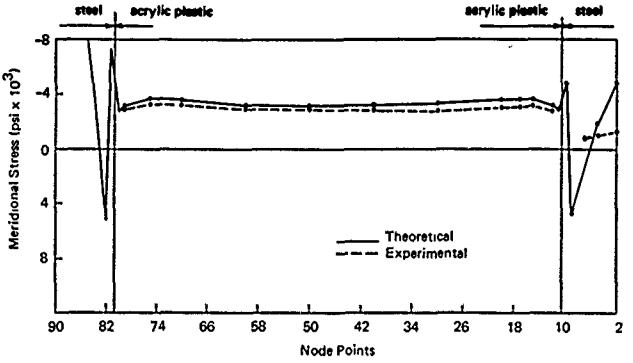

(a) Meridional stresses on the exterior surface.

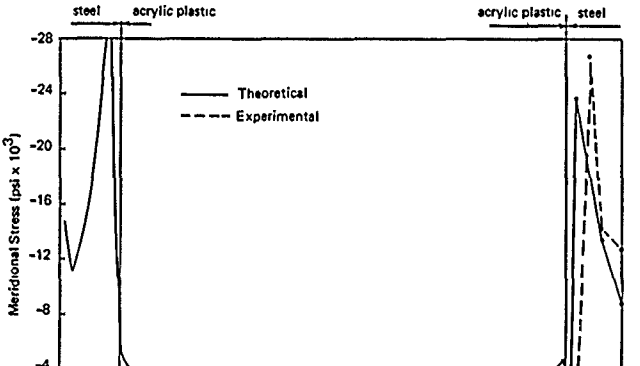

(b) Meridional stresses on the interior surface.

Figure 102. Comparison of analytically and experimentally derived stresses in the 66-inch-diameter capsule under 500-psi short-term hydrostatic loading.

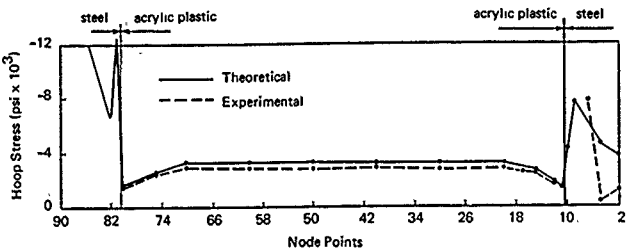

(a) Hoop stresses on the exterior surface.

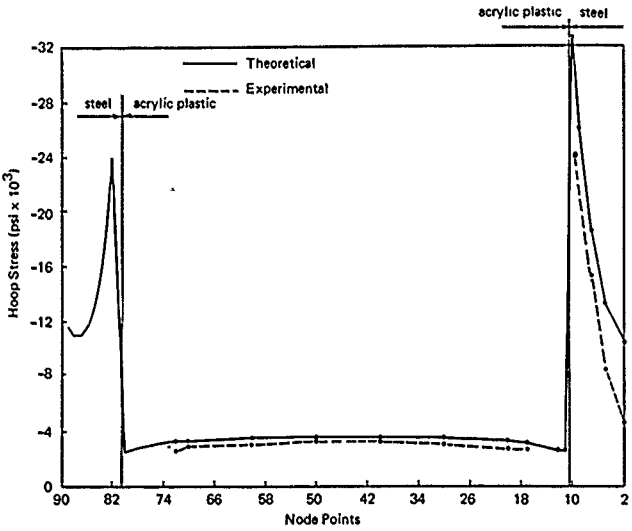

(b) Hoop stresses on the interior surface.

Figure 103. Comparison of analytically and experimentally derived stresses in 66-inch-diameter capsule under 500-psi short-term hydrostatic loading.

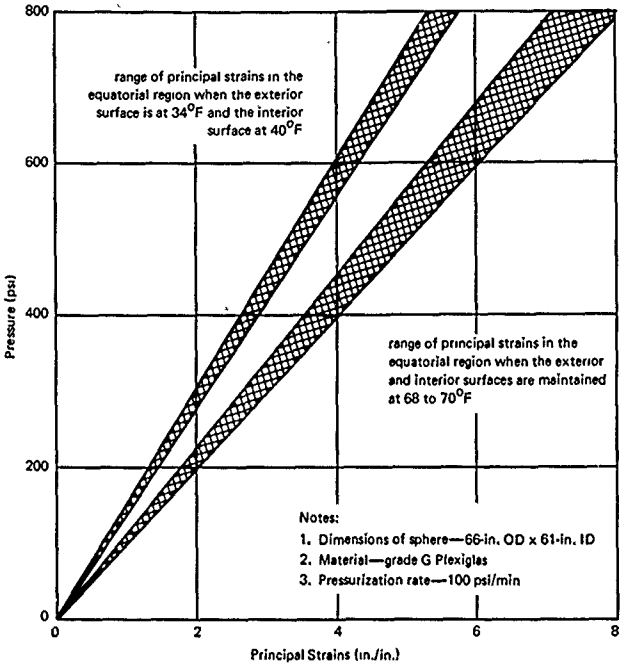

Figure 104. Effect of ambient temperature on strains in 66-inch-diameter capsule under short-term loading: typical strain on interior surface in the equatorial region.

Cyclic strains generated by pressure cycling were recorded at 36 locations on the acrylic plastic hull. Since all the pressure cycles had 500 psi as the upper pressure limit, the following findings pertain only to pressure cycling of that magnitude.

1. The principal strains measured at the equator on the external and internal surfaces of the hull during the pressure rise in each hydrostatic cycle were found to be in same range as those measured during a single short-term loading.

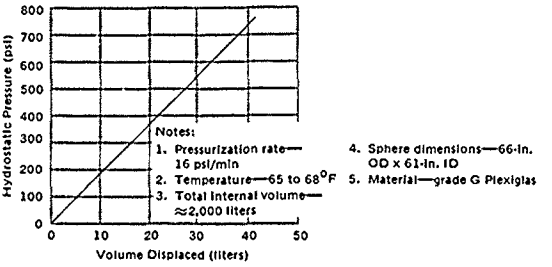

Figure 105. Change in displacement of 66-inch-diameter capsule under short-term loading.

2. The relaxation periods at zero pressure, which were chosen for all pressure cycles to be equal in length or longer than the duration of sustained pressure periods, appeared to be sufficiently long for all strains to return to zero (Figure 107). Thus, the magnitude of strains in acrylic at the initiation of each pressure cycle rose by the last cycle from zero to only 100 μin./in. This took place regardless of whether the length of each cycle was 2, 15 or 60 minutes.

Long-term strains were also recorded at 27 locations while the hull was subjected to long-term loading of 24-hour duration at 100-, 200-, 300-, 400-, 500-, 600-, 700-, and 800-psi external hydrostatic pressure. Since the relaxation periods were sufficiently long between each long-term pressurization to allow for a complete relaxation of the hull, the recorded strain data was not considered to be contaminated by viscoelastic strains still undergoing relaxation when the next pressure cycle was initiated.

1. At room temperature, the magnitude of strains in the equatorial region under long-term hydrostatic loading after a given duration of sustained loading appears to vary linearly with pressure. To what maximum pressure this relationship remains linear is not known, as the long-term pressure tests were conducted only to 800 psi, at which pressure the relationship still continued to be linear (Figures 108, 109, 110).

2. Upon depressurization, the strains in the equatorial region returned almost to zero, even after long-term 800-psi pressure loading. This appears to indicate that even at an 800-psi long-term hydrostatic loading in the 68 to 70°F temperature range, the strains in the capsule (with possible exception of polar regions) are probably still viscoelastic (Figures 109 and 110).

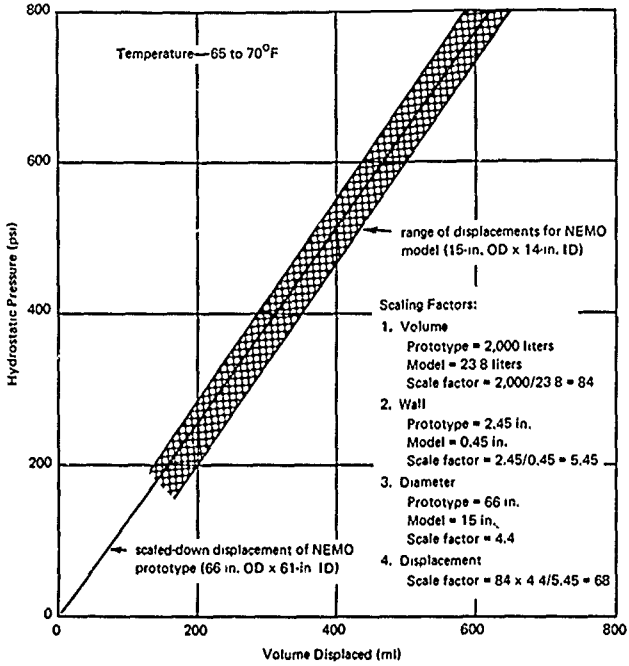

Figure 106. Comparison of displacement change measured on 66-inch diameter capsule and predicted displacement based on extrapolation of displacement change data from 15-inch diameter capsule under short-term loading.

3. The time-dependent strain rate varies with the pressure to which the acrylic plastic hull is subjected during long-term loading. The relationship between the time-dependent strain rate and pressure is probably exponential.

4. Immediately after initiation of long-term pressure loading, the strain and time-dependent strain rate were higher on the interior of the hull in equatorial region than on the exterior of the hull. This was caused by the presence of higher stresses on the interior of the hull at that time. (Figures 109 and 110).

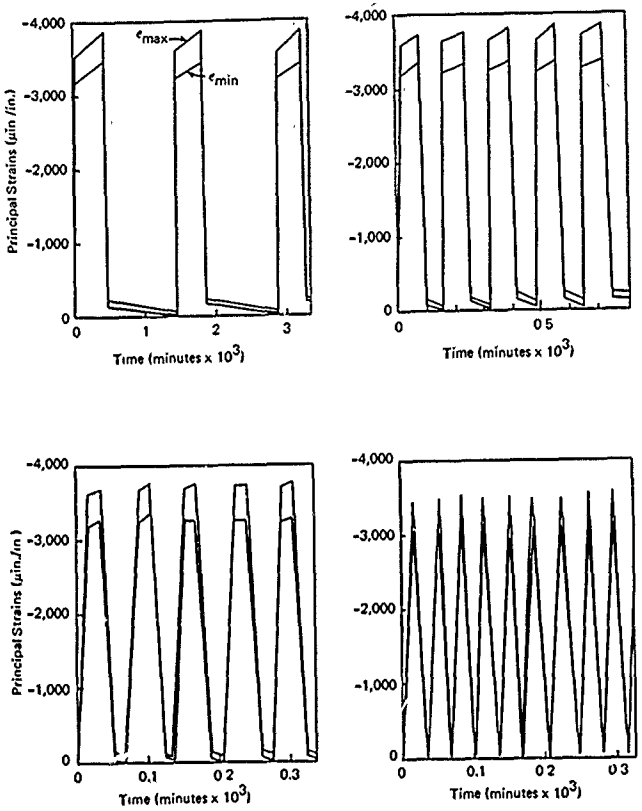

Figure 107. Strains on the interior surface of 66-inch acrylic plastic capsule under cyclic pressure loading to 500 psi.

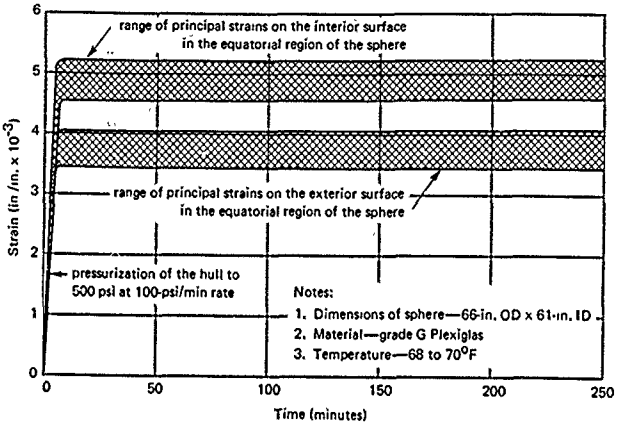

Figure 108. Range of strains at the equatorial region of the 66-inch-diameter capsule under sustained hydrostatic loading of 500 psi.

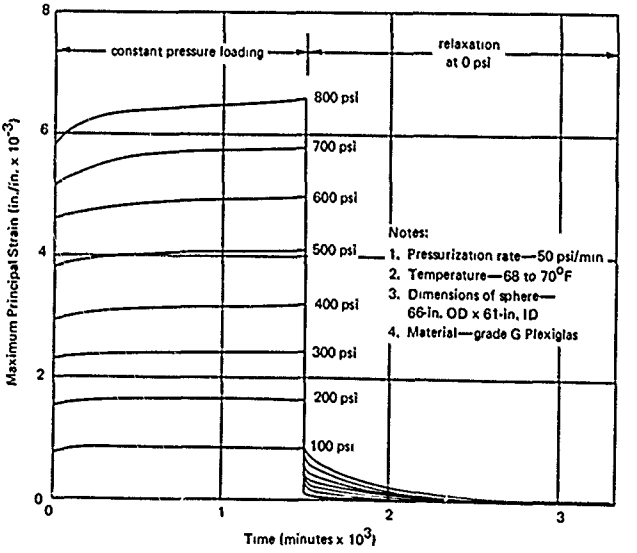

Figure 109. Typical viscoelastic strain on exterior surface of equatorial region in 66-inch-diameter capsule under sustained hydrostatic loadings of different magnitude, and subsequent relaxation.

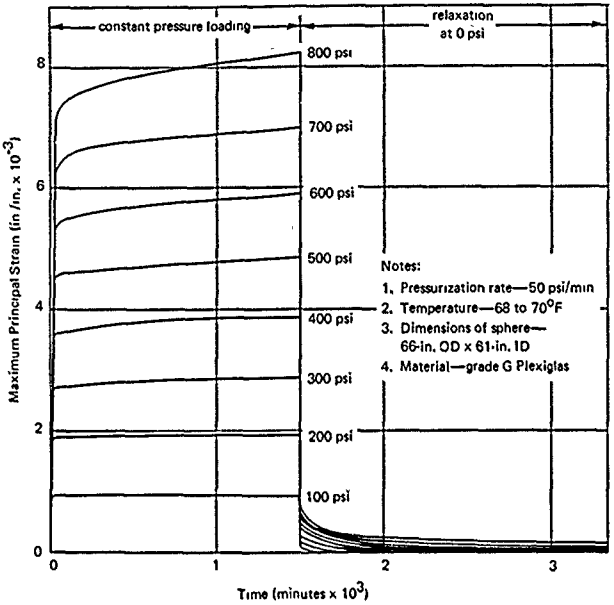

Figure 110. Typical viscoelastic strain on interior surface of equatorial region in the 66-inch diameter capsule under sustained hydrostatic loadings of different magnitude and subsequent relaxation.

5. The strain, as well as the time-dependent strain rate, vary with the temperature of the pressurizing medium. Comparison of strains and strain rates in 32 to 35°F temperature range with those in the 68 to 70°F range shows that in the low temperature range they are smaller by about 20% to 30% (Figure 111).

6. If the acrylic plastic capsule is depressurized to some pressure level above 0 psi, the strains will initially begin to relax as they do when the external pressure level is reduced to 0 psi. After a period of time, the time-dependent relaxation of strains will cease and time-dependent increase in strain will begin, but the rate will be lower than for hulls not previously loaded to higher pressure levels. However, after a sufficiently long period of time, the strains reach the same equilibrium point regardless of whether the hull was first loaded to some overpressure and then depressurized to the operational pressure level or the pressure was raised to the desired level directly from 0 psi. Upon depressurization to operational pressure, the time required for the strains resulting

from overpressure to decrease to the level of strains generated by a simple long-term loading at operational pressure varies with the duration of loading at the overpressure level (Figure 112).

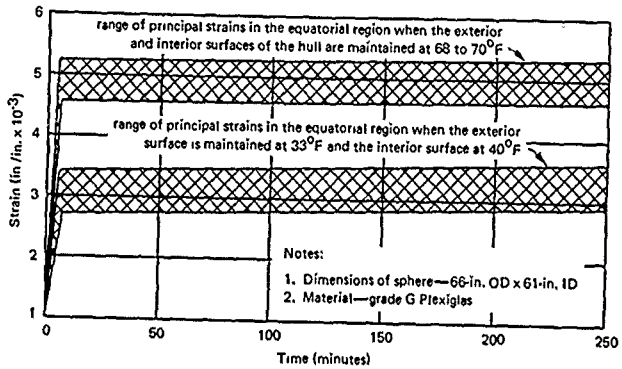

Figure 111. Effect of temperature on viscoelastic strains on interior surface of equatorial region in 66-inch-diameter capsule under 500-psi sustained hydrostatic loading.

Long-term volume decrease, measured by the displacement of water from the interior of the large-scale capsule, was performed only at three different pressure loadings, as compared to nine different pressure loadings for model capsules. From the volume decrease measurements performed on large-scale capsule prototype, the following findings were made:

1. Long-term volume decrease is a function of both time and pressure. However, for any given duration of loading, it is approximately linear with the magnitude of pressure loading. The time-dependent rate of volume decrease for any given pressure loading appears to decrease exponentially with time, and to increase exponentially with the magnitude of pressure loading (Figures 113 and 114).

2. Upon depressurization from the long-term pressure loading, the volume of the large-scale prototype capsule returned to its original size after a relaxation period of approximately the same duration as the long-term pressure loading. The volume increase rates at the beginning of relaxation periods were higher than the volume decrease rates at the beginning of the long-term loading periods (Figure 115).

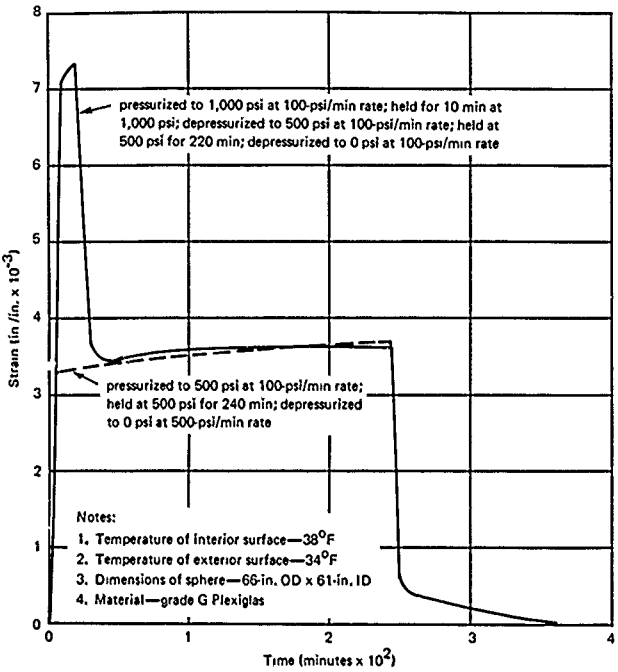

Figure 112. Comparison of strains under 500 psi sustained hydrostatic loading and strains under 500-psi sustained hydrostatic loading following a sustained loading of 1,000 psi; strains were measured on the interior surface in the equatorial region of the 66-inch diameter capsule.

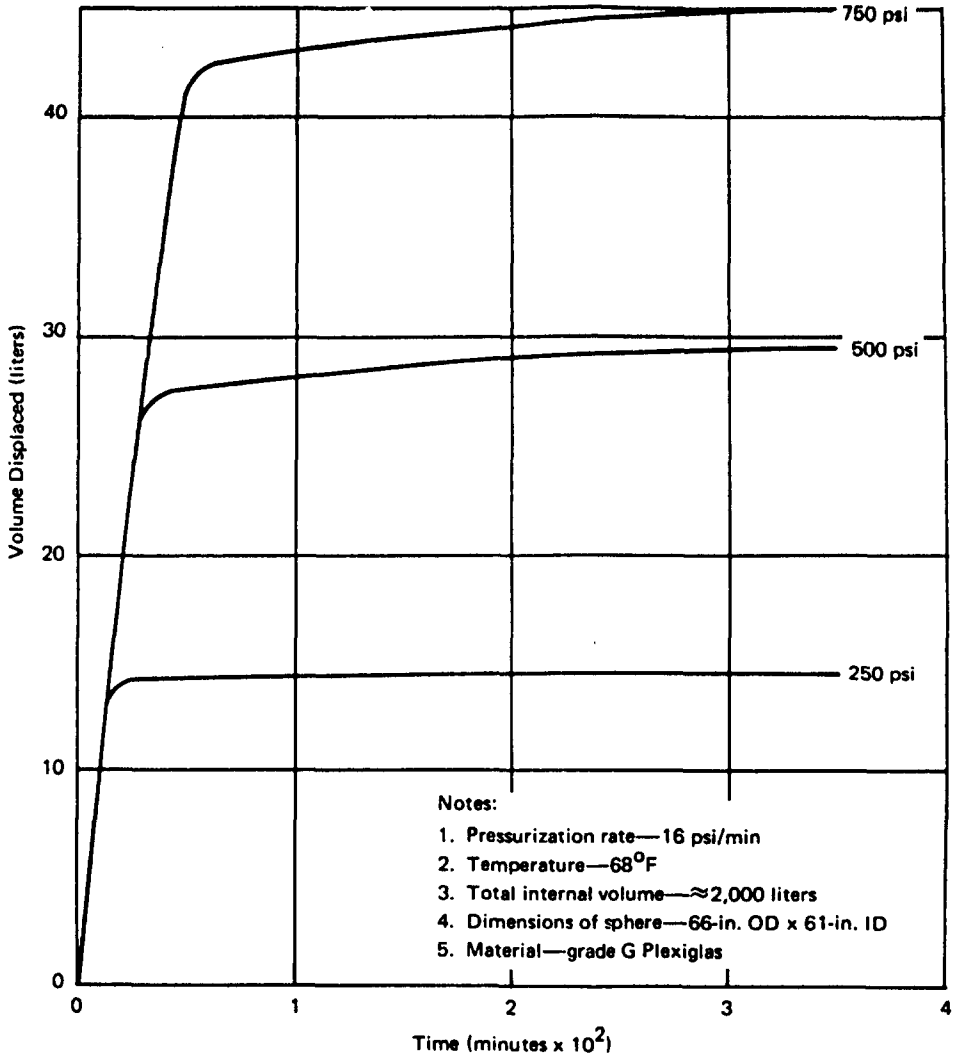

Figure 113. Change in displacement of the 66-inch-diameter capsule under sustained hydrostatic loadings of different magnitudes.

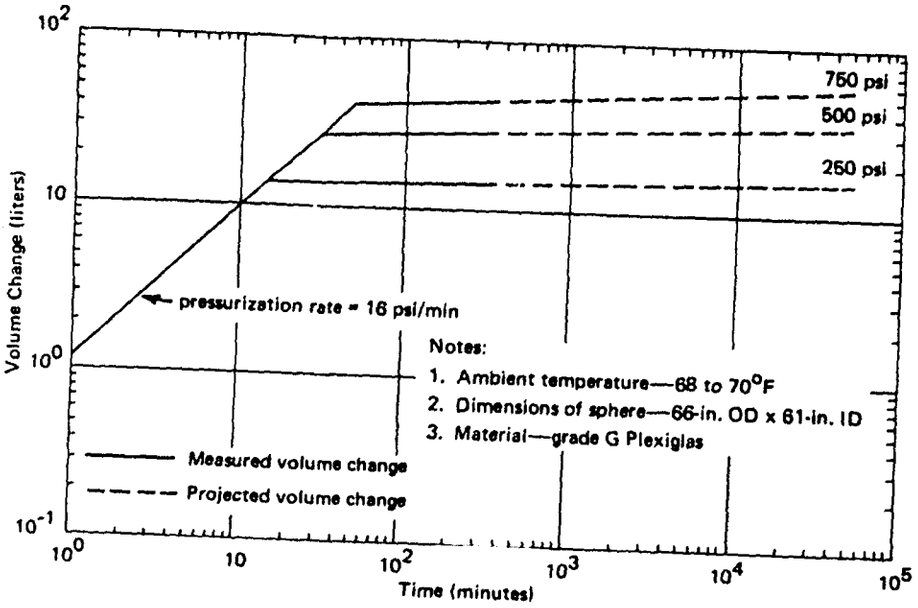

Figure 114. Linear plot of displacement change in a 66-inch-diameter capsule under sustained hydrostatic loading to permit extrapolation of available experimental data.

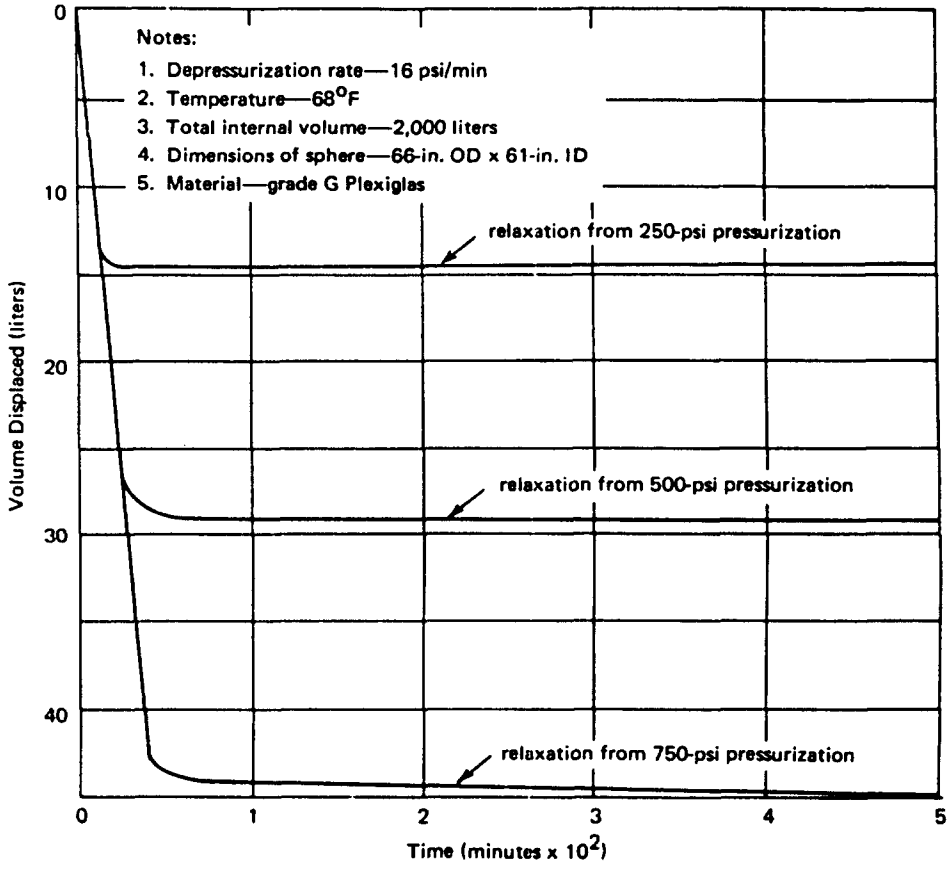

Figure 115. Change in displacement of the 66-inch-diameter capsule during relaxation from sustained hydrostatic loadings of different magnitude.

Short-term strength of the large-scale acrylic plastic capsule was determined by pressurizing it externally to implosion at a 100 psi/min rate with water at 70°F ambient temperature. The implosion took place at 1,850 psi with a failure mechanism similar, if not identical, to that of the models previously imploded under short-term loading. From the observation of the fragments from the imploded sphere as well as comparison of the failure pressure of the large capsule and model capsules the following findings were made:

1. There appears to be no material mass scaling effect, common to glass or concrete structures, in acrylic plastic since the 1,850-psi implosion pressure of the 66-inch capsule matches closely the 1,827-psi pressure predicted for the large-scale capsule on the basis of model capsule tests. This prediction is based on the 1,575-psi average implosion pressure of the 15-inch acrylic plastic models and the fact that the minimum wall thickness of the 66-inch capsule is 16% greater than the minimum thickness of the models.

2. The fragmentation of the large-scale capsule was similar to that of models (Figure 116). In most cases, the fracture planes cross the joint bonds indicating that the joints did not serve as planes of weakness.

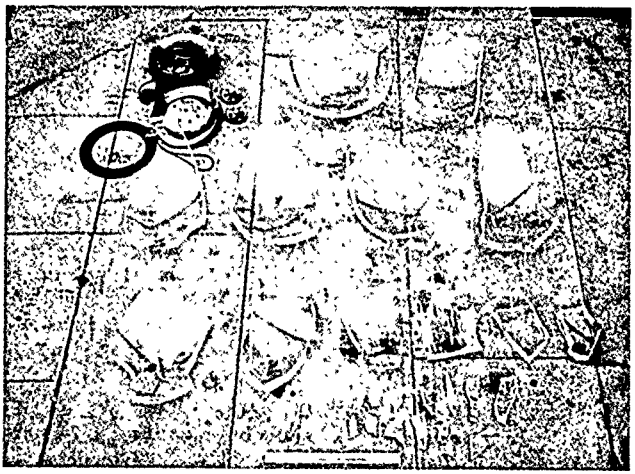

Figure 116. Overview of the structural fragments from the imploded 66-inch-diameter capsule. Note that the acrylic plastic fragments are *not* rectilinear, indicating that fracture did not take place along the bonded joints.

3. All of the steel end closure components except for the top hatch ring and associated split retaining rings showed extensive plastic deformation (Figure 117) indicating that the large-scale polar steel closures underwent *plastic buckling* at approximately the same pressure as the model scale steel closures which failed at 1,800 psi (Figure 80). This validates the linear scaling factor (diameter of prototype capsule/diameter of model capsule) used in the scaling up of model capsule end plates for use in the 66-inch prototype NEMO capsule.

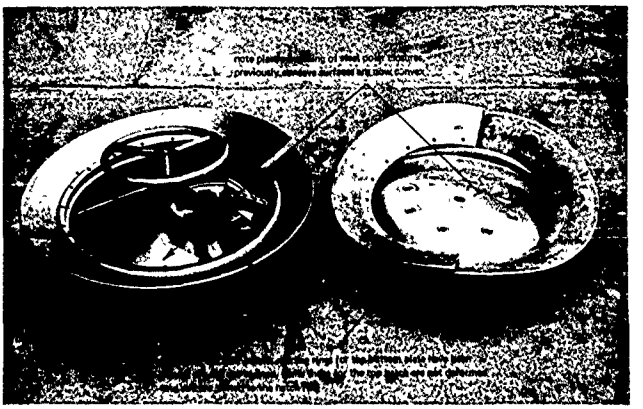

Figure 117. Steel polar closure assemblies from the imploded 66-inch-diameter capsule.

4. The general implosion of the prototype NEMO capsule was triggered by the plastic buckling of the bottom plate. This finding is supported by the fact that (a) only on the bottom plate were the hatch retaining rings twisted, (b) only on the bottom plate was the spherical beveled bearing surface severely distorted, (c) only the bottom polar pentagon had its beveled bearing surface severely damaged (Figures 118 and 119), (d) rosette 3 mounted at the location where plastic hinge in the bottom plate formed showed the highest stress level during previous tests to 500 psi.

5. Since the buckling of the hatch and of the bottom plate was plastic rather than elastic, it can be avoided at pressures less than 2,000 psi by substituting material with a yield point above 60,000 psi for the type 316 stainless steel used in the prototype.

Structural fatigue of the 66-inch hull was evaluated visually by noting the condition of bearing surfaces on the beveled edges of the acrylic plastic hull at the polar penetrations and the condition of the bonded joints between individual spherical pentagons at the conclusion of 107 pressure cycles. The maximum pressure in the individual pressure cycles varied from 100 to 1,070 psi and its duration from 1 minute to 24 hours.

1. Bonded joints did not have any indications of fatigue damage, although the joints had a large number of potential stress raisers in the form of cavities, separation spaces, and hairline cracks introduced during fabrication.

2. The bearing surface on the beveled edge of the polar penetrations had no indications of fatigue in the form of crazing, even though during the preceding 107 pressure cycles the hydrostatic pressure loading was in some cycles 2.4 times higher than pressure at the design depth of 1,000 feet (4 times higher than pressure at the operational depth of 600 feet).

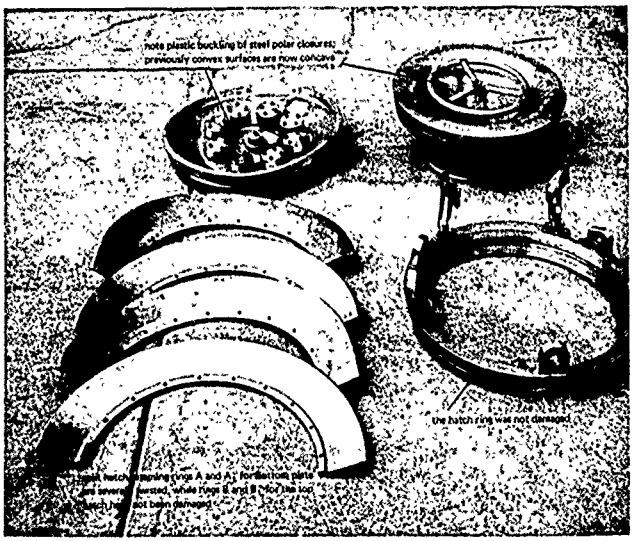

Figure 118. Steel polar closure components from the imploded 66-inch-diameter capsule.

3. The short-term test to failure at conclusion of 107 pressure cycles caused the capsule to fail at 1,850 psi. The actual implosion pressure of the large-scale capsule matches the implosion pressure of 1,827 psi predicted on the basis of implosion tests on model capsules. *Therefore, it can be postulated that no decrease in structural strength occurred as result of the previous pressure cycling to which the capsule was submitted.*

Heat transfer capability of the large-scale capsule was established in a stagnant water environment with a 400-watt interior heat source and forced-air circulation generated by a 100-watt interior fan blowing directly on the bottom polar steel plate.

1. After thermal equilibrium across the wall of the acrylic plastic capsule was established, the temperature measured on the interior surface of the wall was found to be approximately 3 to 4°F higher than the temperature of the water wetting the exterior of the hull.

2. After establishment of thermal equilibrium, the temperature of the air atmosphere contained within the hull was 12 to 12°F higher than the ambient temperature of the stagnant water wetting the exterior of the hull (Figure 120).

Tensile strength of joints in the 2-year-old 66-inch acrylic plastic capsule was established at the completion of the pressure test program by cutting tensile specimens from the fragments of the imploded capsule. Subsequently these bond test specimens were subjected to uniaxial tensile loading to determine their ultimate tensile strength after exposure to atmospheric environment for 2 years alternating with hydrospace environment while undergoing compressive fatigue testing in the vessel. The tensile strength of the joints bonded with PS-18 adhesive was found to be 9,220 psi maximum, 5,680 psi minimum, and 7,350 psi average. When these strength values are compared with the 8,280-psi maximum, 5,150-psi minimum, and 6,700-psi average strength value of PS-18 adhesive (Table 3) measured immediately after casting of a 0.125-inch-thick joint in 2.5-inch-thick acrylic plastic, the following is evident:

1. A 2-year exposure to atmospheric environment alternating with hydrospace environment in the 0-to-2,400-foot-depth range did not significantly alter the original strength of the joints.

2. The 107 pressure cycles in which the typical compressive stress in the joint varied from a minimum of about 600 psi to 11,000 psi had also no significant effect on the tensile strength of the joints bonded with PS-18 adhesive.

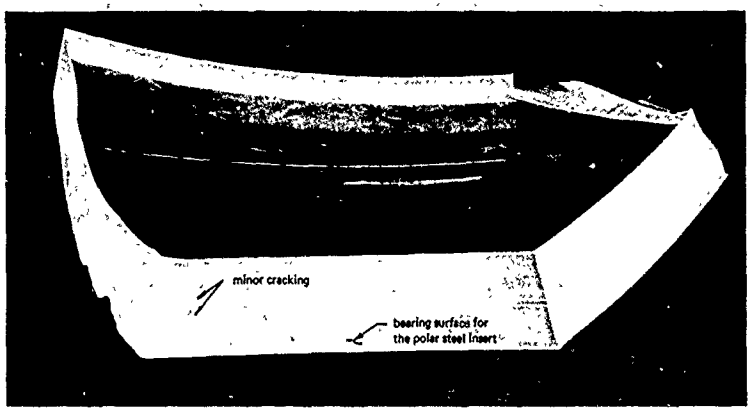

Figure 119a. Fragment from the top polar acrylic plastic pentagon. Note that the beveled bearing surface shows only minor cracking at the location that corresponds to the O-ring groove on the hatch ring.

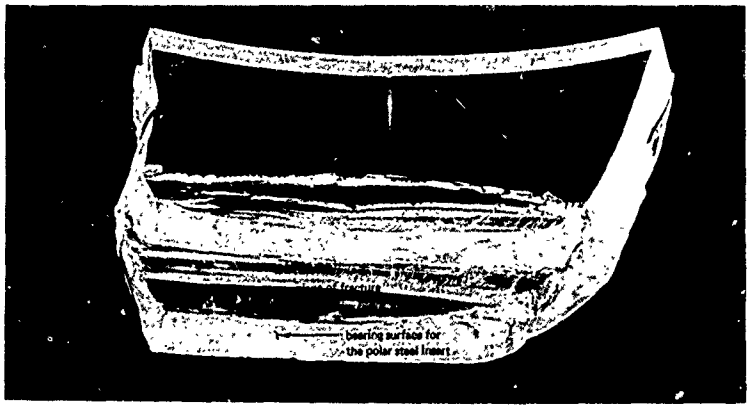

Figure 119b. Fragment from the bottom polar acrylic plastic pentagon. Note that serious spalling has taken place on the beveled bearing surface initiated at the location that corresponds to the O-ring groove on the bottom steel plate. Mechanism of failure is shown in Figure 119c.

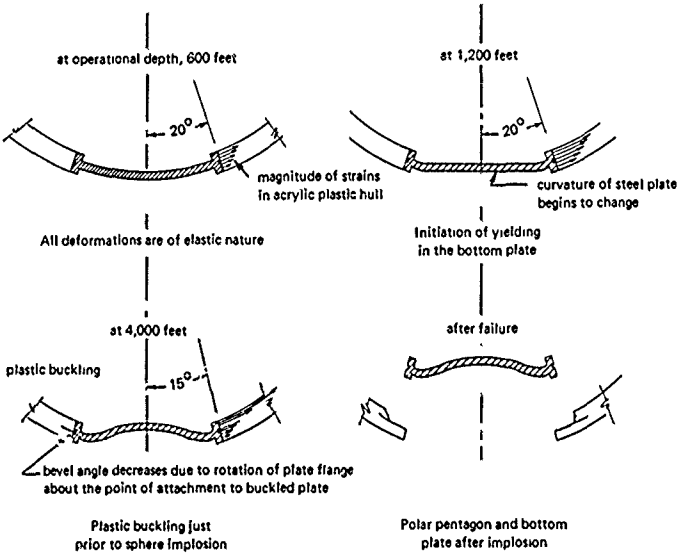

Figure 119c. Mechanism of failure by spalling in the bottom polar acrylic plastic pentagon reconstructed from observation of deformation in the bottom steel plate and fracture in the bottom polar acrylic plastic pentagon.

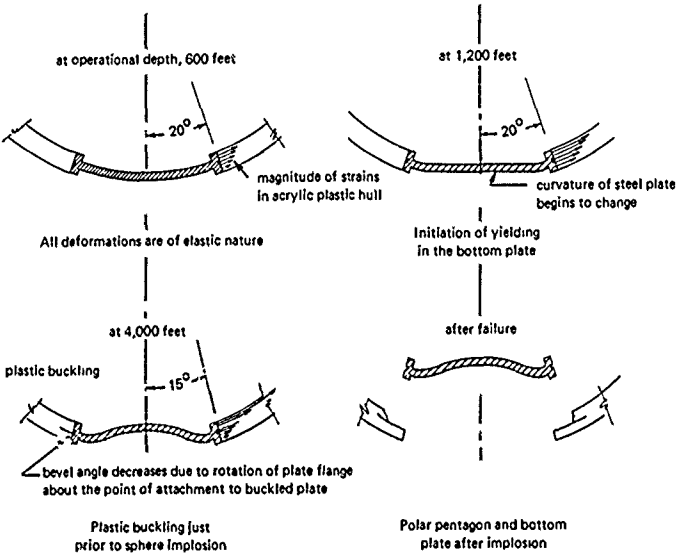

Figure 119c. Mechanism of failure by spalling in the bottom polar acrylic plastic pentagon reconstructed from observation of deformation in the bottom steel plate and fracture in the bottom polar acrylic plastic pentagon.

3. The good reproducibility of material properties and capsule dimensions from one capsule to another as well as from small-scale models to large-scale capsules results in reliable structural performance, which varies for individual capsules less than ± 10% from the average collapse pressure of the group.

4. The 66-inch prototype capsule for incorporation into the NEMO system met the initial requirements for (1) 1,000 dives to design depth of 1,000 feet and (2) implosion under uncontrolled dive conditions only at depth in excess of 3,000 feet.

5. Both the design and the fabrication method developed for the 66-inch large-scale capsule prototype are applicable directly to the 120-inch-diameter capsule concept, the ultimate goal of the acrylic plastic capsule program.

6. Although the chosen polar plate dimensions appear to be adequate for the 1,000-foot design depth when the plate is fabricated from type 316 stainless steel, the safety margin of the metal plates would be substantially increased if they were fabricated instead from Inconel 625 or cadmium plated SAE 4130, both with a minimum yield point of 60,000 psi.

7. The use of models for validation of spherical capsule designs in acrylic plastic is acceptable; there appears to be no mass scaling factor associated with the scaling up of models to full-scale operational capsules.

CONCLUSION

The spherical hull concept of acrylic plastic developed in the NEMO program provides an economical, reliable, and safe pressure resistant capsule with panoramic visibility for continental shelf depths.

RECOMMENDATIONS

These recommendations are based on a conservative engineering evaluation of existing data.

1. On the basis of the experimental and analytical data developed in the 66-inch-OD x 61-inch-ID acrylic plastic capsule program the NEMO capsule merits certification to 600-foot depth. Brief proof-test dives are not to exceed 1,200-foot depth.

2. The crack-free fatigue life of the capsule for dives to 600-foot depth shown in Figure 121 is recommended as a very safe fatigue rating for manned service.

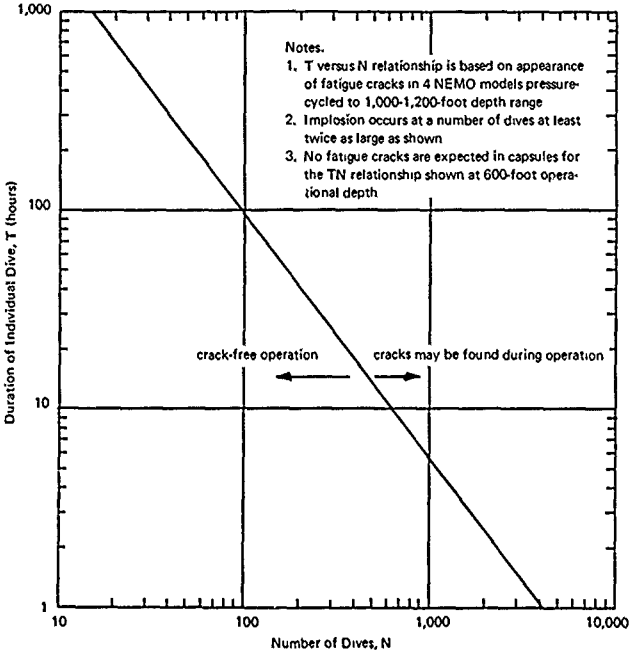

Figure 121. Crack-free fatigue life of 66-inch-OD NEMO capsule at 600-foot depth.

3. The fatigue life depends not only on the number of dives, but also on their maximum depth and duration. When the fatigue value of individual dive is calculated after each dive, both the duration and the maximum depth reached must be noted. The fatigue value of a dive to a lesser depth than 600 feet is calculated on the conservative linear basis (e.g., a dive to 300 feet of 1-hour duration is considered as 1/2 of a dive to 600 feet of 1-hour duration). When the fatigue values for dives of different durations and depths are added up, the procedure is to consider each dive as a fraction of the available fatigue life at 600 feet and specified dive duration. Thus, the fatigue values of a 1-hour dive to 300 feet, a 6-hour dive to 400 feet, and a 100-hour dive to 600 feet are added up as:

$$\Sigma = \frac{1}{4{,}000}\left(\frac{300}{600}\right) + \frac{1}{1{,}000}\left(\frac{400}{600}\right) + \frac{1}{100}\left(\frac{600}{600}\right)$$

to result in a cumulative fatigue value of 0.01079. So long as the summation of all dive fatigues is $\Sigma < 1.000$ the hull is considered safe. When the sum of the dive fatigue values reaches 1.000 the hull will be considered to have no further fatigue life and must be replaced.

4. The fatigue curve of Figure 121 is very conservative as it is based on the appearance of cracks under cyclic proof-test depth loadings to 1,140 feet while the manned operational dives will have a maximum depth limit of only 600 feet. Furthermore, since it is known from the cycling tests conducted on models that extensive fracturing of the acrylic/metal plate interface takes place prior to catastrophic fatigue failure, periodic visual inspection of the hull during its service life will prevent premature fatigue failure.

5. These recommendations also apply to other acrylic plastic capsules that will be fabricated in the future for other systems besides NEMO, provided that:

a. The capsule design is identical to the one developed in this program.

b. Acrylic plastic material has the properties specified in Table 1.

c. Adhesive utilized has a minimum tensile strength of 4,500 psi and service life comparable to PS-18 adhesive in marine environment.

d. Thickness of material in the finished capsule is $2.285 < t < 2.625$ inches.

e. The diameter of the capsule is $65.875 < D < 66.125$ inches.

f. The external radius of the capsule is $32.875 < R < 33.125$ inches.

ACKNOWLEDGMENTS

Many engineers and scientists have contributed to the development of the NEMO concept and the successful completion of the acrylic plastic capsule structural validation program. Messrs. R. G. McCarty,* J. G. Moldenhauer,* initiated the NEMO concept, while Messrs. K. Tsuji* and D. T. Stowell* developed it sufficiently to show its feasibility. The pentagonal acrylic plastic

* Naval Missile Center, Point Mugu, California.

capsule concept was conceived and engineered by Dr. J. D. Stachiw* and designed by Messrs. W. A. Winner** and R. T. Rains.** The successful fabrication of the capsule is the result of close supervision of, and assistance to, shop personnel by Messrs. R. B. Gunyan,** D. O'Connor,** and Jack Marble.**

* Naval Civil Engineering Laboratory, Port Hueneme, California.
** Pacific Missile Range, Point Mugu, California.

Appendix A

DETAILED DIMENSIONS OF 66-INCH-DIAMETER ACRYLIC PLASTIC HULL FOR NEMO SYSTEM

Although the description of the 66-inch acrylic plastic hull in the main body of the report is adequate for discussion of the acrylic plastic hull design and its performance under hydrostatic pressure, it is not detailed enough for the personnel involved in certifying the seaworthiness of the acrylic plastic hull. The Certification Board requires not only a detailed description of the plans from which the hull was built, but also how well the finished product conformed to these plans. Only after the relationship between the dimensions shown on plans and the dimensions of the finished product is well understood can the dimensional deviations of future operational hulls be considered as acceptable or unacceptable. This statement is based on the fact that the prototype 66-inch hull that successfully withstood the many hydrostatic overloads to which it was subjected during the testing program was *not* perfect, but deviated from the specified nominal dimensions in a certain manner. If future hulls built for incorporation into manned submersibles show only as much (or less) dimensional and structural deviation from fabrication plans and specifications as exhibited by the prototype, they will be acceptable. Their performance should then be equivalent or superior to the one shown by the prototype 66-inch acrylic plastic hull discussed in this report.

For this reason the figures and tables comprising Appendix A are grouped to show in detail not only the drawings used in the fabrication, but also the dimensional measurements performed on the hull structure during and after the fabrication. Thus Figures A-1 to A-10 show the fabrication plans, while Figures A-11 to A-13 show the quality control measurements performed on the hull during fabrication.

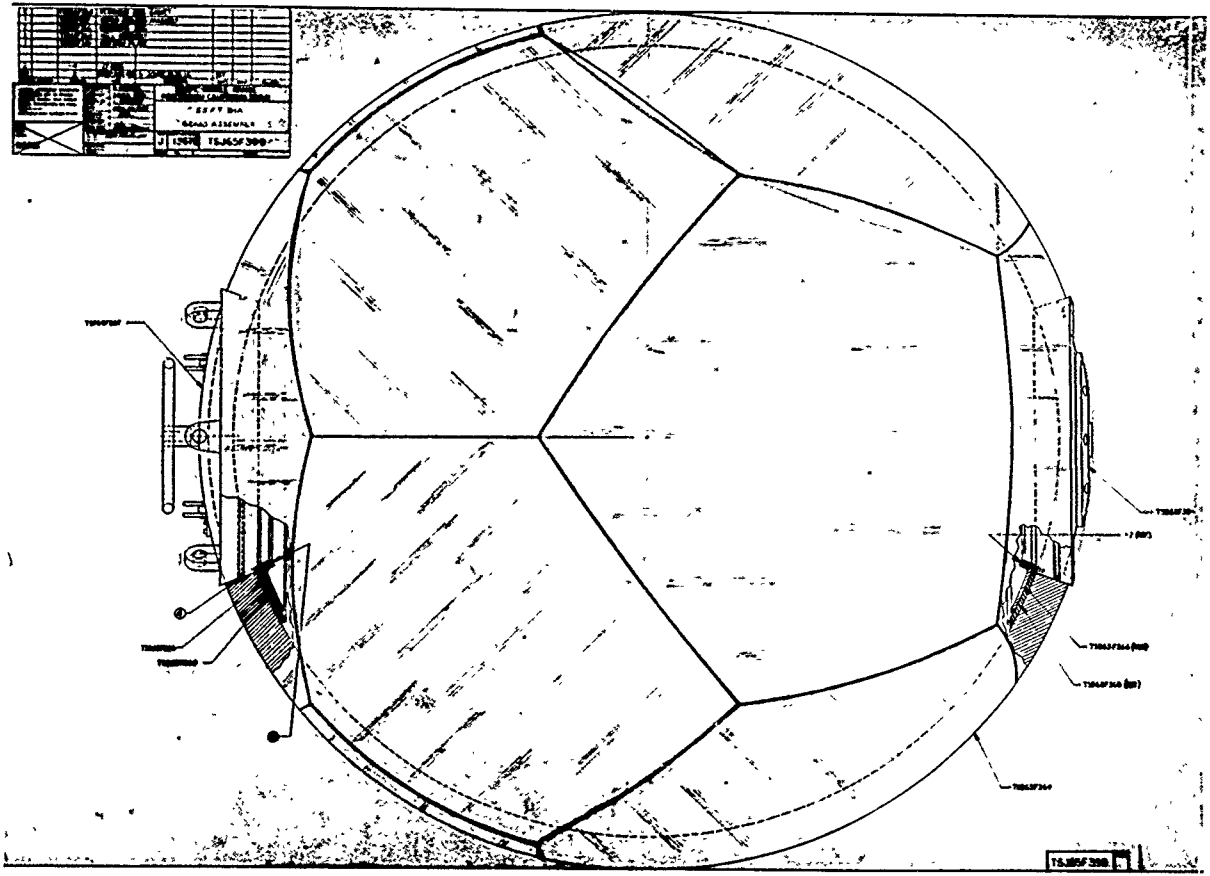

Figure A-1. NEMO system 66-inch-diameter prototype capsule: assembly.

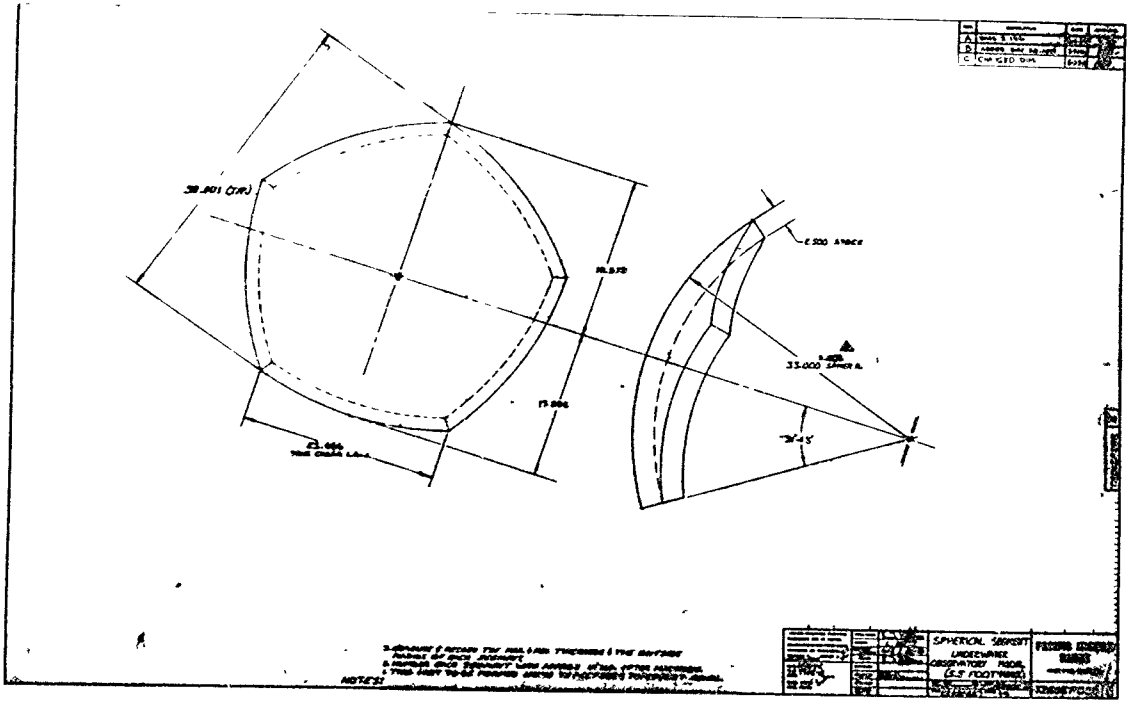

Figure A 2 Typical spherical pentagon for the 66 inch diameter capsule

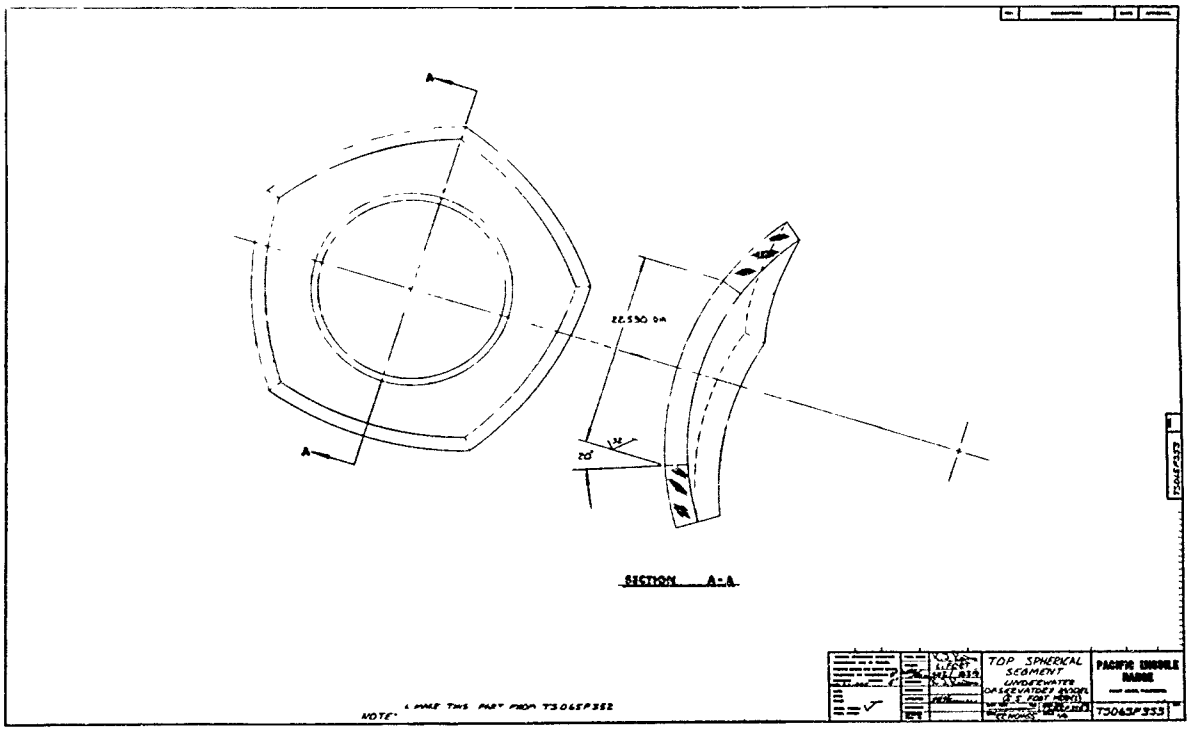

Figure A-3 Polar spherical pentagon for the 66-inch-diameter capsule

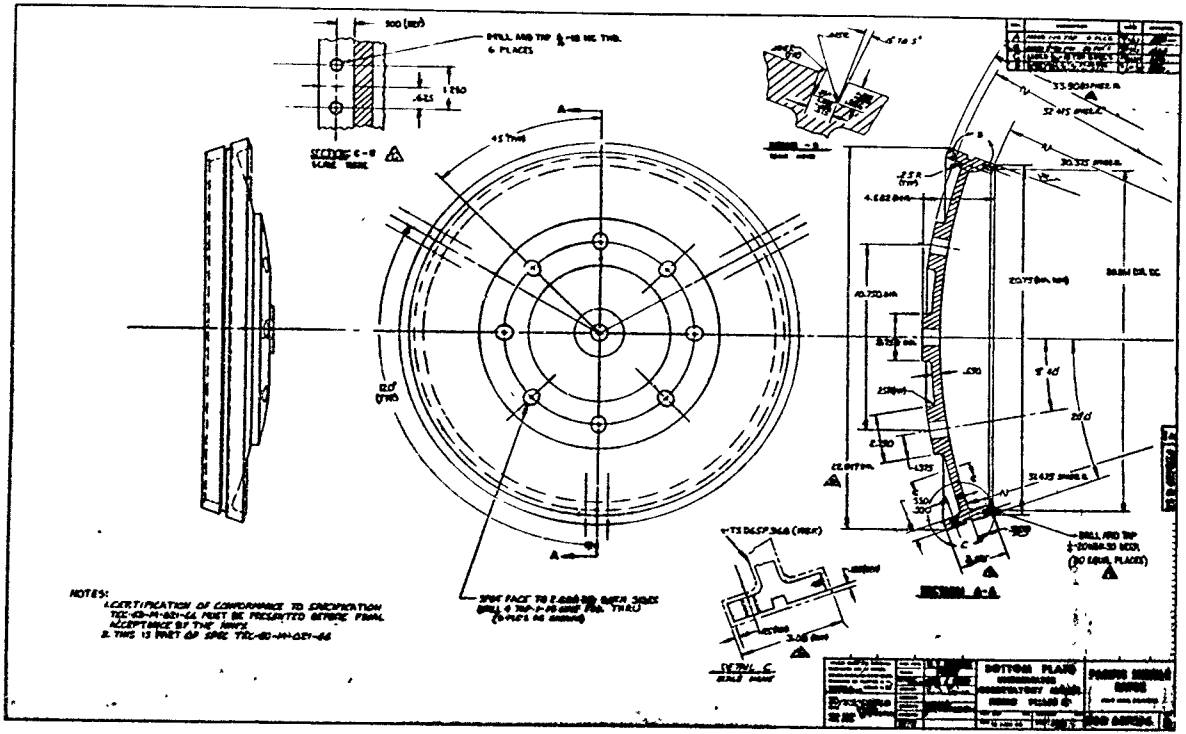

Figure A-4 Bottom plate serving as closure for the lower polar penetration in the 66-inch diameter capsule

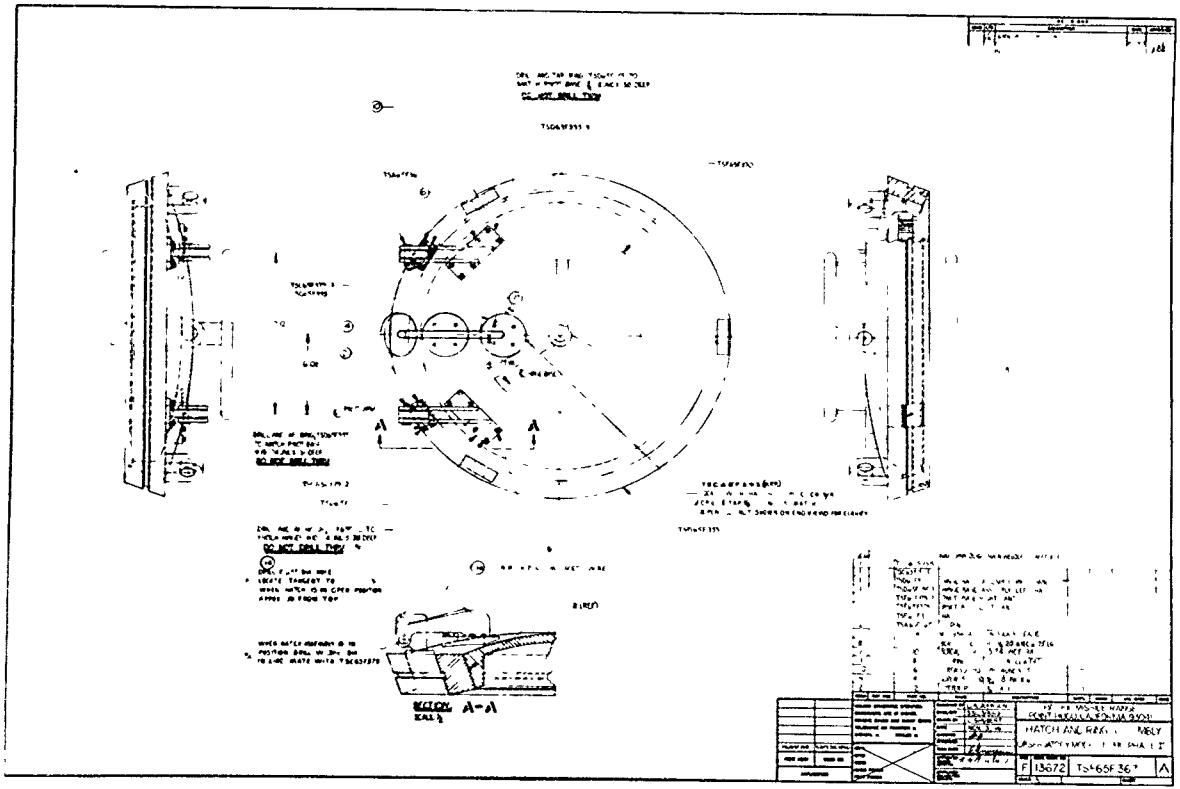

Figure A-5 Hatch subsystem serving as closure for the top polar penetration in the 66 inch-diameter capsule top view

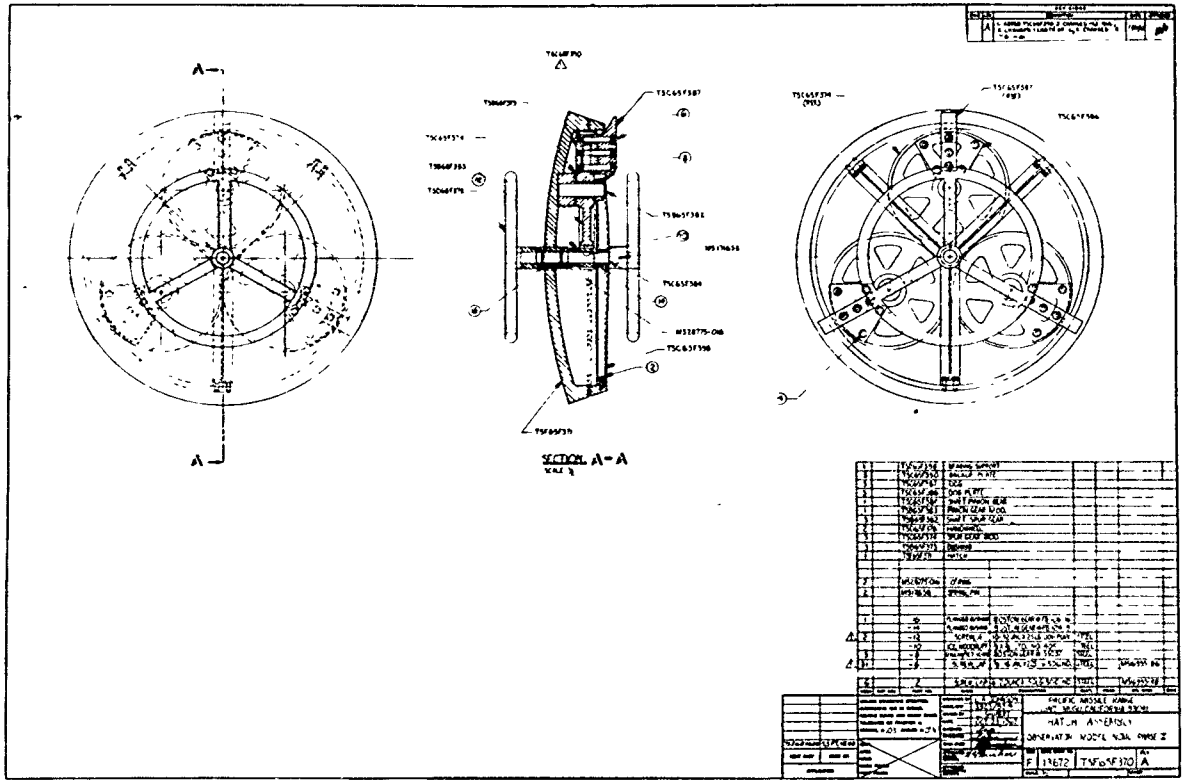

Figure A-6 Cross section and bottom view of the hatch subsystem

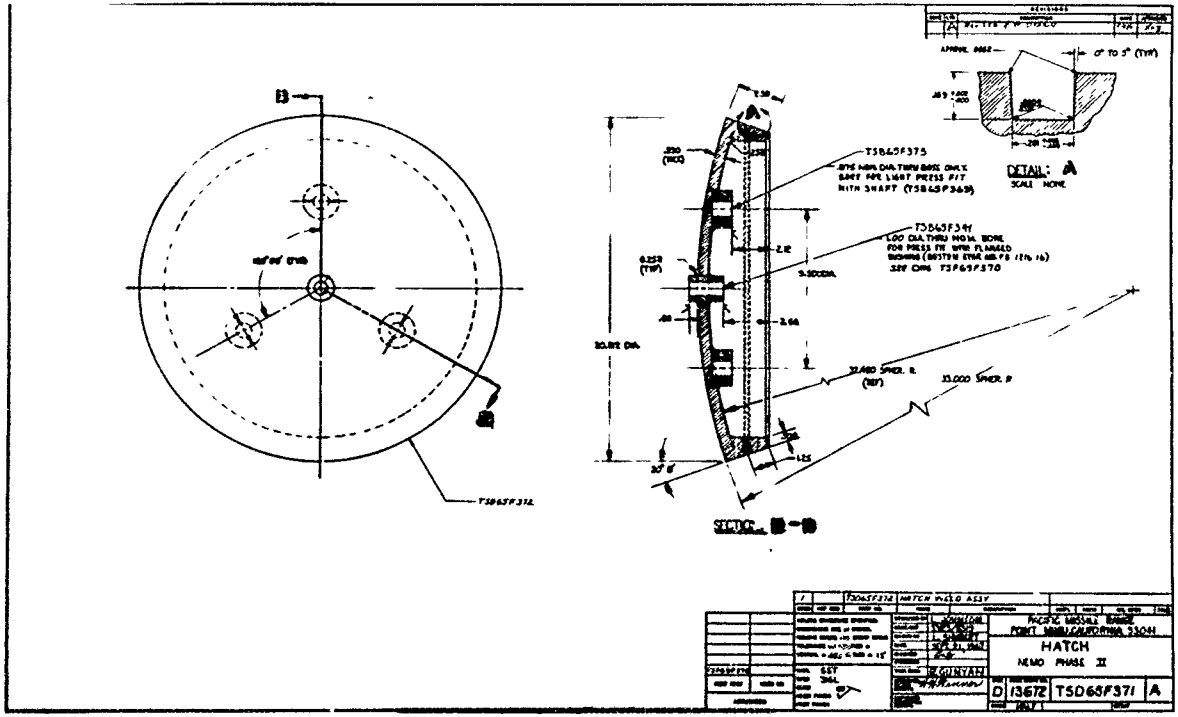

Figure A-7 Hatch plate detail

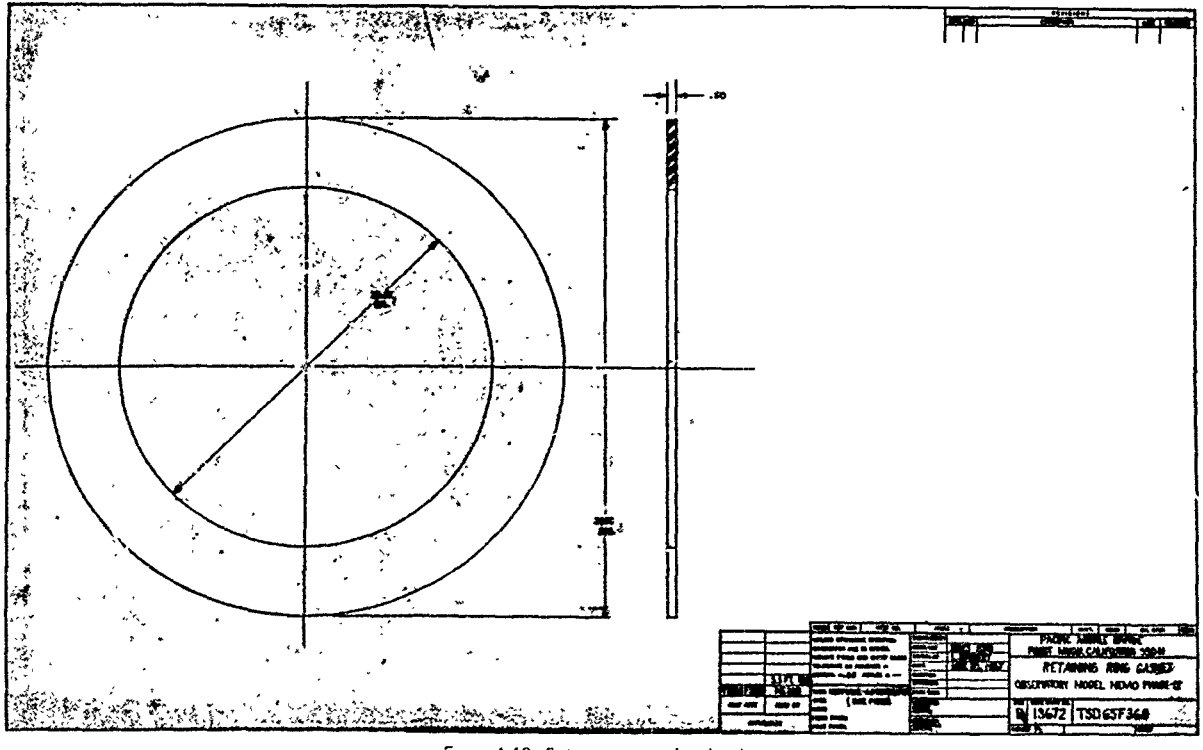

Figure A-10. Retaining ring gasket detail.

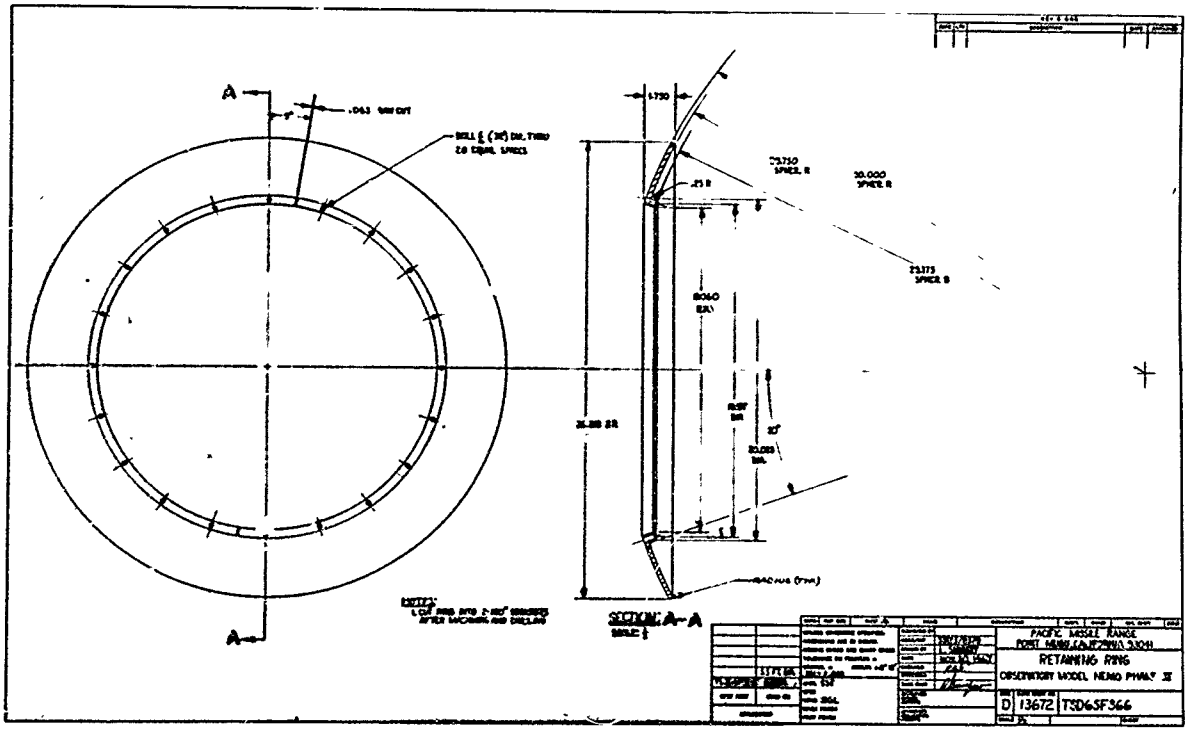

Figure A-9 Retaining ring detail.

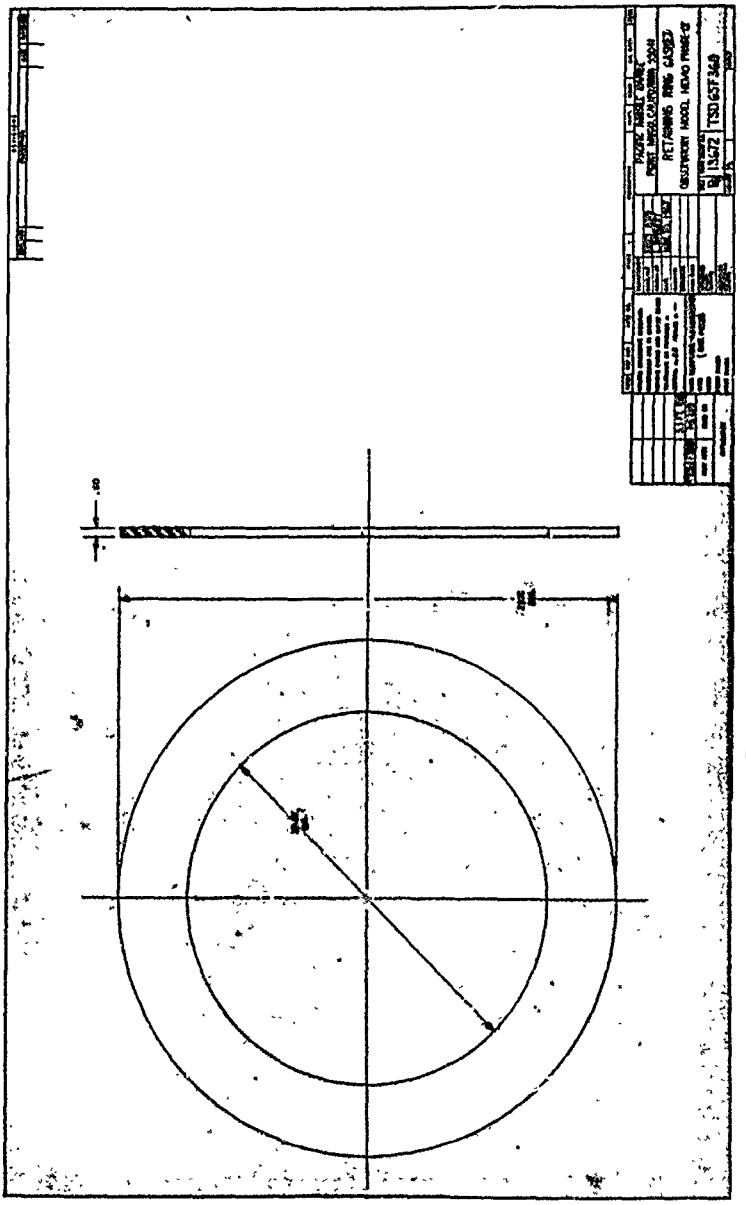

Figure A-10. Retaining ring gasket detail

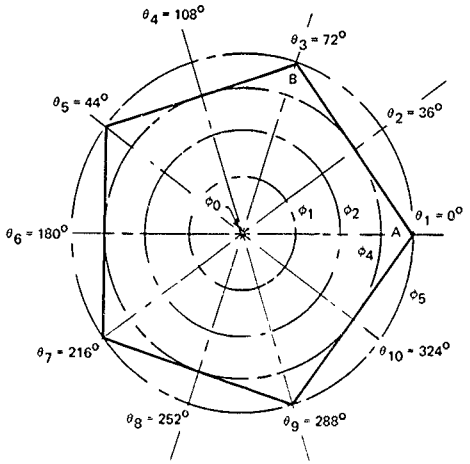

Typical Pentagon

ϕ angle

$\phi_0 = 0^o0'$ $\phi_4 = 31^o30$

$\phi_1 = 10^o30'$ $\phi_5 = 37^o10$

$\phi_2 = 21^o0'$

Notes

1 Points A and B were marked to give orientation

2 Angles ϕ_1 through ϕ_5 are angles through the center of the sphere

3 Angles θ_1 through θ_{10} are measured from the center of the pentagon

4 Pentagons are for the prototype 66-inch NEMO capsule

5 ΔR denotes change in internal surface curvature from specified 30 500 inches, + indicates shorter radius while - indicates longer radius

Point	Pentagon 1		Pentagon 3		Pentagon 4		Pentag
	ΔR	t	ΔR	t	ΔR	t	ΔR
$\theta_1 - \phi_0$	+0 028	2.36	+0 155	2 350	+0.120	2 290	+0 100
$\theta_1 - \phi_1$	+0 015	2 385	+0 140	2 350	+0 112	2 310	+0 099
$\theta_1 - \phi_2$	-0 014	2 410	+0 110	2 375	+0 055	2 360	+0 065
$\theta_1 - \phi_4$	-0 095	2 455	+0 062	2 450	-0 040	2 430	-0 028
$\theta_1 - \phi_5$	-0 170	2 505	+0 025	2 480	-0 103	2 460	-0 098
$\theta_2 - \phi_1$	+0 010	2 38	+0 139	2 350	+0 102	2 315	+0 091
$\theta_2 - \phi_2$	-0 018	2 395	+0 115	2 370	+0 050	2 370	+0 048
$\theta_2 - \phi_4$	-0 097	2 468	+0 068	2 430	-0 050	2 430	-0 057
$\theta_3 - \phi_1$	0	2 385	+0 145	2 350	+0 090	2 330	+0 075
$\theta_3 - \phi_2$	-0 028	2 410	+0 120	2 370	+0 025	2 390	+0 013
$\theta_3 - \phi_4$	-0 081	2 465	+0 074	2 430	-0 080	2 485	-0 105
$\theta_3 - \phi_5$	-0 149	2 485	+0 036	2 465	-0 131	2 500	-0 175
$\theta_4 - \phi_1$	0	2 385	+0 140	2 350	+0 083	2 335	+0 070
$\theta_4 - \phi_2$	-0 035	2 410	+0 105	2 375	+0 025	2 395	-0 010
$\theta_4 - \phi_4$	-0 113	2 470	+0 053	2 430	+0 021	2 455	-0 120
$\theta_5 - \phi_1$	+0 005	2 380	+0 144	2 350	+0 083	2 335	-0 070
$\theta_5 - \phi_2$	-0 029	2 410	+0 106	2 380	+0 033	2 390	0
$\theta_5 - \phi_4$	-0 115	2 475	+0 070	2 490	-0 068	2 455	-0 087
$\theta_5 - \phi_5$	-0 183	2 495	-0 033	2 535	-0 111	2 460	-0 145
$\theta_6 - \phi_1$	+0 013	2 385	+0 137	2 350	+0 087	2 330	+0 060
$\theta_6 - \phi_2$	-0 020	2 410	+0 090	2 390	+0 039	2 380	+0 015
$\theta_6 - \phi_4$	-0 110	2 465	0	2 502	-0 044	2 415	-0 059
$\theta_7 - \phi_1$	+0 021	2 380	+0 120	2 355	+0 098	2 320	+0 074
$\theta_7 - \phi_2$	-0 013	2 410	+0 065	2 430	+0 050	2 370	+0 033
$\theta_7 - \phi_4$	-0 120	2 475	-0 020	2 530	-0 030	2 430	-0 041
$\theta_7 - \phi_5$	-0 202	2 530	-0 067	2 570	-0 083	2 440	0 100
$\theta_8 - \phi_1$	+0 023	2 385	+0 103	2 355	+0 107	2 310	+0 085
$\theta_8 - \phi_2$	-0 020	2 410	+0 040	2 430	+0 055	2 375	+0 050
$\theta_8 - \phi_4$	-0 124	2 470	-0 048	2 550	-0 045	2 425	-0 041
$\theta_9 - \phi_1$	+0 017	2 380	+0 106	2 355	+0 116	2 305	+0 090
$\theta_9 - \phi_2$	-0 023	2 410	+0 042	2 430	+0 060	2 360	+0 050
$\theta_9 - \phi_4$	-0 123	2 470	-0 052	2 565	-0 060	2 450	-0 029
$\theta_9 - \phi_5$	-0 200	2 515	-0 092	2 585	-0 123	2 480	-0 095
$\theta_{10} - \phi_1$	+0 017	2 385	+0 124	2 350	+0 119	2 310	+0 098
$\theta_{10} - \phi_2$	-0 018	2 410	+0 078	2 430	+0 063	2 360	+0 064
$\theta_{10} - \phi_4$	-0 109	2 470	+0 022	2 490	-0 040	2 415	-0 021

(a) Pentagons

Figure A 11 Quality control measurements, deviations from
in completed spherical pentagons prior to assembly

Pentagon 4		Pentagon 5		Pentagon 6		Pentagon 8		Pentagon 9		Pentagon 15		Pentagon 17		Pentagon 18	
ΔR	t	ΔR	t	ΔR	t	ΔR	t	ΔR	t	ΔR	t	ΔR	t	ΔR	t
+0 120	2 290	+0 100	2 295	+0 065	2 335	-0 025	2 415	0	2 385	–	–	+0 010	2 400	+0 007	2 385
+0 112	2 310	+0 099	2 285	+0 036	2 365	+0 010	2 390	-0 009	2 385	-0 050	2 465	+0 010	2 400	-0 018	2 405
+0 055	2 360	+0 065	2 325	+0 006	2 400	+0 027	2 400	-0 025	2 410	-0 036	2 455	-0 004	2 400	-0 045	2 435
-0 040	2 430	-0 028	2 405	-0 068	2 450	-0 016	2 410	-0 080	2 450	-0 059	2 465	-0 055	2 450	-0 089	2 485
-0 103	2 460	-0 098	2 480	-0 124	2 485	-0 064	2 420	-0 145	2 480	-0 111	2 470	-0 112	2 480	-0 127	2 510
+0 102	2 315	+0 091	2 295	+0 067	2 365	+0 010	2 390	-0 007	2 385	-0 052	2 455	+0 008	2 400	0	2 405
+0 050	2 370	+0 048	2 330	-0 007	2 405	+0 021	2 400	-0 021	2 410	-0 038	2 455	-0 008	2 430	-0 015	2 435
-0 050	2 430	-0 057	2 420	-0 095	2 480	-0 035	2 415	-0 081	2 445	-0 068	2 450	-0 057	2 440	-0 065	2 465
+0 090	2 330	+0 075	2 298	+0 035	2 365	-0 005	2 400	-0 008	2 385	-0 063	2 465	+0 002	2 405	+0 015	2 400
+0 025	2 390	+0 013	2 365	-0 010	2 415	-0 002	2 410	-0 037	2 415	-0 060	2 470	-0 017	2 430	+0 013	2 405
-0 080	2 485	-0 105	2 465	-0 120	2 500	-0 051	2 430	-0 102	2 460	-0 085	2 465	-0 073	2 465	-0 038	2 435
-0 131	2 500	-0 175	2 550	-0 200	2 545	-0 104	2 455	-0 156	2 502	-0 130	2 490	-0 134	2 490	-0 083	2 470
+0 083	2 335	+0 070	2 325	+0 047	2 365	-0 025	2 410	-0 001	2 385	-0 075	2 470	0	2 405	+0 023	2 390
+0 025	2 395	-0 010	2 395	+0 005	2 415	-0 032	2 430	-0 035	2 415	-0 075	2 470	-0 020	2 435	+0 017	2 400
+0 021	2 455	-0 120	2 515	-0 093	2 465	-0 090	2 455	-0 102	2 465	-0 105	2 480	-0 070	2 450	-0 024	2 420
+0 083	2 335	-0 070	2 330	+0 060	2 365	-0 040	2 435	-0 002	2 385	-0 076	2 470	0	2 405	+0 018	2 395
+0 033	2 390	0	2 385	+0 020	2 400	-0 051	2 470	-0 015	2 410	-0 080	2 470	-0 025	2 445	+0 017	2 405
-0 068	2 455	-0 087	2 455	-0 067	2 450	-0 091	2 490	-0 090	2 460	-0 110	2 500	-0 083	2 475	-0 039	2 450
-0 111	2 460	-0 145	2 520	-0 134	2 485	-0 147	2 500	-0 143	2 485	-0 148	2 510	-0 135	2 495	-0 100	2 475
+0 087	2 320	+0 060	2 330	+0 069	2 360	-0 055	2 445	-0 005	2 385	-0 075	2 470	0	2 400	+0 004	2 395
+0 039	2 380	+0 015	2 370	+0 043	2 380	-0 073	2 470	-0 018	2 410	-0 078	2 470	-0 020	2 430	+0 020	2 400
-0 044	2 415	-0 059	2 455	-0 045	2 420	-0 129	2 500	-0 079	2 450	-0 108	2 480	-0 075	2 455	-0 073	2 460
+0 098	2 320	+0 074	2 330	+0 072	2 350	-0 060	2 455	-0 005	2 385	-0 078	2 470	+0 003	2 400	-0 010	2 400
+0 050	2 370	+0 033	2 365	+0 055	2 365	-0 085	2 485	-0 018	2 410	-0 078	2 470	-0 017	2 430	-0 014	2 430
-0 030	2 430	-0 041	2 410	-0 035	2 415	-0 145	2 520	-0 075	2 450	-0 115	2 500	-0 075	2 465	-0 134	2 570
-0 083	2 440	-0 100	2 455	-0 100	2 440	-0 187	2 535	-0 135	2 475	-0 173	2 525	-0 137	2 490	-0 187	2 550
+0 107	2 310	+0 085	2 315	+0 066	2 360	-0 049	2 450	-0 007	2 385	-0 078	2 470	+0 005	2 400	-0 023	2 415
+0 055	2 375	+0 050	2 335	+0 037	2 375	-0 069	2 470	-0 026	2 410	-0 077	2 470	-0 012	2 430	-0 070	2 485
-0 045	2 425	-0 041	2 407	-0 037	2 415	-0 125	2 495	-0 076	2 445	-0 110	2 485	-0 088	2 465	-0 168	2 555
+0 116	2 305	+0 090	2 285	+0 053	2 365	-0 026	2 425	-0 008	2 390	-0 068	2 470	0 009	2 400	-0 028	2 428
+0 060	2 360	+0 050	2 335	+0 026	2 395	-0 031	2 430	-0 028	2 410	-0 068	2 470	-0 009	2 420	-0 074	2 485
-0 060	2 450	-0 029	2 400	-0 053	2 435	-0 077	2 455	-0 088	2 460	-0 110	2 500	-0 060	2 450	-0 140	2 545
-0 123	2 480	-0 095	2 475	-0 110	2 460	-0 135	2 485	-0 149	2 500	-0 173	2 530	-0 118	2 470	-0 180	2 560
+0 119	2 310	+0 098	2 290	+0 043	2 365	0 003	2 410	-0 010	2 400	-0 056	2 470	-0 010	2 400	-0 029	2 415
+0 063	2 360	+0 064	2 325	+0 015	2 400	+0 005	2 400	-0 029	2 420	-0 047	2 465	-0 0	2 410	-0 065	2 410
-0 040	2 415	-0 021	2 415	-0 065	2 450	-0 050	2 415	-0 075	2 450	-0 073	2 455	-0 055	2 440	-0 120	2 515

(a) Pentagons without penetrations

Continued

easurements, deviations from nominal 33 000-inch radius and 2 500 inch wall thickness
ufactured pentagons prior to assembly into a sphere

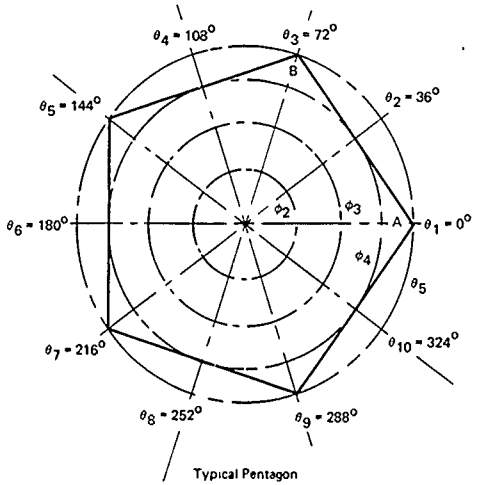

Typical Pentagon

ϕ angle

$\phi_2 = 21^o0'$ $\phi_4 = 31^o30'$

$\phi_3 = 26^o15'$ $\phi_5 = 37^o10'$

Notes

1 Points A and B were marked to give orientation

2 Angles ϕ_1 through ϕ_5 are angles through the center of the sphere

3 Angles θ_1 through θ_{10} are measured from the center of the pentagon

4 Pentagons are for the prototype 66-inch NEMO capsule

5 ΔR denotes change in internal surface curvature from specified 30 500 inches, + indicates shorter radius, while – indicates longer radius

Point	Pentagon 2		Pentagon 7	
	ΔR	t	ΔR	t
$\theta_1 - \phi_2$	+0 105	2 395	+0 041	2 460
$\theta_1 - \phi_3$	+0 043	2.455	+0 017	2 485
$\theta_1 - \phi_4$	–0 013	2 510	–0 022	2 520
$\theta_1 - \phi_5$	–0 085	2 540	–0 075	2 540
$\theta_2 - \phi_2$	+0 105	2 395	+0 030	2 465
$\theta_2 - \phi_3$	+0 053	2 455	+0 006	2 490
$\theta_2 - \phi_4$	0	2.480	–0 035	2 520
$\theta_3 - \phi_2$	+0 110	2 395	+0 028	2 460
$\theta_3 - \phi_3$	+0 061	2 455	0	2 490
$\theta_3 - \phi_4$	+0 007	2.480	–0 042	2 520
$\theta_3 - \phi_5$	–0 065	2 530	–0 107	2 550
$\theta_4 - \phi_2$	+0 100	2 395	+0 039	2 465
$\theta_4 - \phi_3$	+0 053	2 445	+0 021	2 480
$\theta_4 - \phi_4$	–0 005	2 480	–0 004	2 505
$\theta_5 - \phi_2$	+0 100	2 395	+0 047	2 440
$\theta_5 - \phi_3$	+0 061	2 445	+0 032	2 460
$\theta_5 - \phi_4$	+0 015	2 465	+0 002	2 480
$\theta_5 - \phi_5$	–0 045	2 500	+0 045	2 505
$\theta_6 - \phi_2$	+0 102	2 395	+0 083	2 420
$\theta_6 - \phi_3$	+0 040	2 445	+0 069	2 440
$\theta_6 - \phi_4$	+0 005	2 470	+0 042	2 460
$\theta_7 - \phi_2$	+0 087	2 395	+0 105	2 410
$\theta_7 - \phi_3$	+0 051	2 445	+0 095	2 420
$\theta_7 - \phi_4$	+0 003	2 470	+0 060	2 440
$\theta_7 - \phi_5$	–0 055	2 505	+0 003	2 460
$\theta_8 - \phi_2$	+0 090	2 400	+0 102	2 400
$\theta_8 - \phi_3$	+0 060	2 450	+0 093	2 413
$\theta_8 - \phi_4$	+0 037	2 460	+0 052	2 425
$\theta_9 - \phi_2$	+0 095	2 405	+0 095	2 420
$\theta_9 - \phi_3$	+0 081	2 445	+0 072	2 445
$\theta_9 - \phi_4$	+0 048	2 455	+0 040	2 465
$\theta_9 - \phi_5$	–0 002	2 460	–0 010	2 475
$\theta_{10} - \phi_2$	+0 095	2 400	+0 057	2 450
$\theta_{10} - \phi_3$	+0 050	2 455	+0 036	2 475
$\theta_{10} - \phi_4$	–0 005	2 475	–0 006	2 497

(b) Pentagons with penetrations

Figure A 11 Continued

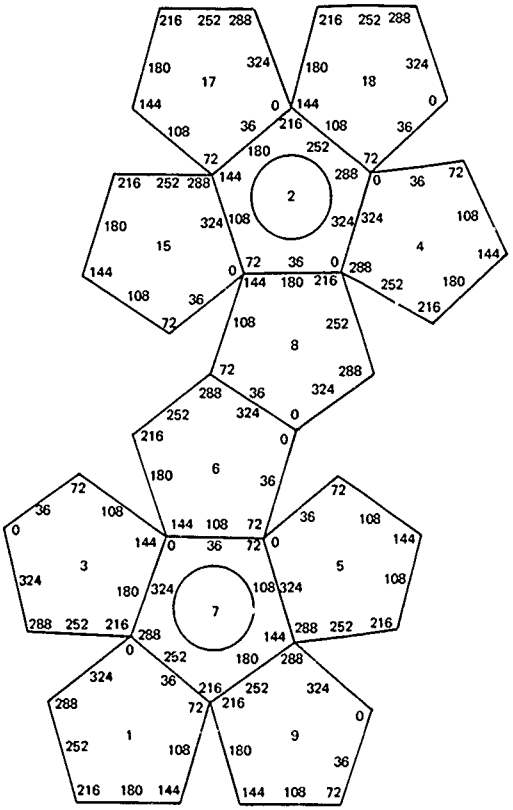

Layout of Prototype 66-inch Capsule For NEMO System

From	To	Diameter (in.)	Date	Time
9	15	66 125	12-19-67	1420
1	8	66.130	12-19-67	1430
4	3	66 084	12-19-67	1440
6	18	66.135	12-19-67	1450
5	17	66 158	12-19-67	1500
2-0	7-288	66 055	12-19-67	1530
2-72	7-216	66 032	12-20-67	0735
2-144	7-144	66 065	12-20-67	0745
2-216	7-72	66 070	12-20-67	0750
2-288	7-0	66 071	12 20-67	0800
4-0	3-144	66 060	12-20-67	0800
4-72	3-72	66 005	12 20-67	0800
4-144	3-0	65 920	12-20-67	0805
4-216	3-288	65 975	12-20-67	0810
4-288	3-216	66 035	12-20-67	0810
8-70	1-216	65 945	12 20-67	0815
8-72	1-144	66 000	12-20-67	0815
8-144	1-72	66 030	12-20-67	0820
8-216	1-0	66 010	12-20-67	0820
8-288	1-288	65 938	12 20-67	0825
15-0	9-216	66 015	12-20-67	0830
15-72	9-144	65 973	12-20-67	0830
15-144	9-72	65 975	12-20-67	0833
15-216	9-0	66 010	12 20-67	0835
15-288	9-288	66 050	12 20-67	0835
18-0	6-216	65 992	12 20-67	0840
18-72	6-144	66 045	12 20-67	0840
18-144	6-72	66 050	12-20-67	0840
18-216	6-0	65 985	12 20-67	0845
18-288	6-288	65 965	12 20-67	0845
8-0	1-216	65 950	1 3-68	0945
8-72	1-144	66 075	1-3-68	0950
8-144	1-72	66 075	1 3-68	10
8-216	1-0	66 080	1 3-68	10
8 283	1-288	66 085	1-3-68	1010
8-0	1-216	65 930	1-3-68	1115
8-72	1-144	66 015	1 3-68	1115
8-144	1-72	66 010	1-3-68	1125
8-216	1-0	66 085	1 3-68	1135
8-288	1-288	66 085	1 3-68	11
8-0	1-216	65 950	1-3-68	1505
8-72	1-144	66 015	1-3-68	1510
8-144	1 72	66 060	1-3-68	1515
8-216	1-0	66 010	1-3-68	1520
8-288	1-288	66 085	1-3-68	1520

Note

1 Diameter measurements taken 0 50 inch from pentagon s co

2 Measurement at 9, 15, etc is center of pentagon

Figure A-12 Quality control measurements, deviations from nominal 66 000 inch diameter after assembly and bonding of pentagons into a 66-inch diameter capsule

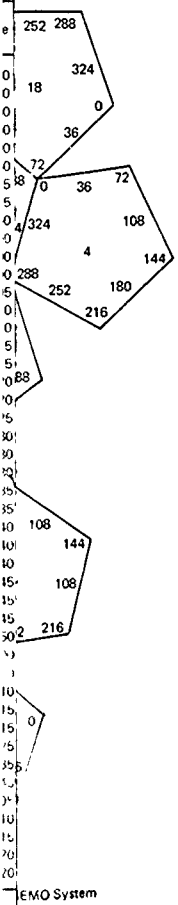

EMO System

From	To	Diameter (in.)	Date	Time	Temperature (°F)	Humidity
9	15	66.125	12-19-67	1420	74	47
1	8	66.130	12-19-67	1430	74	47
4	3	66 084	12-19-67	1440	74	47
6	18	66.135	12-19-67	1450	74	47
5	17	66.158	12-19-67	1500	74	47
2-0	7-288	66 055	12-19-67	1530	74	47
2-72	7-216	66 032	12-20-67	0735	65	44
2-144	7-144	66 065	12-20-67	0745	65	44
2-216	7-72	66 070	12-20-67	0750	66	44
2-288	7-0	66 071	12-20-67	0800	66	44
4-0	3-144	66 060	12-20-67	0800	66	44
4-72	3-72	66 005	12-20-67	0800	66	44
4-144	3-0	65 920	12 20-67	0805	66	44
4-216	3-288	65 975	12-20-67	0810	66	44
4-288	3-216	66 035	12-20-67	0810	66	44
8-70	1-216	65 945	12-20-67	0815	66	44
8-72	1-144	66 000	12-20-67	0815	67	44
8-144	1-72	66 030	12-20-67	0820	67	44
8-216	1-0	66 010	12 20-67	0820	67	44
8-288	1-288	65 938	12-20-67	0825	67	44
15-0	9-216	66 015	12-20-67	0830	68	44
15-72	9-144	65 978	12-20-67	0830	68	44
15-144	9-72	65 975	12-20-67	0830	68	44
15-216	9-0	66 010	12-20-67	0835	68	44
15-288	9 288	66 050	12-20-67	0835	68	44
18-0	6-216	65 992	12-20-67	0840	68	44
18-72	6-144	66 045	12-20-67	0840	68	44
18-144	6-72	66 050	12-20-67	0840	68	44
18-216	6-0	65 985	12-20-67	0845	68	44
18-288	6-288	65 965	12-20-67	0845	68	44
8-0	1-216	65 950	1 3-68	0945	64	40
8-72	1-144	66 075	1-3-68	0950	64	40
8-144	1-72	66 075	1 3-68	1000	64	40
8-216	1-0	66 080	1-3-68	1000	64	40
8-288	1-288	66 085	1-3-68	1010	64	40
8-0	1-216	65 990	1 3-68	1115	67	38
8-72	1-144	66 015	1-3-68	1115	67	38
8-144	1 72	66 010	1 3-68	1125	67	38
8-216	1-0	66 085	1-3-68	1135	67	38
8-288	1-288	66 085	1 3-68	1145	67	38
8-0	1-216	65 950	1-3-68	1505	72	36
8-72	1-144	66 015	1 3-68	1510	72	36
8-144	1-72	66 060	1-3-68	1515	72	36
8-216	1-0	66 010	1-3-68	1520	72	36
8-288	1 288	66 085	1-3-68	1520	72	36

Note

1 Diameter measurements taken 0 50 inch from pentagon's corner as shown on plan layout of NEMO

2 Measurement at 9, 15, etc is center of pentagon

ntrol measurements, deviations from nominal 66 000-inch diameter after assembly and
f pentagons into a 66 inch diameter capsule

Intersection of Pentagons	Corner	I	II	III	IV	V	VI	Center	I	II	III	IV	V	VI	Corner	I
2-4	288-0	–	0 012	0 045	0 045	0 015	0 000	324-324	–	–	0 014	0 025	0 006	0 005	0-288	–
2-8	0-216	–	0 035	0 062	0 062	0 039	0 009	36-180	–	–	0 045	0 045	0 018	0 010	72-144	–
2-15	72-0	–	0 032	0 070	0 072	0 036	0 014	108-324	–	–	0 042	0 042	0 016	0 011	144-288	–
2 17	144-72	–	0 039	0 059	0 061	0 023	0 005	180-36	–	–	0 036	0 045	0 036	0 016	216-0	–
2-18	216-144	–	0 001	0 035	0 039	0 020	0 007	252-108	–	–	0 003	0 012	0 008	0 009	288 72	–
4-18	0-72	0 005	0 013	0 041	0 039	0 019	0 014	36-36	0 013	0 000	0 019	0 036	0 023	0 010	72-0	0 000
4-9	72-72	0 010	0 021	0 064	0 074	0 045	0 025	108-36	0 038	0 045	0 078	0 084	0 045	0 030	144-0	0 040
4-5	144-216	0 042	0 080	0 134	0 115	0 061	0 033	180-180	0 040	0 048	0 090	0 074	0 048	0 034	216-144	0 016
4-8	216-288	0 013	0 018	0 048	0 045	0 006	0 002	252-252	0 023	0 020	0 043	0 039	0 014	0 012	288 216	0 010
8-15	144-0	0 020	0 042	0 075	0 090	0 045	0 028	108 36	0 026	0 037	0 074	0 077	0 045	0 031	72-72	0 013
8-6	0-0	0 036	0 068	0 120	0 118	0 055	0 024	36-324	0 031	0 047	0 080	0 080	0 044	0 028	72-288	0 020
8-5	0-72	0 028	0 057	0 112	0 091	0 045	0 027	324-108	0 026	0 031	0 076	0 074	0 036	0 030	288-144	0 010
15-17	288-72	0 005	0 017	0 015	0 043	0 006	0 000	252-108	0 008	0 008	0 031	0 026	0 008	0 009	216-144	0 000
15-3	144-72	0 004	0 028	0 064	0 055	0 036	0 028	180-36	0 006	0 003	0 020	0 075	0 050	0 036	216-0	0 006
15-6	72-288	0 028	0 048	0 095	0 104	0 050	0 030	108-252	0 040	0 057	0 092	0 091	0 048	0 035	144-216	0 030
17 18	0-144	0 009	0 035	0 076	0 062	0 026	0 014	324-180	0 013	0 020	0 054	0 047	0 026	0 026	288-216	0 009
17-1	216-288	0 032	0 062	0 110	0 110	0 069	0 041	252-252	0 029	0 050	0 080	0 102	0 045	0 036	288 216	0 020
17 3	216-288	0 010	0 036	0 080	0 090	0 065	0 039	180-324	0 010	0 010	0 030	0 090	0 064	0 048	144-0	0 002
18 1	216-216	0 010	0 014	0 057	0 075	0 034	0 010	252-180	0 026	0 035	0 050	0 045	0 015	0 010	288-144	0 024
18-9	0-72	0 019	0 033	0 060	0 070	0 041	0 020	324-108	0 026	0 035	0 050	0 062	0 035	0 023	288-144	0 030
9-1	144-144	0 006	0 030	0 069	0 048	0 011	0 003	180-108	0 020	0 022	0 050	0 032	0 010	0 010	216-72	0 000
9-7	216-216	0 010	0 020	0 045	0 050	0 025	0 012	252-180	0 012	0 012	0 033	0 034	–	–	288 144	0 006
9-5	0-216	0 010	0 035	0 072	0 074	0 032	0 013	324 252	0 011	0 022	0 050	0 045	0 022	0 018	288 288	0 001
5-7	288-144	0 002	0 010	0 033	0 030	0 002	–	324-108	0 010	0 010	0 025	0 020	–	–	0-72	0 010
5-6	0-72	0 003	0 013	0 041	0 055	0 014	0 002	36-36	0 014	0 020	0 047	0 045	0 014	0 006	72 0	0 005
6-7	72 72	0 003	0 013	0 048	0 042	0 007	–	108 36	0 012	0 012	0 029	0 022	–	–	144-0	0 000
6-3	216-72	0 000	0 008	0 046	0 034	0 022	0 007	180-108	0 004	0 002	0 016	0 026	0 021	0 020	216-72	0 000
1 7	72 216	0 010	0 018	0 060	0 064	0 025	–	36-252	0 015	0 016	0 046	0 048	–	–	0-288	0 015
3-7	216-288	0 010	0 015	0 016	0 020	0 000	–	180-324	0 010	0 015	0 016	0 008	–	–	144-0	0 009
3-1	288 288	0 016	0 036	0 039	0 051	0 018	0 005	252 324	0 017	0 034	0 042	0 034	0 008	0 007	216-0	0 017
9-1	144-144	0 007	0 018	0 062	0 043	0 006	0 002	180-108	0 006	0 015	0 045	0 032	0 005	0 005	216-72	0 000
9-1	144 144	0 007	0 018	0 064	0 045	0 003	0 002	180-108	0 009	0 014	0 043	0 027	0 002	0 003	216-72	0 002
9-1	144 144	0 007	0 017	0 069	0 045	0 005	0 002	180-108	0 014	0 018	0 050	0 032	0 006	0 009	216 72	0 001

Prototype 66-Inch Capsule For NEMO System

Notes

1 End of template with Roman numeral I is to be placed on pentagon listed first

2 End of template with Roman numeral VI is to be placed on pentagon listed second

3 Measure sphericity at each Roman numeral on template with a feeler gage and record

4 When taking corner measurement place template 0 50 inch from corner

5 Template should be perpendicular to intersection of pentagons in both directions when taking measurements

6 Locations of points on pentagons can be found on Figure A-12

7 All readings larger than zero denote radius of curvature longer than 33 000 inches

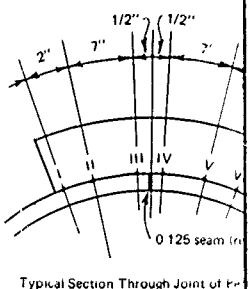

Typical Section Through Joint of Fr

Figure A-13. Quality control measurements, deviations from nominal 33 000 i bonded 66-inch diameter capsule

III	IV	V	VI	Corner	I	II	III	IV	V	VI	Date	Time	Temperature (°F)	Humidity
0 014	0 025	0 006	0 005	0-288	–	0 004	0 045	0 050	0 015	0 000	12-16-67	1250	74	40
0 045	0 045	0 018	0 010	72-144	–	0 041	0 070	0 070	0 041	0 013	12-16-67	1300	74	40
0 042	0 042	0 016	0 011	144-288	–	0 031	0 066	0 066	0 035	0 014	12-16-67	1345	74	40
0 036	0 045	0 036	0,016	216-0	–	0 017	0 055	0 060	0 031	0 010	12-16-67	1400	74	41
0 003	0 012	0 008	0 009	288-72	–	0 000	0 016	0 033	0 017	0 014	12-16-67	1430	74	41
0 019	0 036	0 023	0 010	72-0	0 003	0 000	0 028	0 031	0 013	0 009	12-16-67	1500	74	41
0 078	0 084	0 045	0 030	144-0	0 040	0 075	0 119	0 099	0 038	0 029	12-18 67	1135	74	48
0 090	0 074	0 048	0 034	216-144	0 016	0 035	0 070	0 074	0 046	0 026	12-18-67	1235	75	48
0 043	0 039	0 014	0 012	288-216	0 010	0 027	0 060	0 060	0 029	0 011	12-18-67	0800	68	46
0 074	0 077	0 045	0 031	72-72	0 013	0 028	0 076	0 076	0 037	0 025	12-18-67	0830	70	47
0 080	0 080	0 044	0 028	72-288	0 020	0 041	0 085	0 092	0 040	0 022	12-18-67	1300	75	48
0 076	0 074	0 036	0 030	288-144	0 010	0 027	0.068	0 094	0 045	0 034	12 18-67	1335	76	47
0 031	0 026	0 008	0 009	216-144	0 000	0 003	0 035	0 043	0 005	0 005	12-18-67	1020	72	48
0 020	0 075	0 050	0 036	216-0	0 006	0 002	0 030	0 081	0 060	0 038	12-18 67	1430	76	48
0 092	0 091	0 048	0 035	144-216	0 030	0 064	0 120	0 115	0 060	0 034	12-18-67	1510	76	48
0 054	0 047	0 026	0 026	288-216	0 009	0 020	0 053	0 050	0 014	0 018	12 18-67	1050	73	48
0 080	0 102	0 045	0 036	288-216	0 020	0 060	0 085	0 100	0 045	0 025	12-19-67	0745	68	46
0 030	0 090	0 064	0 048	144-0	0 002	0 002	0 028	0 095	0 068	0 047	12-19-67	0805	70	46
0 050	0 045	0 015	0 010	288 144	0 024	0 042	0 070	0 062	0 016	0 007	12-19-67	0835	70	46
0 050	0 062	0 035	0 023	288 144	0 030	0 047	0 080	0 092	0 047	0 027	12-19-67	0850	70	46
0 050	0 032	0 010	0 010	216-72	0 000	0 012	0 062	0 062	0 006	0 000	12-19-67	0940	72	46
0 033	0 034	–	–	288-144	0 006	0 020	0 048	0 033	0 010	–	12-19-67	1000	72	46
0 050	0 045	0 022	0 018	288-288	0 001	0 012	0 050	0 032	0 010	0 002	12-19-67	1020	72	46
0 025	0 020	–	–	0-72	0 010	0 012	0 040	0 037	0 000	–	12-19-67	1045	72	46
0 047	0 045	0 014	0 006	72 0	0 005	0 025	0 066	0 068	0 029	0 006	12-19-67	1100	72	46
0 029	0 022	–	–	144-0	0 003	0 012	0 044	0 035	0 007	–	12-19-67	1125	73	46
0 016	0 026	0 021	0 020	216-72	0 000	0 005	0 027	0 022	0 008	0 009	12-19-67	1235	74	47
0 046	0 048	–	–	0-288	0 015	0 029	0 076	0 060	0 027	–	12-19-67	1300	74	47
0 016	0 008	–	–	144-0	0 009	0 015	0 015	0 01 /	0 002	–	12-19-67	1315	74	47
0 042	0 034	0 008	0 007	216-0	0 012	0 017	0 033	0 050	0 015	0 000	12 19-67	1330	74	47
0 045	0 032	0 005	0 005	216-72	0 000	0 004	0 035	0 040	0 004	0 002	1-3-68	0920	64	42
0 043	0 027	0 002	0 003	216-72	0 002	0 010	0 037	0 035	0 006	0 001	1 3 68	1105	67	38
0 050	0 032	0 006	0 009	216-72	0 001	0 010	0 042	0 035	0 006	0 002	1 3 68	1500	72	36

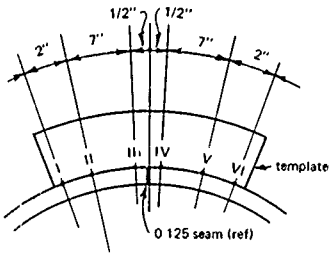

Typical Section Through Joint of Pentagon

measurements, deviations from nominal 33 000-inch radius on the assembled and
diameter capsule

Appendix B

PHOTOELASTIC INVESTIGATION OF CAPSULES

Since acrylic plastic is a photoelastically active material, the acrylic plastic capsule lends itself to photoelastic techniques for investigation of stress distribution in the acrylic plastic parts of the hull. Photoelastic investigations may be used during fabrication for measurement of residual stresses both in the formed spherical pentagons, as well as in the bonded joints. In addition photoelastic investigations may be used for measurement of stresses during actual application of external loads to the capsule. Because the photoelastic effect functions at the molecular level, stresses can be determined quite accurately in the acrylic plastic capsule around any stress concentration, a feat that is difficult to accomplish with other stress measurement techniques.

Before the photoelastic technique, however, was applied to the acrylic plastic capsule, the photoelastic sensitivity of acrylic plastic had to be accurately determined. Since a literature search failed to uncover references to the photoelastic constants of grade G Plexiglas, the material used in the fabrication of the hull, the constants were experimentally determined as a part of the acrylic plastic capsule research program.

The photoelastic properties of the grade G Plexiglas acrylic plastic material were determined under both polarized white light and monochromatic illumination, although monochromatic illumination is generally the only one utilized for detailed experimental stress analysis. The reason for determining the photoelastic properties of acrylic plastic also under white light was that it would be hard to provide uniform monochromatic illumination for the whole 66-inch hull needed during the general overview of the stress distribution in the capsule.

The photoelastic properties of grade G Plexiglas were experimentally determined by uniaxial compression testing of a 2 x 4 x 1/2-inch acrylic plastic test specimen. The uniaxial load was applied parallel to the 4-inch dimension, while the light was transmitted across the 0.5-inch thickness of the material. The Polaroid polarizer and analyzer were equipped with quarterwave plates and placed parallel to the faces of the acrylic plastic specimen through which the light was transmitted. The light, after passing through the polarizer, was circularly polarized and, after passing through the stressed acrylic plastic, was analyzed by the analyzer. (The technically correct description of this photoelastic investigation technique is "determination of materials' fringe constants in a light-field polariscope utilizing circularly polarized transmitted light.")

When a sodium vapor monochromatic light source was utilized, the successive dark fringes were observed in grade G Plexiglas material to be approximately separated by 1,600-psi principal stress or 800-psi maximum shear intervals. When placed into the fringe constant equation

$$f = \frac{(\sigma_1 - \sigma_2)h}{n} \qquad \text{B-1}$$

where f = fringe constant (lb/in./fringe order)

σ_1 = maximum principal stress (psi)

σ_2 = minimum principal stress (psi)

h = thickness of test specimen (in.)

n = order of interference

the fringe constant was determined to be $f = 800$ lb/in./fringe order. Since the modulus of elasticity of grade G Plexiglas is approximately 450,000 psi, the fringe constant when expressed in terms of strain is about 1,770 μin./in./order for a 1-inch specimen thickness.

In a light-field circular polariscope utilizing monochromatic transmitted light, the first dark fringe appears in 0.5-inch-thick acrylic plastic at the 800-psi principal stress magnitude while the first light band appears at the 1,600-psi principal stress magnitude (800-psi maximum shear). That is because in a light-field circular polariscope, isochromatics (black fringes) represent half orders of interference. If the polariscope was set to produce a dark field, the dark field would be present at zero loading, while the first black isochromatic would appear only after the 1,600-psi principal stress (800-psi maximum shear) was reached.

When white light was used in the light-field polariscope utilizing circularly polarized transmission, colored isochromatics replaced the black fringes. Since it is rather difficult to convey in words the subtle changes in color that accompany the loading of acrylic plastic, color photographs were taken at many loading intervals (Figure B-1). With the aid of the colors, it is possible to determine rather readily without any elaborate experimental setup the magnitude of maximum shear stress in the completed acrylic plastic capsules. Using sunlight as the source of white light only two sheets of Polaroid with bonded quarterwave plates are needed to perform a photoelastic stress analysis of an acrylic plastic structure.

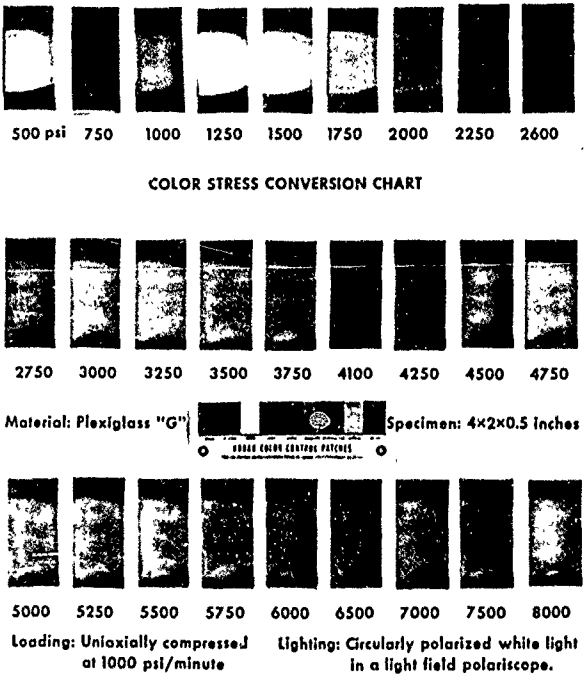

Figure B-1. Color stress conversion table for 0 5 inch-thick grade G Plexiglas acrylic plastic under short-term uniaxial compressive loading in a light-field polariscope utilizing a circularly polarized transmitted white light, stress values shown are for the principal stress

Utilizing such a simple polariscope the residual stresses were investigated in both model and large-scale acrylic plastic capsules after annealing was completed. Since the highest typical stresses in the joints are found at the corners of the pentagons, all of the measurements for typical residual stresses were performed at those locations. Using the photoelastic stress investigation technique the highest *typical residual shear stresses* in the acrylic plastic capsule models were found to be approximately 1,300 psi (blue color) for solvent-bonded joints (blue, Figure 41) and 1,300 psi for cast-in-place self-polymerizing PS-18 bonded joints (blue, Figure 44). In the large-scale acrylic plastic capsule (Figure 54) the typical residual shear stresses in the cast-in-place PS-18 adhesive joint were approximately 500 psi. The magnitude of residual stresses around stress raisers in the joint is described separately, as their magnitude depends more on the quality of bonding rather than type of adhesive.

The worst residual stress raisers were found to be in the cast-in-place PS-18 joints at locations where either a trepanning operation was performed to fill a cavity or interface separation with adhesive (Figure B-2), or where one filling of the joint with adhesive terminated and another one was initiated (Figure B-3). Small or large cavities (air bubbles) in the cast-in-place adhesive joint did not act as residual stress raisers (Figure B-4).

On the basis of the photoelastic investigations into the magnitude and distribution of residual stresses in the bonded joints, several findings have been made

1. Using the magnitude of residual stresses at the tips of the pentagons as a yardstick of comparison, there is very little difference in the effect that the solvent or self-polymerizing adhesive has on the magnitude of typical residual stresses in the joints if all the joints in the sphere are bonded in one or two increments.

2 Joints in capsules bonded in numerous small increments with self-polymerizing standard PS-18 adhesive have more stress raisers than joints in capsules bonded *simultaneously* by the solvent or self-polymerizing adhesive technique

3 The stress raisers in the joints filled incrementally by self-polymerizing adhesive are the result of incremental bonding process, where one section of the joint hardens before the next one is filled with adhesive

4. Trepanning operations (drilling a hole to a cavity in the joint and filling it with self-polymerizing adhesive) creates a serious residual stress concentration

5. Cavities in the joint do not create significant residual stress concentrations

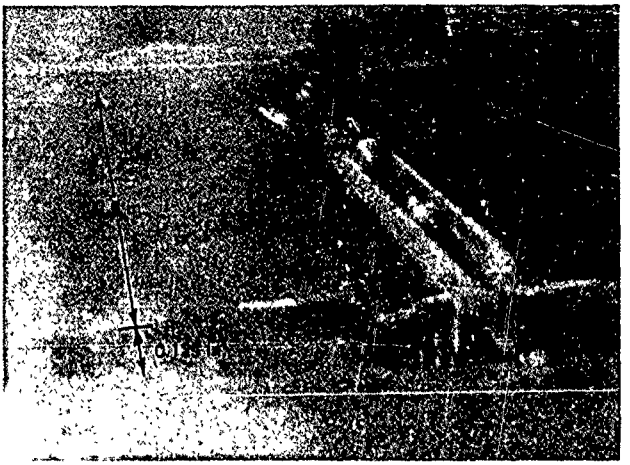

(a) Nonpolarized white light.

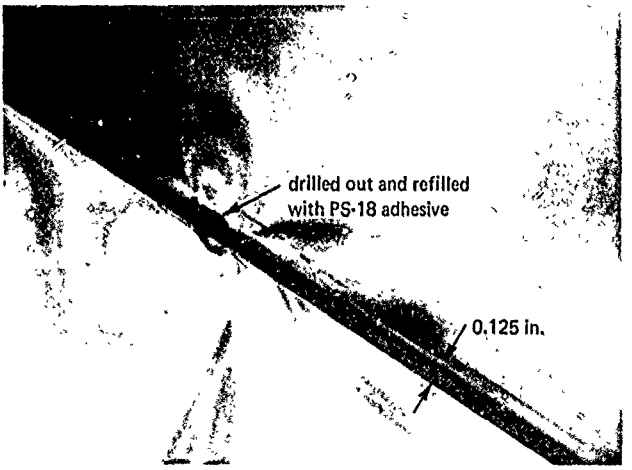

(b) Circularly polarized white light

Figure B 2. Residual stress raiser in the form of a local trepanning and recasting operation performed on an excessively large air cavity formed at the interface between two successive pours of the PS-18 adhesive bonding the joints of the prototype 66 inch capsule

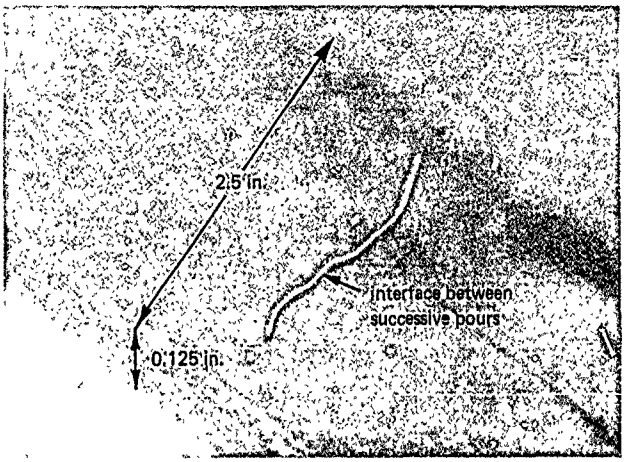

(a) Nonpolarized white light.

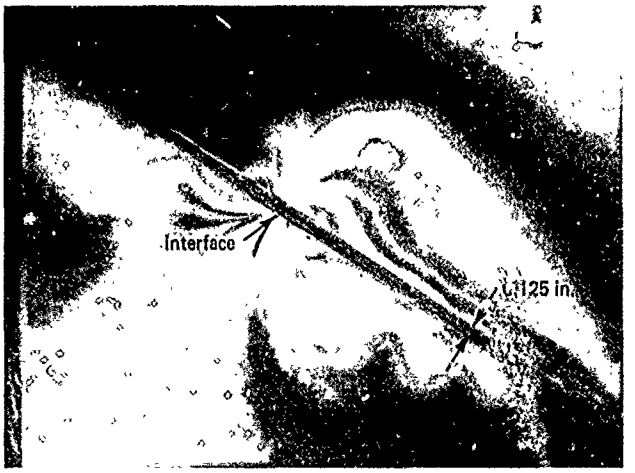

(b) Circularly polarized white light.

Figure B-3 Residual stress raiser in the form of discontinuity at the interface between two successive pours of PS-18 joint bonding material.

(a) Nonpolarized white light.

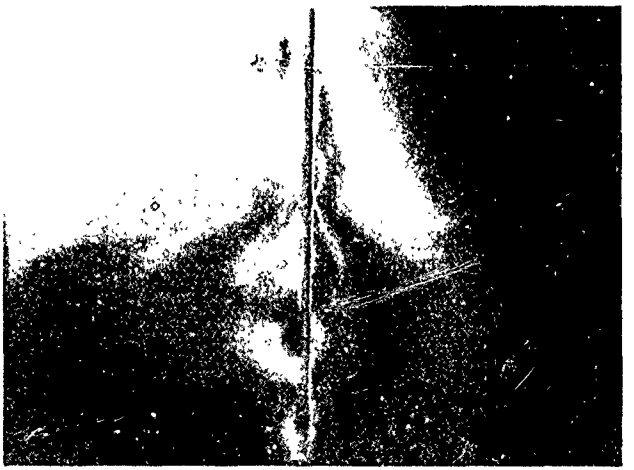

(b) Circularly polarized white light.

Figure B 4 Residual stress raisers in the form of dispersed cavities in the PS-18 joint filler.

From these findings it appears that almost all residual stress concentrations can be eliminated from the joints if the bonding process is modified to permit complete filling of all joints in the capsule with adhesive prior to initiation of the polymerization process. In this manner polymerization of the adhesive in the joints could proceed uniformly. This will not eliminate some of the typical residual stresses in the joint; shrinking of the adhesive in the joint space, whose width is held constant by mechanical spacers, will generate tensile stresses in the filler material. These residual stresses, however, will be fairly uniform, with only a small increase in magnitude at the tips of the pentagons. Because of this uniformity the maximum typical stress will be less than if the joint was cast in increments.

Besides residual stresses, active stresses were also investigated with the photoelastic technique. The tests were performed on a small-scale acrylic plastic capsule subjected to hydrostatic loading inside an internal pressure vessel. Since it was known from other tests that the highest stresses were around the polar steel plates, only that location was investigated photoelastically. When the 15-inch-OD x 14-inch-ID acrylic plastic capsule was externally pressurized to 500 psi, the maximum shear stress value (photoelastically integrated across the wall thickness) near the edge (approximately 0.050 to 0.100 inch from the edge) of the polar penetration in the acrylic plastic was found to be approximately 1,300 psi. This experimental value compares favorably with the maximum shear stress value calculated from the extrapolated strain data measured with electric resistance strain gages at 100 psi of hydrostatic pressure near the edge of the polar penetration (Figures 82 and 83). Shear stresses could not be measured photoelastically at the very edge of the penetration because of the shadow cast by the edge of the steel hatch in the capsule.

SUMMARY

From the discussion of photoelastic investigation of residual and active stresses in the acrylic plastic capsules, it appears that this stress investigation technique is ideal for the evaluation of residual stresses introduced into the capsule by the fabrication process. In fact, the measurement of residual stresses inside the joints between pentagons probably would not have been possible with any other stress investigation technique.

The photoelastic technique is also applicable to measurement of active stresses in the capsule under hydrostatic loading. However, because special equipment (pressure vessel windows and lights and a means of remotely orienting the capsule) is required for such testing, the use of electric resistance strain gages is more attractive.

Appendix C

DIMENSIONAL DEVIATIONS OF NEMO MODELS

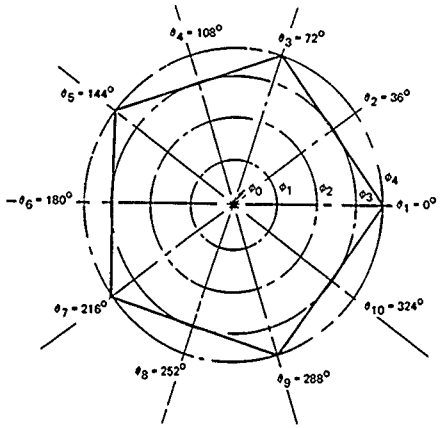

Model Number 18

ϕ angle

$\phi_0 = 0^\circ 0'$

$\phi_1 = 10^\circ 30'$

$\phi_2 = 21^\circ 0'$

$\phi_3 = 31^\circ 30'$

$\phi_4 = 37^\circ 10'$

Note

1 Mark on each pentagon the pentagon number at center and angle numbers at edge, these numbers should be maintained throughout fabrication of the complete sphere

2 Angles ϕ_1 through ϕ_4 are angles through center of sphere

3. Angles θ_1 through θ_{10} are measured from the center of the pentagon

4 Δr denotes change in internal surface curvature from specified 7 000 inches, + indicates shorter radius, while – indicates longer radius.

Point	Pentagon 1		Pentagon 2		Pentagon 3		Pentagon 4	
	Δr	Thickness	Δr	Thickness	Δr	Thickness	Δr	Thickn
$\theta_1 - \phi_0$	+0 004	0 495	+0 005	0 500	+0 006	0 498	+0 005	0 485
$\theta_1 - \phi_1$	+0 002	0 485	+0 003	0 495	+0 0025	0 498	+0 002	0 480
$\theta_1 - \phi_2$	0 005	0 485	0 000	0 495	0 000	0 495	0 000	0 475
$\theta_1 - \phi_3$	-0 0015	0 495	-0 004	0 495	-0 0015	0 498	-0 004	0 475
$\theta_1 - \phi_4$	-0 005	.500	-0 006	0 505	-0 004	0 498	-0 005	0 485
$\theta_2 - \phi_1$	+0 0015	0,485	+0 003	0 495	+0 003	0 498	+0 002	0 475
$\theta_2 - \phi_2$	0 000	0 485	0 000	0 495	0 000	0 498	0 000	0 475
$\theta_2 - \phi_3$	-0 005	0 495	-0 006	0 502	-0 005	0 502	-0 006	0 480
$\theta_3 - \phi_1$	+0 001	0 495	+0 001	0 503	+0 002	0 498	0 000	0 475
$\theta_3 - \phi_2$	0.000	0 495	0 000	0 504	0 000	0 498	0 000	0 475
$\theta_3 - \phi_3$	-0 0025	0 495	-0 0025	0 505	-0 0025	0 498	-0 007	0 475
$\theta_3 - \phi_4$	-0 005	0 495	-0 005	0 505	-0 003	0 502	-0 010	0 485
$\theta_4 - \phi_1$	+0 0015	0 495	+0 002	0 498	+0 004	0 498	+0 002	0 475
$\theta_4 - \phi_2$	0 000	0 495	0 000	0 500	0 000	0 498	0 000	0 475
$\theta_4 - \phi_3$	-0 004	0 495	-0 004	0 500	-0 002	0 500	-0 006	0 475
$\theta_5 - \phi_1$	+0 0025	0 495	+0 002	0 502	+0 003	0 498	+0 0015	0 470
$\theta_5 - \phi_2$	0 000	0 495	0 000	0 502	0 000	0 498	0 000	0 475
$\theta_5 - \phi_3$	-0 000	0 495	-0 002	0 500	0 000	0 500	-0 004	0 475
$\theta_5 - \phi_4$	-0 0025	0 495	-0 004	0 498	-0 003	0 498	-0 007	0 485
$\theta_6 - \phi_1$	+0 003	0,485	+0 003	0 498	+0 004	0 498	+0 003	0 475
$\theta_6 - \phi_2$	0 000	0 485	0 000	0 500	0 000	0 498	0 000	0 475
$\theta_6 - \phi_3$	-0 004	0 490	-0 005	0 495	-0 002	0 498	-0 006	0 480
$\theta_7 - \phi_1$	+0 0015	0 490	+0 002	0 500	0 000	0 498	+0 002	0 475
$\theta_7 - \phi_2$	0 000	0 490	0 000	0 500	0 000	0 498	0 000	0 475
$\theta_7 - \phi_3$	-0 003	0 490	-0 002	0 501	-0 0025	0 498	-0 006	0 485
$\theta_7 - \phi_4$	-0 005	0 485	-0 004	0 498	-0 004	0 498	-0 007	0 495
$\theta_8 - \phi_1$	+0 0015	0 485	+0 002	0 498	0 000	0 498	+0 003	0 47
$\theta_8 - \phi_2$	0 000	0 485	0 000	0 500	0 000	0 498	0 000	0 480
$\theta_8 - \phi_3$	-0 005	0 490	-0 007	0 495	-0 005	0 498	-0 006	0 490
$\theta_9 - \phi_1$	+0 002	0 480	+0 0025	0 498	0 000	0 498	+0 0025	0 475
$\theta_9 - \phi_2$	0 000	0 480	0 000	0 495	0 000	0 493	0 000	0 475
$\theta_9 - \phi_3$	-0 003	0 485	-0 002	0 500	-0 004	0 498	-0 004	0 485
$\theta_9 - \phi_4$	-0 005	0 485	-0 005	0 498	-0 006	0 496	-0 007	0 495
$\theta_{10} - \phi_1$	+0 003	0 480	+0 004	0 495	+0 004	0 493	+0 003	0 475
$\theta_{10} - \phi_2$	0 000	0 480	0 000	0 495	0 000	0 495	0 000	0 475
$\theta_{10} - \phi_3$	-0 005	0 485	-0 005	0 498	-0 004	0 493	-0 006	0 480

Figure C-1. Thickness and sphericity measurements on machined spherical ac and bonding into 15-inch-diameter capsule 18, pentagons without

Pentagon 3		Pentagon 4		Pentagon 5		Pentagon 6		Pentagon 7		Pentagon 8		Pentagon 9		Pentagon 10	
Δr	Thickness	Δr	Thickness	Δr	Thickness	Δr	Thickness	Δr	Thickness	Δr	Thickness	Δr	Thickness	Δr	Thickness
85 006	0 498	+0 005	0 485	+0 003	0 490	+0 003	0 485	+0 0025	0 475	+0 004	0 500	+0 004	0 500	+0 003	0 485
80 025	0 498	+0 002	0 480	+0 001	0 495	+0 0015	0 475	0 000	0 475	+0 002	0 502	+0 0025	0 502	+0 002	0 485
75 00	0 495	0 000	0 475	0 000	0 500	0 000	0 475	-0 001	0 485	0 000	0 510	0 000	0 500	0 000	0 495
75 015	0 498	-0 004	0 475	-0 003	0 495	-0 006	0 475	-0 004	0 485	-0 001	0 512	-0 003	0 500	-0 002	0 502
85 04	0 498	-0 005	0 485	-0 005	0 495	-0 018	0 485	-0 005	0 490	-0 001	0 508	-0 006	0 495	-0 004	0 502
75 03	0 498	+0 002	0 475	+0 0025	0 485	+0 0015	0 475	+0 0015	0 475	+0 002	0 502	+0 003	0 498	+0 003	0 485
75 00	0 498	0 000	0 475	0 000	0 495	0 000	0 475	0 000	0 485	0 000	0 505	0 000	0 500	0 000	0 485
80 05	0 502	-0 006	0 480	-0 003	0 495	-0 011	0 475	-0 004	0 485	-0 005	0 510	-0 0025	0 500	-0 004	0 500
75 02	0 498	0 000	0 475	0 000	0 490	+0 0015	0 470	0 000	0 475	+0 0015	0 498	+0 0015	0 500	+0 002	0 485
75 00	0 498	0 000	0 475	0 000	0 495	0 000	0 472	0 000	0 485	0 000	0 498	0 000	0 502	0 000	0 485
75 025	0 498	-0 007	0 475	-0 004	0 495	-0 004	0 475	-0 0025	0 485	-0 006	0 500	-0 003	0 500	-0 003	0 495
85 03	0 502	-0 010	0 485	-0 005	0 490	-0 018	0 485	-0 005	0 485	-0 013	0 505	-0 004	0 500	-0 007	0 500
75 04	0 498	+0 002	0 475	+0 0015	0 480	+0 002	0 472	+0 003	0 472	+0 003	0 500	+0 002	0 498	+0 003	0 480
75 00	0 498	0 000	0 475	0 000	0 485	0 000	0 472	0 000	0 475	0 000	0 515	0 000	0 495	0 000	0 485
75 02	0 500	-0 006	0 475	-0 006	0 495	-0 009	0 470	-0 007	0 480	-0 009	0 502	-0 005	0 500	-0 004	0 495
70 03	0 498	+0 0015	0 470	+0 0015	0 495	+0 0015	0 475	+0 002	0 475	+0 002	0 498	+0 002	0 500	+0 001	0 485
75 00	0 498	0 000	0 475	0 000	0 490	0 000	0 475	0 000	0 475	0 000	0 499	-0 000	0 495	0 000	0 485
75 00	0 500	-0 004	0 475	-0 003	0 495	-0 004	0 485	-0 005	0 475	-0 004	0 501	-0 004	0 505	-0 004	0 495
85 03	0 498	-0 007	0 485	-0 005	0 495	-0 010	0 485	-0 013	0 485	-0 012	0 500	-0 007	0 505	+0 009	0 502
75 04	0 498	+0 003	0 475	+0 003	0 480	+0 003	0 475	+0 003	0 475	+0 0025	0 497	+0 004	0 495	+0 002	0 475
75 00	0 498	0 000	0 475	0 000	0 485	0 000	0 405	0 000	0 475	0 000	0 495	0 000	0 495	0 000	0 485
80 02	0 498	-0 006	0 480	-0 004	0 490	+0 009	0 485	-0 009	0 475	-0 007	0 510	-0 004	0 500	-0 005	0 492
75 00	0 498	+0 002	0 475	+0 001	0 485	+0 001	0 472	+0 0015	0 475	+0 001	0 500	+0 004	0 495	0 000	0 482
75 00	0 498	0 000	0 475	0 000	0 485	0 000	0 475	0 000	0 470	0 000	0 500	0 000	0 493	-0 002	0 490
85 025	0 498	-0 006	0 485	-0 002	0 493	-0 005	0 485	-0 006	0 472	-0 005	0 515	-0 0025	0 500	-0 007	0 495
95 04	0 498	-0 007	0 495	-0 005	0 500	-0 009	0 485	-0 028	0 480	-0 007	0 515	-0 009	0 502	-0 010	0 495
7 00	0 498	+0 003	0 475	+0 0015	0 485	+0 003	0 475	+0 003	0 475	+0 0025	0 498	+0 004	0 495	+0 001	0 480
80 00	0 498	0 000	0 480	0 000	0 487	0 000	0 482	0 000	0 475	0 000	0 505	0 000	0 495	0 000	0 485
90 05	0 498	-0 006	0 490	-0 004	0 498	-0 007	0 485	-0 010	0 475	-0 004	0 515	-0 004	0 502	-0 007	0 495
75 00	0 498	+0 0025	0 475	+0 001	0 487	+0 0015	0 475	+0 0015	0 475	+0 0025	0 505	+0 0015	0 500	0 000	0 483
75 00	0 493	0 000	0 475	0 000	0 490	0 000	0 480	0 000	0 472	0 000	0 512	0 000	0 502	-0 0015	0 490
85 04	0 498	-0 004	0 485	-0 004	0 498	-0 004	0 487	-0 005	0 475	-0 001	0 515	-0 003	0 502	-0 004	0 500
95 05	0 496	-0 007	0 495	-0 005	0 498	-0 009	0 492	-0 015	0 482	-0 002	0 512	-0 006	0 500	-0 006	0 502
75 04	0 493	+0 003	0 475	+0 002	0 485	+0 0025	0 475	+0 002	0 475	+0 003	0 505	+0 003	0 500	+0 003	0 485
75 00	0 495	0 000	0 475	0 000	0 495	0 000	0 475	0 000	0 475	0 000	0 512	0 000	0 502	0 000	0 495
80 04	0 493	-0 006	0 480	-0 005	0 498	-0 009	0 480	-0 011	0 485	-0 000	0 512	-0 004	0 500	-0 003	0 505

ac asurements on machined spherical acrylic plastic pentagons prior to assembly
ut meter capsule 18, pentagons without penetrations.

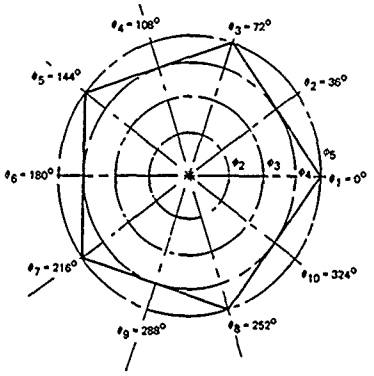

Model Number 18

Points	Pentagon 11		Pentagon 12	
	Δr	Thickness	Δr	Thickness
$\phi_1 - \phi_2$	-0 001	0 475	0 000	0 505
$\phi_1 - \phi_3$	-0 004	0 485	-0 002	0 505
$\phi_1 - \phi_4$	-0 007	0 485	-0 004	0 502
$\phi_1 - \phi_5$	-0 011	0 492	-0 005	0 500
$\phi_2 - \phi_2$	-0 001	0 470	0 000	0 505
$\phi_2 - \phi_3$	-0 002	0 475	-0 001	0 505
$\phi_2 - \phi_4$	-0 009	0 485	-0 003	0 500
$\phi_3 - \phi_2$	0 000	0 475	0 000	0 495
$\phi_3 - \phi_3$	-0 003	0.475	-0 0025	0 502
$\phi_3 - \phi_4$	-0 013	0 480	-0 005	0 500
$\phi_3 - \phi_5$	-0.017	0.482	-0 006	0.498
$\phi_4 - \phi_2$	-0 001	0 470	0 000	0 495
$\phi_4 - \phi_3$	-0 003	0.475	-0 015	0 500
$\phi_4 - \phi_4$	-0 010	0.480	-0 004	0 502
$\phi_5 - \phi_2$	-0 001	0 470	0 000	0 500
$\phi_5 - \phi_3$	-0.004	0 470	-0 002	0.509
$\phi_5 - \phi_4$	-0 016	0.475	-0 004	0 505
$\phi_5 - \phi_5$	-0 022	0.480	-0 006	0 505
$\phi_6 - \phi_2$	-0 003	0.475	0 000	0 508
$\phi_6 - \phi_3$	-0.002	0.475	0 001	0 505
$\phi_6 - \phi_4$	-0 011	0.375	-0 0025	0 505
$\phi_7 - \phi_2$	-0 0015	0 465	0 000	0 505
$\phi_7 - \phi_3$	-0 003	0 470	-0 0015	0 505
$\phi_7 - \phi_4$	-0 011	0 475	-0 003	0 505
$\phi_7 - \phi_5$	-0 019	0 480	-0 004	0 505
$\phi_8 - \phi_2$	-0 0015	0 475	0 000	0.505
$\phi_8 - \phi_3$	-0 004	0.475	-0 0015	0 506
$\phi_8 - \phi_4$	-0 010	0 480	-0 003	0 505
$\phi_8 - \phi_2$	-0 001	0.475	0 000	0 506
$\phi_9 - \phi_3$	-0 003	0.475	-0 0015	0 505
$\phi_9 - \phi_4$	-0 012	0.480	-0 004	0.505
$\phi_9 - \phi_5$	-0 015	0.485	-0 005	0.505
$\phi_{10} - \phi_2$	-0 001	0 480	0 000	0 505
$\phi_{10} - \phi_3$	-0 0015	0 475	-0 0015	0 505
$\phi_{10} - \phi_4$	-0 009	0 480	-0 005	0 505

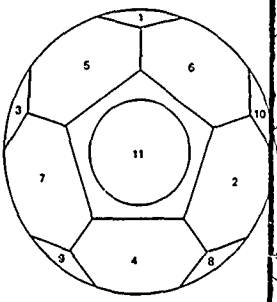

Hull Assembly

ϕ angle

$\phi_2 = 21°0'$
$\phi_3 = 26°15'$
$\phi_4 = 31°30'$
$\phi_5 = 37°10'$

Note

1 Mark on each pentagon the pentagon number at center edge and angle numbers at outer edges, these numbers should be maintained throughout fabrication of complete sphere

2 Angles ϕ_2 through ϕ_5 are angles through center of sphere

3. Angles θ_1 through θ_{10} are measured from the center of the pentagon.

4 Δr denotes change in internal surface curvature from specified 7.000 inches, + indicates shorter radius, while – indicates longer radius.

Note

1 Diameter measurements to be taken 0 50 inch from pentagon edges at number corners θ_1, θ_2, θ_3, etc

2 Measurement at 1, 2, 3, etc is center of pentagon

Figure C-2. Thickness and sphericity measurements on machined spherical acrylic plastic pentagons prior to assembly and bonding into a 15-inch-diameter capsule 18; pentagons with polar penetrations.

Figure C

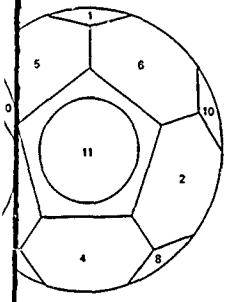

Hull Assembly

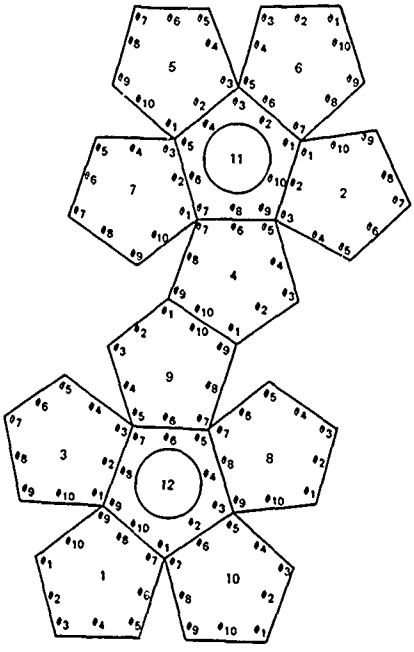

Flat Pattern

From	To	Diameter
$1\text{-}\theta_1$	$4\text{-}\theta_3$	15 010
$1\text{-}\theta_2$	$4\text{-}\theta_2$	15 018
$1\text{-}\theta_3$	$4\text{-}\theta_1$	15 007
$1\text{-}\theta_4$	$4\text{-}\theta_{10}$	15 023
$1\text{-}\theta_5$	$4\text{-}\theta_9$	15 028
$1\text{-}\theta_6$	$4\text{-}\theta_8$	15 037
$1\text{-}\theta_7$	$4\text{-}\theta_7$	15 032
$1\text{-}\theta_8$	$4\text{-}\theta_6$	15 040
$1\text{-}\theta_9$	$4\text{-}\theta_5$	15 026
$1\text{-}\theta_{10}$	$4\text{-}\theta_4$	15 037
1	4	15 038
$2\text{-}\theta_1$	$3\text{-}\theta_3$	15 007
$2\text{-}\theta_2$	$3\text{-}\theta_2$	15 013
$2\text{-}\theta_3$	$3\text{-}\theta_1$	15 011
$2\text{-}\theta_4$	$3\text{-}\theta_{10}$	15 032
$2\text{-}\theta_5$	$3\text{-}\theta_9$	15 030
$2\text{-}\theta_6$	$3\text{-}\theta_8$	15 035
$2\text{-}\theta_7$	$3\text{-}\theta_7$	15 029
$2\text{-}\theta_8$	$3\text{-}\theta_6$	15 033
$2\text{-}\theta_9$	$3\text{-}\theta_5$	15 027
$2\text{-}\theta_{10}$	$3\text{-}\theta_4$	15 030
2	3	15 035
$5\text{-}\theta_1$	$8\text{-}\theta_9$	15 016
$5\text{-}\theta_2$	$8\text{-}\theta_8$	15 017
$5\text{-}\theta_3$	$8\text{-}\theta_7$	15 017
$5\text{-}\theta_4$	$8\text{-}\theta_6$	15 026
$5\text{-}\theta_5$	$8\text{-}\theta_5$	15 024
$5\text{-}\theta_6$	$8\text{-}\theta_4$	15 030
$5\text{-}\theta_7$	$8\text{-}\theta_3$	15.012
$5\text{-}\theta_8$	$8\text{-}\theta_2$	15 [illegible]
$5\text{-}\theta_9$	$8\text{-}\theta_1$	15 013
$5\text{-}\theta_{10}$	$8\text{-}\theta_{10}$	15 018
5	8	15 000

From	To	Diameter
$6\text{-}\theta_1$	$9\text{-}\theta_1$	14 995
$6\text{-}\theta_2$	$9\text{-}\theta_{10}$	14 996
$6\text{-}\theta_3$	$9\text{-}\theta_9$	15 006
$6\text{-}\theta_4$	$9\text{-}\theta_8$	15 027
$6\text{-}\theta_5$	$9\text{-}\theta_7$	15 021
$6\text{-}\theta_6$	$9\text{-}\theta_6$	15 035
$6\text{-}\theta_7$	$9\text{-}\theta_5$	15 028
$6\text{-}\theta_8$	$9\text{-}\theta_4$	15 030
$6\text{-}\theta_9$	$9\text{-}\theta_3$	15 013
$6\text{-}\theta_{10}$	$9\text{-}\theta_2$	15 009
6	9	15 030
$7\text{-}\theta_1$	$10\text{-}\theta_9$	15 028
$7\text{-}\theta_2$	$10\text{-}\theta_8$	15 022
$7\text{-}\theta_3$	$10\text{-}\theta_7$	15.011
$7\text{-}\theta_4$	$10\text{-}\theta_6$	15 011
$7\text{-}\theta_5$	$10\text{-}\theta_5$	14 998
$7\text{-}\theta_6$	$10\text{-}\theta_4$	15.011
$7\text{-}\theta_7$	$10\text{-}\theta_3$	15 000
$7\text{-}\theta_8$	$10\text{-}\theta_2$	15 028
$7\text{-}\theta_9$	$10\text{-}\theta_1$	15 029
$7\text{-}\theta_{10}$	$10\text{-}\theta_{10}$	15 038
7	10	15 033
$11\text{-}\theta_1$	$12\text{-}\theta_7$	15 008
$11\text{-}\theta_2$	$12\text{-}\theta_6$	15.009
$11\text{-}\theta_3$	$12\text{-}\theta_5$	14 995
$11\text{-}\theta_4$	$12\text{-}\theta_4$	15.010
$11\text{-}\theta_5$	$12\text{-}\theta_3$	14 995
$11\text{-}\theta_6$	$12\text{-}\theta_2$	15 015
$11\text{-}\theta_7$	$12\text{-}\theta_1$	15 010
$11\text{-}\theta_8$	$12\text{-}\theta_{10}$	15 030
$11\text{-}\theta_9$	$12\text{-}\theta_9$	15 025
$11\text{-}\theta_{10}$	$12\text{-}\theta_8$	15 027

[illegible]r measurements to be taken 0 50 inch
[illegible]ntagon edges at number corners θ_1,
[illegible]tc
[illegible]ion at 1, 2, 3, etc. is center of pentagon

Figure C-3. Diametrical measurements on 15 inch-diameter capsule 18 after bonding and annealing was completed

Appendix D

FEASIBILITY STUDY OF EQUATORIAL RING FOR THE ATTACHMENT OF THE ACRYLIC PLASTIC CAPSULE TO THE FRAMEWORK OF A SUBMERSIBLE SYSTEM

INTRODUCTION

Although the external cage type of capsule restraint (Figure 8) was selected as the most applicable for securing the 66-inch capsule to the framework of the NEMO system, this does not indicate that the other types of restraint discussed in detail in the main body of the report are not applicable if the design requirements of the submersible system are different from that of the 66-inch first-generation NEMO system. Since the acrylic plastic capsules will be incorporated into submersible systems distinctly different from the first-generation NEMO system, some of the other capsule restraint concepts warranted exploratory investigation. Of the five feasible approaches previously discussed (Figures 5 through 9), only the *bolt-on internal tie rod*, the *equatorial ring*, and the *external cage* types of restraints appeared to show real versatility. For this reason, they were chosen for further exploratory investigation. The *internal tie-rod restraint* was utilized in most of the models tested for the acrylic plastic capsule program (Figures 15 and 64), and thus does not require here any further discussion. The *bolt-on restraint* was used during the extensive testing of the 66-inch-diameter large-scale capsule prototype (Figures 70 and 101), and for this reason no further experimental work was needed on this type of restraint. The *external cage restraint* was chosen for evaluation in the construction of the first generation operational NEMO system built by the Southwest Research Institute, and thus the only type of capsule restraint that remained to be evaluated was the *equatorial ring* type.

EXPERIMENTAL PROGRAM

The exploratory experimental evaluation of the *equatorial ring capsule restraint concept* consisted of designing and fabricating a 15-inch-OD x 14-inch-ID acrylic plastic capsule that would be attached to the submersible's exostructure by means of an equatorial ring incorporating the essential features of that concept. The essential features of this concept (Figure D-1) were (1) an equatorial ring (Figure D-2) to which were attached the capsule, the exostructure of the submersible, and the lifting slings, and (2) tapered pins that were rigidly seated by means of threaded nuts (Figure D-3) in the hull of the acrylic plastic capsule, while in the equatorial ring they were restrained only from lateral displacement but were permitted to translate radially by sliding in oversize holes drilled radially into the ring

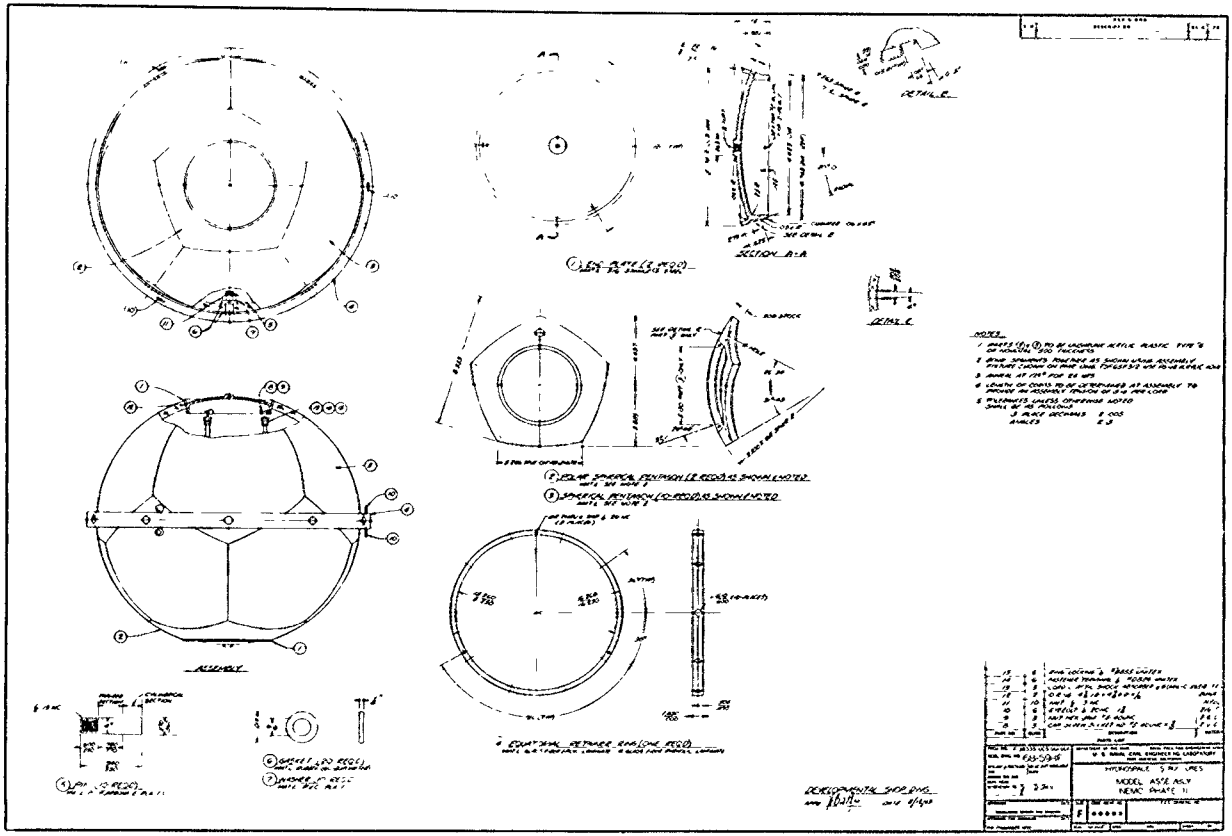

Figure D-1. Design of the 15-inch OD x 14-inch-ID acrylic plastic capsule model with equatorial ring.

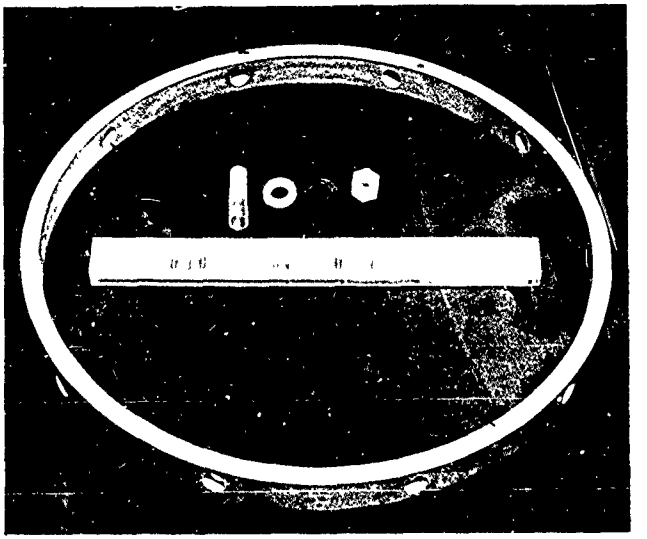

Figure D-2. Equatorial ring and tapered pins needed for attaching the ring to the acrylic plastic capsule.

The model capsule was fabricated in an identical manner to those already discussed in the main body of the report (Figure D-4), except that 10 radially tapered holes were drilled through the wall along the capsule's equator (Figure D-4). For implosion testing, the model was equipped (Figure D-5) with the simplified end closures (Figure 63) described in the main body of the report.

The test condition for imploding the *equatorial ring* capsule was short-term pressurization at 100°F. The choice of this test condition was based on the program's need for implosion data on acrylic plastic capsules at various temperatures to establish the temperature-versus-implosion-pressure relationship of acrylic plastic capsules. Since the total number of model capsules available for the acrylic plastic hull program was limited, the implosion testing of the equatorial ring capsule had to satisfy two requirements. It had to establish the adequacy of the equatorial ring restraint design while at the same time it had to provide additional data for the study on the effect of temperatures on the implosion pressure of acrylic plastic capsules.

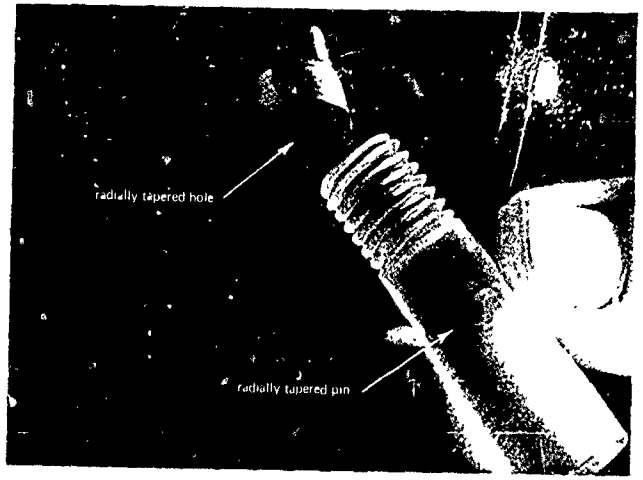

(a) Inserting the pin.

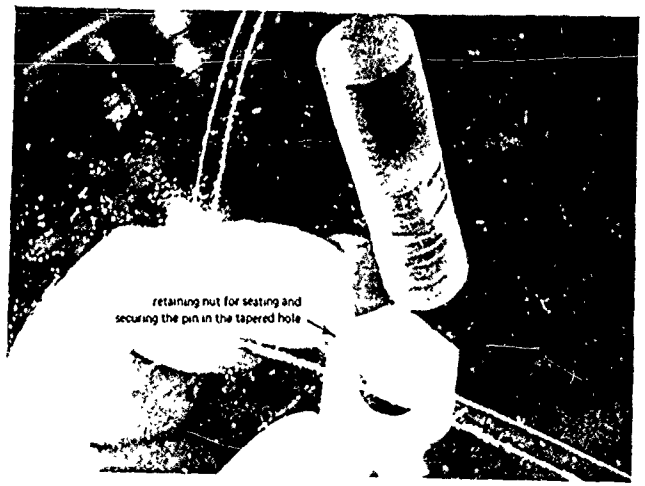

(b) Securing the pin.

Figure D-3. Installation of the tapered pins into the radially tapered holes in the acrylic plastic hull.

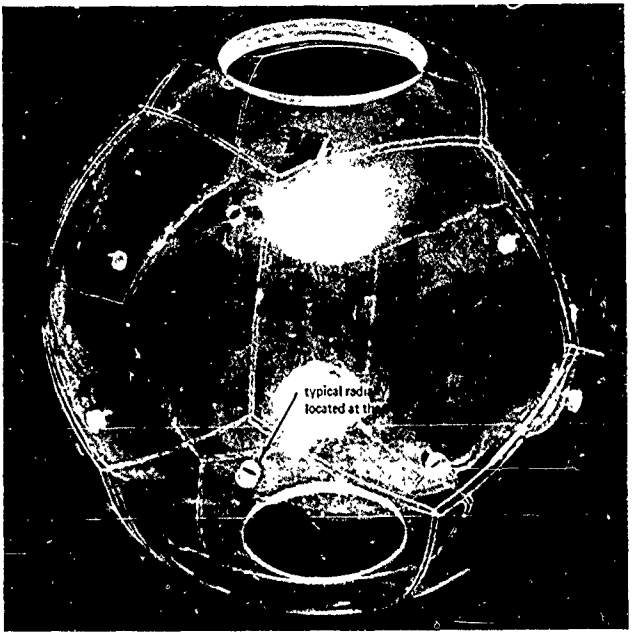

(a) Overall view of the capsule.

(b) Detail of the radially tapered hole.

Figure D-4. Acrylic plastic capsule prior to being outfitted with polar steel end closures, pins, and equatorial ring

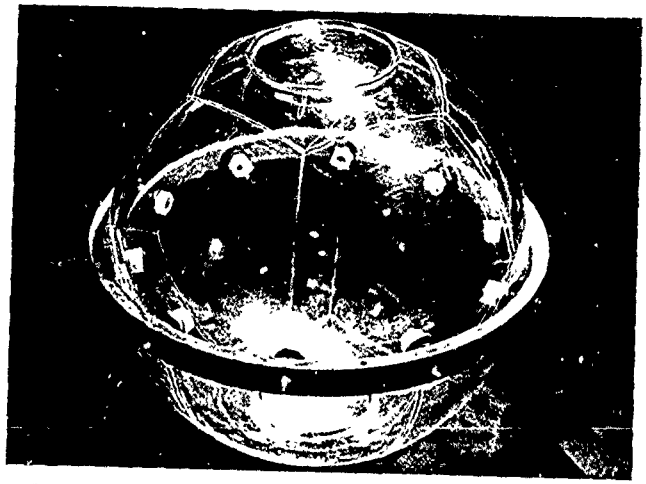

Figure D-5. Assembled 15-inch-diameter acrylic plastic capsule with equatorial ring.

After pressurization of the capsule to implosion at 100°F, the structural adequacy of the concept was to be inferred from a plot of implosion pressure versus temperature generated by implosion testing at different temperatures on an additional eight capsules with internal tie rods. Since the critical-pressure-versus-temperature relationship appears to be linear in the 32 to 114°F test range, it would be easy to see whether the implosion pressure of the equatorial ring capsule fit the linear relationship established by the other capsules. A good fit would be a positive proof that the incorporation of the equatorial ring into the hull of the acrylic plastic capsule did not introduce into the hull structure any stress raisers that decrease the critical pressure of the acrylic plastic hull.

FINDINGS

When the capsule (Figure D-6) with the equatorial ring was pressurized at a 100-psi/min rate to destruction at the ambient temperature of 100°F, it imploded at 1,175 psi. This critical pressure was found to agree (Figure D-7) with the value predicted for this temperature by the linear relationship established by the implosion pressures of other capsules at different temperatures (Figure 78)

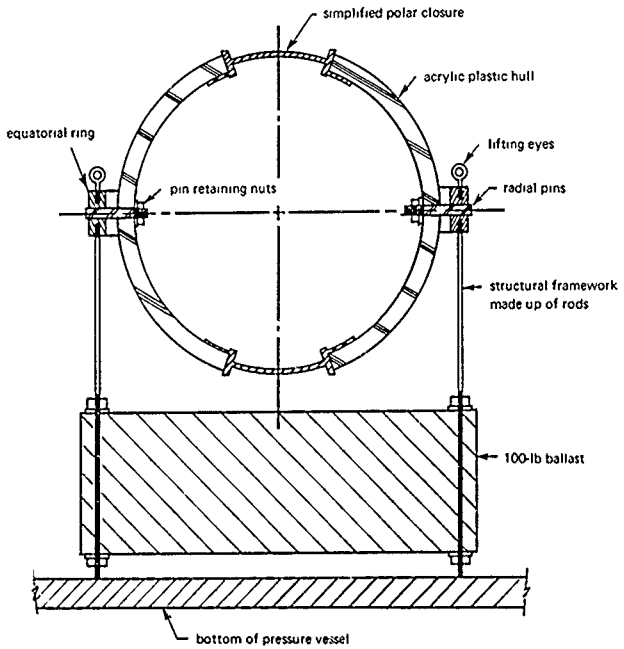

Figure D-6. Test arrangement for implosion testing of the 15-inch-diameter capsule with equatorial ring

CONCLUSION

The equatorial ring restraint concept for attaching a spherical acrylic plastic capsule to the structural framework of a submersible system has been found to be feasible, and its application does not compromise in any manner the structural integrity of the acrylic plastic pressure hull under external hydrostatic loading

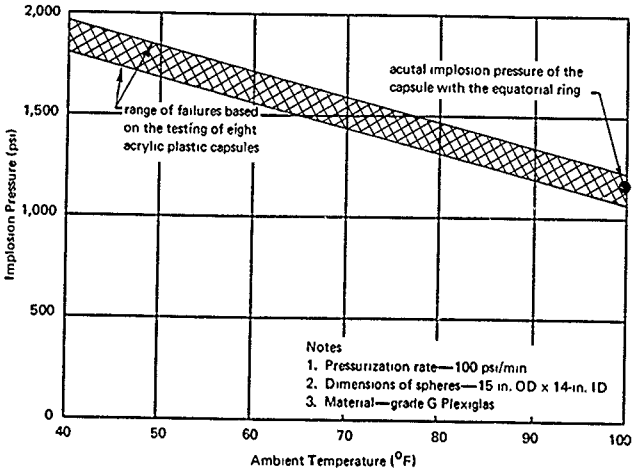

Figure D-7. Comparison of implosion pressure of equatorial ring concept with predicted implosion pressure.

Appendix E

EXPLORATORY INVESTIGATION INTO THE FEASIBILITY OF ACRYLIC PLASTIC CAPSULES FOR OCEAN DEPTHS BEYOND 600 FEET

DISCUSSION

The experiments constituting the main body of this report have shown conclusively that the spherical acrylic plastic capsules with nominal t/D = 0.033 are safe for depths up to 1,000 feet and therefore merit certification for manned use to at least 600 feet. But this information does not provide the necessary basis for predicting the safe operational pressure of thicker acrylic plastic capsules. Since there may be future requirements to predict what the capsule thickness should be for some greater operational depth (for example, 2,000 feet), a brief exploratory study was performed on the collapse depth of thicker acrylic plastic capsules.

EXPERIMENTAL PROGRAM

Model capsules were used to investigate the performance of one nominal t/D ratio only 0.066. The outside diameter and polar opening closure designs remained essentially the same as in the model capsules with t/D = 0.033. The only differences between the simulated end closure used on the thin capsules and on the thick capsules (Figure E-1) are (1) increase in thickness of closure, (2) use of titanium instead of steel, and (3) a gasket instead of an O-ring seal system. Since only four thick capsule models were available for the exploratory study, it was decided to test them under long-term loading conditions, as in this manner a long-term failure prediction curve, similar to the one derived for thin capsules (Figure 87) could be derived On the basis of the long-term failure curve, the safe operational depth of such a capsule could be predicted with reasonable accuracy by selecting the same *span of time* for definition of safe operational pressure as was found to correspond with the 600-foot operational depth for thin capsules (Figure 87).

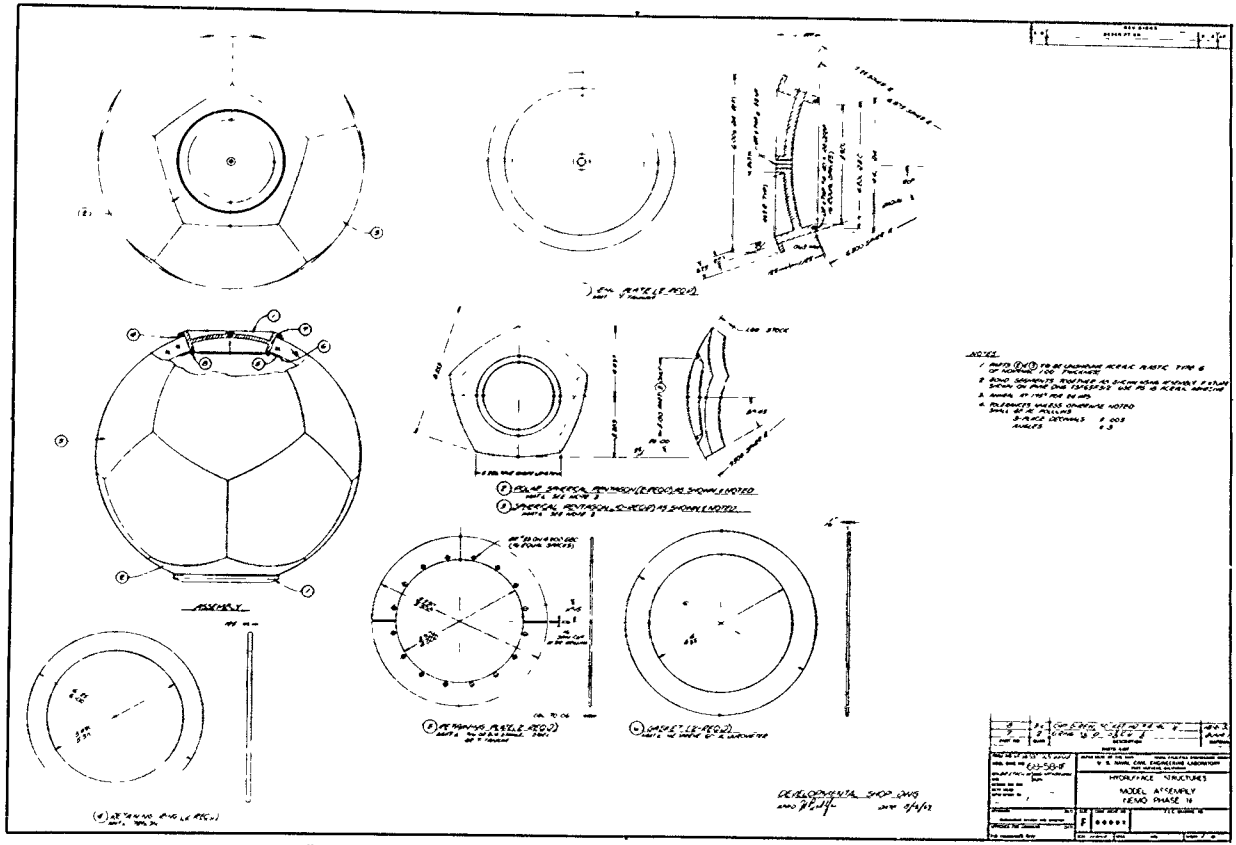

Figure E-1. Models with outside diameter of 15 inches and inside diameter of 13 inches

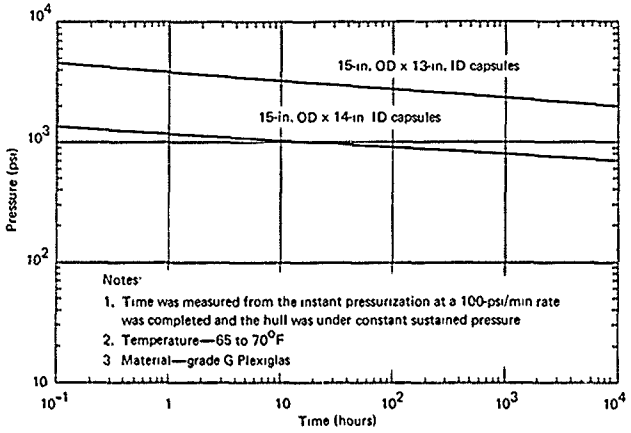

Figure E-2. Comparison of time-dependent implosion pressures for 15-inch-outside-diameter capsules with different wall thicknesses.

FINDINGS

When the four capsules with t/D = 0.066 were tested to implosion under long-term hydrostatic loading, it was found that the implosion pressures were, as expected, a function of time (Table E-1) similar to the capsules with t/D = 0.033. When the time-versus-implosion-pressure relationship was plotted on the same log-log scale, as was used for the t/D = 0.033 capsules (Figure 87), it was found that the slope of the linear graph is the same as that for the thin capsule. The only difference in the results for the thick- and thin-walled capsules was the magnitude of the sustained pressure for a given duration of loading (Figure E-2). From a comparison of these results, the short-term implosion pressure of the capsules with nominal t/D = 0.066 was extrapolated to occur at 5,000 psi, while the design proof depth (cyclic and long-term) was predicted to be 2,400 feet (certifiable for at least 1,200-foot manned operations when the same stress level and time dependent failure criteria are used as for the t/D = 0.033 capsules).

Table E-1. Long-Term Pressurization Tests on 15-Inch-OD x 13-Inch-ID Model Capsules

Specimen Number	Joint	Type of Penetration Closures	Temperature (°F)		Type of Failure	Pressurization Rate (psi/min)	Sustained Pressure (psi)	Duration of Loading (minute)
			Outside	Inside				
22	wide	special titanium plates (Figure E-1)	69	69	general implosion of acrylic plastic capsule	100	4,500	6
23	wide	special titanium plates (Figure E-1)	69	69	general implosion of acrylic plastic capsule	103	4,000	23
24	wide	special titanium plates (Figure E-1)	71	71	general implosion of acrylic plastic capsule	95	3,500	315
25	wide	special titanium plates (Figure E-1)	70	70	general implosion of acrylic plastic capsule	101	3,000	1,575

NOTE: 1. End plates made from Ti-6Al-4V titanium.
2. Acrylic plastic is grade G Plexiglas of nominal 1-inch thickness.
3. Wide joints bonded with PS-18 cement.
4. The same set of end plates was used over and over again

Observation of fragments from the 1-inch-thick polar acrylic plastic pentagons confirmed the observations made previously on the 1/2-inch-thick polar pentagons that the magnitude of cracks in the beveled bearing surface pressing against the steel inserts is *a function of magnitude of time-dependent strain*, not stress level. Thus, for example, the cracks in the fragment (Figure E-3) from the capsule that imploded at 3,000 psi after 1,575 minutes of sustained hydrostatic loading are deeper than those found in the fragment from the capsule that imploded at 4,000 psi after 23 minutes of sustained loading (Figure E-4).

CONCLUSIONS

Acrylic plastic spherical hulls of 66-inch diameter, if fabricated from standard nominally 4-inch-thick plate (thickest commercially available grade G Plexiglas plate), merit certification to an operational depth of 1,050 feet if the stress level, fatigue life, and time-dependent failure criteria are similar to those employed for certification of the nominally 2.5-inch-thick acrylic plastic hull to a 600-foot depth.

RECOMMENDATIONS

For operational depths either greater or lesser than 600 feet, the t/D ratios shown on Figure E-5 are recommended for manned acrylic plastic capsules. These values of t/D have been calculated using the same criteria of safety established experimentally for the NEMO 600-foot operational depth capsules of this report. When more experimental data become available on the relationship between the t/D ratio and safe operational depth the Figure E-5 will be revised to incorporate the new findings.

Figure E-3. Cracks in the beveled bearing surface of the polar acrylic plastic pentagon viewed at a right angle to the cut through the bearing surface. Capsule failed after 1,575 minutes of sustained loading at 3,000 psi.

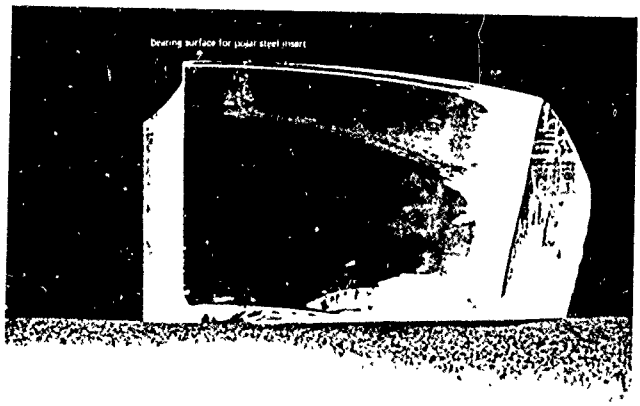

Figure E-4. Cracks in the beveled bearing surface of the polar acrylic plastic pentagon viewed at a right angle to the cut through the bearing surface. Capsule failed after 23 minutes of sustained loading at 4,000 psi.

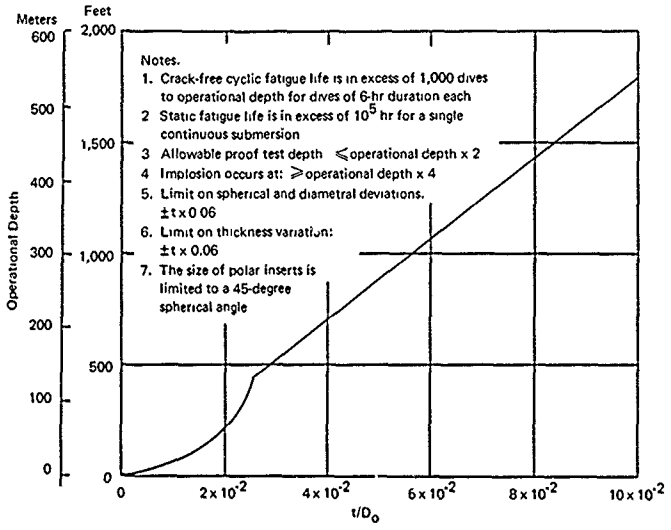

Figure E-5. Recommended dimensions of spherical acrylic capsules for certifiable manned undersea operations.

Appendix F

FABRICATION OF OPERATIONAL 66-INCH-OD x 61-INCH-ID ACRYLIC CAPSULES

INTRODUCTION

The knowledge and experience gained in developing the prototype 66-inch acrylic capsule (NEMO capsule 0) was immediately applied to the production of three additional 66-inch capsules. NEMO capsule 1 was to be mated with the THS (Transparent Hull Submersible) system by the Naval Underwater Research and Development Center; NEMO capsule 2 was to be incorporated into the NEMO system by the Naval Civil Engineering Laboratory, while NEMO capsule 3 was to be utilized for further structural tests.

The three additional acrylic capsules were fabricated on contract by Swedlow Inc. of Los Angeles, California. The reasons for contracting the fabrication of the additional acrylic capsules to an industrial company were: (1) to find out how well the fabrication techniques developed in a model shop environment perform in an industrial shop environment and (2) to develop in the plastics industry capability for mass production of NEMO acrylic capsules. The metal polar plates for the capsules were again manufactured by the shop personnel of the Navy Pacific Missile Range.

DESIGN

The three acrylic capsules were fabricated according to the same design used previously in the prototype 66-inch capsule. The only difference in the specification was that instead of specifying only PS-18 adhesive for the joints, other adhesives could be substituted for it providing their tensile strength was in excess of 4,000 psi and the adhesive was as immune to seawater as PS-18 adhesive.

The metal polar plates were also fabricated to the same basic design as the prototype. Major differences were only the elimination of the planetary gear hatch locking mechanism and the substitution of cadium-plated type 4130 steel for type 316 stainless steel. Both changes were made for economy.

FABRICATION

The procedures for fabrication of capsules 1, 2, and 3 were the same as for the prototype capsule 0 described in the main body of the report except that a different adhesive and acrylic plastic joint spacers were used in capsules 2 and 3. These acrylic joint spacers were not removed prior to setting of adhesive, resulting in considerable labor saving. No changes in tooling were made prior to fabricating capsules 1, 2, and 3 except for changing the curvature of the mold from nominal 33.187 to actual 33.000 inches and giving the newly machined surface a 16-rms finish.

The adhesive selected for capsules 2 and 3 was Swedlow's SS-6217, which has a polymerization rate that can be controlled more accurately during bonding of the joints. Prior to substituting SS-6217 adhesive for PS-18 adhesive, it was evaluated for strength and immunity to seawater. Both its strength and resistance to seawater (6,360-psi average tensile strength prior to immersion and 5,990 psi after 42 days' immersion) were found to be equivalent to that of PS-18. In addition, the cured adhesive was not only transparent but colorless, rather than yellow as PS-18 generally is.

QUALITY CONTROL

Very stringent quality controls were maintained during every step of the fabrication to insure that the completed capsules would perform structurally as well, or better than, the prototype capsule 0 described in the main body of the report. Five different quality controls were applied, and the results were recorded by inspectors

Material Properties

Each sheet of 48 x 60 x 2.5-inch acrylic plastic was accompanied by an invoice from the manufacturer stating the type of material, date cast, and batch number. Upon receipt of the material, a 12 x 48 x 2.5-inch strip was cut from each sheet From this strip a total of 10 (two for each test) specimens were machined and subsequently tested to determine the following material properties

1. Compressive strength and compressive modulus of elasticity
2. Tensile strength and tensile modulus of elasticity
3. Flexural strength and flexural modulus of elasticity

4. Shear strength

5. Compressive deformation under load

If the average value of two test specimens for any of the above-mentioned tests was less than specified in Table 1, the acrylic sheet from which the specimens were cut was rejected. Upon examination of the test data, only one sheet out of 38 had to be rejected. The mechanical properties determined for all the 38 sheets of 2.5-inch-thick acrylic plastic are shown in Table F-1.

After the tests the accepted acrylic plastic sheets were officially released for band-sawing into 46-inch-diameter discs.

Dimensional Tolerance Measurement

After all the discs had been cut from the accepted sheets, the thickness of each disc at seven different points was measured (Figure F-1). If the thickness of the disc was within $2.375 \leq t \leq 2.625$ inches, it was considered to be acceptable, and the given disc was released for thermoforming into sectors. None of the discs were rejected, as all discs met the specified tolerances on thickness (Table F-2).

After forming the disc into spherical sector by means of heat and application of vacuum in a female mold, the thickness was checked again at six locations (Figure F-1). If the thickness was found to be within $2.315 < t < 2.685$ inches, the formed sector was considered to be acceptable, and it was released for machining into a pentagon (Table F-2).

After the pentagons were machined and annealed, they were checked for sphericity and adherence to tolerances specified for the size of the pentagon. None of the finished pentagons were found to exceed the $32.875 \leq R \leq 33.125$-inch tolerance on sphericity measured at six places (Figure F-1) across the outside surface of the pentagon (Table F-2). All but five pentagons met the dimensional tolerance of $37.380 \leq K \leq 38.020$ inches on size measured between nonadjacent tips of the pentagon. The five pentagons, whose K dimension was, in some cases, 0.100-inch less than specified, were also accepted but on the condition that commensurately thicker spacers would be utilized by the contractor in the assembly of the capsule to compensate for some of the undersize pentagons. The capsule in which the undersized pentagons were used was capsule 3 not slated for manned service but structural testing. The diameter of the penetrations in the polar pentagons was checked at this time also. All of the penetrations were found to conform to the $22.568 \leq d \leq 22.578$-inch dimensional tolerance.

Table F-1. Mechanical Properties of Acrylic Plastic Plates

(Test specimens formed from unshrunk, 48 x 60 x 2.5-in. grade G Plexiglas.)

Type of Test	ASTM No.	Specimen Size	Test Condition	Environment	NCEL Material Specification	No. of Test Specimens That Failed to Meet Minimum Specification[a]	Test Result	
							Minimum	Spec M
Tensile strength (ultimate)	D-638	0.250 in. thick x 0.500 in. wide	0.05-in./min crosshead speed	23°C and 50% RH	9,000 psi	1	8,400 psi	1(250 500
Tensile modulus of elasticity[b]	D-638	0.250 in. thick x 0.500 in. wide	0.05-in./min crosshead speed	23°C and 50% RH	400,000	1	390,000	250 500
Tensile elongation at failure	D-638	0.250 in. thick x 0.500 in. wide	0.05-in./min crosshead speed	23°C and 50% RH	2-7%	0	2.5%	250 500
Shear strength (ultimate)	D-732-46	0.250 x 1.000-in. disc, punched out	0.05-in./min crosshead speed	23°C and 50% RH	8,000 psi	0	8,360 psi	1250 sc. f
Compressive deformation under load	D-621-64	0.500 x 0.500 x 0.500 in.	4,000-psi sustained load for 24 hr	122°F	2% max	1	0.6%	500 500
Compressive strength (yield)	D-695	0.500 x 0.500 x 1.500 in.	0.05-in./min crosshead speed	23°C and 50% RH	15,000 psi	1	13,100 psi	500 500
Compressive modulus of elasticity[b]	D 695	0.500 x 0.500 x 1.500 in.	0.05-in./min crosshead speed	23°C and 50% RH	420,000 psi	0	420,000 psi	65500 500
Flexural strength (ultimate)	D-790-66	0.250 in. thick x 0.500 in. wide	0.11-in./min deflection rate on 4.0-in. span	23°C and 50% RH	14,000 psi	1	13,200 psi	1250 500
Flexural modulus of elasticity[b]	D-790-66	0.250 in. thick x 0.500 in. wide	0.11-in./min deflection rate on 4.0 in. span	23°C and 50% RH	420,000 psi	1	390,000 psi	50250 500

[a] 38 specimens for each type of test. All of the specimens that did not meet specifications came from the same acrylic plastic plate, which was rejected as a result of it.

[b] Modulus based on linear stress/strain rate only.

Table F-1 Mechanical Properties of Acrylic Plastic Plates

(Test specimens formed from unshrunk, 48 x 60 x 2 5-in. grade G Plexiglas.)

Specimen Size	Test Condition	Environment	NCEL Material Specification	No. of Test Specimens That Failed to Meet Minimum Specification[a]	Test Results	
					Mimimum	Maximum
250 in. thick x 500 in. wide	0 05-in./min crosshead speed	23°C and 50% RH	9,000 psi	1	8,400 psi	10,800 psi
250 in. thick x 500 in. wide	0 05-in./min crosshead speed	23°C and 50% RH	400,000	1	390,000	510,000
250 in. thick x 500 in. wide	0.05-in./min crosshead speed	23°C and 50% RH	2-7%	0	2.5%	6.3%
250 x 1,000-in. ic, punched out	0 05-in./min crosshead speed	23°C and 50% RH	8,000 psi	0	8,360 psi	13,000 psi
500 x 0.500 x 500 in.	4,000-psi sustained load for 24 hr	122°F	2% max	1	0.6%	2.5%
500 x 0 500 x 500 in.	0.05-in./min crosshead speed	23°C and 50% RH	15,000 psi	1	13,100 psi	17,100 psi
500 x 0 500 x 500 in	0.05-in./min crosshead speed	23°C and 50% RH	420,000 psi	0	420,000 psi	650,000 psi
250 in thick x 500 in. wide	0.11-in./min deflection rate on 4 0-in. span	23°C and 50% RH	14,000 psi	1	13,200 psi	17,200 psi
250 in. thick x 500 in wide	0.11-in./min deflection rate on 4 0 in. span	23°C and 50% RH	420,000 psi	1	390,000 psi	500,000 psi

s specimens that did not meet specifications
.n was rejected as a result of it.

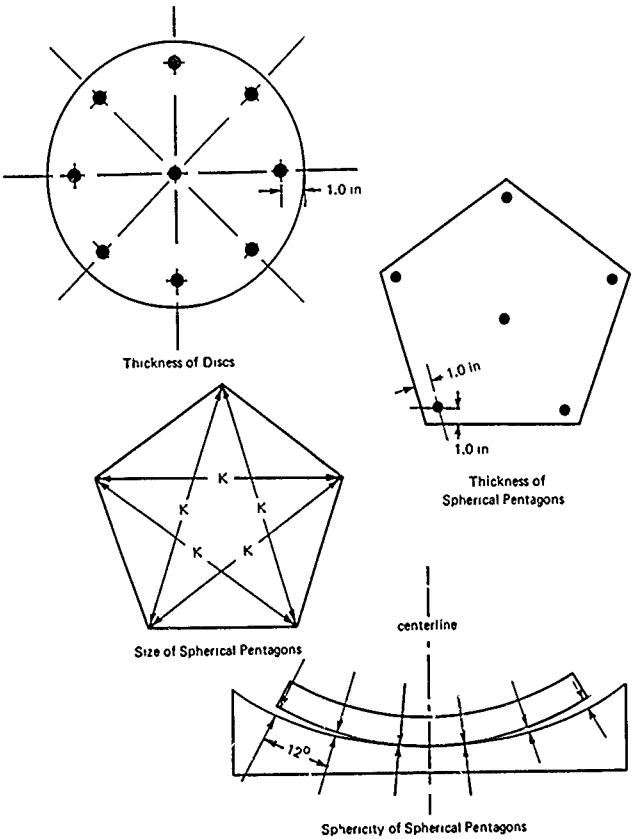

Figure F-1. Location of measurements on structural modules.

Table F-2. Summary of Dimensional Measurements

(Measurements performed on NEMO capsules 1, 2, and 3.)

Specimen	Type of Measurement	Acceptable Range (in.)	Test Results (in.)	
			Maximum	Minimum
Discs prior to forming	thickness	2.375-2.625	2.600	2.385
Pentagons after forming	thickness	2.315-2.685	2.653	2.315
	chord length	37.970-38.030	38.020	37.858
	radius (sphericity)	33.000±0.125	33.100	32.950
Completed spheres	diameter	65.750-66.250	66.100	66.020

After assembly and bonding of the pentagons into three capsules, their diameters were checked at 16 locations and were found to be within the $65.750 \leq D \leq 66.250$-inch specified tolerance for external diameter (Table F-2). The external sphericity was so close to its nominal value that the spheres actually could have met with ease the much more desirable $66.815 \leq D \leq 66.125$-inch tolerance. Since this much tighter diametral tolerance can be apparently met with ease, it is recommended for future capsules

Visual Inspection of Joints

After all the dimensional measurements were completed, the joints (Figure F-2) were visually inspected for undercuts and presence of bubbles. No undercuts were found in any of the joints. Mismatches of thickness were found across some of the joints in the sphere's interior, as could be expected between pentagons of slightly varying thickness. Since all the variations of thickness in pentagons were previously found to be within specified thickness tolerances, the mismatches across the joints were accepted as natural.

The number of bubbles in the joints was found to be drastically fewer than in prototype capsule 0 discussed in the main body of the report and thus acceptable. Capsules 2 and 3 bonded with SS-6217 adhesive had an order of magnitude fewer bubbles than capsule 1 bonded with PS-18, capsule 1 in turn, had several orders of magnitude fewer bubbles than capsule 0, which was also bonded with PS-18 adhesive. Although the multitude of bubbles in capsule 0 did not appear to cause any reduction in the

Figure F-2. Inspection of joints for presence of bubbles and undercuts at Swedlow Inc.

capsule's critical pressure or serve as sources for incipient cracks under hydrostatic loading, the substantial decrease in number of bubbles in capsules 1, 2, and 3 resulted in joints with much better transparency and an improved all around appearance.

Strength of Joints

The quality of the joints was checked for each capsule by bonding together four blocks of 12 x 4 x 2 5-inch acrylic plastic into two 12 x 8.125 x 2 5 inch joint specimens with the same batch of adhesive used on the capsule and in the same controlled environment where capsules were bonded. These joint specimens accompanied the capsule to the oven for annealing. After the capsule was completed and ready to be delivered to the customer, 12 tensile test coupons were cut from each joint specimen, with the joint in the center of each coupon. All of the test coupons were tested to destruction, and the ultimate tensile strength of the joints was noted.

Table F-3. Summary of Joint Evaluation Tests

Capsule No.	Adhesive Used	No. of Test Specimens[a]	NCEL's Specified Minimum Tensile Strength (psi)	Tensile Strength (psi)[b]		
				Maximum	Minimum	Average
1	PS-18 (modified by Swedlow)	16	4,000	9,300	7,250	8,580
2	SS-6217 (developed by Swedlow)	16	4,000	7,970	6,340	7,150
3	SS 6217 (developed by Swedlow)	12	4,000	8,640	6,860	8,300

[a] The test specimens for each capsule were 0.750 in. thick by 0.500 in. wide. The 0.125-in.-wide joint was located in the center of the test specimen length. Overall length of specimens was 8 125 in.

[b] The tensile strength of joints in prototype capsule 0 was by comparison 9,220-psi maximum, 5,680-psi minimum, and 7,350-psi average.

The tensile strength of all the joint test coupons (Table F-3) was found to be in excess of the specified minimum 4,000 psi, and thus acceptable. As can be seen from Table F-3, the tensile strength range of 6,300 to 9,800 psi of the joints in capsules 1, 2, and 3 was approximately the same as for the prototype capsule (NEMO 0), for which the tensile strength of the joints was in the 5,680 to 9,200-psi range.

Metallic Closures

The quality control for the polar metal plates (Figure F-3) consisted of material control, dimensional inspection, visual finish inspection, and structural integrity testing. The material quality control consisted of notarized invoices from the supplier certifying the steel stock to be annealed type 4130 steel (MIL-S-18729C) with Brinell hardness in the 163-170 range. The dimensional control consisted of checking the dimensions of machined steel parts for conformance to the drawings. After electroplating the steel parts with cadmium without any brightener, the parts were visually inspected for appearance and quality. If the dimensional check and the visual inspection showed the parts to be satisfactory, they were accepted for mounting in the acrylic plastic capsules

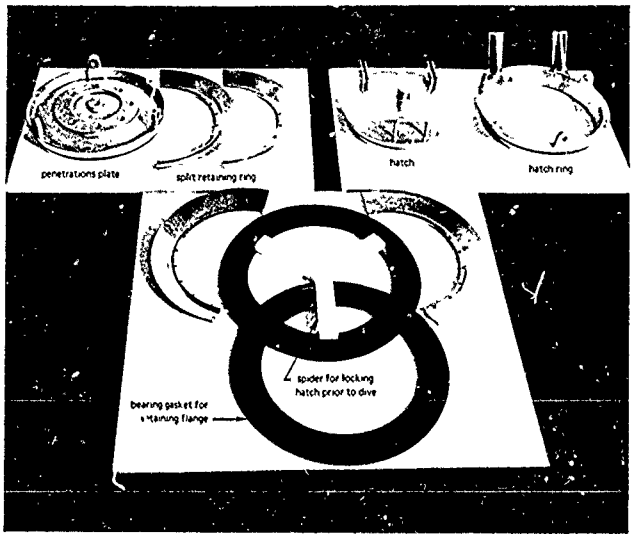

Figure F-3. Components of the top and bottom polar closures used in NEMO capsules 1, 2, and 3.

The structural integrity test was performed on the steel parts in conjunction with the structural integrity testing of the acrylic plastic capsule, as it was felt that only by testing the steel closures mounted in the acrylic plastic capsule (Figure F-4) would it be possible to obtain a realistic evaluation for both

STRUCTURAL INTEGRITY CONTROL

The overall structural integrity of the acrylic plastic capsules was established by a hydrostatic proof test. The acrylic plastic capsules were mated with their steel polar plates, instrumented with electric resistance strain gages, and subjected to a 4-hour hydrostatic loading under 500-psi external pressure If no water was found in the interior of the capsule and the strains measured at the equator matched those on prototype capsule 0 under identical loading (Figure F-5), the performance of the capsule was acceptable Since none of the three capsules leaked and the strains on the equator matched those recorded previously on capsule 0, capsules 1, 2, and 3

were acceptable. In addition to proof-testing capsules 1, 2, and 3, capsule 3 was subjected to extensive cyclic tests to establish the ability of SS-6217 adhesive to withstand without failure cyclic stresses and long-term immersion under compressive loading. Detailed inspection of the bonded joints failed to detect any incipient cracks after 815 cycles of 1 hour duration at 1,200-foot, 178 cycles at 1,500-foot, and 117 cycles at 2,000-foot depths. Fatigue cracks were observed in the acrylic bearing surfaces in contact with steel polar closures only after completion of cycling tests to 1,500-foot depth. The cyclic tests on NEMO capsule 3 concluded the series of quality control tests.

CONCLUSIONS

The successful production run of three 66-inch acrylic plastic capsules by a contractor according to NCEL specifications has shown that almost all of the fabrication processes developed under laboratory conditions were directly applicable with no, or only minor modifications for mass production requirements typical to industry. The only improvement was in bonding. Substitution of a different adhesive and joint spacer system permitted simultaneous bonding of six pentagons into a hemisphere rather than bonding of only a single edge at a time between adjoining pentagons.

The ability of the plastics fabricator and the material supplier to produce by industrial fabrication techniques a series of capsules with the same, or better structural properties than those found in capsule 0, indicates that both the material properties and dimensional tolerances achieved in the prototype capsule are within the range of industrial capability. Thus, it appears that there will be no problems encountered by the industry in producing as many NEMO 66-inch acrylic plastic capsules in the future as may be required by the national undersea program.

The ability of mass-produced capsule 3 to withstand the extensive cyclic pressure testing at 100% overload without generation of fatigue cracks confirms again (1) the validity of cyclic test data generated previously by testing of models and NEMO capsule 0, (2) the presence of 100% overload safety margin for recommended fatigue life (Figure 121) in manned operations to 600-foot depth, and (3) the ability of NEMO capsules to withstand safely brief manned proof-test dives to 1,200 feet.

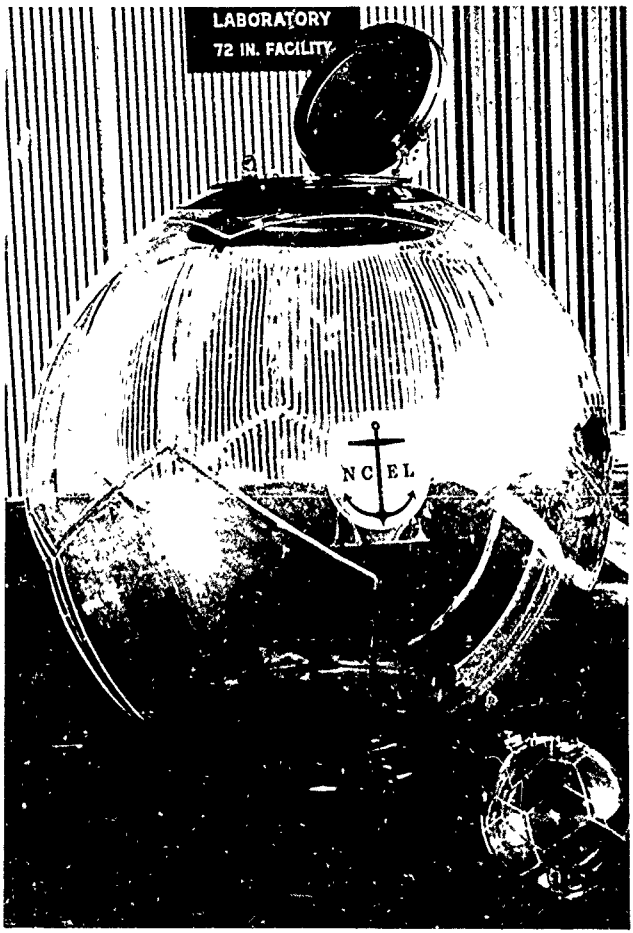

Figure F-4. Assembled NEMO capsule 1 prior to structural integrity testing in NCEL's Deep Ocean Simulation Facility; 15-inch-diameter capsule 16 is shown here for scale.

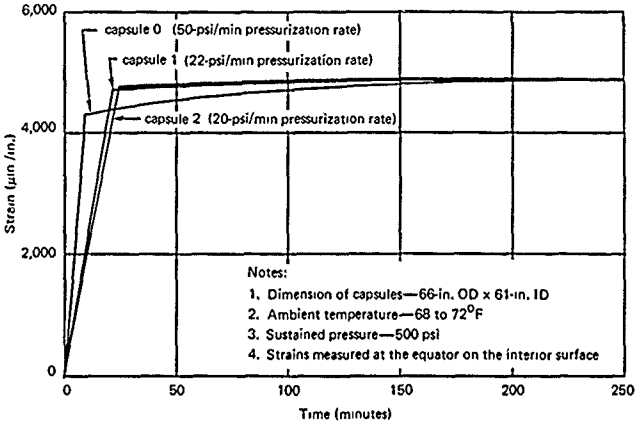

Figure F-5. Comparison of strains on the interior surface of the NEMO capsules under long term 500 psi hydrostatic loading.

RECOMMENDATIONS

The specifications and drawings used in the production of three capsules by the contractor were generally satisfactory, however, as result of the experience gained in the fabrication of the three capsules, the following specification changes should be introduced:

1. Decrease the tolerance on the diameter to $65.875 \leq D \leq 66.125$ inches.

2. Increase the tolerance on the thickness of the finished hull to $2.300 \leq t \leq 2.700$ inches.

3. Increase the tolerance on the chord length between nonadjacent pentagon tips to $32.970 \leq K \leq 33.030$ inches.

4. Increase the minimum tensile strength requirement of the joint from 4,000 psi to 5,000 psi.

5. Increase the tolerance on the thickness of the acrylic plastic discs prior to forming to $2.350 \leq t \leq 2.650$ inches.

REFERENCES

1. A. Piccard. Earth, sky and sea. New York, Oxford University Press, 1956.

2. H. A. Perry. "The argument for glass submersibles," UnderSea Technology, vol. 5, no. 9, Sept. 1964, pp. 31-35.

3. J. G. Moldenhauer, et al. "The design, fabrication and testing of acrylic pressure hulls for manned vehicles," paper presented at American Society of Mechanical Engineers, Winter Annual meeting, Chicago, Ill., Nov. 7-11, 1965. (ASME paper 65-WA/Unt-10).

4. Rohm and Haas Company. Plexiglas handbook for aircraft engineers, 2d ed. Philadelphia, Pa., 1952.

5. Armed Forces Supply Support Center. Military Handbook MIL-HDBK-17 Plastics for flight vehicles, pt. 2. Transparent glazing materials. Washington, D. C., 1961.

6. Pennsylvania State University. Ordnance Research Laboratory. Report no. NOrd 16597-91. General instability of circumferentially stiffened sandwich shells subjected to uniform external pressure, by J. D. Stachiw. University Park, Pa., Dec. 1962. (Contract NOrd 16597)

7. ———. ———. Report no. NOrd 16597-97: The effects of shell joints and bonding on the stability of acrylic resin cellular shells, by J. D. Stachiw. University Park, Pa., Sept. 1964. (Contract NOrd 16597)

8. J. D Stachiw. "The influence of joint strength and its location between cellular sandwich shell facings," Journal of Ocean Technology, vol. 2, no. 4, Oct. 1968, pp. 132-138.

9. J. D. Stachiw. "New approach to the assembly of cylindrical hulls from shell sections," Journal of Ocean Technology, vol. 2, no. 1, Dec. 1967, pp. 50-52.

10 Pennsylvania State University. Ordnance Research Laboratory. Report no. NOw 63-0209-C-2 Solid glass and ceramic external-pressure vessels, by J. D. Stachiw. University Park, Pa., Jan. 1964. (Contract NOw 63-0209-C)

11. David Taylor Model Basin. Report 1741. Tests of stiffened and unstiffened machined spherical shells under external hydrostatic pressure, by M. A. Krenzke and T J. Kiernan. Washington, D. C., Aug. 1963 (AD 422297)

12. ———. Report 1757 The effect of initial imperfections on the collapse strength of deep spherical shells, by M. A. Krenzke and T. J. Kiernan. Washington, D. C., Feb. 1965. (AD 612100)

13.————. Report 1759: The elastic buckling strength of spherical glass shells, by M. A. Krenzke and R. M. Charles. Washington, D. C., Sept. 1963. (AD 423588)

14.————. Report 1713: The elastic buckling strength of near-perfect deep spherical shells with ideal boundaries, by M. A. Krenzke. Washington, D. C., July 1963. (AD 416057)

15. J. W. Mavor. "Observation windows of the deep submersible ALVIN," Journal of Ocean Technology, vol. 1, no. 1, June 27, 1966, pp. 2-16.

16. Naval Civil Engineering Laboratory. Technical Report R-512: Windows for external or internal hydrostatic pressure vessels, pt. 1. Conical acrylic windows under short-term pressure application, by J. D. Stachiw and K. O. Gray. Port Hueneme, Calif., Jan. 1967. (AD 646882)

17.————. Technical Report R-527: Windows for external or internal hydrostatic pressure vessels, pt. 2. Flat acrylic windows under short-term pressure application, by J. D. Stachiw, G. M. Dunn, and K. O. Gray. Port Hueneme, Calif., May 1967. (AD 652343)

18.————. Technical Report R-631: Windows for external or internal hydrostatic pressure vessels, pt. 3. Critical pressure of acrylic spherical windows under short-term pressure applications, by J. D. Stachiw and F. W. Brier. Port Hueneme, Calif., June 1969. (AD 689789)

19. Naval Air Engineering Center. Aeronautical Materials Laboratory. Report no. NAEC-AML-2350. Oceanographic effects on plastic engineering materials, by H. J. Lee. Philadelphia, Pa., Jan. 1966. (AD 481419)

20.————. ————. Report no. NAEC-AML-2260: Oceanographic effects on plastic engineering materials (Part A) and elastomeric engineering materials (Part B), by H. J. Lee and E. J. Colacicco. Philadelphia, Pa., Jan. 1966 (AD 481377)

21 Southwest Research Institute. Final report on Contract N00123-67-C-2123 NEMO stress analysis and material investigation, by R. C. DeHart, T. Wah, and L. R. Calcote San Antonio, Tex., Mar. 1968. (SwRI Project no 03-2159)

22. Naval Civil Engineering Laboratory. Technical Note. The spherical acrylic pressure hull for hydrospace application, part II—experimental stress evaluation of prototype NEMO capsule, by J. D Stachiw and K. Mack Port Hueneme, Calif. (To be published.)

UNCLASSIFIED

Security Classification

DOCUMENT CONTROL DATA - R & D

Security classification of title, body of abstract and indexing annotation must be entered when the overall report is classified)

1 ORIGINATING ACTIVITY (Corporate author) Naval Civil Engineering Laboratory Port Hueneme, California 93041	2a. REPORT SECURITY CLASSIFICATION UNCLASSIFIED 2b. GROUP

3 REPORT TITLE

THE SPHERICAL ACRYLIC PRESSURE HULL FOR HYDROSPACE APPLICATION; PART II - EXPERIMENTAL STRESS EVALUATION OF PROTOTYPE NEMO CAPSULE

4 DESCRIPTIVE NOTES (Type of report and inclusive dates)

5 AUTHOR(S) (First name, middle initial, last name)

J. D. Stachiw and K. L. Mack

6 REPORT DATE October 1970	7a. TOTAL NO OF PAGES 66	7b NO OF REFS 3
8a CONTRACT OR GRANT NO	9a. ORIGINATOR'S REPORT NUMBER(S)	
b PROJECT NO YF 38.535.005.01.006	TN-1113	
c.	9b OTHER REPORT NO(S) (Any other numbers that may be assigned this report)	
d		

10 DISTRIBUTION STATEMENT

This document has been approved for public relase and sale; it's distribution is unlimited.

11 SUPPLEMENTARY NOTES	12 SPONSORING MILITARY ACTIVITY Naval Facilities Engineering Command

13 ABSTRACT

The prototype 66-inch diameter spherical hull of NEMO* with 2.5 inch wall thickness has been subjected to a series of hydrostatic tests under simulated hydrospace environment to determine its structural integrity. After repeated long term and cyclic tests in the 220 to 2400 foot depth range, the hull was tested to implosion at 4150 feet. The magnitude of strains measured on the hull during cyclic and long term loadings, as well as the short term implosion depth of 4150 feet indicate that the hull satisfies the 1000 foot design depth requirement and can be without any further tests incorporated into any man-rated system approved for operation in the 0 to 600 foot depth range.

* Naval Experimental Manned Observatory

DD FORM 1 NOV 65 1473 (PAGE 1)

S/N 0101-807-6801

UNCLASSIFIED

Security Classification

14 KEY WORDS	LINK A		LINK B		LINK C	
	ROLE	WT	ROLE	WT	ROLE	WT
Acrylic Resins						
Spheres						
Pressure vessels						
Deep water						
Underwater structures						
Hydrostatic pressure						
Failure						
Bucking						
Implosions						

Naval Civil Engineering Laboratory
DEVELOPMENT OF A SPHERICAL ACRYLIC PLASTIC PRESSURE HULL FOR HYDROSPACE APPLICATION (Final), by J. D. Stachiw
TR-676 217 p. illus April 1970 Unclassified

1. Pressure hull—Acrylic plastic sphere I. YF 38 535 005.01.006

A spherical, acrylic plastic capsule has been designed for protection of man against the external hydrostatic pressure present at continental shelf depths. Experimental and analytical studies have been conducted to evaluate the performance of both the spherical capsule design and the acrylic plastic construction material at continental shelf depths. Results from testing twenty-two 15-inch-outside diameter models and a large-scale prototype under short term, cyclic, and long-term hydrostatic pressure indicate that the design and material chosen meet the requirements for safe operation at continental shelf depths. A prototype 66-inch-OD capsule of 2.5-inch wall thickness, and 4,000-pound positive buoyancy in seawater has been specifically developed for the NEMO (Naval Experimental Manned Observatory) system. The NEMO prototype capsule successfully withstood 105 simulated dives ranging from 250 to 2,400 feet prior to being tested to implosion at a simulated depth of 4,150 feet. Until more experimental data are generated on the fatigue life of the full scale NEMO capsule under different pressure loadings, the capsule is considered to be safe for manned operation only to the 600-foot depth.

Naval Civil Engineering Laboratory
DEVELOPMENT OF A SPHERICAL ACRYLIC PLASTIC PRESSURE HULL FOR HYDROSPACE APPLICATION (Final), by J. D. Stachiw
TR-676 217 p. illus April 1970 Unclassified

1. Pressure hull—Acrylic plastic sphere I. YF 38 535 005 01.006

A spherical, acrylic plastic capsule has been designed for protection of man against the external hydrostatic pressure present at continental shelf depths. Experimental and analytical studies have been conducted to evaluate the performance of both the spherical capsule design and the acrylic plastic construction material at continental shelf depths. Results from testing twenty-two 15-inch-outside diameter models and a large-scale prototype under short term, cyclic, and long-term hydrostatic pressure indicate that the design and material chosen meet the requirements for safe operation at continental shelf depths. A prototype 66-inch-OD capsule of 2.5-inch wall thickness, and 4,000-pound positive buoyancy in seawater has been specifically developed for the NEMO (Naval Experimental Manned Observatory) system. The NEMO prototype capsule successfully withstood 105 simulated dives ranging from 250 to 2,400 feet prior to being tested to implosion at a simulated depth of 4,150 feet. Until more experimental data are generated on the fatigue life of the full scale NEMO capsule under different pressure loadings, the capsule is considered to be safe for manned operation only to the 600-foot depth.

Naval Civil Engineering Laboratory
DEVELOPMENT OF A SPHERICAL ACRYLIC PLASTIC PRESSURE HULL FOR HYDROSPACE APPLICATION (Final), by J D. Stachiw
TR-676 217 p. illus April 1970 Unclassified

1. Pressure hull—Acrylic plastic sphere I. YF 38 535.005 01.006

A spherical, acrylic plastic capsule has been designed for protection of man against the external hydrostatic pressure present at continental shelf depths Experimental and analytical studies have been conducted to evaluate the performance of both the spherical capsule design and the acrylic plastic construction material at continental shelf depths. Results from testing twenty-two 15-inch-outside diameter models and a large-scale prototype under short-term, cyclic, and long-term hydrostatic pressure indicate that the design and material chosen meet the requirements for safe operation at continental shelf depths A prototype 66-inch-OD capsule of 2.5-inch wall thickness, and 4,000-pound positive buoyancy in seawater has been specifically developed for the NEMO (Naval Experimental Manned Observatory) system The NEMO prototype capsule successfully withstood 105 simulated dives ranging from 250 to 2,400 feet prior to being tested to implosion at a simulated depth of 4,150 feet Until more experimental data are generated on the fatigue life of the full scale NEMO capsule under different pressure loadings, the capsule is considered to be safe for manned operation only to the 600-foot depth.

Naval Civil Engineering Laboratory
DEVELOPMENT OF A SPHERICAL ACRYLIC PLASTIC PRESSURE HULL FOR HYDROSPACE APPLICATION (Final), by J. D. Stachiw
TR-676 217 p illus April 1970 Unclassified

1. Pressure hull—Acrylic plastic sphere I. YF 38 535 005 01 006

A spherical, acrylic plastic capsule has been designed for protection of man against the external hydrostatic pressure present at continental shelf depths. Experimental and analytical studies have been conducted to evaluate the performance of both the spherical capsule design and the acrylic plastic construction material at continental shelf depths. Results from testing twenty-two 15-inch-outside diameter models and a large-scale prototype under short term, cyclic, and long term hydrostatic pressure indicate that the design and material chosen meet the requirements for safe operation at continental shelf depths. A prototype 66-inch OD capsule of 2 5-inch wall thickness, and 4,000-pound positive buoyancy in seawater has been specifically developed for the NEMO (Naval Experimental Manned Observatory) system The NEMO prototype capsule successfully withstood 105 simulated dives ranging from 250 to 2,400 feet prior to being tested to implosion at a simulated depth of 4,150 feet Until more experimental data are generated on the fatigue life of the full scale NEMO capsule under different pressure loadings, the capsule is considered to be safe for manned operation only to the 600-foot depth.

Unclassified

Security Classification

DOCUMENT CONTROL DATA - R & D

(Security classification of title, body of abstract and indexing annotation must be entered when the overall report is classified)

1 ORIGINATING ACTIVITY (Corporate author) Naval Civil Engineering Laboratory Port Hueneme, California 93041	2a. REPORT SECURITY CLASSIFICATION Unclassified 2b GROUP

3 REPORT TITLE

DEVELOPMENT OF A SPHERICAL ACRYLIC PLASTIC PRESSURE HULL FOR HYDROSPACE APPLICATION

4 DESCRIPTIVE NOTES (Type of report and inclusive dates)

Final; October 1964—October 1969

5 AUTHOR(S) (First name, middle initial, last name)

J. D. Stachiw

6 REPORT DATE April 1970	7a TOTAL NO OF PAGES 217	7b NO OF REFS 22
8a CONTRACT OR GRANT NO	9a ORIGINATOR'S REPORT NUMBER(S) TR-676	
b PROJECT NO YF 38.535.005.006	9b OTHER REPORT NO(S) (Any other numbers that may be assigned this report)	
c		
d		

10 DISTRIBUTION STATEMENT

This document has been approved for public release and sale; its distribution is unlimited.

11 SUPPLEMENTARY NOTES	12 SPONSORING MILITARY ACTIVITY Naval Facilities Engineering Command Washington, D. C.

13 ABSTRACT

A spherical, acrylic plastic capsule has been designed for protection of man against the external hydrostatic pressure present at continental shelf depths. Experimental and analytical studies have been conducted to evaluate the performance of both the spherical capsule design and the acrylic plastic construction material at continental shelf depths. Results from testing twenty-two 15-inch-outside diameter models and a large-scale prototype under short-term, cyclic, and long-term hydrostatic pressure indicate that the design and material chosen meet the requirements for safe operation at continental shelf depths. A prototype 66-inch-OD capsule of 2.5-inch wall thickness, and 4,000-pound positive buoyancy in seawater has been specifically developed for the NEMO (Naval Experimental Manned Observatory) system. The NEMO prototype capsule successfully withstood 105 simulated dives ranging from 250 to 2,400 feet prior to being tested to implosion at a simulated depth of 4,150 feet. Until more experimental data are generated on the fatigue life of the full scale NEMO capsule under different pressure loadings, the capsule is considered to be safe for manned operation only to the 600-foot depth.

DD FORM 1 NOV 65 1473 (PAGE 1)

S/N 0101-807-6801

Unclassified

Security Classification

14 KEY WORDS	LINK A		LINK B		LINK C	
	ROLE	WT	ROLE	WT	ROLE	WT
Ocean pressure hulls						
Spherical hulls						
Acrylic plastic hull material						
66-inch-OD prototype						
15-inch model sphere						
Spherical pentagon modules						
Bonding methods						
Metal penetrations						
Metal hatches						
Restraint systems						
Pressure vessel testing						
Photoelastic analysis						
Panoramic visibility						
Submersibles						

Technical Note N- 1113

THE SPHERICAL ACRYLIC PRESSURE HULL FOR HYDROSPACE APPLICATION; PART II - EXPERIMENTAL STRESS EVALUATION OF PROTOTYPE NEMO CAPSULE

By

J. D. Stachiw and K. L. Mack

October 1970

NAVAL CIVIL ENGINEERING LABORATORY
Port Hueneme, California 93041

THE SPHERICAL ACRYLIC PRESSURE HULL FOR HYDROSPACE APPLICATION; PART II
EXPERIMENTAL STRESS EVALUATION OF PROTOTYPE NEMO CAPSULE

Technical Note N- 1113

YF 38.535.005.01.006

by

J. D. Stachiw and K. L. Mack

ABSTRACT

The prototype 66-inch diameter spherical hull of NEMO* with 2.5 inch wall thickness has been subjected to a series of hydrostatic tests under simulated hydrospace environment to determine its structural integrity. After repeated long term and cyclic tests in the 220 to 2400 foot depth range, the hull was tested to implosion at 4150 feet. The magnitude of strains measured on the hull during cyclic and long term loadings, as well as the short term implosion depth of 4150 feet indicate that the hull satisfies the 1000 foot design depth requirement and can be without any further tests incorporated into any man-rated system approved for operation in the 0 to 600 foot depth range.

* Naval Experimental Manned Observatory

INTRODUCTION

A spherical acrylic plastic capsule (Figure 1) has been developed[1] to serve as a pressure resistant hull in a manned observatory (Figure 2) for conducting underwater research and exploration along the continental shelf. The 66-inch external diameter spherical hull of the observatory was fabricated using twelve identical regular spherical pentagons of 2½ inch thick acrylic plastic, bonded together with an acrylic cement. The individual spherical pentagons were thermo-formed in an oven from flat commercial stock using a circular vacuum mold having the required spherical curvature, then machined to their proper shape and dimension, and, finally, annealed prior to assembly and bonding. Two openings of identical diameter were provided at opposite poles of the sphere. To allow entry to and exit from the interior of the sphere, a stainless steel hatch was inserted into the top opening of the sphere (Figure 3). A stainless steel plate mounted in the same manner as the hatch and 180° from it allows penetrations to be made into the hull to accomodate electrical and hydraulic connections.

One of the subjects to be investigated in the development of the capsule was the structural adequacy of the hull when subjected to water pressure and an upward buoyancy force resulting from its submergence to continental shelf depths. To this end, two studies were undertaken, one being a theoretical stress analysis[2] and the other being an experimental stress analysis. This report is concerned with the experimental stress analysis study of the prototype. The theoretical stress analysis and the comparison of experimental to theoretical stress values are discussed in a separate report.[3]

TESTING PROCEDURE

The hydrostatic pressure on the hull exterior due to its being lowered to various depths in the sea was simulated in the Laboratory's 72-inch diameter pressure vessel using seawater compressed by an electric motor-driven positive displacement pump. Prior to being placed in the pressure vessel, the hull was mounted inside a cage (Figure 4) on a support pedestal using brackets attached to the bottom steel plate (Figure 5). The cage offered protection to the test specimen during handling in and out of the pressure vessel. The support pedestal served not only to support the hull wnen it rested on deck but also served as an anchor to resist the 4,000 pound upward acting buoyancy force created by the hull's displacement in water.

The hydrostatic test program, which took approximately fifty days to complete, was divided into six phases (Table 1), each phase

following the other in consecutive order. All phases of the test were completed before the prototype acrylic plastic capsule was tested to implosion inside the pressure vessel. The first five test phases that underlie the experimental stress analysis are:

Phase I consisted of a series of eight tests performed in uninterrupted sequence with the hull in the vessel. For the first test, hydrostatic pressure was applied at the rate of 100 psi/min until 100 psi pressure was reached, stopping at every 50 psi interval to take strain readings. Approximately 90 seconds were required for strain recording and balancing unit to record in digital form - 87 channels of strain data. Upon reaching 100 psi, the pressure was held constant for 24 hours. During the first hour, strain and pressure readings were taken every ten minutes. Thereafter, strain and pressure readings were taken only hourly for the remaining 23 hours. The pressure was then dropped to 0 psi at a rate of 100 psi/min. During the depressurizing cycle, pressure and strain readings were taken at 50 psi intervals. When 0 psi was reached, strain gage readings were taken every ten minutes during the first hour that the pressure was zero, and, then, hourly until strain relaxation ceased. This was considered to have occurred when the strain rate decreased to a value of 50 micro inches/inch or less in a 12 hour period. For the succeeding seven tests, the hull was successively subjected to maximum pressures of 200, 300, 400, 500, 600, 700 and 800 psi, repeating the above noted procedure used for the 100 psi maximum pressure test.

Phase II of the testing program was made up of a series of five identical tests, each test following the other in a fixed sequence. Hydrostatic pressure was applied to the exterior of the hull at a rate of 100 psi/min until a pressure of 500 psi was reached. Pressurization was stopped momentarily at each 100 psi level at which time strain gage readings were taken. Once the 500 psi level was reached, the pressure was held constant for a period of 6 hours during which strain gage readings were taken every 10 minutes during the first hour and every hour for the remaining 5 hours. The pressure was then dropped to 0 psi at a rate of 100 psi/min. The depressurization was stopped momentarily at each 100 psi interval to allow strain gage readings to be taken. Once 0 psi was reached, strain gage readings were taken every 10 minutes during the first hour and then hourly for the period of 18 hours. At the end of the 18 hour period, the test cycle was repeated. After the fifth test cycle was completed, the hull was allowed to relax in the vessel for about 3 days before Phase III of the test program was begun.

Phase III of the test program consisted of a series of consecutively-run pressure cycles. All five cycles of Phase III test series were completed in one day. During each cycle the hull was pressurized to 500 psi at a 100 psi/minute rate. At 100 psi intervals the pressurization

Table 1. SUMMARY OF TESTS FOR EXPERIMENTAL STRESS EVALUATION

Pressure Range psi	Test Designation	Duration of Loading	Duration of Relaxation
Phase I			
0-100	I-1	24 hours	70 hours
0-200	I-2	24	72
0-300	I-3	24	44
0-400	I-4	24	45
0-500	I-5	24	96
0-600	I-6	24	188
0-700	I-7	24	144
0-800	I-8	24	275
Phase II			
0-500	II-1	6	18
0-500	II-2	6	18
0-500	II-3	6	18
0-500	II-4	6	18
0-500	II-5	6	66*
Phase III			
0-500	III-1	1	1
0-500	III-2	1	1
0-500	III-3	1	1
0-500	III-4	1	1
0-500	III-5	1	1
			60*
Phase IV			
0-500	IV-1	15 min.	15 min.
0-500	IV-2	15	15
0-500	IV-3	15	15
0-500	IV-4	15	15
0-500	IV-5	15	15
0-500	IV-6	15	15
0-500	IV-7	15	64*

Table 1. (cont'd)

Pressure Range psi	Test Designation	Duration of Loading	Duration of Relaxation
Phase V			
0-500	V-1	2	2
0-500	V-2	2	2
0-500	V-3	2	2
0-500	V-4	2	2
0-500	V-5	2	2
0-500	V-6	2	2
0-500	V-7	2	2
0-500	V-8	2	2
0-500	V-9	2	2
0-500	V-10	2	2
0-500	V-11	2	2
0-500	V-12	2	2

* Time elapsed from the end of one phase to the beginning of the next phase, hours.

was stopped and strain gage readings were taken. The pressure was held constant at 500 psi for one hour. Strain gage readings were taken every 10 minutes. The pressure was then dropped to 0 psi at 100 psi/min. Depressurization was interrupted and strain gage readings were taken at 100 psi intervals. The relaxation period lasted one hour at which time strain gage readings were taken every 10 minutes.

This procedure was repeated until all 5 cycles had been completed. A period of 60 hours was allowed to elapse after completion of the Phase III test before the Phase IV series of tests were begun.

Phase IV of the test program was accomplished with seven identical consecutively-run tests and took approximately one day to complete. Again, the exterior of the hull was pressurized from 0 psi to 500 psi at a rate of 100 psi/min. As in previous phases, strain gage readings were taken at each 100 psi interval. The pressure was held constant at 500 psi for a period of 15 minutes, with strain gage readings being taken every 5 minutes. The pressure was then released and allowed to return to 0 psi, with strain gage readings being taken at each 100 psi level as before. Zero pressure was maintained for 15 minutes during which time strain gage readings were taken every 5 minutes prior to beginning the next identical test cycle. After the series of seven test cycles were completed, the hull was then allowed to relax in the closed vessel at atmospheric pressure for 64 hours before commencing Phase V of the test program.

Phase V consisted of twelve identical consecutively-run tests which took approximately one day to complete. Hydrostatic pressure was applied to the exterior of the hull at a rate of 100 psi/min until a pressure of 500 psi was reached. Pressurization was stopped momentarily at each 100 psi level to allow strain gage readings to be taken. The 500 psi pressure was held approximately 2 minutes. After strain gage readings were made the pressure was dropped to 0 psi at a rate of 100 psi/min. At each 100 psi drop in pressure, the pressure was held constant to allow strain gage readings to be taken. Upon reaching 0 psi the hull was permitted to relax for 2 minutes during which strain readings were taken. After 2 minutes of relaxation, the next cycle was begun. After completion of 12 cylces the hull was allowed to relax at psi pressure for 48 hours with strain gage readings being taken hourly.

After completion of the five test phases, the hull was removed from the pressure vessel, the strain gage leads were retraced to confirm their locations, and the hull examined for cracks, joint irregularities, and inclusions. Before and during all phases of the test, the interior of the hull was vented to the atmosphere, and the temperature inside and outside the pressure vessel as well as that inside and outside of the hull was stabilized to and maintained between 68°F and 70°F.

Phase VI. After extensive inspection of the hull, it was subjected to many other hydrostatic tests (Table 2). Since no strain readings were taken during Phase VI tests, they are not discussed in this report. (For detailed discussion of these tests see Reference 1). Only the last test during which the hull was pressurized to implosion is discussed in this report as it substantiates some of the findings made solely on the basis of experimental stress analysis.

INSTRUMENTATION

The hull was instrumented using SR-4, type FAER-50D-12S13L, strain gages attached to the surfaces of the hull with epoxy Epy-150. Budd's Gagecoat #2 and #5 were used to waterproof the gages. Three strain gages wired independently and placed in the configuration of a wye constituted a rosette. A total of 29 rosettes were used to instrument the hull (Figure 6), giving a total of 87 channels of readout. Seven rosettes were placed on the bottom stainless steel plate, four being placed on the interior surface and three being placed on the exterior surface (Figure 7). A total of 22 rosettes were placed on the acrylic plastic portion of the hull, eight being located on the interior surface and fourteen on the exterior surface of the hull. Most of the rosettes placed on the exterior surface of the hull had a corresponding rosette oppositely placed on the interior surface (Figure 8). In order to have a common base of reference so that a comparison may be made in the future between the theoretical analysis and experimental results, all of the rosettes were mounted along the same meridian line at points whose relative position with respect to the polar axis of the capsule was recorded in degrees of latitude. One of the legs of the wye making up a rosette was always placed on this meridian line, and the individual strain gage readings at any particular rosette location were always taken in the same given order and referenced to this meridian mounted strain gage to insure proper interpretation of the strain gage readings. The rosettes were numbered beginning with number one at the bottom stainless steel plate (Figure 9) and extended through number eighteen near the top of the hull. As a further identification as to location, rosettes mounted on the exterior surface of the hull were assigned the letter A following their number while those rosettes mounted on the interior surface of the hull have the letter B following their number. The thickness and sphericity of the hull at each rosette and the location of each rosette with respect to a joint were also recorded to aid in subsequent reduction of strain data (Figure 10).

Leads from a thermocouple and the strain gages mounted inside the hull were led to watertight bulkhead connectors which screwed into threaded holes provided for that purpose in the bottom stainless steel plate. After passing through the bottom stainless steel plate (Figure 11), these leads together with those from the exterior gages and a thermocouple inside the pressure vessel were connected to a penetrator assembly in the pressure vessel's head (Figure 12) which allowed passage

Table 2. MISCELLANEOUS TESTS CONDUCTED ON NEMO
AFTER CONCLUSION OF EXPERIMENTAL STRESS ANALYSIS TESTS

Number of Tests	Maximum Pressure (psi)	Duration of Sustained Loading	Temperature (°F)	Damage Observed
1	250	6 hours	68 - 70°F	None
1	500	6 hours	68 - 70°F	None
1	750	6 hours	68 - 70°F	None
1	500	4 hours	38°F	None
1	600	7 hours	36°F	None
1	700	5.5 hours	43°F	None
1	750	8 hours	42°F	None
1	850	8 hours	41°F	None
20	500	4 hrs. per test	32 - 75	None
15	550	1 hr. per test	32 - 40	None
13	550	0.5 hr. per test	32 - 40	None
11	500	1 minute per test	32 - 40	None
1	1070	10 minutes	34	None
1	1850	None	70	Gen. Implosion

of the leads out of the pressure vessel to a 90 channel multiple digital strain indicator and digital temperature indicators (Figure 13).

To monitor leakage of water into the interior of the hull, a 0.250 inch diameter copper tube was inserted through the bottom stainless steel plate flush with the plate's inside surface and sealed against water pressure with an epoxy compound. The tube was connected to a fitting in the vessel head penetrator assembly from where it was connected to an empty graduate. Since the graduate was open to the atmosphere, the atmospheric pressure prevailed at all times in the interior of the acrylic plastic hull. Only once a day when the hull was under pressure, air at a pressure of about 10 psi was introduced into the tube and, consequently, into the interior of the hull. The air pressure was held momentarily after which it was released. The pressurized air was then allowed to escape from the interior of the hull through the tube. The air ejected any water accumulated in the hull ahead of it. Any water forced out of the hull was collected in a graduate and its amount recorded. The amount of water leakage averaged about 5 quarts per day and was caused by an improperly molded plastic penetrator located in the bottom stainless steel plate. The faulty penetrator was not replaced during the testing program as the penetrator would also require the replacement of the custom made cable whose procurement time was approximately 6 months. There was no evidence of leakage from any other source.

Periodically the NEMO capsule was removed from the pressure vessel and inspected for any indications of damage like local yielding or cracking of hull material. Some selected locations on the hull were also photographed each time for later reference.

REDUCTION OF DATA

For any combination of stresses at a point in a stressed body, three mutually perpendicular planes passing through the point can be found on which only normal stresses exist; the normal stresses on these planes on which there are no shearing stresses are called principal stresses. There exist two types of stress fields when one considers the hollow spherical shape. On the interior surface only two principal stresses are present creating what is called a biaxial stress condition. However, on the exterior surface a state of triaxial stress is found.

Biaxial Principal Stresses

The two dimensional stress field was assumed to consist of normal stresses σ_1, σ_2, at right angles to each other. The third stress, σ_3, is zero since there is no internal or external pressure being exerted at right angles to the plane on which the strains are being measured.

Rosettes in a wye configuration were used to measure the strains on the interior and exterior of the acrylic hull, as mentioned earlier. The strain readings were designated ϵ_a, ϵ_b, and ϵ_c, where ϵ_a was always

oriented along the meridian on the sphere.

The maximum and minimum principal strain were found by using the conventional Mohr circle theory and the three strain gage readings ε_a, ε_b, and ε_c.

$$\varepsilon \begin{matrix} \max \\ \min \end{matrix} = \frac{\varepsilon_a + \varepsilon_b + \varepsilon_c}{3} \pm \sqrt{\left(\varepsilon_a - \frac{\varepsilon_a + \varepsilon_b + \varepsilon_c}{3}\right)^2 + \left(\frac{\varepsilon_b - \varepsilon_c}{\sqrt{3}}\right)^2} \qquad \text{(Eq. 1)}$$

The stresses were calculated using E, the modulus of elasticity, and μ, Poisson's ratio:

$$\sigma_{max} = \frac{E}{1 - \mu^2}\left(\varepsilon_{max} + \mu\varepsilon_{min}\right) \qquad \text{(Eq. 2)}$$

$$\sigma_{min} = \frac{E}{1 - \mu^2}\left(\varepsilon_{min} + \mu\varepsilon_{max}\right) \qquad \text{(Eq. 3)}$$

The angle was measured from the meridional axis to the axis along which the maximum principal strain was oriented.

$$\theta = \frac{1}{2}\tan^{-1}\frac{\frac{1}{\sqrt{3}}\left(\varepsilon_b - \varepsilon_c\right)}{\varepsilon_a - \left(\frac{\varepsilon_a + \varepsilon_b + \varepsilon_c}{3}\right)} \qquad \text{(Eq. 4)}$$

This angle lies in the plane of the sphere's surface.

Triaxial Principal Stresses

On the exterior surface of the sphere the third principal stress, σ_3, is not zero, thereby creating a triaxial stress condition. The stress, σ_3, represents the hydrostatic pressure being applied to the hull. This stress generates a radial strain, but its magnitude cannot be measured on the sphere's surface by conventional strain gages as they lie in a plane at right angle to the radial strain. Although the magnitude of the radial strain cannot be measured, the magnitude of the stress causing the radial strain is known, as it is numerically equal to the external hydrostatic pressure. Thus, it is possible to calculate the magnitude of the three principal stresses if the two principal strains on the external surface of the sphere and the radial stress are known.

Using the system of three equations that describe the relationship between three principal stresses in the three dimensional stress field

$$\sigma_1 = \frac{E}{(1+\mu)(1-2\mu)} \left[(1-\mu)\,\varepsilon_{max} + \mu\,(\varepsilon_{min} + \varepsilon_3)\right] \qquad \text{(Eq. 5)}$$

$$\sigma_2 = \frac{E}{(1+\mu)(1-2\mu)} \left[(1-\mu)\,\varepsilon_{min} + \mu\,(\varepsilon_{max} + \varepsilon_3)\right] \qquad \text{(Eq. 6)}$$

$$\sigma_3 = \frac{E}{(1+\mu)(1-2\mu)} \left[(1-\mu)\,\varepsilon_3 + \mu(\varepsilon_{max} + \varepsilon_{min})\right] \qquad \text{(Eq. 7)}$$

and the values of ε_{max} and ε_{min} calculated (Equation 1) from strains measured on the surface of the sphere the values of σ_1, σ_2, and σ_3 have been calculated. In the equations above σ_1 and σ_2 denote principal stresses in the plane of the sphere's external surface, while σ_3 represents the principal stress at right angle to the plane in which σ_1 and σ_2 are acting.

Shear Stresses for Biaxial and Triaxial Loadings

The evaluation of shear stress in the triaxial loading condition was accomplished by using the octahedral shearing stress theory. It is possible by using Mohr's circle to resolve a system of three dimensional stresses into two systems acting on the eight octahedral planes. One system is represented by shearing stresses τ_G, and the other by equal normal stresses σ_G.

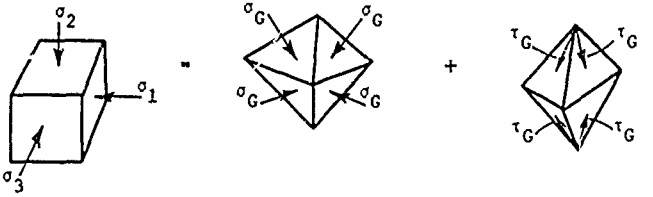

It is postulated that the equal compressive (or tensile) stresses, σ_G, do not initiate yielding of the material but may produce fracture. Therefore, the octahedral shearing stresses are assumed by this theory to be entirely responsible for initiation of yielding in the material. The octahedral shear theory postulates further that yielding at any point in a body under any combination of stresses is initiated only when the octahedral shearing stress τ_G becomes equal to $\sqrt{2}/3\ \sigma_y$, where σ_y is

the tensile or compressive elastic strength of the material as determined by the standard uniaxial test. This value can be found by having a uniaxial stress condition in which $\sigma_2 = \sigma_3 = 0$ (Equation 8). The octahedral shearing stress on each octahedral plane may be expressed:

$$\tau_G = \pm \frac{1}{3} \sqrt{(\sigma_1 - \sigma_2)^2 + (\sigma_2 - \sigma_3)^2 + (\sigma_3 - \sigma_1)^2} \qquad \text{(Eq. 8)}$$

where σ_1, σ_2, and σ_3 are the three principal stresses determined by Equations (5, 6, 7, 8).

The evaluation of shear stress in the biaxial loading condition was accomplished by Mohr's circle. The maximum shear stress was calculated using the Mohr circle:

$$\tau_{max} = \frac{\sigma_1 - \sigma_2}{2} = \frac{\sigma_{max} - \sigma_{min}}{2} \quad \text{where } \sigma_{max} \text{ and } \sigma_{min} \text{ are} \qquad \text{(Eq. 9)}$$

obtained from Equations (2) and (3)

In the calculation of stress values under both the biaxial and triaxial states of stress the modulus of elasticity, E, and Poisson's ratio, μ, were assumed to be 4.5×10^5 psi and 0.35 for the acrylic and 28×10^6 psi and 0.26 for the steel, respectively. The properties of both materials are described at length in Reference 1. It suffices here to state that the yield point of 316 Type stainless steel is in 25,000 - 30,000 psi range while for Plexiglas G acrylic plastic under short-term loading it is 10,000 psi. The strain readings from each rosette were converted to principal strains, principal stresses and octahedral shear stresses by means of an IBM 1620, Model 2 computer.

Since the reduction of all the experimental data into principal stresses and shear stresses would be too voluminous for inclusion into the report and because the validity of some calculated stresses (under long-term creep for example) is doubtful because of necessary simplifications in assumptions underlying the analytical calculations, all experimental data was chosen for reduction to principal strains, but only some for reduction to stresses.

The data that was chosen for reduction to stresses pertained only to short-term loading conditions when NEMO was pressurized repeatedly to 100, 500, and 800 psi sustained pressure levels (Phase I tests Nos. 1, 5, and 8). The reasons for choosing only these test conditions are:

1. Equations (2) through (8) describe accurately only the behavior of isotropic materials in the linear range of elastic deformations. Since the deformation of acrylic plastic can be postulated to represent that of an isotropic material in the linear portion of the elastic strain range only under short-term loading at stress levels less than 8000 psi

calculations of stresses in NEMO under short-term hydrostatic loading can be considered reasonably accurate. The visco-elastic and visco-plastic behavior of the material with the associated time dependent change of modulus of elasticity and Poisson's ratio makes the calculation of stresses in NEMO under long-term loading a very complex operation beyond the scope of this report.

2. The 100, 500, and 800 psi short-term loadings were chosen for calculation of stresses because they represent the minimum, proof and 200% overload test conditions. During the pressurization to the 100 psi pressure level, the lowest sustained pressure loading to which NEMO was subjected, the distribution of stresses (Figures 14a, 15a, 15b, 16a, and 16b) is probably indicative of the true elastic conditions as the stress levels are so low that virtually no visco-elastic or visco-plastic deformations could have been present. The stresses, on the other hand, found during the loading to the 500 psi pressure level are of interest (Figures 14b, 15a, 15b, 17a and 17b) as a comparison between them and those generated by the test to the 100 psi pressure level will clearly show whether any serious yielding of the NEMO hull took place when it was subjected to the proof test. Finally, the stresses recorded during the loading to 800 psi level are important (Figures 14c, 15a, 15b, 18a-20d) because they should show some occurrence of yielding in the steel hatches, or the acrylic plastic material around them at this 200% overload level.

Other data that has been reduced to show only principal strains and is included in this report pertains to (1) sustained loading at 100, 200, 300, 400, 500, 600, 700, and 800 psi pressure levels (Figures 21a-24b),and (2) cyclic loading to 500 psi pressure level (Figures 25-32b). Since inclusion of graphs depicting this data for all of the rosettes would make this report too voluminous, some selectivity was exercised in the presentation of data. For some tests, like the long-term loading to 100, 500 and 800 psi pressure levels principal strains are shown for five rosettes while for the cyclic tests only summaries of the strain distribution and strains from the equatorial rosettes are shown (Figures 25-32).

Although the exclusion of most of the data generated during the hydrostatic testing of the NEMO capsule from this report makes it somewhat less than complete, it was felt that the data selected for inclusion in this report is more than sufficient to support the findings made in the report and that the inclusion of all the generated experimental data would only make the report unwieldly as in most cases the strains generated by the many rosettes in the cyclic and long-term tests were similar, if not identical, and thus most of the data would have been repetitive.

FINDINGS

Short-Term Loading

Acrylic Plastic. The stresses measured on the acrylic plastic hull (Figures 15 and 19) varied from one strain gage rosette to another depending on their location. For all rosettes on the acrylic plastic stresses were higher on the interior of the hull. At the equator of the hull maximum and minimum principal stresses in the plane of the hull's surface were approximately the same. As one progressed, however, from the equatorial rosettes to those located near the polar penetrations in the hull, the difference between maximum and minimum principal stresses in the plane of the hull's surface increased. At the edge of the penetration the highest principal stress was in the meridional direction and its magnitude on the exterior of the hull was approximately the same as the maximum principal stress at the equator, while the least principal stress was in the hoop direction and its magnitude was approximately 45 percent less.

The relationship between the hydrostatic pressure and stresses on the acrylic was linear and approximately the same for the short-term portions of all Phase I tests. This indicates that no yielding of the acrylic occurred under short-term loading at any of the locations where the strain gage rosettes were located even when the NEMO hull was hydrostatically loaded to 800 psi (Figure 19). At 500 psi the maximum principal stress recorded on the external surface in equatorial region was -3008 psi while on the interior it was -3423 psi. No higher stresses than 3423 psi were recorded at any other rosette location on the acrylic hull at 500 psi loading.

It is interesting to note that considerable shifting of principal stress directions occurred during short-term pressurization of the acrylic hull. The magnitude of direction shift varied from rosette to rosette, and from one pressure level to another. The major shifts occurred in the equatorial region while in the vicinity of the polar opening there was almost no change in direction of principal stress axis from one pressure level to another. This indicates that the steel plate presents such a major structural discontinuity with associated well defined stress field in the spherical hull that small changes in acrylic hull deflections are not able to change the orientation of the stress field significantly. This substantiates the findings made previously on 15-inch NEMO models that at the very edge of the penetration in acrylic the meridional stresses are substantially higher than hoop stresses and thus constitute a well defined stress pattern that minor readjustments in hull deflections cannot shift. The presence of major shifts in the principal stress axis orientation on the equatorial region indicates on the other hand that the magnitudes of both meridional and hoop stresses are so well matched that even a minor local change in hull deflections can radically change the direction of principal stress axis. It also shows that because the sphere is made up of 12 non-

identical structural modules the stresses will redistribute themselves in a stepwise manner as each increment in pressure will differently affect each pentagon and the interrelationship between them.

Steel. The stresses measured on steel surfaces of the NEMO hull were considerably higher than on acrylic surfaces. The highest stresses measured at 500 psi were on the interior of the steel plate at rosette locations #4 and #3. The direction of the -26,700 psi maximum principal stress at location #3 was in the meridional direction, while at location #4 the -24,050 psi maximum principal stress was in hoop direction. Although for rosettes #3 and #4 the relationships between hydrostatic pressure and stress were quasi-linear (Figure 20) for each of the individual short-term portions of Phase I hydrostatic tests, they were not identical. Thus, for example, in the Phase I-1 (0 to 100 psi) test the maximum principal stress at rosette #3 at 100 psi hydrostatic pressure was -11,790 psi, in the Phase I-5 (0 to 500 psi) test the same principal stress at 100 psi pressure was -8240 psi, while in the Phase I-8 (0 to 800 psi) test it became at 100 psi pressure -2580 psi. It thus appears that the stress magnitude for a given hydrostatic pressure level like 100 psi at rosette locations #3 and #4 progressively decreased from one hydrostatic test to another. After seven long-term tests the stress magnitude under 100 psi hydrostatic loading at rosette #3 was less than 25 percent of its value measured during the first test.

The reasons for this behavior are many and their inter-relationship not well understood. Three major factors are at work here that cause the stress-strain relationship of the steel bottom plate at locations #3 and #4 to change from one test to another.

Factor A is the change in relative position between the steel plate and the penetration in acrylic. During pressurization, the plate is forced deeper into the opening. Upon depressurization the surface friction between steel and acrylic does not often permit the steel plate to return to its original location in the opening. Because of this, the steel remains under compressive preload whose magnitude increases from test to test by approximately 100 microinches. Since in the calculation of stresses the strain reading at the beginning of each test is taken as the zero datum the determination of residual stresses after each test was not accomplished by comparing stresses from different tests but by comparing the magnitude of residual strains after completion of relaxation periods at the end of all Phase I tests (Figures 21 and 22) with the magnitude of residual strain at the completion of relaxation period following the long-term loading at 100 psi.

Factor B is plastic deformation of the acrylic at the very edge of the penetration. Its magnitude, and the pressure level at which it occurs, has not been accurately determined as no strain gages were located on the acrylic at the very edge of the penetration. Extrapolating the readings taken at rosette #18, the closest one to the edge, indicates that the first permanent set occurred at the edge of the penetration only after the Phase I-4 (0 to 600 psi) test.

Factor C is plastic deformation of the steel plate due to overloading. Analysis of residual strains after each test of Phase I indicates that plastic deformation does probably take place after the Phase I-6 (0 to 600 psi) test (Figure 22).

Shifting of principal stress axis during short-term pressurization of the hull was also observed on the bottom steel plate. No doubt that, in this case, the quality of original fit between the hatch and the acrylic bearing surface was the major contributing factor. From the type of shift observed at rosette 4B (Figure 20d) it would appear that the bottom plate flange contacted the acrylic first at the interior surface of the hull and only later at higher pressure levels the bearing stresses between the steel plate and the acrylic becomes more evenly distributed with the hoop stress becoming the maximum principal stress.

In general, the magnitude of maximum stresses on the bottom steel plate recorded at 500 psi short-term loading indicate that (1) no yielding of the 316 stainless steel plate took place at the 1000 ft design depth, and (2) that failure of the bottom plate will be by plastic buckling with the plastic hinge point located immediately adjacent to the bottom plate flange (Figure 18a).

Long-Term Loading

Acrylic. The long-term loading of NEMO hull showed very clearly that under sustained constant loading an acrylic pressure hull undergoes time dependent deformation which may be elastic or plastic, depending whether upon removal of compressive stresses the hull springs back to its unloaded state, or whether it remains deformed. The rate of time dependent strain increase was found to be a function of applied load as well as time (Figure 23). The time dependent strain rate varied directly with the magnitude of applied load and inversely with duration of loading. These observations, of course, confirm the observations made previously during long-term testing of acrylic windows at NCEL. The significant finding that was made this time, however, was that although the time dependent strain rates at different pressures are quite dissimilar the resultant total strain magnitudes at the termination of the 24-hour long-term loadings appear to be a linear function of pressure for the equatorial region of the spherical hull.

What factors cause this to occur is not known, however, one major factor very well may be the changing magnitude of permanent residual strains remaining in the hull from each preceding long-term test. The magnitudes and character of these permanent strains may just be of the right combination to assure linearity of the relationship between sustained loading level and the magnitude of strains in the equatorial region of the spherical hull. Whether the residual strains indicate in every case compressive plastic deformation of the acrylic material because of the previously applied hydrostatic loading is doubtful. This opinion is based on the fact that the residual strains after completion of Phase I-1, 2 and 3 tests were of tensile in nature while only the succeeding ones were of compressive nature.

The linearity between magnitude of long-term loading and strain magnitude did not exist at the polar penetrations in the acrylic. Although rosette #18A was not at the very edge of the penetration, it registered pronounced deviation from the linear pressure vs. strain relationship during long-term tests at pressures in excess of 600 psi. This would seem to indicate that probably at the acrylic/steel interface permanent deformation does take place during 24-hour long-term loadings in excess of 500 psi.

Steel. The measurements on steel bottom plate failed to detect any time dependent plastic deformation at long-term loadings below 600 psi (Figure 24). This does not mean, however, that the strains remained necessarily constant during the long-term loading. In some of the long-term tests, they increased, in some they decreased, while at still others they remained constant. The variation in response was probably caused by (1) changes in strain magnitude of the acrylic material contacting the steel plate, (2) the amount of relative movement between the steel plate and acrylic bearing surface during the duration of the long-term test, and (3) the residual strains present in the material at the beginning of the particular long-term cycle. From the observation of the magnitude and character of the residual strains at rosettes #3 and #4 (where the largest strains in steel occur) it appears that plastic deformation of the steel probably takes place in long-term tests only if the maximum hydrostatic pressure is in excess of 600 psi.

Cyclic Loading

Acrylic. The reproducibility of strains from one pressure cycle to another one of the same duration was excellent for each one of the rosettes indicating that very little, if any, cumulative gain in plastic strains occurred. This was true regardless of whether the duration of the individual pressure cycle to 500 psi was of 6 hours or 2 minutes, providing the relaxation time between individual cycles was at least as long as the duration of the loading cycle (Figures 25 through 32).

The distribution of strains on the hull changed very little, if any, between cyclic tests of different duration. There was, however, a somewhat perceptible shift in the magnitude as well as the distribution of strains between the initation and termination of an individual pressure cycle. This shift was most noticeable on the rosettes located in the interior of the vessel, but even so, it was of very minor magnitude.

It thus appears that there is not apparent hysteresis, cummulative viscoplastic strain, or cold working in the acrylic hull subjected to cyclic pressure loading, provided that the acrylic hull has not been stressed beyond its viscoelastic yield point during the duration of the individual pressure cycle. Pressure cycling the NEMO hull to 500 psi external hydrostatic pressure with relaxation periods of at least the same duration as the loading cycle did not appear to load the hull past

the viscoelastic yield point at any of rosette locations so long as the duration of the individual loading cycle was equal to, or less than, 6 hours.

Steel. The strains measured on the steel plate did not change significantly from one pressure cycle to another, or from one cycling program to another. It is interesting to note, however, that the magnitude of strains in steel generated during the pressure cycling to 500 psi is noticeably less than the strains generated previously during the first short-term loading to 500 psi (Phase I-5). It is surmised that this has been caused by cold working the steel plate past its yield point, as well as plastically deforming the acrylic plastic hull adjacent to the steel plate during the long-term loading to 800 psi (Phase I-8).

Miscellaneous Loadings

After completing the test Phases I through V the NEMO hull was subjected to an assorted group of miscellaneous tests whose objectives were the determination of (1) displacement change during various kinds of hydrostatic loading, and (2) the rate of heat transfer from the interior of the hull when diving in waters with widely varying ambient temperatures. Since the findings of these tests were thoroughly discussed in another report[1] and since these tests have little bearing on the evaluation of the hull's structural adequacy, they will not be further discussed.

Destructive Testing

The final test in the structural evaluation program of NEMO hull #0 was the short-term implosion testing in which by the observation of fragments and magnitude of loading at which the failure took place some of the postulates formed during previous non-destructive testing could be confirmed or modified.

The implosion that occurred at 1850 psi under 50 psi/minute loading rate was of general, rather than local nature indicating that the ultimate strengths of the acrylic hull and the steel penetration closures were fairly well matched. This finding is supported by the fact that not only was the acrylic hull broken into several orange peel shaped fragments, but also that the metallic chosures were severely dished in (Figure 33). If only the hull had failed, there would not have been any signs of concave dishing in on the initially convex closures as fragmentation of the sphere is incapable of producing such deformations in the metallic end-closures. If on the other hand the metallic end-closures alone had failed, general fragmentation of the hull would not have taken place but just some fracturing and spalling around the edges of the penetration in acrylic.

Since the hull was filled with water, that was vented to atmosphere during the implosion testing, a failed metal plate could not serve as a high-speed projectile that by impacting the interior of the acrylic hull would fracture it into many fragments.

The acrylic fragments resulting from the implosion were in the shape of orange peels with the fracture lines cutting in all cases across bonded joint lines. The ends of fragments that butted previously against the bottom steel plate (Figure 34) were severely spalled indicating serious deformation of the steel bearing surface at the time that the spher imploded. The ends of fragments that butted against the top hatch ring did not show severe spalling but only radial in plane of hull racking (Figure 35). When one observes the deformed steel end-closures of the hull it becomes immediately very clear why only the acrylic bearing surface in contact with the bottom plate showed such e tensive damage while the top one did not.

The deformation of the bottom plate was of such nature (complete reversal of spherical curvature) that the beveled bearing flange rotated (Figure 36) about its line of attachment to the dished head. The rotation of the flange caused it to bear extra hard on the inner half of the acrylic bearing surface while almost completely relieving the bearing stress against the outer half of the acrylic plastic bearing surface. The rotation of the flange was so large that the resulting bearing pressure on the inner half of the acrylic hull caused it to shear off at the bearing surface. The shearing plane formed approximately a 45° angle with the inner surface of the hull.

This was not the case with the upper steel closure. Although the hatch deformed severely like the bottom plate by completely reversing the curvature of the hatch the effect of this buckling process on the acrylic bearing surface was minimal. The reason for this difference is that the hatch ring between the deforming hatch and the acrylic bearing surface formed a rigid barrier which the buckled hatch could not deform. Thus, the acrylic bearing surface in contact with the hatch ring did not experience at any time the uneven bearing pressure that would be exerted by a rotating hatch flange if it was in contact with the acrylic bearing surface without the intervening hatch ring barrier.

The failure mode of the bottom plate also illuminates quite well the strain readings on it during the Phase I tests. The reason that rosette #3B recorded the highest strains on the plate becomes quite obvious. The rosette was mounted at the location where the plastic hinge for the dishing of the plate was located. Since the rosette #3B was on the compression side of the plastic hinge, the compressive flexure strains would be superimposed on the compressive membrane strains in the meridional direction to exceed the strains recorded at rosette 1A and B, 2A and B, and 4B. This is the location where probably yielding also took place first on the bottom plate, and only after formation of the plastic hinge did the plate flange rotate bringing uneven pressure to bear upon the acrylic bearing surface.

Tensile specimens were cut from the acrylic plastic hull fragments to establish the tensile strength of joints after the hull was subjected to the extensive hydrostatic testing program. The tensile strength of the PS-18 bonded joints was found to be in the same range (9220-7350 psi) as the strength of the PS-18 joints in test blocks (8280-5150 psi) tested immediately after fabrication of the NEMO hull #0. This substantiates the claim of the adhesive supplier that long-term submersion in seawater, as well as repeated compressive straining of joints bonded with PS-18, does not decrease its mechanical strength.

No evidence was found of cracks initiating at the many bubbles and discontinuities present in the bonded joints (Figure 37). This substantiates the postulate[1] made at the beginning of the program by the designers of NEMO hull that bubbles and other similar discontinuities in the joints will not act as sources of incipient cracks so long as the bonded joints have not been subjected to (1) tensile stresses, or (2) compressive stresses of such magnitude that plastic deformation of the joint filler material takes place (at approximately 15,000 psi compressive stress). Elimination of the bubbles and discontinuities in the joints is, however, a desirable objective for future NEMO hulls because (1) their presence is unsightly, (2) they may constitute a source of leakage, and (3) they restrict the use of NEMO hulls solely to external pressure loadings.

CONCLUSIONS

The hydrostatic testing program as well as the subsequent experimental stress analysis have conclusively shown that the prototype 66-inch OD x 61-inch ID Plexiglas G plastic NEMO hull #0 bonded with PS-18 adhesive and equipped with 316 Type stainless steel penetration closures has met the design objectives of (1) collapse depth in excess of 3000 feet, (2) design depth of 1000 feet, and (3) operational depth of 600 feet for manned dives.

RECOMMENDATIONS

1. Further experimentation should be conducted on bonding of spherical pentagons to obtain an adhesive system and bonding technique superior to the PS-18 bonding system so that less bubbles and discontinuities are present in the hull joints.

2. For diving operations in excess of 600 feet the Type 316 stainless steel should be replaced in penetration closures with Inconel 625 that has superior corrosion resistance and mechanical strength. If the cost of Inconel 625 end-closures proves to be excessive, SAE 4130 cadmium plated steel may be substituted for it providing the projected life of the system is short.

REFERENCES

1. J. D. Stachiw, "Development of a Spherical Acrylic Plastic Pressure Hull for Hydrospace Application," U. S. Naval Civil Engineering Laboratory, Technical Report R-676, April 1970.

2. R. C. DeHart, "NEMO Stress Analysis and Material Investigation," Technical Report Contract No. N00123-67-C-2123, Southwest Research Institute, San Antonio, Texas, March 1968.

3. H. Ottsen, "The Spherical Acrylic Pressure Hull for Hydrospace Application; Part III - Comparison of Experimental and Analytical Stress Evaluations for Prototype NEMO Capsule" (to be published by NCEL).

Figure 1. Prototype 66-inch OD x 61-inch ID acrylic plastic NEMO capsule.

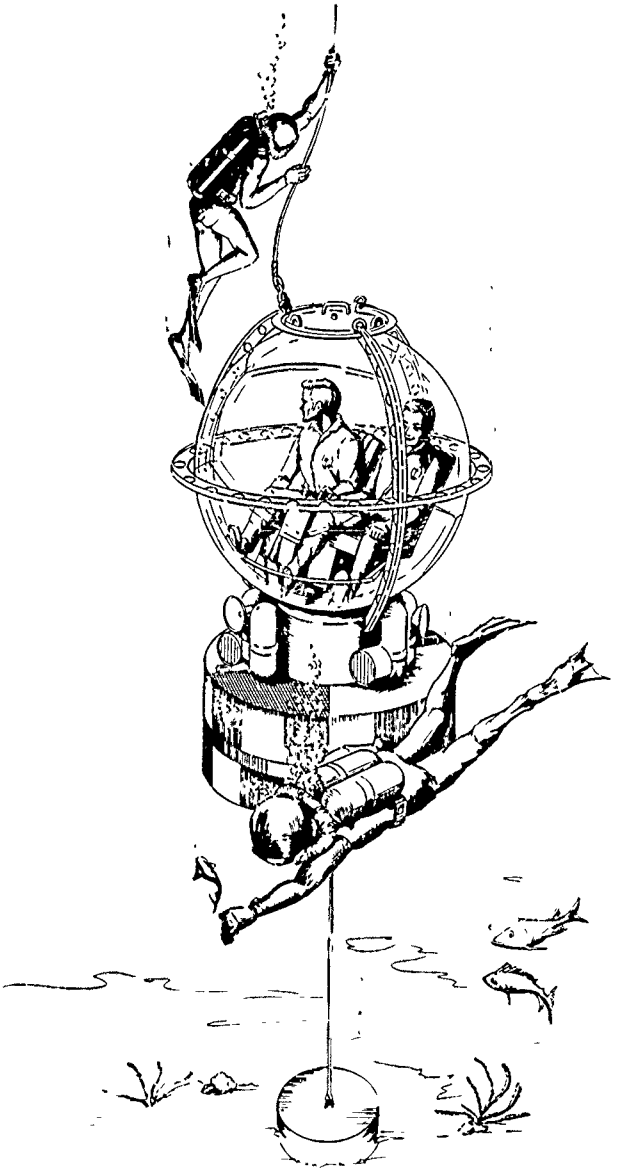

Figure 2. NEMO capsule in tethered self-winching diver control center.

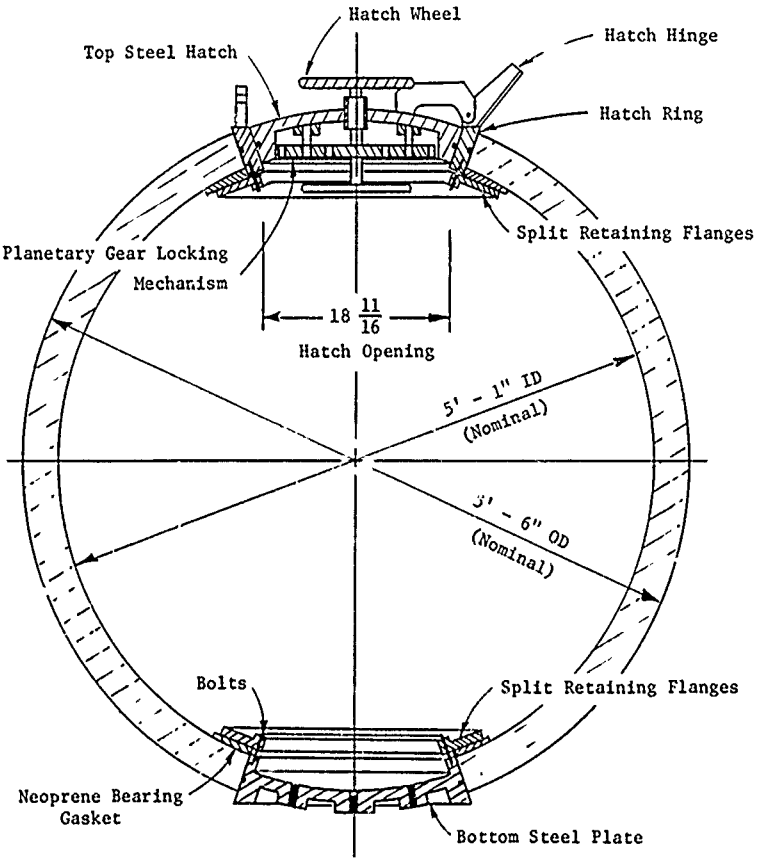

Figure 3. NEMO Hull Cross Section.

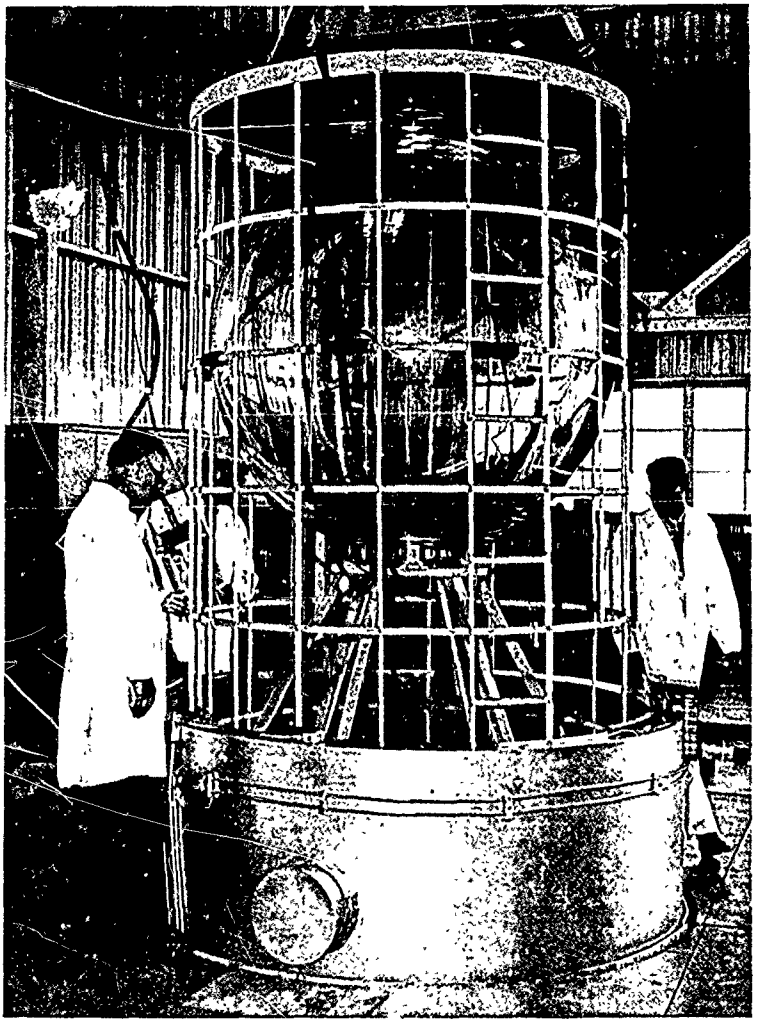

Figure 4. NEMO capsule being lowered into the Deep Ocean Simulation Facility pressure vessel; note the protective cage and support pedestal.

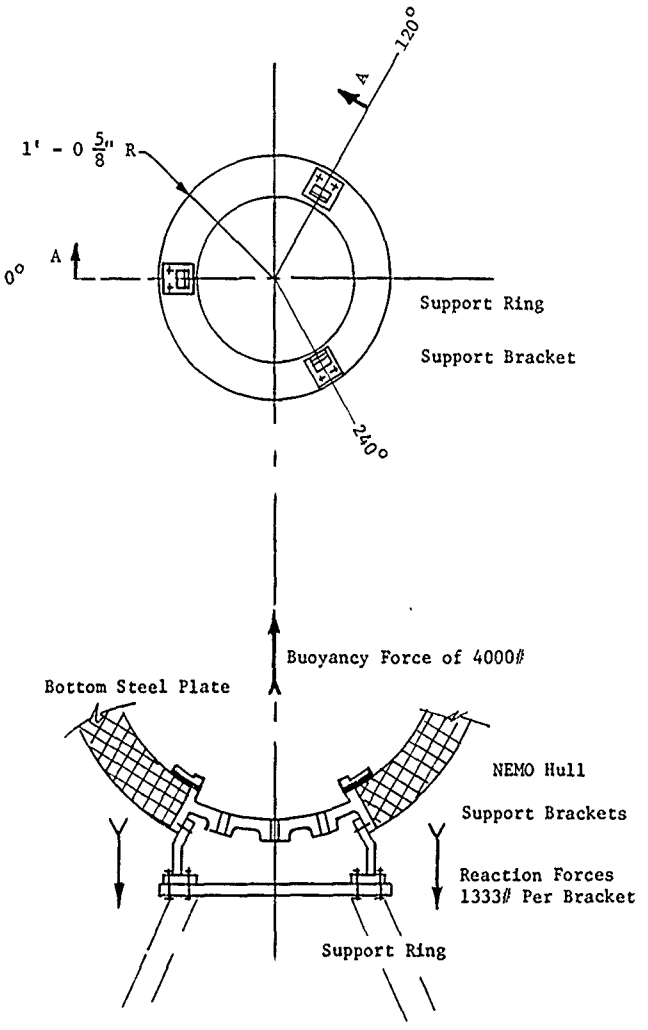

Figure 5. Method of attaching capsule's bottom steel plate to cage support pedestal.

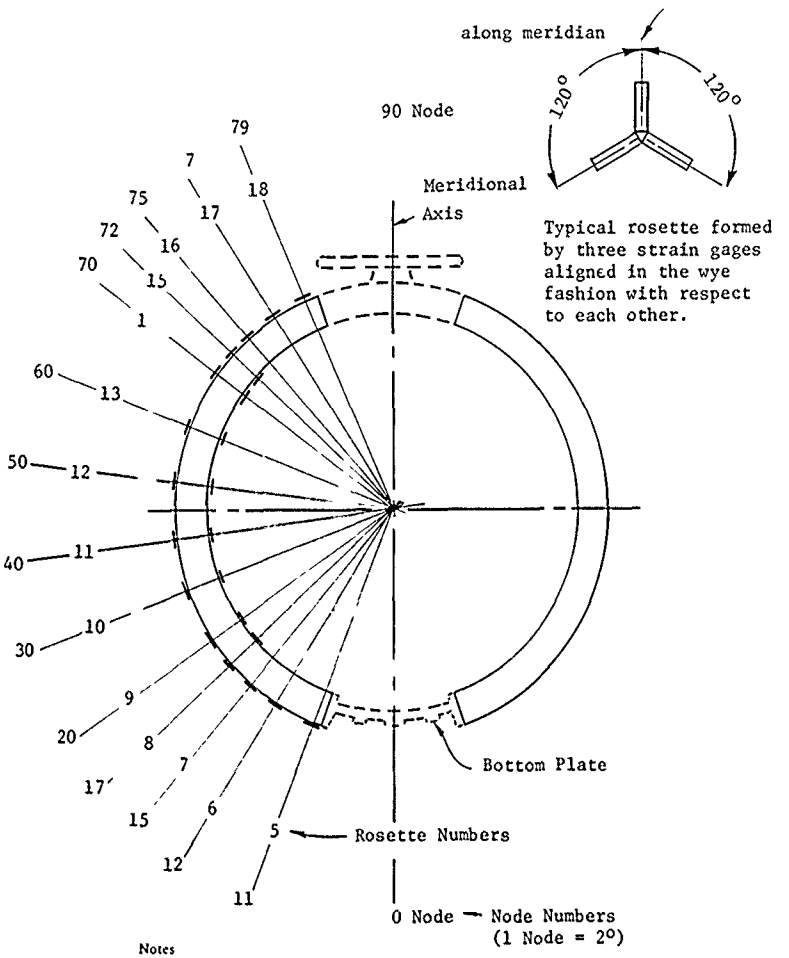

Notes

1 Rosettes on hull exterior have the Suffix A following the number Likewise, interior rosettes have B for the Suffix (e g. 10A and 10B)

2 Node locations have been determined by dividing the sphere into 2 degree increments. Numbering of nodes began on the bottom just as the numbering of the rosettes and continues to the top

Figure 6. Rosette locations on the acrylic portion of the capsule.

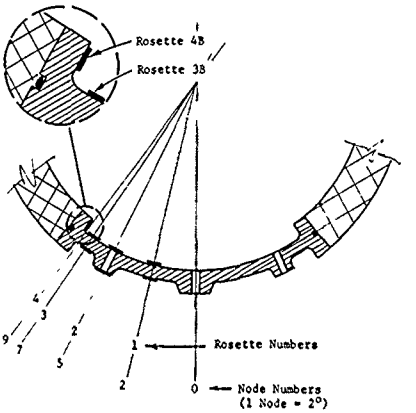

Figure 7. Location of and numbering system for rosettes on the stainless steel plate portion of the capsule.

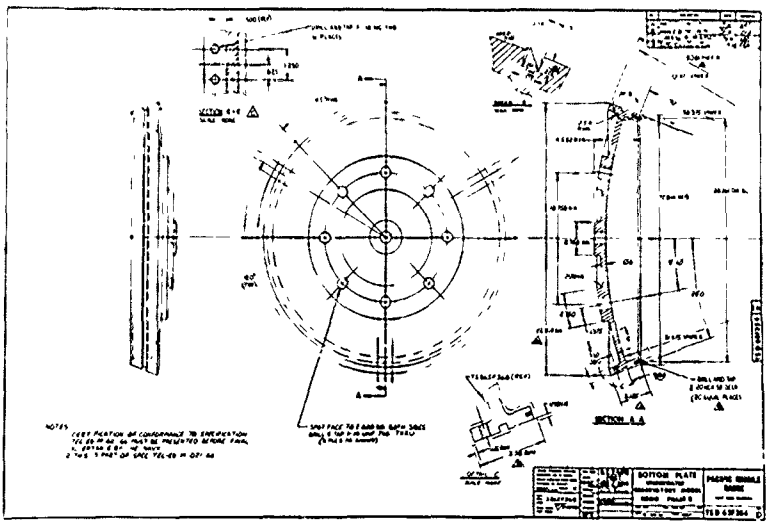

Figure 7a. Detailed dimensions of the bottom steel plate for prototype NEMO fabricated from 316 Type stainless steel

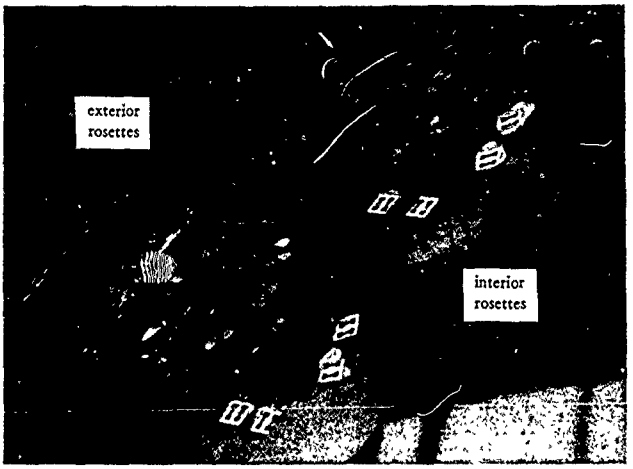

Figure 8. Typical installation of strain gage rosettes on the interior and exterior surfaces of the acrylic hull.

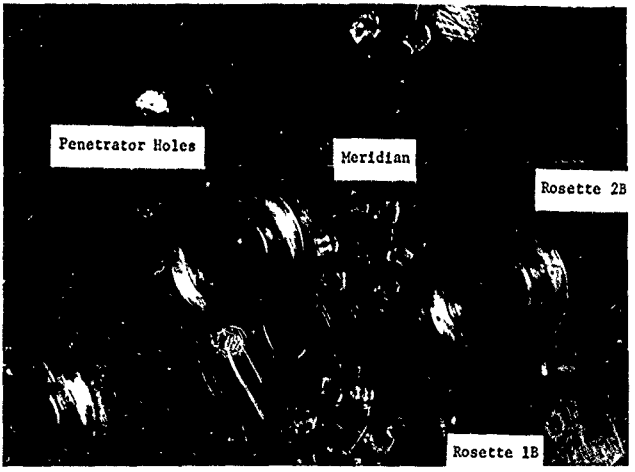

Figure 9. Typical installation of strain gage rosettes on the interior surface of the bottom steel plate.

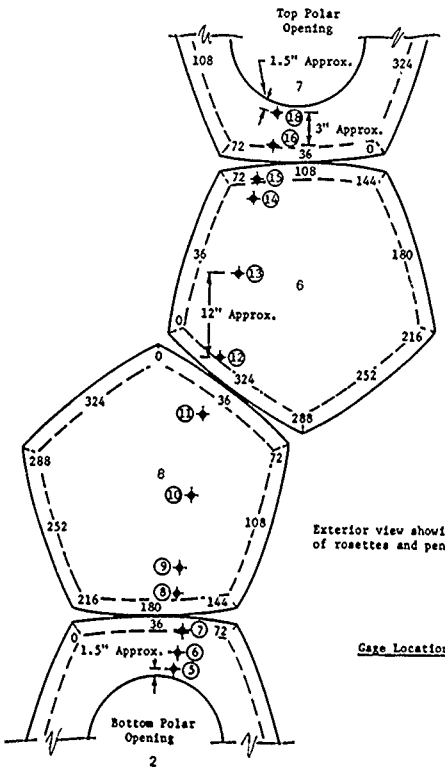

Exterior view showing numbering of rosettes and pentagons

Gage Location

Rosette No.	Thickness of Acrylic (Inches)	Sphericity Deviation*
5	2.395	+.010
6	2.455	+.030
7	2.480	+.050
8	2.495	+.040
9	2.470	+.030
10	2.405	+.026
11	2.400	+.047
12	2.425	+.044
13	2.380	+.010
14	2.500	+.013
15	2.500	+.048
16	2.520	+.042
18	2.460	+.007

* Denotes longer radius of curvature than the nominal 33.000 inch radius

Figure 10. Thickness and curvature of the acrylic hull under strain gage rosettes.

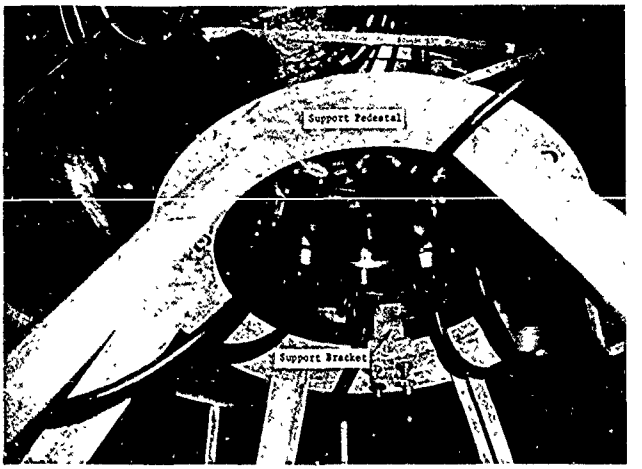

Figure 11. An exterior view of the bottom steel plate showing the support pedestal as well as the penetrators and cables for strain gages located on the interior of the capsule.

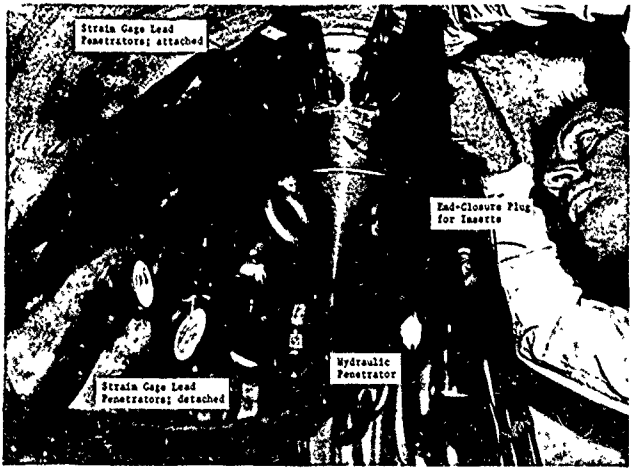

Figure 12. Pressure vessel head plug for accommodating electrical and hydraulic penetrators during hydrostatic testing of NEMO.

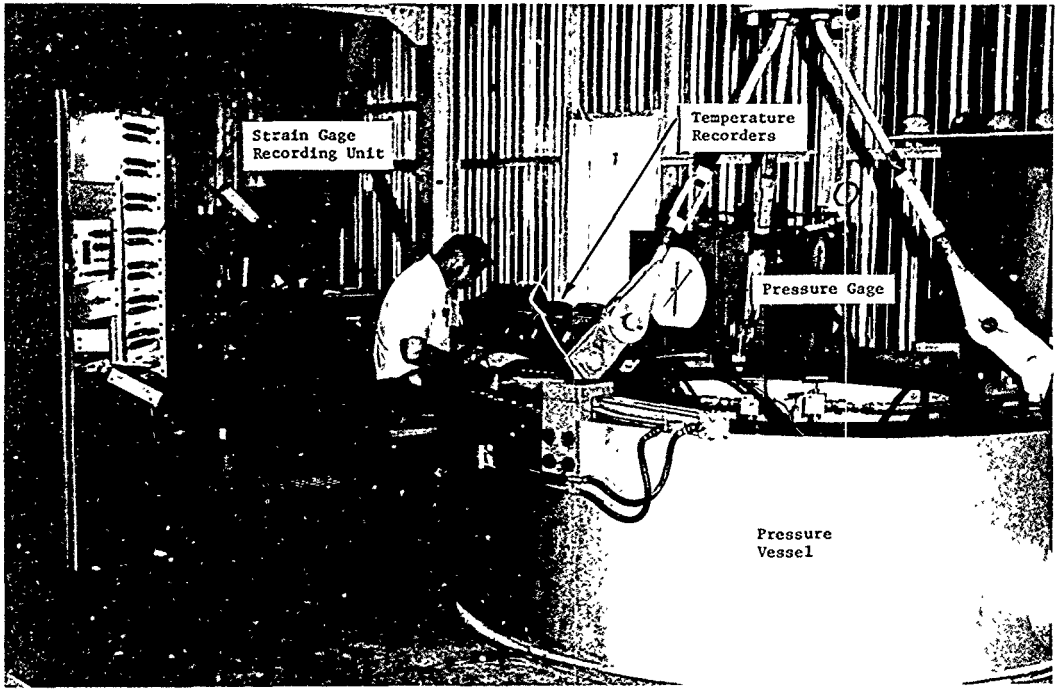

Figure 13. General view of instruments for monitoring the hydrostatic testing of NEMO inside the pressure vessel.

Figure 14a. Strains & Stresses During Short-Term Loading to 100 Psi (Phase 1a)

Press		ϵ_a	ϵ_b	ϵ_c	Principal Strains		$\frac{\tan 2\theta}{2}$	Principal Stresses		Shear Stress
50	1A	126.	119.	167.	167.2	107.3	1.222	5844.1	4513.4	2521.5
100	1A	135.	120.	187.	187.1	113.5	1.091	6471.5	4834.7	2790.3
50	2A	-10.	-10.	-18.	-7.3	-17.9	.866	-378.3	-615.3	231.5
100	2A	-33.	-20.	-16.	-12.7	-33.2	.115	-677.3	-1133.4	422.4
50	3A	17.	15.	-26.	30.0	-26.0	.789	680.8	-564.6	510.5
100	3A	4.	-9.	-61.	17.7	-61.7	.577	15.0	-1750.1	805.5
50	1B	11.	-33.	-20.	12.1	-40.1	-.150	50.3	-1109.7	580.0
100	1B	-41.	-53.	-53.	-41.0	-57.0	0.000	-1676.2	-2031.8	177.7
50	3B	-178.	-49.	-54.	-9.2	-178.0	-.017	-1668.9	-5419.3	1875.1
100	3B	-392.	-96.	-103.	-1.9	-392.0	-.010	-3119.7	-11788.3	4334.2
50	4B	10.	-120.	-65.	19.0	-141.6	-.258	-535.4	-4105.9	1785.2
100	4B	36.	-194.	-141.	39.4	-238.7	-.112	-680.6	-6861.7	3090.5
50	5A	-405.	-210.	-217.	-149.6	-405.0	-.015	-176.3	-261.4	86.8
100	5A	-732.	-293.	-294.	-147.3	-732.0	0.000	-260.7	-455.6	145.2
50	6A	-531.	-326.	-327.	-258.3	-531.0	-.002	-254.7	-345.5	123.5
100	6A	-949.	-537.	-545.	-404.9	-949.0	-.008	-431.8	-613.2	212.2
50	7A	-524.	-370.	-386.	-328.8	-524.4	-.047	-289.7	-354.8	130.9
100	7A	-974.	-658.	-645.	-543.8	-974.1	.017	-507.5	-651.0	233.1
50	8A	-492.	-438.	-342.	-336.2	-511.7	.407	-291.2	-349.7	129.5
100	8A	-895.	-720.	-616.	-580.8	-906.4	.198	-514.4	-622.9	225.1
50	9A	-423.	-378.	-376.	-361.6	-423.0	.018	-288.3	-308.7	117.3
100	9A	-795.	-710.	-671.	-652.1	-798.5	.161	-531.5	-580.4	215.6
50	10A	-385.	-413.	-400.	-383.1	-415.5	-.261	-297.9	-308.7	119.4
100	10A	-698.	-766.	-727.	-690.9	-769.7	-.348	-546.3	-572.5	216.6
50	11A	-410.	-411.	-435.	-402.3	-435.0	.799	-311.3	-322.2	125.7
100	11A	-745.	-761.	-801.	-735.6	-802.3	.481	-575.1	-597.3	229.1
50	12A	-393.	-399.	-433.	-383.4	-433.2	.640	-301.3	-317.9	122.4
100	12A	-759.	-783.	-848.	-743.4	-849.8	.498	-587.6	-623.1	238.4
50	13A	-389.	-418.	-420.	-388.9	-429.0	.028	-303.3	-316.7	122.5
100	13A	-763.	-802.	-801.	-762.9	-814.3	-.011	-591.2	-608.4	235.4
50	14A	-450.	-402.	-456.	-401.8	-470.1	-1.113	-317.3	-340.1	131.6
100	14A	-877.	-798.	-828.	-788.2	-880.3	-.202	-616.1	-646.8	250.5

Figure 14a. (cont'd)

Press		ε_a	ε_b	ε_c	Principal Strains		$\frac{\tan 2\theta}{2}$	Principal Stresses		Shear Stress
50	16A	-468.	-360.	-444.	-358.5	-489.4	-.551	-298.6	-342.2	128.6
100	16A	-959.	-705.	-793.	-670.0	-967.9	-.181	-571.2	-670.4	248.6
50	18A	-514.	-133.	-276.	-85.4	-529.9	-.200	-165.8	-314.0	107.9
100	18A	-1045.	-347.	-446.	-176.5	-1048.7	-.066	-332.6	-623.3	213.8
50	8B	-422.	-472.	-481.	-421.6	-495.0	.071	-305.0	-329.5	12.2
100	8B	-743.	-884.	-826.	-735.8	-899.4	-.224	-538.7	-593.3	27.2
50	9B	-413.	-471.	-471.	-413.0	-490.3	0.000	-299.8	-325.5	12.8
100	9B	-759.	-849.	-856.	-758.8	-883.7	.032	-547.7	-589.4	20.8
50	10B	-462.	-464.	-482.	-456.6	-482.0	.708	-320.6	-329.1	4.2
100	10B	-885.	-868.	-878.	-867.1	-886.8	-.360	-603.8	-610.4	3.2
50	11B	-481.	-471.	-519.	-461.0	-519.5	1.484	-329.7	-349.2	9.7
100	11B	-976.	-983.	-1040.	-959.1	-1040.2	.695	-678.5	-705.5	13.5
50	12B	-444.	-469.	-496.	-439.6	-499.6	.303	-315.1	-335.1	10.0
100	12B	-926.	-952.	-1012.	-912.4	-1014.2	.463	-649.9	-683.8	16.9
50	13B	-449.	-476.	-501.	-445.3	-505.3	.274	-319.0	-339.0	10.0
100	13B	-906.	-992.	-1018.	-904.3	-1039.6	.113	-650.3	-695.4	22.5
50	14B	-362.	-467.	-482.	-361.5	-512.4	.057	-277.3	-327.7	25.1
100	14B	-783.	-934.	-900.	-780.8	-963.7	-.109	-573.4	-634.4	30.4
50	15B	-325.	-442.	-437.	-324.9	-477.7	-.018	-252.3	-303.3	25.4
100	15B	-690.	-871.	-817.	-685.3	-899.9	-.151	-513.0	-584.5	35.7
100	3A	+ 4.	- 9.	- 61.	+ 18.	- 62.	1.15	- 358.	-2122.	900
100	2B	-125.	- 67	- 63.	- 45.	-125.	0.058	- 390.	-3400.	

Figure 14b. Strains & Stresses During Short-Term Loading to 500 Psi (Phase 1e)

Press		ϵ_a	ϵ_b	ϵ_c	Principal Strains		$\frac{\tan 2\theta}{2}$	Principal Stresses		Shear Stress
100	1B	-150.	-20.	-50.	5.2	-151.9	-.112	-1028.1	-4521.4	1746.6
200	1B	-310.	-10.	-130.	24.3	-324.3	-.216	-1801.0	-9550.2	3874.5
300	1B	-330.	-30.	-150.	4.3	-344.3	-.216	-2557.8	-10307.0	3874.5
400	1B	-370.	-60.	-180.	-22.8	-383.8	-.207	-3682.7	-11704.6	4010.9
450	1B	-360.	-80.	-190.	-47.1	-372.8	-.211	-4326.1	-11565.7	3619.7
500	1B	-410.	-80.	-200.	-37.1	-422.8	-.192	-4416.6	-12988.7	4286.0
100	2B	-60.	-60.	10.	9.9	-83.3	.866	-350.3	-2424.4	1037.0
200	2B	-150.	-130.	-40.	-39.0	-174.3	.599	-2532.4	-5539.5	1503.5
300	2B	-240.	-180.	-120.	-110.7	-249.2	.288	-5271.2	-8350.4	1539.6
400	2B	-380.	-250.	-160.	-135.6	-391.0	.222	-7125.8	-12802.0	2838.1
450	2B	-380.	-250.	-170.	-144.2	-389.0	.203	-7370.4	-12809.7	2719.6
500	2B	-430.	-280.	-190.	-160.0	-439.9	.199	-8240.2	-14462.4	3111.1
100	3B	-250.	-150.	-50.	-34.5	-265.4	.288	-3109.6	-8241.6	2566.0
200	3B	-430.	-240.	-150.	-108.2	-438.3	.165	-6674.3	-14010.3	3667.9
300	3B	-540.	-310.	-240.	-182.1	-544.5	.114	-9720.4	-17775.0	4027.3
400	3B	-660.	-370.	-330.	-245.3	-661.2	.055	-12531.9	-21774.3	4621.1
450	3B	-700.	-400.	-370.	-279.2	-700.7	.041	-13858.0	-23223.0	4682.5
500	3B	-810.	-440.	-420.	-303.0	-810.2	.022	-15427.5	-26698.5	5635.4
100	4B	40.	-190.	-90.	53.1	-213.1	-.240	-67.7	-5986.2	2959.2
200	4B	50.	-310.	-230.	54.9	-381.6	-.108	-1329.6	-11030.7	4850.5
300	4B	90.	-400.	-360.	90.8	-537.5	-.036	-1468.6	-15432.2	6981.8
400	4B	120.	-520.	-460.	121.4	-694.8	-.042	-1777.0	-19916.6	9069.7
450	4B	150.	-540.	-520.	150.1	-756.8	-.012	-1400.1	-21554.8	10077.3
500	4B	190.	-590.	-590.	190.0	-850.0	0.000	-930.9	-24042.0	11555.5
100	1A	0.	30.	10.	30.9	-4.3	-.433	861.3	77.4	417.2
200	1A	-10.	10.	-10.	9.9	-16.6	-.866	99.8	-492.6	241.6
300	1A	10.	0.	-20.	14.3	-20.9	.433	160.4	-623.4	321.3
400	1A	-10.	-20.	-40.	-5.6	-40.9	.433	-631.4	-1415.3	434.0
450	1A	-20.	-10.	-40.	-5.6	-40.9	2.598	-649.0	-1432.9	423.8
500	1A	-40.	-10.	-40.	-10.0	-49.9	-.866	-866.3	-1755.2	526.5

Figure 14b. (cont'd)

Press		ϵ_a	ϵ_b	ϵ_c	Principal Strains		$\frac{\tan 2\theta}{2}$	Principal Stresses		Shear Stress
100	2A	0.	30.	30.	40.0	0.0	0.000	1166.0	277.1	530.2
200	2A	-10.	20.	10.	24.3	-10.9	-.173	573.9	-209.9	366.8
300	2A	-20.	10.	0.	14.3	-20.9	-.173	160.4	-623.4	321.3
400	2A	-30.	-10.	-10.	-3.3	-29.9	0.000	-474.8	-1067.4	298.2
450	2A	-40.	0.	-10.	7.3	-40.7	-.123	-254.5	-1322.8	463.9
500	2A	-30.	0.	-10.	4.3	-30.9	-.173	-288.2	-1072.1	330.7
100	6A	-980.	-570.	-600.	-452.7	-980.5	-.032	-462.0	-637.9	223.7
200	6A	-1900.	-1010.	-1030.	-726.5	-1900.1	-.009	-821.3	-1212.5	416.4
300	6A	-2790.	-1430.	-1480.	-1009.5	-2790.4	-.016	-1180.1	-1773.7	604.8
400	6A	-3750.	-1880.	-1960.	-1309.1	-3750.8	-.018	-1559.9	-2373.8	809.1
450	6A	-4130.	-2070.	-2170.	-1448.7	-4131.2	-.021	-1726.7	-2620.9	889.9
500	6A	-4490.	-2180.	-2400.	-1551.1	-4495.4	-.043	-1871.5	-2853.0	964.0
100	7A	-1000.	-550.	-750.	-506.3	-1027.0	-.247	-497.8	-671.3	238.9
200	7A	-1980.	-1030.	-1340.	-890.5	-2009.4	-.168	-925.0	-1298.0	455.4
300	7A	-3000.	-1580.	-1930.	-1315.7	-3024.2	-.121	-1379.0	-1948.5	682.9
400	7A	-3970.	-2290.	-2580.	-1909.7	-3983.6	-.081	-1909.7	-2601.0	918.1
450	7A	-4320.	-2560.	-2860.	-2159.4	-4333.8	-.080	-2127.5	-2852.4	1005.1
500	7A	-5020.	-2930.	-3200.	-2404.0	-5029.2	-.059	-2404.7	-3279.8	1159.3
100	8A	-860.	-740.	-590.	-573.7	-886.2	.333	-507.1	-611.2	220.3
200	8A	-1750.	-1400.	-1230.	-1153.8	-1766.1	.169	-1016.4	-1220.5	440.4
300	8A	-2600.	-2110.	-1870.	-1763.7	-2622.9	.170	-1536.7	-1823.2	660.3
400	8A	-3500.	-2840.	-2550.	-2401.1	-3525.5	.155	-2079.5	-2454.3	892.3
450	8A	-3930.	-3190.	-2860.	-2693.9	-3959.3	.157	-2334.4	-2756.2	1001.6
500	8A	-4340.	-3610.	-3260.	-3100.3	-4372.9	.167	-2644.0	-3068.2	1122.9
100	9A	-880.	-770.	-770.	-733.3	-879.9	0.000	-587.8	-636.7	242.0
200	9A	-1680.	-1450.	-1450.	-1373.3	-1679.9	0.000	-1113.5	-1215.7	456.1
300	9A	-2470.	-2160.	-2160.	-2056.6	-2469.9	0.000	-1659.5	-1797.3	675.0
400	9A	-3290.	-2910.	-2900.	-2776.6	-3290.0	.011	-2229.8	-2490.9	904.7
450	9A	-3690.	-3250.	-3240.	-3096.6	-3690.0	.009	-2492.6	-2690.4	1011.7
500	9A	-4200.	-3670.	-3650.	-3479.8	-4200.1	.016	-2807.6	-3047.7	1147.4

Figure 14b. (cont'd)

Press		ε_a	ε_b	ε_c	Principal Strains		$\frac{\tan 2\theta}{2}$	Principal Stresses		Shear Stress
100	10A	-760.	-800.	-820.	-758.0	-828.6	.173	-591.3	-614.8	237.1
200	10A	-1450.	-1550.	-1540.	-1449.7	-1576.9	-.045	-1134.1	-1176.5	450.2
300	10A	-2080.	-2290.	-2240.	-2076.6	-2329.9	-.117	-1644.7	-1729.1	654.0
400	10A	-2780.	-3000.	-2900.	-2766.1	-3020.5	-.254	-2176.0	-2260.8	857.0
450	10A	-3120.	-3380.	-3330.	-3117.3	-3435.9	-.092	-2457.6	-2563.8	971.4
500	10A	-3480.	-3750.	-3710.	-3478.4	-3814.9	-.069	-2737.7	-2849.9	1081.2
100	11A	-830.	-830.	-830.	-830.0	-830.0	0.000	-628.4	-628.4	248.8
200	11A	-1520.	-1550.	-1610.	-1507.0	-1612.9	.433	-1170.0	-1205.3	465.3
300	11A	-2240.	-2310.	-2350.	-2235.7	-2364.2	.192	-1732.4	-1775.2	684.8
400	11A	-2950.	-2990.	-3010.	-2948.0	-3018.6	.173	-2269.0	-2292.5	885.7
450	11A	-3350.	-3430.	-3460.	-3347.6	-3478.9	.136	-2583.4	-2627.2	1015.1
500	11A	-3780.	-3840.	-3880.	-3775.2	-3891.4	.216	-2903.7	-2942.4	1141.2
100	12A	-730.	-770.	-910.	-694.1	-912.4	.551	-573.6	-646.3	242.0
200	12A	-1440.	-1520.	-1710.	-1396.5	-1716.8	.470	-1132.0	-1238.7	466.0
300	12A	-2130.	-2290.	-2480.	-2097.6	-2502.3	.322	-1686.4	-1821.2	686.8
400	12A	-2720.	-2900.	-3070.	-2694.5	-3098.7	.277	-2153.4	-2288.1	859.2
450	12A	-3180.	-3430.	-3640.	-3150.7	-3682.5	.256	-2519.0	-2696.3	1018.6
500	12A	-3570.	-3830.	-4060.	-3536.9	-4103.0	.265	-2819.4	-3008.2	1139.3
100	13A	-800.	-850.	-850.	-800.0	-866.6	0.000	-619.6	-641.8	250.1
200	13A	-1510.	-1580.	-1580.	-1510.0	-1603.3	0.000	-1169.8	-1200.9	464.2
300	13A	-2250.	-2290.	-2290.	-2250.0	-2303.3	0.000	-1728.8	-1746.5	677.0
400	13A	-2850.	-2950.	-2940.	-2849.7	-2976.9	-.045	-2211.1	-2253.5	863.0
450	13A	-3300.	-3440.	-3420.	-3299.2	-3474.0	-.066	-2557.7	-2616.0	1006.6
500	13A	-3700.	-3830.	-3820.	-3699.8	-3866.8	-.034	-2860.6	-2916.3	1125.0
100	14A	-920.	-880.	-880.	-866.6	-919.9	0.000	-663.4	-681.1	269.6
200	14A	-1740.	-1590.	-1590.	-1540.0	-1740.0	0.000	-1209.7	-1276.4	491.9
300	14A	-2600.	-2350.	-2340.	-2259.9	-2600.0	.016	-1787.1	-1900.5	728.5
400	14A	-3390.	-2990.	-3010.	-2869.7	-3390.2	-.022	-2295.5	-2469.0	936.2
450	14A	-3920.	-3440.	-3440.	-3280.0	-3920.0	0.000	-2627.9	-2841.2	1079.4
500	14A	-4430.	-3850.	-3850.	-3656.6	-4429.9	0.000	-2939.5	-3197.3	1214.1

Figure 14b. (cont'd)

Press		ε_a	ε_b	ε_c	Principal Strains		$\frac{\tan 2\theta}{2}$	Principal Stresses		Shear Stress
100	16A	-1100.	-740.	-800.	-657.2	-1102.7	-.078	-588.8	-737.3	271.9
200	16A	-2020.	-1380.	-1480.	-1229.1	-2024.2	-.073	-1101.3	-1366.3	498.7
300	16A	-3010.	-2080.	-2160.	-1821.5	-3011.7	-.038	-1636.2	-2032.9	740.5
400	16A	-3950.	-2750.	-2860.	-2420.6	-3952.6	-.041	-2166.2	-2676.8	974.5
450	16A	-4410.	-3080.	-3200.	-2713.8	-4412.8	-.040	-2426.0	-2992.3	1088.7
500	16A	-4960.	-3450.	-3600.	-3042.7	-4963.9	-.045	-2720.5	-3360.9	1224.7
100	18A	-1250.	-470.	-540.	-255.0	-1251.6	-.040	-409.2	-741.4	261.6
200	18A	-2090.	-620.	-810.	-389.9	-2090.0	.003	-682.8	-1249.4	428.4
300	18A	-2910.	-1170.	-1130.	-563.1	-2910.2	.009	-972.6	-1755.0	593.9
400	18A	-3780.	-1540.	-1450.	-732.4	-3780.8	.017	-1269.6	-2285.7	769.8
450	18A	-4180.	-1700.	-1610.	-812.5	-4180.8	.015	-1409.3	-2532.1	850.0
500	18A	-4690.	-1910.	-1760.	-881.3	-4691.9	.022	-1563.3	-2833.5	952.9
100	8B	-810.	-980.	-970.	-809.8	-1030.1	-.026	-600.2	-673.6	36.7
200	8B	-1520.	-1840.	-1840.	-1520.0	-1946.6	0.000	-1128.8	-1271.1	71.1
300	8B	-2190.	-2670.	-2680.	-2189.9	-2836.7	.008	-1632.2	-1847.7	107.7
400	8B	-2910.	-3580.	-3570.	-2909.9	-3796.7	-.006	-2173.7	-2469.3	147.7
450	8B	-3210.	-4020.	-4020.	-3210.0	-4290.0	0.000	-2416.1	-2776.1	179.9
500	8B	-3620.	-4530.	-4520.	-3619.9	-4826.6	-.004	-2722.7	-3124.9	201.1
100	9B	-830.	-910.	-960.	-824.2	-975.7	.206	-597.8	-648.3	25.2
200	9B	-1580.	-1800.	-1810.	-1579.8	-1880.1	.019	-1147.6	-1247.7	50.0
300	9B	-2290.	-2670.	-2660.	-2289.9	-2790.0	-.011	-1675.1	-1841.8	83.3
400	9B	-2990.	-3500.	-3570.	-2987.7	-3718.9	.055	-2199.6	-2443.3	121.8
450	9B	-3340.	-3950.	-4020.	-3338.1	-4201.8	.046	-2466.0	-2753.9	143.9
500	9B	-3730.	-4400.	-4510.	-3725.8	-4700.8	.065	-2754.4	-3079.4	162.4
100	10B	-940.	-910.	-920.	-905.6	-940.9	-.173	-633.3	-645.1	5.8
200	10B	-1770.	-1800.	-1790.	-1769.0	-1804.3	-.173	-1231.0	-1242.8	5.8
300	10B	-2640.	-2660.	-2660.	-2640.0	-2666.6	0.000	-1832.4	-1841.3	4.4
400	10B	-3440.	-3540.	-3490.	-3432.2	-3547.7	-.288	-2396.9	-2435.3	19.2
450	10B	-3940.	-4050.	-3930.	-3896.4	-4050.2	-1.039	-2725.1	-2776.3	25.6
500	10B	-4410.	-4520.	-4450.	-4395.7	-4524.2	-.404	-3066.2	-3109.1	21.4

Figure 14b. (cont'd)

Press		ε_a	ε_b	ε_c	Principal Strains		$\frac{\tan 2\theta}{2}$	Principal Stresses		Shear Stress
100	11B	-930.	-850.	-1110.	-809.5	-1117.1	2.251	-615.6	-718.1	51.2
200	11B	-1840.	-1910.	-2060.	-1745.7	-2060.9	1.139	-1265.1	-1370.2	52.5
300	11B	-2790.	-2800.	-3030.	-2715.5	-3030.1	.796	-1936.9	-2041.4	52.2
400	11B	-3640.	-3710.	-3930.	-3585.2	-3934.7	.529	-2544.8	-2661.3	58.2
450	11B	-4090.	-4070.	-4560.	-3919.7	-4560.2	.943	-2828.6	-3042.1	106.7
500	11B	-4660.	-4680.	-5090.	-4529.7	-5090.2	.789	-3236.5	-3423.4	93.4
100	12B	-1020.	-980.	-1080.	-968.5	-1084.7	4.330	-691.3	-730.1	19.3
200	12B	-1960.	-1820.	-2080.	-1803.0	-2103.5	-11.258	-1302.2	-1402.3	50.0
300	12B	-2860.	-2640.	-3000.	-2623.7	-3042.8	-3.897	-1891.6	-2031.3	69.8
400	12B	-3110.	-3430.	-3890.	-3023.9	-3929.4	.362	-2256.0	-2557.8	150.9
450	12B	-4200.	-4010.	-4470.	-3959.7	-4493.5	4.979	-2837.1	-3015.1	88.9
500	12B	-4680.	-4470.	-5010.	-4405.6	-5034.3	3.897	-3162.9	-3372.4	104.7
100	13B	-990.	-1000.	-1020.	-985.6	-1020.9	.433	-688.7	-700.4	5.8
200	13B	-1870.	-1890.	-1920.	-1864.2	-1922.3	.371	-1301.0	-1320.4	9.6
300	13B	-2700.	-2800.	-2910.	-2682.0	-2924.6	.307	-1900.3	-1981.1	40.4
400	13B	-3520.	-3600.	-3840.	-3461.0	-3845.6	.519	-2465.1	-2593.3	64.0
450	13B	-4060.	-4190.	-4440.	-4006.9	-4453.0	.424	-2854.1	-3002.7	74.3
500	13B	-4530.	-4670.	-4970.	-4463.7	-4982.9	.447	-3183.4	-3356.5	86.5
100	14B	-890.	-960.	-960.	-890.0	-983.3	0.000	-632.9	-664.0	15.5
200	14B	-1650.	-1860.	-1820.	-1647.9	-1905.4	-.091	-1187.0	-1272.9	42.9
300	14B	-2480.	-2780.	-2680.	-2470.2	-2823.0	-.173	-1773.5	-1891.1	58.7
400	14B	-3290.	-3540.	-3560.	-3289.6	-3637.0	.033	-2339.7	-2455.5	57.9
450	14B	-3750.	-4160.	-3980.	-3726.0	-4200.6	-.243	-2664.7	-2822.9	79.0
500	14B	-4190.	-4640.	-4440.	-4162.9	-4683.6	-.247	-2975.5	-3149.0	86.7
100	15B	-700.	-960.	-890.	-694.6	-1005.3	-.134	-536.6	-640.2	51.7
200	15B	-1440.	-1790.	-1620.	-1414.5	-1818.7	-.277	-1051.8	-1186.5	67.3
300	15B	-2210.	-2620.	-2440.	-2186.0	-2660.6	-.243	-1598.5	-1756.7	79.0
400	15B	-2910.	-3490.	-3170.	-2854.5	-3525.4	-.329	-2096.6	-2320.2	111.8
450	15B	-3260.	-3920.	-3570.	-3202.0	-3964.6	-.312	-2353.6	-2607.8	127.0
500	15B	-3620.	-4370.	-3980.	-3556.8	-4423.1	-.304	-2617.9	-2906.6	144.3
500	3A	+50.	-200.	-200.	+50.0	-283.0	0	-886.0	-8292.0	3834.0

Figure 14c. Strains & Stresses During Short-Term Loading to 800 Psi (Phase Ih)

Press		ϵ_a	ϵ_b	ϵ_c	Principal Strains		$\frac{\tan 2\theta}{2}$	Principal Stresses		Shear Stress
100	1A	-50.	-10.	-10.	3.3	-49.9	0.000	-325.4	-1510.6	618.0
200	1A	-30.	0.	0.	10.0	-30.0	0.000	-4.2	-893.0	380.9
300	1A	-70.	-30.	-30.	-16.6	-69.9	0.000	-1152.4	-2337.6	834.7
400	1A	-100.	-50.	-40.	-26.2	-100.4	.078	-1712.0	-3361.7	1210.5
500	1A	-100.	-60.	-60.	-46.6	-100.0	0.000	-2357.8	-3543.0	1251.1
600	1A	-130.	-80.	-70.	-56.2	-130.4	.078	-2917.4	-4567.1	1625.6
700	1A	-160.	-80.	-80.	-53.3	-159.9	0.000	-3096.7	-5467.1	1944.2
800	1A	-130.	-100.	-90.	-82.6	-130.7	.123	-3782.9	-4851.2	1712.6
100	2A	-20.	-10.	0.	1.5	-21.5	.288	-156.9	-670.1	256.1
200	2A	40.	10.	20.	40.9	5.6	-.173	1204.5	420.6	574.1
300	2A	0.	-10.	-40.	7.3	-40.7	.519	-201.8	-1270.1	481.6
400	2A	-70.	-40.	-30.	-22.6	-70.7	.123	-1372.1	-2440.4	832.4
500	2A	-10.	-30.	-30.	-10.0	-36.6	0.000	-762.2	-1354.8	357.2
600	2A	-40.	-60.	-50.	-38.4	-61.5	-.288	-1846.1	-2359.3	737.9
700	2A	-30.	-40.	-50.	-28.4	-51.5	.288	-1502.8	-2016.0	541.0
800	2A	-50.	-60.	-70.	-48.4	-71.5	.288	-2294.7	-2807.9	850.9
100	8A	-730.	-740.	-600.	-599.8	-780.1	1.010	-501.4	-561.6	204.6
200	8A	-1500.	-1380.	-1190.	-1176.1	-1537.1	.382	-986.7	-1107.0	401.8
300	8A	-2410.	-2070.	-1830.	-1766.8	-2439.8	.225	-1505.5	-1729.8	627.2
400	8A	-3220.	-2730.	-2410.	-2315.5	-3257.7	.213	-1987.5	-2301.6	831.5
500	8A	-4020.	-3410.	-2980.	-2866.5	-4073.4	.225	-2470.3	-2872.6	1035.7
600	8A	-40.	-4120.	-3530.	-17.1	-5109.5	-.067	-1248.9	-2946.4	988.3
700	8A	-5710.	-4820.	-4150.	-3989.6	-5796.9	.236	-3463.3	-4065.8	1463.9
800	8A	-6510.	-5580.	-4680.	-4533.4	-6646.5	.282	-3948.5	-4652.9	1673.4
100	9A	-670.	-780.	-750.	-667.6	-798.9	-.136	-539.6	-583.4	218.0
200	9A	-1390.	-1470.	-1410.	-1375.2	-1471.4	-.519	-1077.0	-1109.1	420.7
300	9A	-2260.	-2210.	-2130.	-2124.2	-2275.7	.384	-1659.3	-1709.8	652.3
400	9A	-3000.	-2890.	-2790.	-2772.0	-3014.6	.270	-2178.0	-2258.8	857.0
500	9A	-3810.	-3590.	-3490.	-3440.9	-3819.0	.160	-2719.2	-2845.3	1076.0
600	9A	-4630.	-4320.	-4190.	-4118.9	-4641.0	.150	-3268.3	-3442.3	1299.5
700	9A	-5460.	-5090.	-4910.	-4829.5	-5477.1	.169	-3836.6	-4052.5	1530.5
800	9A	-6240.	-5840.	-5660.	-5570.5	-6256.1	.159	-4410.3	-4638.8	1756.5

Figure 14c. (cont'd)

Press		ϵ_a	ϵ_b	ϵ_c	Principal Strains		$\frac{\tan 2\theta}{2}$	Principal Stresses		Shear Stress
100	10A	-650.	-700.	-730.	-646.6	-739.9	.199	-518.2	-549.4	204.7
200	10A	-1250.	-1420.	-1400.	-1249.3	-1463.9	-.054	-1011.1	-1082.6	399.9
300	10A	-1950.	-2100.	-2140.	-1947.6	-2178.9	.101	-1551.4	-1628.5	608.3
400	10A	-2560.	-2790.	-2820.	-2559.0	-2887.5	.053	-2046.0	-2155.5	802.1
500	10A	-3230.	-3500.	-3540.	-3228.6	-3618.0	.059	-2574.3	-2704.1	1008.8
600	10A	-3890.	-4210.	-4270.	-3887.4	-4359.2	.074	-3099.0	-3256.3	1215.6
700	10A	-4540.	-4930.	-5000.	-4537.1	-5109.5	.071	-3620.7	-3811.5	1422.5
800	10A	-5230.	-5660.	-5760.	-5224.8	-5875.1	.090	-4164.6	-4381.4	1637.9
100	11A	-720.	-780.	-780.	-720.0	-800.0	0.000	-566.6	-593.3	226.3
200	11A	-1340.	-1460.	-1490.	-1338.3	-1521.6	.096	-1067.1	-1128.2	423.4
300	11A	-2120.	-2220.	-2250.	-2118.0	-2275.2	.112	-1656.1	-1708.5	651.3
400	11A	-2820.	-2930.	-2960.	-2818.2	-2988.4	.103	-2197.0	-2253.7	859.9
500	11A	-3490.	-3650.	-3680.	-3488.7	-3724.6	.074	-2726.8	-2805.4	1067.6
600	11A	-4190.	-4370.	-4430.	-4185.7	-4474.2	.123	-3272.6	-3368.8	1281.9
700	11A	-4890.	-5090.	-5150.	-4886.1	-5200.5	.112	-3816.0	-3920.8	1492.7
800	11A	-5600.	-5830.	-5910.	-5594.1	-5965.8	.128	-4370.3	-4494.2	1711.3
100	12A	-630.	-630.	-700.	-606.6	-699.9	.866	-490.5	-521.7	191.6
200	12A	-1250.	-1310.	-1420.	-1227.1	-1426.2	.414	-992.9	-1059.3	390.0
300	12A	-1900.	-2020.	-2170.	-1873.7	-2186.2	.333	-1514.8	-1618.9	598.1
400	12A	-2490.	-2670.	-2930.	-2441.2	-2952.0	.363	-1997.1	-2167.4	795.2
500	12A	-3120.	-3400.	-3630.	-3088.4	-3678.2	.252	-2513.2	-2709.8	997.6
600	12A	-3720.	-4080.	-4360.	-3682.8	-4423.7	.242	-3005.7	-3252.7	1195.3
700	12A	-4320.	-4790.	-5100.	-4283.1	-5190.1	.214	-3504.9	-3807.3	1397.6
800	12A	-4950.	-5490.	-5850.	-4906.9	-5953.0	.216	-4015.6	-4364.3	1602.7
100	13A	-690.	-680.	-700.	-678.4	-701.5	0.000	-527.6	-535.3	203.2
200	13A	-1330.	-1350.	-1400.	-1318.3	-1401.6	.481	-1035.3	-1063.1	400.0
300	13A	-2000.	-2060.	-2130.	-1988.2	-2138.4	.319	-1564.9	-1615.0	607.8
400	13A	-2610.	-2710.	-2800.	-2596.9	-2816.4	.268	-2052.6	-2125.8	796.0
500	13A	-3270.	-3430.	-3520.	-3260.4	-3552.8	.190	-2578.9	-2676.4	1002.7
600	13A	-3910.	-4110.	-4260.	-3890.5	-4296.0	.236	-3089.3	-3224.5	1205.4
700	13A	-4540.	-4790.	-4920.	-4526.9	-4973.0	.178	-3591.0	-3739.7	1397.8
800	13A	-5210.	-5500.	-5650.	-5195.0	-5711.6	.177	-4120.0	-4292.2	1605.6

Figure 14c. (cont'd)

Press		ϵ_a	ϵ_b	ϵ_c	Principal Strains		tan 2θ	Principal Stresses		Shear Stress
100	16A	-1180.	-830.	-960.	-785.7	-1194.2	-.197	-671.1	-807.3	306.1
200	16A	-2120.	-1450.	-1630.	-1332.9	-2133.7	-.134	-1174.2	-1441.1	532.8
300	16A	-3060.	-2060.	-2310.	-1875.7	-3077.5	-.123	-1675.8	-2076.4	760.0
400	16A	-4040.	-2690.	-3000.	-2426.8	-4059.8	-.112	-2188.5	-2732.9	995.5
500	16A	-5040.	-3330.	-3710.	-2989.8	-5063.4	-.108	-2711.3	-3402.5	1236.6
600	16A	-6000.	-3910.	-4410.	-3513.1	-6033.5	-.117	-3207.6	-4047.7	1466.4
700	16A	-7000.	-4530.	-5150.	-4076.1	-7043.8	-.124	-3731.5	-4720.7	1708.8
800	16A	-7910.	-5120.	-5940.	-4667.5	-7979.1	-.149	-4256.5	-5360.3	1940.6
100	18A	-1890.	-800.	-690.	-360.6	-1892.6	.041	-578.5	-1089.1	403.4
200	18A	-2760.	-1140.	-980.	-489.5	-2763.7	.040	-854.8	-1612.8	576.7
300	18A	-3610.	-1470.	-1270.	-618.8	-3614.4	.038	-1127.6	-2126.1	745.8
400	18A	-4470.	-1870.	-1590.	-809.5	-4477.1	.044	-1434.1	-2656.6	921.4
500	18A	-5380.	-2230.	-1900.	-951.8	-5388.1	.043	-1724.4	-3203.2	1104.1
600	18A	-6250.	-2580.	-2220.	-1108.2	-6258.4	.040	-2014.7	-3731.4	1279.1
700	18A	-7030.	-2940.	-2520.	-1286.4	-7040.2	.042	-2300.2	-4218.1	1436.8
800	18A	-8000.	-3350.	-2850.	-1453.9	-8012.7	.044	-2614.5	-4800.8	1634.0
100	8B	-660.	-970.	-990.	-659.6	-1086.9	.027	-533.4	-675.8	71.2
200	8B	-1290.	-1810.	-1840.	-1289.5	-2003.7	.024	-1020.9	-1259.0	119.0
300	8B	-2020.	-2720.	-2740.	-2019.8	-2966.8	.012	-1568.3	-1883.9	157.8
400	8B	-2670.	-3570.	-3610.	-2669.5	-3897.1	.018	-2068.4	-2477.6	204.5
500	8B	-3370.	-4420.	-4490.	-3368.8	-4817.7	.027	-2592.3	-3075.3	241.4
600	8B	-4020.	-5380.	-5380.	-4020.0	-5833.3	0.000	-3108.5	-3712.9	302.2
700	8B	-4690.	-6310.	-6290.	-4689.9	-6836.7	-.005	-3632.2	-4347.7	357.7
800	8B	-5330.	-7290.	-7280.	-5329.9	-7936.6	-.002	-4157.8	-5026.7	434.4
100	9B	-820.	-930.	-880.	-813.0	-940.2	-.254	-585.7	-628.1	21.1
200	9B	-1500.	-1770.	-1770.	-1500.0	-1860.0	0.000	-1103.0	-1223.0	59.9
300	9B	-2200.	-2630.	-2700.	-2197.3	-2822.6	.065	-1633.4	-1841.9	104.2
400	9B	-2920.	-3460.	-3500.	-2919.2	-3667.3	.030	-2155.3	-2404.6	124.6
500	9B	-3610.	-4310.	-4490.	-3599.8	-4673.4	.098	-2684.9	-3042.7	178.9
600	9B	-4300.	-5170.	-5330.	-4293.2	-5573.3	.072	-3202.0	-3628.7	213.3
700	9B	-5010.	-6090.	-6230.	-5005.7	-6547.5	.052	-3742.2	-4256.2	256.9
800	9B	-5700.	-7060.	-7200.	-5696.5	-7610.0	.042	-4287.2	-4925.0	318.9

Figure 14c. (cont'd)

Press		ϵ_a	ϵ_b	ϵ_c	Principal Strains		tan 2θ	Principal Stresses		Shear Stress
100	10B	-910.	-890.	-890.	-883.3	-909.9	0.000	-616.3	-625.2	4.4
200	10B	-1750.	-1710.	-1730.	-1706.9	-1753.0	-.288	-1189.9	-1205.3	7.6
300	10B	-2630.	-2650.	-2600.	-2597.6	-2655.7	4.330	-1808.7	-1828.1	9.6
400	10B	-3480.	-3490.	-3460.	-3459.0	-3494.3	2.598	-2401.0	-2412.8	5.8
500	10B	-4370.	-4370.	-4310.	-4310.0	-4389.9	.866	-2998.2	-3024.8	13.3
600	10B	-5260.	-5270.	-5210.	-5209.5	-5283.7	1.299	-3619.9	-3644.6	12.3
700	10B	-6160.	-6190.	-6120.	-6116.1	-6197.2	6.062	-4248.7	-4275.8	13.5
800	10B	-7100.	-7130.	-7050.	-7046.6	-7139.9	3.464	-4895.2	-4926.3	15.5
100	11B	-930.	-930.	-960.	-920.0	-959.9	.866	-644.1	-657.4	6.6
200	11B	-1820.	-1840.	-1930.	-1795.6	-1930.9	.599	-1267.4	-1312.5	22.5
300	11B	-2760.	-2800.	-2960.	-2717.7	-2962.2	.577	-1925.4	-2006.8	40.7
400	11B	-3640.	-3740.	-3920.	-3602.8	-3930.5	.410	-2553.0	-2662.3	54.6
500	11B	-4580.	-4660.	-4960.	-4502.0	-4964.6	.564	-3199.8	-3354.0	77.1
600	11B	-5520.	-5650.	-5940.	-5455.0	-5951.6	.456	-3865.7	-4031.2	82.7
700	11B	-6490.	-6620.	-7000.	-6397.3	-7009.3	.514	-4538.7	-4742.7	102.0
800	11B	-7470.	-7600.	-8070.	-7348.8	-8077.8	.557	-5218.5	-5461.4	121.4
100	12B	-940.	-830.	-1000.	-823.7	-1022.8	-2.944	-606.0	-672.4	33.1
200	12B	-1840.	-1710.	-1970.	-1689.8	-1990.1	0.000	-1223.8	-1323.8	50.0
300	12B	-2750.	-2570.	-2930.	-2542.1	-2957.8	0.000	-1834.5	-1973.1	69.2
400	12B	-3570.	-3440.	-3870.	-3372.0	-3881.3	2.190	-2425.8	-2595.6	84.8
500	12B	-4470.	-4330.	-4880.	-4229.9	-4890.0	1.764	-3046.9	-3266.9	110.0
600	12B	-5350.	-5200.	-5850.	-5073.6	-5859.6	1.608	-3653.6	-3915.6	130.9
700	12B	-6230.	-6080.	-6860.	-5912.0	-6867.9	1.407	-4264.5	-4583.1	159.3
800	12B	-7140.	-7010.	-7910.	-6791.6	-7915.0	1.217	-4903.5	-5278.0	187.2
100	13B	-910.	-910.	-910.	-910.0	-910.0	0.000	-629.9	-629.9	0.0
200	13B	-1790.	-1780.	-1830.	-1769.4	-1830.5	1.443	-1235.9	-1256.3	10.1
300	13B	-2670.	-2700.	-2750.	-2660.0	-2753.3	.393	-1858.2	-1889.4	15.5
400	13B	-3490.	-3530.	-3630.	-3466.7	-3633.2	.481	-2429.9	-2485.4	27.7
500	13B	-4360.	-4420.	-4520.	-4340.0	-4526.6	.393	-3038.1	-3100.3	31.1
600	13B	-5220.	-5300.	-5410.	-5199.8	-5420.1	.352	-3639.4	-3712.8	36.7
700	13B	-6080.	-6160.	-6270.	-6059.8	-6280.1	.352	-4234.8	-4308.2	36.7
800	13B	-6960.	-7140.	-7190.	-6956.9	-7236.3	.105	-4866.5	-4959.6	46.5

Figure 14c. (cont'd)

Press		ε_a	ε_b	ε_c	Principal Strains		$\frac{\tan 2\theta}{2}$	Principal Stresses		Shear Stress
100	15B	-550.	-820.	-740.	-543.1	-863.4	-.150	-433.5	-540.3	53.3
200	15B	-1220.	-1550.	-1350.	-1181.3	-1565.2	-.376	-886.7	-1014.7	63.9
300	15B	-1860.	-2260.	-1930.	-1770.0	-2263.3	-.608	-1313.9	-1478.3	82.2
400	15B	-2450.	-2970.	-2480.	-2296.2	-2970.4	-.771	-1710.7	-1935.4	112.3
500	15B	-3080.	-3690.	-3040.	-2849.3	-3690.6	-.987	-2123.6	-2404.0	140.2
600	15B	-3570.	-4340.	-3520.	-3279.2	-4340.7	-.986	-2460.7	-2814.6	176.9
700	15B	-4110.	-5020.	-3980.	-3715.6	-5024.3	-1.154	-2807.2	-3243.4	218.1
800	15B	-4610.	-5690.	-4390.	-4093.2	-5700.1	-1.309	-3122.1	-3657.8	267.8
100	1B	-130.	-80.	-70.	-56.2	-130.4	.078	-2706.6	-4356.3	824.8
200	1B	-190.	-350.	-80.	-49.8	-363.4	-4.676	-4335.9	-11303.6	3483.8
300	1B	-240.	-140.	-110.	-84.7	-241.9	.112	-4433.5	-7926.8	1746.6
400	1B	-270.	-160.	-150.	-116.4	-270.2	.037	-5606.7	-9023.[illegible]	1708.5
500	1B	-280.	-180.	-170.	-139.7	-280.2	.041	-6385.1	-9506.7	1560.8
600	1B	-300.	-190.	-190.	-153.3	-299.9	0.000	-6946.9	-10206.2	1629.6
700	1B	-310.	-210.	-230.	-188.8	-311.1	-.096	-8101.6	-10817.2	1357.8
800	1B	-330.	-220.	-240.	-195.6	-330.9	-.086	-8460.4	-11467.5	1503.5
100	2B	-90.	-70.	-30.	-28.0	-98.6	.433	-1612.4	-3180.3	783.9
200	2B	-140.	-80.	-50.	-37.0	-142.9	.173	-2229.5	-4581.2	1175.8
300	2B	-220.	-120.	-110.	-79.7	-220.2	.041	-4114.8	-7236.5	1560.8
400	2B	-290.	-140.	-140.	-90.0	-290.0	0.000	-4966.9	-9411.4	2222.2
500	2B	-360.	-150.	-150.	-80.0	-360.0	0.000	-5213.2	-11435.4	3111.1
600	2B	-410.	-160.	-180.	-89.5	-410.4	-.036	-5894.6	-13024.2	3564.8
700	2B	-440.	-160.	-200.	-91.8	-441.5	-.066	-6204.1	-13975.9	3885.8
800	2B	-450.	-220.	-250.	-162.2	-451.0	-.060	-8395.2	-14811.9	3208.3
100	3B	-20.	-90.	10.	25.9	-92.5	-2.165	55.5	-2578.0	1316.7
200	3B	-160.	-120.	-20.	-16.7	-183.2	.481	-1933.4	-5634.1	1850.3

Figure 14c. (cont'd)

Press		ϵ_a	ϵ_b	ϵ_c	Principal Strains		$\frac{\tan 2\theta}{2}$	Principal Stresses		Shear Stress
300	3B	-280.	-140.	-70.	-39.8	-286.8	.173	-3436.4	-8923.9	2743.7
400	3B	-460.	-180.	-110.	-36.1	-463.8	.096	-4707.1	-14211.7	4752.3
500	3B	-590.	-230.	-150.	-52.6	-593.9	.086	-6220.0	-18248.3	6014.1
600	3B	-720.	-240.	-180.	-38.2	-721.7	.050	-6783.7	-21973.0	7594.6
700	3B	-850.	-250.	-200.	-15.6	-850.9	.034	-7114.9	-25677.8	9281.4
800	3B	-990.	-260.	-230.	3.6	-990.3	.017	-7622.9	-29710.4	11043.7
100	4B	-60.	-80.	10.	11.2	-97.9	1.558	-426.9	-2852.2	1212.6
200	4B	0.	-130.	-50.	15.7	-135.7	-.384	-587.6	-3952.9	1682.6
300	4B	30.	-240.	-170.	35.1	-288.4	-.128	-1197.3	-8388.2	3595.4
400	4B	50.	-360.	-270.	55.4	-442.1	-.106	-1785.9	-12844.6	5529.3
500	4B	120.	-450.	-360.	123.8	-583.8	-.074	-839.6	-16565.7	7863.0
600	4B	130.	-520.	-450.	131.9	-691.9	-.049	-1439.3	-19749.8	9155.2
700	4B	170.	-570.	-540.	170.3	-796.9	-.017	-1108.2	-22603.4	10747.6
800	4B	210.	-560.	-620.	211.1	-857.7	.032	-357.4	-24111.0	11876.8
800	3A	190.	100.	50.	195.0	31.0	0.376	5828.0	2187.0	2120.0
800	6A	-7500.	-4200.	-4100.	-3033.0	-7500.0	0.0258	-3332.0	-4822.0	1660.0

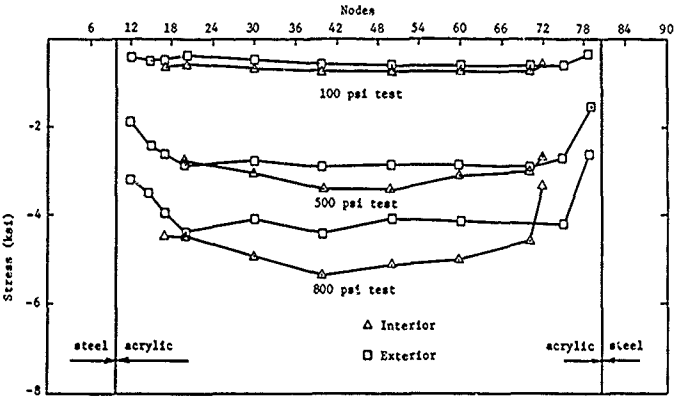

Figure 15a. Distribution of Hoop Stresses on the NEMO acrylic hull.

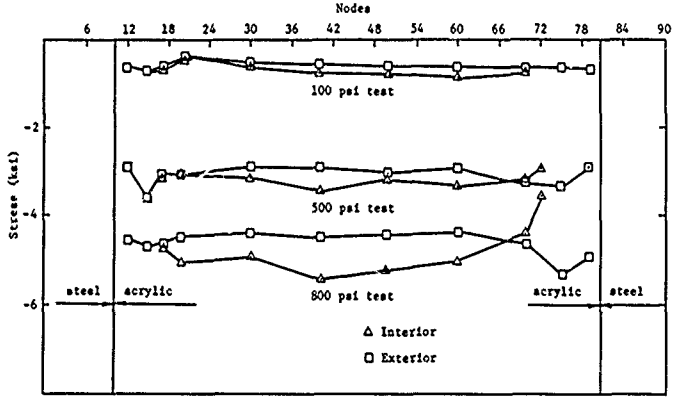

Figure 15b. Distribution of Meridional Stresses on the NEMO acrylic hull.

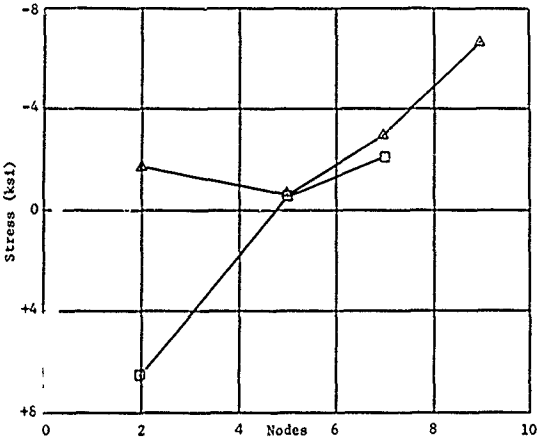

Figure 16a. Hoop stresses on bottom steel plate under 100 psi hydrostatic loading.

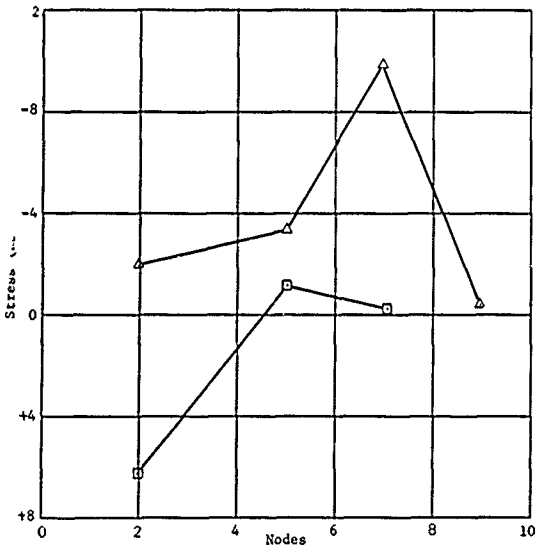

Figure 16b. Meridional Stresses on Bottom Steel Plate Under 100 psi Hydrostatic Loading.

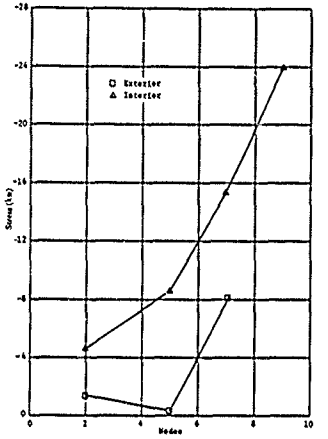

Figure 17a Hoop stresses on bottom steel plate under 500 psi hydrostatic loading

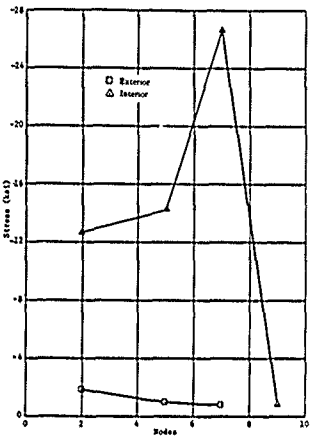

Figure 17b Meridional stresses on bottom steel plate under 500 psi hydrostatic loading

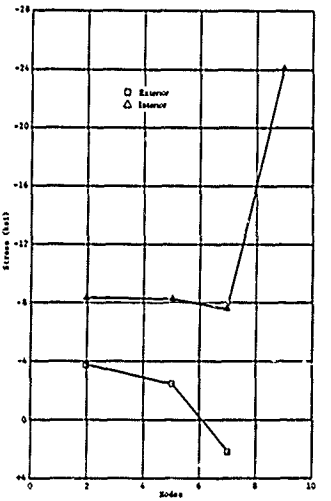

Figure 18a Hoop stresses on the bottom steel plate under 800 psi hydrostatic loading.

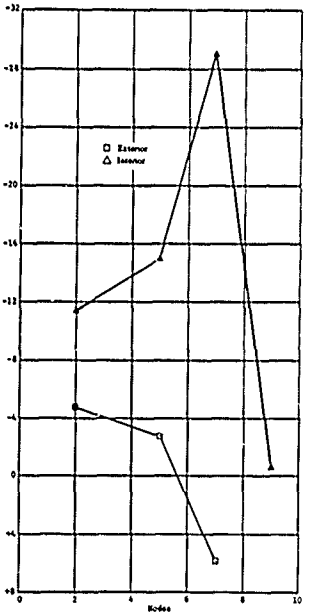

Figure 18b Meridional stresses in bottom steel plate under 800 psi hydrostatic loading

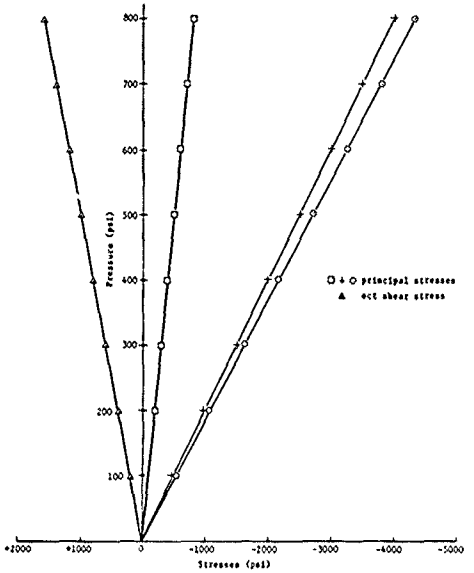

Figure 19a Typical stresses on the exterior of acrylic hull in the equatorial region, Rosette 12A under short-term loading to 800 psi

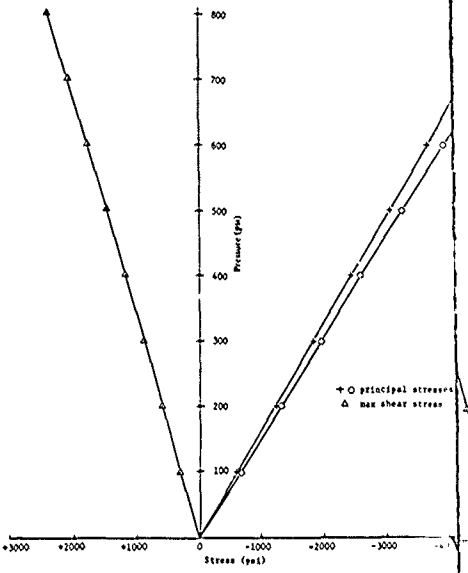

Figure 19b Typical stresses on the interior of acrylic hull in the equatorial region, Rosette 12B under short-term loading to 800 psi

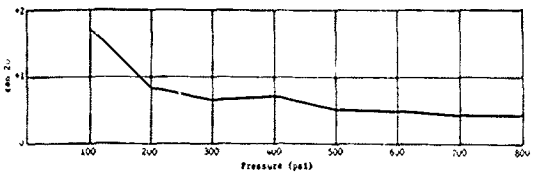

Figure 19d Change in orientation of principal strains on the exterior surface of the acrylic hull in equatorial region, Rosette 12A under short-term loading to 800 psi

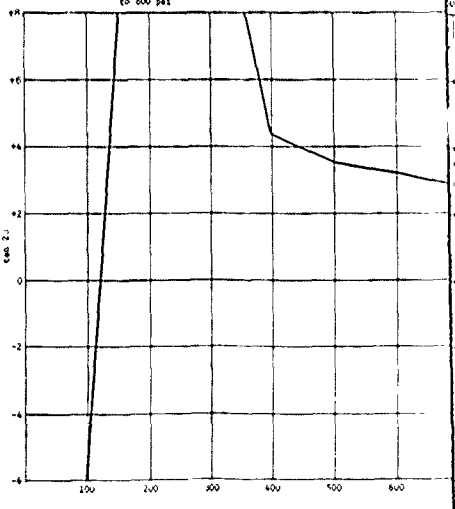

Figure 19e Change in orientation of principal strains on the interior surface of the acrylic hull in equatorial region Rosette 12B under short-term loading to 800 psi

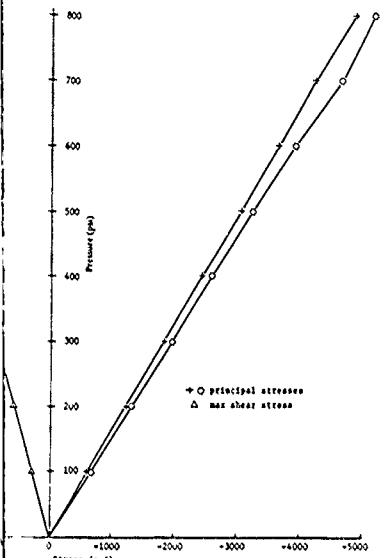

al stresses on the interior of acrylic hull in the
rial region, Rosette 12B under short-term loading
0 psi

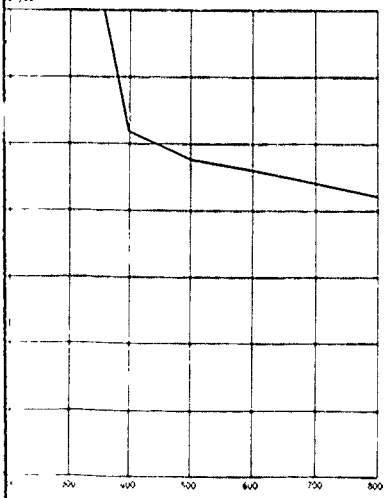

rientation of principal strains on the interior
the acrylic hull in equatorial region, Rosette 12B
rt-term loading to 800 psi

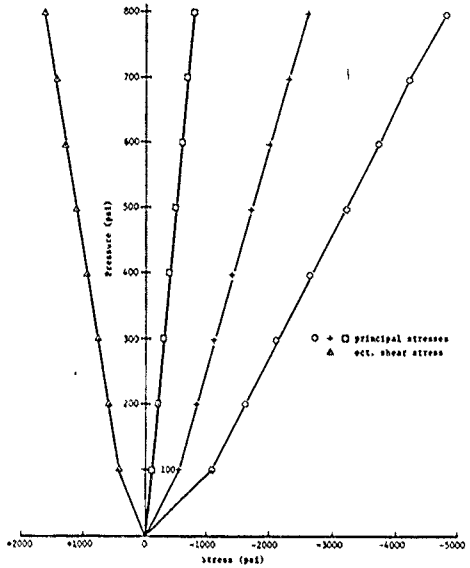

Figure 19c Stresses on the exterior of the hull near polar penetration, Rosette 18A under short-term loading to 800 psi

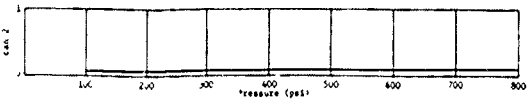

Figure 19f Change in orientation of principal strains on the exteri r surface of the acrylic hull near polar penetration, Rosette 18A under short-term loading to 800 psi

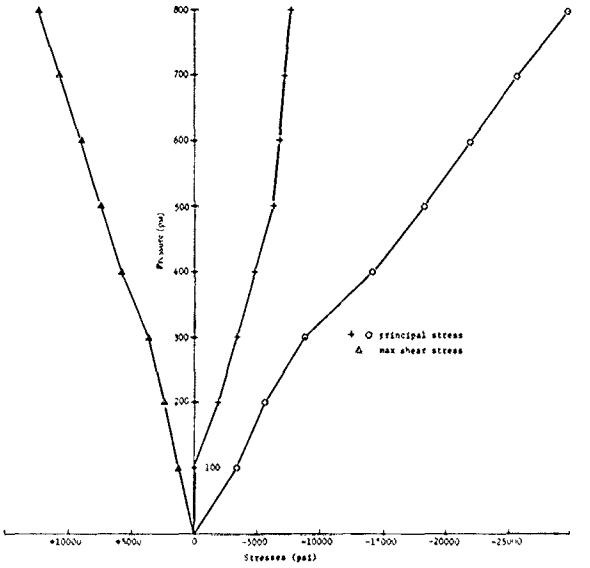

Figure 20a Stresses on the highest stressed location on the interior surface of bottom steel plate, Rosette 3B under short-term loading to 800 psi

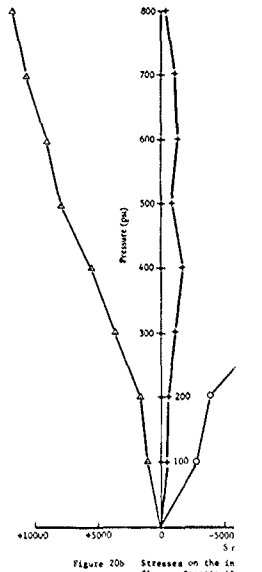

Figure 20b Stresses on the in flange, Rosette 4B

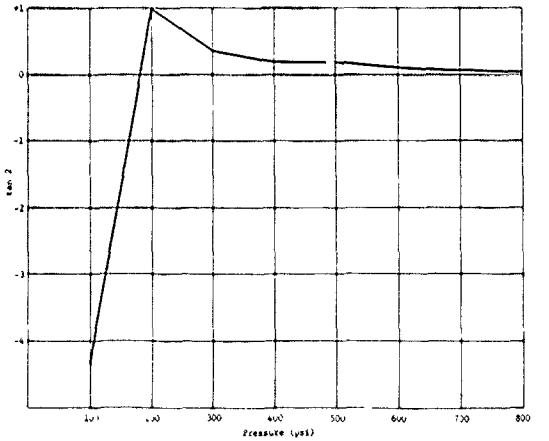

Figure 20c Change in orientation of principal strains on the interior surface of the bottom steel plate, Rosette 3B under short-term loading to 800 psi

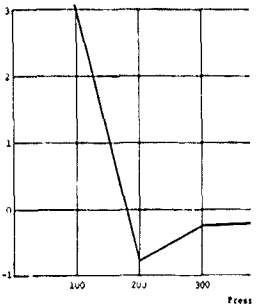

Figure 20d Change in orientatio surface of the botto term loading to 80

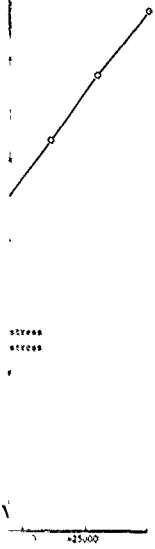

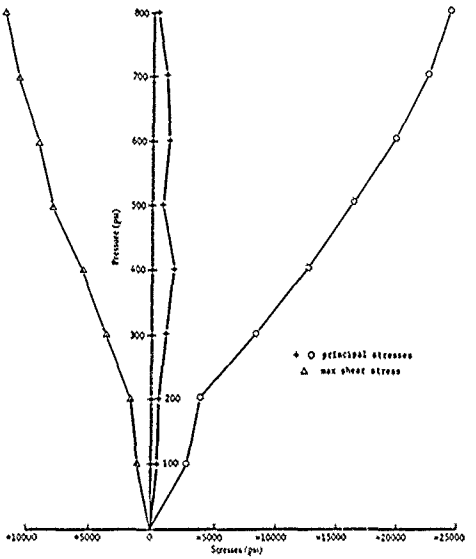

Figure 20b. Stresses on the interior surface of steel bottom plate flange, Rosette 4B under short-term loading to 800 psi.

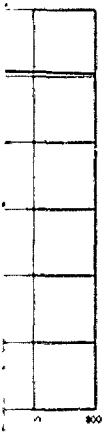

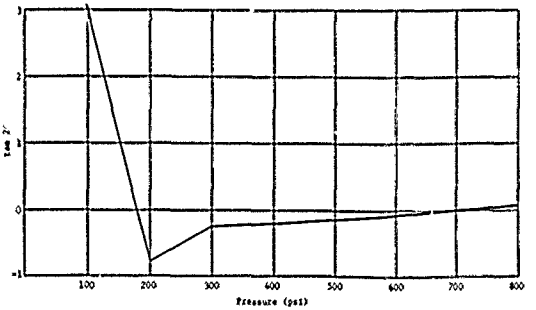

Figure 20d. Change in orientation of principal strains on the interior surface of the bottom steel plate, Rosette 4B under short-term loading to 800 psi.

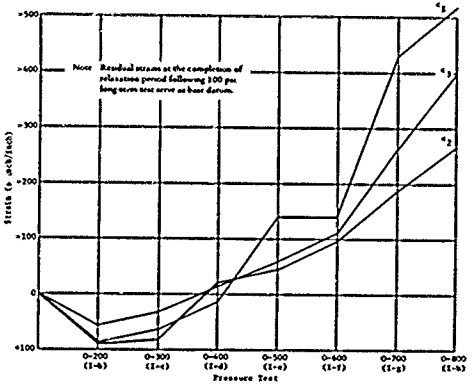

Figure 21a Residual strains on the exterior of the hull in the equatorial region at the conclusion of each long-term test; Rosette 12A

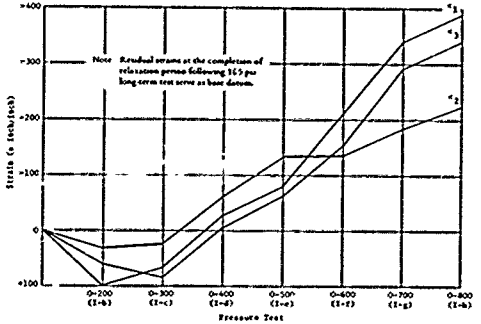

Figure 21b Residual strains on the interior of the hull in equatorial region at the conclusion of each long-term test; Rosette 12B

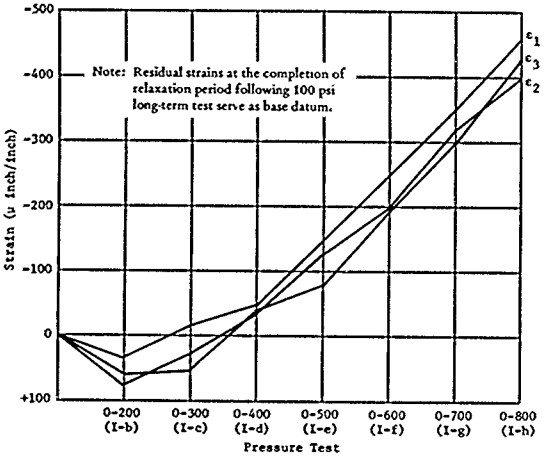

Figure 21c. Residual strains on the exterior of the acrylic hull at the polar penetration at the conclusion of each long-term test; Rosette 18A.

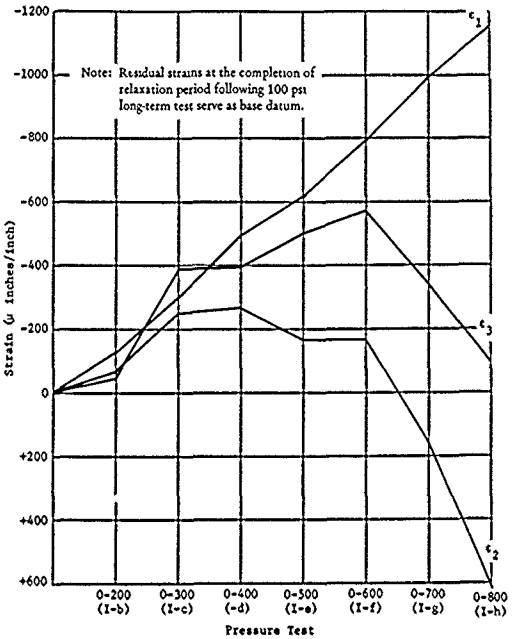

Figure 22a. Residual strains on the interior of bottom steel plate at the conclusion of each long-term test; Rosette 3B.

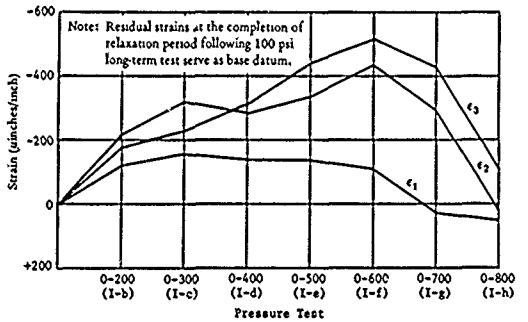

Figure 22b. Residual strains on the interior surface of steel bottom plate flange; Rosette 4B under short-term loading to 800 psi.

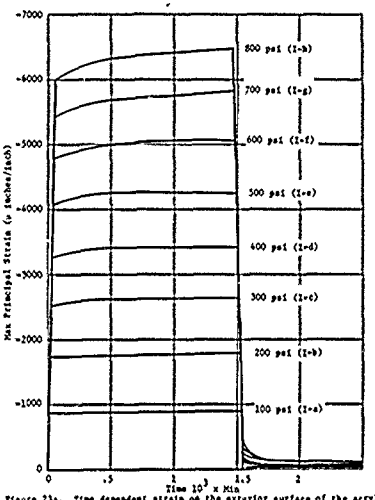

Figure 23a. Time dependent strain on the exterior surface of the acrylic hull in equatorial region; Rosette 12A under long-term hydrostatic loadings to different pressures.

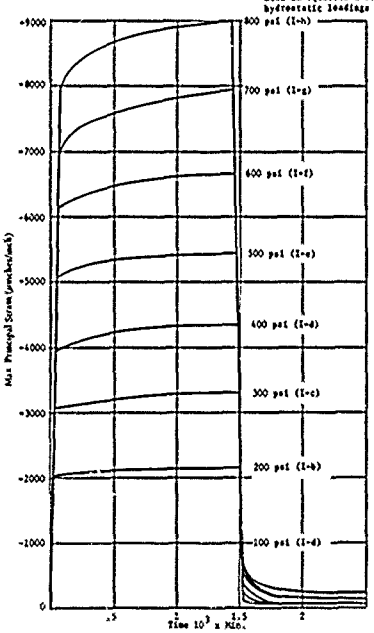

Figure 23b Time dependent strain on the interior surface of the acrylic hull in the equatorial region; Rosette 22b under long-term hydrostatic loadings to different pressures.

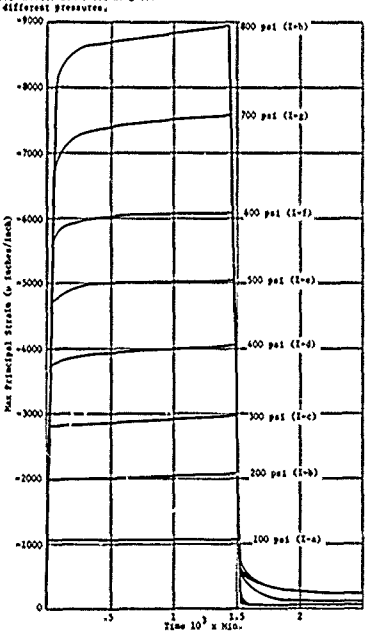

Figure 23c Time dependent strain on the exterior surface of the acrylic hull near polar penetration, Rosette 18A under long-term hydrostatic loadings to different pressures.

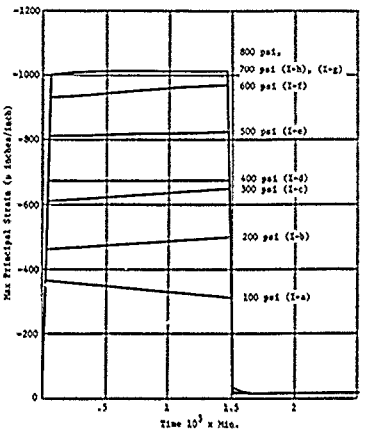

Figure 24a. Time dependent strain on the internal surface of the bottom steel plate; Rosette 38 under long-term hydrostatic loadings to different pressures.

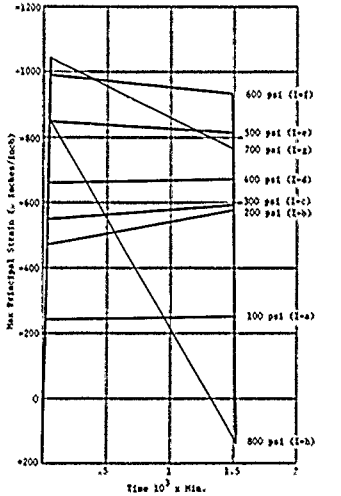

Figure 24b. Time dependent strain on the internal surface of the bottom steel plate flange; Rosette 43 under long-term hydrostatic loadings to different pressures.

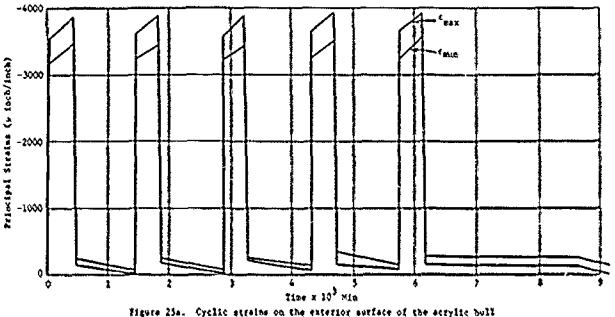

Figure 25a. Cyclic strains on the exterior surface of the acrylic hull in equatorial region; Rosette 10A under pressure cycles of 500 psi magnitude and 6-hour duration.

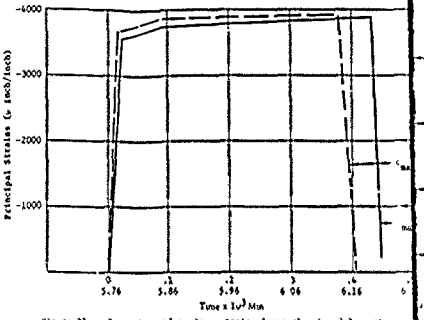

Figure 25c Comparison of maximum strains for cycles 1 and 5 on the exterior surface of the acrylic hull in equatorial region; Rosette 10A under pressure cycles of 500 psi magnitude and 6-hour duration.

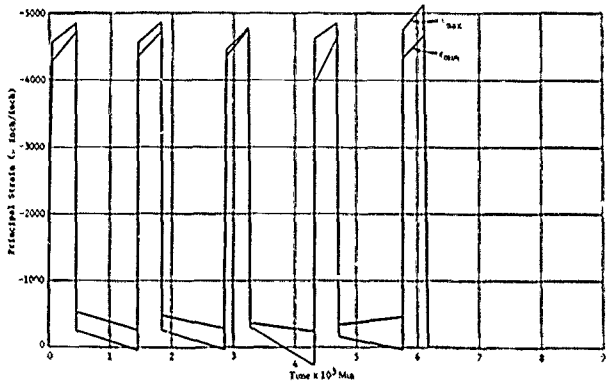

Figure 25b. Cyclic strains on the interior surface of the acrylic hull in equatorial region, Rosette 10B under pressure cycles of 500 psi magnitude and 6-hour duration.

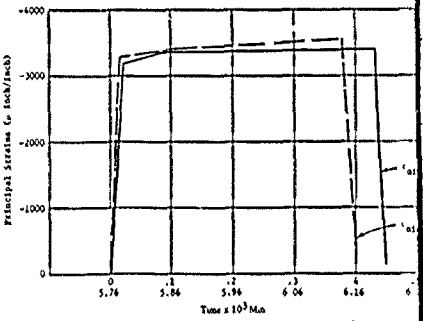

Figure 25d Comparison of minimum strains for cycles 1 and 5 on the exterior surface of the acrylic hull in equatorial region Rosette 10A under pressure cycles of 500 psi magnitude and 6-hour duration

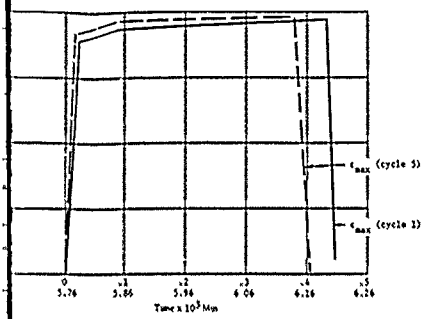

re 25c. Comparison of maximum strains for cycles 1 and 5 on the exterior surface of the acrylic hull in equatorial region; Rosette 10A under pressure cycles of 500 psi magnitude and 6-hour duration.

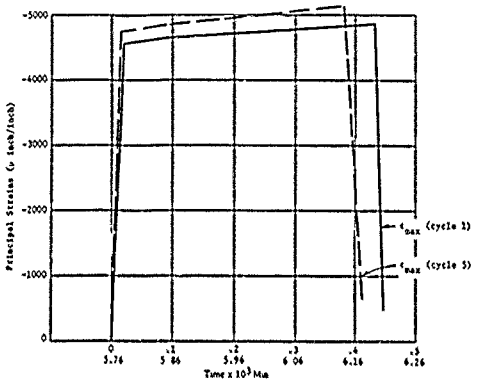

Figure 25e. Comparison of maximum strains for cycles 1 and 5 on the interior surface of the acrylic hull in equatorial region; Rosette 10B under pressure cycles of 500 psi magnitude and 6-hour duration.

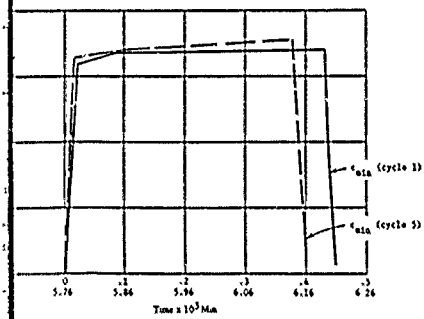

re 25d Comparison of minimum strains for cycles 1 and 5 on the exterior surface of the acrylic hull in equatorial region, Rosette 10A under pressure cycles of 500 psi magnitude and 6-hour duration.

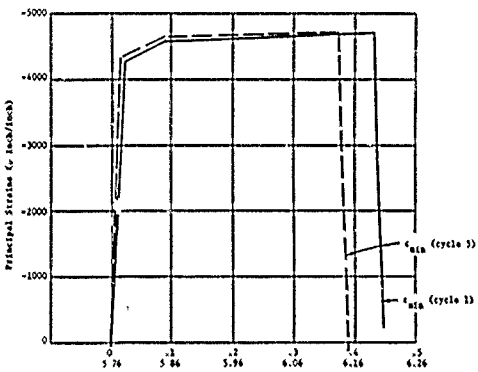

Figure 25f. Comparison of minimum strains for cycles 1 and 5 on the interior surface of the acrylic hull in equatorial region, Rosette 10B under pressure cycles of 500 psi magnitude and 6-hour duration.

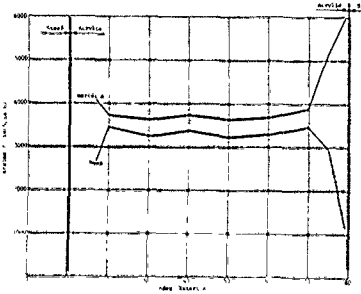

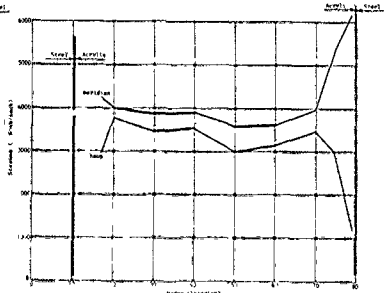

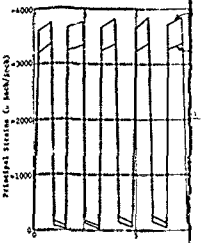

Figure 27a Cyclic stress in equatorial 500 psi magn

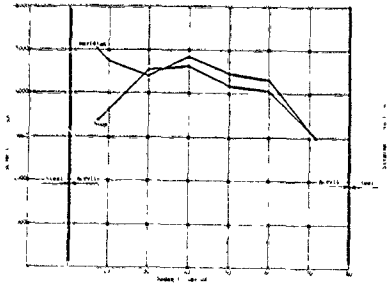

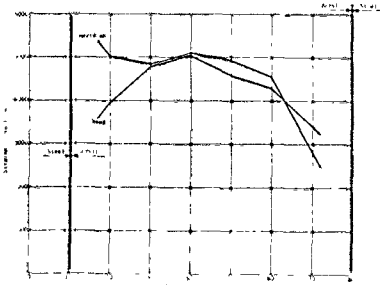

Figure 27c Comparis

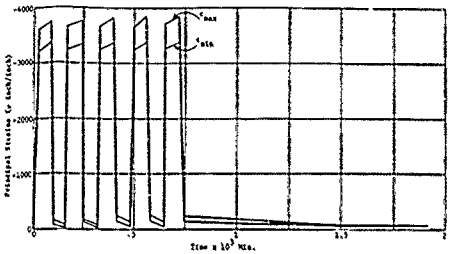

Figure 27a. Cyclic strains on the exterior surface of the acrylic hull in equatorial region; Rosette 10A under pressure cycles of 500 psi magnitude and 1-hour duration.

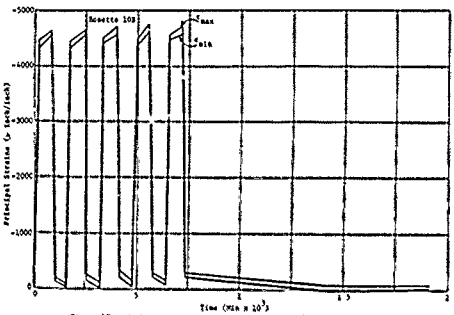

Figure 27b Cyclic strains on the interior surface of the acrylic hull in equatorial region; Rosette 10A under pressure cycles of 500 psi magnitude and 1-hour duration

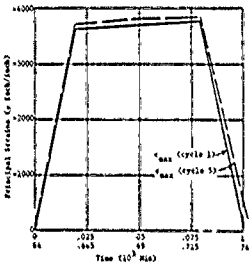

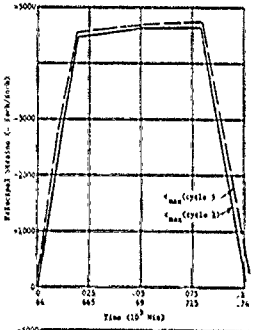

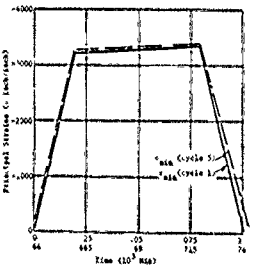

Figure 27c Comparison of maximum and minimum strains for cycles 1 and 5 at the interior surface of the acrylic hull in equatorial region, Rosette 10A under pressure cycles of 500 psi magnitude and 1-hour duration.

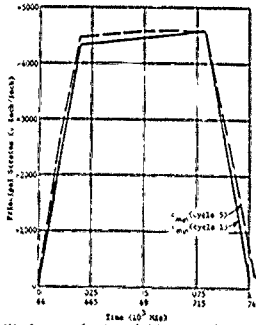

Figure 27d Comparison of maximum and minimum strains for cycles 1 and 5 at the interior surface of the acrylic hull in equatorial region, Rosette 10B under pressure cycles of 500 psi magnitude and 1-hour duration

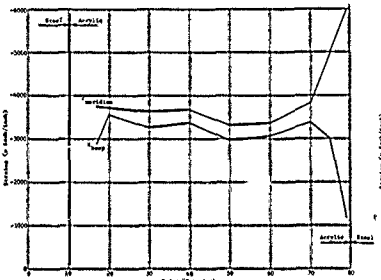

Figure 24a Distribution of hoop and meridional strains on the exterior surface of acrylic hull at the beginning of the second 1-hour pressure cycle at 300 psi

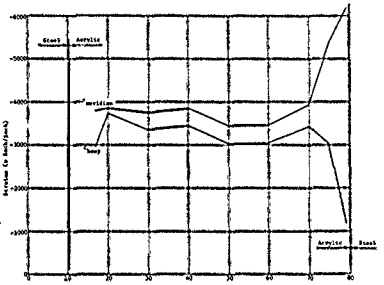

Figure 24b Distribution of hoop and meridional strains on the exterior surface of acrylic hull at the termination of the second 1-hour pressure cycle at 300 psi

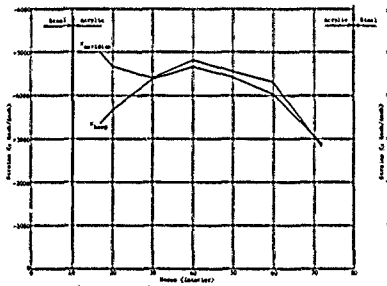

Figure 24c Distribution of hoop and meridional strains on the interior surface of acrylic hull at the beginning of the second 1-hour pressure cycle at 300 psi

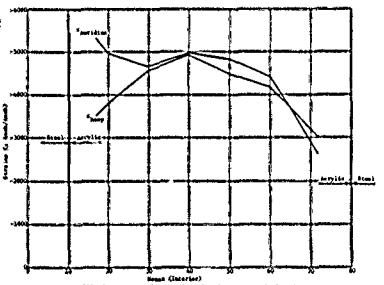

Figure 24d Distribution of hoop and meridional strains on the interior surface of acrylic hull at the termination of the second 1-hour pressure cycle at 300 psi

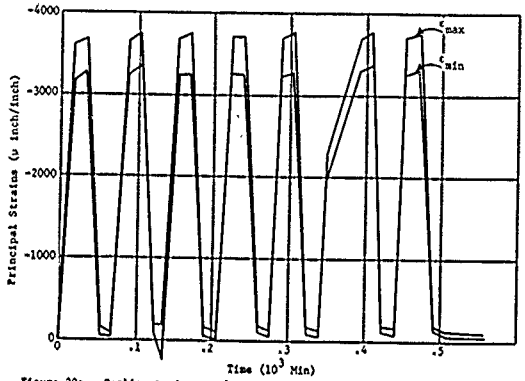

Figure 29a. Cyclic strains on the exterior surface of the acrylic hull in equatorial region; Rosette 10A under pressure cycles of 500 psi magnitude and 15-minute duration.

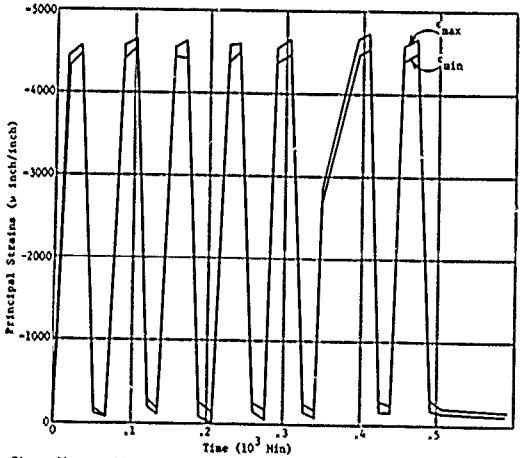

Figure 29b. Cyclic strains on the interior surface of the acrylic hull in equatorial region; Rosette 10B under pressure cycles of 5000 psi magnitude and 15-minute duration.

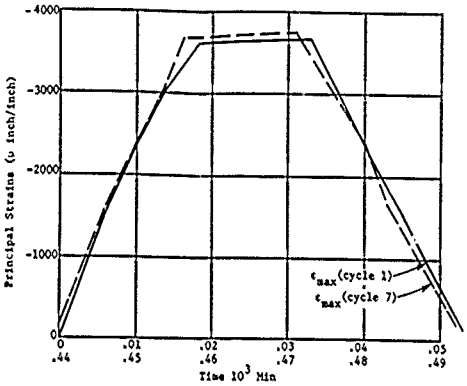

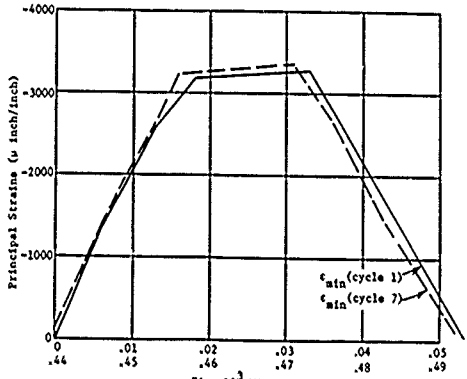

Figure 29c. Comparison of maximum and minimum strains for cycles 1 and 7 on the exterior surface of the acrylic hull in equatorial region; Rosette 10A under pressure cycles of 500 psi magnitude and 15-minute duration.

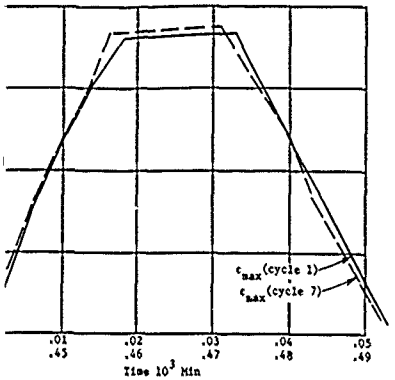

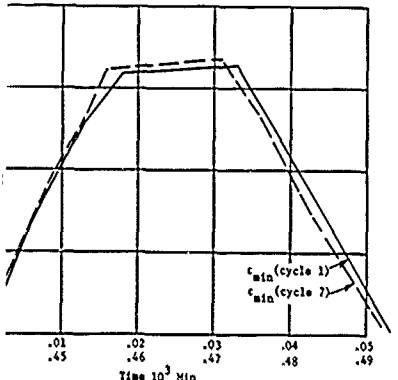

Comparison of maximum and minimum strains for cycles 1 and 7 on the exterior surface of the acrylic hull in equatorial region; Rosette 10A under pressure cycles of 500 psi magnitude and 15-minute duration.

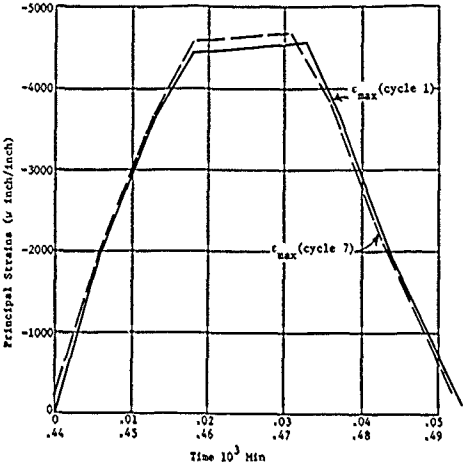

Figure 29d. Comparison of maximum strains for cycles 1 and 7 on the interior surface of the acrylic hull in equatorial region; Rosette 10B under pressure cycles of 500 psi magnitude and 15-minute duration.

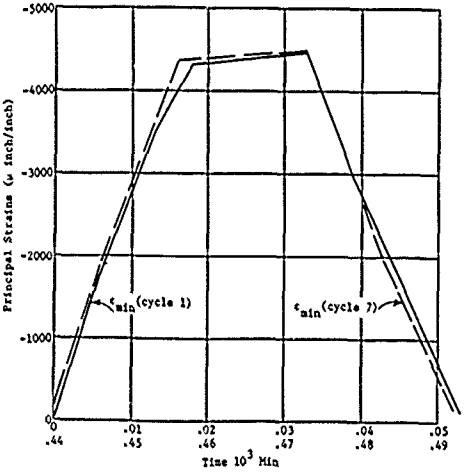

Figure 29e. Comparison of minimum strains for cycles 1 and 7 on the interior surface of the acrylic hull in equatorial region; Rosette 10B under pressure cycles of 500 psi magnitude and 15-minute duration.

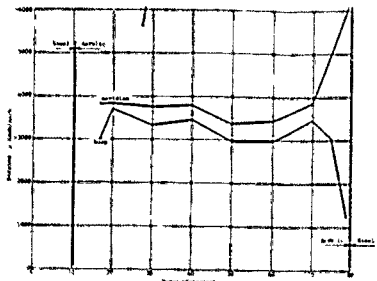

Figure 34b. Distribution of hoop and meridional stresses on the exterior surface of acrylic hole at the horizontal at the second pressure cycle at 500 psi

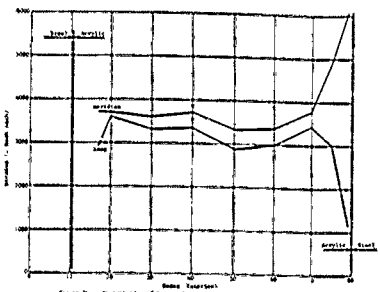

Figure 34c. Distribution of hoop and meridional stresses on the exterior surface of acrylic hole at the beginning of the second pressure cycle at 500 psi

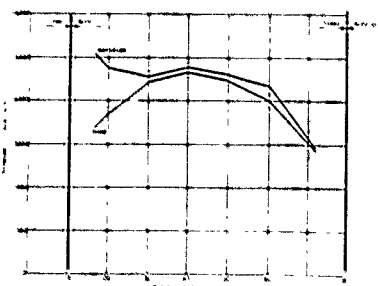

Figure 34e. Distribution of hoop and meridional stresses on the exterior surface of acrylic hole at the beginning of the second pressure cycle at 500 psi

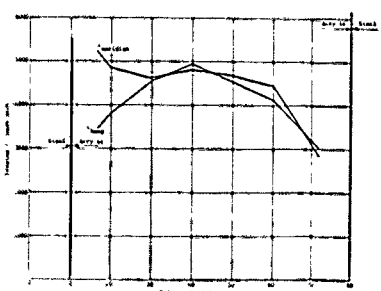

Figure 34d. Distribution of hoop and meridional stresses on the exterior surface of acrylic hole at the termination of the second pressure cycle at 500 psi

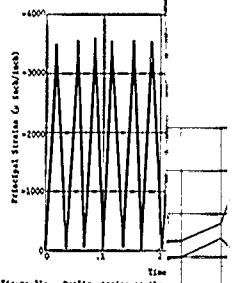

Figure 34a. Cyclic strains on the in equatorial region: 500 psi magnitude and

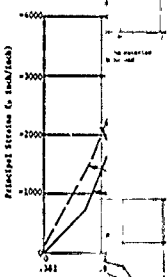

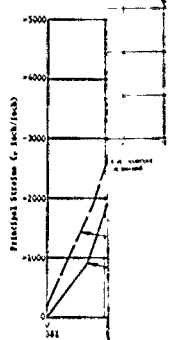

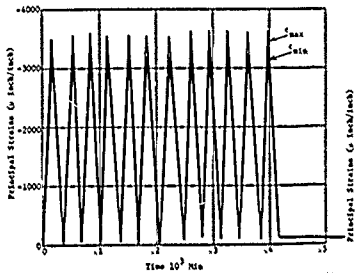

Figure 31a. Cyclic strains on the exterior surface of the acrylic hull in equatorial region; Rosette 10A under pressure cycles of 500 psi magnitude and 2-minute duration.

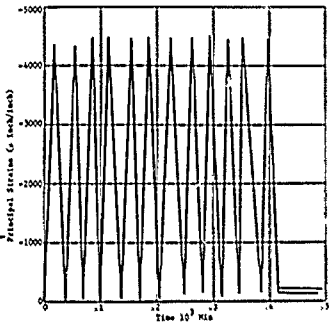

Figure 31b. Cyclic strains on the interior surface of the acrylic hull in equatorial region; Rosette 10B under pressure cycles of 500 psi magnitude and 2-minute duration.

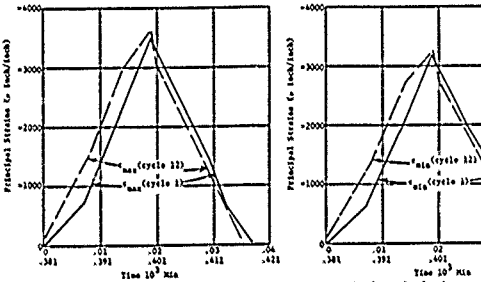

Figure 31c. Comparison of maximum and minimum strains for cycles 1 and 12 on the exterior surface of the acrylic hull in equatorial region; Rosette 10A under pressure cycles of 500 psi magnitude and 2-minute duration.

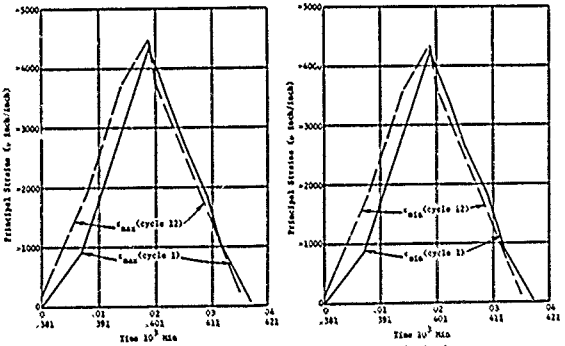

Figure 31d Comparison of maximum and minimum strains for cycles 1 and 12 on the interior surface of the acrylic hull in equatorial region; Rosette 10B under pressure cycles of 500 psi magnitude and 2-minute duration.

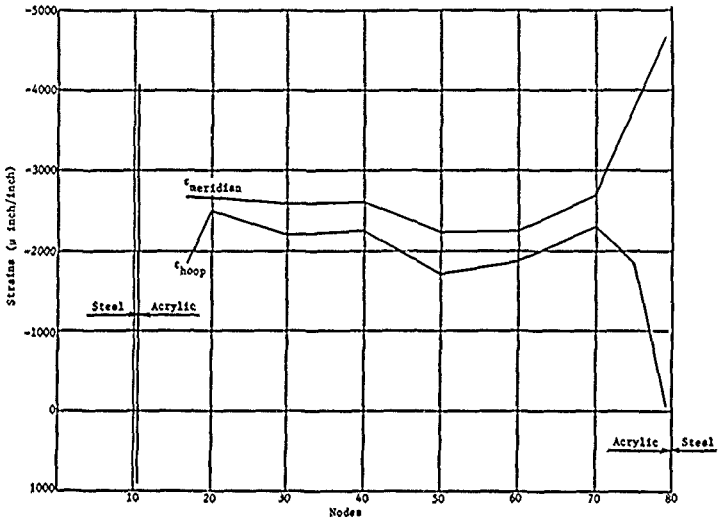

Figure 32a. Distribution of hoop and meridional strains on the exterior surface of acrylic hull at the midpoint of the second 2-minute pressure cycle at 500 psi.

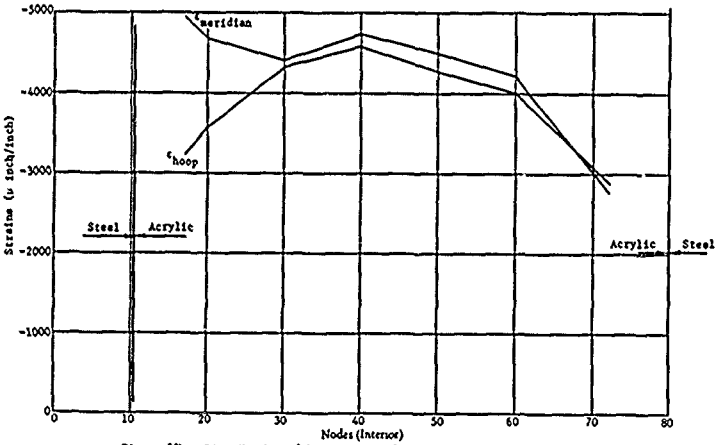

Figure 32b. Distribution of hoop and meridional strains on the interior surface of acrylic hull at the midpoint of the second 2-minute pressure cycle at 500 psi.

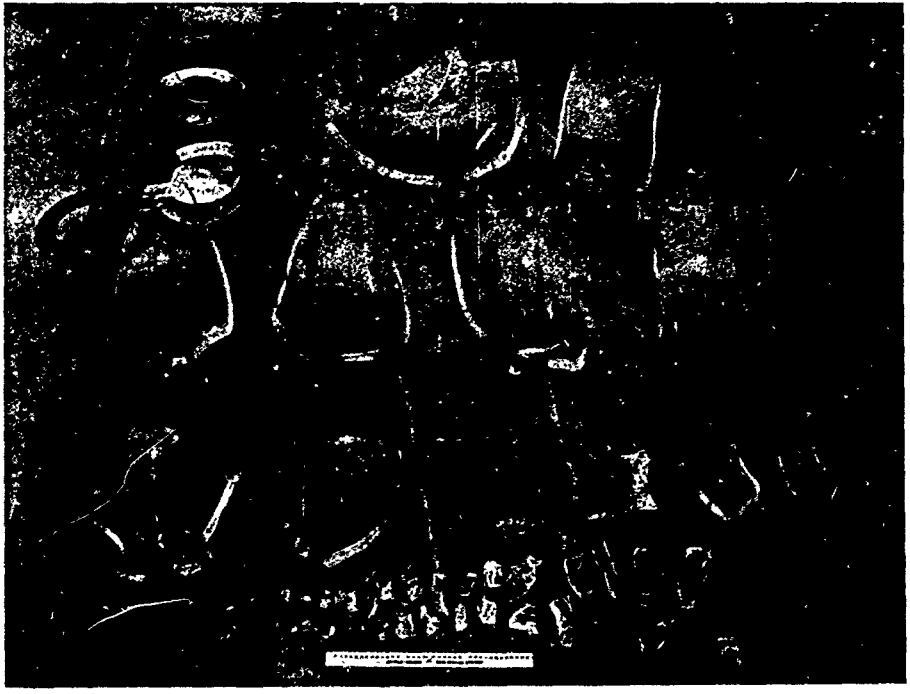

Figure 33. Fragments of imploded NEMO capsule.

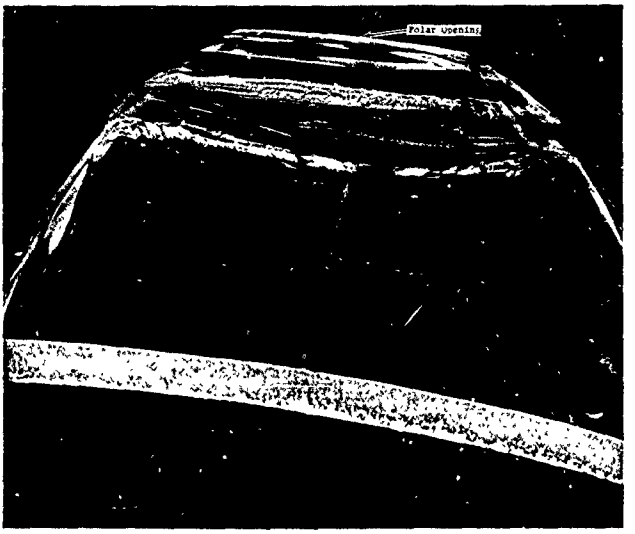

Figure 34a. Fragment from the polar pentagon in contact with the bottom steel penetration plate; exterior surface.

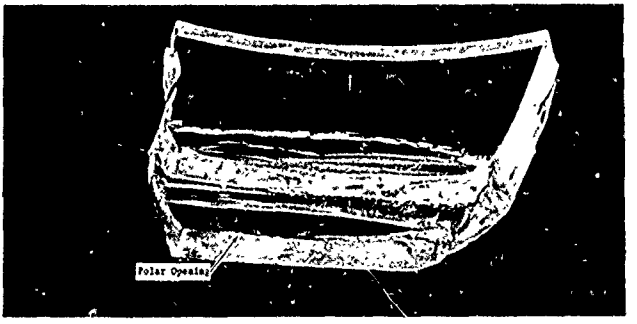

Figure 34b. Fragment from the polar pentagon in contact with the bottom steel penetration plate; interior surface. Note extensive spalling on the acrylic bearing surface in contact with steel plate.

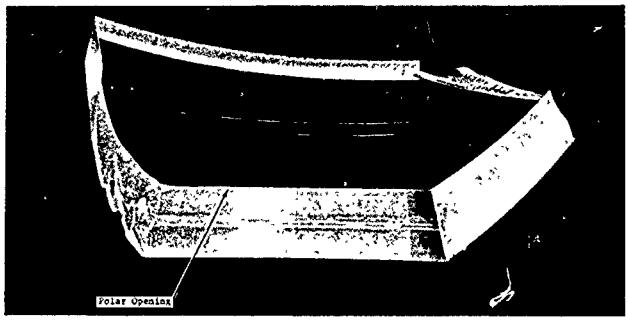

Figure 35a. Fragment from the polar pentagon in contact with the top hatch ring; interior surface. Note only minor cracking on the acrylic bearing surface.

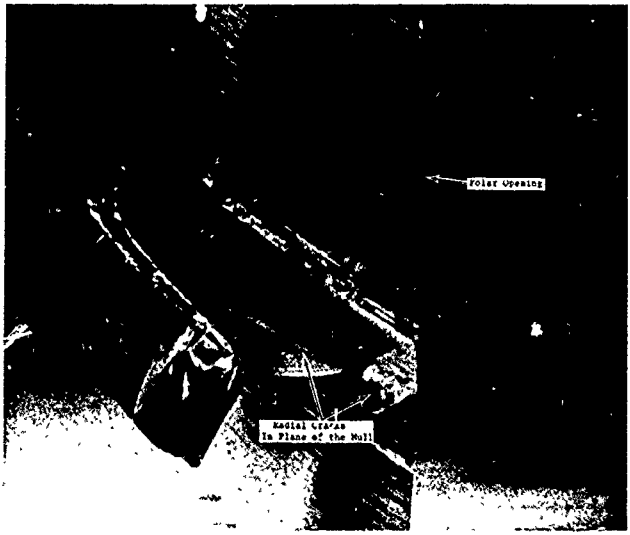

Figure 35b. Section through the top polar pentagon in contact with the top hatch ring. Note that the crack is in the plane of hull and approximately at middle of its thickness.

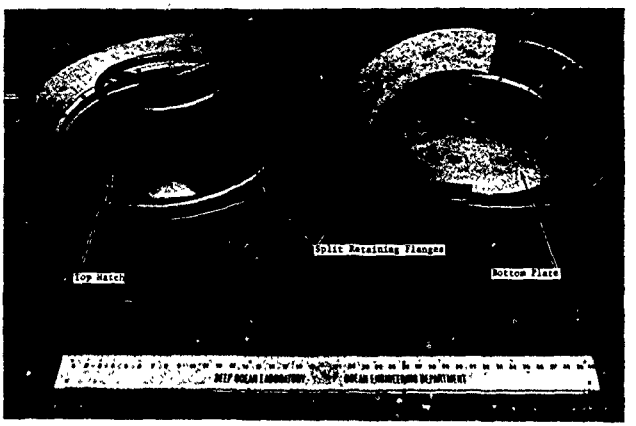

Figure 36a. Plastically deformed steel parts from the imploded NEMO hull.

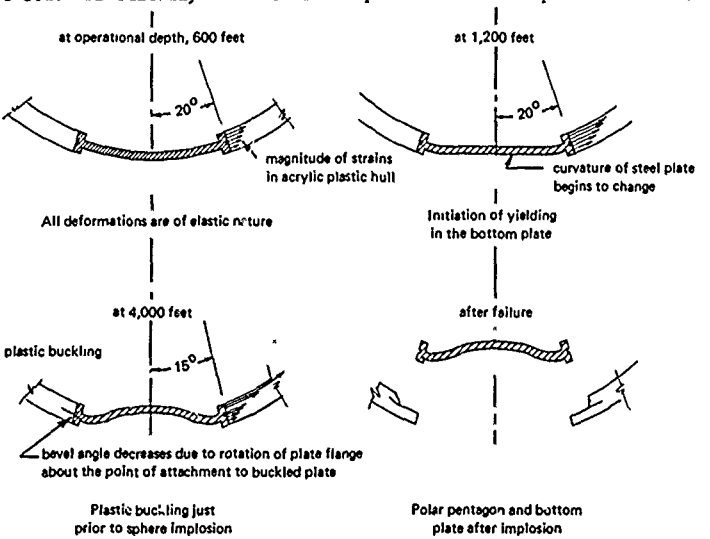

Figure 36b. Mechanism of spalling in the bottom polar acrylic pentagon reconstructed from observation of deformation in the bottom steel plate and fracture in the bottom polar acrylic pentagon.

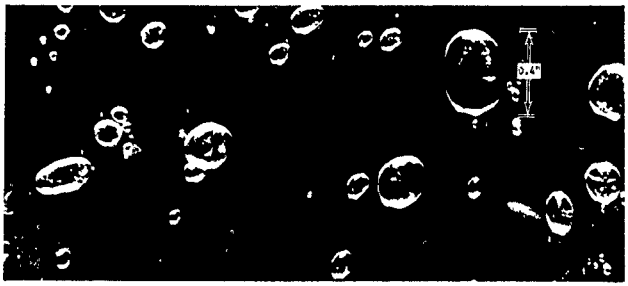

Figure 37a. Typical air cavities in the NEMO joints bonded with PS-18 self-polymerizing adhesive.

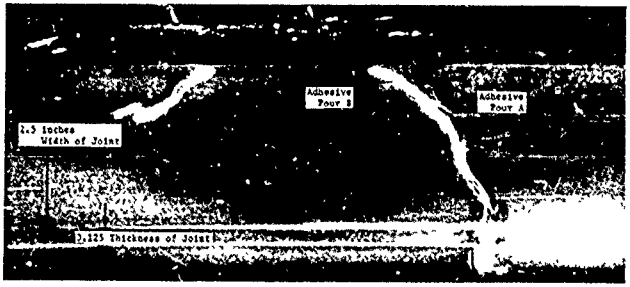

Figure 37b. Typical joint discontinuity at the interface of two successive adhesive pours.

Figure 37c. Typical joint discontinuity that has been routed out and refilled with new adhesive. Note the presence of fine incipient cracks at the edges of the refilled cavity.

Technical Note N-1094

THE SPHERICAL ACRYLIC PRESSURE HULL FOR HYDROSPACE APPLICATION; PART III - COMPARISON OF EXPERIMENTAL AND ANALYTICAL STRESS EVALUATIONS FOR PROTOTYPE NEMO CAPSULE

By

H. Ottsen and J. D. Stachiw

March 1970

NAVAL CIVIL ENGINEERING LABORATORY
Port Hueneme, California 93041

THE SPHERICAL ACRYLIC PRESSURE HULL FOR HYDROSPACE APPLICATION; PART III COMPARISON OF EXPERIMENTAL AND ANALYTICAL STRESS EVALUATIONS FOR PROTOTYPE NEMO CAPSULE

Technical Note N-1094

YF-38.535.005.01.006

by

H. Ottsen

ABSTRACT

A comparison is presented of results obtained from analytical and experimental stress analyses of the NEMO pressure hull (an acrylic submersible with steel polar penetrations). The general procedures of the analytical investigation are reviewed and the assumptions stated. Excellent agreement between the two sets of results was observed for the acrylic portion of the hull. Due to the severe structural simplification necessary in the analytical simulation of the steel polar penetrations, discrepancies were noted in the two sets of stresses obtained in these regions; general trends were, however, similar. It was concluded that the acrylic to steel transitions incorporated in the prototype design provide an optimum transfer of load without inducing a concentration of stresses.

INTRODUCTION

It has been stated[1] that a safe and efficient means of protecting man in hydrospace may be provided by a system with the following characteristics: (1) undistorted and extensive observation capabilities, and (2) the same breathing mixture and ambient pressure as that found on land. These features were incorporated in an observatory called NEMO (Naval Experimental Manned Observatory) which was proposed by the Naval Missile Center (NAVMISCEN). The concept introduced with the NEMO is basically that of a transparent pressure hull manufactured from cast acrylic sheets which are thermo-formed and machined into spherical pentagons and then bonded together. Provisions are made to incorporate the means necessary for entering and exiting the capsule, the life support and communication systems, the power supply, and the anchoring and hoisting devices in the design of the observatory.

The structural concept of NEMO is illustrated in Figure 1. The acrylic sphere is, as indicated, formed by cementing twelve pentagons together. The two polar pentagons are fitted with stainless steel hatches for entering and exiting the vehicle and to provide the necessary penetrations for power, communication and control conduits. The steel cage shown in Figure 1b, is included in the design in order to relieve the acrylic hull of any tensile stresses which would otherwise result in the hull during hoisting of the submersible. Besides providing this tensile restraint, the only other function of the cage would be to offer some protection of the hull against possible accidental impacts. Structurally the cage would - under normal operating conditions - have no effect on hull stresses.

The general dimensions of the NEMO prototype are: 66-inch outside diameter and 2.5-inch hull thickness. The purpose of the NEMO is to permit non-divers to enter hydrospace to observe and evaluate working operations and conditions in the submarine environment.

An extensive experimental study has been made of the response of acrylic hulls to short term, cyclic and sustained loadings.[1] This work involved the testing of twenty-two 15-inch diameter models in addition to the thorough testing of a full-sized capsule. A detailed description of the testing program and the results obtained may be found in Reference 1.

In order to support some of the experimental findings, an analytical determination[2] was made of the response of the NEMO sphere to various short term loading conditions. The present report will review the procedures used in this analysis and the results obtained relating to the hydrostatic loading conditions examined experimentally. A discussion will be included comparing the analytical and experimental findings.

Description of Analysis

Program Features. The main part of the analysis was performed using a computer program called SEAL-SHELL-2, a digital computer program for the stress analysis of a thick shell of revolution with axisymmetric pressures, temperatures, and distributed loads. The shell is divided into 2 to 100 segments each of which have the following characteristics:

1. Each segment may have different elastic properties.
2. Each segment may be loaded with different pressures.
3. Each segment may have a curved middle surface, or it may be straight as part of a flat plate, cylinder, or cone.
4. Each segment may have a temperature distribution varying arbitrarily through the thickness but varying linearly along the segment.
5. Each segment may have a linearly varying thickness.
6. Each segment may have a radial load, an axial load, and a bending moment applied externally.
7. Middle surface shifts are allowed between segments.

Using segments with the above mentioned characteristics, the analysis of the shell may be performed as described in the following section.

Basic Procedure for Analysis. An arbitrary set of 11 deflection shapes is applied to each segment and the resulting strain energy is determined with the restrictions posed by the following basic assumptions:

1. The Bernoulli-Navier assumption from beam theory that plane cross sections which are plane before bending remain plane after bending, and
2. The assumption that shear stress varies parabolically through the thickness (this, also, is taken from beam theory).

By the principle of virtual work, the strain energy of each segment is used to determine the forces on the segment in terms of the deflections they produce. Solving the resulting set of simultaneous equations and using the requirement that displacements and rotations at the joint between adjacent segments be equal, the stresses in the shell may be determined for a given external loading.

The first step in this procedure is to define segment strain in terms of the segment displacements U, V, and W. The above mentioned arbitrary set of 11 displacements is then defined in terms of U, V, and W. From these two relationships, the segment strains are expressed in terms of the arbitrary displacements.

With these expressions for the strain and utilizing the stress-strain temperature relations pertaining to the material in question, expressions may be generated relating stresses to the arbitrary displacements. Combining the obtained expressions for stresses and strains, the internal work done during an arbitrary virtual displacement, as defined by the mentioned arbitrary set of displacements, may be determined. Equating the internal work to the work done by the externally applied forces through the above virtual displacement, equations are obtained relating segment deflections to segment forces. Equating displacements and rotations at the joints of the segments, the stresses connecting the segments are then defined.

In order to include shear deformations in the analysis, simple beam theory is applied to each segment and the resulting flexibility in shear is included in the expression for the total flexibility of the segment.

By these general procedures, equations have been generated relating internal stresses in the hull to the externally applied loads. Simple back-substitution yields the corresponding deflections.

For purposes of the present study, the hull is divided into ninety 2° segments. The segments corresponding to the steel hatches include Nos. 1-10 and 81-90, while segment Nos. 11-80 represent the acrylic hull.

Presentation of Results

Analytical Results. A variety of loading conditions were analyzed using the SEAL-SHELL-2 program in an effort to determine the most severe combination of loadings to which the shell could be exposed. The present report will concern itself only with the short term loading conditions which were investigated experimentally, namely the hydrostatic pressure combined with the tether force loading. The stresses induced by a 500 psi pressure and a 4000 lb tether force are plotted in Figure 2.* The following observations may be made from the analytically obtained stress distributions:

1. Significant effect of the polar end-closures is limited to regions within 10° - 20° of the penetration.
2. Stresses in the remaining portions of the hull reveal very small bending moments and good correspondence of meridional and hoop stresses.
3. The meridional and hoop stresses in the equatorial regions range between 3.0 and 3.5 ksi approximately. Somewhat higher stresses are encountered in the polar inserts due to the mismatch in rigidity between the steel hatches and the acrylic hull. It should be noted, in observing the stress distributions in the hatches, that simplifying

* A tabulation of the calculated stresses is presented in Table 1.

assumptions were necessary in the analytic treatment of this portion of the vessel. Thus, the analytical results in this region may not be entirely correct, although they probably reflect the trends well.

Comparison of Analytic and Experimental Results - Acrylic Hull. Strain gage data was obtained from both 15" diameter NEMO models and two 66" diameter prototypes.[1] The data from the 15" diameter models provides detailed stress distributions in the immediate vicinity of the polar hatch openings in addition to stress values in the equatorial region. The prototype was instrumented to yield the stress distributions along a meridian with some concentration of readings occurring in the regions of the hatch openings.

In order to make the data from the 15" diameter model compatible with the analytical data obtained, a simple dimensional analysis was necessary. The results of this analysis provide the following scaling laws as related to applied pressures, concentrated loads, buoyancy, and weight of spherical hulls:

1. Hull stresses in spheres of equal c/d ratio (thickness to diameter ratio) resulting from applied pressures of the same magnitude are equal;
2. Hull stresses in two spheres of equal t/d ratio, resulting from applied concentrated loads, are related to these concentrated loads by the reciprocal of the ratio of the diameters squared:

$$\frac{\sigma_1}{\sigma_2} = \left(\frac{d_2}{d_1}\right)^2 \frac{P_1}{P_2}$$

3. Hull stresses are linearly related to the magnitude of applied pressures and concentrated loads;
4. The buoyancy of the vessel scales according to the cube of the hull diameter, and
5. Weight of the hull scales according to the cube of the hull diameter for constant t/d ratios.

From these observations, it may be noted that comparisons of data obtained from spheres of varying sizes cannot be made when the loadings consist of various combinations of applied pressures and concentrated loads. These combined loading conditions do exist when the spheres are subjected to hydrostatic pressure and the pressurizing agent is water. Besides being subjected to the hydrostatic pressure, the spheres must, under these conditions, also resist the effects of the tether force and the net buoyancy of the vessel. However, as shown in Reference 2, these additional effects are insignificant and may be neglected in the comparisons. Thus, the data obtained from the 15" diameter NEMO models may be compared to data obtained experimentally and analytically for the 66" diameter prototype, and the comparisons may be based solely upon applied hydrostatic pressure.

The experimental results, as reported in References 1, 4, and 5 showing the stress distributions in the immediate vicinity of the polar hatch openings, have been reproduced in Figures 3 and 4. Also included in these plots, for purposes of comparison, are the appropriate analytical results.[2] Much of the experimental data in this region was obtained from a 15" NEMO model; these stresses were measured at an applied hydrostatic pressure of 100 psi. In order to obtain a common basis for the comparisons and since the analytic results are based upon a pressure level of 500 psi, the experimentally obtained stresses (for the 15" diameter model) have been scaled up by a factor of five. This scaling, which is justified assuming elastic conditions, accounts for the high stress levels in Figures 3 and 4, which in some cases, are shown to be above the compressive short term strength of the acrylic of 15,000 psi. In the actual model, localized plastic flow would, of course, have occurred at the 500 psi pressure level, thus relieving the high stresses.

Experimental data obtained from the testing of two 66" diameter NEMO prototypes has also been included in Figures 3 and 4. It may be observed that the data obtained from the prototypes is in excellent agreement with the analytical results, whereas the data obtained from the model reveals a substantial stress concentration within two node points (0.07 radians) of the hatch. This discrepancy may be attributed to (1) differences in hatch design, and (2) different hatch placement procedures for model and prototype. Figure 5 shows the prototype, model, and the analytically simulated hatch designs. The different conditions prevailing at the acrylic to steel transition in the three cases may clearly be observed. The most gradual transition seems to have been incorporated in the prototype design due to the presence of the neoprene gaskets and the retaining flanges (Figure 5a). The hatch placement procedure for the 66" diameter prototype involves a tightening of the bolts connecting the retaining flange to the hatch ring. This "pre-tensioning" will also tend to provide for a continuous transfer of stresses between the acrylic and steel portions of the hatch. The design of the 15" diameter model, on the other hand, does not include the gasket and the retaining flange. Furthermore, the hatch is secured, initially, by a set of tension springs, the effects of which are relaxed when the sphere deforms under hydrostatic loading. Thus, a lower degree of structural continuity appears to be provided in the hull to hatch transition in the case of the 15" diameter model.

The transition between the acrylic hull and the steel hatch is analytically assumed to be a simple change of materials with a gradual reduction in thickness from the acrylic to the steel portions of the hull (Figure 5c). The ratio of the two thicknesses employed* provides for a good continuity of flexibility across the transition as evidenced by the relatively constant stress level predicted analytically in the acrylic hull right up to the acrylic-steel interface (Figures 3 and 4).

* The hatch thickness was originally chosen to provide a hatch collapse strength approximately equal to that of the acrylic hull.

A high stress level is then predicted in the steel because of the equilibrium requirements imposed upon the thinner hatch section.

Thus, it appears that the stress levels predicted analytically in the acrylic hull are in excellent agreement with the empirical results. The experimental data obtained from the 66" diameter prototypes practically coincides with the analytical results. The stresses in a small region adjacent to the hatch, as measured in a 15" diameter model, deviate somewhat from those measured in the prototype and those predicted analytically. As discussed above, this discrepancy is peculiar to the 15" diameter model only and is probably caused by variations in hatch designs. In mentioning the stress concentrations measured in the model, it should be noted that applied hydrostatic pressures substantially higher than 500 psi were successfully resisted by all the models subjected to short term loading.[4] This demonstrates that the acrylic hull has a propensity to flow and will relax conditions in regions of severe stress concentration.

The stress distributions in regions of the acrylic hull away from the hatches, obtained from the testing of the 66" diameter spheres, [1, 5] are presented in Figures 6 and 7. Also included for comparison are the corresponding stresses obtained analytically. In these comparisons, also, excellent agreement is noted between empirical and analytical results.

Comparison of Analytic and Experimental Results-Steel Hatch. The comparisons of the analytically and experimentally determined stresses in the steel hatch portion of the NEMO hull present some basic difficulties due to the simplifications necessary in the analytic study. These simplifications included:

1. The mentioned analytic treatment of the transition between the acrylic hull and the steel hatch. As discussed previously, the analytic study assumes a simple, gradual change in thickness at the acrylic-steel interface, whereas, the actual hatch design contains several thick ring elements.
2. The actual bottom plate includes several thickness variations which provide reinforcement at the conduit penetrations (Figure 5a). The analytical model assumes a constant thickness (0.8 in.) slightly larger than the nominal thickness of the hatch (0.550 in.) to account for the reinforcement. Thus, the structural characteristics of the actual and analytical models are sufficiently different to prevent a detailed comparison of the two sets of results. General trends may, however, be examined.

Figures 8 and 9 show the analytical stress distributions along with the appropriate experimental values. It may be noted that the gross trends in the two sets of results are similar and the stresses found by the two methods are of the same order of magnitude. In examining the variation of the meridional stresses on the internal and external

surfaces, and noting that the difference between these two stresses at any given section is a measure of the bending moment induced at that section, the stiffening effect of the thickness increase at node 5 is clearly distinguishable. Similar trends may also be observed in the distribution of the hoop stresses.

A closer analytical simulation of the hatches would require a more detailed analysis than the one performed in the present study.

Summary and Conclusions

An analytical study[2] was made of the response of an acrylic pressure hull with steel polar penetrations (NEMO) to a variety of loadings.

The program used (SEAL-SHELL-2) utilized a displacement method to analyze shells of revolution subjected to axisymmetric loads. Modifications were included in the analysis to make it applicable to thick shells. The present report analyzes the results of the study and compares them with experimental data. The findings are:

1. The most severe loading case was found to be the hydrostatic loading.
2. The effects of tether force and net buoyancy were found to be negligible in comparison with the effect of hydrostatic loading, allowing experimental data obtained from a 15" diameter NEMO model to be compared with the results (experimental and analytical) obtained for the 66" diameter prototype.
3. With the structural simplifications of the polar penetrations assumed in the analytical study, good continuity of flexibility across the acrylic to steel interface was observed in the analytical results.
4. Comparisons of analytical results and the experimental data obtained from the 66" diameter NEMO prototypes revealed an excellent agreement between the two sets of results.
5. Experimental data obtained from the 15" diameter NEMO model indicated that stress concentrations were present in the model in regions immediately adjacent to the steel hatches. However, these increases in stress levels appear to be peculiar to the 15" diameter model only and appear to be caused by differences in model and prototype hatch designs.
6. The general trends in the analytically and experimentally determined stress distributions in the steel hatches were found to be similar. Deviations in the specific stress values in the two sets of results may be attributed to the structural simplifications necessary in the analytic study of the steel hatches.

In summary it may be concluded that excellent agreement exists between the analytically and experimentally determined stress distributions. Particularly good agreement was observed for the stresses found in the acrylic portions of the hull. It was noted that the acrylic to steel transitions incorporated in the prototype design provide an optimum transfer of loads without inducing a concentration of stresses.

Table 1. TABULATION OF ANALYTICAL RESULTS

Node	External Surface		Internal Surface	
	Meridional Stress (psi)	Hoop Stress (psi)	Meridional Stress (psi)	Hoop Stress (psi)
1	- 4608	- 2091	- 9743	-11013
2	- 4901	- 3709	- 8947	-10579
3	- 4682	- 4583	- 9441	-10767
4	- 3562	- 4847	-11001	-11707
5	- 1830	- 4804	-13295	-13335
6	+ 232	- 4747	-16060	-15632
7	+ 2289	- 4989	-19004	-18589
8	+ 3909	- 5874	-21742	-22161
9	+ 4518	- 7769	-23744	-26217
10	- 4850	- 4308	- 3387	-32907
11	- 2898	- 1490	- 4806	- 2723
12	- 3184	- 1861	- 4221	- 2829
13	- 3386	- 2184	- 3806	- 2922
14	- 3523	- 2457	- 3520	- 3008
15	- 3608	- 2684	- 3331	- 3088
16	- 3655	- 2869	- 3216	- 3163
17	- 3672	- 3017	- 3154	- 3232
18	- 3668	- 3132	- 3132	- 3294
19	- 3650	- 3220	- 3136	- 3350
20	- 3622	- 3285	- 3159	- 3400
21	- 3588	- 3332	- 3194	- 3443
22	- 3552	- 3363	- 3234	- 3479
23	- 3515	- 3383	- 3278	- 3509
24	- 3480	- 3394	- 3320	- 3533
25	- 3447	- 3397	- 3361	- 3552
26	- 3418	- 3397	- 3398	- 3567
27	- 3391	- 3392	- 3431	- 3578
28	- 3369	- 3386	- 3460	- 3586
29	- 3350	- 3378	- 3485	- 3591
30	- 3334	- 3370	- 3505	- 3594
31	- 3322	- 3362	- 3522	- 3595
32	- 3312	- 3355	- 3535	- 3595
33	- 3605	- 3348	- 3545	- 3594
34	- 3299	- 3342	- 3553	- 3593
35	- 3295	- 3337	- 3558	- 3591
36	- 3293	- 3332	- 3562	- 3589
37	- 3292	- 3329	- 3564	- 3586
38	- 3291	- 3326	- 3566	- 3584
39	- 3291	- 3324	- 3566	- 3582

Table 1. (cont'd)

Node	External Surface		Internal Surface	
	Meridional Stress (psi)	Hoop Stress (psi)	Meridional Stress (psi)	Hoop Stress (psi)
40	- 3292	- 3322	- 3566	- 3581
41	- 3292	- 3321	- 3566	- 3579
42	- 3293	- 3320	- 3565	- 3578
43	- 3293	- 3320	- 3565	- 3578
44	- 3294	- 3320	- 3564	- 3577
45	- 3294	- 3320	- 3564	- 3577
46	- 3295	- 3321	- 3564	- 3578
47	- 3295	- 3322	- 3564	- 3579
48	- 3295	- 3323	- 3564	- 3580
49	- 3294	- 3324	- 3564	- 3581
50	- 3294	- 3326	- 3564	- 3583
51	- 3294	- 3329	- 3564	- 3585
52	- 3294	- 3331	- 3563	- 3588
53	- 3295	- 3335	- 3562	- 3590
54	- 3296	- 3338	- 3560	- 3593
55	- 3298	- 3343	- 3557	- 3595
56	- 3302	- 3348	- 3552	- 3598
57	- 3307	- 3354	- 3546	- 3600
58	- 3313	- 3361	- 3537	- 3602
59	- 3322	- 3369	- 3525	- 3602
60	- 3334	- 3377	- 3510	- 3602
61	- 3348	- 3385	- 3491	- 3600
62	- 3366	- 3392	- 3468	- 3595
63	- 3387	- 3399	- 3441	- 3589
64	- 3412	- 3404	- 3409	- 3579
65	- 3441	- 3406	- 3373	- 3566
66	- 3473	- 3404	- 3332	- 3548
67	- 3509	- 3396	- 3289	- 3525
68	- 3546	- 3380	- 3245	- 3497
69	- 3584	- 3353	- 3201	- 3463
70	- 3622	- 3312	- 3161	- 3422
71	- 3655	- 3254	- 3130	- 3375
72	- 3682	- 3173	- 3114	- 3321
73	- 3696	- 3067	- 3121	- 3260
74	- 3693	- 2928	- 3163	- 3192
75	- 3664	- 2753	- 3252	- 3118
76	- 3601	- 2535	- 3408	- 3038
77	- 3493	- 2269	- 3653	- 2951
78	- 3326	- 1951	- 4018	- 2857
79	- 3084	- 1577	- 4544	- 2750
80	- 2745	- 1148	- 5283	- 2619

Table 1. (cont'd)

Node	External Surface		Internal Surface	
	Meridional Stress (psi)	Hoop Stress (psi)	Meridional Stress (psi)	Hoop Stress (psi)
81	- 7453	-12943	-15341	-24635
82	+ 5282	- 6831	-31187	-24047
83	+ 313	- 7430	-25739	-18821
84	- 4375	- 8941	-20962	-15210
85	- 8314	-10807	-17169	-12930
86	-11340	-12667	-14382	-11654
87	-13447	-14336	-12457	-11090
88	-14644	-15819	-11133	-11052
89	-14514	-17705	- 9831	-11763
90	- 5019	-33935	- 1881	-22166

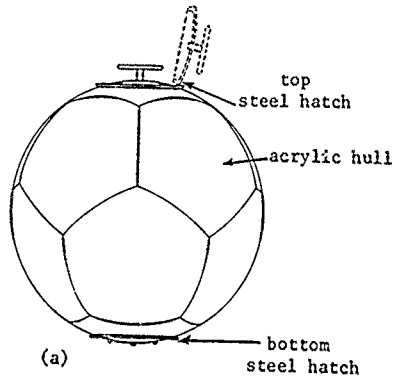

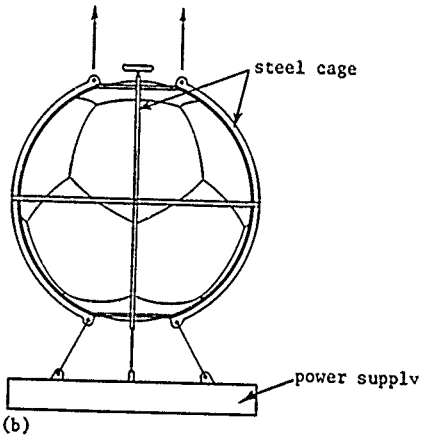

Figure 1. Structural Concept of NEMO (Ref. 1)

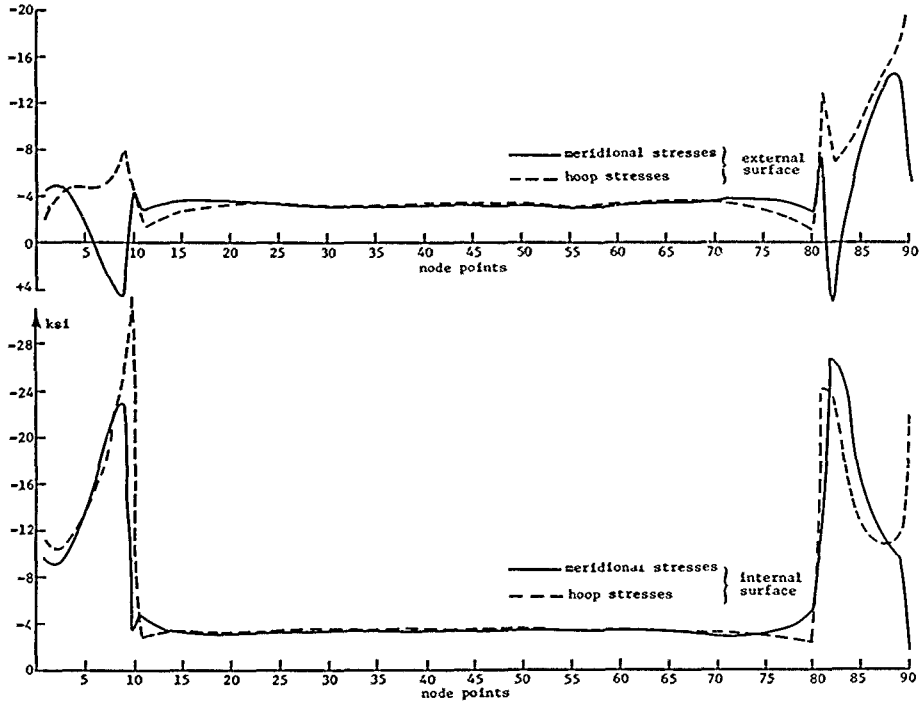

Figure 2. Analytically Determined Stresses in NEMO Hull; 500 psi Hydrostatic Pressure and 4000 Pound Tether Force

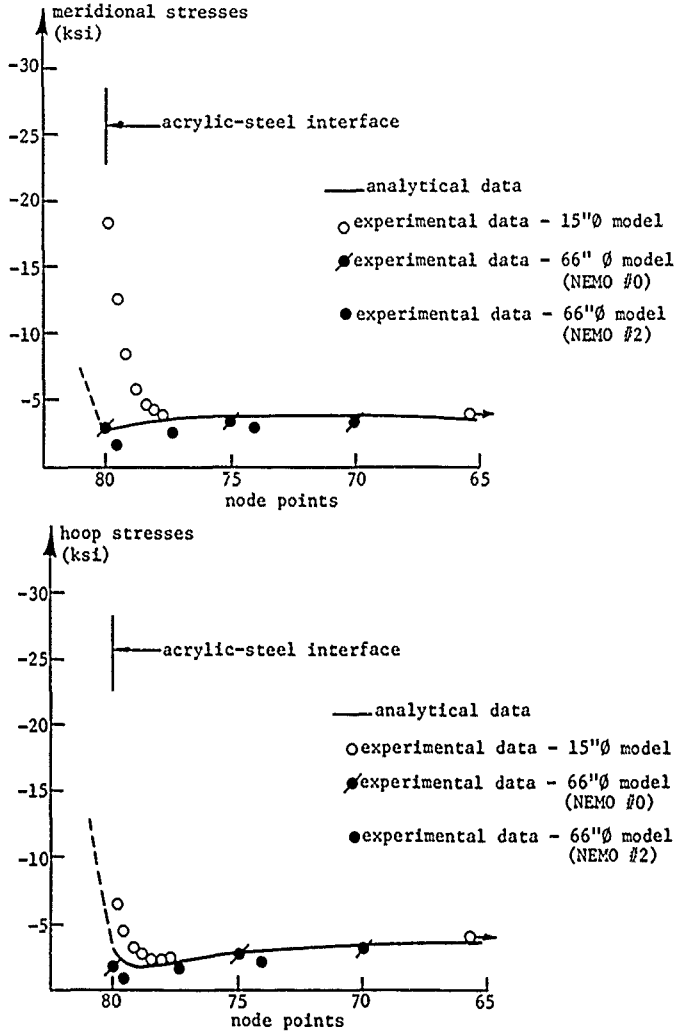

Figure 3. Comparison of Analytically and Experimentally Determined Stresses on External Surface of NEMO Hull in Immediate Vicinity of Hatch Opening; 500 psi Hydrostatic Pressure.

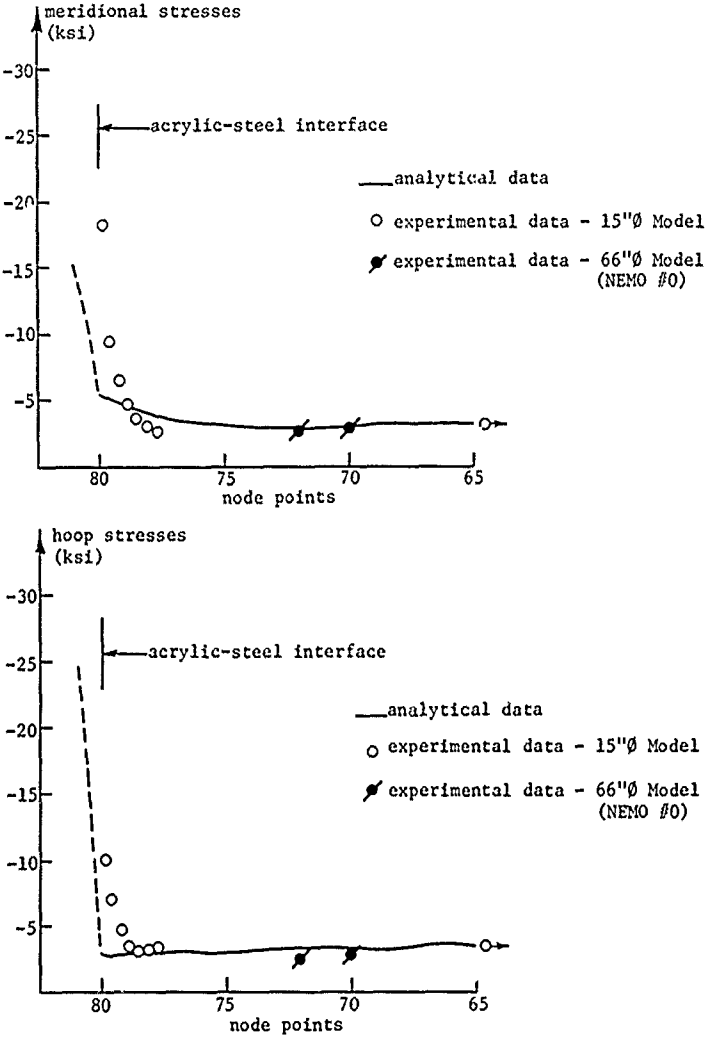

Figure 4. Comparison of Analytically and Experimentally Determined Stresses on Internal Surface of NEMO Hull in Immediate Vicinity of Hatch Opening; 500 psi Hydrostatic Pressure.

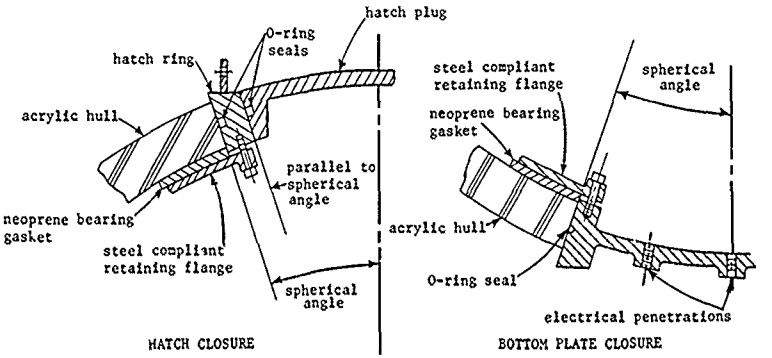

(a) Actual Acrylic-Steel Transitions - 66" Diameter NEMO Prototype

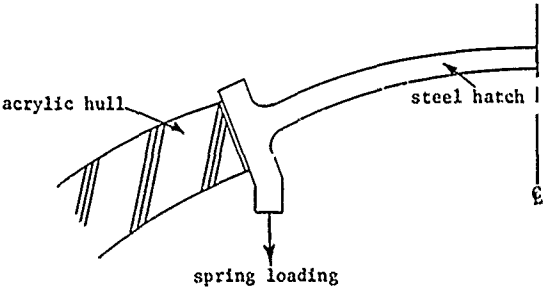

(b) Actual Acrylic-Steel Transition - 15" Diameter NEMO Model

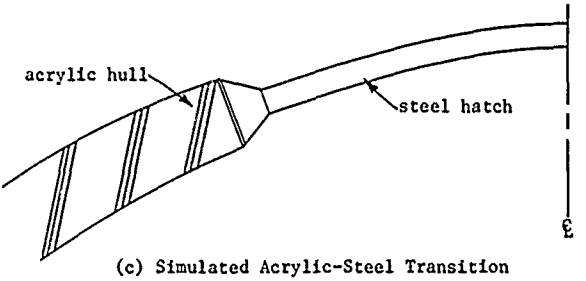

(c) Simulated Acrylic-Steel Transition

Figure 5. Actual and Simulated Acrylic-Steel Transitions (Refs. 1, 2, and 4).

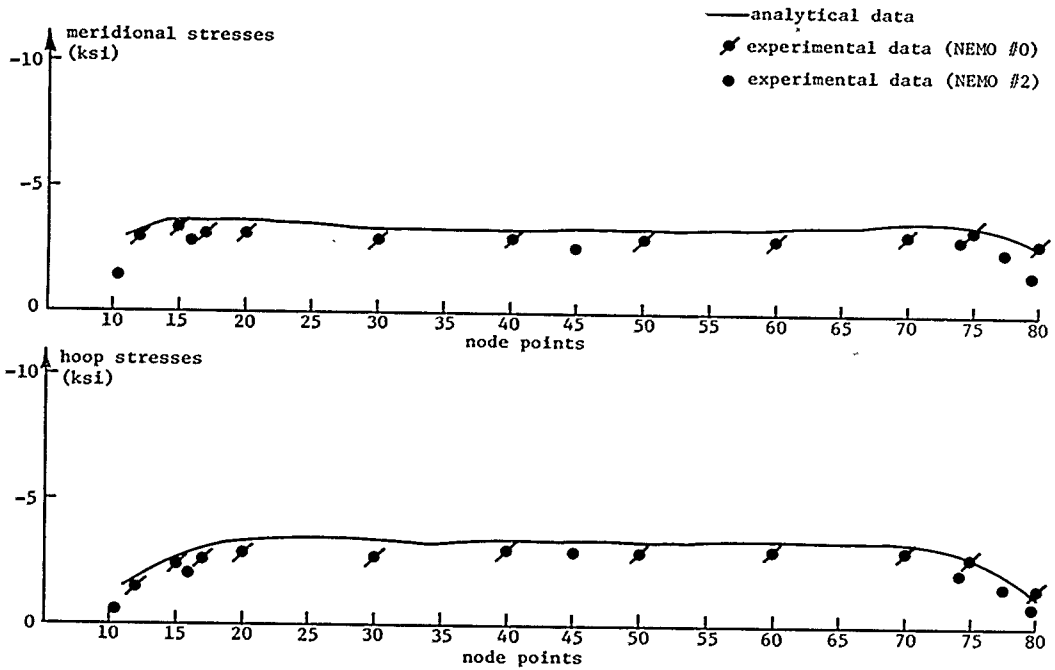

Figure 6. Comparison of Analytically and Experimentally Determined Stresses Along Meridian on External Surface of NEMO Hull; 500 psi Hydrostatic Pressure.

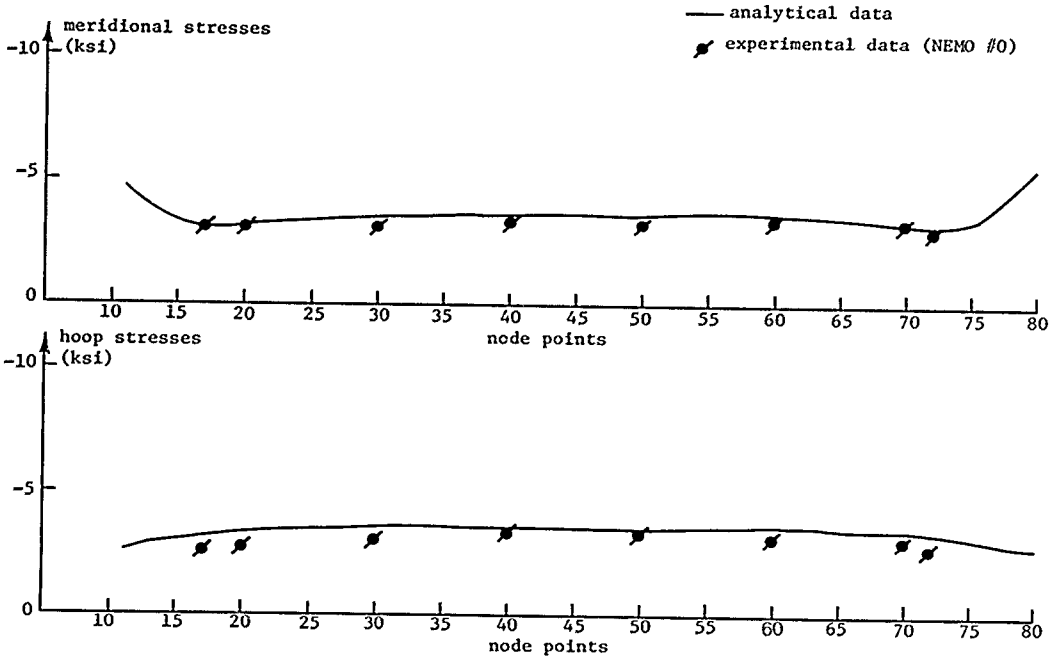

Figure 7. Comparison of Analytically and Experimentally Determined Stresses Along Meridian on Internal Surface of NEMO Hull; 500 psi Hydrostatic Pressure.

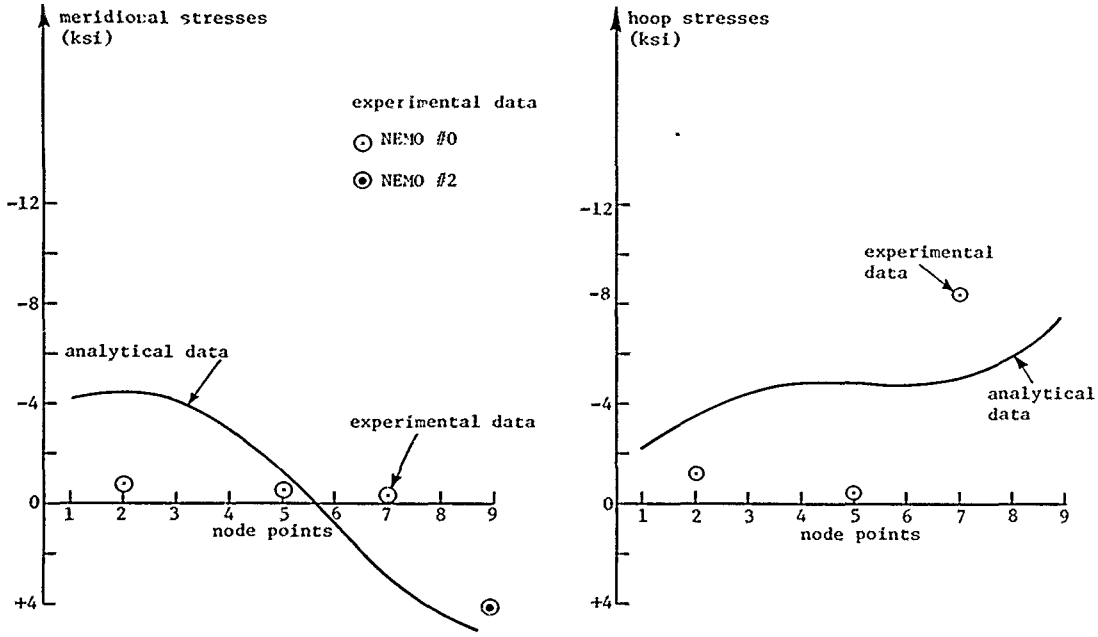

Figure 8. Comparison of Analytically and Experimentally Determined Stresses in NEMO Hatch - External Surface; 500 psi Hydrostatic Pressure.

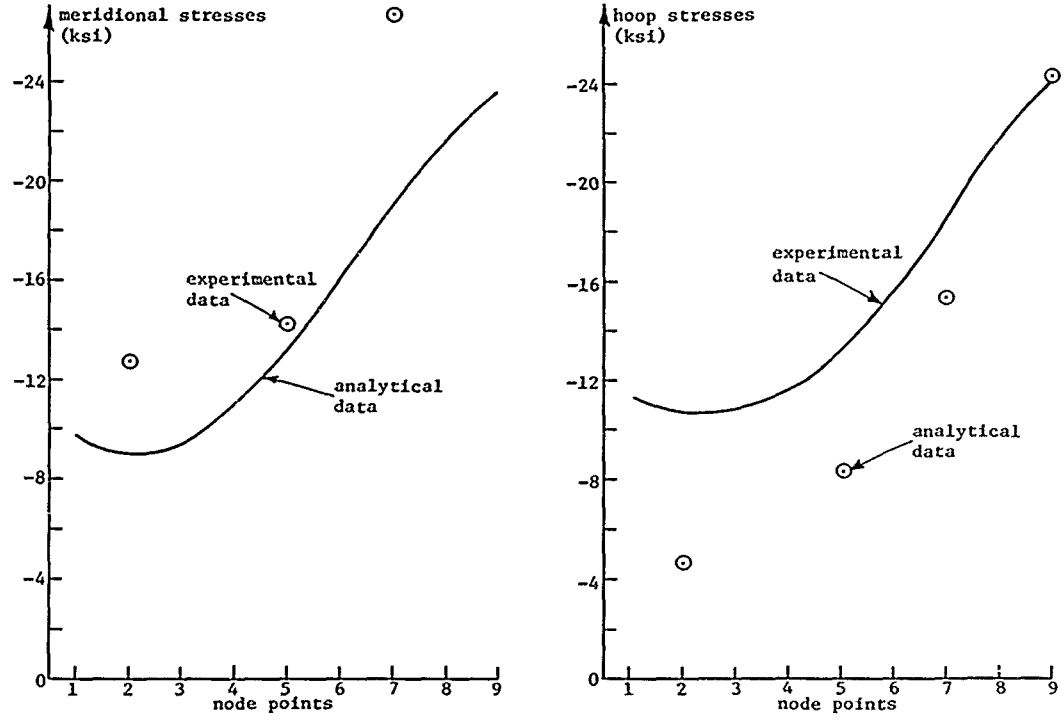

Figure 9. Comparison of Analytically and Experimentally Determined Stresses in NEMO Hatch - Internal Surface; 500 psi Hydrostatic Pressure.

REFERENCES

1. Stachiw, J. D., "The Development of the Spherical Acrylic Pressure Hull for Hydrospace Application", Naval Civil Engineering Laboratory, Port Hueneme, California (publication pending).

2. DeHart, R. C., Wah, T., and Calcote, L. R., "NEMO Stress Analysis and Material Investigation", Final Report to NAVMISCEN, Point Mugu, California, Contract No. N00123-67-C-2123, March 1968.

3. Friedrich, C. M., "SEAL-SHELL-2 - A Computer Program for the Stress Analysis of a Thick Shell of Revolution with Axisymmetric Pressures, Temperatures, and Distributed Loads", WAPD-TM-398, December 1963.

4. Stachiw, J. D., Mack, K. L., "The Spherical Acrylic Pressure Hull for Hydrospace Application; Part II - Experimental Stress Evaluation of Prototype NEMO Capsule", Naval Civil Engineering Laboratory, Port Hueneme, California (publication pending).

5. Snoey, M. R., Katona, M. G., "Structural Analysis of a Spherical Acrylic Pressure Hull", Naval Civil Engineering Laboratory, Port Hueneme, California (publication pending).

UNCLASSIFIED
Security Classification

DOCUMENT CONTROL DATA - R & D

(Security classification of title, body of abstract and indexing annotation must be entered when the overall report is classified)

1 ORIGINATING ACTIVITY (Corporate author)	2a. REPORT SECURITY CLASSIFICATION
Naval Civil Engineering Laboratory Port Hueneme, California 93041	UNCLASSIFIED
	2b. GROUP

3 REPORT TITLE

The Spherical Acrylic Pressure Hull for Hydrospace Application; Part III - Comparison of Experimental and Analytical Stress Evaluations for Prototype NEMO Capsule

4. DESCRIPTIVE NOTES (Type of report and inclusive dates)

Final February 1970 - March 1970

5 AUTHOR(S) (First name, middle initial, last name)

Henning Ottsen

6. REPORT DATE	7a. TOTAL NO. OF PAGES	7b. NO OF REFS
June 1970	20	5

8a. CONTRACT OR GRANT NO	9a. ORIGINATOR'S REPORT NUMBER(S)
b. PROJECT NO. YF-38.535.005.01.006	TN-1094
c.	9b. OTHER REPORT NO(S) (Any other numbers that may be assigned this report)
d.	

10 DISTRIBUTION STATEMENT

This document has been approved for public release and sale; its distribution is unlimited.

11. SUPPLEMENTARY NOTES	12. SPONSORING MILITARY ACTIVITY
	Naval Facilities Engineering Command Washington, D. C. 20360

13 ABSTRACT

A comparison is presented of results obtained from analytical and experimental stress analyses of the NEMO pressure hull (an acrylic submersible with steel polar penetrations). The general procedures of the analytical investigation are reviewed and the assumptions stated. Excellent agreement between the two sets of results was observed for the acrylic portion of the hull. Due to the severe structural simplification necessary in the analytical simulation of the steel polar penetrations, discrepancies were noted in the two sets of stresses obtained in these regions; general trends were, however, similar. It was concluded that the acrylic to steel transitions incorporated in the prototype design provide an optimum transfer of load without inducing a concentration of stresses.

DD FORM 1 NOV 65 1473 (PAGE 1)

S/N 0101-807-6801

UNCLASSIFIED
Security Classification

14 KEY WORDS	LINK A		LINK B		LINK C	
	ROLE	WT	ROLE	WT	ROLE	WT
Pressure vessels						
Hulls (structures)						
Acrylic resins						
Stress analysis						
Spherical shells						
Hydrospace						
Underwater vehicles						

Technical Note N-1134

THE SPHERICAL ACRYLIC PRESSURE HULL FOR HYDROSPACE APPLICATION: PART IV - CYCLIC FATIGUE OF NEMO CAPSULE #3

By

J. D. Stachiw

October 1970

NAVAL CIVIL ENGINEERING LABORATORY
Port Hueneme, California 93041

THE SPHERICAL ACRYLIC PRESSURE HULL FOR HYDROSPACE APPLICATION: PART IV CYCLIC FATIGUE OF NEMO CAPSULE #3

Technical Note N-1134

YF 38.535.005.01.006

by

J. D. Stachiw

ABSTRACT

The 66-inch outside diameter 2.5-inch thick NEMO Model 600 spherical hull #3 has been hydrostatically pressure cycled till fatigue cracks appeared in the acrylic plastic and the top hatch plastically buckled. The plastic buckling of the hatch, fabricated from annealed 4130 alloy steel, took place during simulated repeated dives in the 2080 to 2250 foot depth range. The cracks in the acrylic plastic hull were located in the beveled surface in contact with the metallic polar closures. The first crack was observed only after the hull had been subjected to 993 consecutive pressure cycles, of which 815 cycles were to 1200 feet followed immediately by 178 cycles to 1540 feet. An additional 257 pressure cycles to 2080 foot depth did not implode the pressure hull but only caused the cracks to extend further into the hull. The duration of sustained pressure loading in each pressure cycle was approximately 45 minutes followed by 45 minute relaxation period.

The cyclic tests conclusively prove that (1) an adequate cyclic fatigue safety factor exists for NEMO hulls performing, routinely, extended manned dives to 600-foot depth, and that (2) manned proof test dives of 1 hour duration to 1200-foot depth can be performed providing the total number of proof test dives does not exceed 100. To prevent plastic buckling of the polar steel closures prior to general implosion of the capsule it is necessary to specify heat treated 4130 steel alloy for the polar penetration closures.

INTRODUCTION

The Naval Civil Engineering Laboratory, under sponsorship of the Naval Facilities Engineering Command, has completed[1] in 1969 the successful development of spherical acrylic plastic pressure hull NEMO* Model 600 for manned exploration of continental shelf depths. These hulls have a 66-inch outside diameter (D), 2.5-inch wall thickness (t), are equipped with two metallic penetration closures located at the top and bottom poles of the sphere, and utilize bonded spherical pentagon modules for construction of the hull.

The prototype hull #0 of the NEMO Model 600 series has been tested to destruction after 107 pressure cycles in which its behavior under short-term and long-term hydrostatic loadings was evaluated.[1,2,3] The 4150-foot implosion depth of the NEMO Model 600 hull #0 proved that the 600-foot depth operational rating given to the NEMO Model 600 hulls is sufficiently safe for manned operation.

Two questions, however, remained that needed further elucidation. It was not known at what depth plastic buckling of the annealed 4130 steel alloy hatches would occur and it remained to be proven that the fatigue data generated by testing of 15-inch NEMO models was applicable to the full-scale NEMO hull. To answer these two questions, it was decided to pressure cycle a full-scale NEMO Series 600 hull until significant cracks occurred in the acrylic material and plastic buckling of the metallic penetration closures took place.

TEST SPECIMEN

NEMO Model 600 hull #3 served as the test specimen (Figure 1). The construction of hull #3 (Tables 1 and 2) was very similar (Figures 2 through 8) to that of hull #0 imploded previously[1] at 4150-foot depth during the full-scale NEMO hull development tests. The only significant difference between hull #3 built by Swedlow Inc. together with hulls #1 and #2 (Appendix A) and hull #0 built by the Pacific Missile Range was the use of different adhesive and steel alloy for the polar penetration closures (Figure 8).

Instead of PS-18 adhesive, hull #3 utilized SS-6217 adhesive developed by Swedlow Inc. The SS-6217 adhesive was especially formulated for this application to permit slower polymerization which resulted in almost complete absence of air bubbles in the bonded joint. The average tensile strength of the SS-6217 adhesive filled joints in hull #3 was 8300 psi with 8640 psi maximum and 6860 psi minimum strength. The 8300 psi average tensile strength of SS-6217 adhesive compared very favorably with the 9220 psi maximum, 5680 psi minimum and 7350 psi average strength established[1] for PS-18 adhesive in hull #0.

The polar penetration closures were fabricated from annealed 4130 alloy steel instead of type 316 stainless steel used in hull #0. The substitution of annealed 4130 alloy steel for 316 stainless steel was prompted by economy. Application of corrosion resistant plating to 4130

*Naval Experimental Manned Observatory

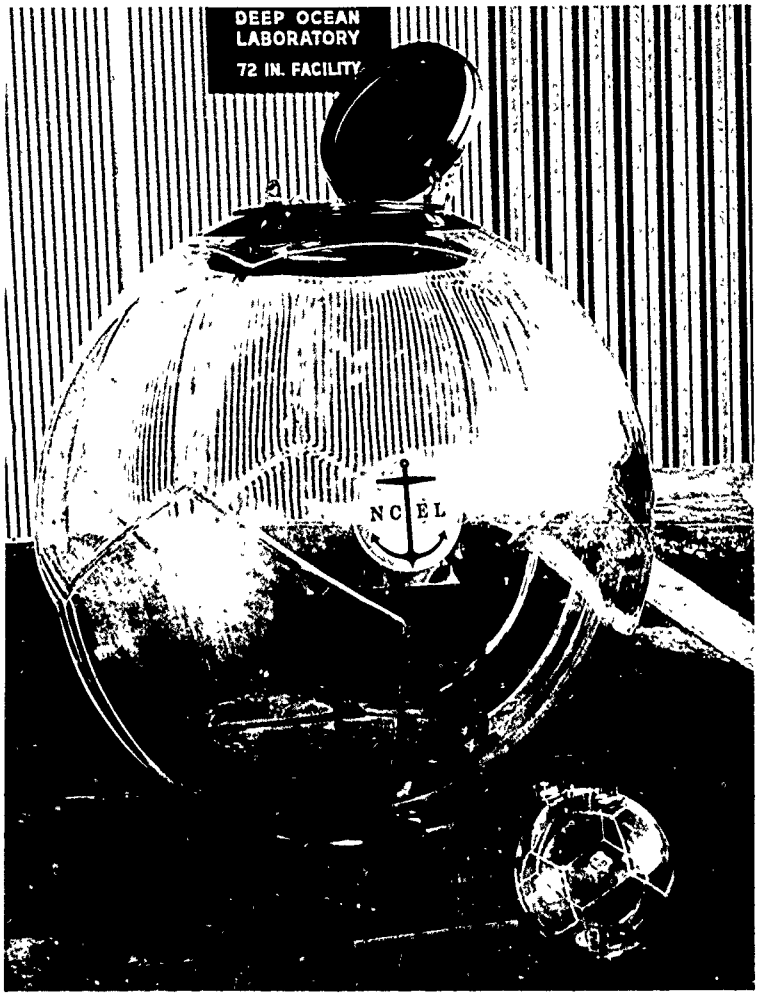

Figure 1. NEMO Model 600 capsule with hull #3; 15-inch NEMO model is shown for scale.

Table 1. NEMO Model 600 Capsule #3 Fabrication Data

MATERIALS*

Metal Closures[1]

Material	Annealed 4130 steel
Tensile Yield Strength, psi	45,850 (average)
Tensile Ultimate Strength, psi	81,800 (average)
Elongation (2-inch gage length), percent	29 (average)

Acrylic Hull[2]

Material	Plexiglas G			
Tensile Ultimate Strength, psi	10,700	max.	10,000	min.
Elongation at Rupture, percent	6.0	max.	3.5	min.
Tensile Modulus, psi	5.1×10^6	max.	4.2×10^6	min.
Shear Strength, psi	11,200	max.	9,400	min.
Flexural Strength, psi	17,100	max.	14,000	min.
Flexural Modulus, psi	4.8×10^6	max.	4.5×10^6	min.
Compressive Yield Strength, psi	17,100	max.	16,500	min.
Compressive Modulus, psi	4.9×10^6	max.	4.5×10^6	min.
Deformation Under Comp. Load, percent (4000 psi at 122°F for 24 hours)	1.2	max.	0.7	min.

DIMENSIONS

Thickness, inches (70 measurements)	2.607	max.	2.498	min.
Radius, inches (70 measurements)	33.100	max.	32.956	min.
Diameter, inches (16 measurements)	66.090	max.	66.035	min.

JOINTS[3]

Tensile Ultimate Strength, psi (Tests performed by NCEL)	8640	max.	6860	min.
Tensile Ultimate Strength, psi (Tests performed by Swedlow Inc)	9150	max.	8000	min.

*Number of test specimens taken are: (1) 2, (2) 120, (3) 16

Table 2. Specified* Properties of Acrylic Plastic

Physical Properties

Property	Typical	Test Method
Hardness, Rockwell M	90	ASTM-D785-62
Hardness, Barcol	90	ASTM-D2583
Specific gravity	1.19 ± 0.01 (2 tests within 0.005)	ASTM-D792-64T
Refractive index; 1/8 inch	1.50 ± 0.01	ASTM-D542-50
Luminous transmittance; 1/8 inch	91%	ASTM-D1003-61
Haze, 1/8 inch	2.3	ASTM-D1003-61
Heat distortion temperature		ASTM-D648-56
+3.6°F/min at 264 psi	200°F	
+3.6°F/min at 66 psi	220°F	
Thermal expansion/°F at 20°F	35×10^{-6}	Fed. Stan. 406 Method 2031
Water absorption; 1/8 inch		ASTM-D570-63T
(a) 25 hours at 73°F	0.3%	
(b) to saturation	1.9%	

Mechanical Properties

Tensile strength, rupture (0.2 in./min)	9,000 psi (min)	ASTM-D638-64T
Tensile elongation, rupture	2% (min)-7% (max)	ASTM-D638-64T
Modulus of elasticity, tension	400,000 psi (min)	ASTM-D638-64T
Compressive strength, (0.2 in./min)	15,000 psi (min)	ASTM-D695-63T
Flexural strength, rupture	14,000 psi (min)	ASTM-D790-63
Shear Strength, rupture	8,000 psi (min)	ASTM-D732-46
Impact strength, 1 zod (per inch of notch)	0.4 ft-lb (min)	ASTM-D256-56
Compressive deformation under load (4,000 psi at 122°F for 24 hours)	2% (max)	ASTM-D621-64

*Specification developed by NCEL for procurement of acrylic plastic plates to be utilized in the fabrication of man-rated pressure resistant windows and pressure hulls.

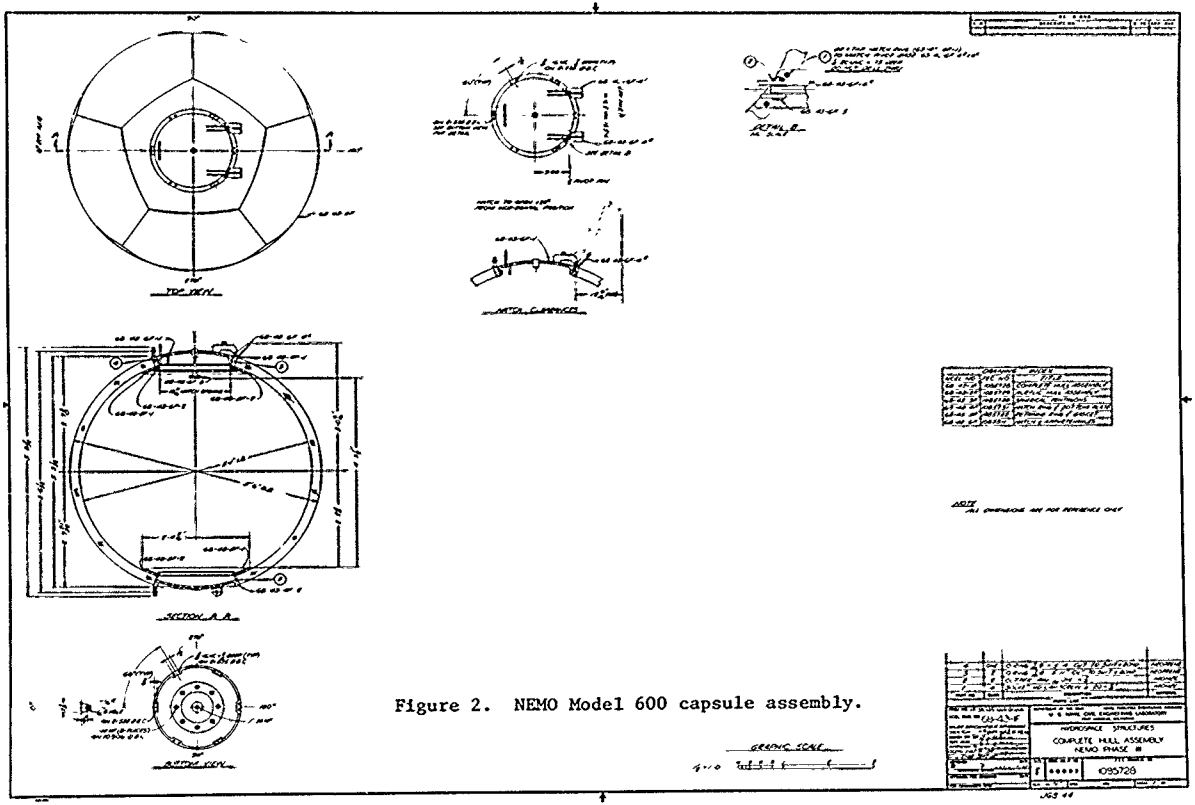

Figure 2. NEMO Model 600 capsule assembly.

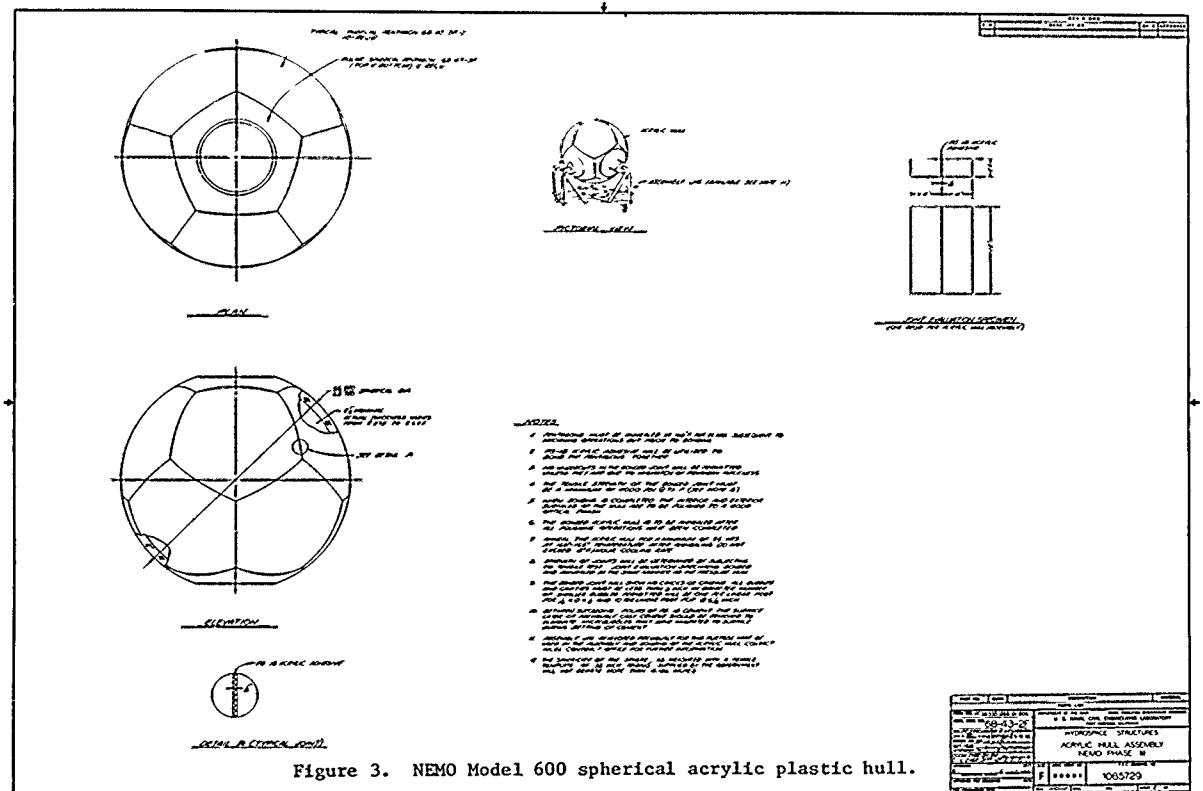

Figure 3. NEMO Model 600 spherical acrylic plastic hull.

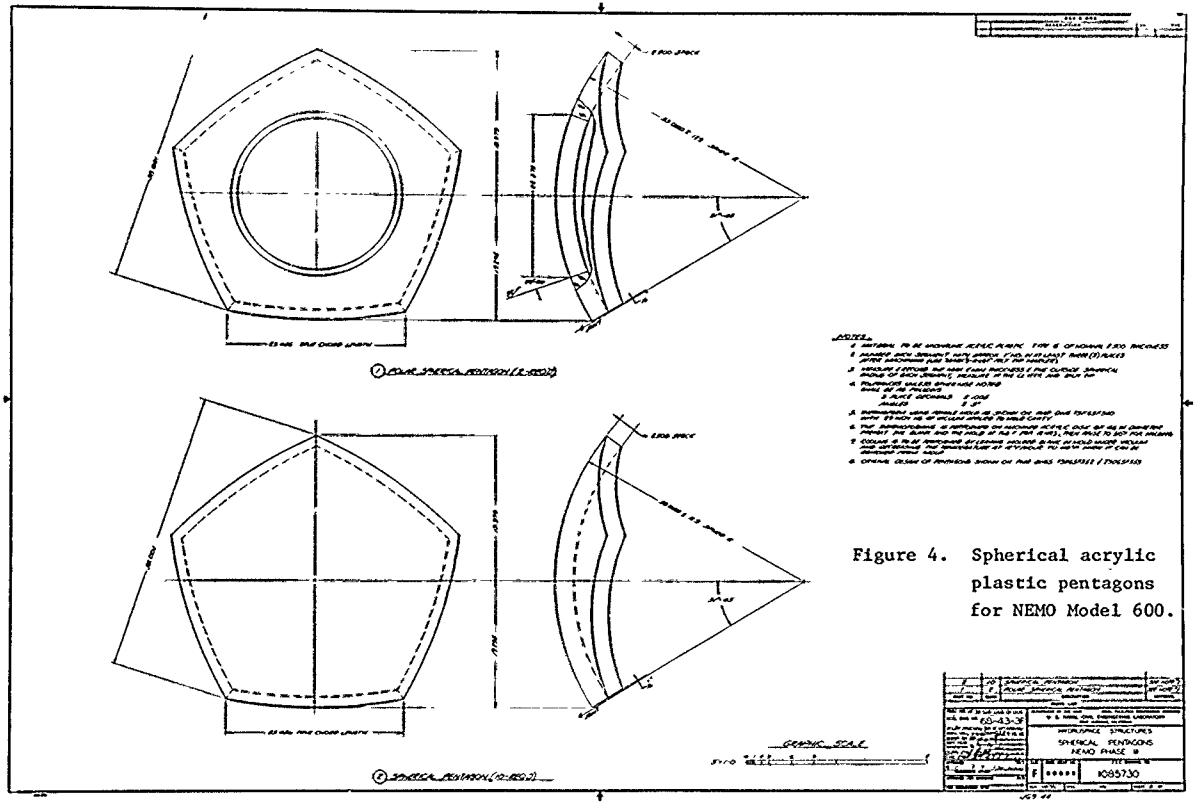

Figure 4. Spherical acrylic plastic pentagons for NEMO Model 600.

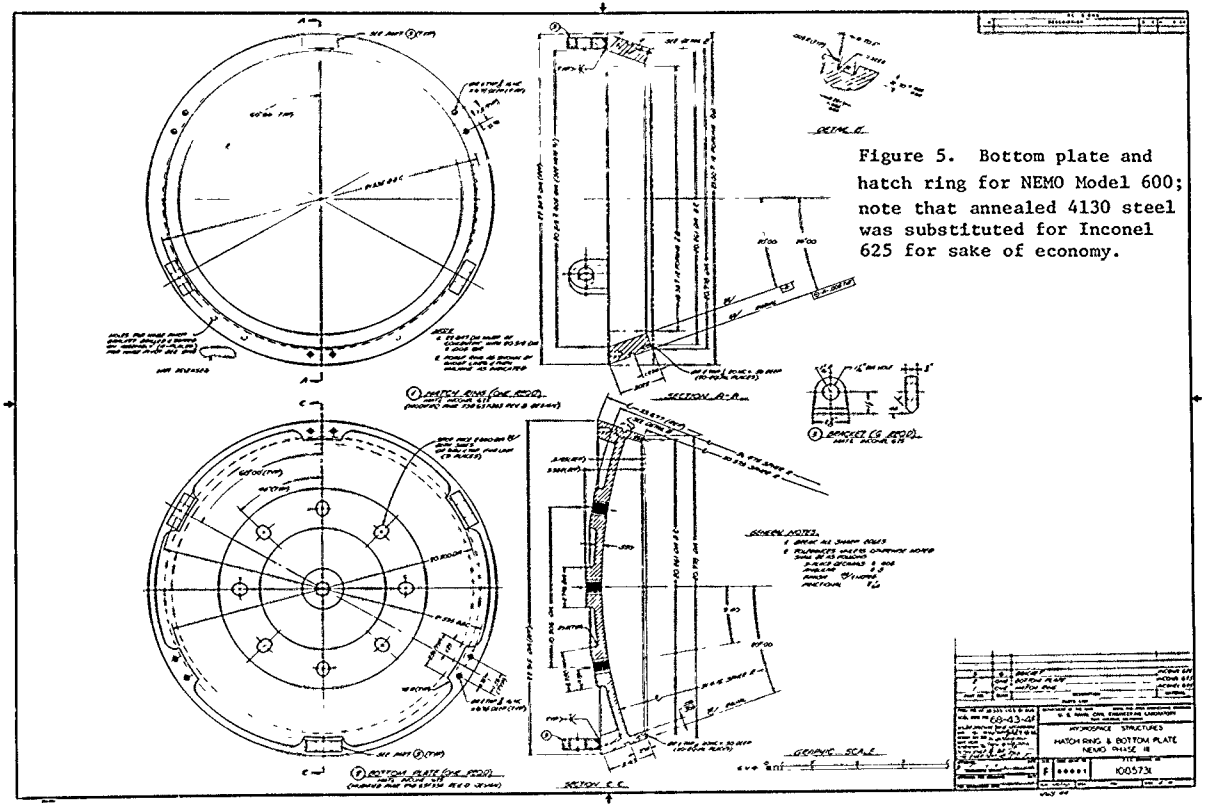

Figure 5. Bottom plate and hatch ring for NEMO Model 600; note that annealed 4130 steel was substituted for Inconel 625 for sake of economy.

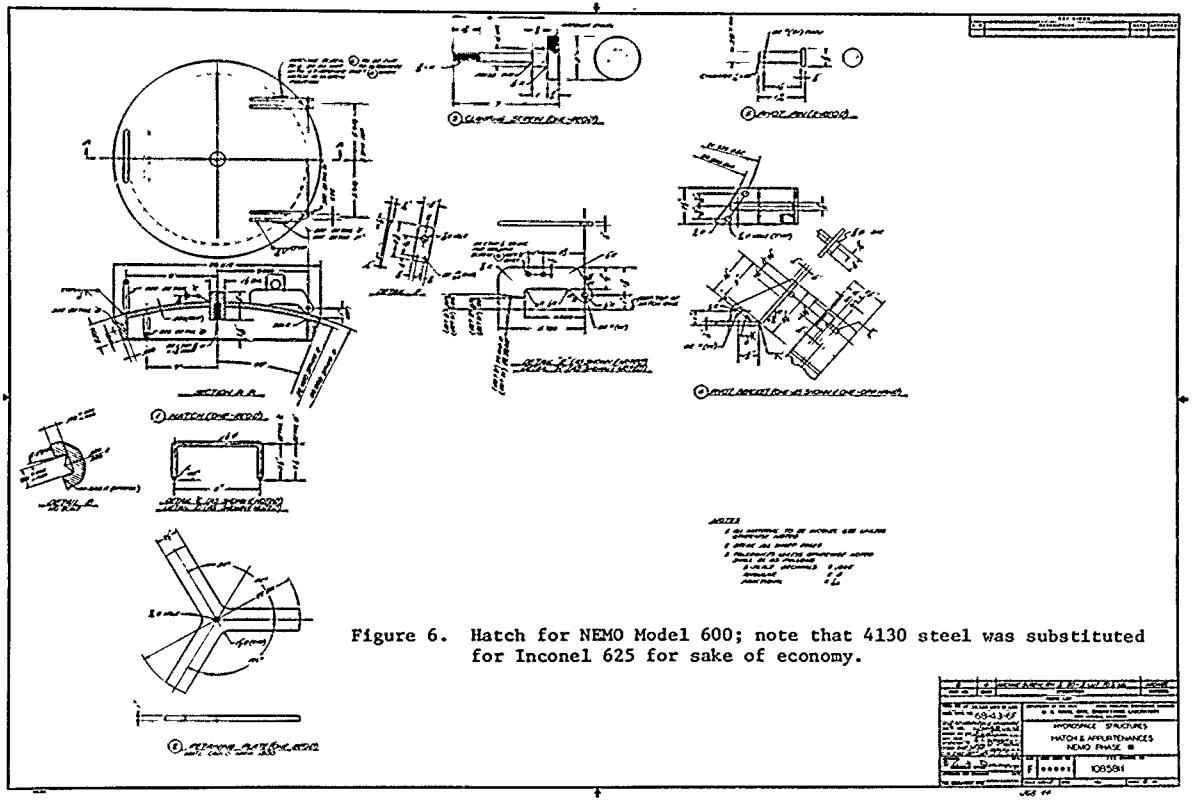

Figure 6. Hatch for NEMO Model 600; note that 4130 steel was substituted for Inconel 625 for sake of economy.

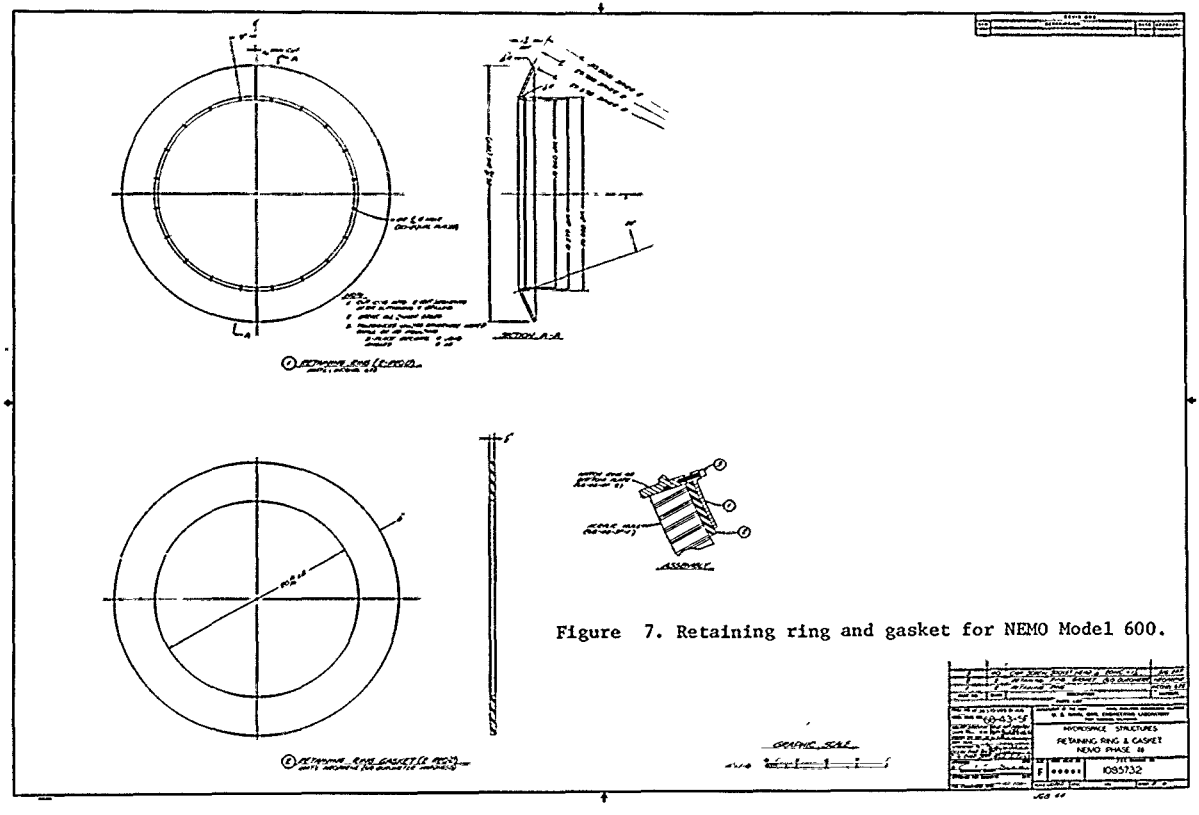

Figure 7. Retaining ring and gasket for NEMO Model 600.

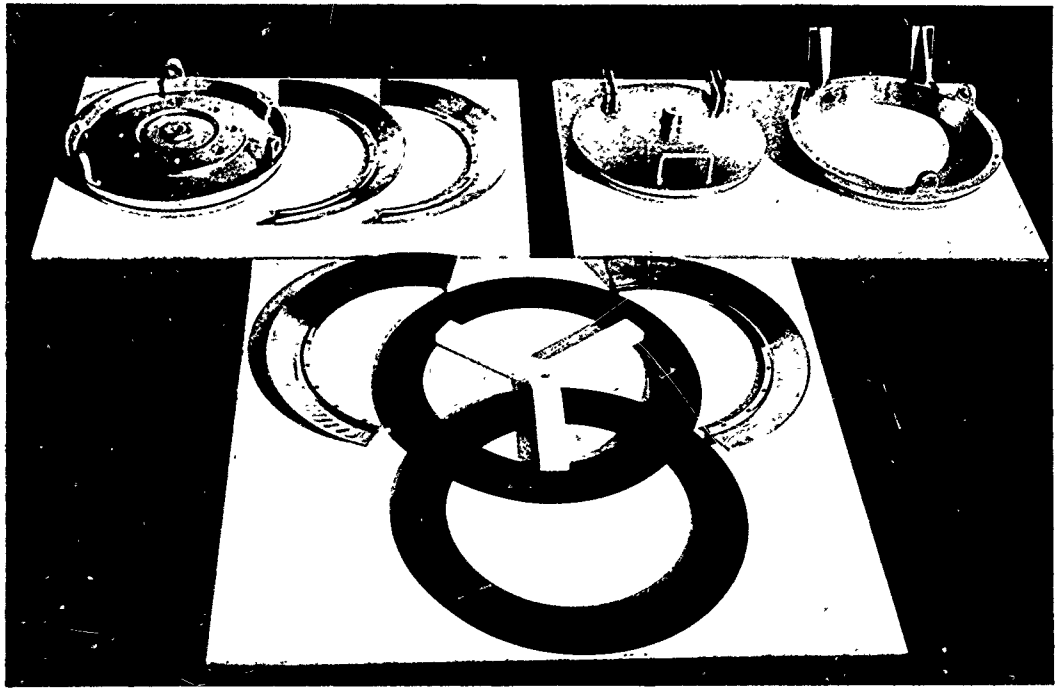

Figure 8. Components for the metallic polar closures in NEMO Model 600.

alloy closures gave them fair protection against the corrosive action of seawater. The 45,000 - 50,000 psi yield strength of annealed 4130 alloy was supposed to give the metal penetration closures approximately the same yield strength as that of medium cold worked 316 stainless steel forging.

TEST ARRANGEMENT

The same test arrangement was used for hull #3 as was previously used for hydrostatic testing of hull #0 (Figure 9). The assembled hull was placed inside a cage-like test jig and was fastened to it by bolting the bottom penetration plate to the support pedestal integral with the cage. Since hull #3 was not filled with water for the tests, the bottom plate had to resist 4000 lb upward pull when the cage assembly was placed in the water-filled 72-inch diameter pressure vessel.

TEST PROCEDURE

The hydrostatic pressure cycling procedure consisted of pressurizing the pressure vessel interior with 70°F tap water at 100 psi/minute rate till the desired pressure level was reached. Once the desired pressure level was reached, the valves were closed locking the pressurized water inside the vessel. After approximately 45 minutes, the valves were opened and the vessel was depressurized at 100 psi/minute rate. The vessel remained unpressurized for the same length of time that it was previously pressurized. The complete fatigue cycle consisting of pressurizing, sustained pressure loading, depressurizing, and relaxation required approximately 120 minutes.

The pressure cycling program consisted of four phases separated by removal and inspection of the hull for cracks in the acrylic and plastic deformation of the metallic penetration closures.

Phase 1 - Pressure cycle hull #3 to 550 psi 815 times. During a typical sustained pressure loading, the pressure dropped from 550 to 528 giving an average 539 psi pressure level equivalent to 1200-foot depth (Figure 10).

Phase 2 - Pressure cycle hull #3 to 700 psi 178 times. During a typical sustained pressure loading the pressure dropped from 700 to 675 psi giving an average 687 psi pressure level equivalent to 1540-foot depth (Figure 11).

Phase 3 - Pressure cycle hull #3 to 950 psi 117 times. During a typical sustained pressure loading the pressure dropped from 950 psi to 910 giving an average 930 pressure level equivalent to 2080-foot depth (Figure 12).

Phase 4 - Pressure cycle hull #3 to 950 psi 140 times. During a typical sustained pressure loading the pressure dropped from 950 psi to 830 psi giving an average 890 psi pressure level equivalent to 2000-foot depth.

The magnitude of pressure drop during sustained loading was the sum of (1) hull shrinkage under load, (2) changes in temperature, and

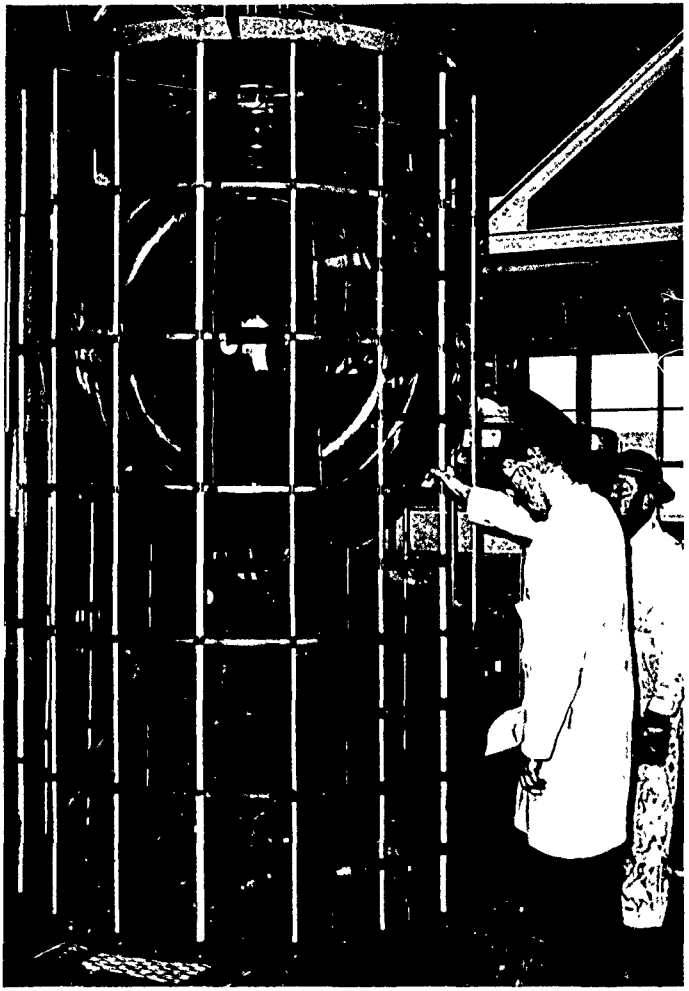

Figure 9. Jig for hydrostatic testing of NEMO Model 600 in NCEL's 72-inch diameter Deep Ocean Simulator.

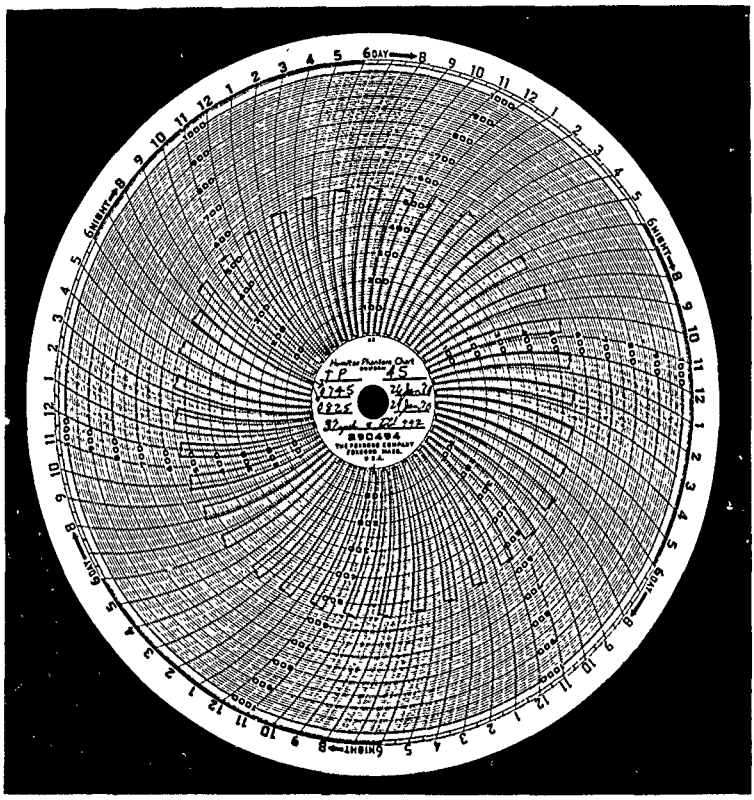

Figure 10. Typical pressure versus time record of cyclic tests to 1200 foot depth.

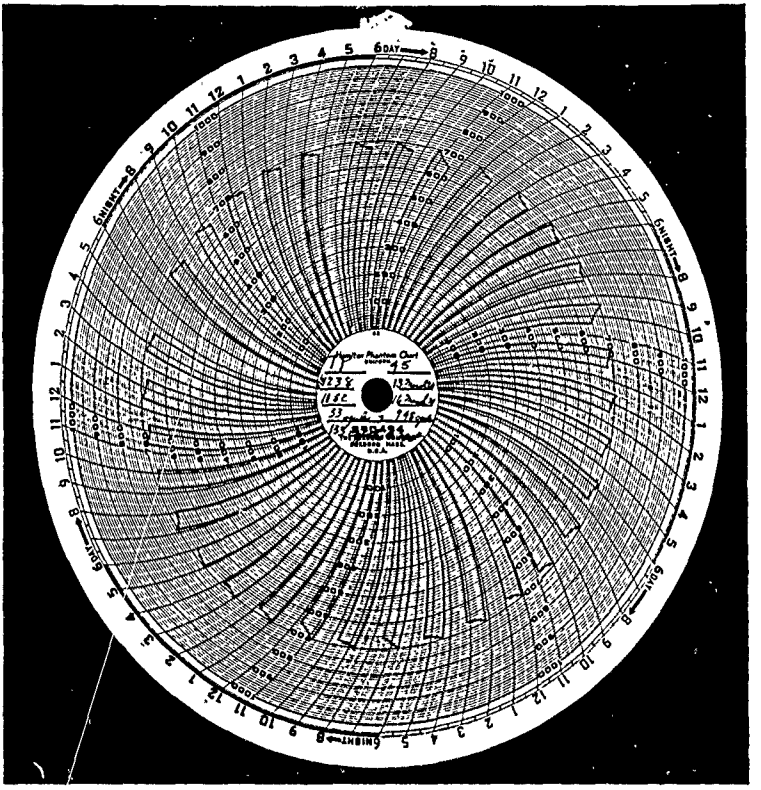

Figure 11. Typical pressure versus time record of cyclic tests to 1540 foot depth.

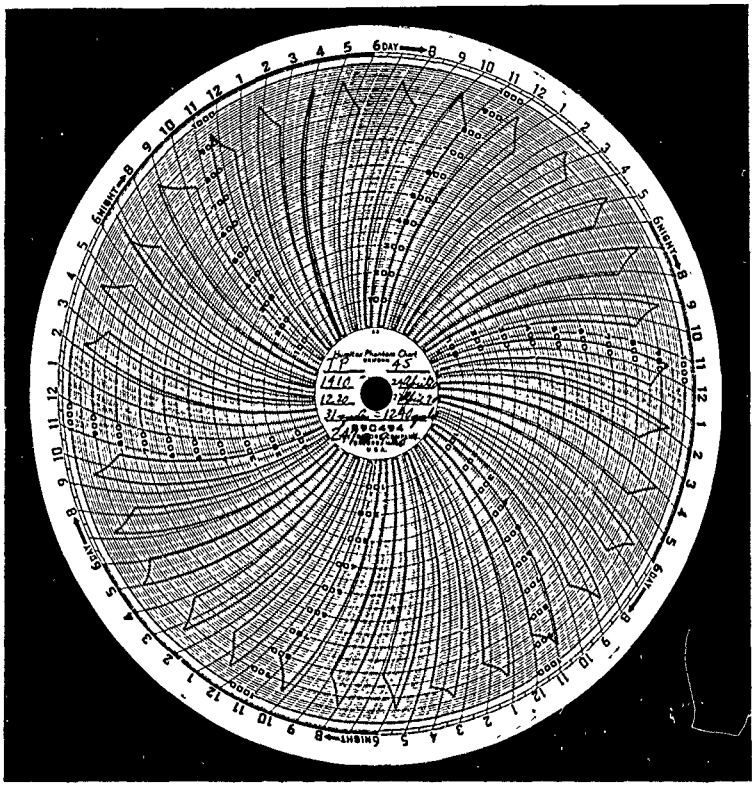

Figure 12. Typical pressure versus time record of cyclic tests to 2000 foot depth.

(3) leakage past the solenoid operated shut-off valve. Since the pressure cycling control mechanism operated unattended malfunctions often occurred. These malfunctions generally resulted in pressure cycles of unequal length, some sustained loadings being only 15 minutes long while others were 100 minutes long. Such malfunctions occurred seldom, influencing only about 1 percent of the pressure cycles.

There was one malfunction of the cycling control mechanism that was more serious than the others as it caused the pressurization to continue to approximately 1000 psi. This malfunction occurred in Phase 4 of the program at the 101st pressure cycle.

TEST OBSERVATIONS

Since hull #3 was visually inspected five times during the cyclic fatigue evaluation program, the results of the observations are stated accordingly.

Inspection of Hull #3 Prior to Cycling

Detailed inspection of the hull failed to detect any separation cracks or crazings in the acrylic plastic or components of the metallic penetration closures. The adhesive bonded joints contained a small number of air bubbles whose location was carefully noted.

Inspection of Hull #3 After Phase 1 of Cyclic Tests

No cracks or crazing was found anywhere in or on the acrylic plastic hull, or components of the metallic end-closures. The air bubbles inside the adhesive bonded joints did not enlarge or serve as crack initiators.

Inspection of Hull #3 After Phase 2 of Cyclic Tests

No cracks were found inside the adhesive filled joints of the acrylic plastic hull, or components of the metallic end-closures. The air bubbles inside the adhesive bonded joints did not enlarge or serve as crack initiators. Slight surface crazing was observed on all the acrylic plastic bearing surfaces in contact with the metallic penetration closures. Two small cracks of 0.250 penetration and 0.250 length were found in the plastic bearing surface in contact with the bottom steel penetration closure (Figure 13).

Inspection of Hull #3 After Phase 3 of Cyclic Tests

Several cracks of 0.250-inch penetration, 0.500-inch length, and less than 0.001-inch width were found in the acrylic plastic bearing surface in contact with the bottom steel penetration closure. The cracks were located around the circumference of the polar opening in the midplane of the hull wall. In all cases, these cracks originated at the bearing

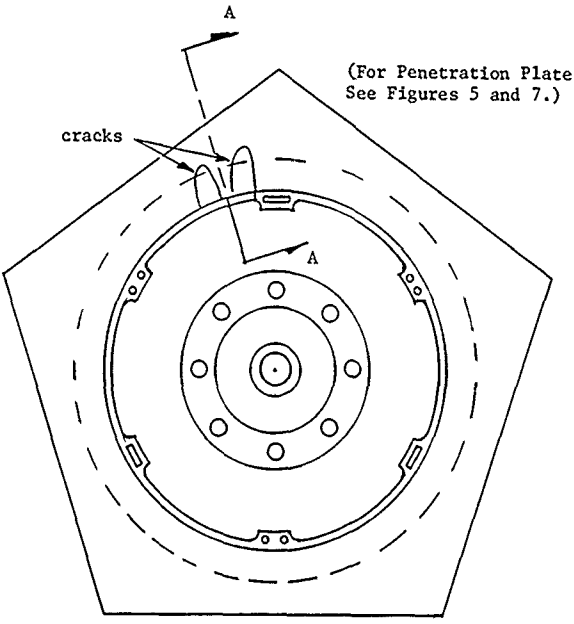

Bottom View of Polar
Opening for the Bottom
Penetration Plate

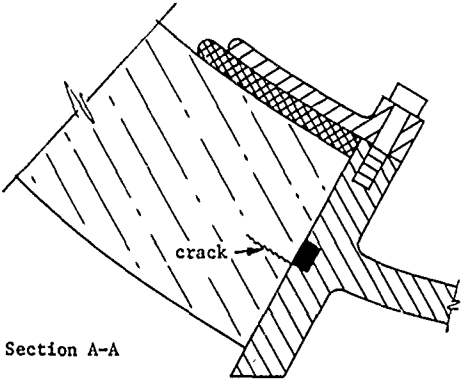

Section A-A

Figure 13. Appearance of first cracks at the conclusion of Phase 2 cyclic tests.

surface and their penetrations were oriented at right angle to it. As the cracks penetrated further they tended to follow the curvature of the hull. The cracks were located in the same place and were of the same shape as those in the 15-inch NEMO models tested in the previous study. No cracks or crazing was observed in the adhesive filled joints and the voids there did not enlarge or serve as crack initiators.

Inspection of Hull After Phase 4 of Cyclic Tests

The previously observed cracks on the acrylic plastic bearing surface in contact with bottom steel closure penetrated the hull further, reaching approximately 0.500 inches in penetration. Only a few more cracks also 0.500 inches in penetration were noted on the same bearing surface.

A multitude of new cracks were noted on the top acrylic plastic bearing surface in contact with the hatch ring. Those cracks were of approximately 2.0-inch penetration and several inches long. They were located at midplane and in the inner half of hull thickness (Figures 14, 15, and 16).

Several separation voids were found inside the adhesive filled joints. They did not originate at existing air bubbles inside the adhesive. These separation voids were less than 0.5-inch in diameter, about 0.001 inches thick, and oriented parallel to the edges of the acrylic pentagons. In all cases, they were located at midplane of the hull thickness in contact with the pentagon edge (Figure 17). The separation voids were characterized by their knife edge thickness and scallop marks on the top and bottom surfaces of the separation voids.

The top hatch exhibited typical plastic buckling of sufficient magnitude to result in complete reversal of hatch curvature (Figure 18). Where previously the hatch was convex, now it is concave. No cracks were observed in the plastically buckled hatch and the cadmium plating did not spall off from the yielded steel.

Neither the hatch ring nor the bottom penetration plate showed any signs of plastic deformation.

FINDINGS

1. Plastic buckling of metallic hull components occurs first in the top hatch assembly in the 2080 to 2250-foot depth range.

2. The first cracks in the acrylic plastic were observed in the plastic bearing surface in contact with the bottom penetration after the hull has been consecutively subjected to approximately 993 pressure cycles of 45 minutes each sustained loading duration. Of these cycles 815 were to 1200-foot depth followed by 178 cycles to 1540-foot depth.

3. Cracks appeared in the plastic bearing surface in contact with the top hatch ring after a total of 1250 cycles. Of these 815 cycles were

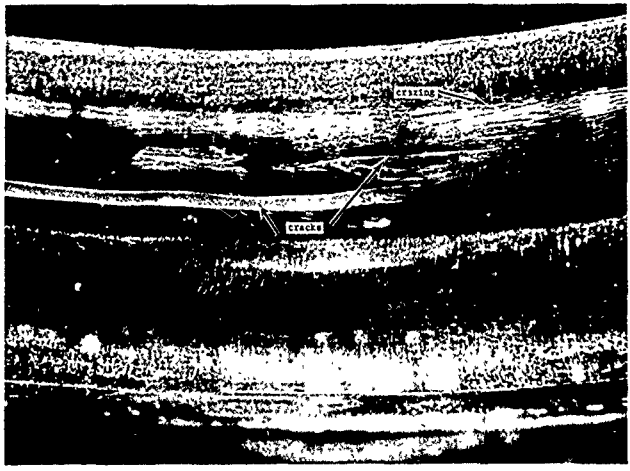

Figure 14. Typical crack in the acrylic plastic bearing surface in contact with the hatch ring at the conclusion of Phase 4 cyclic tests; view normal to the bearing surface.

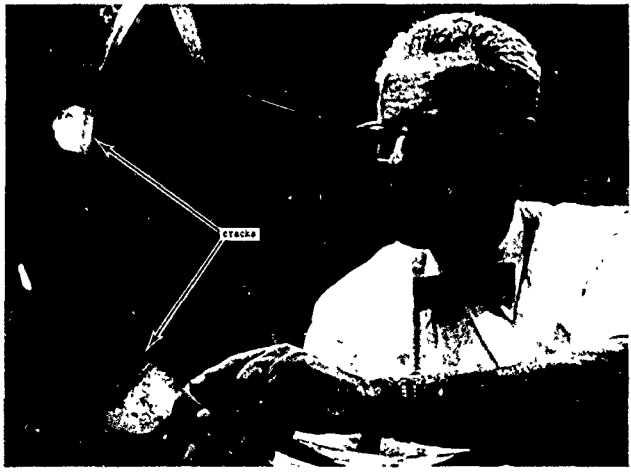

Figure 15. Typical cracks in the acrylic plastic bearing surface in contact with the hatch ring at the conclusion of Phase 4 cyclic tests; view parallel to the bearing surface.

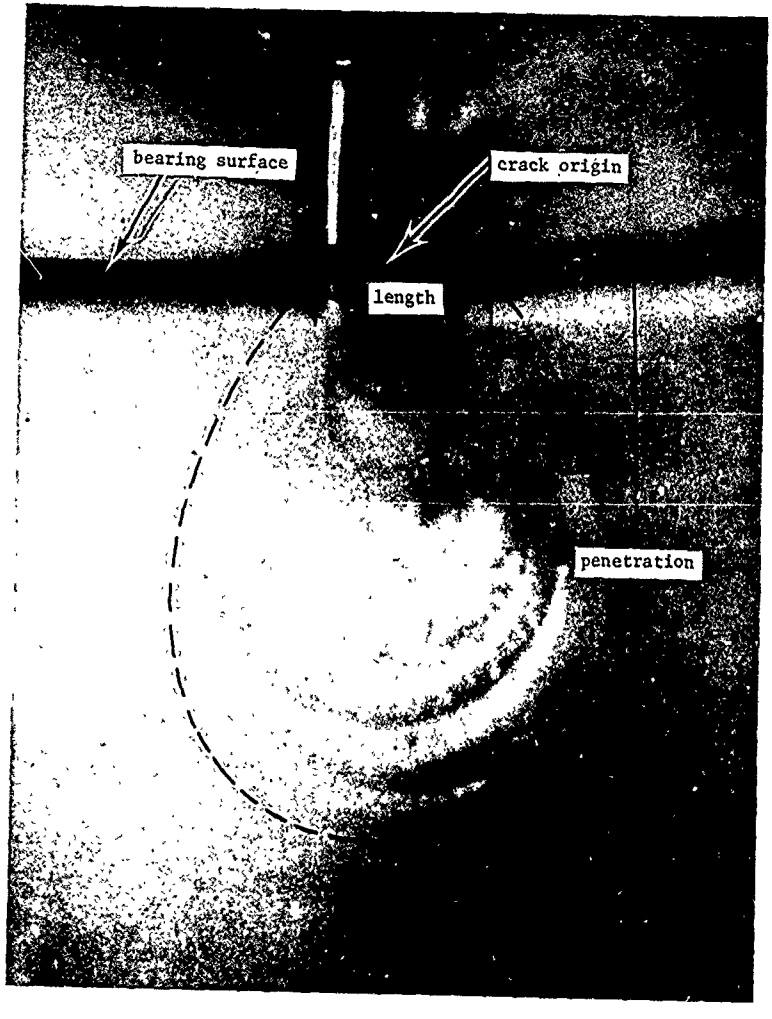

Figure 16. Detail of a typical crack shown in Figures 14 and 15.

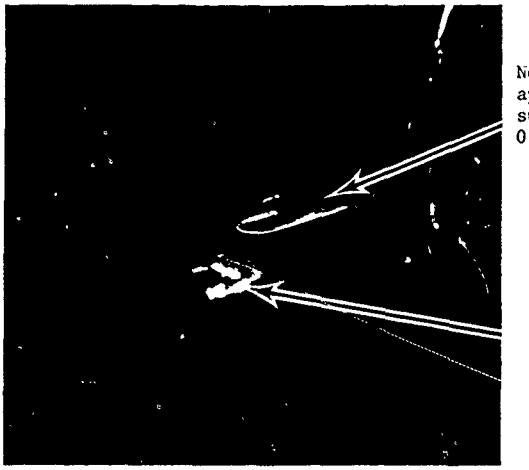

Note the scalloped appearance of the surface (approx. 0.25-inch diameter).

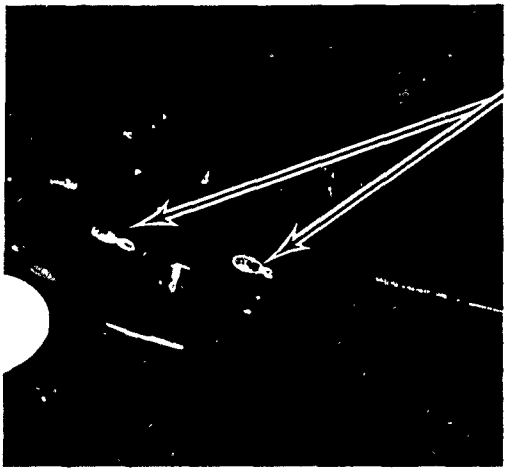

Note the scalloped appearance of the surface (approx. 0.5-inch wide x 1.0-inch long).

Acrylic joint spacer (0.5 x 0.5 x 0.125 inches).

Figure 17. Separation voids in the joint at the conclusion of Phase 4 cyclic tests.

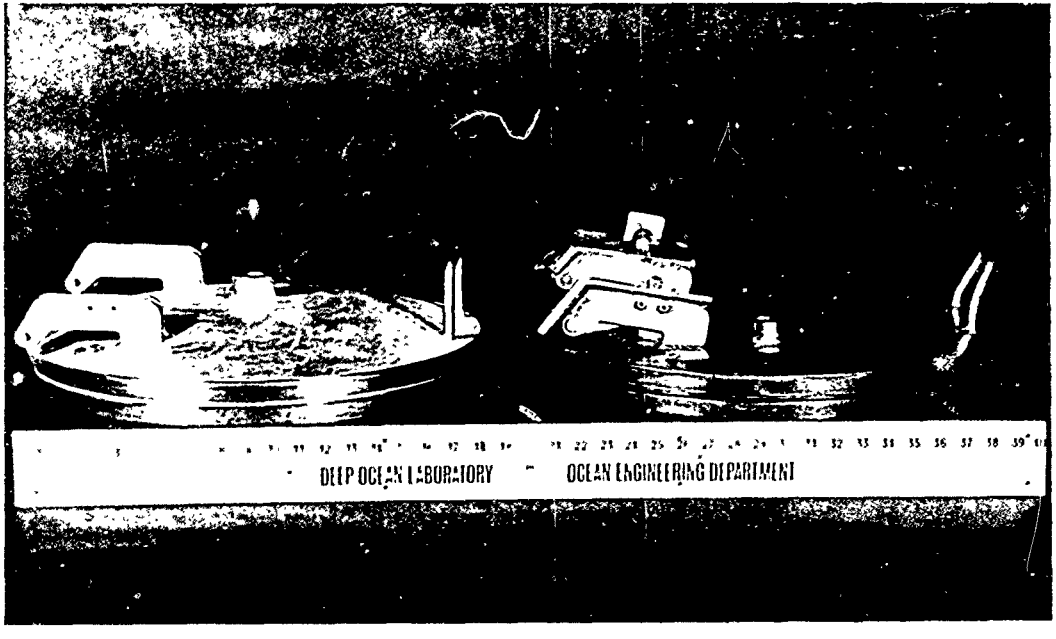

Figure 18. Comparison between the plastically buckled and a brand new hatch of annealed 4130 steel for NEMO Model 600 capsule.

to 1200-foot depth, 178 cycles to 1540-foot depth, and 257 cycles to 2080-foot depth.

4. Cracks were observed in the adhesive bonded joints at a few locations only after the hull was subjected to a total of 1250 cycles. Of these, 815 cycles were to 1200-foot depth, 178 cycles to 1540-foot depth, and 257 cycles to 2080-foot depth.

5 ıe location and character of the fatigue cracks were the same as in th. .5-inch models tested previously indicating that cyclic fatigue data generated by testing of models is applicable to the 66-inch diameter NEMO capsules.

CONCLUSION

The hatch in the NEMO Model 600 possesses a safety factor of 3.8 based on the relationship between the 2250-foot depth where plastic buckling of 4130 annealed steel hatch occurs after repeated dives, and the 600-foot maximum operational depth.

The acrylic plastic hull of NEMO Model 600 possesses a safety factor of 7 based on the relationship between the 4150-foot implosion depth[1] under short-term loading and the 600-foot maximum operational depth.

The NEMO Model 600 can repeatedly withstand 1 hour long proof test dives to 1200-foot depth without generating fatigue cracks in acrylic plastic providing that the number of such proof test dives does not exceed 100.

RECOMMENDATIONS

When future NEMO Model 600 pressure hulls with 4130 steel end-closures are built, the minimum yield strength of the 4130 steel alloy could be increased, if so desired, to 130,000 psi by heat treatment to eliminate plastic buckling of the hatch prior to general implosion of the acrylic hull at 1850 psi.

REFERENCES

1. Technical Report R-676, "Development of a Spherical Acrylic Plastic Pressure Hull for Hydrospace Application," by J. D. Stachiw, U. S. Naval Civil Engineering Laboratory, April 1970.

2. Technical Note N-1113, "The Spherical Acrylic Pressure Hull for Hydrospace Application; Part II - Experimental Stress Evaluation of Prototype NEMO Capsule," by J. D. Stachiw and K. L. Mack, U. S. Naval Civil Engineering Laboratory, April 1970.

3. Technical Note N-1094, "The Spherical Acrylic Pressure Hull for Hydrospace Application; Part III - Comparison of Experimental and Analytical Stress Evaluations," by H. Ottsen, U. S. Naval Civil Engineering Laboratory, March 1970.

Appendix A

FABRICATION REPORT - NEMO ACRYLIC SPHERE NO. 3

1. Twelve acrylic sheets, 48 inches by 60 inches by 2-1/2 inches thick were rough sawed to a 46-inch diameter. The periphery was machined to a 200 micro-inch finish. One edge was then chamfered to 1/16-inch by 1/16-inch.

   Each machined blank was serialized and the thickness measured. The results of the thickness measurement are contained in Attachment I (Figure A-1).

2. One blank at a time was set in a female form die, Drawing Number TSF65F325, with the chamfered edge against the die.

3. The flat acrylic blank and form die were placed in an oven. A vacuum line was run from a vacuum pump outside the oven, to the center of the form die where the vacuum holes are located.

   The oven was preheated to +165°F over night.

4. After preheating, forming was accomplished as follows:

   a) The oven temperature was raised to +310°F

   b) After eight hours at +310°F, vacuum was applied and the blank formed to contour

   c) After fifteen minutes under vacuum, the oven was turned off. Vacuum was left on and the oven doors remained closed.

   d) The oven was allowed to cool overnight, a minimum of sixteen hours. The oven doors were opened and the formed part in the form die was allowed to cool to room temperature.

5. The above procedure was followed for all twelve acrylic blanks.

6. Each of the formed spherical blanks were checked for contour and thickness. The results of the thickness measurement are contained in Attachment 1.

7. Each of the formed spherical blanks were annealed for twenty-four hours at +160°F. The blanks were cooled at a rate not exceeding eight degrees per hour, to room temperature. Each spherical blank was annealed in the form die.

8. Each of the formed spherical blanks were machined into a pentagon section, on a milling machine, in accordance with Drawing Number 1085730.

9. A hole was machined in two of the spherical pentagon sections with a vertical boring mill. This was done in accordance with Drawing Number 1085730. These two sections are used at the polar regions of the sphere.

10. Each of the machined spherical pentagons were annealed for twenty-four hours at +160°F. The pentagons were cooled at a rate not exceeding eight degrees per hour, to room temperature. Each spherical pentagon was annealed in the form die.

    The machined spherical pentagons were reinspected for contour. The results are contained in Attachment I.

11. The periphery of each pentagon was sanded using 240 to 400 grit sandpaper.

12. One polar zone pentagon and five regular spherical pentagons were positioned in the handling fixture, Drawing Number SK67154, hemispherically with the polar zone pentagon at the bottom center and the other five encompassing it. The pentagons were spaced 0.125 inches apart with acrylic spacers (0.250 inch by 0.500 inch). These spacers were located two on a pentagon side and approximately two inches in from each corner. The joints between the segments were matched on the outside surface so the external curvature across the joint was continuous.

13. The 0.125 inch spaces between the pentagon segments were prepared for cementing as follows:

    a) The joint on each side was covered with an adhesive backed aluminum foil (Scotch Brand No. 425). The adhesive backed aluminum foil was formed in a manner to allow it to protuberate slightly over the joint area. This protuberance left a bead in the cementing operation which compensated for shrinkage in the cemented joint.

14. Swedlow's proprietary casting material, identified as SS-6217, was utilized to bond the pentagons together. SS-6217 was evaluated before and after sea water exposure. The results were forwarded to and approved by NCEL.

15. A filling arrangement was adapted to the taped joints to allow cementing of the six pentagon sections in two operations.

16. The hemisphere was poured and the adhesive cured. (Details of the adhesive and cure are proprietary to Swedlow Inc.)

17. The first hemisphere was removed from the fixture with a hoist and sling. The second hemisphere was constructed in the same manner in accordance with paragraphs 11 through 16 using 0.188 inch acrylic spacers and was left positioned in the fixture.

18. The first hemisphere was elevated above the second one with a hoist and sling. It was positioned in place on the second hemisphere with the 0.125 inch acrylic spacers as described in paragraph 12. The joints were prepared and the adhesive poured as described in paragraphs 13 through 16. The joining of the two hemispheres completed the acrylic sphere.

19. When the adhesive backed aluminum foil was removed from the sphere, a number of bubbles were evident in the cement joint.

20. To repair the joint required that the bubbled area be removed by machining or drilling.

    After the bubbled area was removed the sphere was annealed at 160°F for a period of twenty-seven hours. The sphere was cooled at a rate not exceeding eight degrees per hour until it reached room temperature. It was then removed from the oven.

21. The areas to be repaired were then filled with Swedlow's adhesive identified as SS-6217 and then cured.

22. This procedure, paragraphs 20 and 21, was followed until the majority of the bubbles were repaired.

23. After repair, the adhesive beads were removed and cleaned.

24. The completed sphere was then polished to remove scratches.

25. The completed sphere was then annealed, in the fixture, for a period of twenty-seven hours at 160°F. The sphere was cooled at a rate not exceeding eight degrees per hour until it reached room temperature. It was then removed from the oven.

26. The annealed acrylic sphere was moved to a temperature controlled room where it was allowed to equalize to the temperature of the room. The sphere was then measured for conformance to FEC Drawing Number 1085729, "Hydrospace Structures - NEMO Phase III Acrylic Hull Assembly".

27. The completed and accepted acrylic sphere was protected with Protex 20V protective paper, packaged and delivered to Naval Civil Engineering Laboratory.

28. Four test coupons, four inches wide by twelve inches long by 2.5 inches thick, were bonded together using the Swedlow adhesive SS-6217 and annealing procedures representative of the full acrylic hull. One test coupon was identified and delivered to the Naval Civil Engineering Laboratory for testing.

29. The second test coupon was tested by Swedlow. The results are contained in Attachment III.

Attachment #1 FINAL PENTAGON INSPECTION

Pentagon No. #107

Inspector _____

Date 30 September 1969

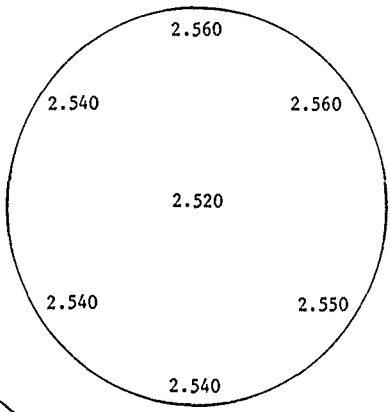

THICKNESS CHART BEFORE FORMING

SHORT CORD MEASUREMENT	LONG CORD MEASUREMENT
1. 23.500	1. 38.003
2. 23.501	2. 37.999
3. 23.495	3. 37.996
4. 23.497	4. 37.996
5. 23.498	5. 37.999

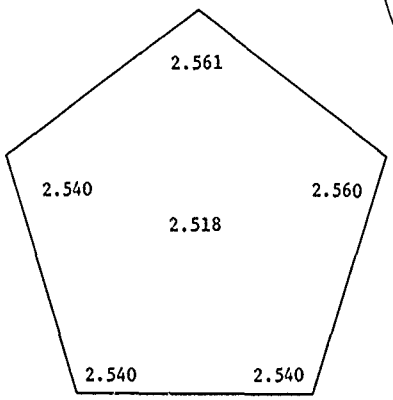

THICKNESS CHART AFTER FORMING

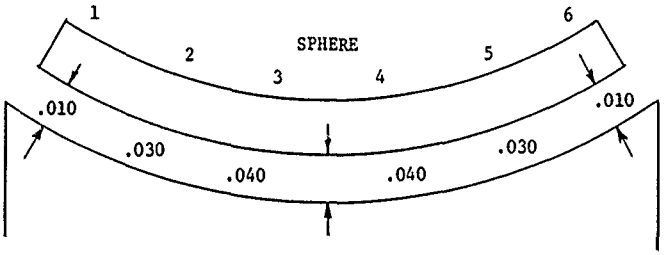

CONTOUR TEMPLATE AFTER MACHINING

Figure A-1. Typical Dimensional Control Form for Individual Pentagons Used by Swedlow Inc. During Fabrication of NEMO Hull #3.

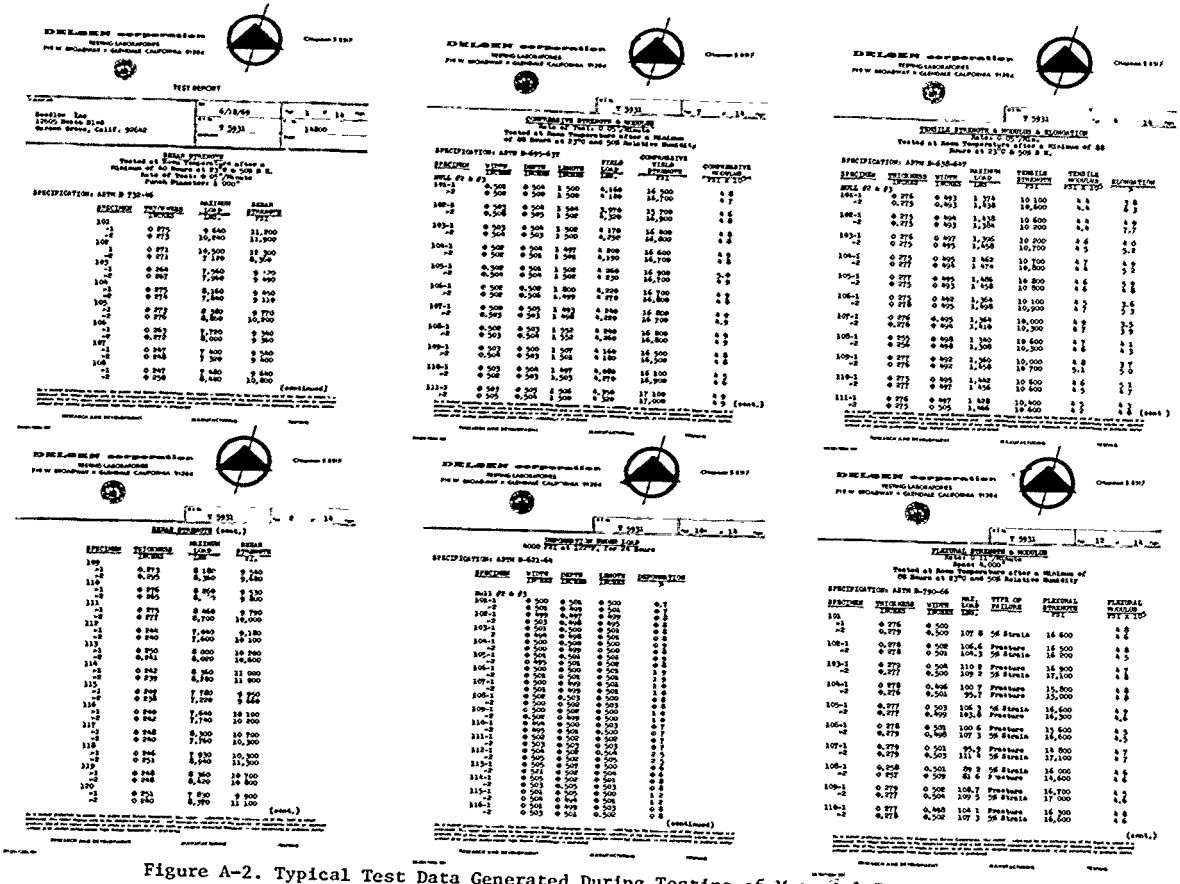

Figure A-2. Typical Test Data Generated During Testing of Material Properties.

Figure A-3. Control of Bond Strength Quality
by Swedlow Inc.

ATTACHMENT #3 - DETERMINATION OF BOND STRENGTH

Swedlow control for Hull No. 3.

Tensile specimens per Federal Test Method Std. No. 406, Method 1011A with the bonded joint located in the center of the reduced area.

Test Temperature: +75°F

Test Speed: 0.050 inches/minute

Specimen Number	Bond Strength (psi)	Type Failure
1 (1)	8000	Bond joint
2 (1)	9150	Bond joint
3 (1)	8540	Bond joint
4 (1)	8830	Bond joint
	Average: 8630	
5 (2)	8240	Bond joint
6 (2)	8320	Bond joint
7 (2)	8080	Bond joint
8 (2)	8330	Bond joint
	Average: 8242	

(1) 0.90 inch thick specimens.

(2) 0.25 inch thick specimens.

Appendix B

NEMO CAPSULES FOR OTHER DEPTHS

The experimental and analytical studies conducted in the development of 66-inch OD x 61-inch ID NEMO capsules with 600-foot operational depth rating (NEMO Model 600) are only indirectly applicable to design of NEMO capsules for other depths. Still, requirements may arise in the future for acrylic plastic capsules either with greater, or lesser operational depth than the NEMO capsule. Although the data generated in the NEMO program will allow to design with a reasonable degree of confidence NEMO capsules for other depths, some additional experimental data will be necessary to confirm the design parameters.

Foreseeing this need, several additional 15-inch diameter capsules of 1.0, 0.75, and 0.25 wall thickness have been built, equipped with polar penetration closures (compressibility mismatch factor of 35) and imploded under short- and long-term hydrostatic loadings. The linear plot of implosion pressure versus time on log-log coordinates permits extrapolating implosion pressures of the few capsules that failed in hours to implosion pressure that occur when the capsules are subjected to lower pressure levels for days, or months (Figure B-1 and Table B-1).

On the basis of implosion data from the additional models and all of the data from the NEMO Model 600 program[1], a plot has been made for predicting the safe* operational depth of acrylic capsules with different t/D ratios (Figure B-2). The recommended t/D ratios for various depths are conservative, as they are based on similar relationship between operational depth, and (1) static fatigue, (2) cyclic fatigue*, (3) short-term implosion, and (4) material strength as was formulated for man-rated NEMO Model 600 capsule. Needless to say, that the compressibility of polar inserts for these capsules must be adjusted to the compressibility of the particular hull so that the compressibility mismatch factor is always less than 35, and preferably less than 20 as otherwise undue stress risers will be present at the insert/acrylic interface.

Although from the theoretical viewpoint, there is no valid reason why 66-inch diameter capsules with as little as 0.250-inch or as much as 8-inch wall thickness cannot be built there are practical limits to the minimum and maximum wall thickness. These practical limits imposed by inherent limitations of the current fabrication process devised for the NEMO type capsules are probably 1.0-inch for the minimum thickness and 5.0 inches for the maximum thickness. The minimum thickness is based on the inability to maintain the required sphericity and wall thickness tolerances in a 66-inch diameter hull of less than 1.0-inch thickness.

*Based on a minimum cyclic life of 1000 dives of 6-hour duration to the operational depth. Dives to a lesser depth are counted as a fraction of the pressure cycle. The fatigue value of dives of lesser or longer duration than 6 hours is computed on the same basis as developed for NEMO capsule[1].

The maximum thickness is based on the inability to thermoform acrylic plate in excess of 5-inch thickness to 33-inch radius of curvature. Unless other fabrication methods for spherical hulls are developed, it appears that the maximum safe* operational depth for the thickest (5-inch) 66-inch diameter man-rated acrylic capsules will remain 1350 feet, while for the thinnest (1-inch) 66-inch diameter capsules the maximum safe operational depth will be 150 feet.

Table B-1. Long-Term Pressurization Tests on 15-inch OD Model Acrylic Plastic Capsules

Specimen No.	ID Inches	Joint	Type of Penetration Closures	Temperature °F	Type of Failure	Sustained Pressure, psi	Duration of Loading, min
22	13	Wide (PS-18 adhesive)	Titanium Plate (Ti-6Al-4V)	69	General Implosion	4500	6
23	13	Wide (PS-18 adhesive)	Titanium Plate (Ti-6Al-4V)	69	General Implosion	4000	23
24	13	Wide (PS-18 adhesive)	Titanium Plate (Ti-6Al-4V)	71	General Implosion	3500	315
25	13	Wide (PS-18 adhesive)	Titanium Plate (Ti-6Al-4V)	70	General Implosion	3000	1575
26	13.5	Wide (PS-18 adhesive)	Titanium Plate (Ti-6Al-4V)	71	General Implosion	2900	0.5
27	13.5	Wide (PS-18 adhesive)	Titanium Plate (Ti-6Al-4V)	72	General Implosion	2500	6
28	13.5	Wide (PS-18 adhesive)	Titanium Plate (Ti-6Al-4V)	70	General Implosion	2000	215
29	13.5	Wide (PS-18 adhesive)	Titanium Plate (Ti-6Al-4V)	69	General Implosion	1600	6300
30	14.5	Wide (PS-18 adhesive)	Titanium Plate (Ti-6Al-4V)	70	General Implosion	350	0.5
31	14.5	Wide (PS-18 adhesive)	Titanium Plate (Ti-6Al-4V)	71	General Implosion	320	6
32	14.5	Wide (PS-18 adhesive)	Titanium Plate (Ti-6Al-4V)	70	General Implosion	275	18
33	14.5	Wide (PS-18 adhesive)	Titanium Plate (Ti-6Al-4V)	75	General Implosion	200	8640

NOTE: 1. The polar openings were identical, subtending a 40° spherical angle at the center of the sphere.

2. The penetration closures were of the same thickness and curvature as the acrylic shell.

3. Pressurization rate was 100 psi/minute.

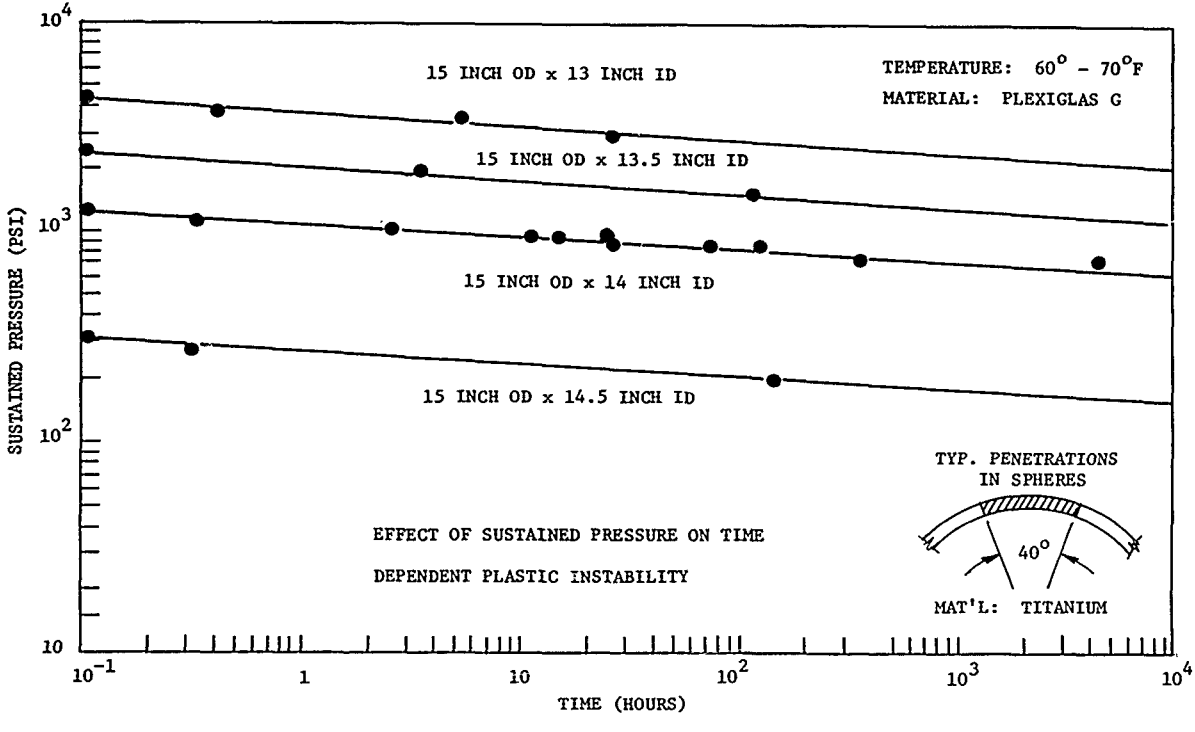

Figure B-1. Implosion pressure of NEMO type acrylic plastic capsules under sustained hydrostatic loading.

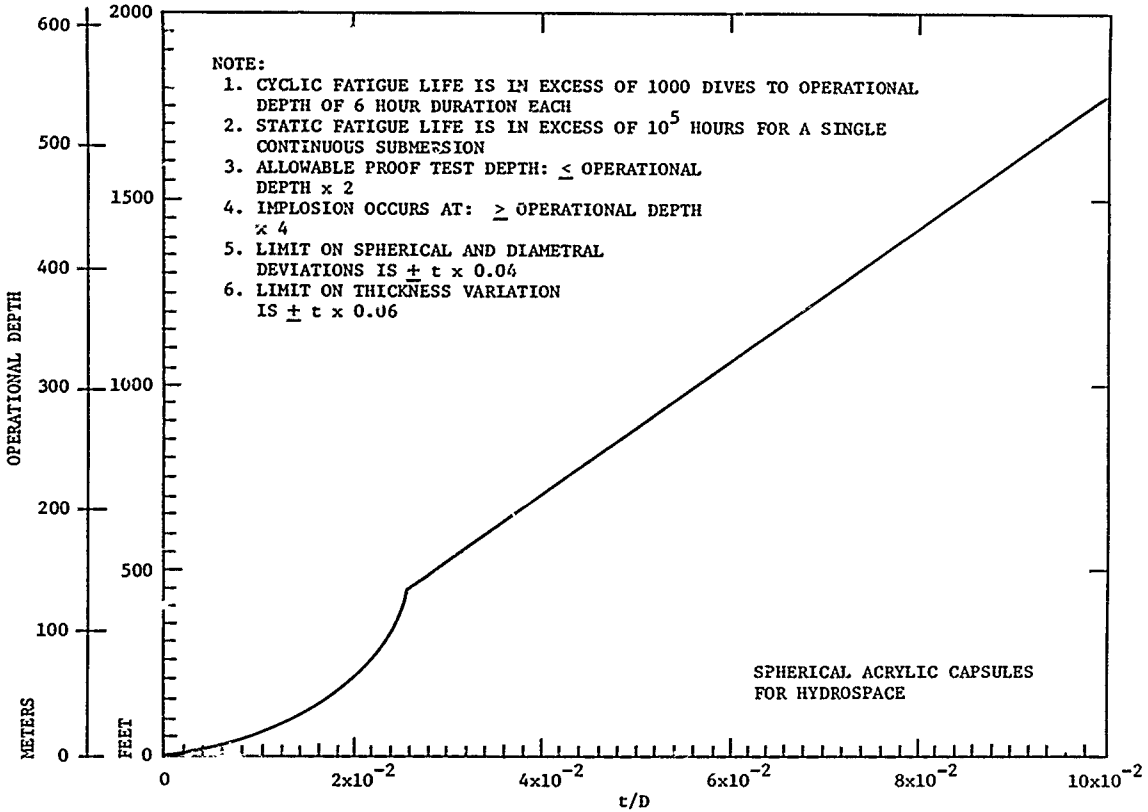

Fig[illegible] 2. Recommended operational depths for man-rated submersibles with acrylic pressure hulls of spherical shape.

UNCLASSIFIED

Security Classification

DOCUMENT CONTROL DATA - R & D

(Security classification of title, body of abstract and indexing annotation must be entered when the overall report is classified)

1. ORIGINATING ACTIVITY (Corporate author)	2a. REPORT SECURITY CLASSIFICATION
Naval Civil Engineering Laboratory Port Hueneme, California 93041	UNCLASSIFIED 2b. GROUP

3. REPORT TITLE

THE SPHERICAL ACRYLIC PRESSURE HULL FOR HYDROSPACE APPLICATION: PART IV - CYCLIC FATIGUE OF NEMO CAPSULE #3

4. DESCRIPTIVE NOTES (Type of report and inclusive dates)

5. AUTHOR(S) (First name, middle initial, last name)

J. D. Stachiw

6. REPORT DATE	7a. TOTAL NO. OF PAGES	7b. NO. OF REFS
October 1970	37	3

8a. CONTRACT OR GRANT NO.	9a. ORIGINATOR'S REPORT NUMBER(S)
b. PROJECT NO. YF 38.535.005.01.006	TN-1134
c.	9b. OTHER REPORT NO(S) (Any other numbers that may be assigned this report)
d.	

10. DISTRIBUTION STATEMENT

This document has been approved for public release and sale; it's distribution is unlimited.

11. SUPPLEMENTARY NOTES	12. SPONSORING MILITARY ACTIVITY
	Naval Facilities Engineering Command

13. ABSTRACT

The 66-inch outside diameter 2.5-inch thick NEMO Model 600 spherical hull #3 has been hydrostatically pressure cycled till fatigue cracks appeared in the acrylic plastic and the top hatch plastically buckled. The plastic buckling of the hatch, fabricated from annealed 4130 alloy steel, took place during simulated repeated dives in the 2080 to 2250 foot depth range. The cracks in the acrylic plastic hull were located in the beveled surface in contact with the metallic polar closures. The first crack was observed only after the hull had been subjected to 993 consecutive pressure cycles, of which 815 cycles were to 1200 feet followed immediately by 178 cycles to 1540 feet. An additional 257 pressure cycles to 2000 foot depth did not implode the pressure hull but only caused the cracks to extend into the hull. The duration of sustained pressure loading in each pressure cycle was approximately 45 minutes followed by 45 minute relaxation period.

The cyclic tests conclusively prove that (1) an adequate cyclic fatigue safety factor exists for NEMO hulls performing, routinely, extended manned dives to 600-foot depth, and that (2) manned proof

Cont'd

DD FORM 1 NOV 68 1473 (PAGE 1)

S/N 0101-807-6801

UNCLASSIFIED

Security Classification

UNCLASSIFIED

Security Classification

14 KEY WORDS	LINK A		LINK B		LINK C	
	ROLE	WT	ROLE	WT	ROLE	WT
Acrylic resins						
Spheres						
Pressure vessels						
Deep water						
Underwater structures						
Hydrostatic pressure						
Failure						
Buckling						
Implosions						

DD FORM 1 NOV 68 1473 (BACK)
(PAGE 2)

UNCLASSIFIED

Security Classification

dives of 1 hour duration to 1200-foot depth can be performed providing the total number of proof test dives does not exceed 100. To prevent plastic buckling of the polar steel closures prior to general implosion of the capsule it is necessary to specify heat treated 4130 steel alloy for the polar penetration closures.

R 716

Technical Report

STRUCTURAL ANALYSIS OF A FULL-SCALE SPHERICAL ACRYLIC PLASTIC PRESSURE HULL

March 1971

Sponsored by

NAVAL FACILITIES ENGINEERING COMMAND

NAVAL CIVIL ENGINEERING LABORATORY

Port Hueneme, California

STRUCTURAL ANALYSIS OF A FULL-SCALE SPHERICAL ACRYLIC PLASTIC PRESSURE HULL

Technical Report R-716

YF 38.535.005.01.006

by

M. R. Snoey and M. G. Katona

ABSTRACT

This study was initiated to: (1) perform a finite element structural analysis on an acrylic plastic pressure hull, (2) compare the finite element results with available experimental results, and (3) present an operating-depth curve and make recommendations for future designs. The design analyzed was a pressure hull incorporating 12 spherical pentagons of acrylic plastic bonded together to form a sphere with an outside diameter of 66 inches and a wall thickness of 2.5 inches. Steel penetrations were located at the two poles. The experimental results were obtained from strain gage data from two independent pressure tests to 500 psi on two acrylic plastic hulls of the same design.

The finite element analysis of the hull structure placed particular emphasis on the acrylic plastic–steel boundary. The boundary conditions at the acrylic plastic–steel interface were two extreme cases: fixed and free. A time-dependent yield–failure criterion for acrylic plastic was combined with the structural analysis to provide an operating depth curve as a function of both time and temperature. Comparison of the finite element and experimental results indicated excellent agreement. At a temperature of 70°F and a maximum of 50 hours' load duration, the acrylic plastic hull can operate to 1,000 feet with a safety factor of 1.5 based on yield and a safety factor of 2.6 based on collapse. Design recommendations are also presented to provide guidelines for future design of the hull and its integration with an undersea vehicle.

CONTENTS

INTRODUCTION

Statement of the Problem

Today's undersea vehicles need greater visibility. The importance of improved visibility is evidenced by the increasing number and size of viewports placed in modern submersibles.[1] Ultimately, the most efficient and effective visibility will be gained from a transparent pressure hull, as Piccard[2] recognized when he proposed a spherical hull made of 12 spherical acrylic plastic pentagons with a manhole and hatch in one of the pentagons. This report is concerned with one of a series of important steps between Piccard's concept and a fabricated, operationally safe acrylic plastic pressure hull: the structural analysis.

Background

A full-scale spherical acrylic plastic pressure hull design is shown in Figure 1. The acrylic plastic hull design analyzed in this report was developed for use in the NEMO (Naval Experimental Manned Observatory) submersible; however, the sphere may be integrated in any undersea vehicle system. The acrylic plastic sphere is fabricated from 12 spherical pentagons of Plexiglas G* bonded together at the 30 joints with a SS-6217** clear adhesive. As shown in Figure 2, the sphere has a wall thickness of 2.5 inches with an outside diameter of 66 inches. Located at each pole is a steel retainer ring and closure plate in a 40-degree spherical angle cutout. The upper closure plate is a hatch for personnel ingress and egress, while the lower one is fixed and accommodates electrical and hydraulic penetrations. Reference 3 contains details on the design, development, and fabrication processes for the acrylic plastic sphere.

* Rohm and Haas trade name.

** Swedlow trade name.

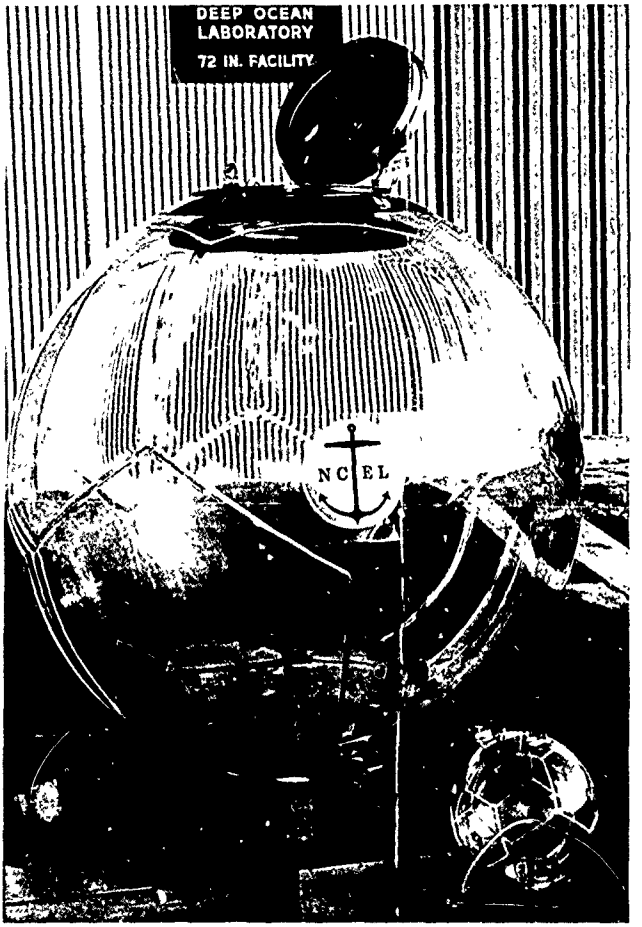

Figure 1. Full-scale, 66-inch outside diameter spherical acrylic plastic pressure hull with walls 2-1/2 inches thick.

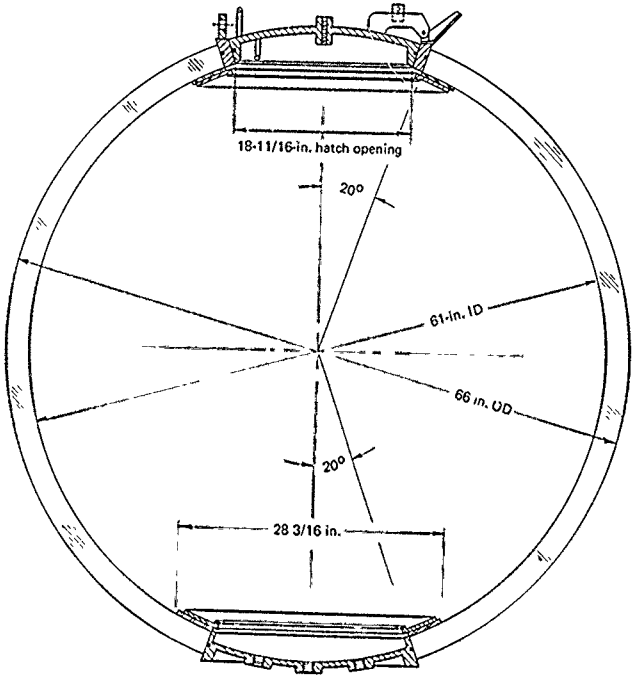

Figure 2. Cross section of the acrylic plastic spherical pressure hull.

Figure 3 indicates the method of retaining the steel penetrations in the acrylic plastic hull: retainer rings bolted to the top hatch ring and the bottom plate. A neoprene gasket is used as a cushion between the acrylic plastic hull and the retainer ring. O-rings serve to seal both the hatch–hatch ring interface and the acrylic plastic–steel interfaces. A hatch ring is used so the wear due to opening and closing the hatch is borne by hard metallic surfaces. The boundary condition (fixed or free) at the acrylic plastic–steel interface is a partial function of the tightness of the retainer-ring bolts, a fact which will be discussed in more detail later.

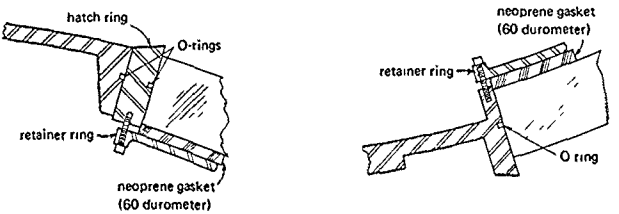

(a) Top hatch. (b) Bottom plate.

Figure 3. Details of the acrylic plastic–steel interfaces.

Objectives

For effective hull design it is extremely important to understand the structural behavior of the spherical plastic hull with steel penetrations. To design a penetration-free spherical hull is a relatively simple matter for both steel and acrylic plastic hulls. But to design acrylic plastic viewports in steel hulls or steel penetrations in acrylic plastic hulls is another problem altogether, due to the large modulus difference which results in relative displacements at the interface. The most important area to consider, then, is in the region of the penetrations in the hull where the continuity of a perfect sphere is interrupted. The objectives of this study are as follows:

1. To perform a finite element structural analysis on an acrylic plastic pressure hull with steel penetrations.
2. To compare the analytical results* with available experimental results.
3. To develop an operating-depth curve and make recommendations for future designs.

The purpose of this study is to provide information on (1) the effects of time and temperature on local yielding (Appendix A) and collapse, and (2) the effects of load cycling on the areas of high stress concentrations so that the conditions for a safe operational life for acrylic plastic hulls can be stipulated.

* For brevity, the results obtained by the finite element structural analysis will be referred to as "analytical results" in this report.

SCOPE OF INVESTIGATION

Experimental Study

The second objective of this report was to compare the analytical results with available experimental results in order to test the validity of the analytical results. Two independent tests with strain gages on two different pressure hulls of the same design were performed; one at NCEL (Naval Civil Engineering Laboratory) and one at SWRI (Southwest Research Institute). The NCEL test is documented in Reference 3, while the results of the test run at SWRI appear in this report. The tests were run on full-scale hulls, which provide more credible results than do models.

Figure 4 shows the instrumented acrylic plastic hull going into the NCEL 72-inch-diameter pressure vessel, rated at 5,500 psi. The cage around the sphere is for protection during handling. The tests at NCEL and SWRI were run at a temperature of 70°F and a loading rate of 100 psi/min. The maximum test pressure was 500 psi (1,125 feet), with all recorded strains exhibiting linear behavior to this load.

During the tests it was necessary to tether the buoyant pressure hull in the test tank, creating a 4,020-pound force on the bottom plate. This force can be considered negligible with respect to the pressure loading on the hull since force equilibrium on the bottom plate occurs at about a 26-foot depth with the hydrostatic pressure being the principal force for depths below that level.

The hull tested at NCEL had strain gage rosettes on both the internal and external surfaces, while the hull tested at SWRI had them only on the external surface. Detailed information on the strain gages can be found in Appendix B.

Analytical Study

General. Since the acrylic plastic hull is fundamentally a solid of revolution, it lends itself to analysis by Lamé field equations for axisymmetric solids. However, due to its complex geometry and composite material construction, numerical methods must be employed to obtain solutions. For this reason, a finite element computer program, written by Wilson,[4] was adopted as the basic tool for analysis. In brief, the idealizations are: axisymmetric structure and loading conditions, linear elastic response, infinitesimal strain, and applicability of small deformation theory. The first portion of Appendix C is devoted to summarizing the program's capabilities, and the assumptions involved in solving a solid of revolution by the finite element technique. Previous uses of the finite element technique in analyzing acrylic plastic structures include analyses of conical viewports and an acrylic plastic hull.[5-9]

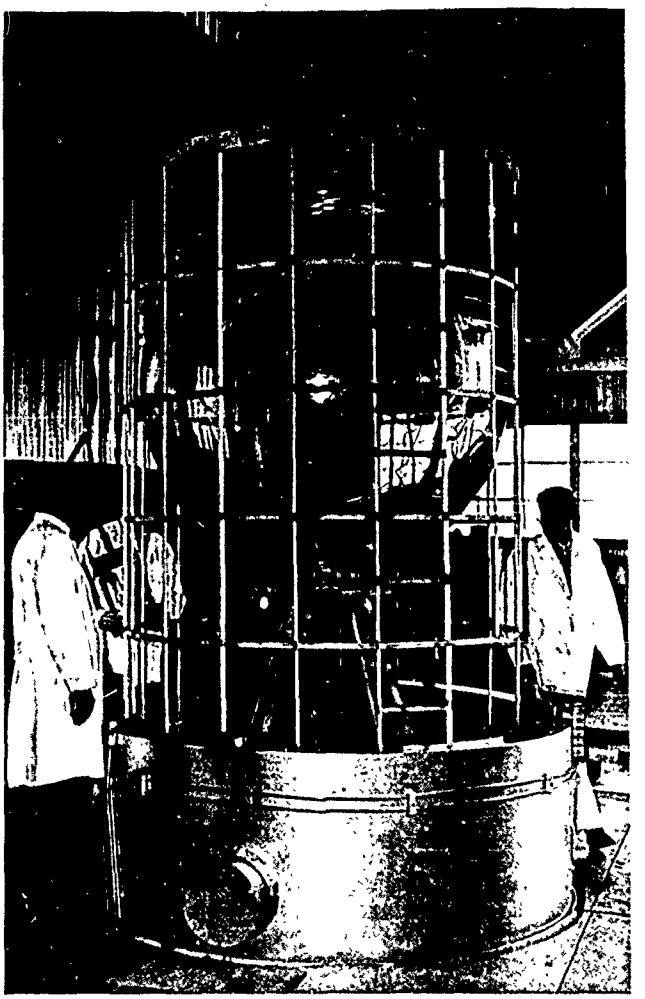

Figure 4. Instrumented acrylic plastic spherical pressure hull undergoing test at NCEL.

The structural idealizations in treating the pressure hull as an axisymmetric solid will now be discussed followed by a discussion of the material properties of acrylic plastic.

Structural Idealization. Aside from unintentional anomalies arising during fabrication of the acrylic plastic hull, there are some inherent structural details that do not conform to the concept of a solid of revolution. In particular the pentagonal construction of the acrylic plastic hull, the circle of bolt holes in the boss on the bottom plate, and the scallops on the bottom plate flange (Figure 5) do not strictly conform to the concept of an axisymmetric solid. However, each of these anomalies occurs periodically with θ, the angle of revolution, so that the net integrated effect over one period of 2π would result with zero net θ-displacement. Hence, on a global level, the primary assumption of no θ-displacements is still valid for the axisymmetric assumption. Moreover, the bonding adhesive which joins the pentagons together has material properties similar to those of the acrylic plastic pentagons, thus minimizing local stress concentrations. The assumption of nearly homogeneous material properties appears valid because imploded models[3] had lines of fracture crossing the bonds indicating the bonds were not the weak region. Minimal local stress concentrations should also occur around the holes in the boss because they will contain stiff penetrators of similar steel. In order to model the scallops on the flange of the bottom plate as a solid of revolution, the scallops were idealized as a uniform ring of equivalent mass, thus averaging the periodic stiffness. With these idealizations, the representation of the acrylic plastic hull as a true solid of revolution is very close to physical reality.

By far the most significant structural consideration is the appropriate modeling of the interfaces between the steel penetrations and the acrylic plastic hull. Under the Coulomb friction hypothesis, normal forces are transmitted undiminished across the interface, whereas the friction or shear force has an upper maximum limited by the product of normal force and coefficient of friction. In reality, the interfacing surfaces are polished and greased, suggesting a frictionless boundary which allows full relative movement between the acrylic plastic and steel until wedging equilibrium occurs.

On the other hand, there are two factors which tend to retard the relative movement. First, the magnitude of the pressure normal to the interface is approximately seven times greater than the hydrostatic pressure load and thus may compensate for the low coefficient of friction. Second, the retainer rings with neoprene gaskets (Figure 3) may inhibit relative movement, depending upon the magnitude of torque on the bolts. Hence, because of the physical uncertainties in representing the response at the interface, two limiting cases were analyzed with the intention of bracketing the actual response.

In the first case (Figure 6a), it was assumed the frictional force and retainer ring restricted all relative movement and thus provided a complete continuum across the interfaces. For the second solution (Figure 6b), a completely frictionless boundary was assumed. This allowed the hull and penetrations to wedge into equilibrium unrestricted as if the coefficient of friction was zero.

The analysis of the continuum assumption is a straightforward application of axisymmetric finite element programs previously cited. However, the solution of axisymmetric problems with structural members connected by frictionless interfaces of arbitrary orientation had not been included in any of the standard computer programs. This program extension was developed by the authors and incorporated into the above-mentioned program. An outline and discussion of this effort are presented in the second part of Appendix C.

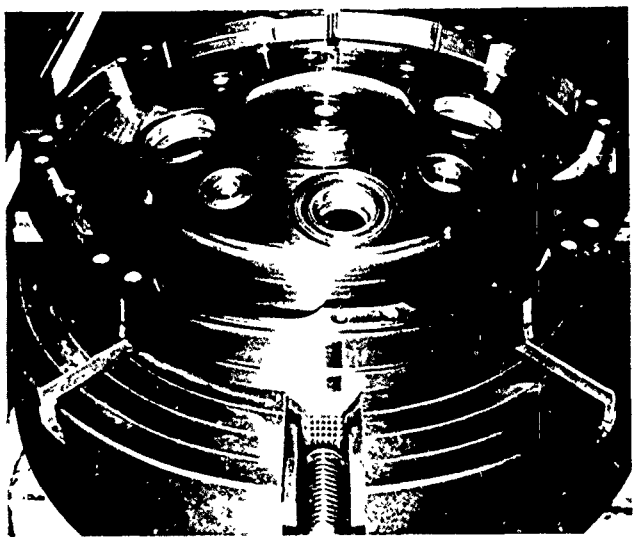

Figure 5. Full-scale bottom plate for acrylic plastic spherical pressure hull.

Failure Criterion. The mechanical properties of the structural materials that comprise the spherical hull are given below:

Component	Material	Modulus of Elasticity, E (psi)	Poisson's Ratio, ν	Yield Stress, σ_y (psi)
Top hatch and bottom plate	steel, AISI 4130, annealed	29,500,000	0.29	55,000
Pressure hull	acrylic Plexiglas G	444,000[6]	0.4[6]	see Figure A-1 in Appendix A

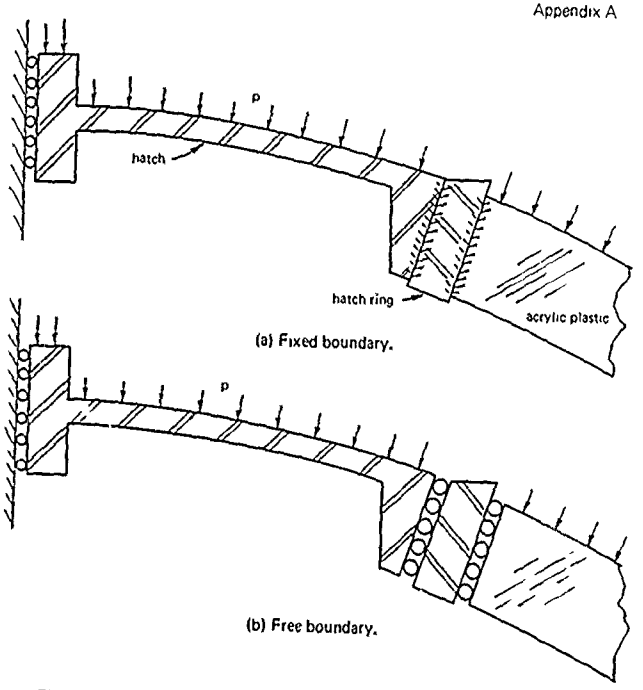

Figure 6. Boundary conditions for the finite element analysis of acrylic plastic hull with steel penetrations.

The failure concept for the acrylic plastic hull is based on a lower limit analysis, that is, when the distortional energy at any point in the structure exceeds the energy which initiates yielding of a one-dimensional test specimen, then the structure is defined to be at failure. The distortion-energy theory or the Huber–von Mises–Hencky theory,[10] normalized for hydrostatic loading, is defined as follows.

$$\sigma_o = \sqrt{\frac{(\sigma_1 - \sigma_2)^2 + (\sigma_2 - \sigma_3)^2 + (\sigma_1 - \sigma_3)^2}{2}} \qquad (1)$$

where σ_o = effective stress per unit of applied pressure, psi/psi

$\sigma_1, \sigma_2, \sigma_3$ = principal stresses per unit of applied pressure, psi/psi

The applicability of the distortional energy failure criterion to steel is well documented, and the behavior of acrylic plastic has also been found to obey this criterion for yielding.[11, 12] However, the time and temperature dependence of the properties of acrylic plastic requires an extension of the material failure laws. These dependent properties were discussed in a previous investigation[7] and are summarized in Appendix A. The present study considers the effect of time, temperature, and state of stress on the yield strength of acrylic plastic.

In analyzing structures made of viscoelastic materials, both the loading history and loading paths are taken into consideration. To apply the failure criteria for acrylic plastic to the pressure hull, the following assumptions have been made.

1. *Residual stresses.* Under normal operations, there will be enough time between dives so that residual or "memory" stresses will be negligible.

2. *Path of loading.* The path generating maximum stresses is an instantaneous step loading to maximum pressure, which is held for a specified loading duration.

The specified loading path corresponds to a "crash" dive to an operational depth which is maintained for the duration of the dive. The viscoelastic solution from this loading path is equivalent to the elastic solution at time = 0+. Moreover, the initial stresses are maximum in terms of magnitude and stress concentrations because, as time progresses, the stresses redistribute and relax. Consequently, the elastic solution produces the governing maximum stresses and may be conservatively assumed constant with time. The degree of conservatism in this assumption is quite small as

can be deduced by applying the elastic-to-viscoelastic correspondence principle to the Lamé elastic solutions for stresses in a perfect thick-walled sphere[13] which are given below:

$$\sigma_1 = \sigma_2 = \frac{-b^3(a^3 + 2r^3)}{2r^3(b^3 - a^3)} \quad (2)$$

$$\sigma_3 = \frac{b^3(r^3 - a^3)}{r^3(b^3 - a^3)} \quad (3)$$

where $\sigma_1, \sigma_2, \sigma_3$ = principal stresses per unit of applied pressure, psi/psi

a = inside radius of sphere, in.

b = outside radius of sphere, in.

r = radial coordinate, in.

Since these stresses are independent of material properties, the correspondence principle dictates the stresses are time-independent for a viscoelastic sphere. Thus, with the hull approximating a sphere, the stress redistribution is minimal.

In summary, the operational depth of the acrylic plastic hull is determined by applying the time-dependent, yield–failure criterion to the computed effective stress which is maximum in both time and space. The time relationship between the operational depth in seawater, effective stress, and yield stress is as follows:

$$d(T) = 2.25\frac{\sigma_y(T)}{\sigma_o} \quad (4)$$

where $d(T)$ = operational depth as a function of time, ft

$\sigma_y(T)$ = yield stress as a function of time, psi

σ_o = effective stress per unit of applied pressure, psi/psi

RESULTS AND DISCUSSION

Comparison of Experimental and Analytical Results

The second objective of this report specifies that data from a finite element stress analysis of the acrylic plastic pressure hull will be compared to available experimental data. Figures 7 through 10 contain results for

both the free and fixed boundary conditions and thus enable a thorough comparison with the experimental results. All the stresses in the acrylic plastic portion of the pressure hull were found to be in compression. Since stress is determined at the centroids of the elements, it was necessary in the regions of high bending to linearly extrapolate to get correct values at the internal and external surfaces.

Figure 7 shows both NCEL and SWRI hoop-stress results for the external surface and demonstrates the excellent agreement between the experimental and analytical stress data. The fixed and free boundary conditions provided the two bracketing extremes for the analysis, as is shown in Figure 7, the experimental results more closely fit the fixed boundary case. This is reasonable because in both experimental spheres the torque applied to the retainer-ring bolts was in excess of that necessary to form a seal at the O-ring.

The experimental and analytical hoop stress results for the internal surface are shown in Figure 8. Figures 7 through 10 clearly indicate the bending in the top hatch and bottom plate. The differences in the stress levels of the acrylic plastic due to the fixed and free boundary conditions are clearly shown in Figure 8.

Figure 9 shows the experimental and analytical meridional stress results for the external surface. This figure indicates how much worse the bending is in the top hatch than in the bottom plate. Figure 9 also clearly shows that the bosses in the bottom plate reduce the stresses in that region.

The experimental and analytical meridional stress results for the internal surface are shown in Figure 10. It can be seen that the presence of the bosses on the external face of the bottom plate affects the stress distribution on the internal surface, but to a lesser degree than on the external surface.

Analytical Stress Response

The data provided by the finite element program emphasize the effective stresses because they are the best indicators of failure regions. Figure 11 gives the maximum effective stress distribution around the sphere independent of the r-coordinate. Thus, Figure 11 points out the locations of the worst points in the hull and compares all points to the Lamé solutions for a perfect sphere. This figure gives a good indication of where the fixed and free cases differ and shows how quickly the stress concentrations in the acrylic plastic diminish to membrane values.

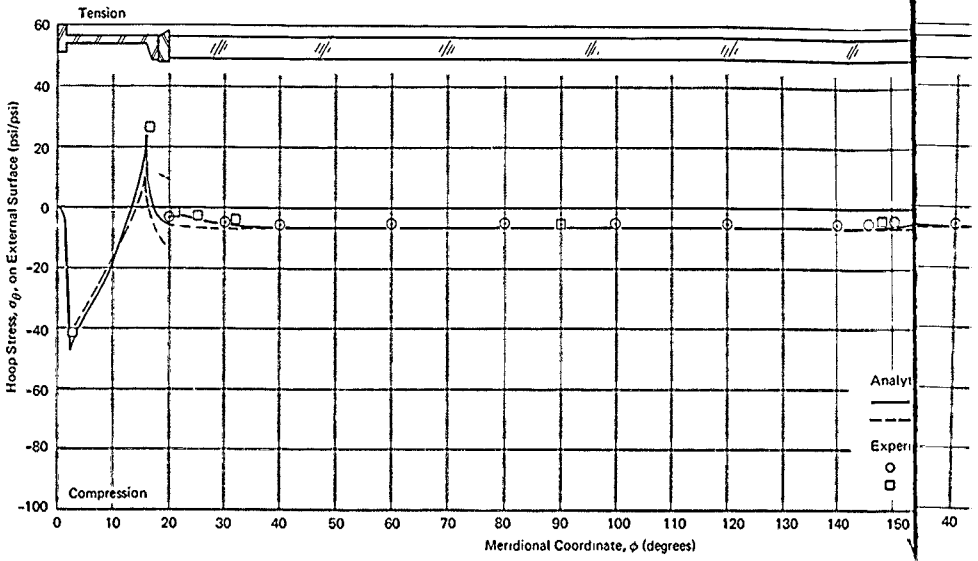

Figure 7. Comparison of experimental and analytical hoop stress results for external surface of acrylic plasti

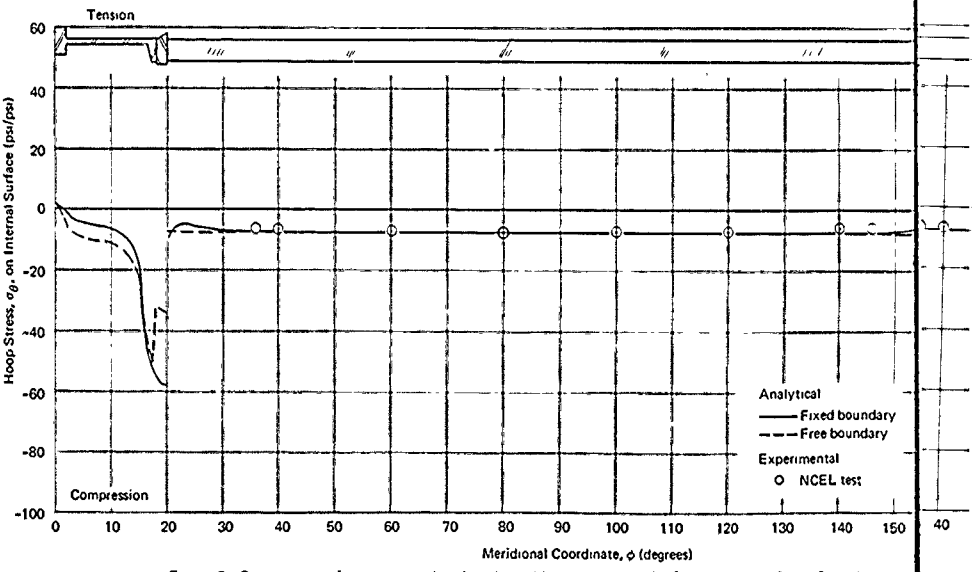

Figure 8. Comparison of experimental and analytical hoop stress results for internal surface of acrylic plasti

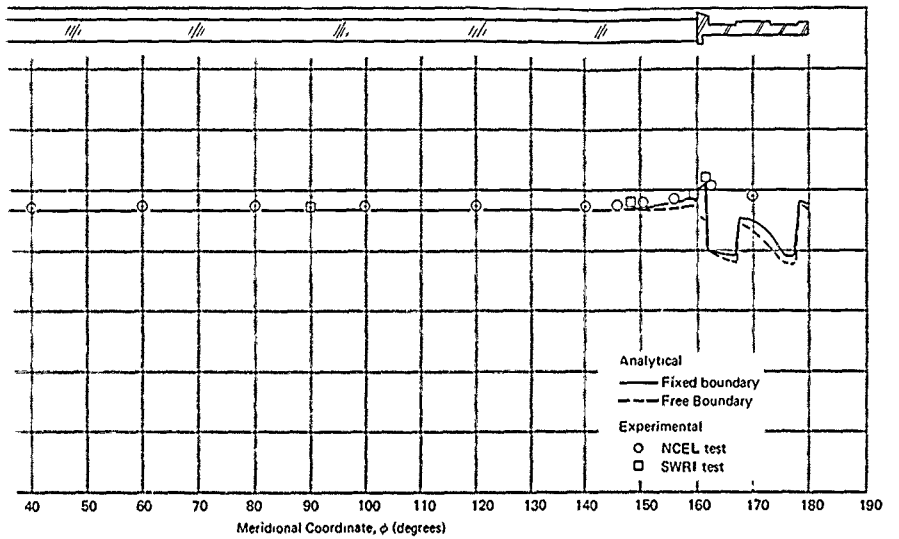

parison of experimental and analytical hoop stress results for external surface of acrylic plastic spherical hull.

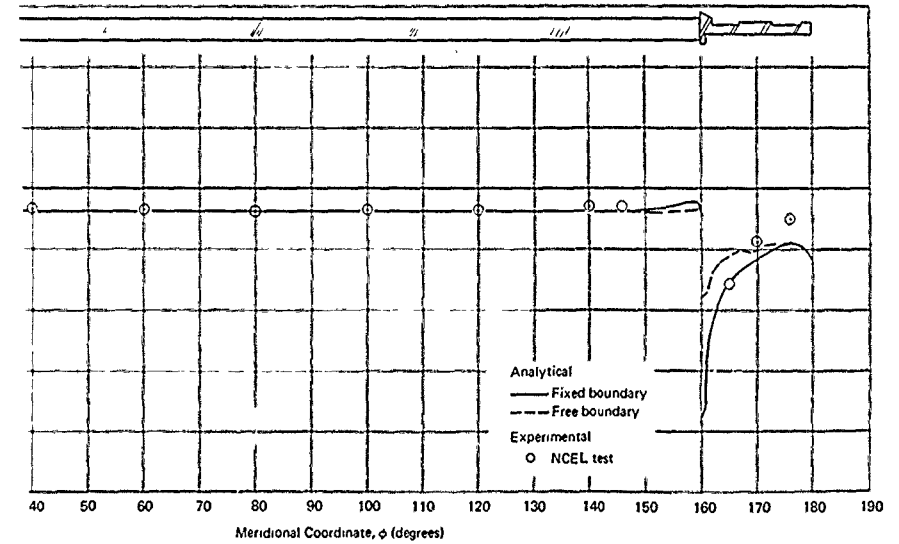

parison of experimental and analytical hoop stress results for internal surface of acrylic plastic spherical hull.

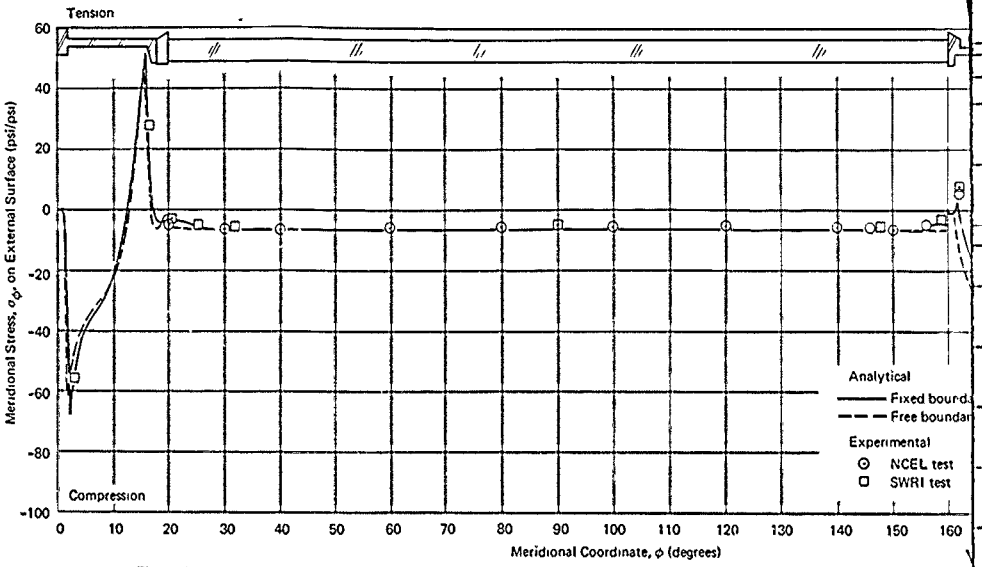

Figure 9. Comparison of experimental and analytical meridional stress results for external surface of acrylic plastic spher

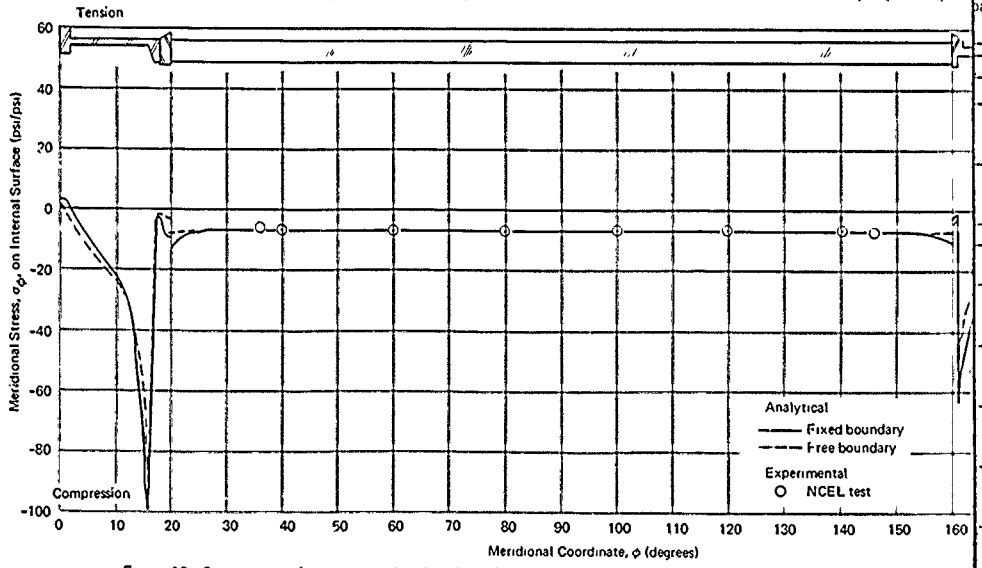

Figure 10 Comparison of experimental and analytical meridional stress results for internal surface of acrylic plastic spher

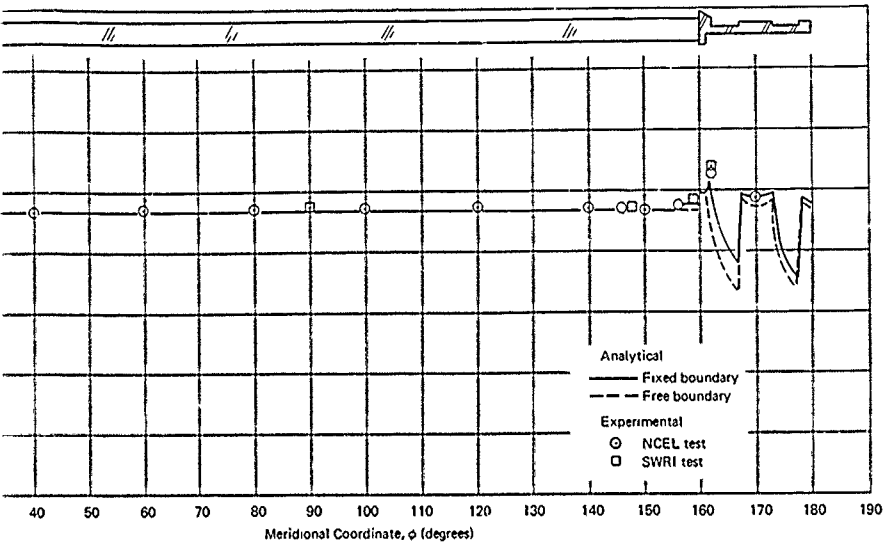

arison of experimental and analytical meridional stress results for external surface of acrylic plastic spherical hull.

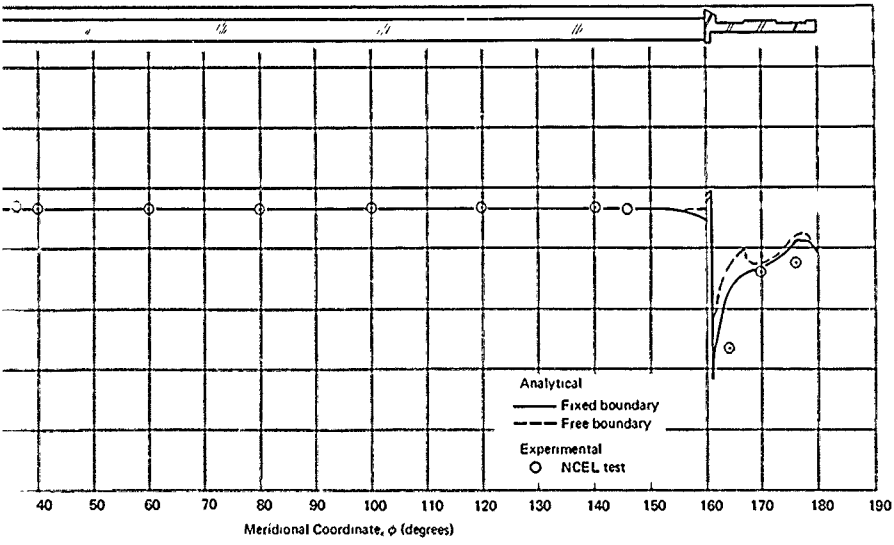

arison of experimental and analytical meridional stress results for internal surface of acrylic plastic spherical hull.

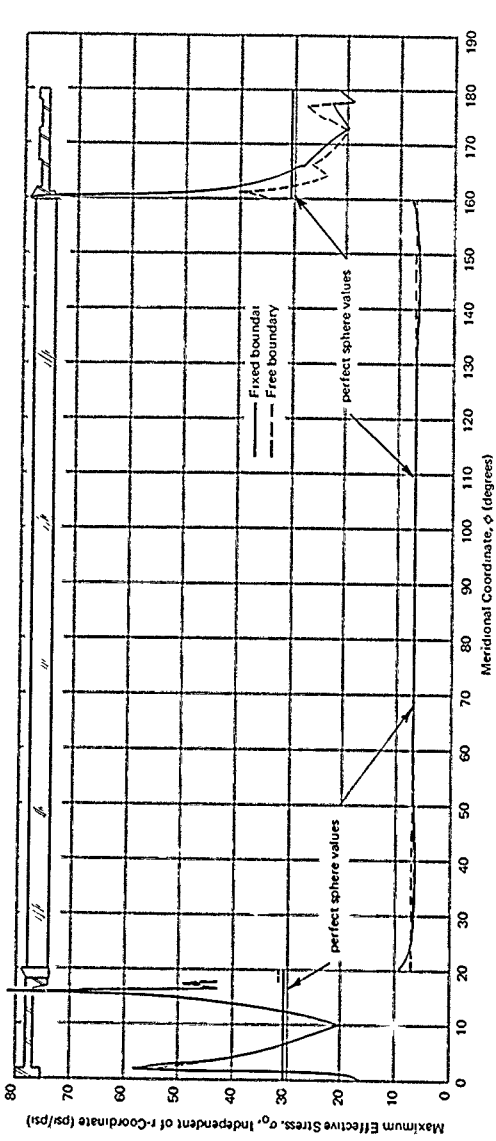

Figure 11. Maximum effective stresses in acrylic plastic spherical pressure hull independent of r-coordinate.

Table 1. Maximum Effective Stresses

Material	Meridional Coordinate, ϕ (deg)	Radial Coordinate, r (in.)	Comments	Effective Stress, σ_o (psi/psi) for—	
				Fixed Boundary	Free Boundary
Acrylic plastic	20.3	30 50	near top hatch (internal surface)	9.1	7.1
	90.0	30.50	at the equator (internal surface)	7.1	7.1
	90 0	33.00	at the equator (external surface)	5.6	5 6
	159.7	30.50	near bottom plate (internal surface)	7.4	7.1
Steel	2.0	33.00	bending near center of top hatch (external surface)	58	51
	15.8	32.45	bending near periphery of top hatch (internal surface)	82	74
	160 3	30.40	bottom plate flange (internal surface)	79	35
	161.3	31.50	bending near periphery of bottom plate (internal surface)	56	40

Table 1 lists some effective stress sensitivity values at specific locations. For the acrylic plastic, the maximum effective stress was at the acrylic plastic–top hatch ring interface and was 1.3 times the membrane effective stress. The maximum effective stress in the steel was in the top hatch and was 2.7 times the membrane effective stress. The fixed boundary condition was the worst case for both the steel and acrylic plastic. At the equator, the fixed and free cases were equal, but the fixed case produces a higher bending stress in the top hatch than does the free case. This is because the moment on the hatch is increased by the additional shear force at the boundary.

Figures 12 through 19 display effective stress contour and surface plots for the very important acrylic plastic–steel interface region. These regions were magnified in the plots for better understanding and more accurate interpretation. The stress contour plots provide visual quantitative data, whereas the surface plots provide a visual qualitative measure of the locations of maximum stress concentrations.

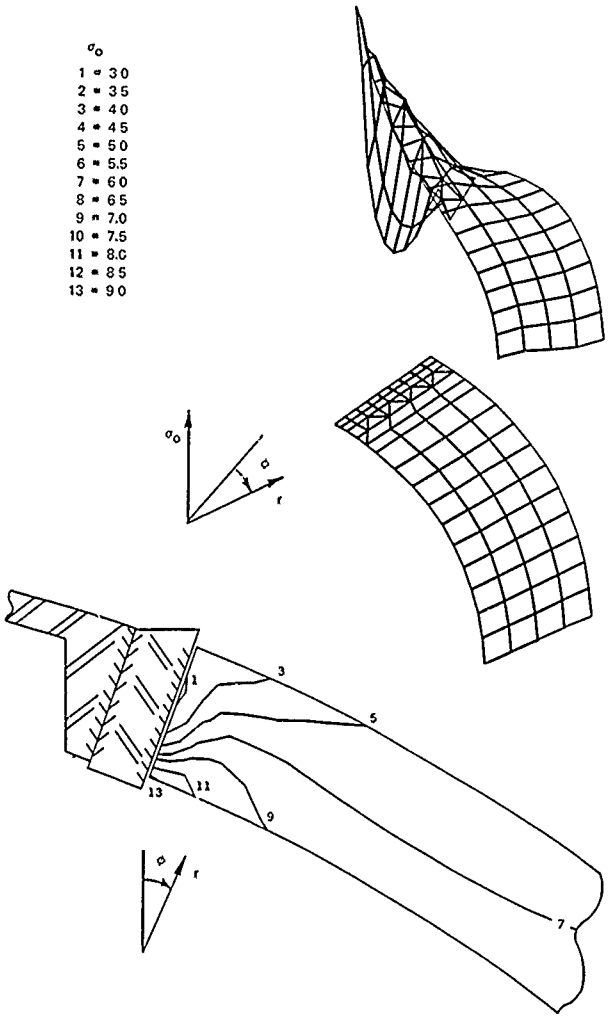

Figure 12. Effective stress contour and surface plots for acrylic plastic at top hatch for fixed boundary condition.

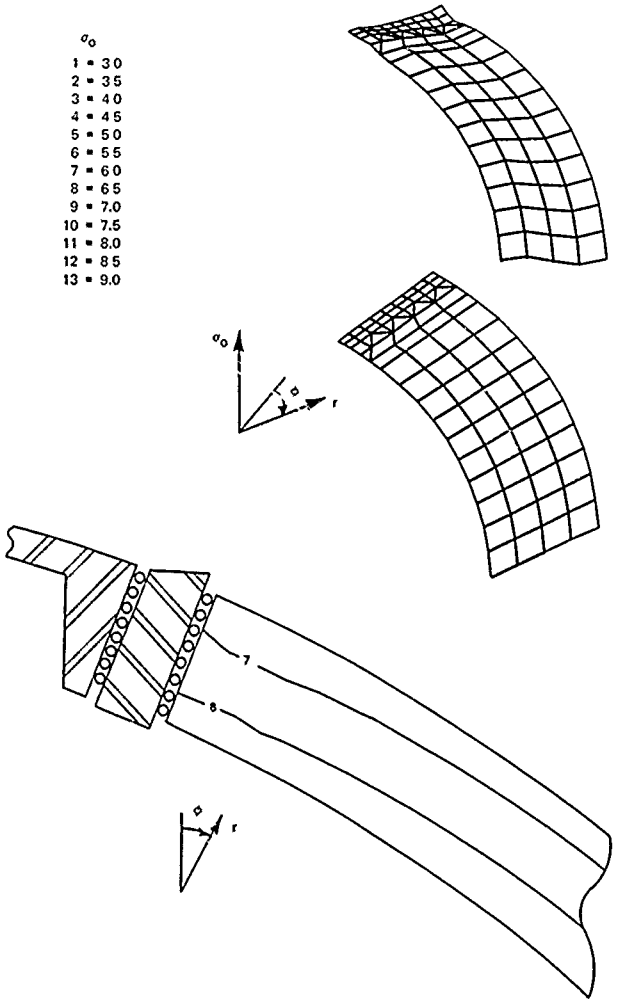

Figure 13. Effective stress contour and surface plots for acrylic plastic at top hatch for free boundary condition.

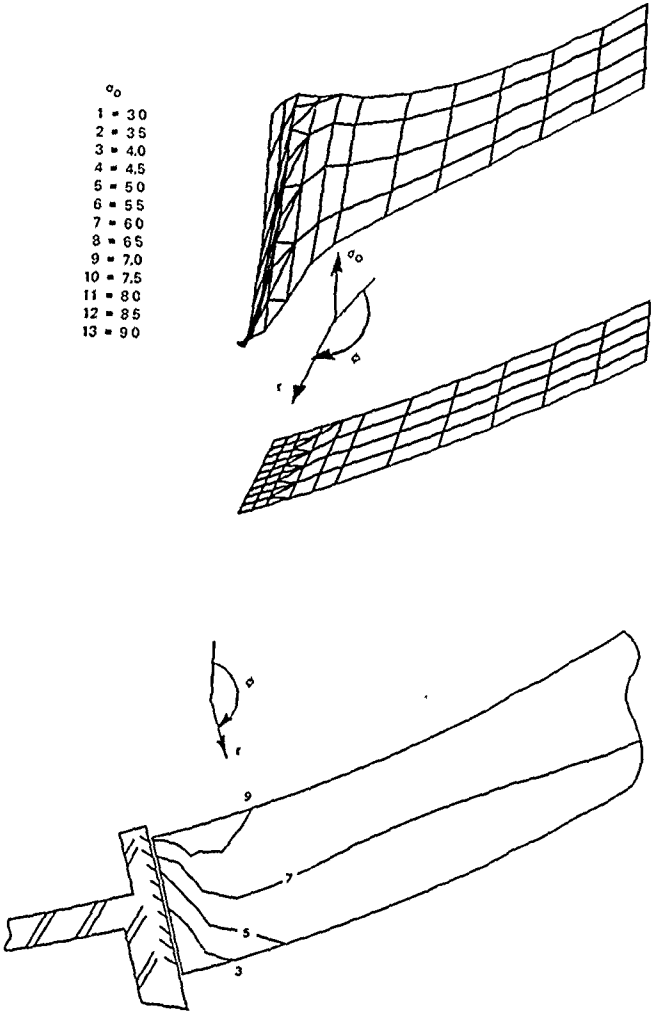

Figure 14. Effective stress contour and surface plots for acrylic plastic at bottom plate for fixed boundary condition.

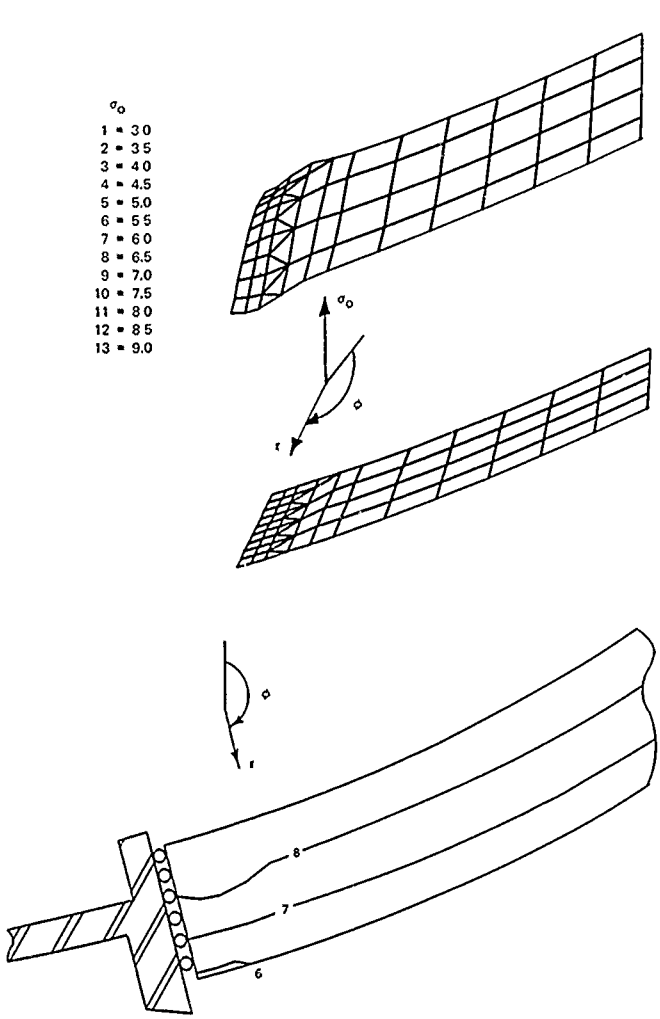

Figure 15. Effective stress contour and surface plots for acrylic plastic at bottom plate for free boundary condition.

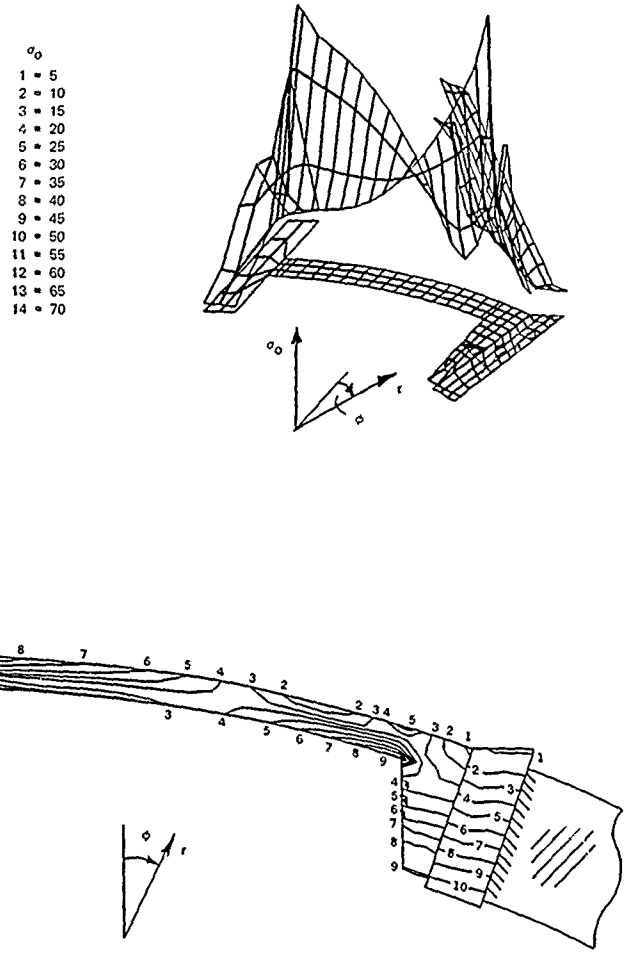

Figure 16. Effective stress contour and surface plots for top hatch for fixed boundary condition.

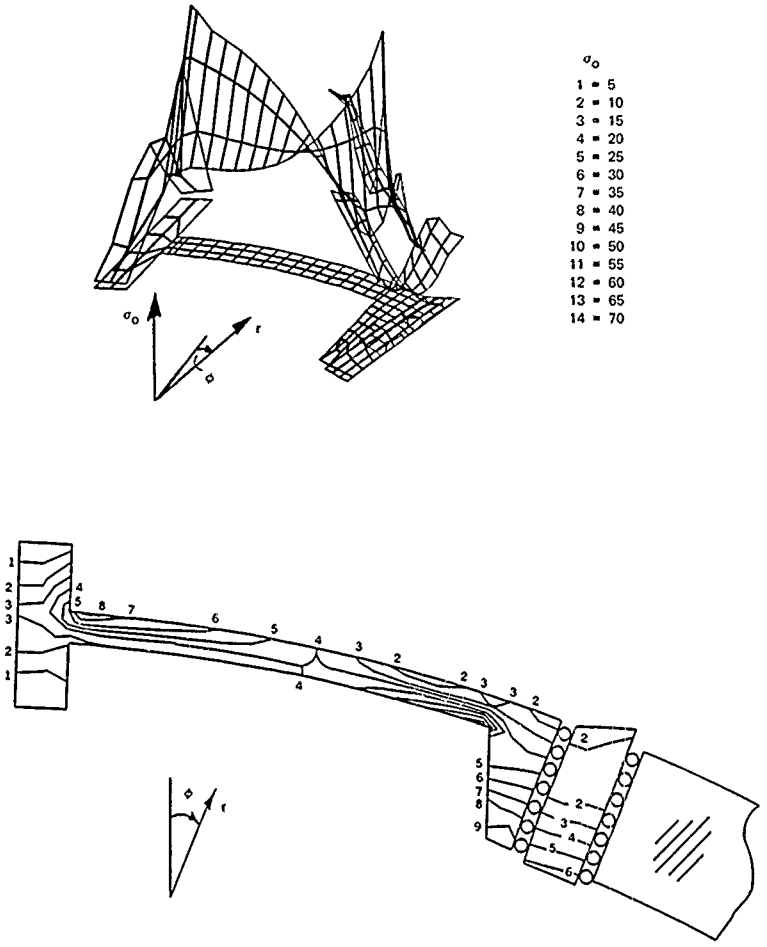

Figure 17. Effective stress contour and surface plots for top hatch for free boundary condition.

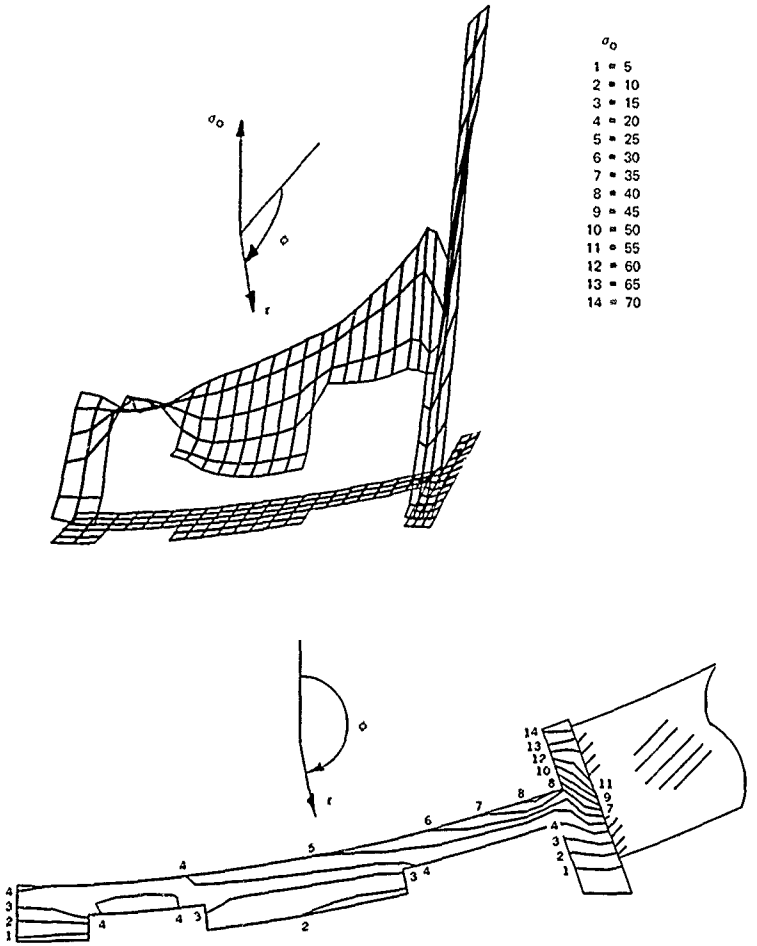

Figure 18. Effective stress contour and surface plots for bottom plate for fixed boundary condition.

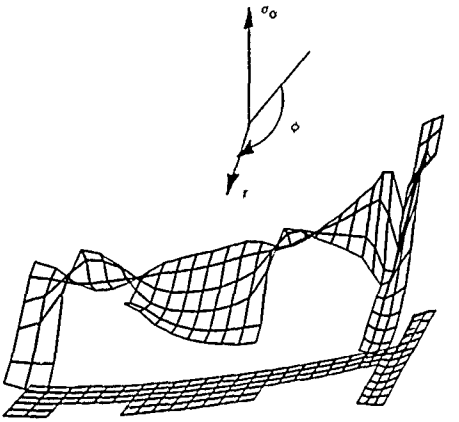

σ_o
1 = 5
2 = 10
3 = 15
4 = 20
5 = 25
6 = 30
7 = 35
8 = 40
9 = 45
10 = 50
11 = 55
12 = 60
13 = 65
14 = 70

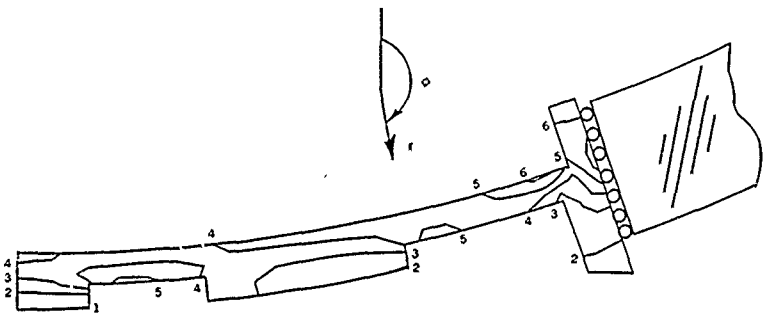

Figure 19. Effective stress contour and surface plots for bottom plate for free boundary condition.

Figures 12 and 13 present the effective stress contour and surface plots for acrylic plastic at the top hatch with fixed and free boundary conditions. The fixed case in Figure 12 shows a stress concentration in the acrylic plastic at the corner on the internal surface, whereas the free case in Figure 13 indicates a stress distribution similar to the Lamé solutions.

Figures 14 and 15 show the effective stress contour and surface plots for acrylic plastic at the bottom plate for both the fixed and free boundary conditions. Although the fixed case solution appears to exhibit a small stress concentration near the internal surface, the maximum effective stress value from Table 1 for the fixed case at this location is approximately equal to that for the free case.

The fixed and free cases for the steel top hatch are shown in Figures 16 and 17. It is evident from both figures that the bending in the top hatch produces high effective stresses in the "neck" section. The effective stress contour and surface plots for the bottom plate are shown in Figures 18 and 19 for both fixed and free boundary conditions. The bottom plate exhibits some bending, but the maximum value occurs as a bearing stress on the flange with a fixed boundary condition.

Analytical Displacement Response

Table 2 lists maximum radial displacements of the pressure hull at several specific locations. As would be expected, the acrylic plastic displaces more at the equator than at any other location. 0.13 inch inward at a 1,000-foot depth. Caution must be exercised in designing internal equipment so that compression of the hull is not impeded in any manner. The displacements at the equator are equal for the fixed and free cases, but because of the small polar displacements for the fixed case the acrylic sphere becomes ellipsoidal for the fixed case while it remains almost spherical for the free case.

The top hatch does move inward relative to the hatch ring for the free boundary condition, but neither the top hatch ring nor bottom plate moves inward relative to the acrylic plastic. In fact, just the opposite occurs with the acrylic plastic moving inward relative to the steel. Thus, if the torque on the retainer ring bolts is increased, retarding movement of the acrylic plastic, the boundary condition approaches the fixed case. From past experience with viewports, one would believe the free case to be the operational boundary condition, but the retainer ring has some influence. The maximum instantaneous relative movement at the acrylic plastic–steel interface for a 1,000-foot depth is 0.11 inch, while the maximum relative movement at the hatch–hatch-ring interface is only 0.01 inch.

Table 2. Maximum Radial Displacements

Material	Meridional Coordinate, ϕ (deg)	Radial Coordinate, r (in.)	Comments	Radial Displacements, $\delta_r \times 10^5$ (in./psi) for—	
				Fixed Boundary	Free Boundary
Acrylic plastic	20	30 50	acrylic plastic–steel interface (internal surface)	-1.9	-26
	90	30 50	at the equator (internal surface)	-30	-30
	160	30 50	acrylic plastic–steel interface (internal surface)	-2 6	-28
Steel	0	31.23	center of top hatch (internal surface)	-15	-4 3
	18	30 50	top hatch (internal surface)	-1.7	-2.3
	18	30.50	top hatch ring (internal surface)	-1.7	-0.1
	20	30 50	acrylic plastic–steel interface (internal surface)	-1.9	-0.8
	160	30 50	acrylic plastic–steel interface (internal surface)	-2.6	-5.4
	180	31.48	center of bottom plate (internal surface)	-14	-5 5

Discussion

Table 3 is a comparison of the finite element results with the exact Lamé solutions at the equator of the sphere. The effects of the penetrations were negligible here; the values for the fixed and free cases are equal. The finite element values are equal to those for Lamé solutions for both stresses and displacements, which provides yet another check on the accuracy of the computer program. Thus, since there has been excellent correlation between the experimental results, Lamé solutions, and the finite element results, application of this validated program to spheres of different geometries can be undertaken with confidence.

Structural adequacy of a pressure hull must be checked for two modes of failure (1) material yielding, and (2) elastic instability of thin shells. Yielding was treated earlier in this report, however, since this hull design has a wall thickness/outside radius ratio of 0.076, or less than the rule of thumb value (0.1) for treating a shell as thin-walled, stability must be investigated. Because

of (1) the lack of experimental data; (2) the complex interrelationship of both elastic modulus and Poisson's ratio with time, temperature, and stress level; and (3) the absence of a well-defined linear region and yield point, it is extremely difficult to apply stability equations to an acrylic plastic sphere. Although collapse cannot be calculated for any point in time with a stability equation, the equation is still helpful for understanding the functional variables. The classical stability equation is:[14]

$$p_{cr} = \frac{2E}{\sqrt{3(1-\nu^2)}}\left(\frac{t}{b}\right)^2 \qquad (5)$$

where p_{cr} = critical collapse pressure, psi

E = modulus of elasticity, psi

ν = Poisson's ratio

t = wall thickness of sphere, in.

b = outside radius of sphere, in.

Table 3. Comparison of Lamé and Finite Element Results for Acrylic Plastic Hull (66-inch OD, 61-inch ID)

Location	Solution	Meridional Coordinate, ϕ (deg)	Radial Coordinate, r (in.)	Effective Stress, σ_o (psi/psi)	Radial Displacement, $\delta_r \times 10^5$ (in /psi)
Internal surface	Lamé	90	30.5	7 1	-30.0
	finite element[a]	90	30.5	7.1	-30.0
External surface	Lamé	90	33.0	5.6	-26.5
	finite element[a]	90	33.0	5 6	-26.5

[a] Fixed and free boundary results are equal at this point.

Figure 20 presents the yield depth and collapse depth curves for the acrylic plastic pressure hull plotted on a semi-log scale because a log-log scale tends to smear the data into a straight line. Instead of attempting to calculate collapse depths, experimental test results from Reference 3 were plotted However, a small difficulty was encountered. The models tested in Reference 3 were not perfect scale models because the t/b ratio was different from that of the full-scale hull. But since the terms in Equation 5 can be separated into two categories, material properties and geometrical properties, it was easy to correlate the critical pressures. The models and full-scale hull were fabricated of identical material, Plexiglas G, so it was necessary only to use the scale factor for size

$$\frac{(t/b)^2 \text{ full scale}}{(t/b)^2 \text{ model}} = \frac{(2.5/33)^2}{(0.5/7.5)^2} = 1.29$$

After equalizing the full-scale and model collapse-depth values, there was good agreement between them as shown in Figure 20.

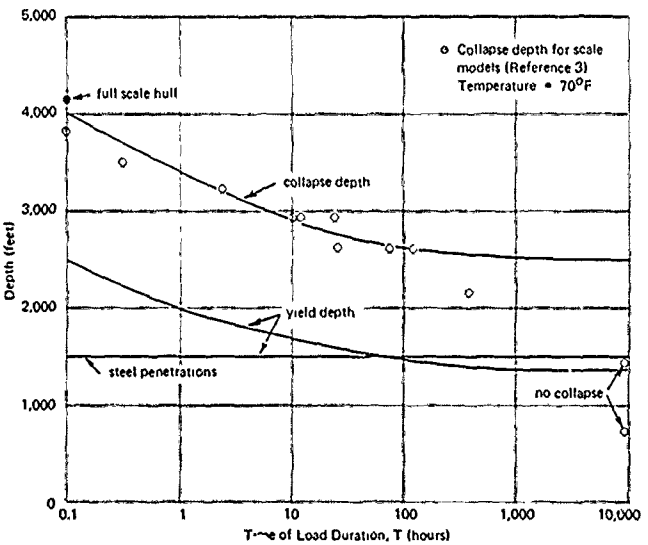

Figure 20. Yield depth and collapse depth curves for the acrylic plastic spherical pressure hull.

As anticipated, the collapse depth curve had the same general shape as the yield depth curve. This is reasonable because with a constant t/b ratio, the critical collapse depth is dependent on the material-properties portion of the equation, therefore, critical collapse depth should reflect the general dependence of acrylic plastic on time.

As Figure 20 indicates, yielding always occurs before the catastrophic stability failure of the hull. With a temperature of 70°F, and a load duration of 50 hours, the 66-inch OD acrylic plastic hull with 2-1/2-inch thick walls can operate to 1,000 feet with a safety factor of 1.5 based on yield and a safety factor of 2.6 based on collapse.

Figure 21 shows a before-test and after-test picture of the AISI 4130 steel top hatch. Notice the complete reversal of curvature in the hatch after the test to 2,000 feet. The hatch yielded without collapse of the hull, which appears to verify the 1,500-foot yield depth. Although Table 1 indicates yielding in the bottom plate, this is probably not actually the case because of the increased material in the flange due to the retainer ring. Any significant deformation of the bottom-plate flange would probably require shearing of the retainer-ring bolts.

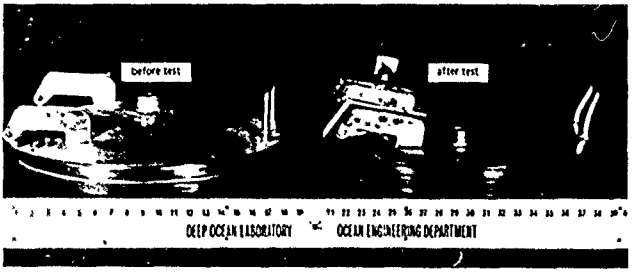

Figure 21. Top hatch after test of full-scale hull to 2,000 feet.

FINDINGS

1. The spherical acrylic plastic pressure hull's operating depth is dependent on both load duration and temperature of environment.

2. There was excellent agreement between the experimental results and the finite element results, with the experimental results agreeing more closely with the fixed case results than with the free case results.

3. At a temperature of 70°F and a maximum of 50 hours' load duration, the the acrylic plastic hull can operate to 1,000 feet with a safety factor of 1.5 based on yield and with a safety factor of 2.6 based on collapse.

4. At a temperature of 70°F and a load duration of 50 hours or less, yielding of the top hatch and bottom plate determines the operating depths, at 50 hours or greater, the behavior of the acrylic plastic hull under loading governs the operating depths.

5. The maximum stress concentration in the acrylic plastic hull was at the acrylic plastic–top hatch ring interface for a fixed boundary condition. The local effective stress at the interface was 1.3 times the membrane effective stress.

6. The maximum stress concentration in the steel penetrations was in the top hatch for a fixed boundary condition. The effective stress in the hatch was 2.7 times the membrane effective stress.

7. The stress concentration in the acrylic plastic hull due to the steel penetrations dissipated within 15 degrees of the acrylic plastic–steel interface.

DESIGN RECOMMENDATIONS

This section presents useful information for (1) present operation of the acrylic plastic hull as used in the NEMO system and (2) future design modifications. Integration of the sphere with a submersible vehicle is also discussed because it can affect the structural behavior of the sphere.

Operating-Depth Curve

Figure 22 presents an operating-depth curve, for the design investigated in this report, which includes both time and temperature. The curve originates from utilizing the maximum effective stresses in Table 1 together with the yield strength of steel and acrylic plastic as shown in Equation 4.

The load duration time used in the abscissa is directly influenced by the mission profile of the vehicle. To aid in selecting the proper load duration time, Figure 23 was included. If a series of dives is scheduled with a turn-around time less than the dive time as shown in Figure 23a, then the creep during the dives is cumulative and the dive times should be added to determine load duration time. Reference 3 experimentally verified this with strain gage tests. Pressure cycling tests indicated no cumulative gain in strains in the sphere for either a 6-hour or 2-minute cycle period as long as the relaxation time was at least as long as the load-duration time. Possible effects at the interface are discussed later.

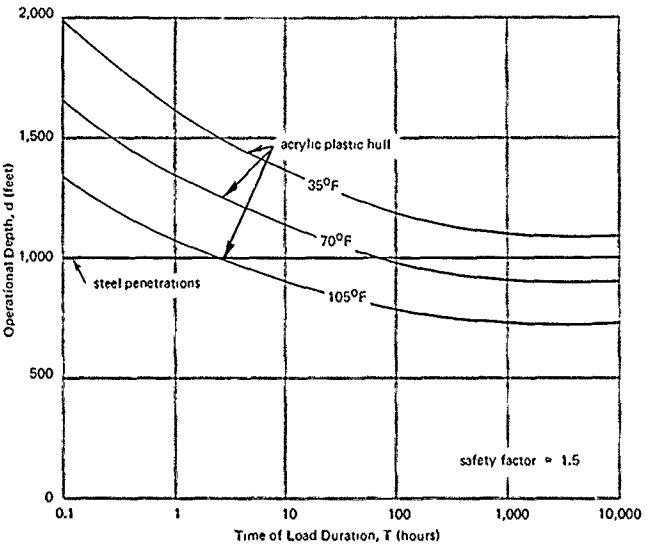

Figure 22. Operating depth curves for the acrylic plastic spherical pressure hull.

Figure 23b illustrates a case in which the dive time is less than or equal to the turn-around time. In this case, the creep strains are given a chance to relax, and the load time duration (Figure 22) is equal to the dive time. It should be pointed out that all undersea vehicles have emergency life support systems, additional load duration time should be provided in the design to preclude yield failure of the hull in the event that it must remain submerged awaiting rescue.

Following is an example to demonstrate how the operating-depth curves are used to find the safe operating depth. The following data are assumed:

Mission profile = three 2-hour dives

Turn-around time = 1 hour

Vehicle's emergency life support = 24 hours

Maximum ambient temperature = 70°F

Safety factor for yield = 1.5

Since the dive times are longer than the turn-around times (Figure 23a), the sum of the individual dives should be used to determine load duration time, T

$$T = 2(3) + 24 = 30 \text{ hours}$$

Utilizing 30 hours as the abscissa value in Figure 22, the following values for the ordinate are found:

Safe depth for acrylic plastic hull = 1,050 feet

Safe depth for steel penetrations = 1,000 feet

The lowest value, 1,000 feet, is selected as the safe operating depth for this example.

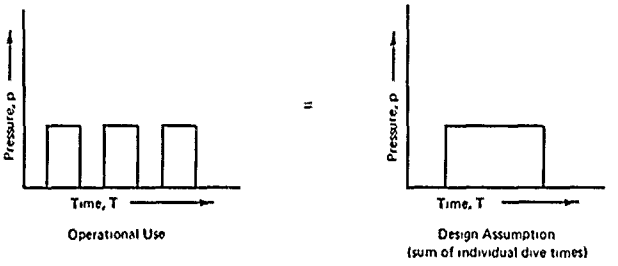

(a) Turn around time < Dive time

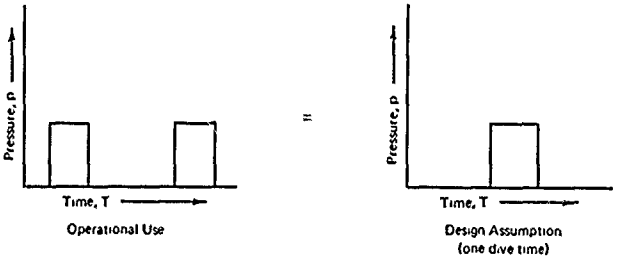

(b) Turn-around time ≥ Dive time

Figure 23. Determination of load duration time.

The number of dives taken during the life of the vehicle is another factor to be considered. As the vehicle dives repeatedly to the seafloor and returns to the surface, cyclic loads are imposed on the pressure hull. Two types of damage to the acrylic plastic pressure hull can result from repetitive dives: (1) localized yield failure of the material, or (2) localized crack failure due to pressure cycling. The former may result when cumulative strains in the viscoelastic material exceed the yield point, as was discussed in the previous section. While yield failure may also occur with high short-term static loads or long-term static loads, the localized crack failure is a function solely of the number of dive cycles and would not ordinarily occur with static loads.

Although there is the possibility of cycling damage in this hull as explained in the next few paragraphs, the authors believe that with proper operation the present hull design is easily capable of 1,000 cycles, and this would probably exceed the operating life of the vehicle. A full-scale hull of this design was cycled 815 times to 1,238 feet (550 psi) with *no* sign of crazing or cracks *anywhere*.[3] The test was run at 70°F with a 1-hour dwell period for both load-on and load-off conditions.

In the acrylic plastic sphere, the cycling damage appears as circumferential cracks at the acrylic plastic–steel interface.[3] This is expected as that is where stress analysis indicates the highest effective stresses were located. The cycling damage or material fatigue is a complicated process in this design because changes in the structure cause changes in the stress level in the acrylic plastic. The fatigue properties of acrylic plastic are discussed in Appendix A.

There are two unique factors to consider concerning fatigue effects on the acrylic plastic.

1. Shear forces that cause high tensile strains in the acrylic plastic at the acrylic plastic–steel bearing surfaces
2. High stress concentrations in the acrylic plastic caused by the O-ring groove in the steel

As mentioned previously, the normal force gradient across the thickness of the acrylic plastic gives rise to a frictional shear force. As seen in Figures 12 and 14, the fixed boundary condition would cause the highest gradient in the frictional shear force. The resulting imposed strains across the thickness, in conjunction with the already present Poisson strain due to compression of the hull will create high tensile strains in the acrylic plastic. For a static load, stress analysis has indicated such a combination will not cause failure, but the following possibility should be considered. As the load is applied and released, more and more lubricating grease is squeezed out. Thus, after X number of cycles, the acrylic plastic near the internal surface develops extremely high

local tensile strains and the acrylic crazes or cracks Thus the combination of a shear force gradient resulting from a fixed boundary condition, reduction of grease as cycling continues, and acrylic plastic's susceptibility to crazing and cracking under high tensile strains may cause cycling damage.

A similar situation occurs with the O-ring groove and, in fact, has occurred in experimental hull tests. That is, the O-ring groove located near a region of high stresses creates a discontinuity which results in even higher stresses. During the pressure cycles on the hull, acrylic plastic material may extrude into the O-ring groove thereby creating a tendency for the acrylic plastic to delaminate upon release of the pressure.

Regardless of the cause of the cycling damage, structural details exist in the present hull design that, if modified, would lessen the chances of failure as a function of the number of cycles. (See next section.) Periodic checks of the bearing surfaces of the acrylic plastic in the operational vehicle would disclose crazing or cracks. Minor crazing is not a dangerous condition if watched closely as it will not result in catastrophic failure.

Safety factors are a necessary adjunct to the design of undersea vehicles to compensate for such items as manufacturing imperfections, tolerances on material properties, tolerances on pressure-hull fabrication, and other unknowns. With the well-documented fabrication processes,[3] the reproducibility of acrylic plastic and 4130 steel material properties, and the excellent correlation between experimental and analytical results in this study, the authors recommend a safety factor of 1.5 based on yield. Besides the use of a factor in design to insure human safety, an unmanned proof test of the hull is also required. It is recommended that this hull design be proof-tested to 1,250 feet and a few strain gages be strategically placed to provide data for comparison with the data in this report and to insure linear behavior.

Recommended Design Changes

The stress analysis contained in this report provides information on the mechanical behavior of the 66-inch OD acrylic plastic pressure hull. Although this hull design is being used in a system operating to a depth of 600 feet, improvements in the design for future applications can be made, especially in the region of the acrylic plastic–steel interfaces.

Recommended design changes for the spherical acrylic plastic pressure hull are contained in Figure 24. The numbers in Figure 24 are keyed to the following paragraphs

1. *Decrease spherical radii of steel penetrations.* The large magnitude of bending in both the top hatch and bottom plate is due to the misalignment of the steel and acrylic plastic cross-section centerlines. This problem has

really not existed in the past because of the thin walls of the steel hulls, but as shown in this report, the alignment of centerlines is important because of the thickness of the acrylic plastic hull. Ideally the radius of the centerline of the steel should equal the radius for the center of pressure of the acrylic plastic hull. Solving for the radius of the center of pressure from the Lamé stress distribution across the wall:

$$\bar{r} = \frac{a^3 b\,[\ln(b/a)]}{b^3 - a^3} + \frac{2}{3} b \qquad (6)$$

where $\bar{r}$ = radius for center of pressure, in.

a = inside radius of sphere, in.

b = outside radius of sphere, in.

Substituting the appropriate values into Equation 6, the radius of the center of pressure, $\bar{r}$, is found to equal 31.4 inches or the centerline of the steel penetration should be located 36% of wall thickness from the inside surface of the acrylic plastic hull. This modification allows the flanges to function primarily as a transition zone for stresses and not for resistance to bending moments. Operationally, this design change might allow collection of water on the top hatch after a dive. Therefore, it is recommended that a light, nonmetallic filler material be placed in the trough to prevent water collection on the hatch.

2. *Increase fillet radii of steel penetrations.* As noticed in the stress analysis results, there were stress concentrations at the fillets on the top hatch and bottom plate. Although decreasing the spherical radii will eliminate some of the stress concentrations, material in the fillet areas should be increased and smoothly faired to a 1/2-inch radius.

3. *Decrease initial torque on retainer ring bolts.* As discussed previously, the initial torque determines whether the acrylic plastic–steel interface will approach a fixed-boundary or a free-boundary condition. Results of the stress analysis indicate that the free-boundary case is more desirable. Therefore, it is recommended that only enough torque be applied to the bolts to squeeze the O-ring for proper sealing. External pressure will keep the conical penetrations in place at depth. There will be no danger of pulling the steel penetrations out with the system integration method described in the next section. If another integration method is used, it may be necessary to place a higher torque on the retainer-ring bolts to insure a seal at the boundary.

4. *Locate O-ring grooves near external surface.* An O-ring seal is the best type for the acrylic plastic–steel interface because it can maintain a seal even with large relative movements of the conical surfaces. Figures 12 through 15 show that the stress concentrations in the acrylic plastic are highest near the internal surface, and thus unnecessarily high stresses will occur around a discontinuity in this region such as an O-ring groove. In fact, it is hypothesized that after long-term loading the acrylic plastic may extrude into the O-ring groove, and this ultimately may cause cracks in this region as the pressure is released. Two advantages would be gained by moving the O-ring groove out to within 1/2 inch of the external surface. (1) it would lower the stresses in the acrylic plastic around the O-ring groove, and (2) it would reduce contact between seawater and the steel surface. The O-ring's ability to seal is independent of its location on the faying surfaces. There need not be so much concern about the seal at the hatch–hatch ring interface because this surface is wiped and silicone grease is reapplied after each dive

5. *Decrease thickness of hatch ring.* The purpose of the hatch ring is to provide a hard sealing surface for the hatch flange, which should be about 1/2-inch thick. Because the stresses exhibited by the hatch ring are low (Figures 16 and 17), the ring thickness can be reduced to 1/2 inch with no adverse structural effects. Such a reduction results in two advantages (1) a lower stiffness in the steel (which should result in stresses in the acrylic plastic approaching those near the bottom plate) and (2) a reduction in the weight of the vehicle by about 25 pounds.

6. *Increase thickness of bottom plate flange and eliminate scallops.* Figures 18 and 19 indicate the presence of high stresses in the flange of the bottom plate. It is therefore necessary to increase the flange thickness (and thereby its stiffness) to about 1 inch to reduce the stresses. Elimination of the scallops is based solely on economic factors. They serve no useful purpose and require considerable more time and cost to machine.

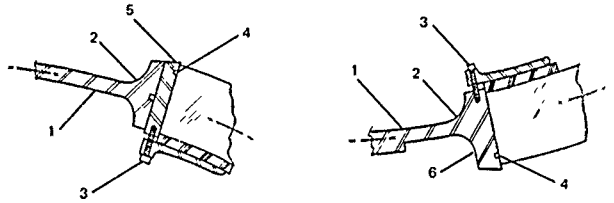

(a) Top hatch. (b) Bottom plate.

Figure 24. Recommended design changes for spherical acrylic pressure hull. (See text for explanation of keyed numbers)

Integration With Undersea Vehicle

To integrate the acrylic plastic pressure hull with an undersea vehicle hull requires attachment to either the steel penetrations or to the acrylic plastic hull. There are several potential problems.

1. With an attachment to the steel penetrations, a shock load either to the acrylic hull or to the rest of the system would transfer a great force across the O-ring seal. This could easily jar the faying surfaces apart momentarily and allow foreign material to enter the O-ring region. The probability of this event is much higher near the ocean surface, where the external pressure is lowest.

2. An event that might occur near the seafloor when the external pressure is highest is the transfer of high shock loads through an already highly stressed region. Such a shock load might overstress an area and result in plastic response.

3. Another problem is that at some point during the operation (that is, either in or out of the water) the hard attachment between the steel penetration and the rest of the system will result in a force that tends to pull the steel penetration out of the hull. Such a force creates tensile stresses in the acrylic plastic and requires higher torque on the retainer ring bolts than otherwise necessary.

Since possibilities for attachment to the steel penetrations are not encouraging, an investigation of attachment to the acrylic plastic hull is warranted. Direct attachment of an undersea vehicle to the acrylic plastic hull is not feasible because of the low strength of acrylic plastic and the possibility of high tensile stresses.

Figure 25 shows the recommended design for integration of the acrylic plastic pressure hull with an undersea vehicle. This concept provides the following advantages:

1. No effect on O-ring seal at acrylic plastic–steel interfaces
2. No transmission of shock loads through already highly stressed areas
3. No structural effects such as restraint on contraction of the hull
4. No induction of tensile stresses in the acrylic plastic hull either in or out of the sea

5. Only sufficient torque need be applied to the retainer-ring bolts to cause the O-ring to seal
6. Minimum infringement on the panoramic visibility
7. Protection of the hull from impact loads by the structural cage

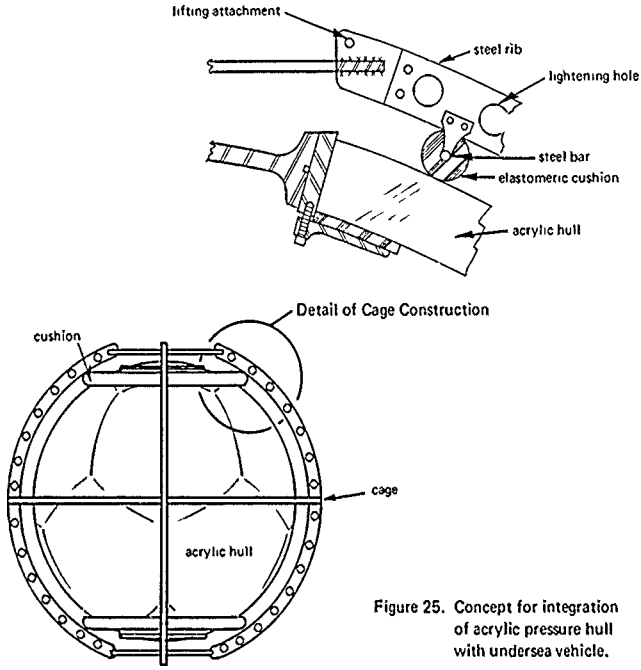

Figure 25. Concept for integration of acrylic pressure hull with undersea vehicle.

By placing the two cushioned rings around the acrylic plastic hull, all shock loads transmitted to and from the sphere are thus distributed and easily absorbed. The steel penetrations would be subject to only external pressure loads and not impact loads near the O-ring seal. The shock loads would be applied to the acrylic plastic hull in a region of equal biaxial stress or the region of lowest stress in the ball. The recommended design has optimum simplicity, so necessary for work in the ocean, and creates no unnecessary structural loads on the hull With this method of attachment, the acrylic

plastic hull rides free, like a ball in a check valve. When the system is lifted out of the water and is sitting on land, the hull sits against the lower cushion and is subject to compressive loading. Compressive loading also results when the vehicle is in the water with the buoyant hull pushing against the upper cushion. As the stress analysis indicated, it is desirable to maintain a free boundary condition at the steel–acrylic plastic interface. The concept in Figure 25 does just that. By eliminating attachment of the undersea vehicle to the steel penetrations of the acrylic plastic sphere, the retainer-ring bolts need be torqued only enough to form a seal with the O-ring. Because there will be some movement between the sphere and the rest of the system with this method, flexible hydraulic lines and electrical cables should be used in conjunction with the design.

Locating the cushions about 30 degrees from the vertical centerline (Figure 25) not only places them in a low-stressed area but also creates minimum interference with the panoramic visibility.

ACKNOWLEDGMENT

The strain gage tests and subsequent data reduction at NCEL were performed by the NCEL Deep Ocean Simulation Laboratory staff and Mr. Kit Mack of NCEL, respectively. Mr. Ed Briggs of the Southwest Research Institute (SWRI) and the SWRI Underwater Engineering Laboratory staff performed the strain gage tests at SWRI.

Appendix A

MATERIAL PROPERTIES OF ACRYLIC PLASTIC

INTRODUCTION

Design of a structure can be subdivided into two categories, structure and material. The finite element method provided the structural analysis, while this appendix provides the necessary information on material properties of the acrylic plastic. Additional information is provided on operational use of acrylic plastic as a structural material.

GENERAL PROPERTIES

One of the primary advantages of using acrylic plastic as a structural material is that its low modulus of elasticity and plastic flow characteristics permit localized yielding and thus a redistribution of stresses. This is extremely important because of the interfaces with other materials such as in the NEMO concept. Acrylic plastic, unlike glass, flows plastically and cracks before failing catastrophically, thus providing a measure of safety in addition to the safety factor based on the yield failure criterion. Reproducibility of physical properties from one commercial sheet of acrylic plastic to another is excellent.

Time and Temperature Dependence

As with all thermoplastics, the material properties of acrylic plastic are extremely time and temperature dependent. Because of this time dependence, yield stress values as a function of time are necessary for calculation of an operating-depth curve. Figure A-1 presents tensile and compressive yield-stress-versus-time curves. Origin of these curves is covered in detail in Reference 7, but a cursory review is presented here.

Creep data were first obtained from several sources.[8, 15-17] The strain–time curves were then transformed into a family of isochronous stress–strain curves from which yield stress values were determined and plotted in Figure A-1.

The general dependence of acrylic plastic on temperature is shown in Figure A-2, in which the properties are shown to have a linear inverse relationship with temperature. The variation of collapse depth of model acrylic plastic hulls with temperature is clearly shown as curve B. Figure A-2 was used to generate the temperature dependence data in Figure 22

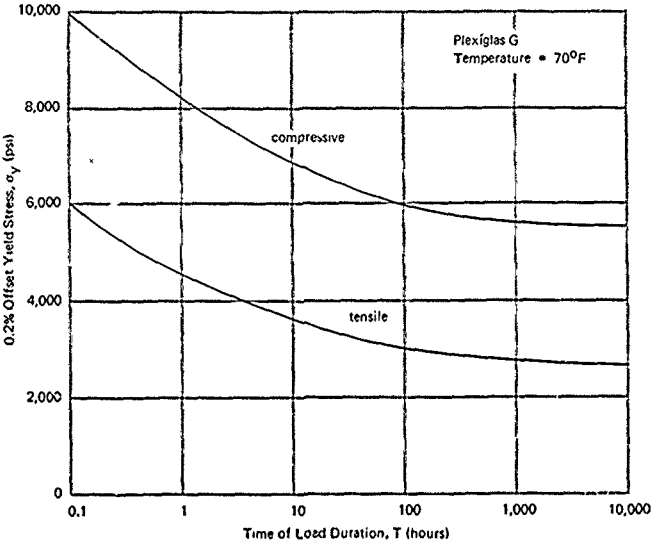

Figure A-1. Yield stress–time curves for acrylic plastic.

Fatigue

Some fatigue data were available for acrylic plastic, but they were by no means extensive.[16,18] It was found that acrylic plastic had a well-defined S-N curve, just as many well-researched metals, with a knee at 10,000 cycles and 6,500 psi. The material also exhibited a fatigue limit or a stress below which fracture by fatigue would not occur even after an infinite number of cycles. The fatigue strength was a function of both the frequency and the number of cycles. The frequency of cycles was shown to have an inverse relationship with the fatigue strength, although it is believed this was partially because of the heat buildup within the test sample as a result of its low thermal conductivity. Attempts have been made to reduce heating during the tests by using blowers, but the degree of success is not known.

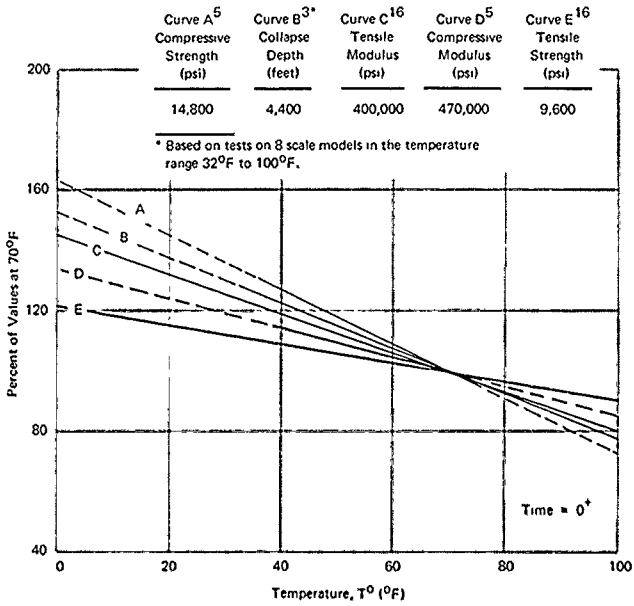

Figure A-2. Properties of acrylic plastic (Plexiglas G) as a function of temperature.

For comparison with these data,[16, 18] the cycling conditions for the acrylic plastic hull are

Frequency ≈ 1 cycle/hour

Number of cycles (dives) = 1,000

Maximum effective stress* at 1,000-foot depth = 4,050 psi

No exact correlation is possible between data from uniaxial fatigue curves and those for spherical acrylic plastic hulls because the acrylic plastic is in either biaxial or triaxial stress states when used in such hulls. Although because of the lack of experimental data it is difficult to do a quantitative fatigue analysis, a qualitative judgment is possible. Since the acrylic plastic

* Although the true relationship between uniaxial and multiaxial fatigue for most materials is unknown, Professor W. N. Findley of Brown University has had some success in correlating the two types of fatigue data for aluminum and 4340 steel.

hull has such an extremely low stress application frequency, low number of cycles, and a low stress level (after incorporation of the design recommendations), fatigue does not appear to be a factor in calculating cycling loads. (See "Operating-Depth Curve" in the "Design Recommendations" section of the main report for further discussion.)

Impact Strength

Impact strength of a pressure hull is important because of the possibility of collision with another object resulting in damage to the hull and possible injury to its occupants. Figure A-3 shows the impact strength of acrylic plastic as a function of temperature. Although its strength is considerably lower than that for metals, acrylic plastic does not exhibit any nil-ductility temperature as many metals do. Caution is required when comparing impact strengths of acrylic plastic and metals, however, because the plastic is amorphous whereas metals have a crystalline structure.

No impact test data were available for the acrylic plastic pressure hull, but two sources were found that provided background information for impact tests on the external faces of acrylic viewports. Results in Reference 19 from tests in a room-temperature, one-atmosphere environment indicate that viewport impact strength was a function of the kinetic energy of the projectile.

Reference 20 reports tests to determine impact strengths of viewports by varying both the hydrostatic pressure and temperature. Five spherical attachments were available for varying the sharpness (radius) of the impacting projectile. These results indicated that viewport strength was a function of the kinetic energy of the projectile and its nose shape. As the radius of the projectile increased, the impact strength of the viewport increased. Just as shown in Figure A-3, the critical impact strength of the viewports was found to be independent of the ambient temperature. The most important aspect of the tests, however, concerned comparison of the test results for viewports under pressure and those under no load. By placing the viewport under load and thus placing the impacted surface in a triaxial stress state, the effects of impact were reduced for a given projectile shape. This is a significant result because the external surface of a spherical acrylic plastic hull is in a similar stress state.

Nevertheless, the impact strength of acrylic plastic is low and therefore must be compensated by design innovations. A structural cage as in Figure 25 would afford some protection for impact loads. Another possible solution would be a free-flooding transparent shield made of polycarbonate plastic. It has an impact strength an order of magnitude higher than acrylic plastic and would not interfere with visibility in the free-flooded state.

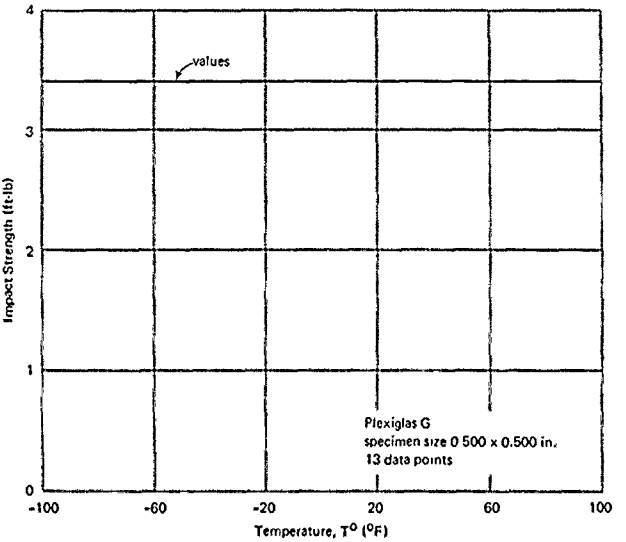

Figure A-3. Impact strength–temperature curve for acrylic plastic.[16]

Degradation

To insure safety of the acrylic plastic null system and its occupants, it is important to know how the properties of acrylic plastic are affected by long-term weathering and exposure to seawater.

Weathering. The Navy has performed tests to determine the effects of outdoor weather aging of acrylic plastic under various climatogical conditions.[21,22] The five locations selected were. (1) Panama Canal Zone (tropical), (2) New Mexico (dry desert), (3) New York (temperate), (4) Fort Churchill, Canada (subarctic); and (5) Point Barrow, Alaska (arctic). In these widely varying climates, extreme conditions of temperature, moisture, wind, sun, and other meteorological factors were present.

The specimens were mounted on rocks at a 45-degree angle of inclination, facing due south, for exposure periods from 1 to 36 months. The standard ASTM tests for tensile strength, tensile modulus, flexural strength, light transmission, and haze were performed. After 3 years' exposure, material properties at all locations had decreased slightly.

There was also slight yellowing of the acrylic at the New Mexico location from strong ultraviolet irradiation. The effects were so minimal, however, that no serious impairment of serviceability of the material occurred.

Seawater. Although an acrylic plastic hull may never be in the ocean as much as it is out, it still is necessary to determine the effects of ocean environment on acrylic plastic. There are many properties of the ocean involved: salinity, temperature, pressure, pH level, currents, and marine organisms. Two separate tests have been reported. one at 2,300 feet for 195 days and one at 6,780 feet for 403 days.[23,24] Both tests were in the Pacific Ocean. Mechanical tests included: flexural strength, modulus of elasticity, tensile strength, and compressive strength. Both relaxed and stressed coupons were exposed to the ocean environment. The test results were somewhat erratic with both increases and decreases of property values within about ±10%, thus generally indicating no severe deleterious effects.

Operations

The use of acrylic plastic for submersible hulls does necessitate a few new operational requirements, but if the properties and limitations of the material are properly understood no trepidations should exist. Acrylic plastic is extremely susceptible to scratching and cracking unless precautions are taken. These scratches interfere with visibility, but those on the external surface disappear when the hull is submerged. Thus care must be taken to not scratch the internal surface with feet or equipment. The acrylic plastic should not be wiped with a dry rag, but rather with soapy water. Care should also be taken in the selection of a solvent for additional cleaning. Carbon tetrachloride or acetone should not be used, isopropyl alcohol or kerosene is recommended.

Greases used around O-ring seals should not be a petroleum derivative, but rather a silicone type. The silicone grease at the acrylic plastic–steel boundary must be periodically replenished to maintain the free boundary condition.

The acrylic plastic hull should be periodically visually inspected to check for stress crazing cracks at the regions of highest effective stress. For a 1,000-cycle lifetime, the acrylic plastic–steel bearing surfaces should be checked every 100 dives.

Appendix B

EXPERIMENTAL TEST PROGRAM

INTRODUCTION

To provide validity for the analytical results, two independent tests on full-scale (66-inch OD) spherical acrylic plastic hulls were run with strain gage instrumentation. One test was run at NCEL and is documented in Reference 3, while the other one was run at SWRI with the results appearing in this report. Figure B-1 shows the instrumented acrylic plastic hull being lowered into the 90-inch-diameter pressure vessel at SWRI rated at 4,000-psi.

Table B-1 summarizes the pertinent facts for the two experimental tests on the acrylic plastic hull. The acrylic plastic was cleaned with 99% isopropyl alcohol, wiped, and air dried. The gages were mounted using standard procedures in the locations indicated by the data points in Figures 7 through 10. Removal of the gages after the tests consisted of pulling off the larger pieces of gage, waterproofing, and terminal strip, after which an abrasive agent (jeweler's rouge) was used to rub off the remains of the adhesive. Light buffing completed the cleanup job.

DISCUSSION

In instrumentation of the acrylic plastic hull with strain gages there were four possible problem areas.

1. Heat dissipation
2. Creep of acrylic plastic
3. Waterproofing
4. High-pressure environment

Since thermal conductivity is low in acrylic plastic, special precautions must be taken to insure dissipation of heat from the strain gage. Heat buildup would cause zero drift in the gage readings and might change the material properties of acrylic. This problem was solved by using (1) foil strain gages instead of wire strain gages, (2) a low excitation voltage, and (3) high-resistance strain gages. Both the Datron and Gilmore strain recording units cycle through the channels so there are short-time voltage applications to the gages at each location. Figure B-2 shows the experimental setup at NCEL with the acrylic plastic hull in the pressure vessel undergoing tests.

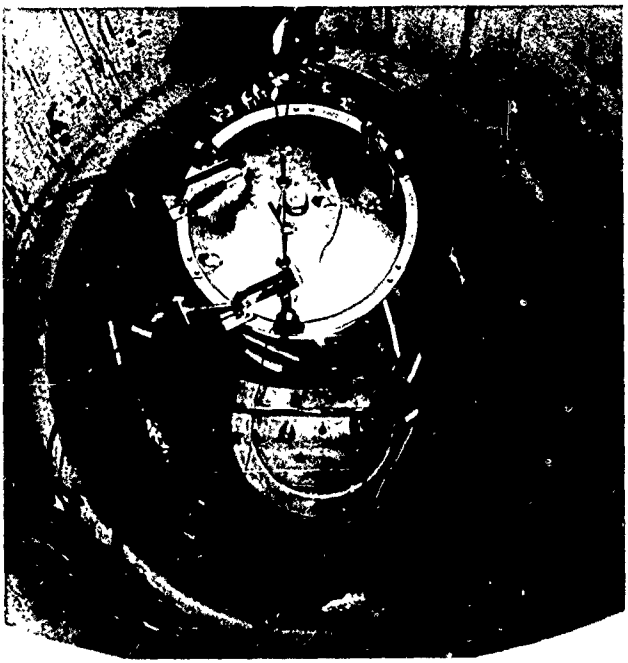

Figure B-1. Instrumented acrylic pressure hull undergoing test at SWRI.

To eliminate the effects of creep on the strain readout, the tests were performed at a rate of 100 psi/min with only short pauses at each 50 psi increment to record the data.

An agent was required that would stick to the acrylic plastic, waterproof the strain gages, and yet have no deleterious effect on the acrylic plastic. The Gagekote series of waterproofing agents was suitable.

As discussed in Reference 6, the maximum magnitude of apparent strain due to hydrostatic pressure and measured by a foil strain gage is 5.5 μin./in. per 1,000 psi. The lowest strain recorded in this study was 100 μin./in. at 500 psi. Using the value of 5.5 μin./in. per 1,000 psi, the maximum error due to the hydrostatic effect on the strain gages was only 2.8%. Flat as opposed to stacked rosettes were used to insure no additional induced errors in measurement due to hydrostatic pressure.

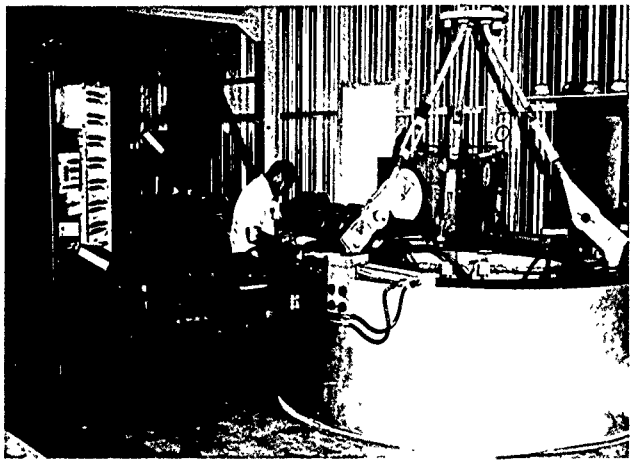

Figure B-2. Experimental test setup at NCEL.

Table B-1. Gage Instrumentation for Pressure Vessel Tests of 66-Inch OD Acrylic Plastic Hull

Item	NCEL Test[3]	SWRI Test
Number of rosettes	24 (no redundant rosettes)	14 (5 redundant rosettes)
Strain gages	BLH FAER-50D-12S13	MM EA 50-125AC-350
Rosette type	three-gage, 60° delta	two-gage, 90° rectangular
Strain gage	foil, epoxy backed	foil, epoxy backed
Gage resistance	120 ohms	350 ohms
Gage length	1/2 inch	1/8 inch
Gage factor	2.04	2.14
Cement	Epy-150	Eastman 910
Waterproofing	Gagekote #2 Gagekote #5	Gagekote #1 Gagekote #2 Gagekote #5
Temperature compensation	half bridge with dummy gage	half bridge with dummy gage
Strain recorder	Budd Datran	Gilmore
Excitation voltage	4.2	6
Pressure medium	seawater	tap water

Appendix C

FINITE ELEMENT ANALYSIS

COMPUTER PROGRAM

The finite element method is now so well documented in many papers and in the book by Zienkiewicz and Cheung[25] that little need be said here about the formulation of finite elements. Instead, the emphasis will be on application and special features of the program used in this investigation.

In general, the Wilson program[4] is applied to determine stresses and displacements in solids of revolution of arbitrary geometry and composition. Loadings must be axisymmetric and can be thermal or mechanical. The material formulation includes elastic response with a bilinear option and anisotropic material properties. The applicability of infinitesimal strain and small displacement theory is assumed. The structure is approximated by triangular elements with six degrees of freedom or quadrilateral elements with ten degrees of freedom of which two are precipitated out prior to formation of the total stiffness matrix. There are no global structural assumptions other than the axisymmetric assumption of no tangential displacements. From variational theorems, it can be shown that the finite element technique approaches the exact solution as the element density increases. Thus experience and sound engineering judgment are required for effective mesh configuration—specifically, the placement of fine mesh in areas of suspected high stresses, as shown in Figure C-1.

IDEALIZATION OF ACRYLIC PLASTIC—STEEL INTERFACE

The general capability of analyzing structural boundaries that transmit only normal forces across a common interface of arbitrary orientation was programmed and incorporated by the authors into the Wilson finite element program. The scope of this routine allows the consideration of generalized plane stress and plane strain as well as axisymmetric structures. The defined interface is completely arbitrary in that any piecewise continuous or discontinuous curve may be assumed. Moreover, the interface may be assumed to be either fixed (that is, to be a continuum) or free, thus, mesh numbering and configuration remain exactly the same so that comparisons of fixed versus free solutions were not confounded with mesh variations. In addition, the program was coded to allow for ease of future inclusion of iterative procedures such as friction response and tensile cracking.

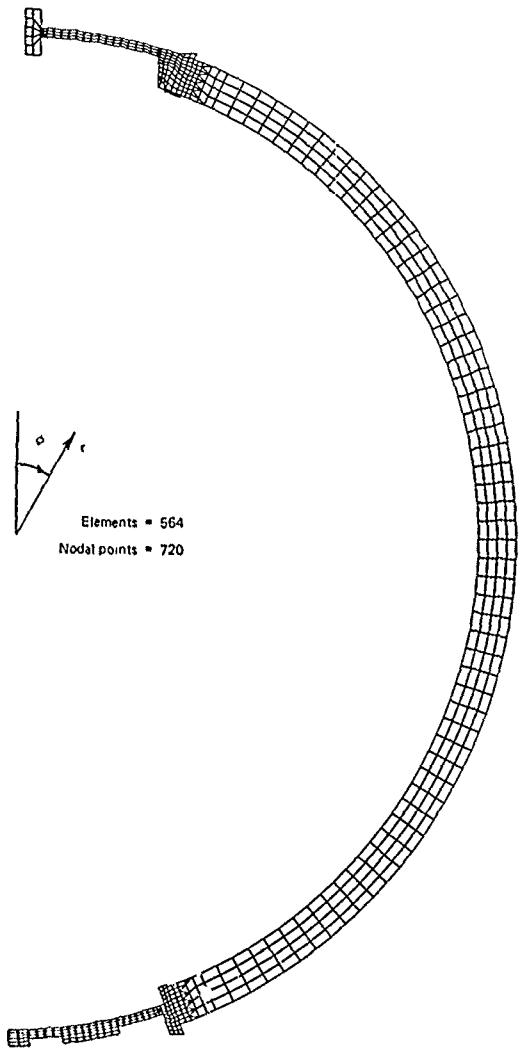

Figure C-1. Finite element mesh for acrylic plastic spherical pressure hull analysis.

The formulation and solution technique is carried out at the stiffness matrix level rather than at the element level. The method resolves to considering a pattern of nodal points along a common interface between two structural members. At each nodal coordinate location on the interface, two nodes are so specified and defined that one node belongs to one member and the second belongs to the other member. Thus at the outset, each node pair is completely uncoupled and represents four degrees of freedom, two for each node. In order to represent a free-slipping boundary, the four degrees of freedom are selectively reduced to three degrees of freedom as follows. First, the corresponding stiffness relations for each node pair are transformed to the local coordinate system defined by the normal and tangent directions of the interface at the particular point. Next, by demanding equilibrium and continuity in the normal direction, the stiffness row and column of each redundant degree of freedom are added to the row and column of the governing degree of freedom. Rather than shrink the stiffness matrix by one for each node pair, a dummy identity relation is inserted in place of the redundant degree of freedom. After the equation has been solved for the displacements, the interface displacements are transformed back into global coordinates.

For the case in which a continuum or fixed solution is desired from the same mesh configuration, the original four degrees of freedom of the interface node pairs are reduced to two degrees of freedom by demanding equilibrium and continuity for any two orthogonal directions. This is done by simply adding corresponding stiffness relations of the redundant node to the governing node and filling in the stiffness matrix with dummy identity relations.

The additional input data required to make use of these interface capabilities is a trivial matter. A user need only specify the number of nodal pairs, the node numbers defining each pair, the interface angle of each pair, and a code number indicating whether the nodes are fixed or free.

REFERENCES

1. M. R. Snoey and J. D. Stachiw. "Windows and transparent hulls for man in hydrospace," in a critical look at marine technology, transactions of the 4th Annual MTS Conference and Exhibit, Washington, D. C., July 8-10, 1968. Washington, D. C., Marine Technology Society, 1968, pp. 419-463.

2. A. Piccard. Earth, sky and sea. New York, Oxford University Press, 1956.

3. Naval Civil Engineering Laboratory. Technical Report R-676: The development of the spherical acrylic pressure hull for hydrospace application, by J. D. Stachiw. Port Hueneme, Calif., Apr. 1970.

4. E. L. Wilson. "Structural analysis of axisymmetric solids," American Institute of Aeronautics and Astronautics, Journal, vol. 3, no. 12, Dec. 1965, pp. 2269-2274.

5. Naval Ship Research and Development Center. Technical Report 2944 Evaluation of full-scale DSRV-1 acrylic windows under external pressure, by M. A. Krenzke, M. C. Breiter, and L. N. Gifford. Washington, D. C., Jan. 1969. (AD 849354)

6. Naval Civil Engineering Laboratory. Technical Report R-675: Stress analysis of a conical acrylic viewport, by M. R. Snoey and J. E. Crawford. Port Hueneme, Calif., Apr. 1970.

7.————. Technical Report R-686 Structural design of conical acrylic viewports, by M. R. Snoey and M. G. Katona. Port Hueneme, Calif., June 1970.

8. Southwest Research Institute. Final Report on Contract N00123-67-C-2123: NEMO stress analysis and material investigation, by R. C. DeHart, T. Wah, and L. R. Calcote. San Antonio, Tex., Mar. 1968.

9. Naval Civil Engineering Laboratory. Technical Note N-1094. The spherical acrylic pressure hull for hydrospace application, pt. III. Comparison of experimental and analytical stress evaluations for prototype NEMO capsule, by H. Ottsen. Port Hueneme, Calif., Mar. 1970.

10. A. Nadai. Theory of flow and fracture of solids, vol. 1. New York, McGraw-Hill, 1950.

11. General Electric Company. Advanced Technology Laboratories. Report No. 61GL181. The effects of biaxial stresses on the deformation and fracture of polymethylmethacrylate, by R. L. Thorkildsen and W. V. Olszewski. Schenectady, N. Y., Apr. 1962.

12. Army Missile Command. Physical Sciences Laboratory. Report No. RR-TR-64-15. Combined stress properties for acrylic tube specimens, by R. E. Ely. Redstone Arsenal, Ala., Aug. 1964. (AD 450662)

13. S. P. Timoshenko and J. N. Goodier. Theory of elasticity, 2nd ed. New York, McGraw-Hill, 1951.

14. S. P. Timoshenko and J. M. Gere. Theory of elastic stability, 2nd ed. New York, McGraw-Hill, 1961.

15. J. Marin and Y. Pao. "On the accuracy of extrapolated creep-test relations for plexiglas subjected to various stresses," American Society of Mechanical Engineers, Transactions, Oct. 1952, pp. 1231-1240.

16. Rohm and Haas Company. PLEXIGLAS handbook for aircraft engineers, 2nd ed., Philadelphia, Pa., 1952.

17. Armed Forces Supply Support Center. Military Handbook MIL-HDBK-17. Plastics for flight vehicles, pt. 2. Transparent glazing materials. Washington, D. C., Aug. 1961.

18. J. M. Zarek. "Accelerated fatigue testing of poly (methyl methacrylate)," British Plastics, vol. 30, 1957, pp. 399-402, 421.

19. Allied Research Associated, Inc. Technical Report ARA 350-3: Tests of acrylic deep submergence windows under simulated operational conditions, by R. Winter and J. Pozerycki. Concord, Mass., Sept., 1968. (Contract no. N00024-67-C-5351) (AD 848287)

20. F. M. Schwartz. "The structural performance of acrylic viewports for deep submersibles," in the decade ahead, 1970-1980; transactions of the 5th Annual MTS Conference & Exhibit, Miami, Florida, June 16-18, 1969. Washington, D. C., Marine Technology Society, 1969, pp. 557-622.

21. S. E. Yustein, R. R. Wihans, and H. J. Stark. "Outdoor weather aging of plastics under various climatological conditions," American Society for Testing Materials, Bulletin 173, Apr. 1951, pp. 31-43.

22.———. "Three years' outdoor weather aging of plastics under various climatological conditions," American Society for Testing Materials, Bulletin 196, Feb., 1954, pp. 29-39.

23. Naval Air Engineering Center. Aeronautical Materials Laboratory. Report No. NAEC-AML-2260, pt. A: Oceanographic effects on plastic engineering materials and elastomeric materials, by H. J. Lee. Philadelphia, Pa., Jan. 1966. (AD 481377)

24. ———. Report No. NAEC-AMNL-2350: Oceanographic effects on plastic engineering materials, by H. J. Lee. Philadelphia, Pa., Jan. 1966. (AD 481419)

25. O. C. Zienkiewicz and T. Cheung. The finite element method in structural and continuum mechanics. New York, McGraw-Hill, 1967.

LIST OF SYMBOLS

a	Inside radius of sphere, in.
b	Outside radius of sphere, in.
d	Operational depth, ft
E	Modulus of elasticity, psi
p	Pressure applied to sphere, psi
p_{cr}	Critical collapse pressure, psi
r	Radial coordinate, in.
$\bar{r}$	Radius for center of pressure, in.
SF	Safety factor
T	Time, hours
T^{O}	Temperature, ^{O}F
t	Wall thickness of sphere, in.
δ_r	Radial displacement of sphere, in./psi
θ	Angle of revolution, deg
ν	Poisson's ratio
$\sigma_1, \sigma_2, \sigma_3$	Principal stresses per unit of applied pressure, psi/psi
σ_o	Effective stress per unit of applied pressure, psi/psi
σ_y	Yield stress, psi
$\sigma_\theta, \sigma_\phi$	Hoop and meridional stresses per unit of applied pressure, psi/psi
ϕ	Meridional coordinate, deg

Naval Civil Engineering Laboratory
STRUCTURAL ANALYSIS OF A FULL-SCALE SPHERICAL ACRYLIC PLASTIC PRESSURE HULL (Final), by M. R. Snoey and M. G. Katona

TR-716 57 p. illus March 1971 Unclassified

1. Acrylic pressure hull—Structural analysis I. YF 38.535.005 01.006

This study was initiated to: (1) perform a finite element structural analysis on an acrylic plastic pressure hull, (2) compare the finite element results with available experimental results, and (3) present an operating-depth curve and make recommendations for future designs. The design analyzed was a pressure hull incorporating 12 spherical pentagons of acrylic plastic bonded together to form a sphere with an outside diameter of 66 inches and a wall thickness of 2.5 inches. Steel penetrations were located at the two poles. The experimental results were obtained from strain gage data from two independent pressure tests to 500 psi on two acrylic plastic hulls of the same design.

The finite element analysis of the hull structure placed particular emphasis on the acrylic plastic–steel boundary. The boundary conditions at the acrylic plastic–steel interface were two extreme cases: fixed and free. A time-dependent yield–failure criterion for acrylic plastic was combined with the structural analysis to provide an operating depth curve as a function of both time and temperature. Comparison of the finite element and experimental results indicated excellent agreement. At a temperature of 70°F and a maximum of 50 hours' load duration, the acrylic plastic hull can operate to 1,000 feet with a safety factor of 1.5 based on yield and a safety factor of 2.6 based on collapse.

Naval Civil Engineering Laboratory
STRUCTURAL ANALYSIS OF A FULL-SCALE SPHERICAL ACRYLIC PLASTIC PRESSURE HULL (Final), by M. R. Snoey and M. G. Katona

TR-716 57 p. illus March 1971 Unclassified

1. Acrylic pressure hull—Structural analysis I. YF 38.535 005 01.006

This study was initiated to: (1) perform a finite element structural analysis on an acrylic plastic pressure hull, (2) compare the finite element results with available experimental results, and (3) present an operating-depth curve and make recommendations for future designs. The design analyzed was a pressure hull incorporating 12 spherical pentagons of acrylic plastic bonded together to form a sphere with an outside diameter of 66 inches and a wall thickness of 2.5 inches. Steel penetrations were located at the two poles The experimental results were obtained from strain gage data from two independent pressure tests to 500 psi on two acrylic plastic hulls of the same design.

The finite element analysis of the hull structure placed particular emphasis on the acrylic plastic–steel boundary. The boundary conditions at the acrylic plastic–steel interface were two extreme cases. fixed and free. A time-dependent yield–failure criterion for acrylic plastic was combined with the structural analysis to provide an operating depth curve as a function of both time and temperature. Comparison of the finite element and experimental results indicated excellent agreement. At a temperature of 70°F and a maximum of 50 hours' load duration, the acrylic plastic hull can operate to 1,000 feet with a safety factor of 1.5 based on yield and a safety factor of 2.6 based on collapse.

Naval Civil Engineering Laboratory
STRUCTURAL ANALYSIS OF A FULL-SCALE SPHERICAL ACRYLIC PLASTIC PRESSURE HULL (Final), by M. R. Snoey and M. G. Katona

TR-716 57 p. illus March 1971 Unclassified

1. Acrylic pressure hull—Structural analysis I. YF 38 535 005 01.006

This study was initiated to: (1) perform a finite element structural analysis on an acrylic plastic pressure hull, (2) compare the finite element results with available experimental results, and (3) present an operating-depth curve and make recommendations for future designs. The design analyzed was a pressure hull incorporating 12 spherical pentagons of acrylic plastic bonded together to form a sphere with an outside diameter of 66 inches and a wall thickness of 2.5 inches. Steel penetrations were located at the two poles. The experimental results were obtained from strain gage data from two independent pressure tests to 500 psi on two acrylic plastic hulls of the same design.

The finite element analysis of the hull structure placed particular emphasis on the acrylic plastic–steel boundary. The boundary conditions at the acrylic plastic–steel interface were two extreme cases: fixed and free. A time-dependent yield–failure criterion for acrylic plastic was combined with the structural analysis to provide an operating depth curve as a function of both time and temperature. Comparison of the finite element and experimental results indicated excellent agreement. At a temperature of 70°F and a maximum of 50 hours' load duration, the acrylic plastic hull can operate to 1,000 feet with a safety factor of 1.5 based on yield and a safety factor of 2.6 based on collapse.

Naval Civil Engineering Laboratory
STRUCTURAL ANALYSIS OF A FULL-SCALE SPHERICAL ACRYLIC PLASTIC PRESSURE HULL (Final), by M. R. Snoey and M. G. Katona

TR-716 57 p. illus March 1971 Unclassified

1. Acrylic pressure hull—Structural analysis I. YF 38 535 005 01.006

This study was initiated to: (1) perform a finite element structural analysis on an acrylic plastic pressure hull, (2) compare the finite element results with available experimental results, and (3) present an operating-depth curve and make recommendations for future designs. The design analyzed was a pressure hull incorporating 12 spherical pentagons of acrylic plastic bonded together to form a sphere with an outside diameter of 66 inches and a wall thickness of 2.5 inches. Steel penetrations were located at the two poles. The experimental results were obtained from strain gage data from two independent pressure tests to 500 psi on two acrylic plastic hulls of the same design.

The finite element analysis of the hull structure placed particular emphasis on the acrylic plastic–steel boundary. The boundary conditions at the acrylic plastic–steel interface were two extreme cases: fixed and free. A time-dependent yield–failure criterion for acrylic plastic was combined with the structural analysis to provide an operating depth curve as a function of both time and temperature. Comparison of the finite element and experimental results indicated excellent agreement. At a temperature of 70°F and a maximum of 50 hours' load duration, the acrylic plastic hull can operate to 1,000 feet with a safety factor of 1.5 based on yield and a safety factor of 2.6 based on collapse.

Unclassified

Security Classification

DOCUMENT CONTROL DATA - R & D

(Security classification of title, body of abstract and indexing annotation must be entered when the overall report is classified)

1. ORIGINATING ACTIVITY (Corporate author)	2a. REPORT SECURITY CLASSIFICATION
Naval Civil Engineering Laboratory Port Hueneme, California 93043	Unclassified
	2b. GROUP

3. REPORT TITLE

STRUCTURAL ANALYSIS OF A FULL-SCALE SPHERICAL ACRYLIC PLASTIC PRESSURE HULL

4. DESCRIPTIVE NOTES (Type of report and inclusive dates)

Final; July 1969—June 1970

5. AUTHOR(S) (First name, middle initial, last name)

M. R. Snoey and M. G. Katona

6. REPORT DATE	7a. TOTAL NO. OF PAGES	7b. NO. OF REFS
March 1971	57	25

8a. CONTRACT OR GRANT NO.	9a. ORIGINATOR'S REPORT NUMBER(S)
b. PROJECT NO YF 38.535.005.01.006	TR-716
c.	9b. OTHER REPORT NO(S) (Any other numbers that may be assigned this report)
d.	

10. DISTRIBUTION STATEMENT

Distribution limited to U. S. Government agencies only; Test and Evaluation; March 1971. Other requests for this document must be referred to the Naval Civil Engineering Laboratory.

11. SUPPLEMENTARY NOTES	12. SPONSORING MILITARY ACTIVITY
	Naval Facilities Engineering Command Washington, D. C. 20390

13. ABSTRACT

This study was initiated to: (1) perform a finite element structural analysis on an acrylic plastic pressure hull, (2) compare the finite element results with available experimental results, and (3) present an operating-depth curve and make recommendations for future designs. The design analyzed was a pressure hull incorporating 12 spherical pentagons of acrylic plastic bonded together to form a sphere with an outside diameter of 66 inches and a wall thickness of 2.5 inches. Steel penetrations were located at the two poles. The experimental results were obtained from strain gage data from two independent pressure tests to 500 psi on two acrylic plastic hulls of the same design.

The finite element analysis of the hull structure placed particular emphasis on the acrylic plastic—steel boundary. The boundary conditions at the acrylic plastic—steel interface were two extreme cases: fixed and free. A time dependent yield—failure criterion for acrylic plastic was combined with the structural analysis to provide an operating depth curve as a function of both time and temperature. Comparison of the finite element and experimental results indicated excellent agreement. At a temperature of 70°F and a maximum of 50 hours' load duration, the acrylic plastic hull can operate to 1,000 feet with a safety factor of 1.5 based on yield and a safety factor of 2.6 based on collapse. Design recommendations are also presented to provide guidelines for future design of the hull and its integration with an undersea vehicle.

DD FORM 1 NOV 65 1473 (PAGE 1)

S/N 0101-807-6801

Unclassified

Security Classification

Unclassified
Security Classification

14 KEY WORDS	LINK A		LINK B		LINK C	
	ROLE	WT	ROLE	WT	ROLE	WT
NEMO						
THS (Transparent hull submersible)						
Acrylic plastic						
Plexiglas						
Undersea vehicles						
Design curves						
Habitats						
Viscoelastic						
Submersibles						
Finite element						
Deep submergence						
Stress analysis						
Yield failure criterion						
Spheres						
Elastic contact						
Penetrations						
Pressure hulls						

DD FORM 1 NOV 68 1473 (BACK)
(PAGE 2)

Unclassified
Security Classification